The University of Nottingham

UNITED KINGDOM · CHINA · MALAYSIA

Punching Shear in Waffle Slabs

In the Presence of Biaxial Moment Transfer

Dickson Wen Jing FONG

A thesis regarding the punching shear failure in waffle slabs in the presence of biaxial moment transfer is submitted to the University of Nottingham in part of consideration of the degree of Doctor of Philosophy on the September 2017.

Abstract

An extensive amount of works have been carried out to develop the current understanding in punching shear mechanism noted in reinforced concrete slabs. However, despite the increasing popularity of waffle slabs, the current understanding about punching behaviour is mainly focused on solid flat slabs, and only limited amount of works have been carried out on waffle slabs and in the presence of biaxial moment. Thus, there is a need to carry out a research in this area to aid the understanding about punching mechanism of waffle slabs in the presence of biaxial moment for the internal column and edge column connections.

The experimental work carried out in this research included destructive testing of thirty-eight 1/10th scale model waffle slab specimens, which consists of fifteen internal column slabs and twenty-three edge column slabs. The main variables were, for the internal column slab, the principle angles of biaxial moment transfer, the column eccentricity, the column orientation and the size of solid sections, and for the edge column slab, the principle angles of biaxial moment transfer, the column eccentricity, the column location and the size of solid sections.

From the experimental investigations, three distinct failure mechanisms were observed: the concentric punching at internal column mechanism; the eccentric punching at internal column mechanism; and the edge punching mechanism. In general, the observed punching shear failure mechanisms of waffle slabs were found identical to solid flat slabs; but the punching shear capacities reduced due to some losses in potential failure surface within the waffle section. The principle angle of biaxial moment transfer was found varying the shear surface area that was being mobilized, thus affecting the punching capacity of the slabs.

An analytical study was carried out, using an upper-bound plastic model, to simulate the observed punching shear mechanisms, and hence, to predict the punching capacity of the slabs. A theoretical model was developed for each of the identified failure mechanism. In addition, three design models based on the current UK code, Eurocode 2, have been developed. In all cases, these models have achieved good agreements with the test results.

Acknowledgements

I would like to express my sincere gratitude to my supervisor, Dr. Lau Teck Leong for his continuous guidance, untiring advices, encouragement and interest in the work. The present work would not be possible without his patience and support throughout the research and during the preparation of this thesis.

I would like to thank the University of Nottingham Malaysia Campus for the scholarship awarded and the Department of Civil Engineering for the financial support to this project, which gave me the opportunity to undertake this research.

Thanks are extended to the technical staffs of the Civil Engineering Mixing Lab at the University of Nottingham Malaysia Campus, especially Mr. Adzarudin Abu Zarim for their friendly assistance and encouragement throughout the research programme.

I would like to express my deepest gratitude to my parents for their understanding, patient and generous encouragement during my study in the University of Nottingham Malaysia Campus. To my parents, I dedicate this work.

Table of Contents

List of Tables

Chapter 3

Chapter 4

Chapter 5

Chapter 6

List of Figures

Chapter 1

Chapter 2

Chapter 3

Chapter 4

Chapter 5

Chapter 6

Chapter 1 Introduction

1.1 Background

One of the many types of reinforced concrete slabs is the reinforced concrete flat plate floor system. The floor system consists of a slab of uniform thickness supported directly on columns without using intermediary beams as shown in Figure 1.1. The flat plate floor system is well-favoured by many designers due to its simplicity in construction, functional form and construction economy as compared to the conventional beam and slab system.

However, a major concern on this design system is the brittle punching failure that may occur due to the transfer of shear forces and unbalanced moment between the slabs and columns. Inclined shear cracks may develop within the slab thickness, which leads to brittle punching shear failure at the slab-column connection. This concern is illustrated in Figure 1.2.

The biggest fear upon the flat plate floor system is that the diagonal shear cracks are not visible on the slab surfaces. These unseen cracks will form across the slab thickness forming a cone, at the supporting column, and leads to a sudden punch through the slab and a sudden drop in the load-carrying capacity of the slab. Therefore, it is utmost important to be able to predict the ultimate strength of slab-column connections.

Since the introduction of flat slab structure, an extensive amount of research has been made to help understanding concentric punching, eccentric punching, and edge punching behaviour of a solid flat slab. The primary and the oldest approach in concentric punching mechanism is developed by Talbot[76] in 1913 in which he introduced an empirical approach to predict the punching failure loads of solid flat slabs. The model was later developed by other researchers (Richart[68]; Hognestad[36]; Whitney[78]; Moe[53]; Yitzhaki[82]; Rankin & Long[65];

Gardner[25]), and was finally adopted by most of the design codes such as ACI[1] and BS8110[14]. An extensive amount of theoretical study has also been made to understand the punching failure mechanism better, such as, the mechanical model introduced by Kinnunen & Nylander[43] and the plastic model introduced by Braestrup et al.[12] and Jiang & Shen[39].

For the eccentric punching mechanism, Di Stasio & Van Buren[17] presented a working stress method for the strength of slab-column connections in the presence of combined shear and unbalanced moment. The model was then modified by Moe[53], the ACI-ASCE committee 326[2] and Hanson & Hanson[30]. The first theoretical beam approach was initiated by Hawkins & Corley[34] based on modifications made upon Andersson's[6] approach, which was done for concentric loading only. Hawkins & Corley[34] developed an interaction diagram for interior slab-column connections transferring shear and unbalanced moment followed by Islam & Park[38], who developed a simpler design procedure. For edge column punching mechanism, an example is the beam analogy approach introduced by Hawkins & Corley[34].

In today's construction industry, waffle slabs are becoming widely popular as waffle slabs provide a lighter and stronger slab (because it gives added strength in both directions) than an equivalent flat slab, thus reducing the extend of foundations. Besides that, with the advancement of today's technology, formworks are invented to accommodate the ease of waffles slab's installation process, leading to construction time saved. Waffle slabs provide a very good form in which dynamic loading may be present, such as laboratories and hospitals.

Waffle slabs are described in that they have a thin topping slab and narrow ribs spanning in both directions between column heads. These column heads are built such that they are constructed at the same depth as the ribs as illustrated in Figure 1.3.

1.2 Problem Statement

Due to the increasing popularity of using waffle slabs in various buildings (e.g. commercial and industrial buildings), it is important to ensure that these waffle slabs are designed to behave satisfactorily under working load conditions as well as to achieve the required strength according to the Ultimate Limit State design.

Many investigators[16,63,66] have carried out experimental studies to determine the behaviour of reinforced concrete flat slab structures under punching shear loading. However, these data are mainly obtained from testing solid flat slab specimens. Very little effort has been made to study the behaviour of waffle slab structures under punching shear loading.

Various design codes[1,14,22] have suggested different design methods to design waffle slabs against punching shear failure. However, the majority of these codes, if not all, are derived from solid flat slabs[1,14,22]. These design methods become questionable as there are obvious differences in terms of structural properties (e.g. punching shear failure mechanism and punching shear capacity) between the solid flat slabs and the waffle slabs. Most previous researches[4,37,47,81] on the waffle slabs and ribbed slabs have shown that the differences in cross section between both slabs lead to a different punching shear failure mechanism and hence, different punching shear capacity.

1.3 Objective and Scope

The main objective of this research is to investigate the punching shear mechanisms of waffle slabs in the presence of unbalanced moment transfer through experimental tests and analytical study. The experimental works carried out in this research involve destruction testing of thirty-eight 1/10th scale slab specimens, which were cast using micro-concrete mixed from scaled aggregates. The tests covered testing at the internal column and the edge column situations.

The objectives of the research are listed in the followings:

1 To investigate the punching shear mechanisms of waffle slabs in the presence of biaxial unbalanced moment transfer for interior, and edge slab-column connections.

2 To study the effects of the principle angle of biaxial moment, the size of the solid section, the column's eccentricity and the column's orientation on the punching shear capacity of waffle slabs at internal column connections.

3 To study the effects of the principle angle of biaxial moment, the size of the solid section, the column's eccentricity and the column's location on the punching shear capacity of waffle slabs at edge column connections.

4 To develop theoretical models, using an upper bound plastic approach and the observed shear failure surface to predict the shear carrying capacities.

5 To develop simple design models for design purposes.

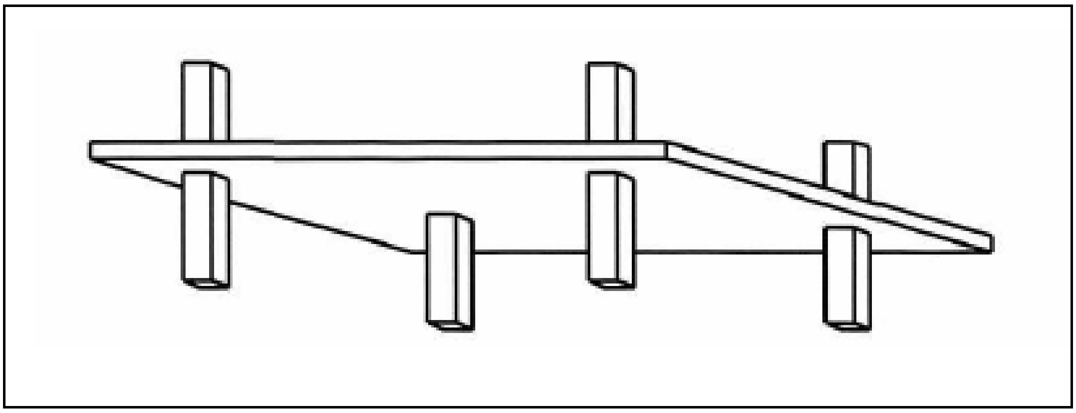

Figure 1.1 Flat Plate Floor System

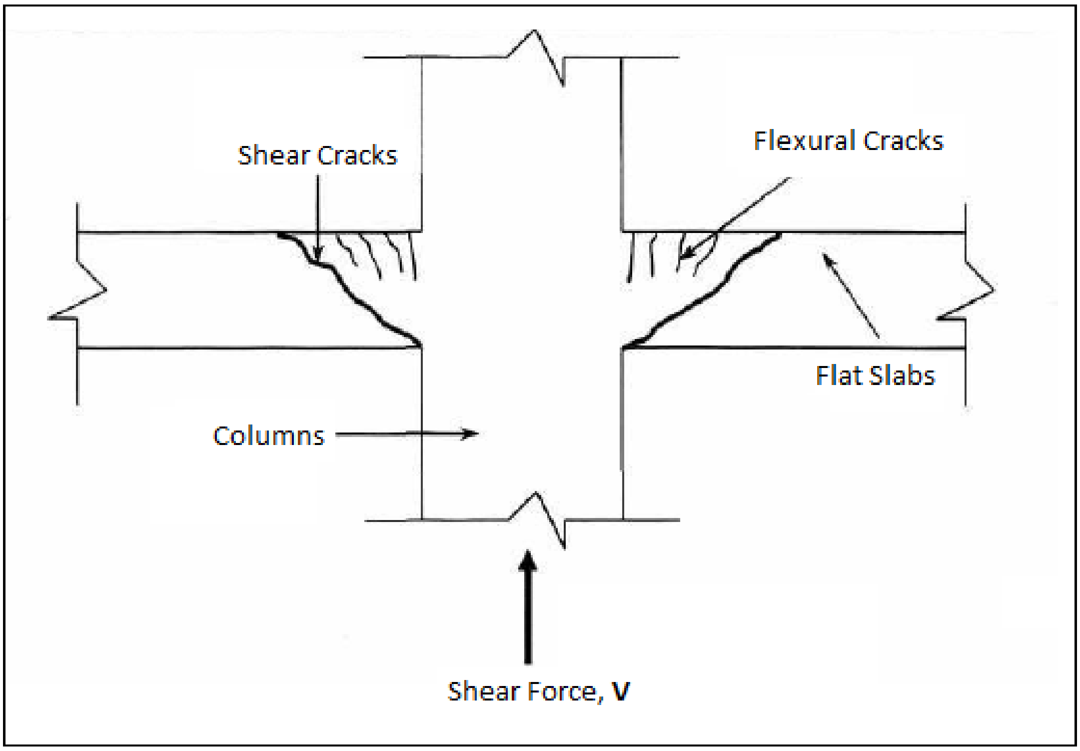

Figure 1.2 Punching Shear Failure

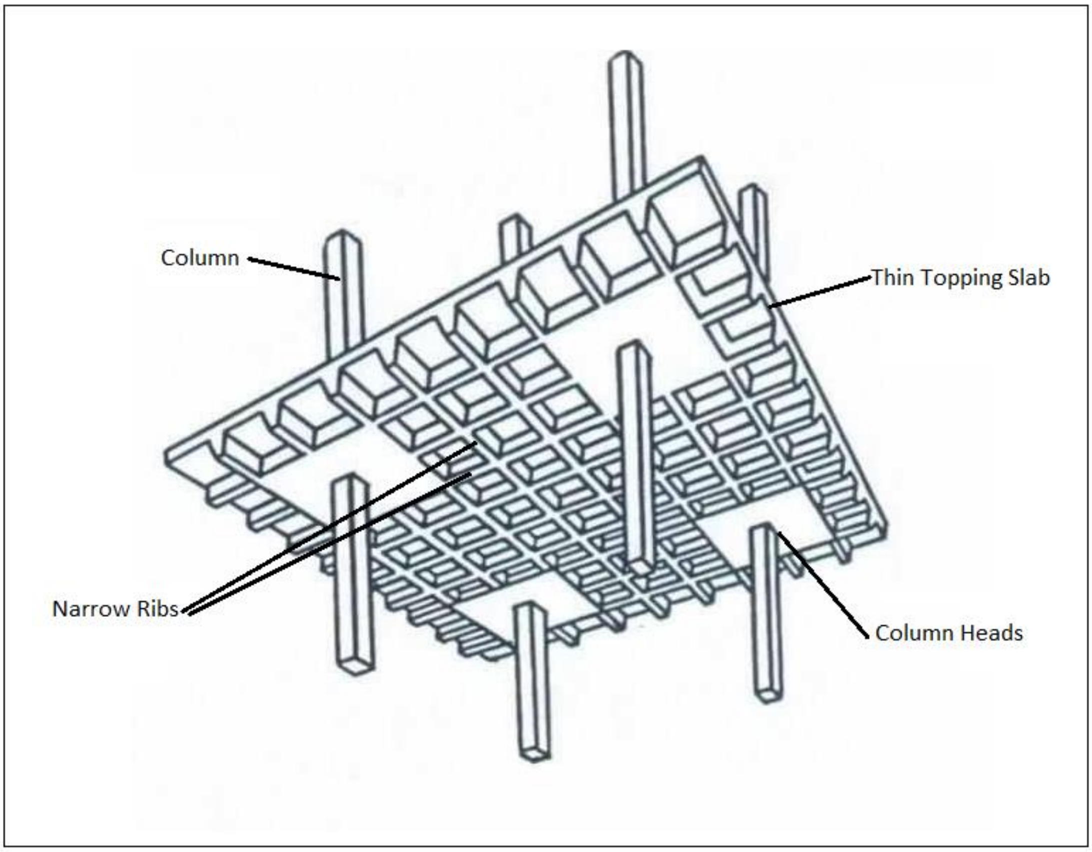

Figure 1.3 Waffle Slab System and its Components

Chapter 2 Literature Review

2.1 Introduction

Extensive amount of works[16,63,66] have been carried out in the last century, which developed all the current understanding in punching shear mechanism in reinforced concrete slabs. However, despite the increasing popularity of waffle slabs, the current understanding with regards to punching shear mechanism has been derived from tests carried out on flat slabs. And, only very limited amount of works have been carried out on waffle slabs. Therefore, previous researches on flat solid flat slabs and waffle slabs[4,37,47,81] have been reviewed to form the basic understanding with regards to the punching shear mechanism of waffle slabs.

In this chapter, a literature review is made on both empirical and theoretical approaches that have been introduced to predict the punching shear strength at internal column, and edge column connections.

2.2 Concentric Punching Shear

In this section, a review upon past models that were proposed to predict the behaviour of solid flat slabs in the absence of unbalanced moment transfer is proposed. In this chapter, the literature on concentric punching shear, consists of the empirical approaches with the building codes approaches, and the theoretical approaches, is presented.

2.2.1 Empirical Approach

2.2.1.1 Control Surface Approach

The earliest study on the shear strength of slab was conducted on reinforced concrete footings and published by Talbot[76] in 1913. Talbot tested a total of 114 wall footings and 83 column footings where the column footings were 5 ft square, 1 ft thick and having a 1 ft square column stub loaded at the center. From about 20 column footing specimens which failed in shear, Talbot proposed that the nominal shear stress, v_c, of a footing without shear reinforcement, corresponds to an assumed perimeter of critical section, u, at a distance equal to the slab depth, d, from the column faces, c, and with its height equals to the section's lever arm, z, as indicated in the following equation:

$$v_c = \frac{V_u}{u.z} \qquad \text{(Eq. 2.1)}$$

Where:

V_u = the ultimate punching load

u = the perimeter of the critical section, $u = 4(c + 2d)$

c = the column width

d = the effect depth of a footing

z = the section lever arm

Richart[68] in 1948 reported the next major study on shear strength of slabs. Richart's model was distinct from Talbot's model[76] in that the effective depth of the column footing was introduced as the major variable. Other variables such as the amount and strength of tensile reinforcement and concrete strength were also being investigated and contributed to the

140 column footings in which all were tested to failure. Richart concluded that the shearing stresses at failure changed as accordance to the effective depth of the footing. The shear stress was found to be lower for thick footings and higher for thin footings.

In 1953, Hognestad[36] re-evaluated Richart's findings[68] on the shear failures of footings. In Hognestad's analysis, under concentric load, the regions of high shear and flexural stresses coincided. For the first time, Hognestad introduced a new ratio, ϕ_o, which represents the ratio of ultimate shear capacity to yield line capacity of the section, as one of the parameters in his statistical study of the test results. Hognestad found valid reasons to believe that the best way to measure shearing strength is to calculate from a control shear surface, which located at the faces of the loading column. Based on the above findings, an empirical equation was proposed to compute the punching shear stress.

$$v_c = \frac{V_u}{jud} = \left(0.035 + \frac{0.07}{\phi_o}\right)\sigma_c + 130psi \qquad \text{(Eq. 2.2)}$$

Where:

V_u = the ultimate punching load

j = 7/8 constant

$u = 4c$, perimeter of critical section

d = effective depth

c = the column width

σ_c = the cylinder concrete compressive strength

ϕ_o = the ratio of ultimate shear capacity to yield line capacity

In 1956, Elstner & Hognestad[20] further explored into the punching shear behavior of solid flat slabs and reported results of 39 square slab specimens being loaded centrally using column stubs and most of the specimens were supported along all four edges. However, only 34 of these slabs were failed in punching shear. The main test variables were: the concrete compressive strength, the percentage of flexural reinforcement (for both tension and compression) and shear reinforcement, the size of column, the concentration of tension reinforcement over the column stub, the support conditions and the type of loadings upon the slabs. Based on the experimental results, Elstner & Hognestad found that the punching shear capacity is highly dependent on the concrete compressive strength and the flexural reinforcement. Besides that, the concentration of tension reinforcement over the column stub and the presence of compression reinforcement show no significant effect on the shear strength of the slab specimens. Elstner & Hognestad agreed that the equation Hognestad[36] proposed in 1953 was unsafe for flat solid slabs cast from high strength concrete. Therefore, based on statistical analysis, Elstner & Hognestad proposed a new equation to compute shear stress for slab specimens without shear reinforcement:

$$v_c = \frac{V_u}{jud} = \left(\frac{0.046}{\phi_o}\right)\sigma_c + 333psi \qquad \text{(Eq. 2.3)}$$

Where:

V_u = the ultimate punching load

j = 7/8 constant

$u = 4c$, perimeter of critical section

c = the column width

d = effective depth

σ_c = the cylinder concrete compressive strength

ϕ_o = the ratio of ultimate shear capacity to yield line capacity

Whitney[78] in 1957 proposed a slightly different ultimate strength theory from those have been presented by others[20,36,68,76]. Whitney presented an ultimate strength theory for shear, derived from the re-evaluation of the previous data[20,36]. Whitney reported that two types of failure modes were noticed. One was the gradual failure after yield had been reached in the flexural steel, while the other was for slabs reinforced with heavy reinforcement, a sudden failure before yield was reached in the flexural bars at the vicinities of the column. From this finding, Whitney further concluded that shear stress could not simply be expressed as a function of cylinder strength for any types of solid flat slabs. Shear stress is principally a function of reinforcement percentage for under-reinforced slabs and is principally a function of concrete strength for over-reinforced slabs. The following equation was proposed to predict the punching shear failure loads:

$$v_c = \frac{V_u}{ud} = 0.75\left(\frac{M_u}{d^2}\right)\left(\sqrt{\frac{d}{a}}\right) + 100psi \qquad \text{(Eq. 2.4)}$$

Where:

V_u = the ultimate punching load

$u = 4(c + d)$, perimeter of critical section

c = the column width

d = effective depth

M_u = the ultimate flexural moment of resistance

a = the distance from column face to load position

Judging from Whitney's equation[78], it is believed that the shear strength of a slab is highly dependent on the concentration of the flexural reinforcement that passed through the failure zone. That is, the shear strength of the slab increases with the increase in flexural reinforcement that passes through the failure zone. This coincided with the method used in the 1956 ACI Building Code and the ideas proposed by Talbot[76] and Richart[68], but contradict the experimental outcomes of Elstner & Hognestad[20].

In 1961, Moe[53] reported tests carried out on 43 nos. of 1.8m square solid flat slabs that were very similar to those tested by Elstner & Hognestad[20]. In this study, the principal variables considered were the effect of column size, the effect of openings column, the effect of eccentricity of applied load, and the effect of concentration of tensile reinforcement within the column. In addition, Moe reported a statistical study of 260 reinforced concrete slabs and footings tested by others. Moe's report concludes:

1. The critical section regulating the ultimate shear strength of slabs should be measured along the perimeter of the loaded area.

2. The flexural strength of the slabs have some influence on the shear strength of the slabs

3. The shear strength of the slabs increases as the column size decreases with respect to the slab thickness.

4. The concentration of flexural reinforcement in the narrow band across the column did not affect the shear strength of the slabs but it increased the flexural rigidity of slabs, and indirectly increased the load at which yielding began in the flexural reinforcement.

5. The shear strength of slabs was found to be more accurate when square root is being applied to the concrete compressive strength and when being related to the relative size of the column, $c/_d$, so as to allow for the effect of size and shape of column. Thus, he introduced a new formula to predict the ultimate shear strength of slabs:

$$v_c = \frac{V_u}{ud} = \sqrt{\sigma_c}\left(15\left(1 - 0.075\frac{c}{d}\right) - 5.25\phi_o\right) \quad \text{(Eq. 2.5)}$$

Where:

V_u = the ultimate shear force

$u = 4c$, the periphery length of critical section inside of the column faces

c = the column width

d = effective depth

$\sigma_c =$ the cylinder concrete compressive strength

ϕ_o = the ratio of ultimate shear capacity to flexural capacity

In 1966, Yitzhaki[82] tested 14 nos. of circular slab-column specimens. Yitzhaki then proposed an equation to predict the vertical punching strength located for the interior column, the coupling critical shear perimeter area was located at distance, d, away from the column face. Another highlight of Yitzhaki's work was that the shear strength has been mainly derived from the reinforcement and the column size, while the effect of concrete strength is the same for both flexural and shear strengths. The equation proposed to predict the punching shear strength is as shown as below:

$$v_c = \frac{V_u}{ud} = 0.164\rho f_y + 149.3\ psi \qquad \text{(Eq. 2.6)}$$

Where:

V_u = the ultimate shear force

$u = 4(c + 2d)$, the critical perimeter

c = the column width

d = effective depth

ρ = the ratio of flexural reinforcement

f_y = yield strength of reinforcement

In 1968, ACI-ASCE Committee 326[2] modified Moe's equation[53] into a simpler model. The committee stated that in any normal design, the punching and flexural resistance to be designed to overcome the same amount of load and therefore, the parameter proposed by Moe, ϕ_o which is a ratio of ultimate shear capacity to flexural capacity is assumed to be equal to unity. Therefore, Moe's equation is simplified to:

$$v_c = \frac{V_u}{ud} = \sqrt{\sigma_c}\left(9.75 - 1.125\frac{c}{d}\right) \qquad \text{(Eq. 2.7)}$$

Where:

V_u = the ultimate shear force

$u = 4c$, the periphery length of critical section inside of the column faces

c = the column width

d = effective depth

$\sigma_c =$ the cylinder concrete compressive strength

In 1987, Rankin & Long[65] reported on concentric punching mechanism of solid flat slabs. Rankin & Long tested a total of 27 isolated interior column slab specimens, in which, the main variables were total depth of the slab and the presence of steel reinforcement. Besides that, another variable being investigated was the concrete compressive strength. Two failure modes were identified in Long's[48] previous work in 1975, which were flexural punching failure and shear punching failure leading to the extension of Long's work to predict the punching strength capacity. The flexural punching mode of slabs can be initiated in three different conditions: flexural failure after the full yielding of steel reinforcement, flexural failure with the partial yielding of flexural steel reinforcement, and concrete crushing failure at the periphery of column.

The shear punching initiated via formation of diagonal tension cracks prior to any yielding in the flexural steel reinforcement or via concrete crushing failure at the periphery of the column. The shear punching mode, however, contradicts the flexural punching mode. Therefore, Rankin & Long[65] proclaimed that the shear punching mechanism is a function of the concrete tensile strength, $\sqrt{\sigma_c}$. The critical control surface is assumed to be located at $0.5d$, from the column faces. Rankin & Long further added that the shear stress to be carried by the concrete in compression only, thus introducing x, to represents the depth of the neutral axis.

$$v_c = \frac{V_u}{ux} = r_f\sqrt{\sigma_c} \qquad \text{(Eq. 2.8)}$$

Where:

V_u = the ultimate shear force

$u = 4(c + d)$, the critical perimeter

c = the column width

d = effective depth

$x = 0.35d^4\sqrt{100\rho}$

r_f = column shape factor proposed by Regan in 1981

σ_c = the cylinder concrete compressive strength

In 1990, Gardner[25] reported studies on the variation of punching shear capacity with the concrete compressive strength. A total of thirty slabs were cast and tested to aid the investigation. Two main variables were investigated by Gardner, the concrete compressive strength and the slab thickness. From this investigation, Gardner reported that the punching shear strength of concrete slab to be proportional to the cube root of concrete strength and flexural steel reinforcement ratio. But, to be inversely proportional to the fourth root of slab's effective depth. The control surface perimeter was reported to be rectangular in shape and located at a distance 1.5 times the effective slab depth from the column faces. From this study, Gardner proposed a new equation to predict the punching shear capacity of solid flat slabs:

$$v_c = \frac{V_u}{4(c+3d)d} = 0.99\left(\sqrt[3]{\rho\sigma_c}\right)\left(\sqrt[4]{\frac{400}{d}}\right) \qquad \text{(Eq. 2.9)}$$

Where:

V_u = the ultimate shear force

c = the column width

d = effective depth

ρ = the ratio of flexural reinforcement

σ_c = the cylinder concrete compressive strength

2.2.1.2 Regan's Approach

In 1981, Regan[67] proposed an alternative control failure surface approach to predict the behavior of solid flat slabs during punching shear loading. Regan proposed that the curved area of an assumed conical failure surface should be used instead of the product of slab depth and the critical surface area.

In a simplified model, Regan portrayed a shear failure surface in a three-dimensional manner as shown in Figure 2.1 where the punching shear surface is a truncated cone inclined at a slope of $\cot\theta = 2.5$ to the plane of the slab from the column faces and this assumed punching shear surface is expressed as:

$$A_c = d\sqrt{1+\cot^2\theta}\,(\Sigma c + \pi d \cot\theta) \qquad \text{(Eq. 2.10)}$$

Where:

d = effective depth

c = the column width

θ =inclination of the failure surface relative to the plane of slab, θ=22°

Regan[67] reported a series of studies to understand the influence of the concrete compressive strength, the type of concrete used, the reinforcement ratio, the thickness of the slab, and the column shape and size on the punching shear strength. Regan's findings were as follows:

1. The punching shear strength was found to increase with the specimen's concrete compressive strength.
2. The type of concrete has a pronounced effect on the punching shear strength. Regan found that a slab cast from normal concrete would give a 20 % increase in punching capacity that a slab cast from lightweight concrete.
3. The punching shear strength was increased when the amount of steel reinforcement increased.
4. The shape of the column has a significant effect on the punching shear strength. A circular column with an identical perimeter length to a square one would give 10 – 15% increase in punching shear strength.
5. The punching shear strength was increased with the column size.

With these findings, Regan[67] concluded that the ultimate punching capacity of a flat slab in the absence of moment transfer to be calculated from the following equation:

$$V_u = K_a K_{sc} v_c A_c \qquad \text{(Eq. 2.11)}$$

Where:

K_a = Concrete type factor, 0.13 for normal concrete and 0.105 for lightweight concrete

K_{sc} = Column shape factor, $1.15\sqrt{\frac{4\pi * column\ area}{(column\ perimeter)^2}}$

v_c = Normal concrete shear strength, $(\sqrt[3]{\rho f_{cu}})(\sqrt[4]{\frac{300}{d}})$

The advantage of applying Regan's approach[67] over the control surface approach[76] is that in Regan's approach, the actual failure surface is being taken into account during the calculation of punching shear resistance. This would ease the adoption to any modifications in the situation of non-solid slabs, such as waffle slabs.

2.2.2 Building Code Approach

The current building codes of practice[1,14,22] adopted the control surface approach to design against concentric punching shear. However, the design procedure of each code differs in terms of the location of the critical section and the derivations of concrete shear strength. In this section, the American Code ACI 318-11[1], the British Standard BS8110[14] and the European Code EC2[22] are reviewed.

2.2.2.1 ACI 318-11

ACI 318-11[1] defines the location of the critical perimeter to be at a distance, $0.5d$, from the column faces, as shown in Figure 2.2. The height of the critical section to be the effective depth of the slab, d. The shear strength of a non-shear reinforced concrete slab is a function of concrete compressive strength and the ratio of the column's sides.

$$v_c = \left(2 + \frac{4}{\beta_c}\right)\sqrt{\sigma_c} \qquad \text{(Eq. 2.12)}$$

Where:

β_c = the ratio of long side to short side of the column

σ_c = the concrete cylinder compressive strength

The ultimate punching capacity of a slab is defined as the product of the shear strength and the critical area, as shown in the following equation.

$$v_c = \frac{V_u}{4(c+d)d} \qquad \text{(Eq. 2.13)}$$

Where:

V_u = the ultimate shear force

c = the column width

d = effective depth

2.2.2.2 BS8110

BS8110[14] defines the location of the critical perimeter to be at a distance, $1.5d$, from the column faces, as shown in Figure 2.3. The height of the critical section to be the effective depth of the slab, d. The shear strength of a non-shear reinforced concrete slab is a function of the concrete compressive strength, the steel reinforcement ratio, and the effective depth of the slab.

$$v_c = \frac{0.79}{\gamma m}\left(\sqrt[3]{\rho f_{cu}}\right)\left(\sqrt[4]{\frac{400}{d}}\right) \qquad \text{(Eq. 2.14)}$$

Where:

γ_m = the material safety factor

ρ = the ratio of flexural reinforcement

f_{cu} = the concrete cube compressive strength

d = effective depth

The ultimate punching capacity of a slab is defined as the product of the shear strength and the critical area, as shown in the following equation.

$$v_c = \frac{V_u}{4(c+3d)d} \quad \text{(Eq. 2.15)}$$

Where:

V_u = the ultimate shear force

c = the column width

d = effective depth

2.2.2.3 Eurocode 2

Eurocode 2[22] defines the location of the critical perimeter to be at a distance, $2d$, from the column faces, as shown in Figure 2.4 for both the square and the circular column stub. The height of the critical section to be the effective depth of the slab, d. The shear strength of a non-shear reinforced concrete slab is a function of the concrete compressive strength, the steel reinforcement ratio and the effective depth of a slab.

$$v_c = \frac{0.18}{\gamma_m} k(100\rho\sigma_c)^{1/3} \quad \text{(Eq. 2.16)}$$

Where:

γ_m = the material safety factor

k = the size effect factor, where $k = 1 + \sqrt{\frac{200}{d}}$

ρ = the steel reinforcement ratio

σ_c = the concrete cylindrical compressive strength

The ultimate punching capacity of a slab is defined as the product of the shear strength and the critical area, as shown in the following equation.

$$v_c = \frac{V_u}{4(c+\pi d)d} \qquad \text{(Eq. 2.17)}$$

Where:

V_u = the ultimate shear force

c = the column width

d = effective depth

2.2.3 Theoretical Approach

2.2.3.1 Mechanical Model

The first mechanical model was introduced by Kinnunen & Nylander[43] in 1960. This mechanical model explains the punching shear phenomenon and predicts the failure load of slab-column connection.

This model, as shown in Figure 2.5(a), is based on the equilibrium of forces acting upon circular slab supported on a circular column, and loaded at the free edges. This mechanical model consists of a central truncated cone confined by the shear cracks and the slab is separated into rigid segments by radial cracks. The separated segments are assumed to be carried on an imaginary conical shell, between the column and the root of the shear crack, as shown in Figure 2.5(b). Each segment is acted on by the resultant forces as shown in Figure 2.5(c). The internal forces comprises of functions of the angle of rotation, ψ, and the mechanical properties of concrete and steel. In technical terms, failure is assumed to occur when the tangential strains at the bottom of the slab under the root of the shear crack reach a characteristic value, ε_{ct}, which is dependent on B/d, at the same time as the stress in the imaginary conical shell is at the concrete's characteristic value.

At failure, $\psi = \varepsilon_{ct}\big(1 + B/(2x)\big)$. The yield stress f_y is reached in the reinforcement within a slab area of radius, r_s:

$$r_s = \psi(d - x)\frac{E_s}{f_y} \qquad \text{(Eq. 2.18)}$$

Where:

ψ = angle of rotation of the rigid segments

d = the effective depth

x = the neutral axis depth

E_s = Young's Modulus of reinforcement

f_y = yield stress of reinforcement

By using this method, it is able to predict the ultimate load irrespective of whether the failure is a flexural failure or a punching failure. If the ratio of reinforcement, ρ, is low, then $r_s > {}^{c}/_{2}$ at failure. This means if f_y has been fully mobilized in all the reinforcement, the failure is categorized as a flexural failure. However, if the ratio of reinforcement, ρ, is high, then $r_s < {}^{c}/_{2}$ at failure. This means if f_y has been fully mobilized in all the reinforcement, thus the failure is categorized as a punching failure. This method gives a continuous transition between these two types of failure. Besides that, it predicts the deformations of the slab at failure.

2.2.3.2 Plastic Model

2.2.3.2.1 Braestrup et al. Model

A plastic solution for the punching shear strength of solid flat slabs was first introduced by Braestrup et al.[12] in 1976. It is based on the failure mechanism as shown in Figure 2.6. The deformations are assumed to be concentrated in a rotationally symmetric failure surface being punched out perpendicularly from the slab, while the rest of the slab remained rigid.

The relative displacement vector is considered to be perpendicular to the slab, leaving that the flexural reinforcement does not contribute to the punching strength and that the punching strength mainly rely on the geometric factor and the concrete compressive strength. However, certain amount of reinforcement is necessary to prevent the surface outside of the critical section to fail or deform before the slab fails in punching.

From these works, Braestrup et al.[12] introduced a upper bound equation to replicate the failure mechanism as shown in Figure 2.6. The internal work dissipated, w_i, per unit length is defined as below:

$$w_i = 0.5\, \delta f_c (l - m\, sin\alpha) \qquad \text{(Eq. 2.19)}$$

Where:

δ = total downward displacement

f_c = plastic concrete compressive strength, $f_c = v_c \sigma_c$

v_c = effectiveness factor

σ_c = concrete cylinder compressive strength

$l = 1 - (k-1)\, f_t/f_c$

$m = 1 - (k+1)\, f_t/f_c$

$$k = \frac{1 + sin\varphi}{1 - sin\varphi}$$

φ = angle of friction in concrete, 37°

α = inclination of discontinuity lines with respect to the direction of displacement

Therefore, the punching shear failure load is derived by equating the external work done by the applied load to the internal work dissipated, w_i.The dissipation is found by integration over the failure surface, thus allowing the work equation to yield as:

$$P\delta = \int_0^h 0.5\, \delta f_c (l - m \sin \alpha) 2\pi r \frac{dx}{\cos \alpha} \qquad \text{(Eq. 2.20)}$$

Where:

r = radius of failure surface, $r = r(x)$

h = depth of slab

The lowest upper bound is obtained by reducing the functional on the right hand side with respect to $r(x)$, subject to $r' \geq \tan\varphi$, imposed by the normality condition. Such variational calculus can be solved by proposing a catenary curve and a straight line inclined at angle φ joined at the depth of $x = h_0$

$$r(x) = r_0 + x \tan\varphi \qquad \text{for } 0 \leq x \leq h_0 \qquad \text{(Eq. 2.21)}$$

$$r(x) = a \cosh\left(\frac{x - h_0}{c}\right) + b \sinh\left(\frac{x - h_0}{c}\right) \qquad \text{for } h_0 \leq x \leq h \qquad \text{(Eq. 2.22)}$$

The corresponding upper bound, $P = P_1 + P_2$, where the contributions, $P_1$and P_2, from the straight line and catenary parts are respectively found to be:

$$P_1 = 0.5\, \pi\, f_c\, h_0\, (d_0 + h_0 \tan\varphi) \left(\frac{1 - \sin\varphi}{\cos\varphi}\right) \qquad \text{(Eq. 2.23)}$$

$$P_1 = 0.5\,\pi\, f_c\,\left(l_c(h-h_0)\right) + \,l\left(r_1\sqrt{{r_1}^2 - c^2} - ab\right) - m({r_1}^2 - a^2) \qquad \text{(Eq. 2.24)}$$

The constants a, b, c and h_0 are determined by the equations:

$$c^2 = \,a^2 - \,b^2$$

$$a = \,r_0 + h_0 \tan\varphi$$

$$\frac{b}{c} = \tan\varphi$$

$$r_1 = a\cosh\left(\frac{h-h_0}{c}\right) + b\,\sinh\left(\frac{h-h_0}{c}\right)$$

Therefore, this solution requires an assumed value of the opening diameter, d_1 and the lowest upper bound is found by minimization with respect to this parameter.

The punching force is a function of the diameter, d_0 and the slab depth, h. This load may be represented by the parameter, τ/σ_c, where $\tau = P/h(d_0 + 2h)$ as shown in Figure 2.7. The solution is very dependent of the value of the concrete tensile strength but independent of the punch diameter, d_0. Besides that, plastic analysis showed that the punching failure surface is dependent on the assumed contribution from the effective tensile strength, f_t. When $f_t = 0$, the failure surface will extend to the support, and this does not replicate the actual punching shear mechanism. Therefore, it is necessary to use an effective tensile strength, $f_t = f_c/400$, in the predictions. When the effective tensile strength is used, the corresponding effectiveness factor, v_c, is found to be a function of the concrete strength as shown in the following equation:

$$v_c = \frac{4.22}{\sqrt{f_c}} \qquad \text{(Eq. 2.25)}$$

The plastic solution only covers the upper bound. In order to establish the plastic model as a complete solution, it would be necessary to indicate a stress distribution in the entire slab which:

-satisfied the equilibrium equations and the statical boundary conditions

-corresponded to a yield line along the optimal failure generatrix

-did not violate the yield condition at any point.

2.2.3.2.2 Jiang & Shen model

In 1986, Jiang & Shen[39] proposed a simpler method as compared to Braestrup et al.[12] to represent the punching strength of a concrete slab. Jiang & Shen presented a second-degree parabola used for a Coulomb-Mohr yield envelope as the failure criterion for the concrete. The main highlight of their proposal was the description of failure as compared to Nielsen's proposal[57]. Nielsen[57] pointed out that punching shear of slab is mainly governed by the tensile strength of concrete whereas Jiang & Shen rebutted that the failure is rather a three-dimensional one. The failure happens mostly in the region of tension-compression-compression or compression-compression-compression, which proves that compression is more vital in this finding. The solution proposed by Jiang & Shen is as follows:

$$P = \pi\sigma_t \left(\frac{{d_1}^2 - d^2}{4} + \frac{2Kh^2}{\ln d_1 - \ln d}\right) \qquad \text{(Eq. 2.26)}$$

Where:

σ_t = effective tensile strength of concrete

d = diameter of loaded area

d_1 = diameter at base of failure cone

h = thickness of concrete slab

K = parameter depending upon the ratio between the effective compressive strength to the effective tensile strength of concrete.

Jiang & Shen[39] also incited that punching shear failure of concrete slab is possible to happen with a smaller angle but requires a higher ultimate strength.

2.2.3.2.3 Salim & Sebastian model

In 2002, Salim & Sebastian[71] proposed another simplified upper-bound plasticity model to that of Braestrup et al.[12], In that the punching shear failure surface is represented by a straight line surface (see Figure 2.8) instead of an integration of a catenary curve and a straight line surface (see Figure 2.6). Therefore, the equation of the generatrix simplifies to:

$$r = \frac{d_0}{2} + x \tan \alpha \qquad \text{(Eq. 2.27)}$$

In addition, Salim & Sebastian found that the effectiveness factor, when taken as a function of slab thickness, concrete strength and tensile reinforcement ratio, has significant effect on the shear strength estimations.

$$v_c = \frac{1.47}{\sqrt{\sigma_c}}\left(1 + \frac{0.48}{\sqrt{h}}\right)(1 + 0.125\rho) \qquad \text{(Eq. 2.28)}$$

Where:

σ_c = cylindrical compressive strength

h = height of slab

ρ = reinforcement ratio

Using previous researches' test results, Braestrup's complex method[12] was compared with the simplified method using both Braestrup's effectiveness factor[12] (see Eq. 2.25) and the proposed effectiveness factor (see Eq. 2.28), Salim & Sebastian found that the proposed simplified method along with the proposed effectiveness factor achieved very good agreement, with only slightly more scatter than that of Braestrup's complex method[12] with Braestrup's effectiveness factor[12].

2.2.3.2.3 Crack Sliding Theory model

In 2011, Nielsen[57] presented the crack sliding theory to predict the punching shear capacity of flat slab. This idea was adopted from the crack sliding theory developed for beams without shear reinforcement.

This model simulates the punching mechanism of a square slab loaded by a rigid square loading plate, as shown in Figure 2.9. The slab is assumed to be isotropically reinforced and the reinforcement ratio is assumed to be sufficiently large to withstand flexural failure. The punching failure load is estimated by equating the external work done by the applied load, W_E, to the internal work dissipated on the failure surface, W_I.

Upon punching shear failure, a system of four inclined cracks is developed as shown in Figure 2.10 and these cracks are assumed to be plane, causing a downward displacement of the pyramidal concrete block. The total dissipation for all four cracks is found to be:

$$W_I = 8\frac{\tau_c}{\frac{x}{h}}(b + x)h\delta \qquad \text{(Eq. 2.29)}$$

Where:

τ_c = Concrete shear strength

b = the column size

x = the inclination of the cracks

h = thickness of the slab

δ = total downward displacement

The external work done is simply $W_E = P_u\delta$ and by equating both equations together, when punching shear failure occurs in the four cracks considered, the punching capacity is represented by:

$$P_u = 8\frac{\tau_c}{\frac{x}{h}}(b + x)h \qquad \text{(Eq. 2.30)}$$

Nielsen[57] found that by minimizing the result of Eq. 2.30 with respect to x will always end up with $x = a$ corresponding to the smallest possible inclination of the cracks and this does not tally with experimental observations. Instead, Nielsen proposed to assume x as a value that the load required to develop the cracks, P_{cr}, equals the load required to cause shear failure in them.

The cracking mechanism is described as, the central pyramidal block moves downward by δ and the other four parts of the slab rotate an angle $\theta = \delta/\alpha$ around lines coinciding with the sides of loading plate resulting in opening of the vertical cracks by the angle $\sqrt{2\theta}$. As shown in Figure 2.11, the rotation also results in a horizontal shift of the reaction forces.

The cracking load, P_{cr}, is found from integrating the effective concrete tensile strength, f_{tef}, of the assumed cracking mechanism.

$$P_{cr} = \frac{4f_{tef}\left[\frac{2}{3}x^3 + \frac{b}{2}x^2 + h^2\left(\frac{b}{2} + a\right)\right]}{a} \qquad \text{(Eq. 2.31)}$$

Where:

f_{tef} = the effective concrete tensile strength, $f_{tef} = 0.156 f_c^{\frac{2}{3}} s(h)$

$s(h)$ = the size effect factor, $s(h) = \left(\frac{h}{0.1}\right)^{-0.3}$

a = the shear span = distance from edge of the loading plate to the nearest support

Lastly, according to the crack sliding theory, the inclination of the critical cracks as well as the load-carrying capacity are found by solving the equation $P_u(x) = P_{cr}(x)$. Therefore, by equating both Eq. 2.30 and Eq. 2.31, the following equation is obtained and to be solved with respect to x/h:

$$P_u = P_{cr} \rightarrow \left(\frac{x}{h}\right)^4 + \frac{3}{4}\frac{b}{h}\left(\frac{x}{h}\right)^3 + \left(\frac{3}{4}\frac{b}{h} + \left(\frac{3}{2} - 3\frac{\tau_c}{f_{tef}}\right)\frac{a}{h}\right)\frac{x}{h} - 3\frac{\tau_c}{f_{tef}}\frac{b}{h}\frac{a}{h} = 0 \qquad \text{(Eq. 2.32)}$$

2.3 Eccentric Punching Shear

In this section, a review upon past models that were proposed to predict the behaviour of solid flat slabs subjected to applied unbalanced moment is proposed. Shear strength of a slab-column connection is undeniably greatly affected by the presence of the unbalanced moment acting upon the connection. In this chapter, eccentric punching shear will only be discussed in the building code approach and theoretical approach, ie. the plastic model.

The author has decided to derive a new design model equation from the existing building code approach and a new theoretical model from the existing plastic model. Therefore, an in-depth literature review on these two approaches is reported.

2.3.1 Elastic model

2.3.1.1 Linear Distribution of Shear Stress on Control Surface Approach

In 1960, Di Stasio & Van Buren[17] introduced a working stress method to predict the punching shear strength of slab-column connections in the presence of combined shear and unbalanced moment. The sum of all vertical shear stresses acting upon the critical section determines the punching shear capacity of solid flat slabs as shown in Figure 2.12(b). In the same Figure 2.12(a), the control surface that was proposed was shown to be located at a distanced equal to the slab overall height from the column faces.

Di Stasio & Van Buren proposed the following equation to estimate the shear stresses at the critical section:

$$v = \frac{8h}{7d}\left[\frac{V}{A_c} + \frac{(M - m_{AB} - m_{CD})C_1}{J_C}\right] \qquad \text{(Eq. 2.33)}$$

Where:

V = Punching shear resistance due to vertical load

M = Unbalanced moment transferred from the vertical load

m_{AB} , m_{CD} = Flexural moments on sides AB and CD of the critical section respectively

h = Overall thickness of the slab

d = The effective depth

A_c = The area of the critical section

J_C = The polar moment of inertia of the critical section about its centroid

C_A = The distance from centroid to the end of the critical section

In Eq. 2.33, the factor $\frac{7}{8}$ was used to comply the American design practice for the calculation of shear stress by $\frac{V_u}{jud}$, as proposed by Hognestad[36] earlier, assuming $j = \frac{7}{8}$. This method proposed by Di Stasio & Van Buren[17] were adopted in the ACI 318[1] for the design of solid flat slabs at the internal column against the punching shear failure in the presence of moment transfer mainly due to its simplicity.

In 1961, Moe[53] introduced another method to analyse the strength of slab-column connections under the presence of combined shear and unbalanced moment. This is different from the Di Stasio's & Van Buren's model[17] because the critical section was assumed to be directly adjacent to the column face. In Moe's model, the slabs were simply supported so as to prevent negative reactions at the supports and allow the corners to lift freely. Load was applied at different eccentricities (varied from 0 to 24 inches) over a square column stub located centrally.

Figure 2.13(a) shows a model proposed by Moe[53] in that a square column stub is loaded with a vertical shear, P, and a moment, M, in one of the planes symmetrical to the faces of the column. As shown in the Figure 2.13(a), the external moment, M is being countered by 3 internal moments: the torsional moments, M_t which are acting on the sides BC and AD, the resultant flexural moments, M_f generated from sections AB and CD, and lastly the vertical shear acting with the presence of eccentricity, Pe. Therefore, by assuming a value for the proportion of the moment provided by uneven shear and then determines the resulting shear stresses with an assumption that these shear stresses vary linearly around the control perimeter, Moe suggested:

$$v = \frac{P}{A_c} + \frac{KMc}{J_C} \tag{Eq. 2.34}$$

Where:

v = the maximum vertical shear stress

P = the vertical load acting with an eccentricity

$A_c = u * d$ = area of the critical section

$J_C = \int x^2 \, dA$ over the entire area of the critical section = the moment of inertial for the critical section

c = the distance from the column center to the most remote part of the critical section

KM = the part of the external unbalanced moment being resisted by uneven shear and torsional moments

Through further investigation by Moe[53], two assumptions were reported. Firstly, the nominal vertical shear stresses are uniformly distributed across the effective depth, d of the slab and secondly, when the slabs were loaded concentrically, it was found that the shear stress at failure is similar to the maximum vertical shear stress during eccentric loading. For the empirical value of K, Moe suggested a value of $1/3$ to find the ultimate shear strength.

In 1962, the ACI-ASCE committee 326[2] reviewed Moe's work[53] and proposed that a limiting shear stress to be estimated using:

$$v_c = 4\left(\frac{c}{d} + 1\right)(\sigma_c)^{1/2} \qquad \text{(Eq. 2.35)}$$

Where:

c = the column width

d = the effective depth

σ_c = the cylindrical strength of concrete

In this equation, the critical section was said to be as according to the periphery of the column. Besides reviewing Moe's work[53], the committee recommended similar procedure to Di Stasio's & Van Buren's work[17] to calculate the moment and shear transfer with an addition of two new modifications. Firstly, the critical section has to be taken at a distance of $d/2$ from the column faces and the effective depth is used instead of the height of the slab during the calculation of A_c and J_c. Therefore, the committee recommended the following equation for interior column:

$$v = \frac{P}{A_c} + \frac{KMc}{Jc} < 4{\sigma_c}^{1/2} \qquad \text{(Eq. 2.36}$$

Judging from the work of Moe's[53] and Hanson's & Hanson's[30], the committee agreed on the empirical value, $K = 0.2$ instead of $1/3$.

In 1968, Hanson & Hanson[30] reported an experimental study which involves the findings of solid flat slabs being vertically loaded at the edges to simulate a single direction load transfer while the column stubs were in a fixed position. Hanson & Hanson further concluded that the ultimate design method recommended by the ACI-ASCE Committee 326[2] is valid in predicting the punching strength of slabs only if the moment reduction factor, K is taken as 0.4.

2.3.1.2 Regan's Approach

In 1981, Regan[67] further researched upon the punching shear mechanism under eccentric loading. When moment transfer is acting on the solid flat slabs, Regan assumed that the transferred moment, αM is being resisted mainly by the flexural strength at both front and back of the column faces, along with unbalanced shear stresses on the assumed failure surface. The distribution of shear corresponding to the pure moment loading is shown in Figure 2.14. It can be seen that the lever arm between the forces and the column faces is described as, $(c_1 + 2d)$. Regan proposed the following equation to calculate the maximum vertical stress on the inclined surface as:

$$v_{max} = \frac{\alpha M}{d\sqrt{1+\cot^2\theta}(c_1+2d)[c_2+0.5\pi d\cot\theta+c_1(3c_1+6d)]} \qquad \text{(Eq. 2.37)}$$

Where:

αM = the magnitude of the unbalanced moment

d = the effective depth

$c_1,\ c_2$ =sizes of a column, which are parallel and perpendicular to the directions of the transferred moment, respectively

θ = the ratio of side of the failure surface perpendicular to applied moment / side of the failure surface parallel to the applied moment

Combining the shear stresses resulting from the unbalanced moment transferred and the shear stresses resulting from concentric shear, V_{uo} and with eccentricity, e:

$$V_{ue} = \frac{V_{uo}}{1+\beta\left[\frac{e}{(c_1+2d)}\right]} \quad \text{(Eq. 2.38)}$$

Where:

V_{ue} = the ultimate shear capacity for eccentric load

V_{uo} = the ultimate shear capacity for concentric load

c_1 = size of column which is parallel to the direction of the transferred moment

d = the effective depth

$e = \frac{M}{V_{uo}}$ = column's eccentricity

$$\beta = 2\alpha\left[\frac{\frac{c_2}{c_1}+\frac{\pi d\cot\theta}{2c_1}+1}{\frac{c_2}{c_1}+\frac{\pi d\cot\theta}{2c_1}+\frac{1}{3\left[1+(\frac{2d}{c_1})\right]}}\right]$$

2.3.1.3 Building Code Approach

The current building codes of practice[1,14,22] adopted the control surface approach to design against eccentric punching shear. However, the design procedure of each code differs in terms of the location of the critical section, the derivations of concrete shear strength and the effect of moment transfer. In this section, the American Code ACI 318-11[1], the British Standard BS8110[14] and the European Code EC2[22] are reviewed.

2.3.1.3.1 ACI 318-11

The ACI 318-11[1] propose a model to calculate the ultimate shear stresses under the presence of shear force and unbalanced moment. This model states that shear stresses acting upon the slab are originated from part of the unbalanced moment transferred and the direct shear force acting on the slab. These distributions of forces are illustrated in Figure 2.15.

Punching shear failure occurs when total of shear stresses exceeds the shear strength calculated using the equation below.

$$v = \frac{V_u}{b_0 d} + \frac{\gamma_v M_u c_{AB}}{J_C} \qquad \text{(Eq. 2.39)}$$

Where:

V_u = applied shear force

M_u = applied unbalanced moment

b_0 = perimeter of the critical section

d = the effective depth

c_{AB} = distance from face AB to the most remote part of the critical section

J_C = the polar moment of inertia of the critical section:

$$J_C = \frac{{b_x}^3 d}{6} + \frac{b_x d^3}{6} + \frac{{b_x}^2 b_y d}{2}$$

γ_v = part of unbalanced moment transferred by shear:

$$\gamma_v = 1 - \gamma_f$$

γ_f = part of unbalanced moment transferred by flexure:

$$\gamma_f = \frac{1}{1 + \left(\frac{2}{3}\right)\sqrt{\frac{b_x}{b_y}}}$$

$b_x, b_y = c_x, c_y + d$ = sides of critical section parallel and perpendicular to the direction of the unbalanced moment, respectively

c_x, c_y = sides of column parallel and perpendicular to the unbalanced moment, respectively

In cases where biaxial moment is being transferred, the maximum shear stresses acting on the critical section can be calculated by summing the effects coming from these biaxial moments as shown in Figure 2.16.

This can be explained using the equation below:

$$v = \frac{V_u}{b_0 d} + \frac{\gamma_{v1} M_{u1} c_{AB}}{J_{C1}} + \frac{\gamma_{v2} M_{u2} c_{BD}}{J_{C2}} \quad \text{(Eq. 2.40)}$$

Where:

c_{AB}, c_{BD} = the distances from center of the critical section to face AB and BD of the critical section, respectively

Subscripts 1,2 = the perpendicular directions in which the unbalanced moment are transferred.

On a side note, for unbalanced moment transfer at interior column connections, ACI allows the fraction of the unbalanced moment transferred by shear to be reduced to 0.25 in cases where the applied shear force, V_u does not exceed $0.4\ V_c$.

2.3.1.3.2 BS8110

In BS8110[14], a plasticity approach is used in computing the effective shear stresses. The critical section is remained unchanged from that of the concentric punching shear. The transferred moment is assumed to be transmitted by the vertical shear stresses and is added along with those stresses from the vertical load. BS8110 introduced a moment transfer factor to represent the reduction in shear resistance caused by the presence of moment transfer.

$$v_c = \frac{V_u}{u}\left(1 + \frac{1.5M_u}{V_u b_x}\right) \qquad \text{(Eq. 2.41)}$$

Where:

V_u = applied shear force

M_u = applied unbalanced moment

$u = 2c_x + 2c_y + 4\pi d$ = the perimeter of rectangular column critical section

$b_x = c_x + 3d$ = side of critical section parallel to the direction of the unbalanced moment

c_x = side of column parallel to the unbalanced moment

Another method proposed by BS8110 is that the nominal shear force can be increased by 15% in cases where unbalanced moments are being transferred at an interior column.

2.3.1.3.3 Eurocode 2

In EC2[22], the transferred moment is taken to be transmitted by a series of unbalanced shear stresses which are distributed at the critical section as shown in Figure 2.17. According to EC2, a moment transfer factor, β is required to be added into the calculation of punching shear capacity due to the effect of eccentric loading as shown below:

$$v_f = \beta \frac{V_u}{ud} \qquad \text{(Eq. 2.42)}$$

Where:

$$\beta = 1 + K \frac{M_u u}{V_u W_1}$$

V_u = applied shear force

M_u = applied unbalanced moment

$u = 2c_x + 2c_y + 4\pi d$ = the perimeter of rectangular column critical section

d = the effective depth

K = coefficient dependent on ratio between column dimensions, c_x and c_y (can be obtained from EC2 Table 6.1)

W_1 = corresponds to distribution of shear stress

Where for rectangular column,

$$W_1 = \frac{{c_x}^2}{2} + c_x c_y + 4c_y d + 16d^2 + 2\pi d c_x$$

c_x, c_y = sides of column parallel and perpendicular to the unbalanced moment, respectively

2.3.2 Plastic Model

2.3.2.1 Beam Analogy Model

The first theoretical beam approach was introduced by Andersson[6] who made three tests in which Andersson reported that the criterion of failure in interior columns is the attainment of a limiting tangential compressive stress on the bottom surface of the concrete. However, this model is only done for concentric loading. Further considerations using beam analogy method have been proposed by a number of authors including Hawkins & Corley[34].

Hawkins & Corley[34] proposed in the beam analogy method to assume the area of the slab-column junction as four beams framing into the column faces as shown in Figure 2.18. Each section is assumed to have the combined effects of bending, shear and torsion and the resistance towards those combined effects can be calculated using standard method. In any cases where the applied shear or moment is greater than the ultimate capacity of one of the beams, some portion of the applied shear or moment is believed to be supported by the adjacent beam. A failure can only be considered when at least three of the four beams failed. Two possible modes of failure were recognized from the different possible combinations of bending, shear and torsional moments formed at failure: moment-torsion and shear-torsion as shown in Figure 2.19.

In 1976, Islam & Park[38] introduced a modified beam analogy method in which it became simpler and easier to be applied upon interior column slab connections. As shown in Figure 2.20 the internal actions were being redistributed from Hawkins' & Corley's model[34] in terms of bending, shear and torsion. The strength of the connection is obtained by summing the flexural, shear and torsional capacity of all acting beams.

2.4 Punching at Edge Column

2.4.1 Elastic Model

2.4.1.1 Linear Distribution of Stress

Di Stasio and Van Buren[17] applied the similar method as the method used to find the effect of eccentric loading as described in Section 2.3.1.1, to investigate the punching shear strength of exterior slab-column connections subjected to moment transfer perpendicular to the free edge of the slab. Most of the experimental variables such as position and size of the critical section remained the same as the eccentric punching shear model except that the critical section was now three-sided instead of four-sided to simulate the situation of edge connections, as shown in Figure 2.21.

A similar set of equation is used to estimate the shear stresses at the critical section for edge punching mechanism:

$$v = \frac{8h}{7d}\left[\frac{V}{A_c} + \frac{(M - m_{AB} - m_{CD})C_A}{J_C}\right] \qquad \text{(Eq. 2.43)}$$

Where:

V = punching shear resistance due to vertical load

M = unbalanced moment transferred from the vertical load

m_{AB} , m_{CD} = flexural moments on sides AB and CD of the critical section respectively

h = overall thickness of the slab

d = the effective depth

A_c = the area of the critical section

J_C = the polar moment of inertia of the critical section about its centroid

C_A = the distance from centroid to the end of the critical section

2.4.1.2 Regan's Approach

Along with Regan's eccentric punching model, Regan[67] proposed an elastic model to identify the local strengths of connections with edge columns with moments perpendicular to the slab edge.

As shown in Figure 2.22, Regan proposed an extreme case of an edge column-slab connection as a condition in which the slab contacts only the inner face of the column. A moment about the center of the column is produced by the presence of shear at the face, except that the distribution of shear is unaffected by the transferred moment. Based on the similar fracture surface in Figure 2.22, Regan presented the limiting shear force as:

$$V_u = d\sqrt{1+\cot^2\theta}\,(c_2 + 0.5\pi d\cot\theta)\sigma_{vu} \qquad \text{(Eq. 2.44)}$$

Where:

d = the effective depth

c_2 = side of the inner face of the column

$\sigma_{vu} = 0.13\varepsilon_s \sqrt[3]{\frac{100A_S}{bd}} * f_{cu}$ = the concrete compressive strength

At the failure stage, the ultimate moment, M_u about the centre of the column is presented as the total of the flexural moment, M_f resisted from the flexural reinforcement passing through the column face and anchored on both sides of the faces, and a moment produced from the shear force, V times the lever arm, ${}^{c_1}/_2$, as shown in following equation:

$$M_u = M_f + V\frac{c_1}{2} \quad \text{(Eq. 2.45)}$$

For edge punching shear mechanism, the slab is usually connected with three column faces, the maximum moment produced from flexural reinforcement, M_f is generated from the reinforcement bars crossing the inner face of the columns and the two local yield lines passing from the inner corners to the edge of the slab, as illustrated in Figure 2.23:

From this model, Regan[67] was able to classify the punching shear mechanism of an edge slab-column connection into three different cases:

Case 1: In scenario where the ultimate moment, M_u is greater than the total of the flexural moment, M_f and the moment produced from the shear force, V times the lever arm, ${}^{c_1}/_{2}$, two yield lines will be formed shaping a triangular zones and there will be no shear acting within these triangular zones and the cracking pattern is in the torsional direction as shown in Figure 2.24(a).

Case 2: In scenario where the ultimate moment, M_u is equal or smaller than the total of the flexural moment, M_f and the moment produced from the shear force, V times the lever arm, ${}^{c_1}/_{2}$, shear is distributed in a more uniformly manner, but it will only happen if diagonal yield lines are not formed. This condition is being visualized in Figure 2.24(b).

Case 3: In scenario where the ultimate moment, M_u is smaller than the total of the flexural moment, M_f, the connection behave largely as a pair of beams framing into the side of column faces and mainly subjected to bending shear and torsion. This condition is being visualized in Figure 2.24(c).

Regan[67] added that the approach above seems to give good prediction of ultimate resistance but is rather complex to be of general use. Regan then proposed a simplified equation to predict the edge punching shear under the effect of moment transfer perpendicular to the slab edge as:

$$V \leq 0.80V_2 \tag{Eq. 2.46}$$

$$M \leq M_{f1}+M_{c2}\frac{V}{V_2} \tag{Eq. 2.47}$$

Where:

M_{f1} = the flexural moment of flexural reinforcement from Case 1

V_2 = the shear capacity from Case 2

M_{c2} = the shear moment acting on the inner face from Case 2

The two general equations above has an advantage of being applicable for all column shapes and is very compatible for estimating the punching shear capacity for corner slab-column connection which will be discussed in the following section.

2.4.1.3 Building Codes

The current building codes of practice[1,14,22] adopted the control surface approach to design against edge punching shear. However, the design procedure of each code differs in terms of the location of the critical section, the derivations of concrete shear strength and the effect of moment transfer. In this section, the American Code ACI 318-11[1], the British Standard BS8110[14] and the European Code EC2[22] are reviewed.

2.4.1.3.1 ACI 308-11

For calculation, ACI 318[1] proposed two different methods for two different scenarios. Firstly, for an unbalanced moment transferred about an axis parallel to the edge of the slab, the distribution of shear stresses is assumed as shown in Figure 2.25. Figure 2.25 shows the unbalanced moment acting at the center of the critical section, M_s is calculated as $(M_u - V_u g)$ in which g is representing the distance from the center of the column to the center of the critical section. Therefore, the maximum shear stress in the slab may occur either at face AB or free edge CD (located totally opposite of each other) can be calculated using the equation:

$$v_{AB} = \frac{V_u}{b_0 d} + \frac{\gamma_v (M_u - V_u g) c_{AB}}{J_C} \qquad \text{(Eq. 2.48)}$$

$$v_{CD} = \frac{V_u}{b_0 d} - \frac{\gamma_v (M_u - V_u g) c_{CD}}{J_C} \qquad \text{(Eq. 2.49)}$$

For the other scenario, in cases where an unbalanced moment transferred about an axis perpendicular to the edge of the slab, the calculation for ultimate shear stresses are calculated as in the case of an interior connection.

On a side note, for unbalanced moment transfer about an axis parallel to the slab free edge at exterior support, ACI Code allows the fraction of unbalanced moment transferred by shear to be reduced to zero in cases where the V_u applied does not exceed $0.75V_c$. This means the unbalanced moment can be considered to produce no shear stresses.

2.4.1.3.2 BS8110

In cases for edge slab-column connections with unbalanced moment about an axis perpendicular to the free edge, BS8110[14] proposed the following equation.

$$v_c = V_t \left(1.25 + \frac{1.5 M_t}{V_t x}\right) \qquad \text{(Eq. 2.50)}$$

Where:

V_t = design shear force

M_t = design moment

x = the perimeter length of the critical section (parallel to axis of bending)

On the other hand, for edge slab-column connections with unbalanced moment about an axis parallel to the free edge and for corner slab-column connections, BS8110 proposed a simple expression independent to the eccentricity of the applied load:

$$v_c = 1.25V_t \quad \text{(Eq. 2.51)}$$

2.4.1.3.3 Eurocode 2

EC2[22] reported that in edge slab-column connections, when the unbalanced moment is about an axis parallel to the slab edge, the punching force is considered to be uniformly distributed along the critical section, u_{1*} as shown in Figure 2.26.

Therefore, the equation used to calculate the punching shear stress is proposed as follows:

$$v_f = \beta \frac{V_u}{ud} \quad \text{(Eq. 2.52)}$$

Where:

$$\beta = \frac{u}{u_{1*}} + k\frac{u}{W_1}e_{par}$$

u = the basic control perimeter

u_{1*} = the reduced basic control perimeter

k = coefficient dependent on ratio between column dimensions, $c_1/2c_2$ (can be obtained from EC2 Table 6.1)

e_{par}= eccentricity parallel to free slab edge due to moment about an axis perpendicular.

W_1 = corresponds to distribution of shear stress

Where for rectangular column,

$$W_1 = \frac{{c_2}^2}{4} + c_1 c_2 + 4c_1 d + 8d^2 + \pi d c_2$$

However, if the unbalanced moment is about an axis perpendicular to the slab edge, use

$$\beta = 1 + K\frac{M_u u}{V_u W_1} \qquad \text{(Eq. 2.53)}$$

2.4.2 Plastic Model

2.4.2.1 Beam Analogy

In 1971, Hawkins & Corley[34] explained further on beam analogy to estimate the punching shear capacity for edge column connection under the presence of unbalanced moment. In this analogy, the critical section is said to be positioned at $d/2$ from the column faces and is formed as a junction of three imaginary beams as shown in Figure 2.27. Any loads applied and moments transferred are assumed to be resisted by the components of these imaginary beams and in any cases where the applied loads are greater than the resistance of these imaginary beams, the excess loads would be redistributed onto the adjacent imaginary beams. Hawkins & Corley stated that two modes of failure exist within the edge column connections which are:

Moment torsion failure: the failure occurs when the flexural strength on the inner face of the critical section (BC) and the torsion strength on the side faces (AB and CD) are reached simultaneously

Shear torsion failure: the failure occurs when the shear strength on the inner face of the critical section (BC) and the torsion strength on the side faces (AB and CD) are reached simultaneously

Therefore, the modes of failure mainly depend on the type of failure that occurs on the inner face of the critical section (BC), deciding whether it is flexural failure or punching shear failure.

2.5 Punching of Waffle Slabs and Ribbed Slabs

2.5.1 Concentric Punching Shear

In 1993, Xiang[81] reported his investigation on 14 waffle slab specimens in the absence of any unbalanced moment transfer subjected to concentric punching shear. The main variables tested were the size of the solid section, the top slab thickness and the reinforcement ratio.

The results of the punching shear failure were divided into two types, obtained from the findings of the size of the solid section. The first observation was that specimens with a small solid section ($2.1h$ to $2.4h$) had their punching failure surface formed outside the solid region area, while specimens with a large solid area ($4h$ to $4.6h$) had their punching failure surface formed within the solid region area, as shown in Figure 2.28.

Xiang compared the test results to the predictions obtained using the BS8110 approach[14] and concluded that the BS8110 provide a good agreement to the test results with some minor changes being applied. These modifications involved the location and the section area of the control surface area. For waffle slabs with small solid section, the control surface is located at 1.5d from the edge of the solid area, and the cross sectional area of the control perimeter is taken into account in the punching shear calculations. For waffle slabs with large solid section, in which the failures take place within the solid area, the control surface area is same as that in BS8110, which is located at 1.5d from the column faces, with a reduction factor of 0.9 used in calculating the punching shear strength. Xiang proposed equations of the models as shown below.

For slab with small solid section,

$$v_c = \frac{V_u}{A_w} \qquad \text{(Eq. 2.54)}$$

Where:

V_u = the ultimate shear force

v_c= the shear strength, to be determined from Eq. 2.14

A_w=the section area of waffle slab

For slab with large solid section,

$$v_c = \frac{V_u}{0.9(4c+12d)d} \qquad \text{(Eq. 2.55)}$$

Where:

V_u = the ultimate shear force

v_c= the shear strength, to be determined from Eq. 2.14

c = the column size

d = the effective depth

Both Eq. 2.54 and Eq. 2.55 have achieved good agreement with the test results[81]. The mean ratios of test to estimated strength of Eq. 2.54 and Eq. 2.55 were 0.99 and 0.97, respectively.

Xiang reported that the punching shear failure surface of a waffle slab is an inclined surface instead of the vertical surface adopted in the control surface approach. Therefore, when the solid section is not large enough, the failure surface would occur into the waffle section, leading to some shear area of the failure surface would be lost. Based on these findings, Xiang applied a factor of 0.9 to the waffle slabs with a large solid section and changing the solid slab section area to the actual waffle slab section area for waffle slabs with small solid section.

In 2004, Lau[46,47] reported experimental testing that had been carried out on 12 1/10th ribbed slab specimens subjected to the internal punching mechanism of ribbed slabs in the absence of any unbalanced moment transfer. The main variables in this experiment were the concrete strength, the top slab thickness, the column shape, and the column size.

Lau explained that when punching occurred, the column was pushed into the slab leading to the internal cracks propagated from the column faces through the slab thickness at about 22 degrees and intersected with the slab top surface at a distance of $2.5h$. However, observations showed that when the width of the wide beam is less than $5h$, an incomplete revolution was formed with lower punching capacity and the reason for that was due to the loss of shear failure surface.

Lau then proposed a design model to predict the concentric punching shear strength of ribbed slab. This model is based on modifications made towards BS8110[14]. The location of the critical perimeter remains unchanged at $1.5d$ from the column faces, but the critical shear areas are reduced depending on the width of the wide beam and top slab thickness of the ribbed slab. Thus, an effective shear area factor, γ, is introduced.

$$V_u = v_c \alpha\, u\, d \qquad \text{(Eq. 2.56)}$$

Where:

V_u = the ultimate shear force

v_c= the shear strength, to be determined from Eq. 2.14

α = the shear retention factor, 0.7 for micro-concrete and 1.0 for normal concrete

u = the perimeter of the critical section,

$$u = 2(c_x + 3d\gamma_x) + 2(c_y + 3d\gamma_y)$$

$c_x,\ c_y$ =sizes of column

$\gamma_x,\ \gamma_y$ = the effective shear area factor,

$$\gamma_x = 1 - \frac{a_{x2}d_2}{a_x d}$$

$$\gamma_y = 1 - \frac{a_{y2}d_2}{a_y d}$$

$a_x,\ a_y$ =the shear span in x and y directions, respectively, and is $\leq 2.6d$

$a_{x2},\ a_{y2}\,, d_2$ =as defined in Figure 2.29

d = the effective depth

Eq. 2.56 has achieved good agreement with the test results[46,47]. The mean ratio of test to estimated strength was 0.99.

In 2013, Al-Bayati[3,4] reported experimental testing that had been carried out on 15 1/10th scale waffle slab specimens regarding to the internal punching mechanism of waffle slabs in the absence of any unbalanced moment transfer. The main variables in this experiment were the size of the solid section, the column shape and size, and the concrete compressive strength.

Al-Bayati described the failure as shear cracks propagated from the column faces through the slab thickness at about 22 degrees and intersected with the slab top surface at a distance of $2.5h$. However, differing from solid flat slab, an incomplete surface of revolution was observed when entering the waffle section. Al-Bayati also reported that the punching capacities increase with the area of solid section and the column sizes, with circular columns being stronger than square columns.

Al-Bayati then proposed a design model to predict the concentric punching shear strength of waffle slab. This model is based on modifications made towards EC2[21]. The location of the critical perimeter remains unchanged at $2d$ from the column faces, but the critical shear areas are reduced depending on the size of the solid section and top slab thickness of the waffle slab. Thus, a depth retention factor, φ, is introduced.

$$P_u = v_c \alpha \, u_{waffle(conc)} \, d \qquad \text{(Eq. 2.57)}$$

Where:

P_u = the ultimate shear force

v_c= the shear strength, to be determined from Eq. 2.16

α = the shear retention factor, 0.7 for micro-concrete and 1.0 for normal concrete

$u_{waffle(con)}$ = the perimeter of the critical section

$$u_{waffle(con)} = \left(c_x\varphi_x + c_y\varphi_y + 4\pi\varphi_{avg}\right)$$

$c_x,\ c_y$ = sizes of a column

$\varphi_x,\ \varphi_y$ = the depth retention factor

$$\varphi_x = 1 - \left[\left(\frac{a_{x2}d_2}{a_x d}\right)\left(\frac{\sum w}{B_x}\right)\right]$$

$$\varphi_y = 1 - \left[\left(\frac{a_{y2}d_2}{a_y d}\right)\left(\frac{\sum w}{B_y}\right)\right]$$

$a_x,\ a_y$ =the shear span in x and y directions, respectively, and is $\leq 2.6d$

$a_{x2},\ a_{y2}, d_2$ =as defined in Figure 2.30

$B_x,\ B_y$ = the side of the solid section in x and y directions, respectively

w = the size of waffle perpendicular to the solid section

d = the effective depth

$$\varphi_{avg} = \frac{\varphi_x + \varphi_y}{2}$$

Eq. 2.57 has achieved good agreement with the test results[3,4]. The mean ratio of test to estimated strength was 1.00.

2.5.2 Eccentric Punching Shear

Al-Bayati[4] in 2013 reported experimental testing that had been carried out on 6 1/10th scale waffle slab specimens regarding the internal punching mechanism of waffle slabs in the presence of unbalanced moment transfer. The main variables in the experiment were the size of the solid section and the column eccentricity.

It is observed that the punching failure surface is dependent on the ratio of column eccentricity, e to the column size, c_x. The punching shear capacity of waffle slabs is reported to be inversely dependent on the column's eccentricity and that it increases as the size of the solid section increases.

Al-Bayati proposed a design model to predict the eccentric punching shear strength of waffle slab. This model is done quite similarly to concentric model. The location of the critical perimeter remains unchanged at $2d$ from the column faces along with the concrete shear strength. As introduced in the concentric model earlier, the depth retention factor, φ, is again used to represent the lost shear area of the incomplete failure surface of the waffle slab onto the shear surface of the critical section.

$$P_u = v_c \alpha \, u_{waffle(eccen)} \, d \qquad \text{(Eq. 2.58)}$$

Where:

P_u = the ultimate shear force

v_c= the shear strength, to be determined from Eq. 2.16

α = the shear retention factor, 0.7 for micro-concrete and 1.0 for normal concrete

$u_{waffle(eccen)}$ = the perimeter of the critical section, as obtained from $u_{waffle(con)}$ in Eq. 2.57

d = the effective deptH

Eq. 2.58 has achieved good agreement with the test results[4]. The mean ratio of test to estimated strength was 1.04

2.5.3 Edge Punching Shear

In 1994, Hussein[37] reported test results of 18 waffle slab specimens regarding the edge punching mechanism of waffle slabs in the presence of moment transfer perpendicular to the slab. The main variables in the experiment were the ribs width at free edge, the column's eccentricity and the reinforcement ratio.

The test results showed that there is an increase in the ultimate capacity with an increase in the rib width, while the ultimate capacity decreases as the load eccentricity increases. The failure mechanism was shown by all specimens in that inclined shear cracks propagated from the faces of the solid section towards the support. From the experimental results, Hussein reported that the critical section is located at a distance of $1.5d$ from the faces of the solid section, and the cross sectional area of the control perimeter is taken into account in the punching shear calculations. The proposed model has shear strength similar to as proposed by BS8110[14]. The proposed equation to compute the punching shear strength of waffle slab at the edge column in the present of moment transfer perpendicular to the slab free edge is shown below.

$$V_u = A_w v_c \alpha \qquad \text{(Eq. 2.59)}$$

Where:

V_u = the ultimate shear force

v_c= the shear strength, to be determined from Eq. 2.14

A_w=the section area of waffle slab

α = the moment reduction factor, $\alpha = \frac{1}{1.5+\left(\frac{1.5e}{S+3d}\right)}$

e = the moment eccentricity, $e = \frac{M}{V}$

S = the width of solid section

d = the effective depth

Eq. 2.59 has achieved good agreement with the test results[37]. The proposed method achieved a mean test to prediction ratio of 0.997.

In 2004, Lau[45,47] reported experimental testing that had been carried out on 6 1/10th ribbed slab specimens subjected to the edge punching mechanism of ribbed slabs in the presence of moment transfer perpendicular to the slab. The main variables in this experiment were the size of the column and the location of the column from the slab free edge.

Lau explained that when punching occurred, the internal shear cracks propagated from the column faces inner-corner regions through the slab thickness at about 22 degrees and intersected with the slab top surface at a distance of $2.5h$. However, observations showed that when the width of the wide beam is small, an incomplete revolution was formed with lower punching capacity and the reason for that was due to the loss of shear failure surface. Lau also reported that the punching capacities increases with the column size and decreases with an increase in the column eccentricity.

Lau then proposed a design model to predict the edge punching shear strength of ribbed slab in the presence of moment transfer. This model is based on modifications made towards BS8110[14]. The critical shear area within the column width is not altered. The model is as shown below:

$$V_u = \frac{1}{1.25} v_c \alpha \, u \, d \qquad \text{(Eq. 2.60)}$$

Where:

V_u = the ultimate shear force

v_c= the shear strength, to be determined from Eq. 2.14

α = the shear retention factor, 0.7 for micro-concrete and 1.0 for normal concrete

u = the perimeter of the critical section,

$$u = (c_x + 3d\gamma_x) + 2(c_y + 1.5d\gamma_y + a_{\gamma 4})$$

$c_x,\ c_y$ =sizes of a column

$\gamma_x,\ \gamma_y$ = the effective shear area factor,

$$\gamma_x = 1 - \frac{a_{x2}d_2}{a_x d}$$

$$\gamma_y = 1 - \frac{a_{y2}d_2}{a_y d}$$

$a_{\gamma 4}$ =the edge beam width as defined in Figure 2.31

d = the effective depth

Eq. 2.60 shows that the model is being more conservative with the test results[45,47], which is as expected. The mean ratio of test to estimated strength was 1.48.

In 2013, Al-Bayati[4] reported experimental testing that had been carried out on 11 1/10th scale waffle slab specimens regarding to the edge punching mechanism of waffle slabs in the presence of moment transfer. Al-Bayati further divided into two series which were, 6 waffle slabs were tested in a perpendicular manner to the slab edge, while the remaining 5 waffle slabs were tested in a parallel manner to the slab edge. The main variables in this experiment were the size of the solid section and the column's eccentricity.

Al-Bayati also reported that the punching shear capacities increase with the area of solid section and that the punching shear capacities are inversely related to the column's eccentricity. Al-Bayati then proposed a design model to predict the edge punching shear strength of waffle slab in the presence of moment transfer perpendicular or parallel to the free edge. This model is based on modifications made towards EC2[22]. The location of the critical perimeter remains unchanged at $2d$ from the column faces and the concrete shear strength are retained. As introduced in the concentric and eccentric models earlier, the depth retention factor, φ, is again used to represent the lost shear area of the incomplete failure surface of the waffle slab onto the shear surface of the critical section.

For the punching shear capacity of waffle slab in the presence of moment transfer perpendicular to the slab free edge,

$$P_{u\perp} = v_c \alpha \, u_{waffle(edge)} \, d \qquad \text{(Eq. 2.61)}$$

Where:

P_u = the ultimate shear force

v_c= the shear strength, to be determined from Eq. 2.16

α = the shear retention factor, 0.7 for micro-concrete and 1.0 for normal concrete

$u_{waffle(edge)}$ = the perimeter of the critical section

$$u_{waffle(edge)} = \left(c_x\varphi_y + c_y\varphi_x + 2\pi\varphi_{avg}\right)$$

d = the effective depth

For the punching shear capacity of waffle slab in the presence of moment transfer parallel to the slab free edge,

$$P_{u\parallel} = \frac{1}{\beta} v_c \alpha \, u_{waffle(edge)} \, d \qquad \text{(Eq. 2.62)}$$

Where:

P_u = the ultimate shear force

v_c= the shear strength, to be determined from Eq. 2.16

β = the moment transfer factor, to be determined from Eq. 2.42

α = the shear retention factor, 0.7 for micro-concrete and 1.0 for normal concrete

$u_{waffle(edge)}$ = the perimeter of the critical section

d = the effective depth

Eq. 2.61 and Eq. 2.62 has achieved good agreement with the test results[4]. The proposed method achieved a mean test to prediction ratio of 0.95.

2.6 Size Effects

The size effect has always been a problem of scaling for every physical theory. This issue is indifferent in concrete structures as well, for which there is a large gap between the scales of large structures (e.g. dams, bridges) and of laboratory scaled-down tests. This gap involves in such structures about one order of magnitude and even when a full-scale test is carried out, it is impossible to obtain a sufficient statistical basis on the full scale.

Since the tests carried out in this study are one order of magnitude lower (1/10th scale micro-concrete specimen), it is important to understand the size effect on the concrete strength in terms of compression, tension and shear.

2.6.1 Size effect in compressive strength tests

In 1925, Gonnerman[29] experimentally showed that the ratio of the compressive failure stress to the concrete compressive strength decreases as the specimen size increase. Gonnerman conducted an investigation into the compressive strength of different size cylinders, while varying other variables such as curing age, cement-aggregate ratio, relative consistency and the aggregate fineness in the tests, as shown in Figure 2.32.

Gonnerman's research prompted many other researchers to study the size effect in compressive strength tests, in which some of the worthy mentions are listed as follows.

In 1963, Harris et al.[32] experimented on a series of model cylinder test to investigate the effect of size on the compressive strength at different curing ages. Harris et al. reported that smaller specimens have higher compressive strength mainly due to the differential curing rates, differential drying and differences in quality of material. Smaller specimens have a larger surface area to volume ratio, which allow them to have a shorter moisture migration path, therefore prompting better curing and drying rates. The quality of material differs in that smaller specimens are generally better compacted, hence, having a higher density and higher compressive strength, as pointed out by Popovics[64].

Neville[55] in 1966 conducted a statistical study for the size effects in concrete compressive strength using results from previous researchers. Neville's main concerns on the effect of size were the type of concretes, curing method and the age of the specimen during testing. Neville found that the size effect to be a function of the volume of the specimen, the maximum lateral dimension and the height to lateral dimension ratio. Hence, a relationship was developed using regression analysis:

$$\frac{P}{P_6} = 0.56 + 0.697\frac{d}{\left(\frac{V}{6h}\right)+h} \qquad \text{(Eq. 2.63)}$$

Where:

P = predicted concrete cube strength of the specimen

P_6 = concrete cube strength of a 6-inch cube

d = maximum lateral dimension of the specimen

V = volume of the specimen

h = height of the specimen

Neville[55] also highlighted that factors such as the modulus of elasticity of the aggregate, Poisson's ratio, aggregate-cement ratio were ignored due to limitation of data, but the relationship still managed to achieve good agreement with the test results, as shown in Figure 2.33.

In 1967, Endersbee[21] commented that the behaviour of concrete in compression is similar to any other quasi-brittle materials, in which the compressive strength of concrete is inversely related to the specimen size. Thus, in a discussion on the paper of William and Mario[79], Endersbee[21] suggested that the relationship between the relative strength and the relative linear dimensions of the specimens is as shown in Figure 2.34. From this suggestion, Endersbee proposed that the concrete strength is a function of the size specimens, as indicated in the equation below:

$$Concrete\ strength = (Specimen\ size)^{-0.106} \qquad \text{(Eq. 2.64)}$$

In 1964, Pahl & Soosaar[60] reported that both concrete and mortar are fairly brittle materials, which explained that failure at a few points will contribute to an overall collapse in the specimen and agreed by Sabnis[70]. Pahl & Soosaar found that smaller specimen has fewer points as compared to larger specimen, where failure can initiate, therefore, the strength of the smaller specimens on the average re higher than that of the larger specimens. Pahl & Soosaar[60] suggested that the size effect can be represented by the following equation, in the function of the volume of specimen.

$$f = a + bV^{-c} \qquad \text{(Eq. 2.65)}$$

Where:

f = compressive strength of concrete

V = volume of concrete specimen

a, b, c = positive constants depending on concrete mix

2.6.2 Size effects on concrete tensile strength

The concrete tensile strength is another fundamental property which carries great influence in the characteristics of reinforced concrete specimens. As observed by many researchers[58,69,80], the specimen size has a prominent effect on the concrete tensile strength, as illustrated in Figure 2.35.

As reported by Kadlecek et al.[41] in 2002, a mathematical statistical methods on 1600 results from previous researchers was conducted by finding the relationship between concrete tensile strength and the size of the corresponding fracture area or the size of the highly stressed volume in the loaded cross-section. From the analysis of 1600 test results, Kadlecek et al. reported that the tensile strength of concrete is dependent on the specimen size, in which, the mutual correlation between both quantities can be represented by an exponential function, as follows: (see Figure 2.36)

$$f_t = aV^{-b} \tag{Eq. 2.66}$$

Where:

f_t= tensile strength of concrete

V = volume of concrete specimen

a, b= constants for best fit data

2.6.3 Size effects on concrete shear strength

In 1966 and 1967, Kani[42] first confirmed the effect of size specimen on the shear strength of RC beam upon the shear failure of RC members at a warehouse located on Wilkins Air Force Depot in Ohio, USA in 1955. Kani investigated on three main variables, which are the depth of the beam, longitudinal steel ratio and shear span-to-depth ratio, in which test results showed an increase in the depth of the beam by 400% decreases the concrete shear strength by 40%. Kani also found that there is transition point, when the shear span-to-depth ratio of about 2.5, at which the RC beams become vulnerable to shear failures.

Bazant & Kim[9] in 1984 proposed a shear strength equation based on non-linear fracture mechanics (see Figure 2.37), where the equation accounts the size effect phenomenon with the longitudinal steel ratio and incorporates the effect of aggregate size, which is as follows:

$$v = \frac{10\sqrt[3]{\rho}}{\sqrt{1+d/25d_o}}\left(\sqrt{\sigma_c} + 3000\sqrt{\frac{\rho}{\left(\frac{a}{d}\right)^5}}\right) \qquad \text{(Eq. 2.67)}$$

Where:

v = concrete shear strength

ρ = longitudinal steel ratio

d = depth of specimen

d_o = aggregate size

σ_c = cylindrical compressive strength

a = shear span

Bazant & Kim's equation gained confidence over 295 previous test results and added that the size effect was mainly due to the strain energy released from the beam being dispersed into the cracking zone as the cracking zone increases.

In 1987, Bazant & Cao[8] investigated the effect of size specimen on the punching shear capacity of reinforced concrete slab. Bazant & Cao found that the nominal shear stress at failure is not constant, as assumed by design codes, but instead it decreases as the slab size increases. The application of size effect law in the improved design formula proved the presence of size effect in punching shear strength. The use of size effect law is further validated by the measurements on deflection diagrams, in which agrees that the post-peak load declines much faster as the slab size increases, as illustrated in Figure 2.38.

2.6.4 Aggregate size effects on concrete shear strength

In 1981, Boswell & Wong[11] conducted shear tests on Mattock[51] type push-off specimen (see Figure 2.39) in order to investigate the effects of aggregate size on concrete shear strength.

From the test results, it was obvious that the peak shear stress is independent of the aggregates size but the residual shear stress is dependent of the aggregate size. That is, when the shear displacement increases, the shear resistance of concrete cast with 2 mm aggregates reduces to a mean residual value of about 70% of its peak, while the shear resistance of concrete cast with 20 mm and 10 mm aggregates remained at their peak, as illustrated in Figure 2.40. Boswell & Wong explained that this may be due to the less surface roughness provided by the 2 mm aggregates in comparison with the 20 mm and 10 mm aggregates.

2.7 Behaviour of micro-concrete in punching shear failure

The use of scaled specimens have become increasing popular owing to their economic benefits and ease of handling specimens, in the exploration of punching behaviour of ribbed slabs and waffle slabs. However, attention should be provided to maintain the section similitude using small size reinforcements and micro-concrete cast with scaled aggregates.

Swamy & Falih[75] investigated the behaviour of micro-concrete slab specimens in punching. A total of nineteen slab specimens was tested, which consisted of a full scale flat slab, six 1/3 scale flat slabs, six ¼ scale flat slabs and six 1/6 scale flat slabs. All scale specimens were reinforced with 3.25 mm diameter steel bars, crimpled and plain. Two specimens from each scale were cast from micro-concrete, with a maximum aggregate size of 2.36 mm and concrete using scaled aggregates, with a maximum of 6.7 mm and 2.36 mm, were used to cast one slab specimen of each of the aforementioned scales.

Swamy & Falih found that shear cracks were dominant on the tension side of the slab specimens and no crack was observed on the compression side of the slabs. Furthermore, the cracks were observed to be finer and increasing in numbers as the scale of the slabs increases. This is believed to be due to the lack of scaling the reinforcement bars. When they compared their test results with CP110[13], the comparisons revealed that CP110 overestimated the test results of specimens cast from micro-concrete by about 30% to 60%, despite taking into account the size effect in shear.

Similar behaviour of micro-concrete slab specimen in punching was observed[3,4,23,45,46,47]. Lau[45,46,47] conducted a laboratory testing on twenty-six ribbed slabs and during the comparison of test results with BS8110[14], Lau revealed that the ratio of test results to prediction from BS8110 is close to unity when a factor of 0.7 is applied during the prediction of ribbed slabs cast from micro-concrete.

In 2015, Al-Bayati[3,4] reported the behaviour of micro-concrete waffle slab specimens under concentric and eccentric loading. During the comparison of test results with ACI[1], Al-Bayati too agreed with Lau that a factor of 0.7 to be applied during the prediction of micro-concrete waffle slab specimens. This application of factor was found to be consistent regardless the slab specimens were loaded concentrically or eccentrically.

2.8 Summary

The current understanding about punching shear mechanisms has been focused on solid flat slabs and only a small amount of study has been carried out on waffle slabs. Based on the literature review gathered, these studies were limited to investigate the concentric punching shear mechanism, the eccentric punching shear mechanism, and the edge punching shear mechanism in the presence of perpendicular and parallel moment transfer to the slab free edge. Very few, or none studies were conducted to investigate the concentric punching shear mechanism in the presence of biaxial moment transfer and the edge punching mechanism in the presence of biaxial moment transfer. As a result, the design procedures for design against the punching shear mechanism for waffle slabs have not been covered as a whole in the present design codes. Therefore, it is considered that there is an importance in experimental investigation and theoretical study to enhance the current design requirements.

Based on the literature review conducted, the author has decided to use the fundamentals of plasticity approach to introduce a new theoretical model which can illustrate the punching failure mechanisms in waffle slabs at internal, and edge column connections, along with to develop the relevant design model based on EC2[22].

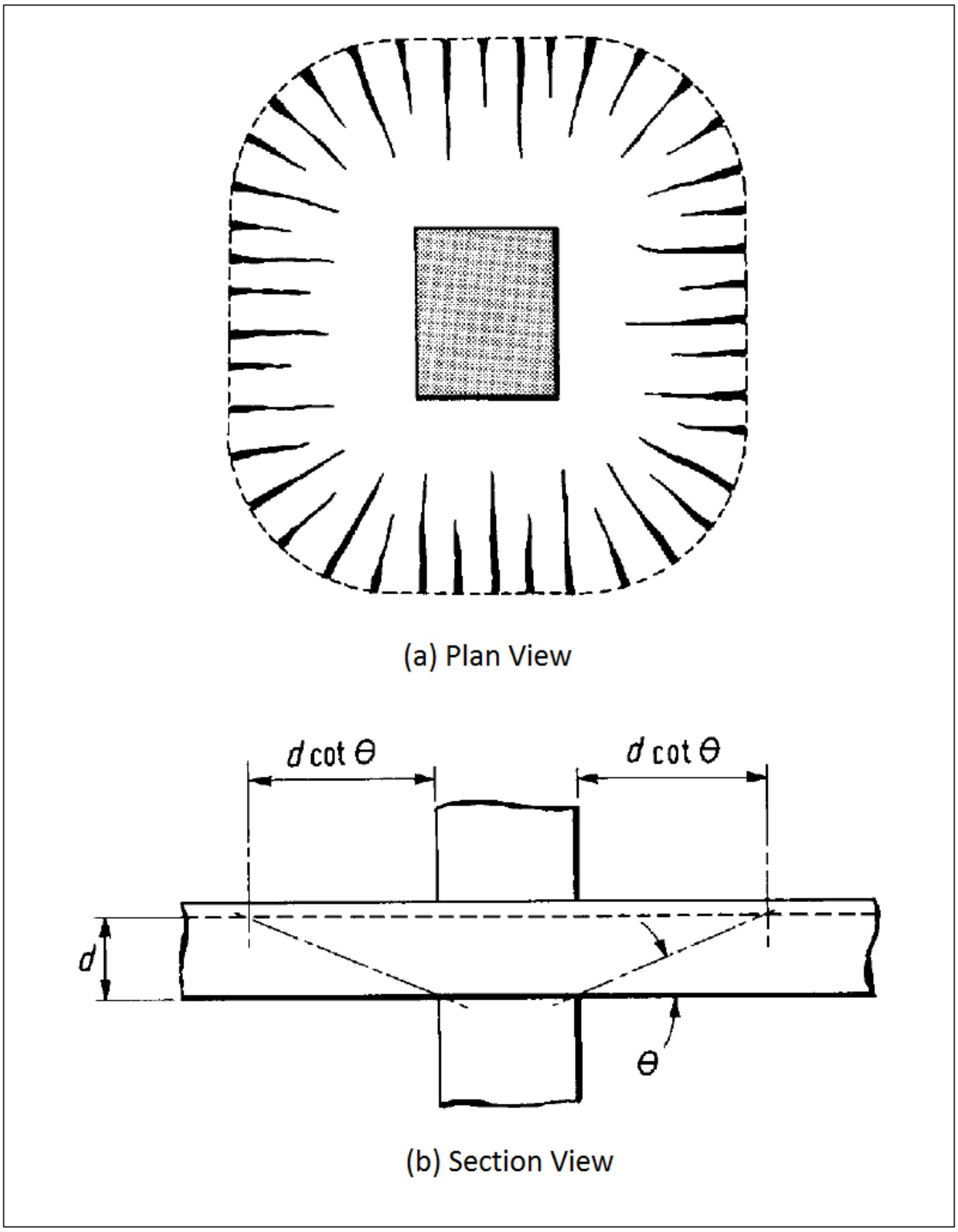

Figure 2.1 Regan's Fracture Surface Approach[67]

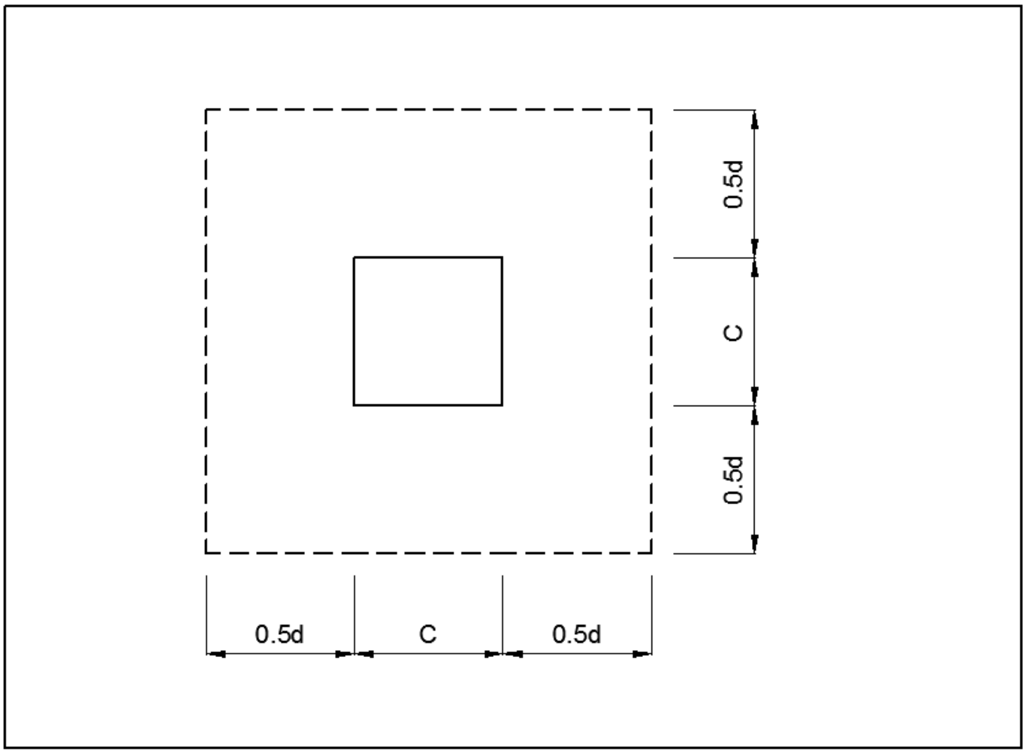

Figure 2.2 Critical Perimeter of ACI 318-11 for Internal Punching Mechanism[1]

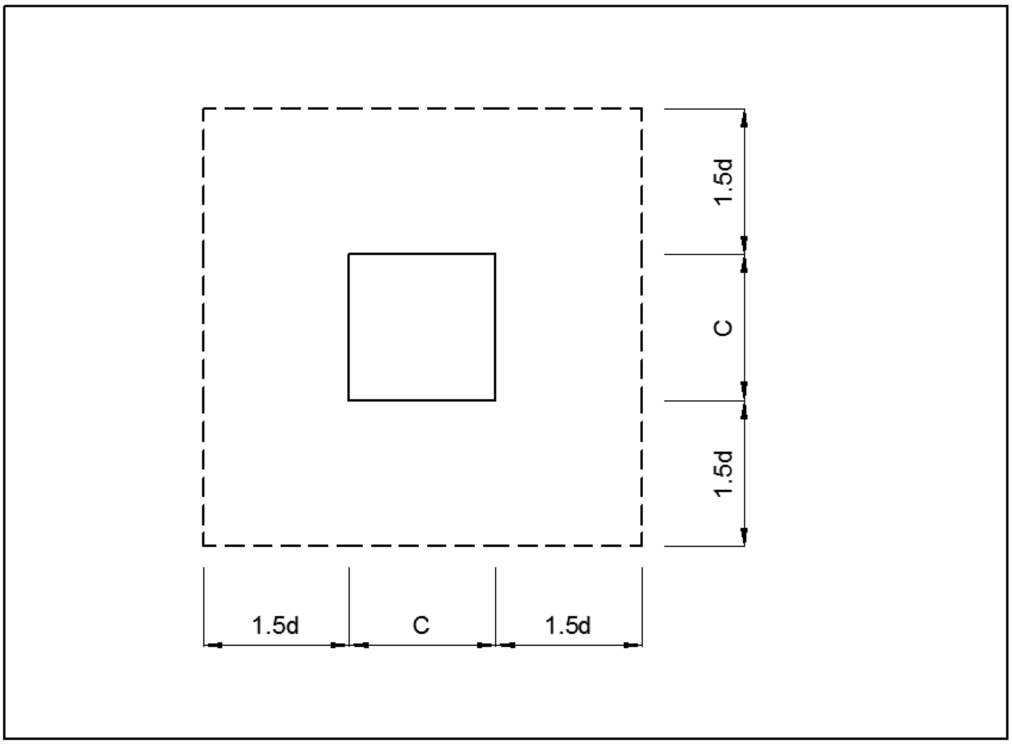

Figure 2.3 Critical Perimeter of BS8110 for Internal Punching Mechanism[14]

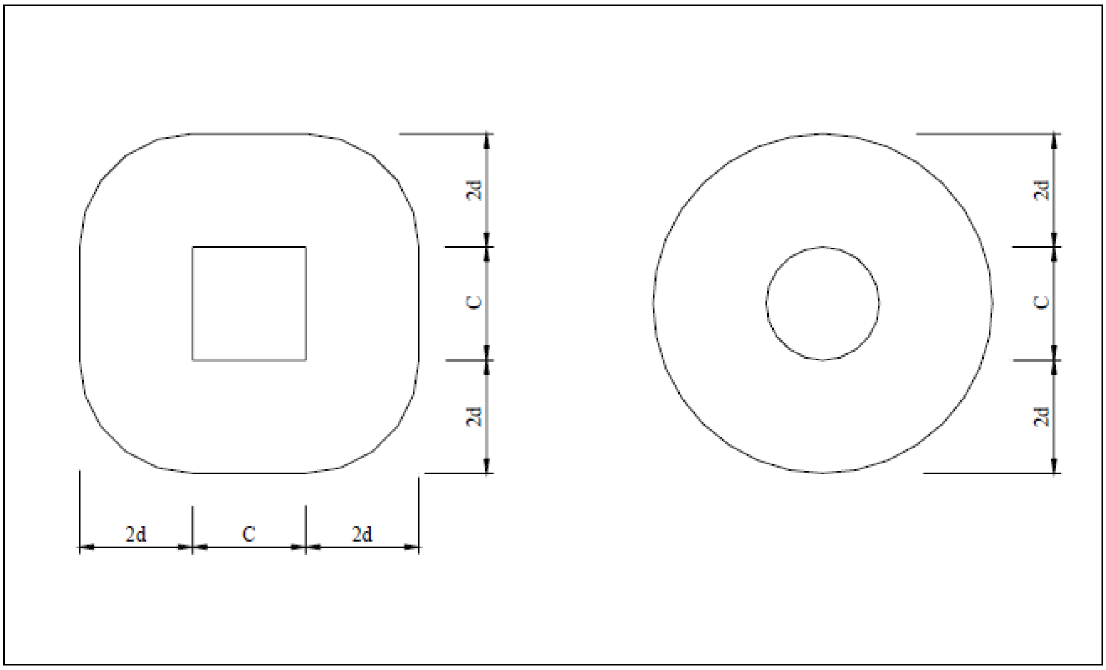

Figure 2.4 Critical Perimeter of EC2 for Internal Punching Mechanism[22]

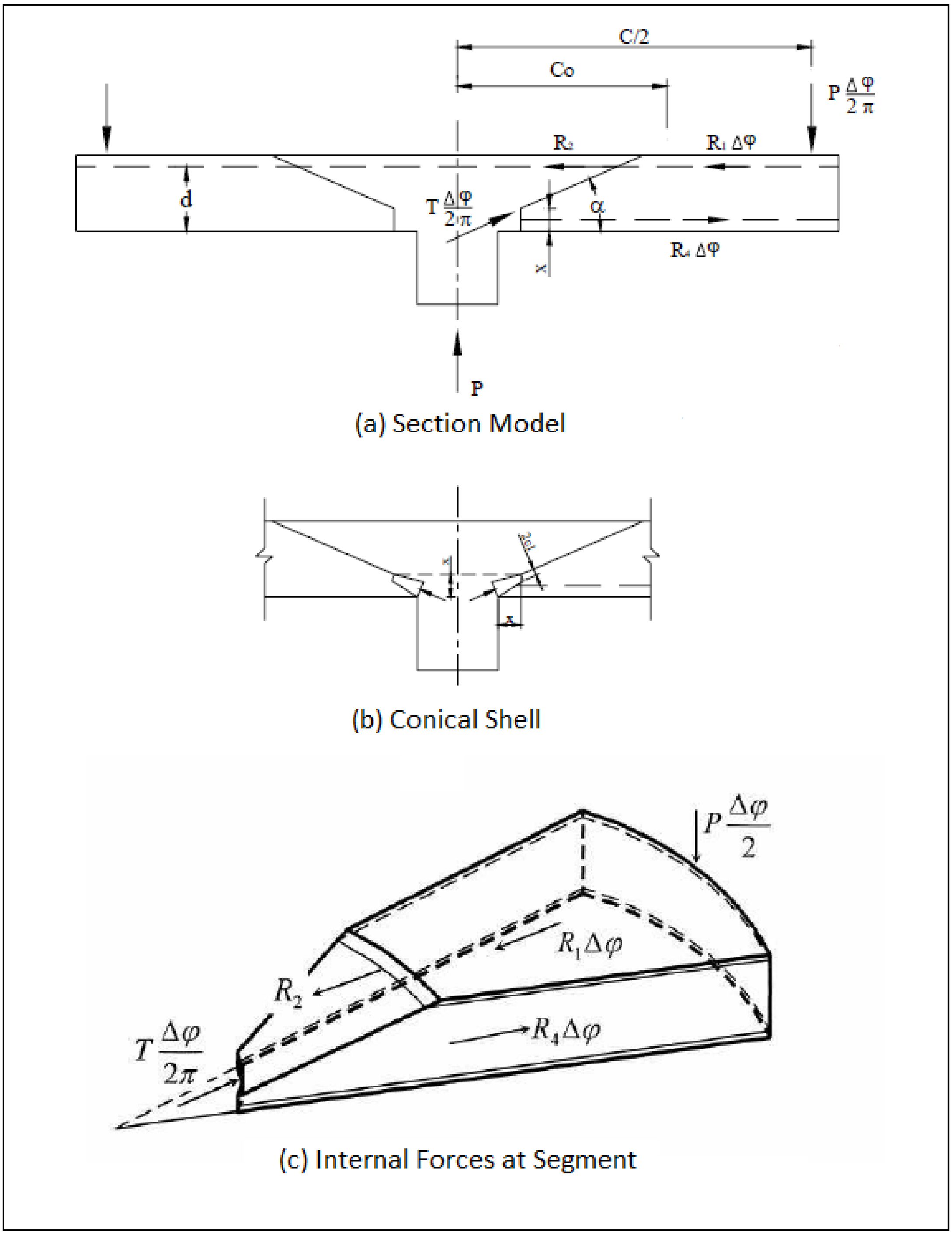

Figure 2.5 Mechanical Model (Kinnunen & Nylander[43])

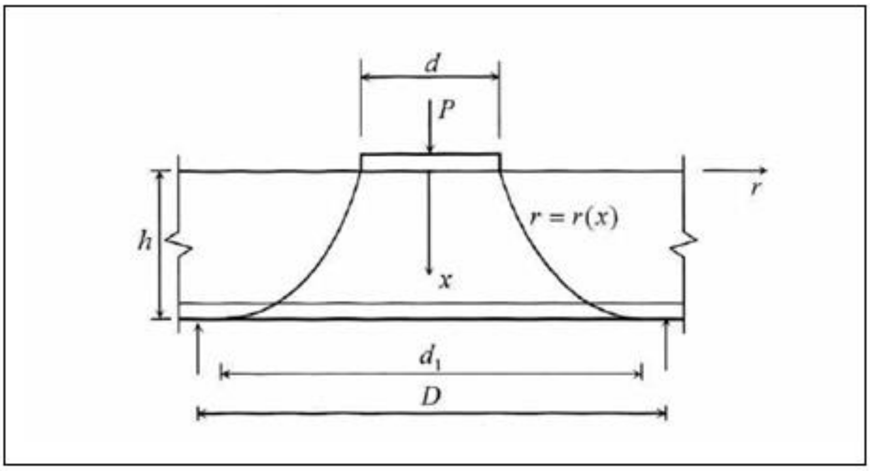

Figure 2.6 Plastic Model by Braestrup et al.[12]

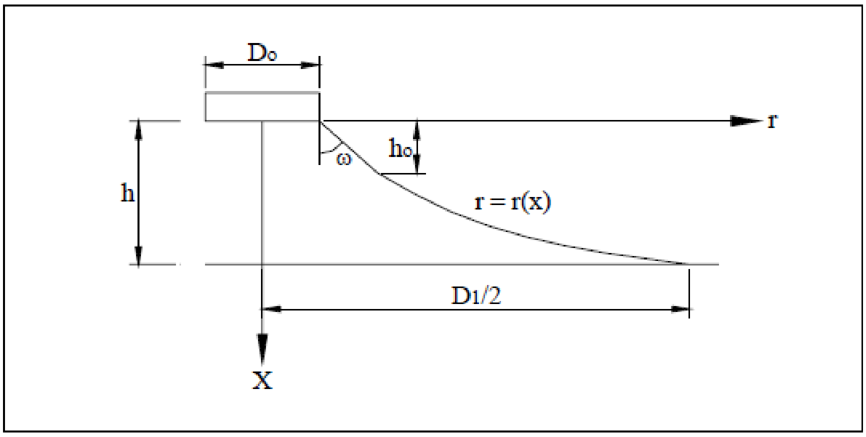

Figure 2.7 Plastic Model-Punching Failure Surface[12]

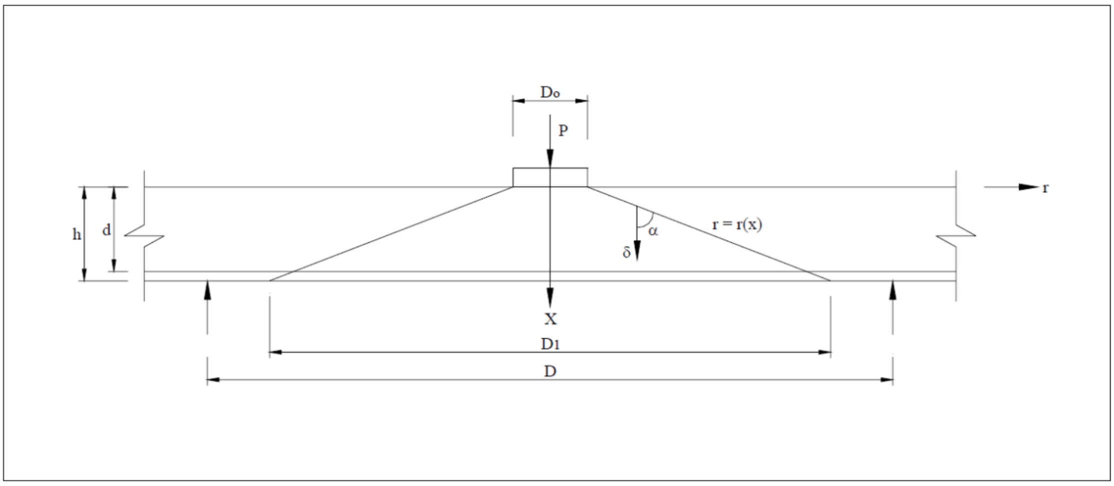

Figure 2.8 Simplified Plastic Model by Salim & Sebastian[71]

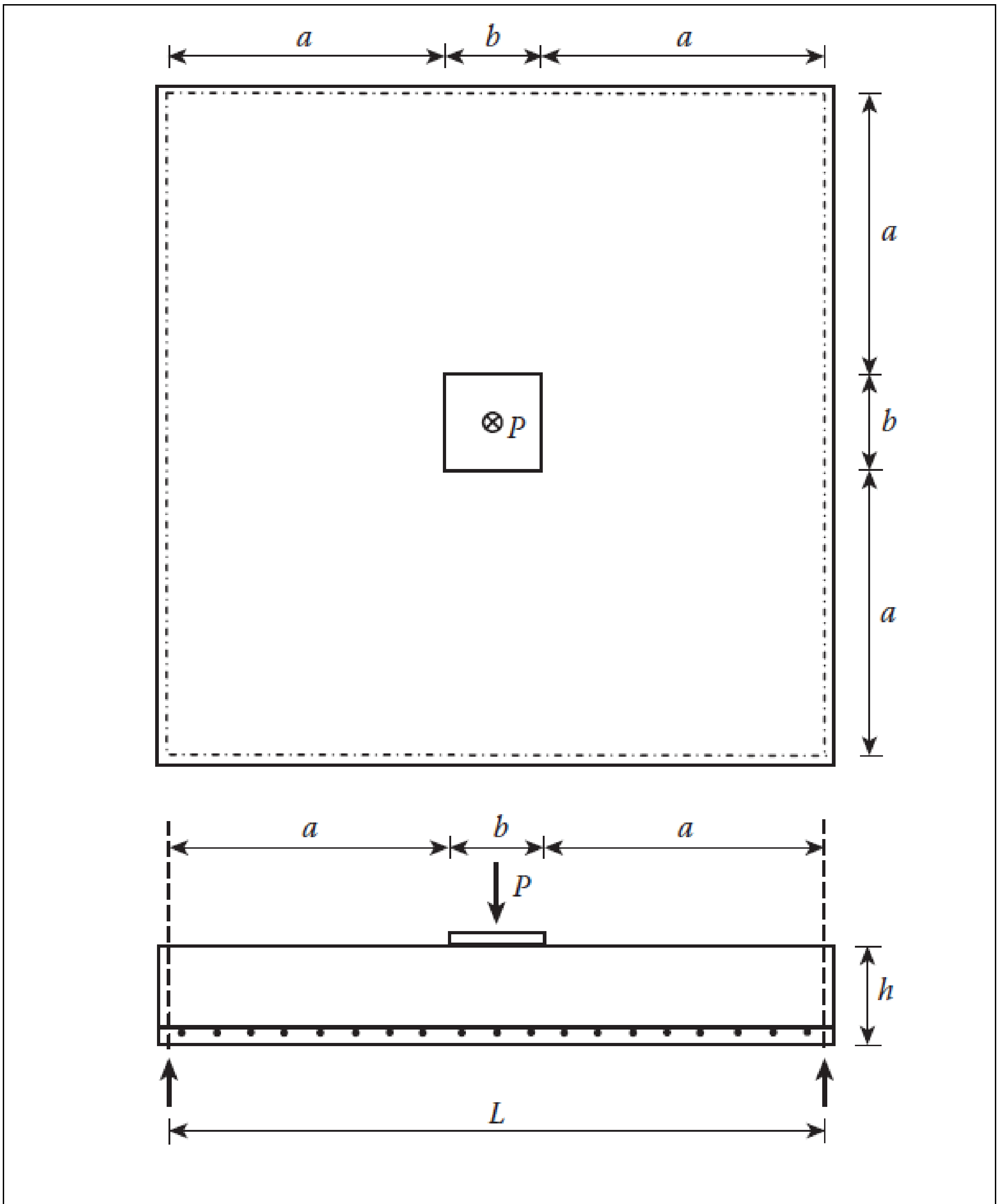

Figure 2.9 Square slab subjected to concentrated load, plane view and cross section[57]

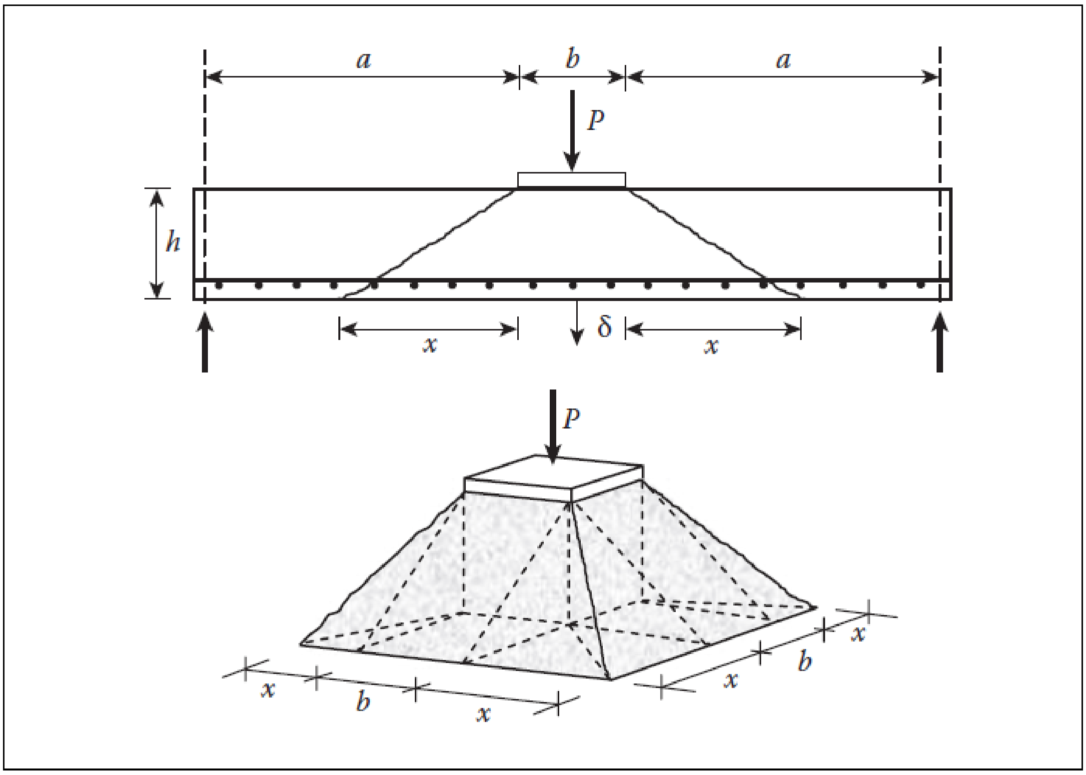

Figure 2.10 Punching shear failure in inclined crack planes[57]

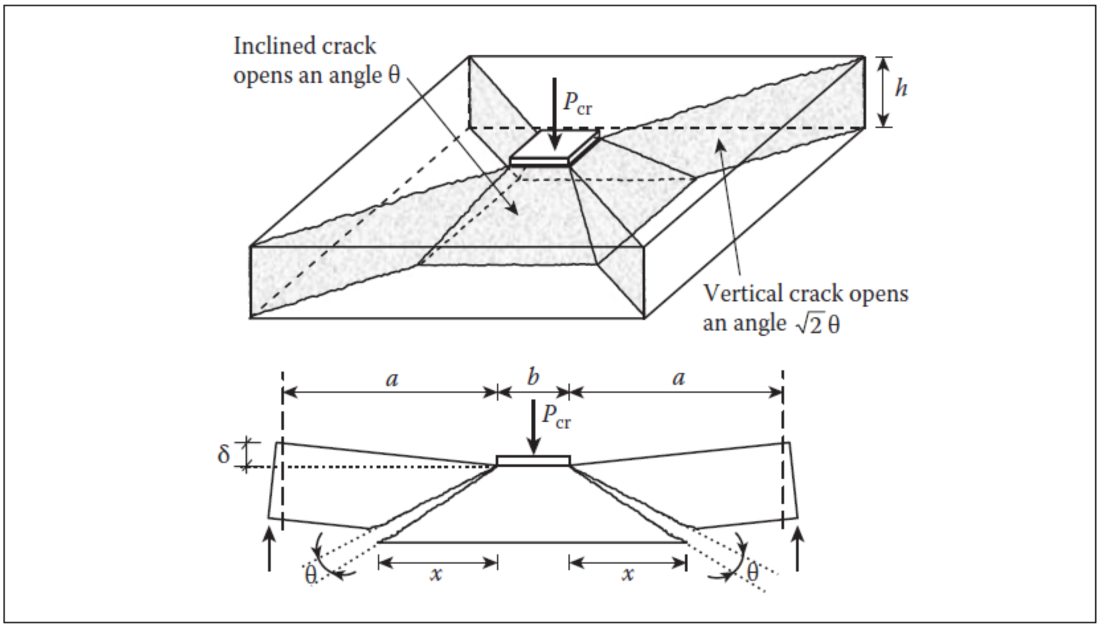

Figure 2.11 Cracking mechanism[57]

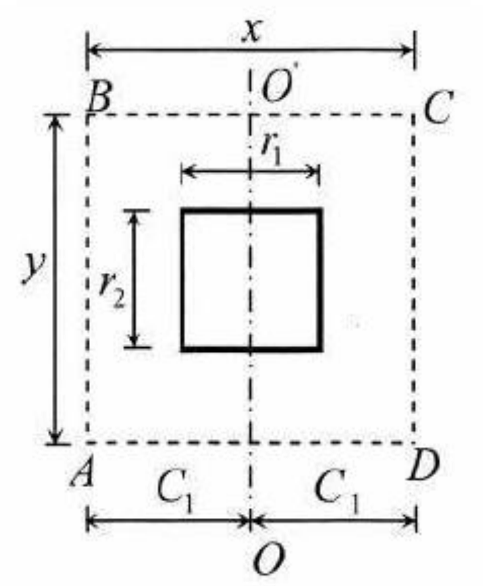

(a) Critical Section

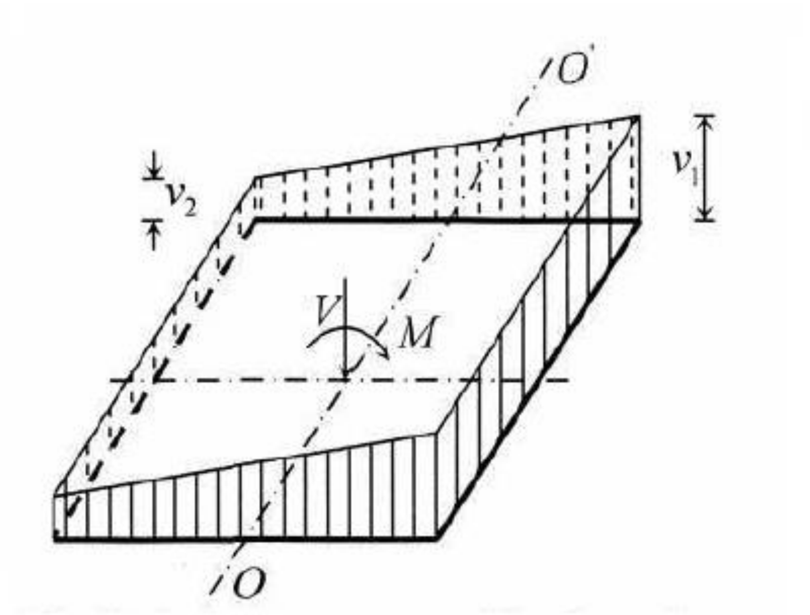

(b) Distribution of Vertical Shear Stress

Figure 2.12 Assumed Shear Stress Distribution for Interior Column[17]

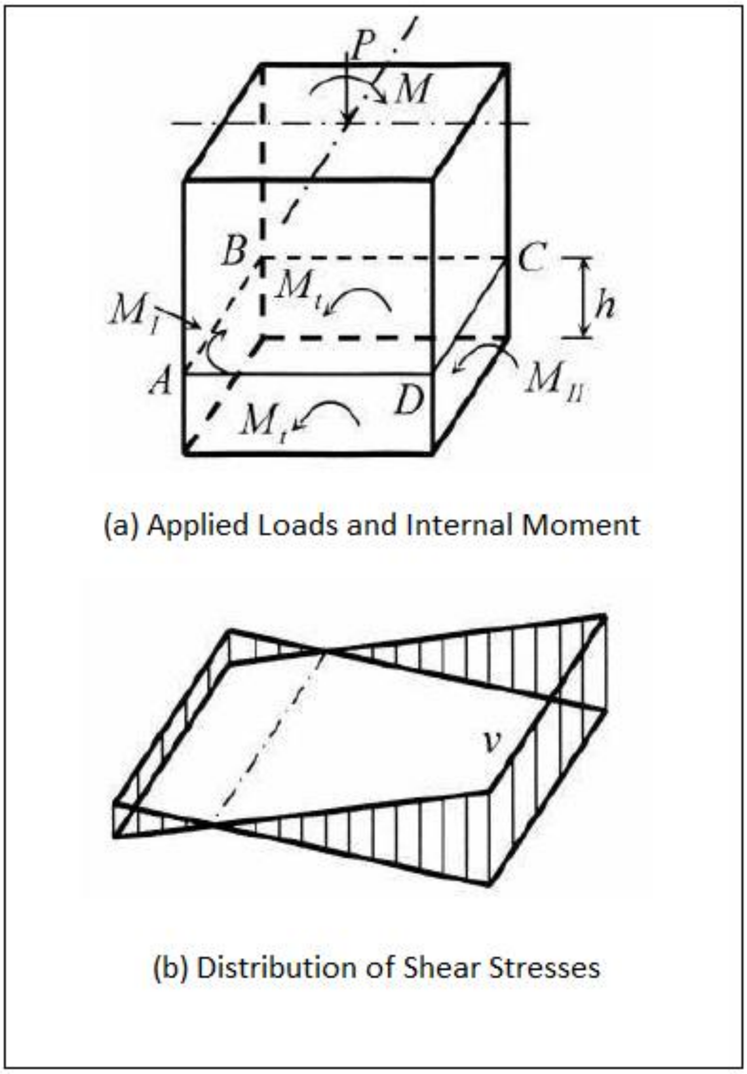

Figure 2.13 Model proposed by Moe[53]

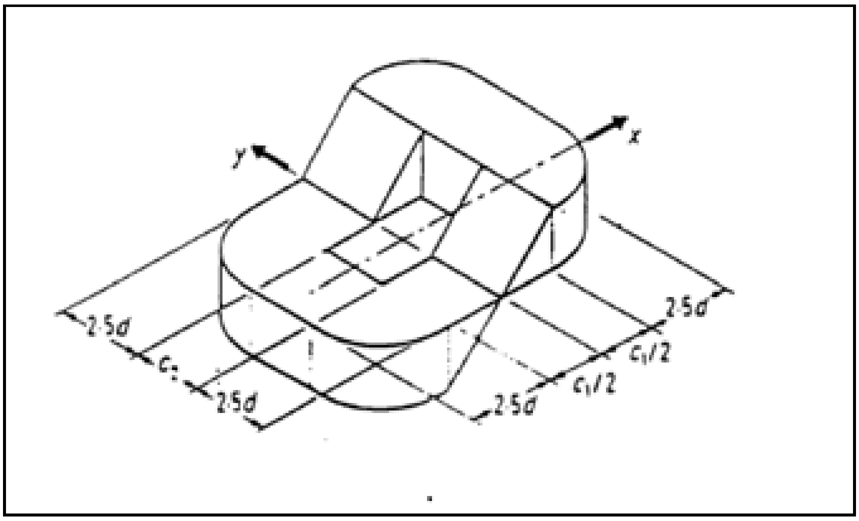

Figure 2.14 Distribution of Shear stresses due to unbalanced moment by Regan[67]

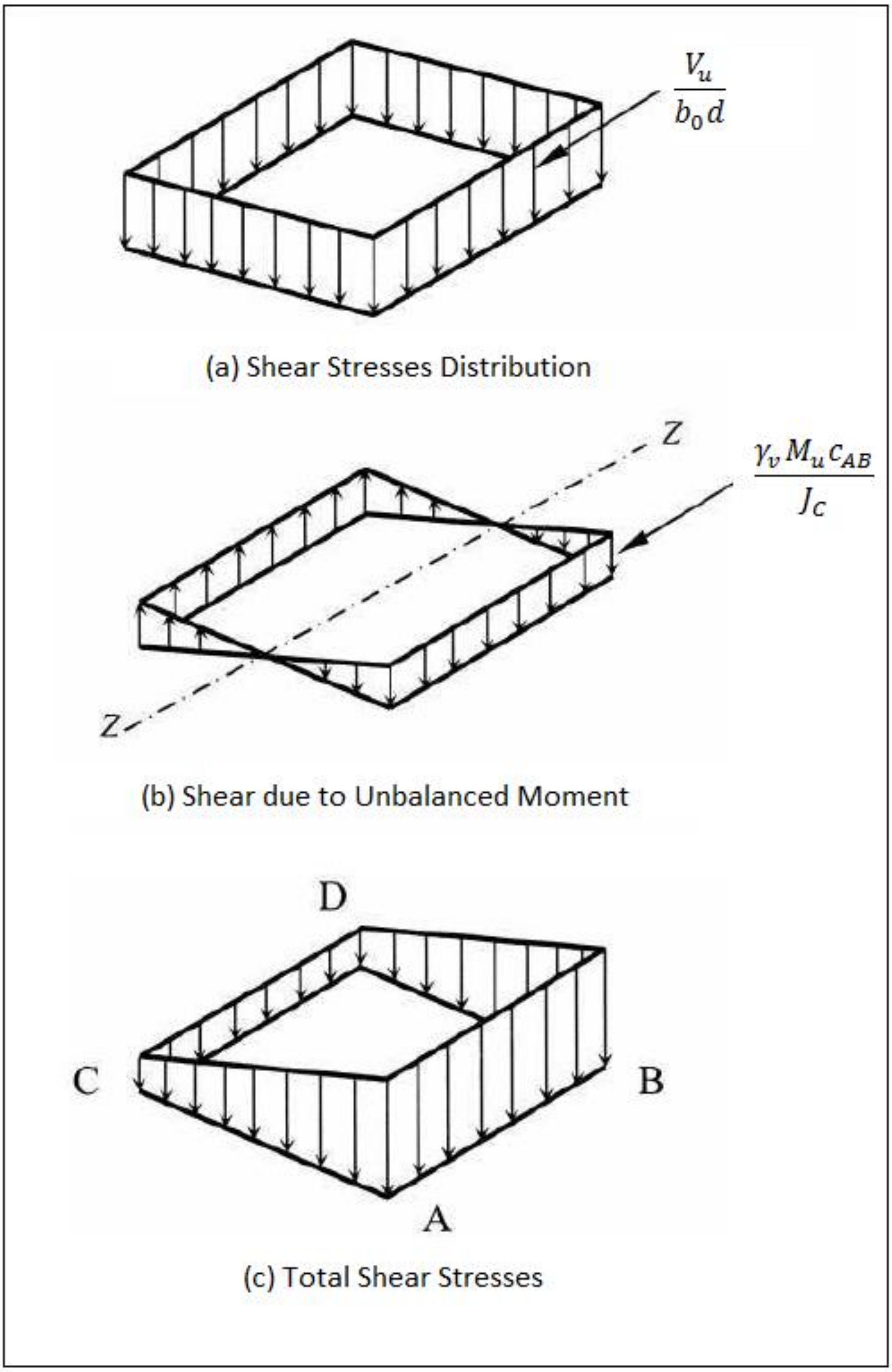

(a) Shear Stresses Distribution

(b) Shear due to Unbalanced Moment

(c) Total Shear Stresses

Figure 2.15 Shear Stresses due to Shear and Moment Transfer at an Interior Column (ACI[1])

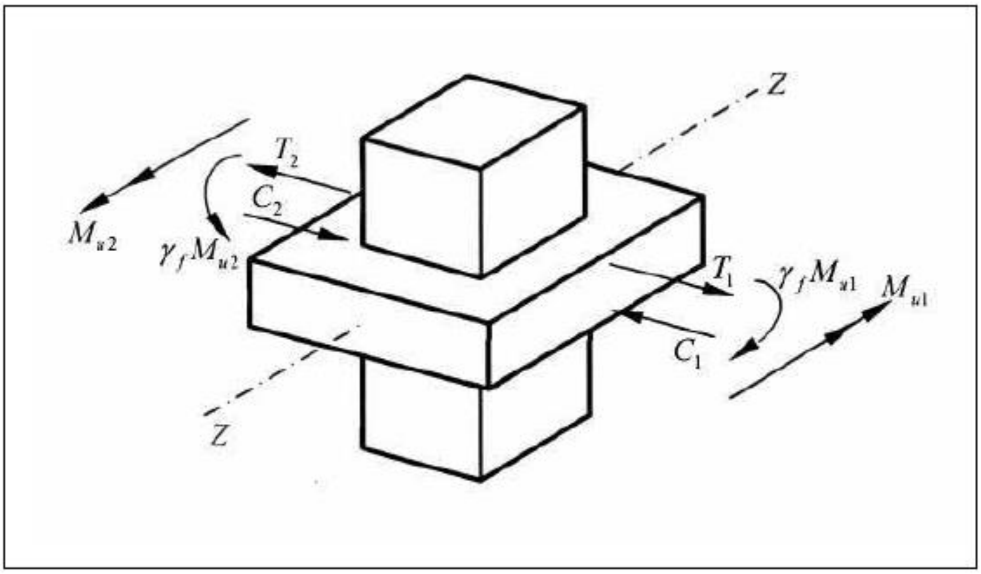

Figure 2.16 Transfer of Biaxial Moment at an Interior Column (ACI-318-11[1])

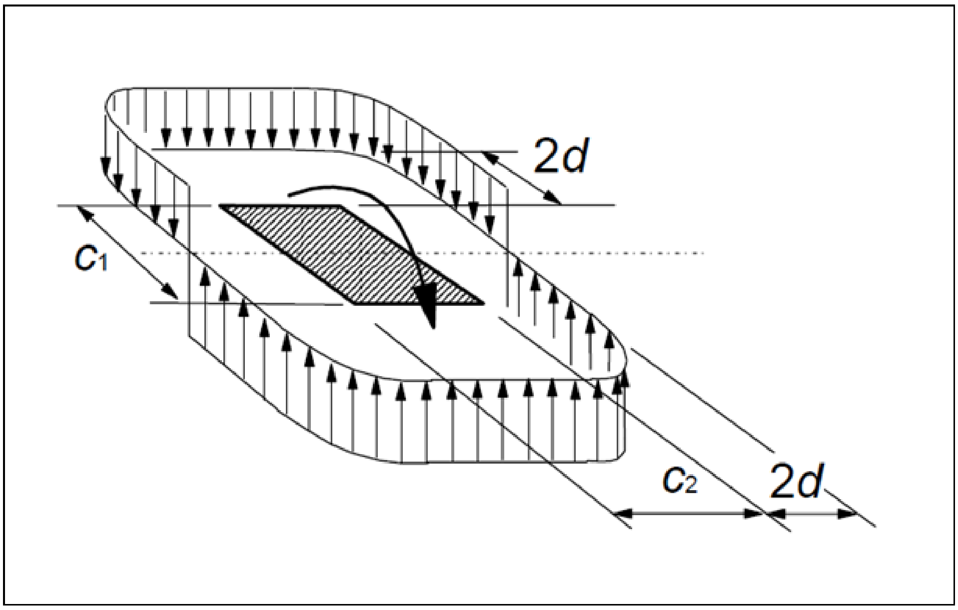

Figure 2.17 Shear distribution due to unbalanced moment at a slab-internal column connection[22]

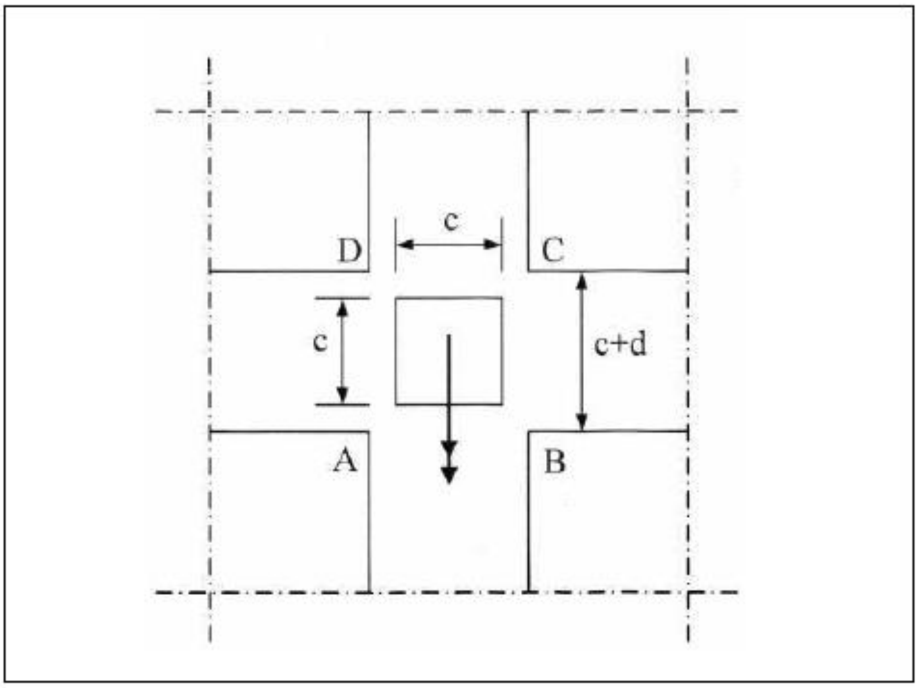

Figure 2.18 Basic Concept of Beam Analogy (Hawkins & Corley[34])

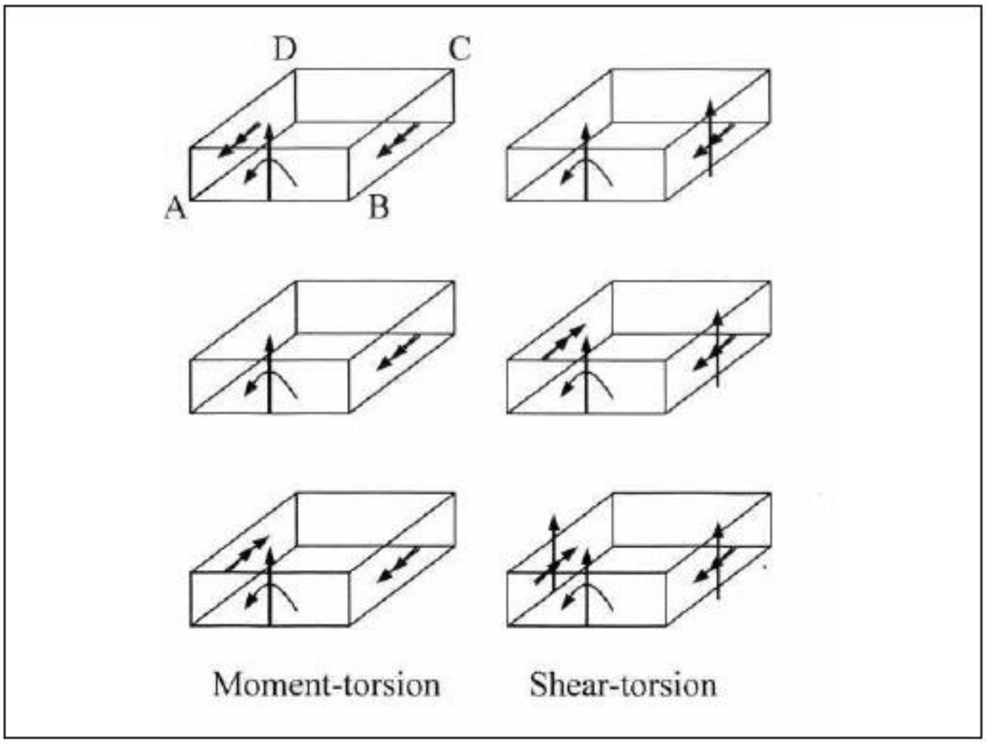

Figure 2.19 Possible failure modes of beam analogy (Hawkins & Corley[34])

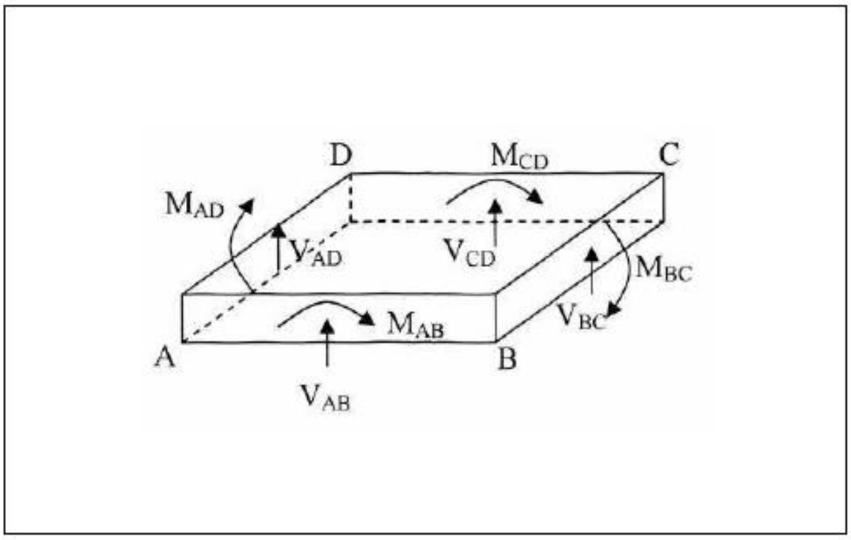

Figure 2.20 Internal Actions based on Beam Analogy Model (Park & Islam[38])

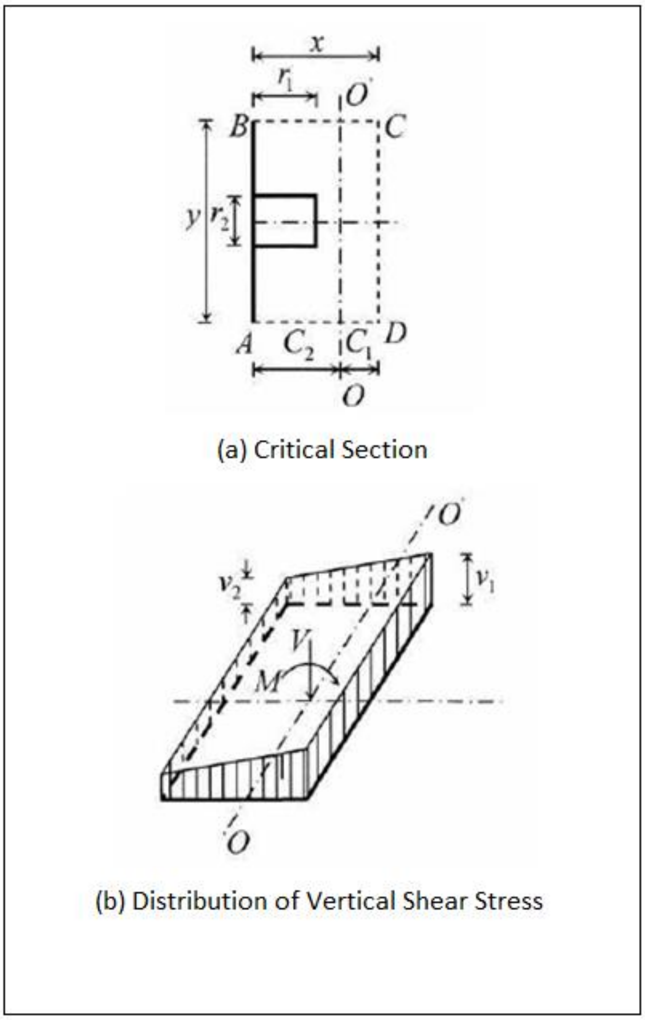

Figure 2.21 Assumed Shear Stress Distribution Edge Column[17]

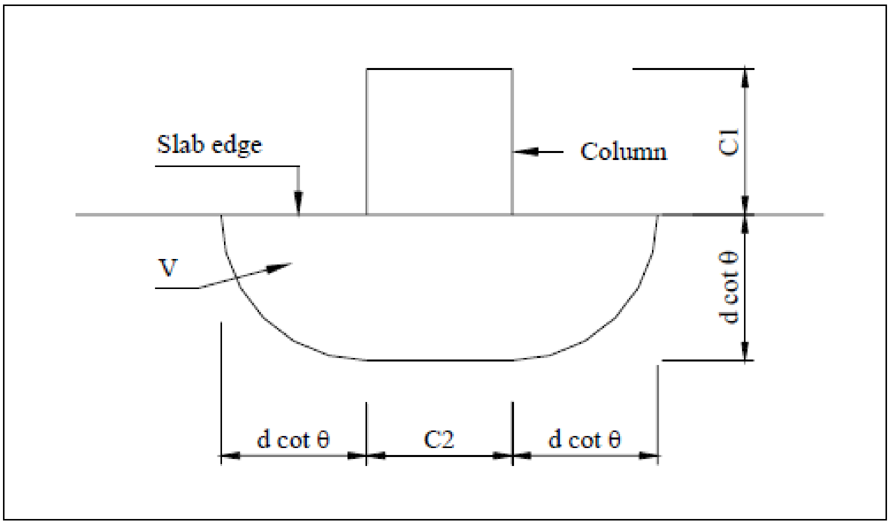

Figure 2.22 Shear Fracture Surface for Punching Failure (Regan[67])

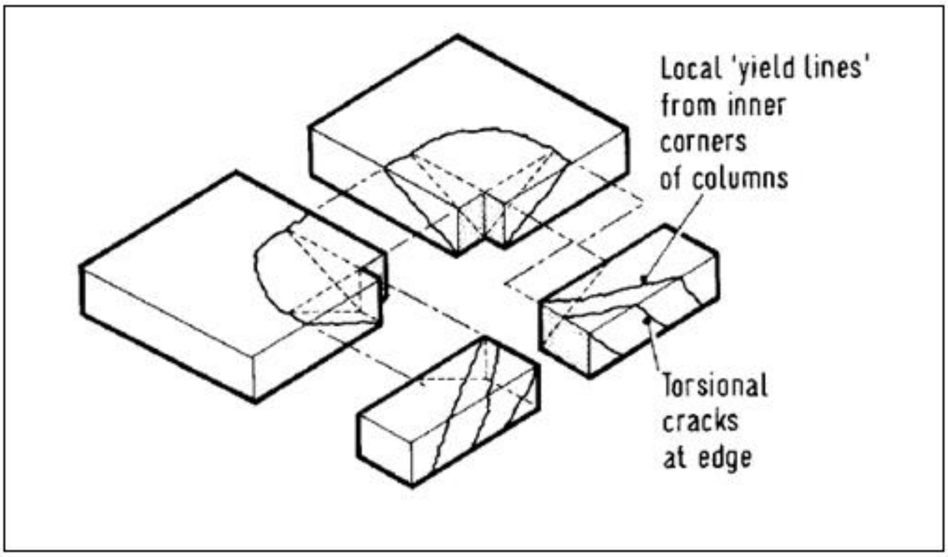

Figure 2.23 Typical Punching at Edge Column (Cracking mode)[67]

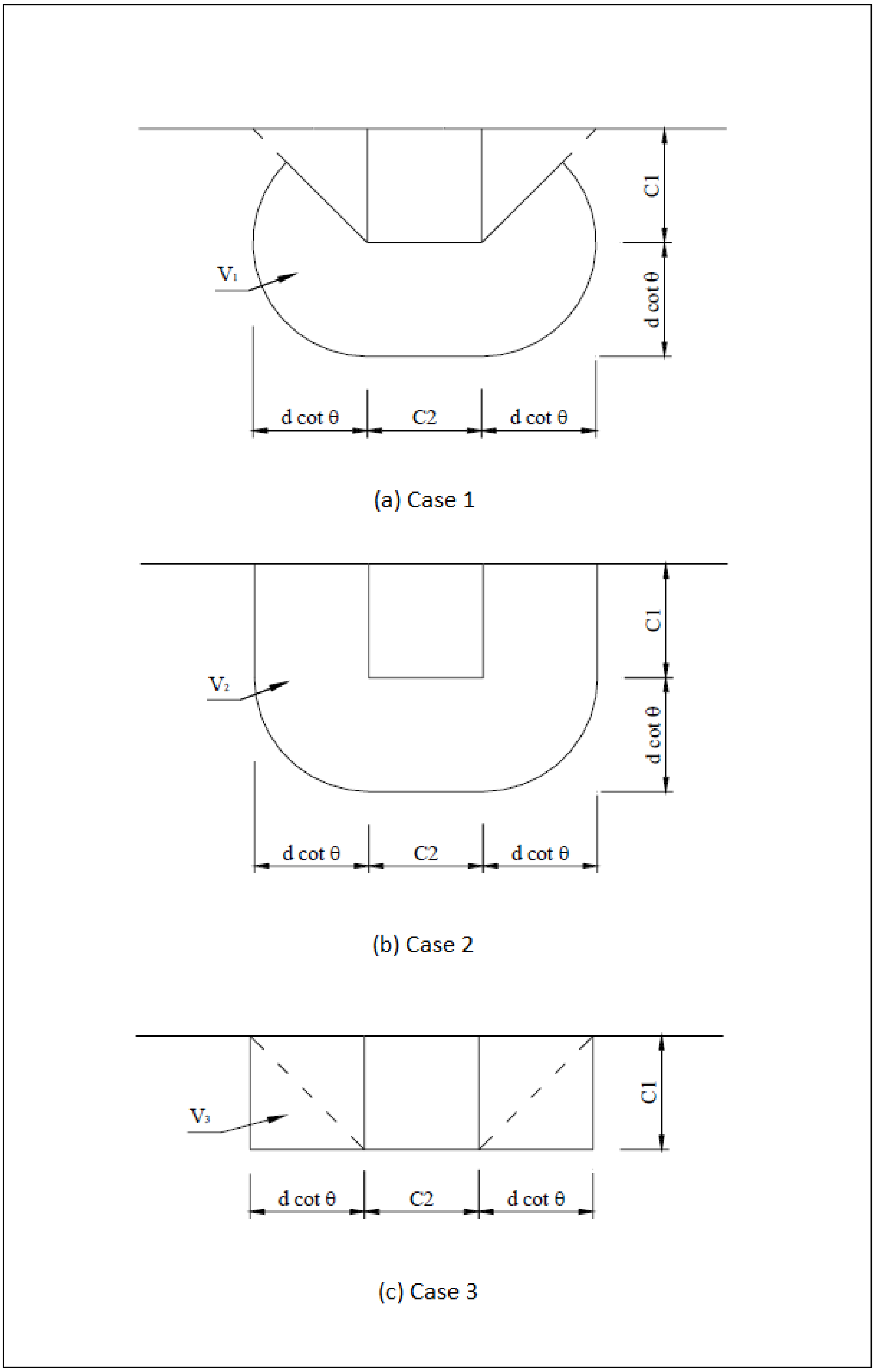

(a) Case 1

(b) Case 2

(c) Case 3

Figure 2.24 Shear fracture surfaces for various magnitudes V and M (Regan[67])

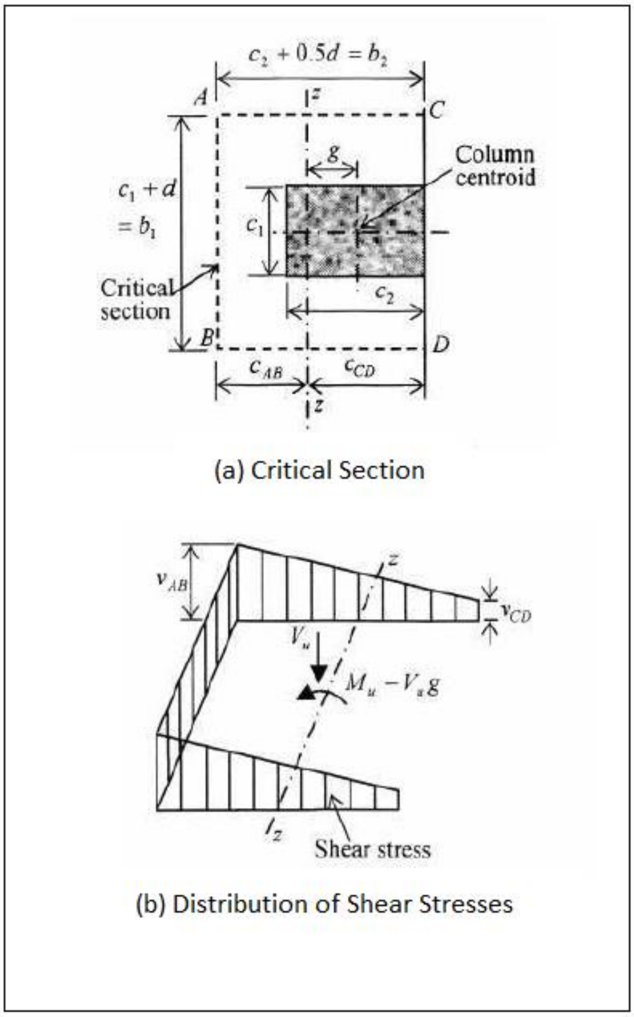

Figure 2.25 Edge Connections (ACI 318-11[1])

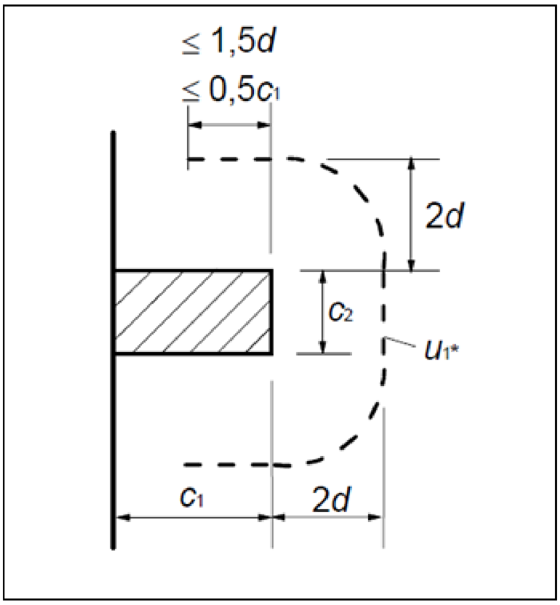

Figure 2.26 Reduced basic control perimeter, u1*[22]

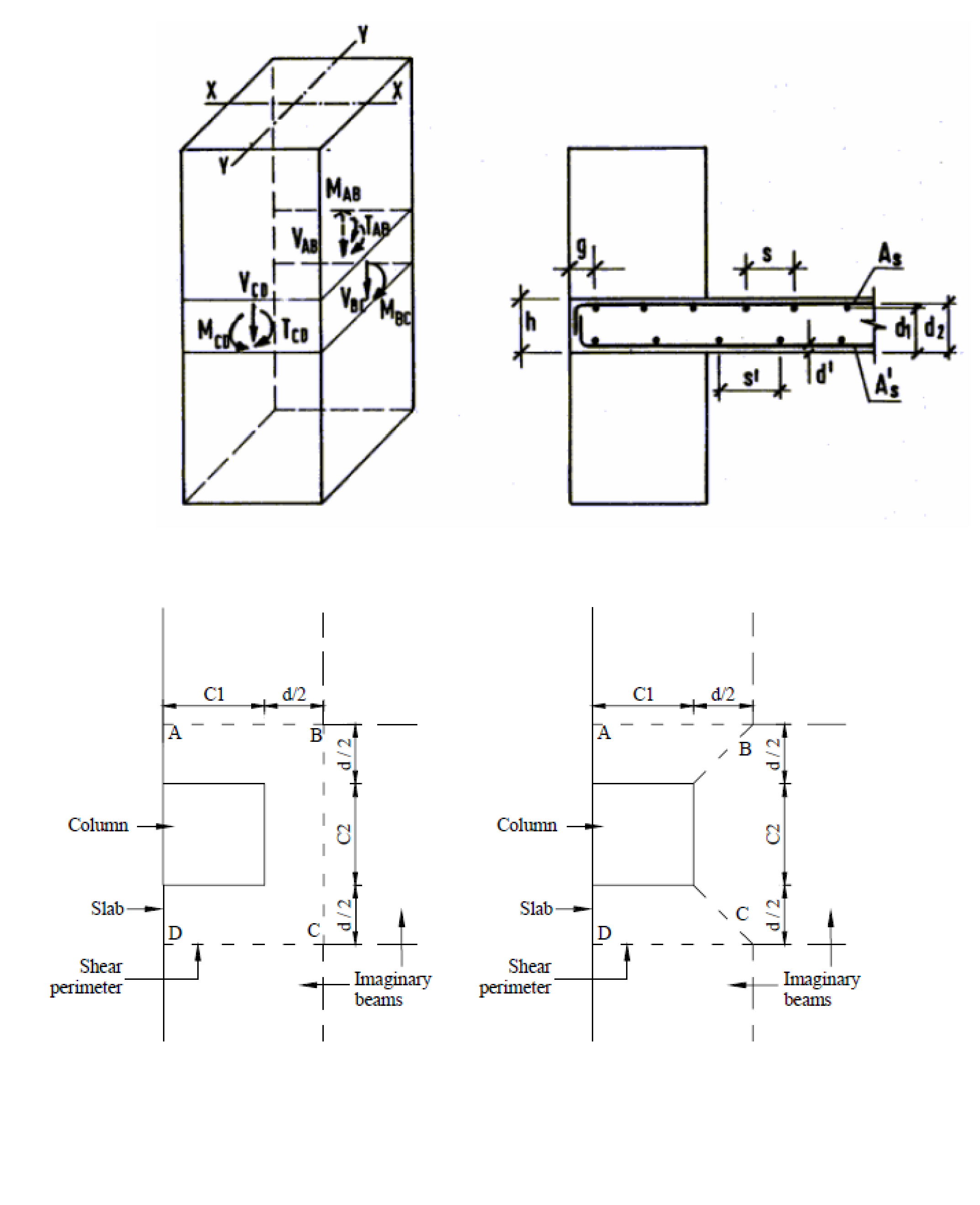

Figure 2.27 Beam Analogy for Edge Column (Hawkins & Corley[34])

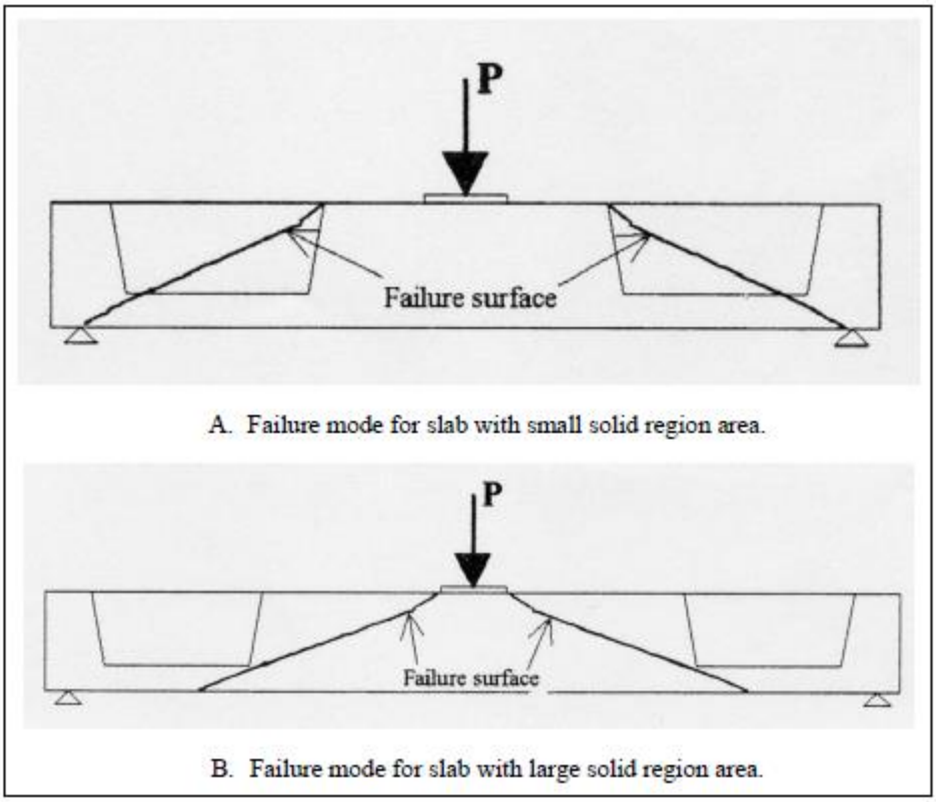

Figure 2.28 Internal Punching Failure Mechanism for Internal Waffle Slabs[81]

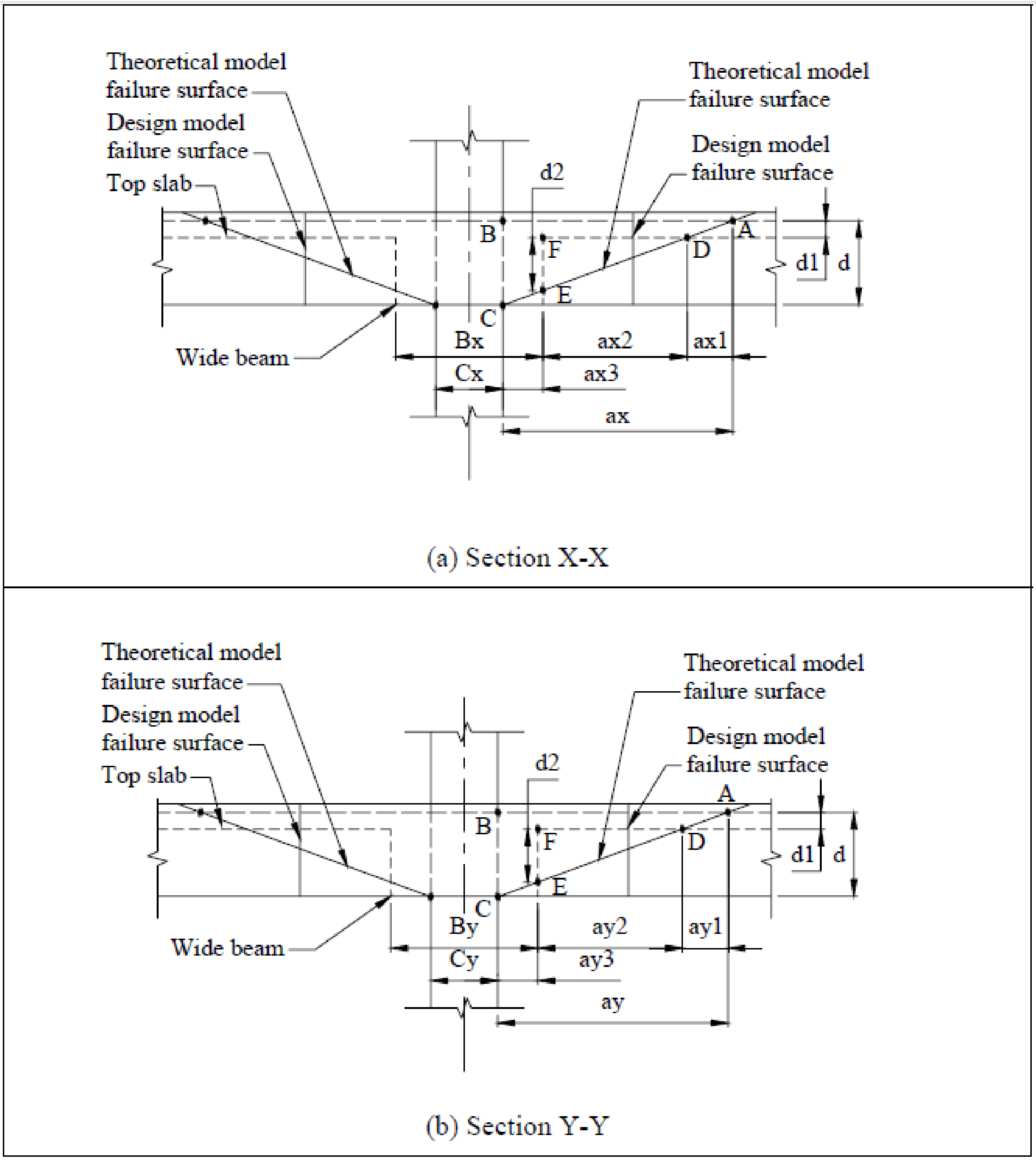

Figure 2.29 Design Model by Lau – Critical Shear Area[46,47]

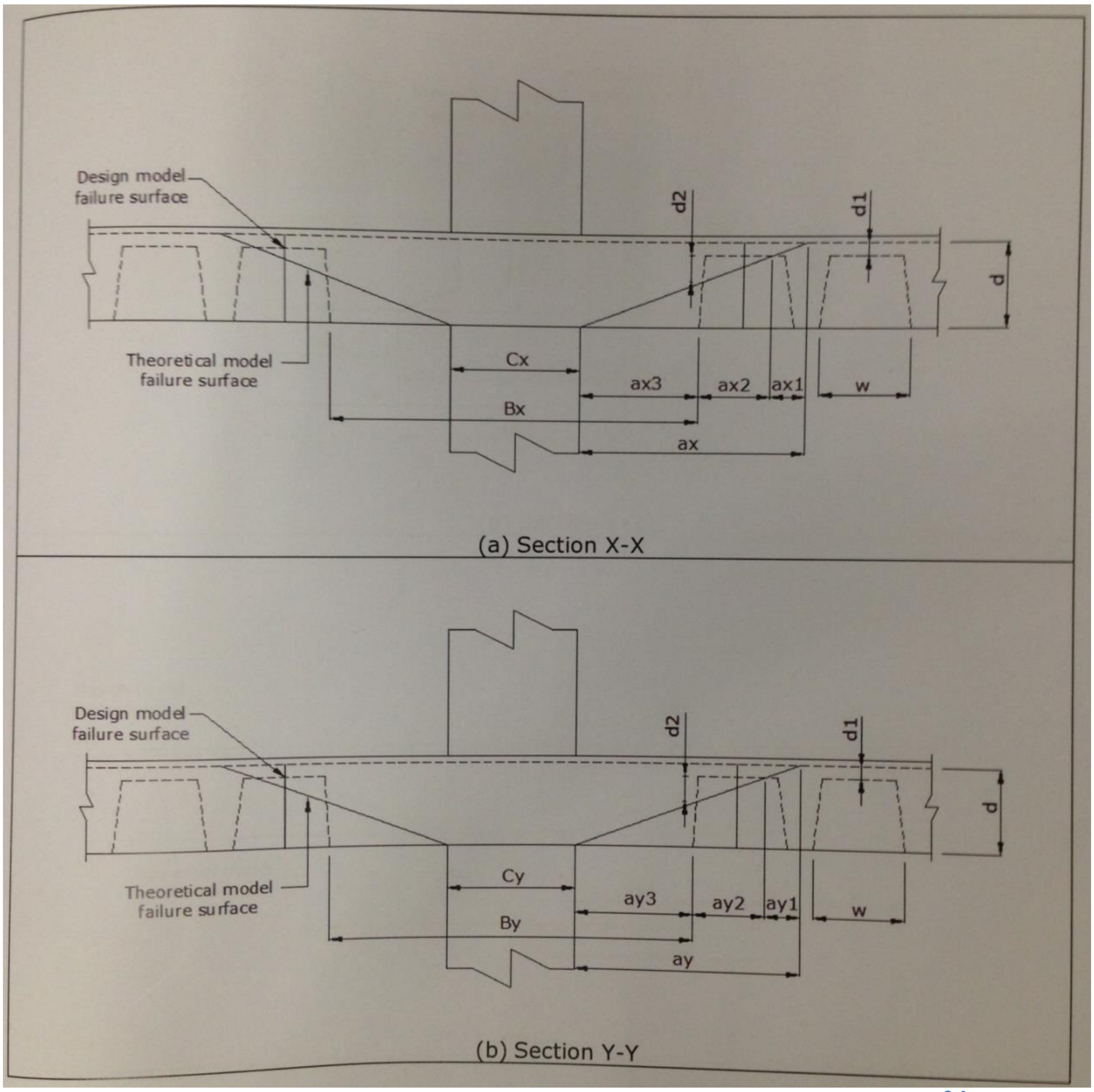

Figure 2.30 Design Models proposed by Al-Bayati -Critical Shear Area[3,4]

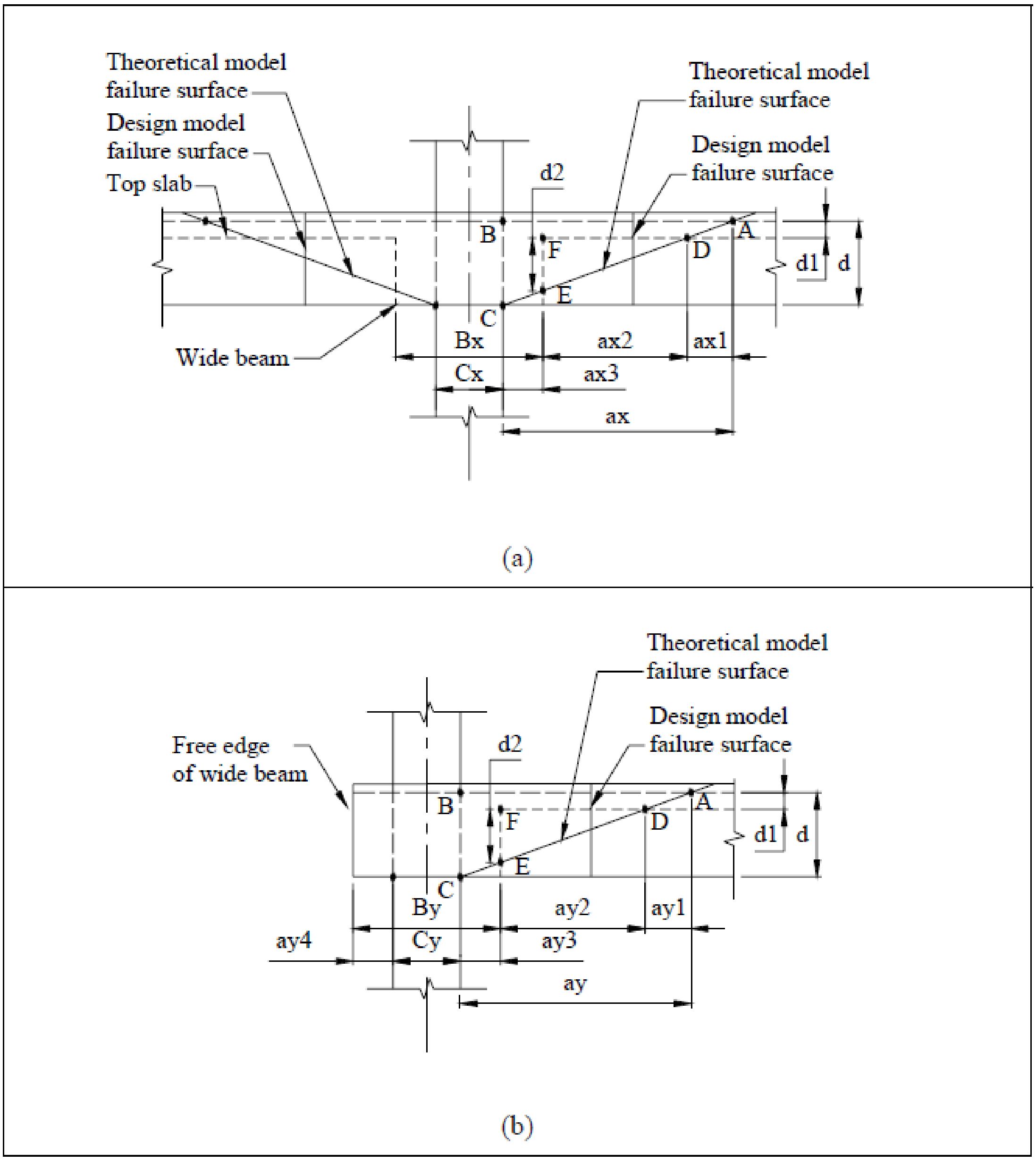

Figure 2.31 Design Model by Lau – Critical Shear Area[45,47]

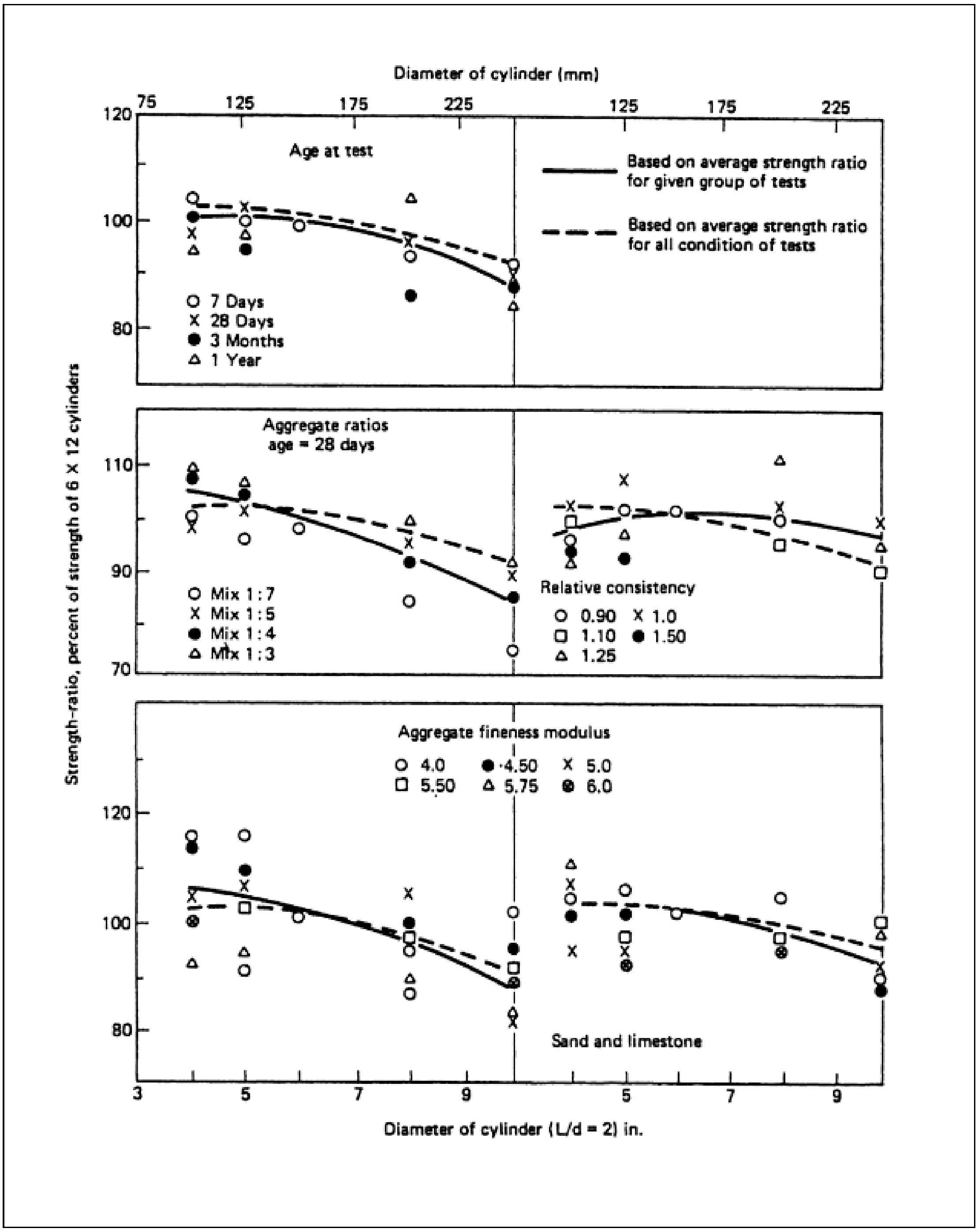

Figure 2.32 Effect of size on compressive strength by Gonnerman[29]

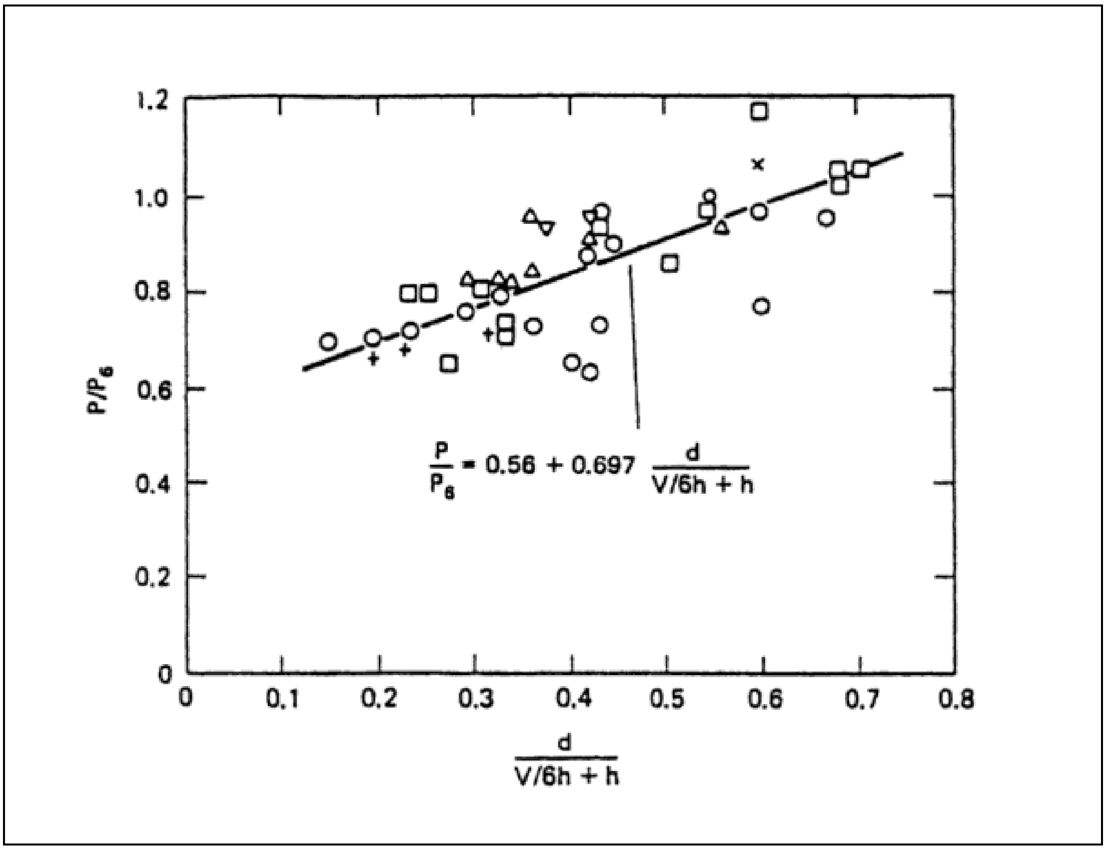

Figure 2.33 Comparison between $\frac{P}{P_6}$ and $\frac{d}{\frac{V}{6h}+h}$ (Neville[55])

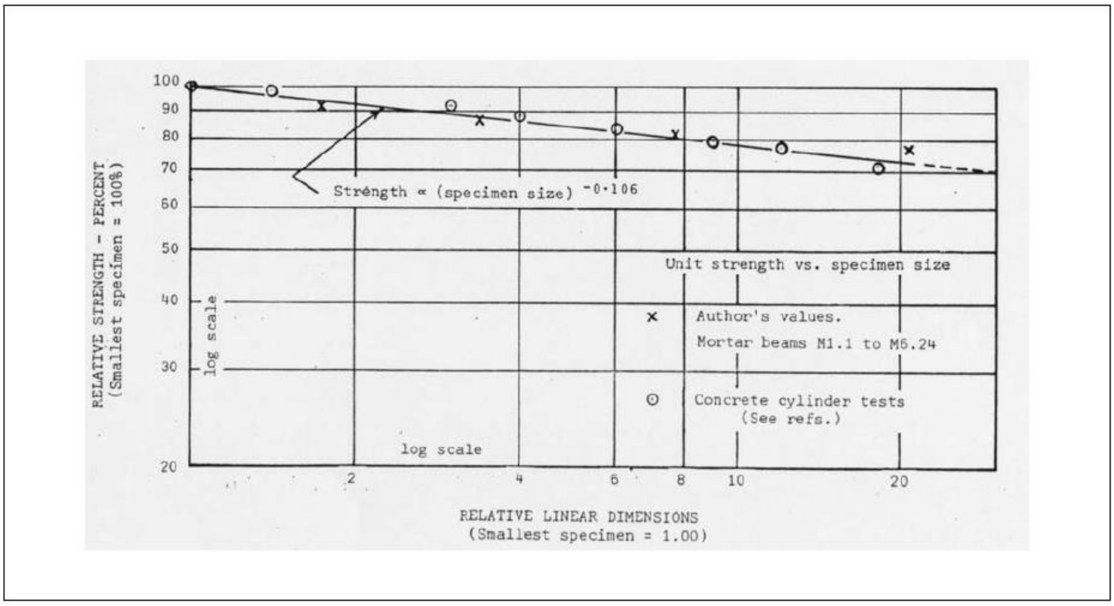

Figure 2.34 Relative strength vs relative linear dimensions by Endersbee[21]

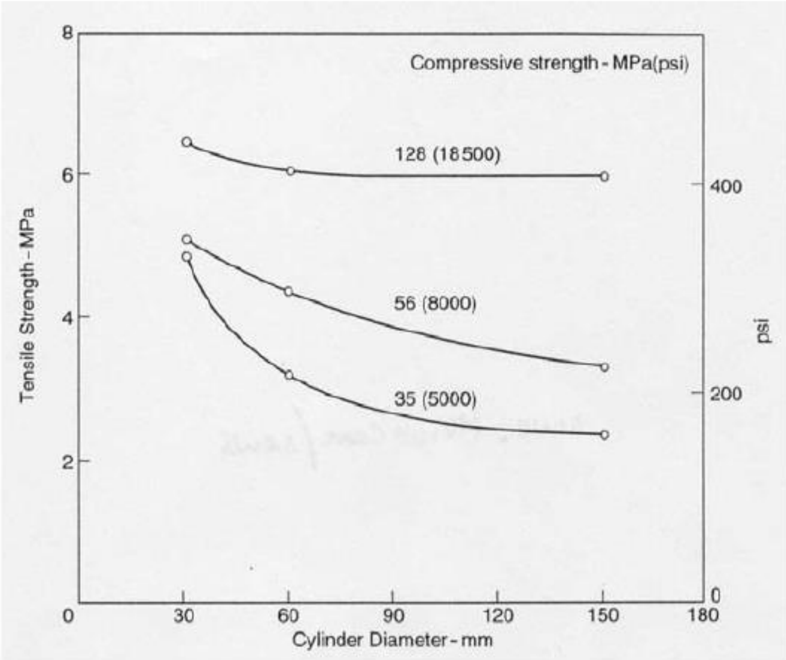

Figure 2.35 Effect of size specimen on concrete tensile strength by Rossi[69]

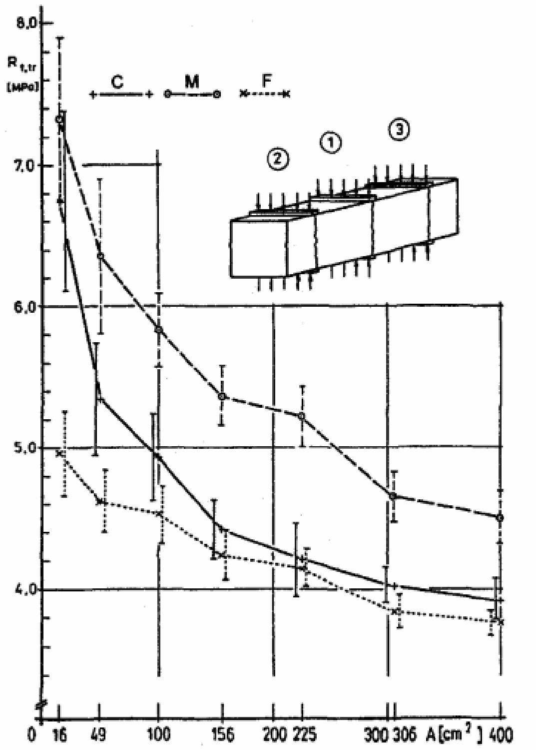

Figure 2.36 Relationship between concrete tensile strength and size of fracture area by Kadlecek et al.[41]

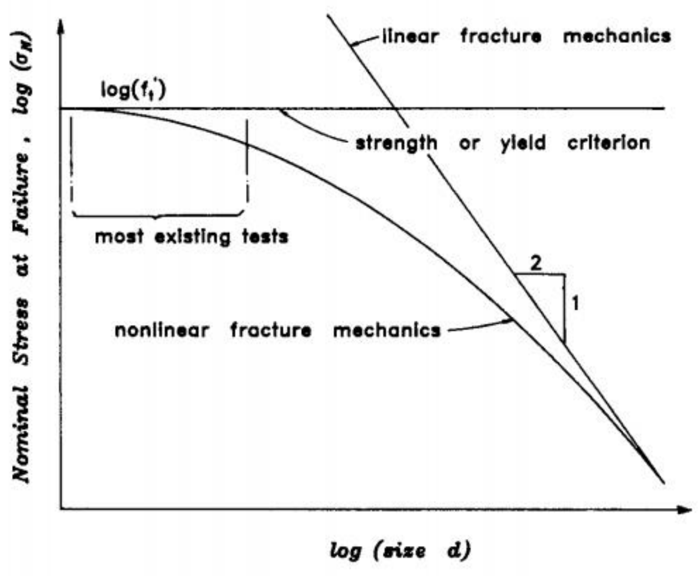

Figure 2.37 Size Effect Law by Bazant & Kim[9]

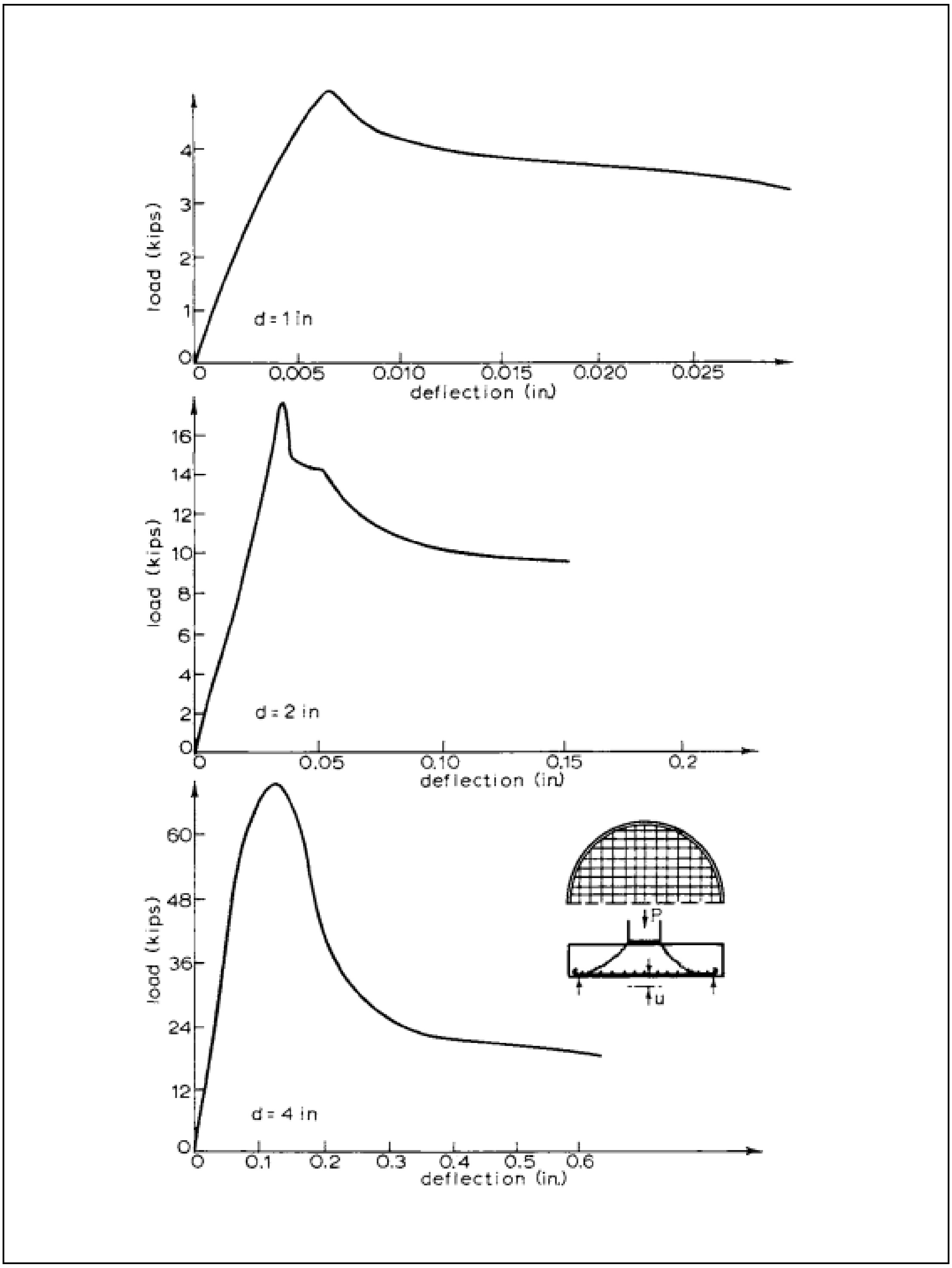

Figure 2.38 Measured load-deflection diagrams for slabs with different thickness by Bazant & Cao[8]

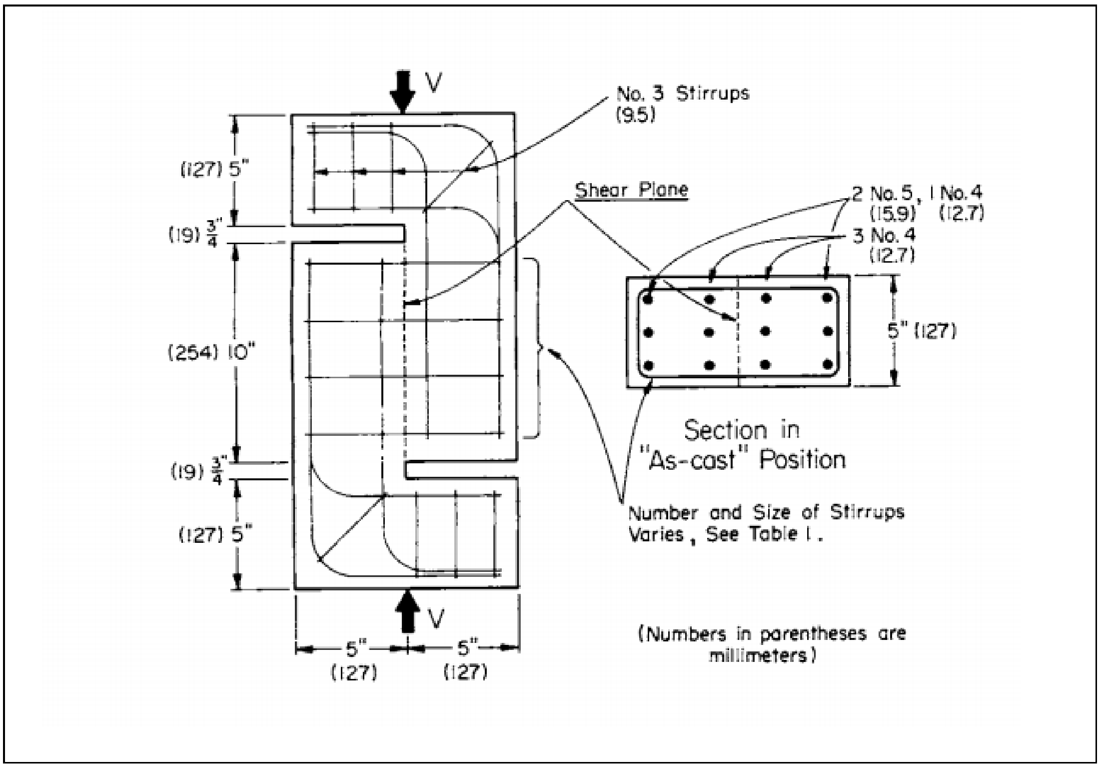

Figure 2.39 Mattock type push off specimen[51]

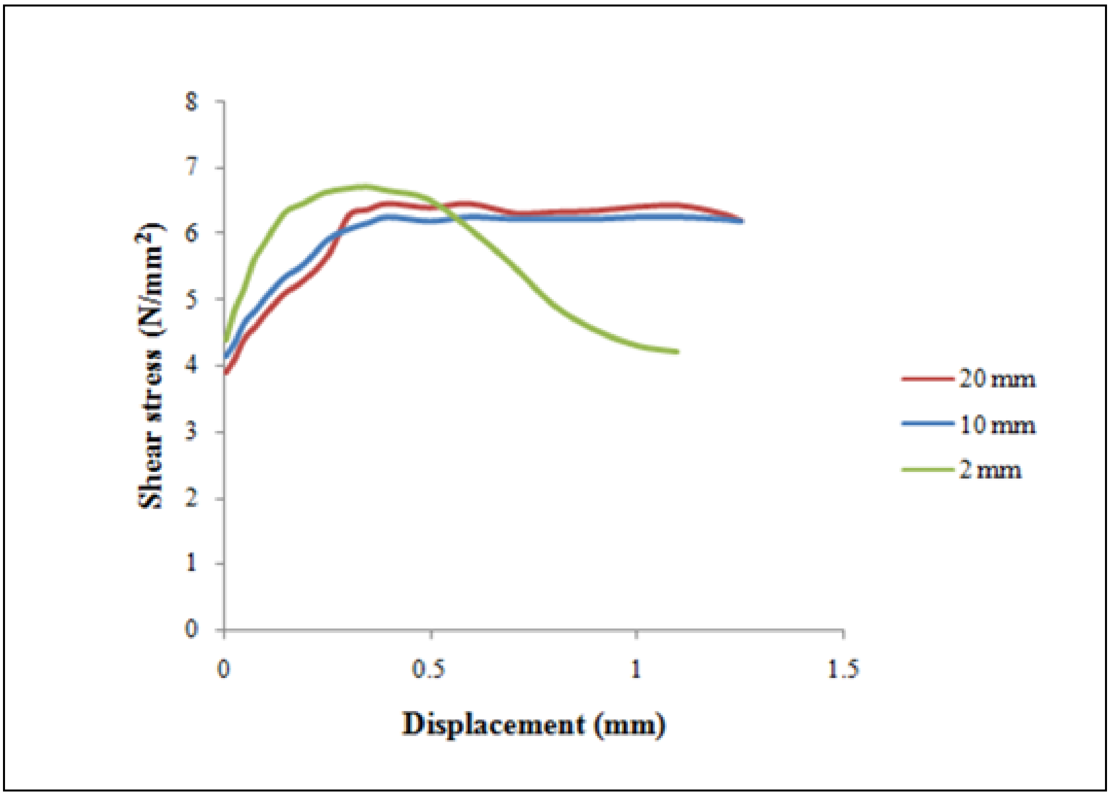

Figure 2.40 Shear stress vs displacement

Chapter 3 Methodology

3.1 Introduction

As mentioned in Chapter 2, the current understanding about the punching shear mechanism has been mainly focusing on both the concentric loads and the uniaxial eccentric loads, none on the biaxial eccentric loads. Therefore, experimental investigation is required to study the effect of principle angle of moment transfer on the punching shear failure mechanism.

A total of thirty-eight waffle slab and solid flat slab specimens were cast and tested to investigate the punching shear mechanism at both the internal and edge column connections. Since no work has been done to investigate the effect of biaxial moment transfer on waffle slabs and solid flat slabs, only small-scale specimens ($1/10^{th}$) were cast to explore the punching shear mechanism due to the economic benefits, and the ease of handling. The maximum size of the aggregates used in the micro-concrete is 2.36 mm, and the diameter of the reinforcement bars used is 3.4 mm.

The slab specimens in this research were categorized into two main series: Internal Column and Edge Column. All slab specimens were cast without a column, and all the columns were simulated using a steel L-column stub bolted onto the slab specimens. The arrangements of the column are explained in detailed in Section 3.4.2.

The effects of biaxial moment transfer were simulated through the rotation of the column stub along with the load eccentricities. Other variables considered were the size of solid section and the column location.

In this chapter, a detailed explanation on the specimens, fabrication and preparation of specimens, test set-up and test procedure used in this experimental study are presented.

3.2 Slab Specimens for Internal Column Series

The Internal Column series consisted of fifteen scaled specimens that were cast and tested to simulate the punching shear failure mechanism at the internal column slab connection in the presence of biaxial moment transfer. As shown in Figure 3.1, the specimens cast in this series were 560 mm x 560 mm. During the tests, all specimens were centrally loaded, and supported at the four edges. All specimens were cast with an overall depth of 70 mm and top slab thickness of 20 mm.

The variables considered were: column eccentricity, principle angle of moment transfer, size of the solid section and column orientation. The reinforcement bars were kept consistent for all slab specimens; all waffle ribs were doubly reinforced to ensure for sufficient bending capacities, and 5 mm covers to reinforcement bars were provided.

The Internal Column Series was subdivided into 4 sub-series: IWS, IWSB, IFSB and IWSBC to achieve the objectives separately.

3.2.1 Series IWS

In Series IWS, only one scaled specimen was cast and tested to simulate the punching shear failure mechanism at the internal column slab connection in the absence of biaxial moment transfer and eccentricity. Table 3.1 lists the test set up and slab details.

This series served as the control specimen for Series IWSB.

3.2.2 Series IWSB

In the IWSB series, a total of nine specimens were cast and tested to simulate the punching shear mechanism at the internal column in the presence of biaxial moment transfer and load eccentricity. Table 3.2 lists the test set up and slab details.

The aim here is to identify the effect of biaxial moment transfer (see Figure 3.3) and load eccentricities on the punching shear failure mechanism at the internal column slab connection.

3.2.3 Series IFSB

In the IFSB series, a total of three specimens were cast and tested to simulate the punching shear mechanism at the internal column in the presence of biaxial moment transfer. Table 3.3 lists the test set up and slab details.

The aim here is to identify the effect of size of solid section on the punching shear failure mechanism at the internal column slab connection.

3.2.4 Series IWSBC

In the IWSBC series, a total of two specimens were cast and tested to simulate the punching shear mechanism at the internal column with the column orientation rotated in accordance to the direction of load eccentricity. Table 3.4 lists the test set up and slab details.

The aim here is to identify any potential effects that may arise from the orientation of the column with respect to the punching capacity.

3.3 Slab Specimens for Edge Column Series

The Edge Column series consisted of twenty-four scaled specimens that were cast and tested to simulate the punching shear failure mechanism at the edge column slab connection in the presence of biaxial moment transfer. As shown in Figure 3.2, the specimens cast in this series are 560 mm x 380 mm. During the tests, all specimens were loaded at the centre of the slab free edge, and supported at three edges. (except Series EWSCE (see Figure 3.29)) All specimens were cast with an overall depth of 70 mm and top slab thickness of 20 mm.

The variables considered were: column eccentricity, principle angle of moment transfer, size of the solid section and column's location. The reinforcement bars were kept constant among all slab specimens; all waffle ribs were doubly reinforced to ensure for sufficient bending capacities, and 5 mm covers to reinforcement bars were provided.

The Edge Column Series was further sub-divided into 3 series: EWSB, EFSB and EWSCE to achieve the objectives separately.

3.3.1 Series EWSB

In the EWSB series, a total of fifteen specimens were cast and tested to simulate the punching shear mechanism at the edge column in the presence of biaxial moment transfer and load eccentricities. Table 3.5 lists the test set up and slab details.

The aim here is to identify the effect of biaxial moment transfer (see Figure 3.4) and the load eccentricities on the punching shear failure mechanism at the edge column slab connection.

3.3.2 Series EFSB

In the EFSB series, a total of five specimens were cast and tested to simulate the punching shear mechanism at the edge column in the presence of biaxial moment transfer. Table 3.6 lists the test set up and slab details.

The aim here is to identify the effect of size of solid section on the punching shear failure mechanism at the edge column slab connection.

3.3.3 Series EWSCE

In the EWSCE series, a total of three specimens were cast and tested to simulate the punching shear mechanism at the edge column in the presence of biaxial moment transfer. Table 3.7 lists the test set up and slab details.

The aim here is to identify the effect of the column's location on the punching shear failure mechanism at the edge column slab connection.

3.4 Fabrication of Specimens

3.4.1 Mould

In the Internal Column Series, all slab specimens were cast using one size steel mould. This mould consisted of a square steel plate, thirty-two aluminium blocks, four angle sections and a plywood board. The steel plate was predrilled with holes to receive the aluminium blocks and the angle sections, and was used to form the base of the mould. The aluminium blocks were used to form the waffle sections and the angle sections were used to hole the slab in position during casting. However, for Series EFSB, an additional plywood board was used to cover the predrilled holes in order to cast solid flat slabs. The detailing of these components used to construct all slab specimens in the Internal Column Series are presented in Figure 3.5, and the complete setup is shown in Figure 3.6.

In the Edge Column series, all slab specimens were cast using one size steel mould as well. This mould consisted of a rectangular steel plate, twenty aluminium blocks, four angle sections and a plywood board. The above described mould worked similarly to the mould in this series. The detailing of these components used to construct all slab specimens in the Edge Column Series are presented in Figure 3.7, and the complete setup is shown in Figure 3.8.

In every cast, nine 50 mm cubes were cast together with the slab specimen. These cubes were cast in steel mould readily available in the laboratory, as shown in Figure 3.9.

3.4.2 Column

To simulate for load eccentricities, a steel column stub with overhang (see Figure 3.10) was fabricated to allow for the required positioning. To simulate the principle angle of moment transfer, a base disc with pre-set rotation was attached to the column stub which further allowed for rotation of the column plate. Such freedoms have allowed for facilitation of the required principle angle of moment transfer and the column rotations.

Furthermore, two holding down bolts were installed through the slab thickness to prevent uplift at the rear of the column when eccentric loads were applied (see Figure 3.11).

3.4.3 Concrete

The concrete used in this research was micro-concrete. The mix was intended to give compressive cube strength of 38 to 42 N/mm^2 at 14 days from a 50 mm cube, and, can be compacted readily under light vibration. In order to obtain the desired compressive strength, several trial mixes were carried out and the mix, as described in the following paragraph, was found to be suitable.

All slab specimens were cast using micro-concrete which constituted of ordinary Portland cement and scaled aggregate with a maximum size of 2.36 mm. The water/cement ratio was proposed to be 0.53 and the aggregate/cement ratio to be 1.6. All aggregates were sieved and re-mixed to the required grading distribution as proposed by Johnson[40] and its sieve distribution is shown in Table 3.9 and Figure 3.12. This was done to ensure that a uniform compaction and a small concrete cover can be achieved.

The concrete compressive strength for 1/10th scale specimen should, however, be obtained from 150 / 10 = 15 mm cubes to accommodate size effects. Hence, the measured 50 mm cube compressive strengths have been modified to represent the intended 15 mm cube compressive strengths as accordance to Endersbee's equation[21]:

$$f_{cu15} = f_{cu50}\left(\frac{15}{50}\right)^{-0.106} \qquad \text{(Eq. 3.1)}$$

3.4.4 Reinforcement

The flexural reinforcement was designed to prevent flexural failure. These steel reinforcements were made of plain steel bars with diameter of 3.4 mm. All steel bars have an ultimate tensile strength of 550 N/mm^2 and yield strength of 460 N/mm^2. A typical stress-strain curve of these steel bars is shown in Figure 3.13.

These bars were spaced at 11 mm within the tension region of the slab while the ribs of the waffle sections were doubly reinforced to enhance bending capacities. The bars in the tension region were bent down with a 90^o hook at both ends while the bars in the ribs of the waffle section were bent up with a 180^o hook at both ends.

All the reinforcement was fabricated manually from plain steel bars. The fabricated reinforcement cage (see Figure 3.14 and Figure 3.15) was placed into the steel mould before pouring the concrete. The reinforcement arrangements in the slab specimens are shown in Figure 3.16 and Figure 3.17, for Internal Column Series and Edge Column Series, respectively.

3.4.5 Casting and Curing

All slab specimens were cast in an upright position to simulate the casting position of the prototype structures. Nine 50 mm cubes were cast together with every slab specimen. Prior to casting, the mould for slabs and cubes were cleaned and oiled with releasing agent.

The prefabricated reinforcement cage was placed within the mould right before the pouring of concrete (see Figure 3.18). Plastic spacers were used during casting to allow for the required reinforcement cover.

The specimen and cubes were cast from a single batch of concrete mix. After the micro-concrete was mixed using a mechanical mixer, the micro-concrete was poured into the mould in three equal layers interval with compaction on a vibrating table. After the completion of the three layers, a steel trowel was used to level and finish the top surface of the slab specimen and cubes.

The slab specimen and cubes were left to cure for 24 hours before striking. Both slab specimen and cubes were stripped on the following day and left to cure together until the desired compressive strength have been achieved.

3.5 Test Set-up

All the slab specimens were tested in an inverse manner, in which the topping slab was faced downwards during the test. The load was applied using a 30 tonnes hand operated hydraulic jack.

Steel rollers were used to support the slab specimens. These rollers were then supported by a square ring beam as shown in Figure 3.19.

3.5.1 Internal Column Series

The slab specimens were supported on steel rollers at four edges, and they were loaded with a 30 tonnes hand operated hydraulic jack onto steel L-column stub mounted centrally on the slab specimens as shown in Figure 3.20. This moment transferring column was replicated using a steel L-column stub and steel plates bolted onto the compression face and tension face of the slab specimens. The direction(s) of the column stub was positioned according to the principle angle(s) of moment transferred, which were 0^{o}, 22.5^{o} and 45^{o}, as shown in Figure 3.21, Figure 3.22 and Figure 3.23, respectively.

3.5.2 Edge Column Series

The edge slab specimens were tested in a manner similar to the Internal Column Series. However, these specimens were only supported on three edges and loaded at the centre of the free edge with a 30 tonnes hand operated hydraulic jack onto steel L-column stub as shown in Figure 3.24. The direction(s) of the column stub was positioned as according to the principle angle(s) of moment transferred, which were 0^{o}, 22.5^{o}, 45^{o}, 67.5^{o} and 90^{o}, as shown in Figure 3.25, Figure 3.26, Figure 3.27, Figure 3.28 and Figure 3.29, respectively.

In Series EWSCE, the column location was re-positioned from the free-edge of the slab to the centre of the edge solid region, as shown in Figure 3.30.

3.6 Deflection

Mechanical dial gauges were used to measure the deflection of the test specimen during loading, with an accuracy of up to 0.01mm. The dial gauges were positioned at the vicinity of the column stub as shown in Figure 3.31 and Figure 3.32, for the Internal Column Series and Edge Column Series, respectively.

For the Internal Column Series, two mechanical dial gauges were used and placed at the front face of the column and the back face of the column, and positioned along the principle axis of the moment transfer. However, for the Edge Column Series, three mechanical dial gauges were used, the position of these dial gauges were fixed and not varied with respect to the principle axis of the moment transfer. The test results are plotted and discussed in Chapter 4.

3.7 Test Procedure

The steel column stub with overhang and the mechanical dial gauges were installed in the designated positions along with the recording of initial readings from the dial gauges and the load cells prior to testing. For both series, the loads were applied onto the column stub by means of hand operated hydraulic jack in increments of 4.21 kN until failure occurred.

The loads were positioned with different column eccentricities and different principle angle of moment transfer in accordance with Table 3.1 to Table 3.8 with respect to the Internal Column Series and the Edge Column Series. In all cases, the loads and deflections were recorded after every load increment and the cracks were marked on the slab upon failure.

Immediately after the completion of each test, the compressive strength of the slab specimen was obtained from compression tests on the 50 mm cubes. The average from six

50 mm cubes was taken as the concrete compressive strength of the slab specimens. The average cube strength for all slab specimens are presented in Chapter 4.

Following the tests, some of the slabs were sawn to examine the internal shear cracks. Details of the observed internal shear cracks are presented in Chapter 4.

3.8 Summary

A total of thirty-eight slab specimens were tested to investigate the internal and edge punching shear failure mechanisms of both waffle slabs and solid flat slabs, with the internal punching mechanism divided into concentric loading and eccentric loading. All slab specimens were cast from micro-concrete with a maximum aggregate size of 2.36 mm and the reinforcements were fabricated from plain steel bars of 3.4 mm diameter.

The experimental results and test observations are presented in the following chapter.

Table 3.1 Specimen Details for Series IWS

Slab Specimen	Size of Solid Section (mm)	Height of Slab, h (mm)	Effective Depth of Slab, d (mm)	Column Size, C_x (mm)	Column Shape	Column Eccentricity e (mm)	Principle Angle of Biaxial Moment Transfer, ∀ (°)
IWS1	200x200	70	62	100	Square	0	0

Table 3.2 Specimen Details for Series IWSB

Slab Specimen	Size of Solid Section (mm)	Height of Slab, h (mm)	Effective Depth of Slab, d (mm)	Column Size, C_x (mm)	Column Shape	Column Eccentricity, e (mm)	Principle Angle of Biaxial Moment Transfer, ∀ (°)
IWSB1	200x200	70	62	100	Square	50	0
IWSB2	200x200	70	62	100	Square	50	22.5
IWSB3	200x200	70	62	100	Square	50	45
IWSB4	200x200	70	62	100	Square	100	0
IWSB5	200x200	70	62	100	Square	100	22.5
IWSB6	200x200	70	62	100	Square	100	45
IWSB7	200x200	70	62	100	Square	150	0
IWSB8	200x200	70	62	100	Square	150	22.5
IWSB9	200x200	70	62	100	Square	150	45

Table 3.3 Specimen Details for Series IFSB

Slab Specimen	Size of Solid Section (mm)	Height of Slab, h (mm)	Effective Depth of Slab, d (mm)	Column Size, C_x (mm)	Column Shape	Column Eccentricity, e (mm)	Principle Angle of Biaxial Moment Transfer, ∀ (°)
IFSB1	360x360	70	62	100	Square	100	0
IFSB2	360x360	70	62	100	Square	100	22.5
IFSB3	360x360	70	62	100	Square	100	45

Table 3.4 Specimen Details for Series IWSBC

Slab Specimen	Size of Solid Section (mm)	Height of Slab, h (mm)	Effective Depth of Slab, d (mm)	Column Size, C_x (mm)	Column Shape	Column Eccentricity, e (mm)	Column Location, Rotation (°)
IWSBC1	200x200	70	62	100	Square	100	22.5
IWSBC2	200x200	70	62	100	Square	100	45

Table 3.5 Specimen Details for Series EWSB

Slab Specimen	Size of Solid Section (mm)	Height of Slab, h (mm)	Effective Depth of Slab, d (mm)	Column Size, C_x (mm)	Column Shape	Column Eccentricity, e (mm)	Principle Angle of Biaxial Moment Transfer, $\forall$ (°)
EWSB1	200x200	70	62	100	Square	50	0
EWSB2	200x200	70	62	100	Square	50	22.5
EWSB3	200x200	70	62	100	Square	50	45
EWSB4	200x200	70	62	100	Square	50	67.5
EWSB5	200x200	70	62	100	Square	50	90
EWSB6	200x200	70	62	100	Square	100	0
EWSB7	200x200	70	62	100	Square	100	22.5
EWSB8	200x200	70	62	100	Square	100	45
EWSB9	200x200	70	62	100	Square	100	67.5
EWSB10	200x200	70	62	100	Square	100	90
EWSB11	200x200	70	62	100	Square	150	0
EWSB12	200x200	70	62	100	Square	150	22.5
EWSB13	200x200	70	62	100	Square	150	45
EWSB14	200x200	70	62	100	Square	150	67.5
EWSB15	200x200	70	62	100	Square	150	90

Table 3.6 Specimen Details for Series EFSB

Slab Specimen	Size of Solid Section (mm)	Height of Slab, h (mm)	Effective Depth of Slab, d (mm)	Column Size, C_x (mm)	Column Shape	Column Eccentricity, e (mm)	Principle Angle of Biaxial Moment Transfer, $\forall$ (°)
EFSB1	360x280	70	62	100	Square	100	0
EFSB2	360x280	70	62	100	Square	100	22.5
EFSB3	360x280	70	62	100	Square	100	45
EFSB4	360x280	70	62	100	Square	100	67.5
EFSB5	360x280	70	62	100	Square	100	90

Table 3.7 Specimen Details for Series EWSCE

Slab Specimen	Size of Solid Section (mm)	Height of Slab, h (mm)	Effective Depth of Slab, d (mm)	Column Size, C_x (mm)	Column Shape	Column Eccentricity, e (mm)	Column Location, Rotation (°)
EWSCE1	200x200	70	62	100	Square	50	0
EWSCE2	200x200	70	62	100	Square	100	0
EWSCE3	200x200	70	62	100	Square	150	0

Table 3.8 Sieve Analysis by Johnson[40]

Sieve Size (mm)	Mass Retained (kg)	%Retained	%Passing
2.36	0.00	0.00	100.00
1.18	38.48	42.23	57.77
0.60	10.47	11.49	46.29
0.30	3.95	4.33	41.95
0.15	30.36	33.32	8.64
≤0.15	7.87	8.64	0.00

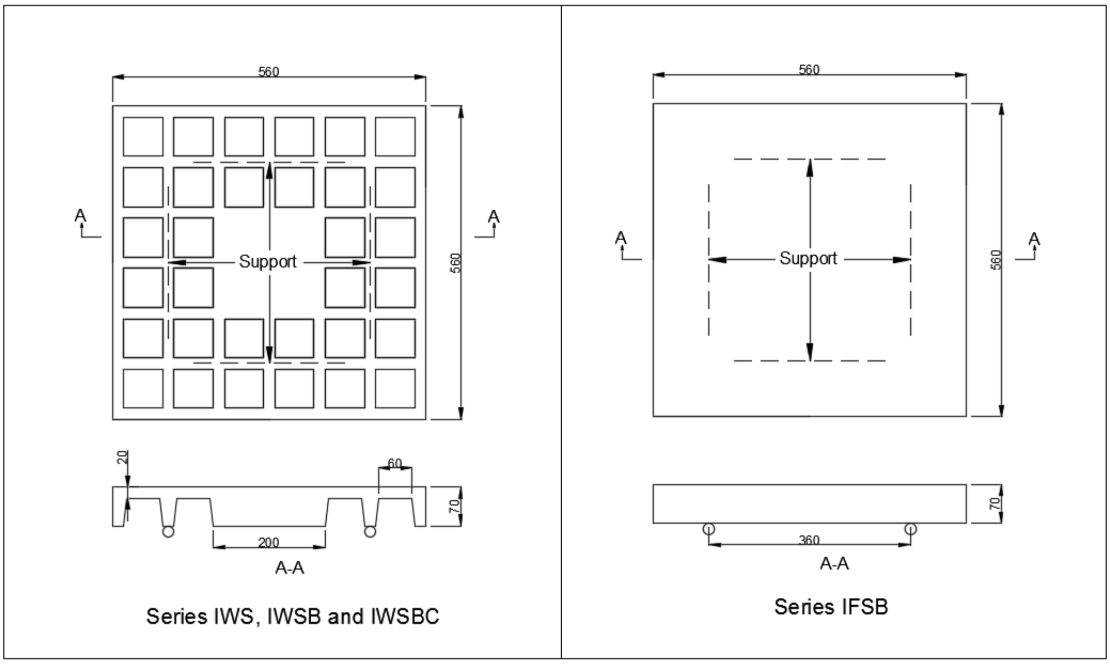

Figure 3.1 Specimen details in the Internal Column Series

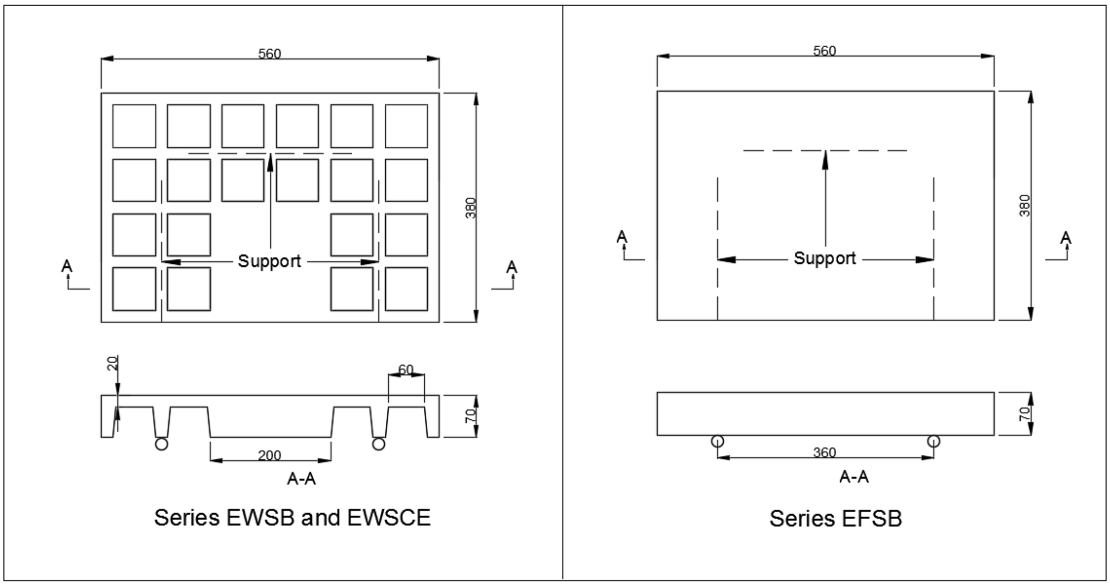

Figure 3.2 Specimen details in the Edge Column Series

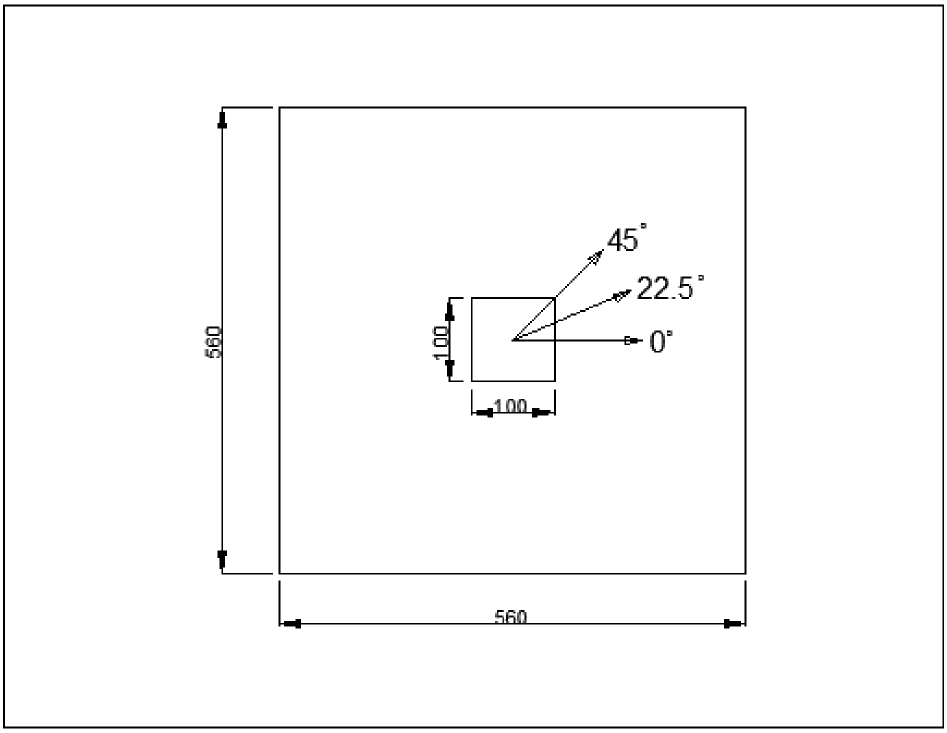

Figure 3.3 Principle angle of moment transfer for waffle slab with 200x200mm solid section and 100x100mm column (IWSB series)

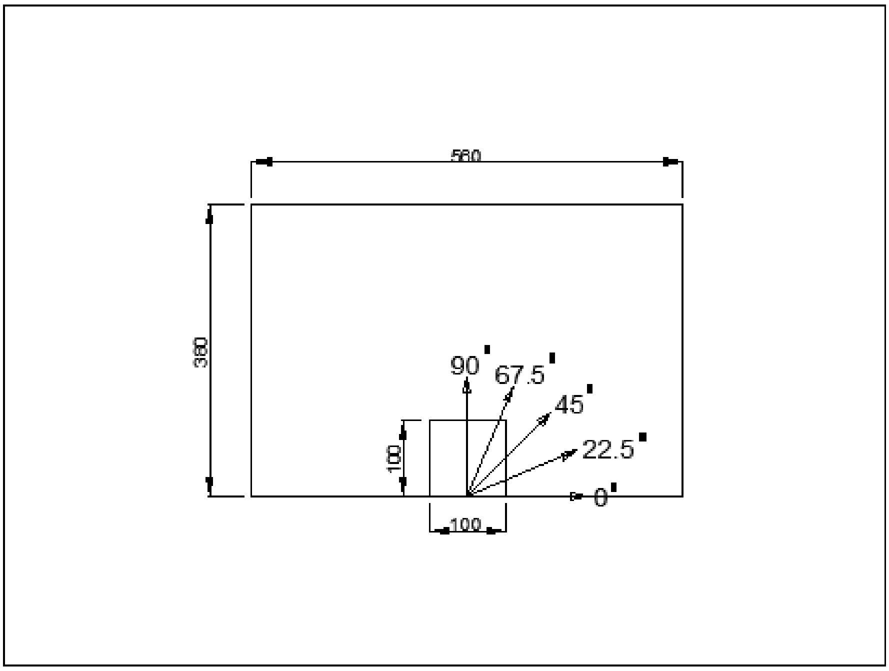

Figure 3.4 Principle angle of moment transfer for waffle slab with 200x200mm solid section and 100x100mm column (EWSB series)

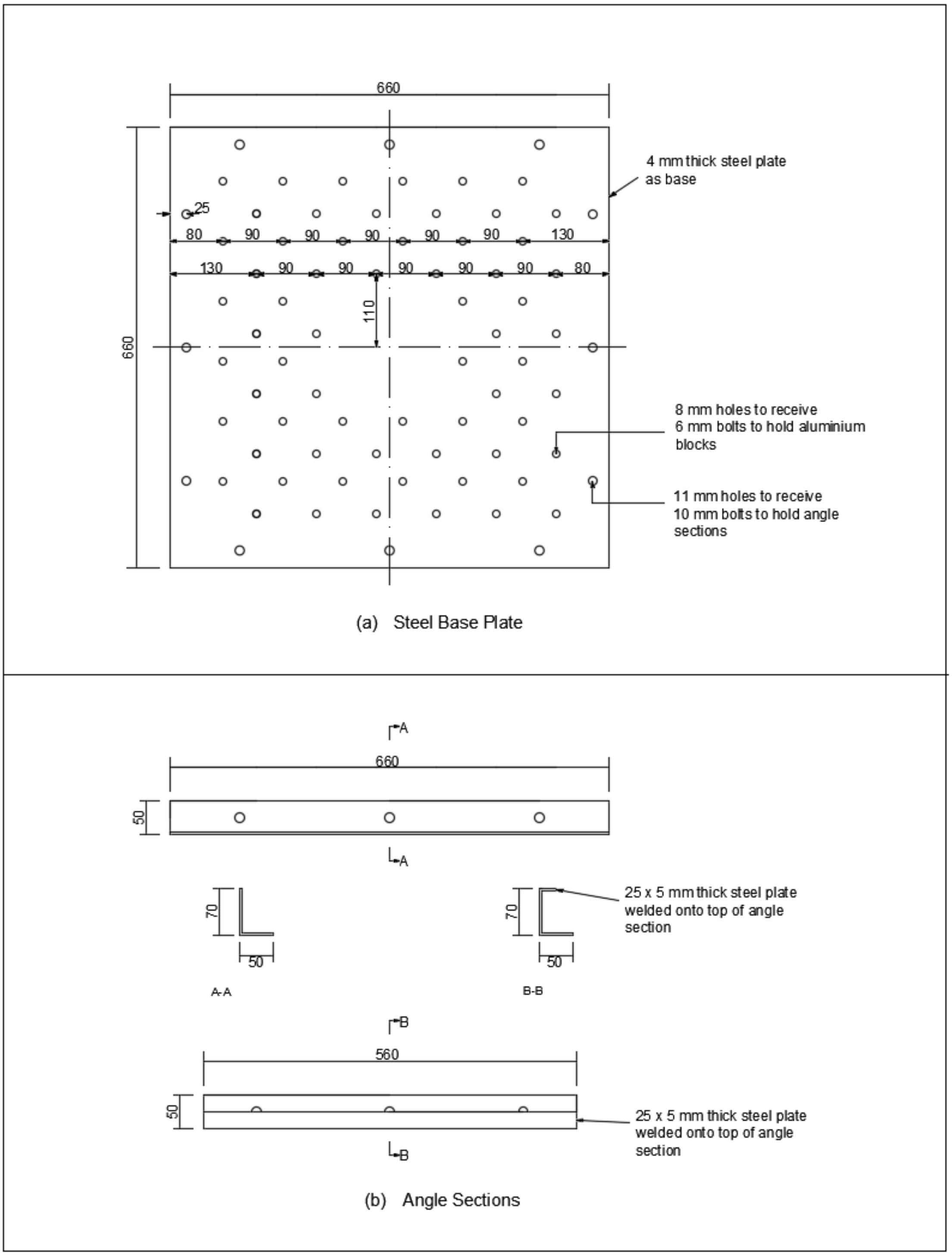

Figure 3.5 Detailing of steel mould components for Internal Column Series

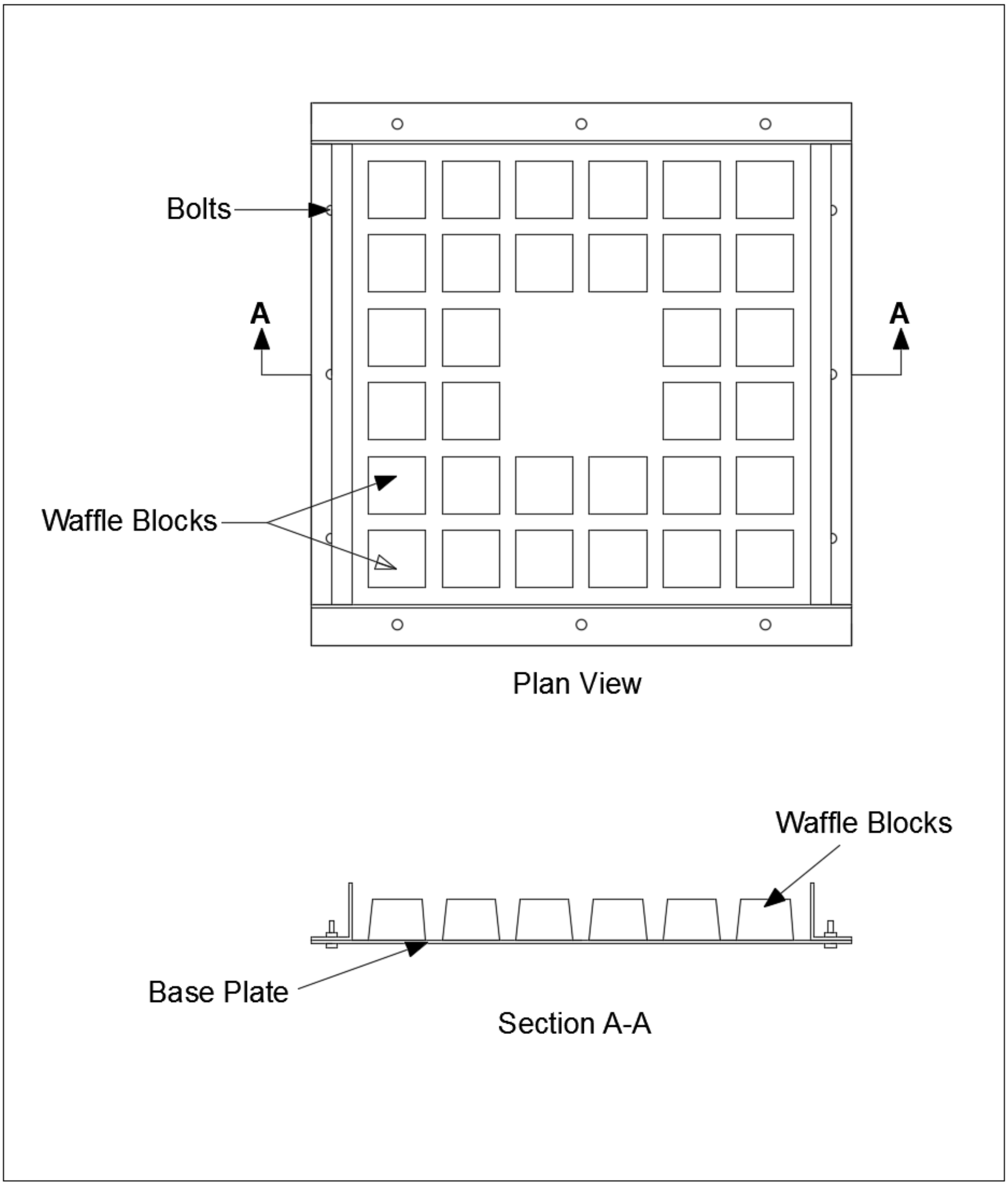

Figure 3.6 Mould Setup for Internal Column Series

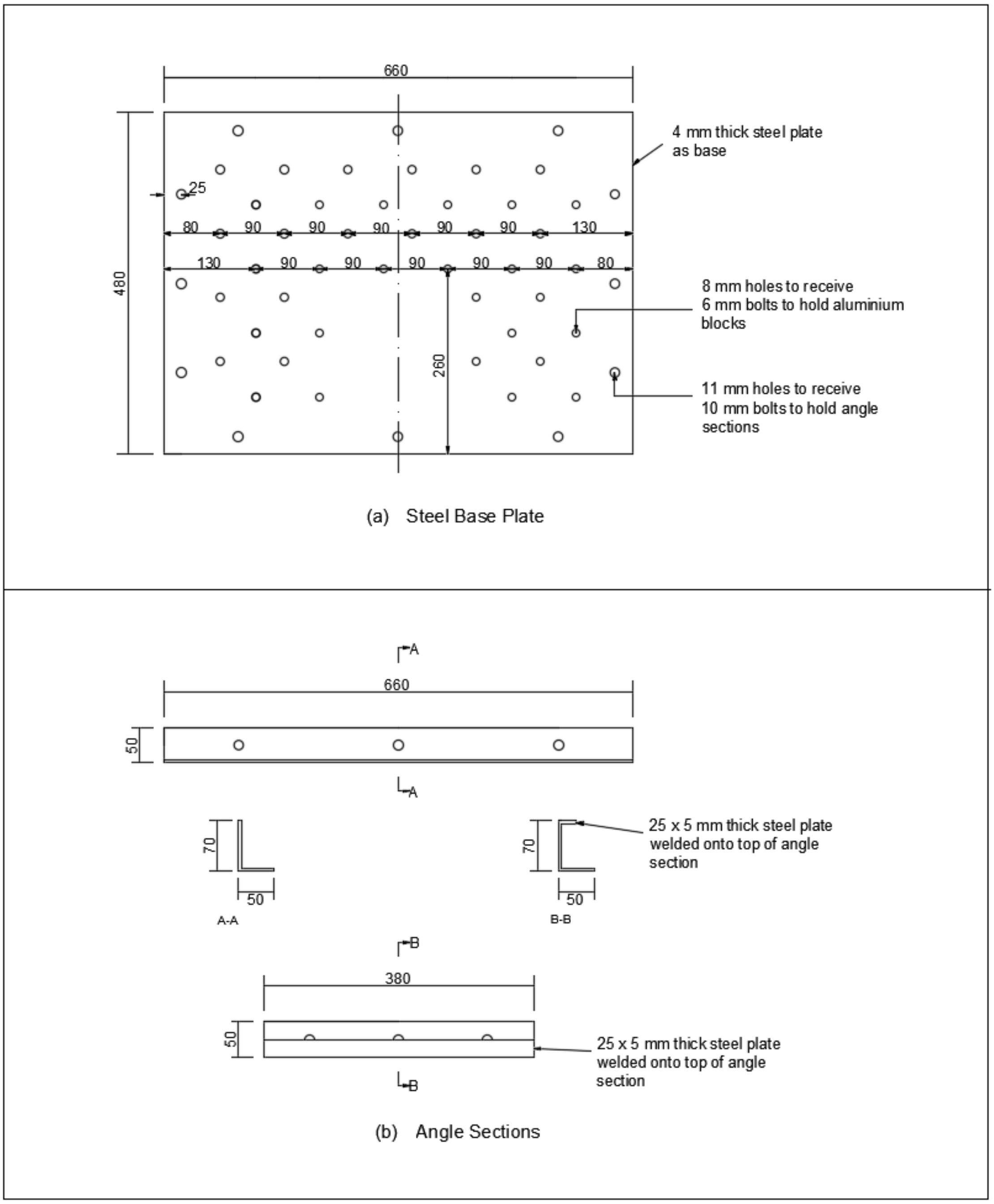

Figure 3.7 Detailing of steel mould components for Edge Column Series

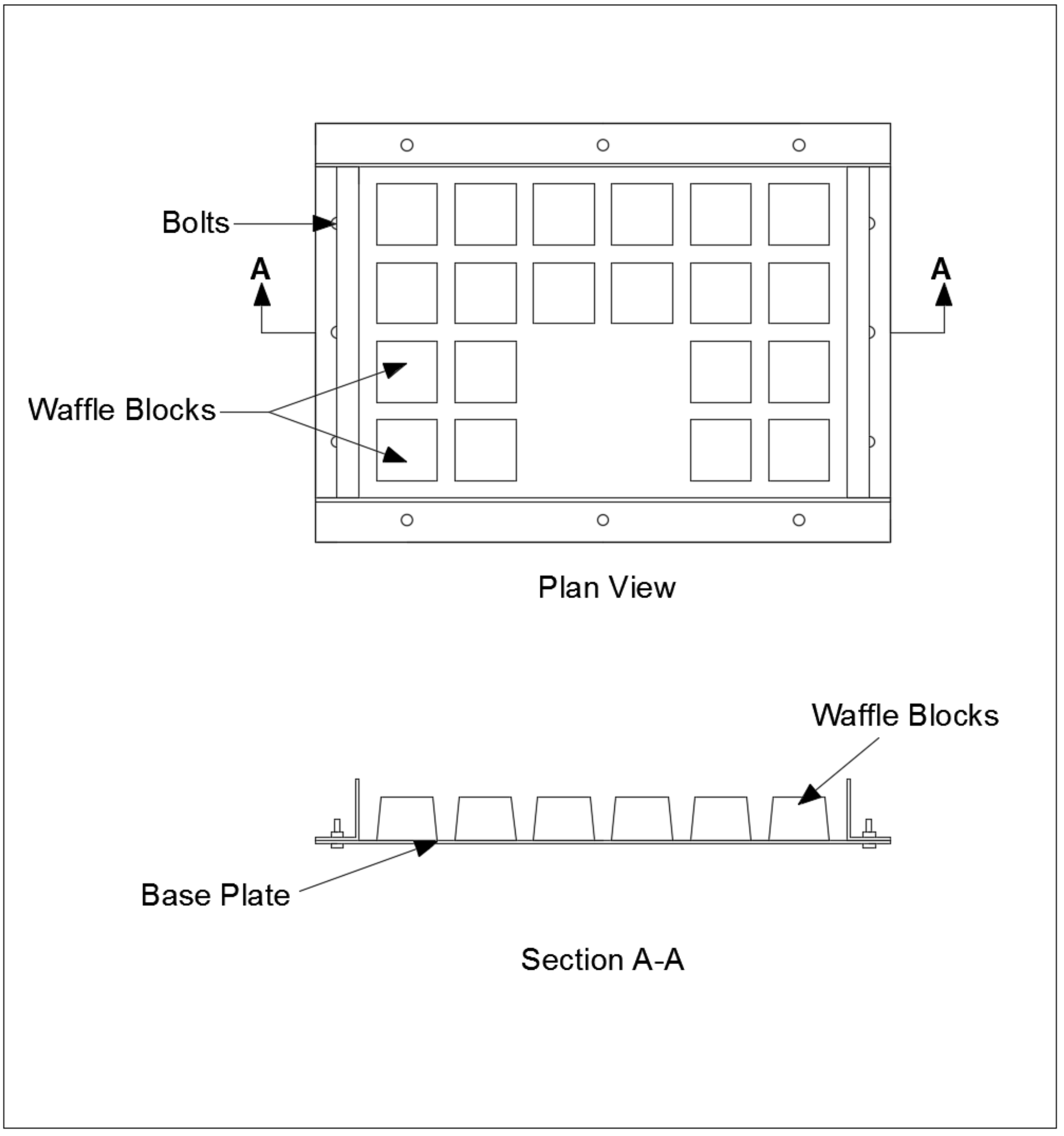

Figure 3.8 Mould setup for Edge Column Series

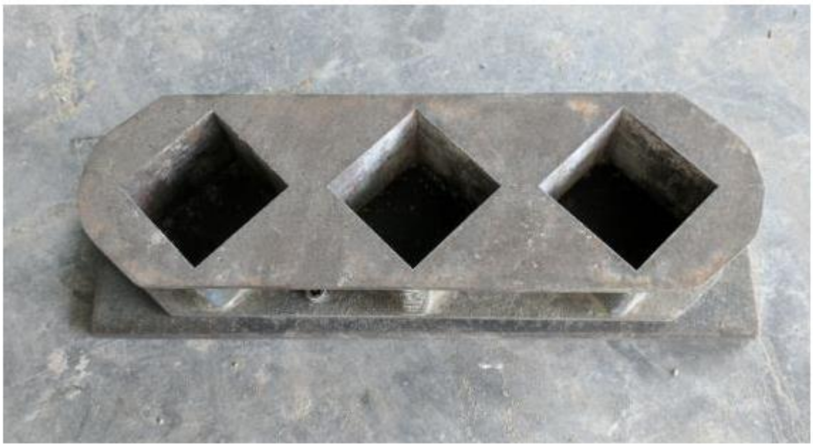

Figure 3.9 Steel mould of 50 mm cubes

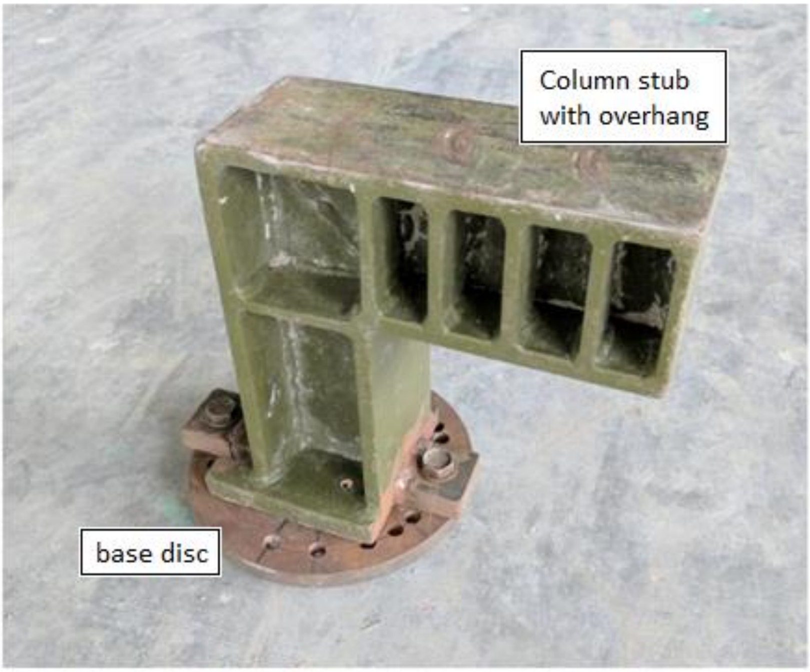

Figure 3.10 Steel L-Column Stub

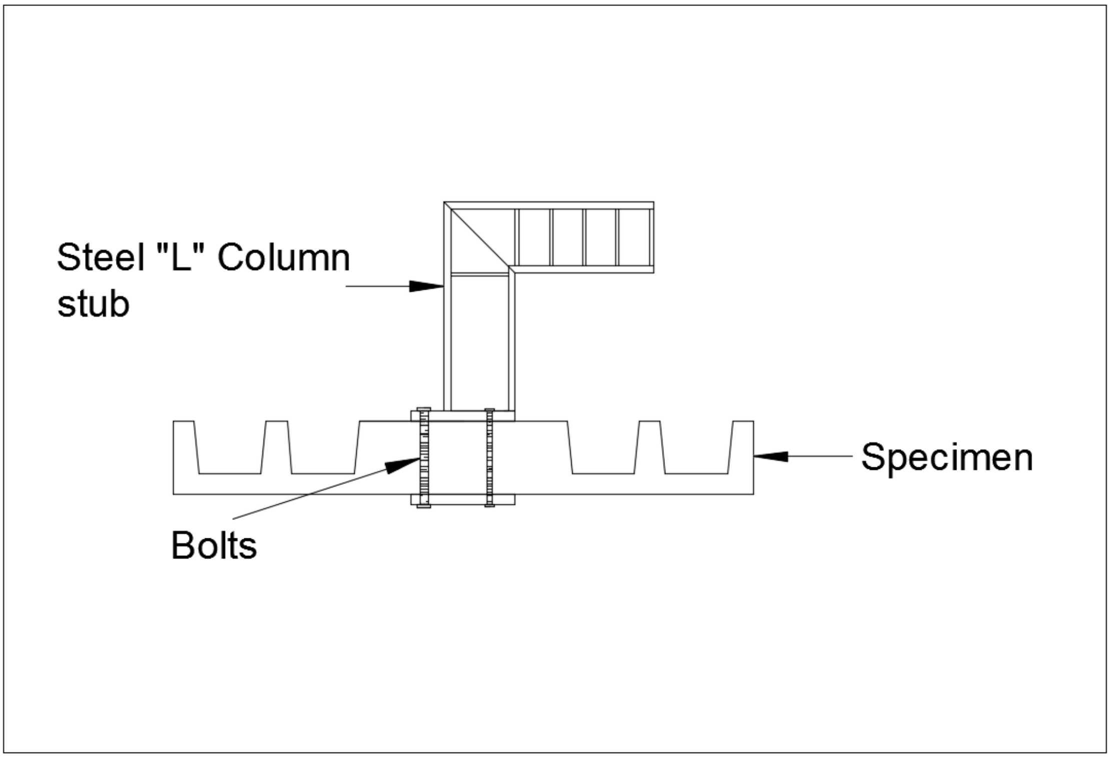

Figure 3.11 Illustration of holding down bolts to prevent uplift

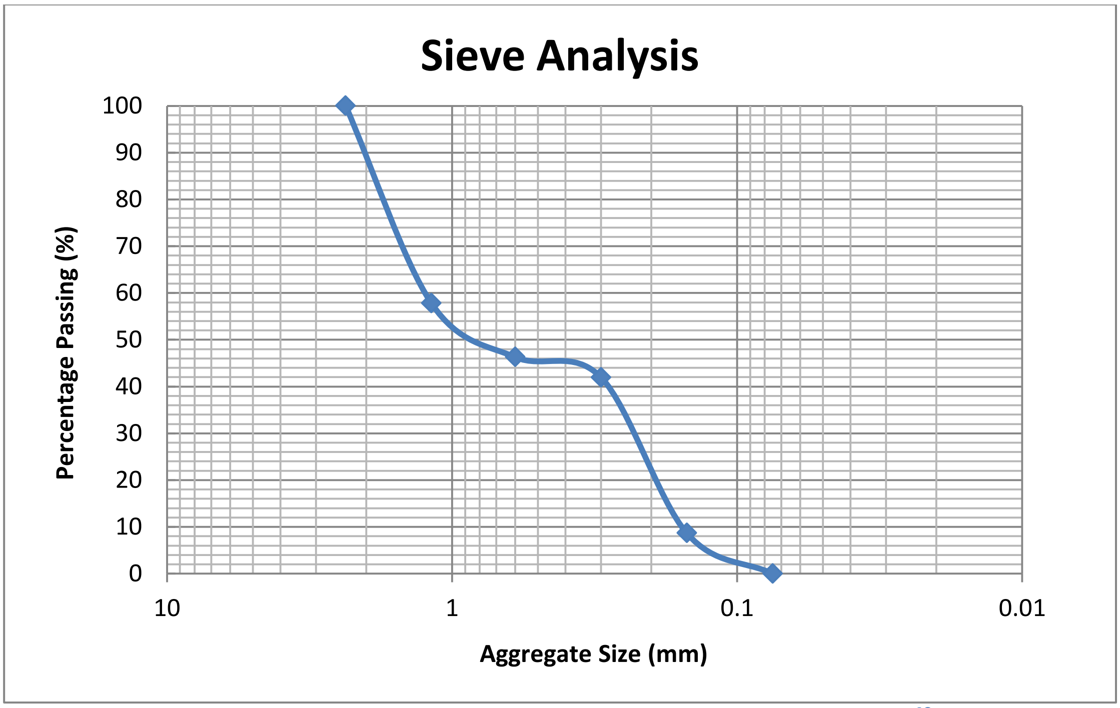

Figure 3.12 Aggregate sieve grading as according to Johnson[40]

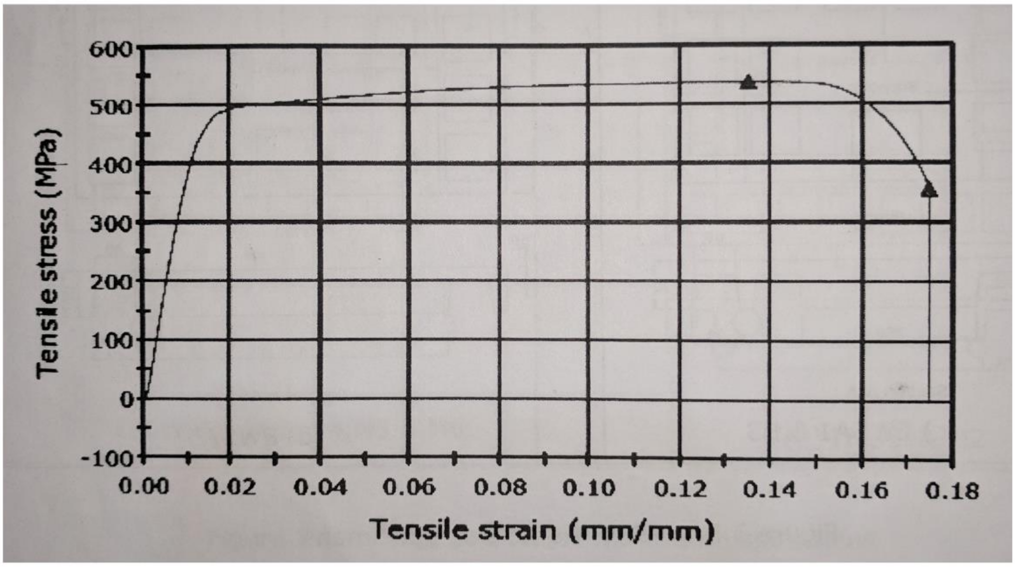

Figure 3.13 Stress vs Strain curve of 3.4 mm bars

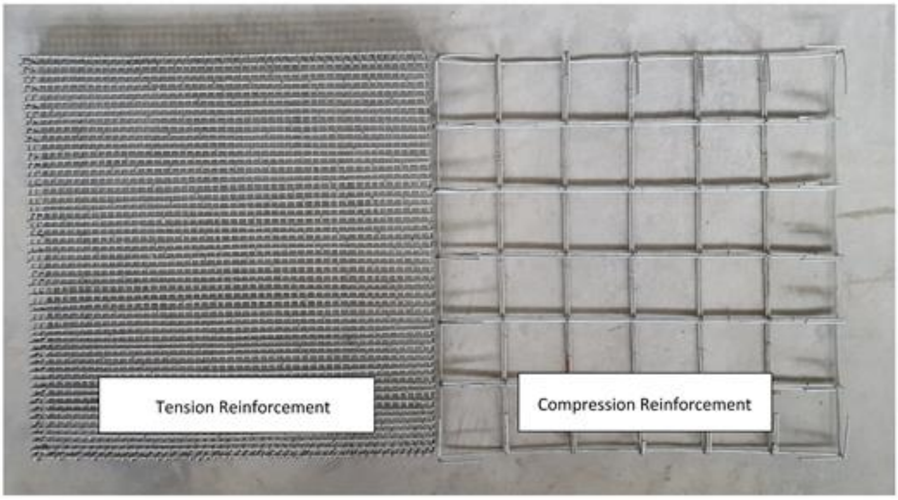

Figure 3.14 Fabricated reinforcement cage for Internal Column Series

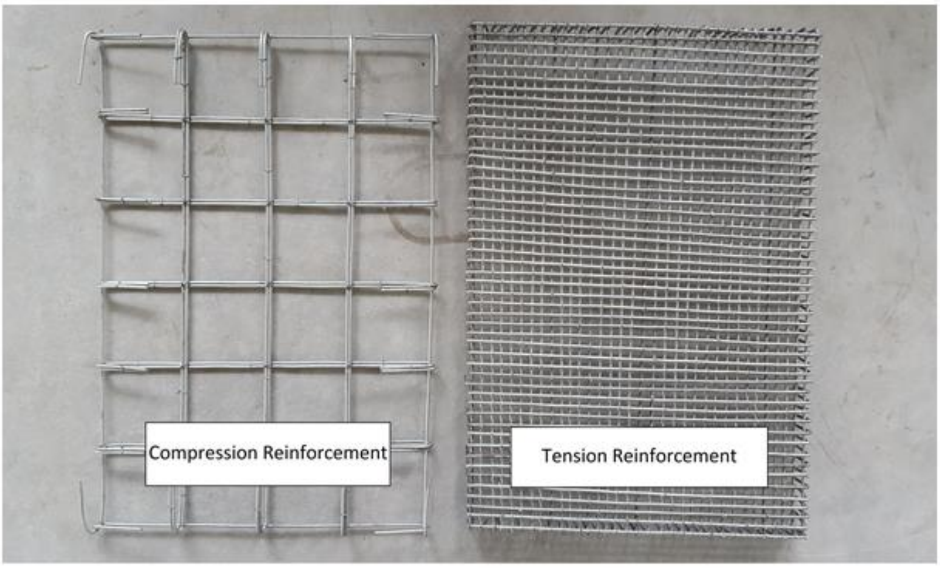

Figure 3.15 Fabricated reinforcement cage for Edge Column Series

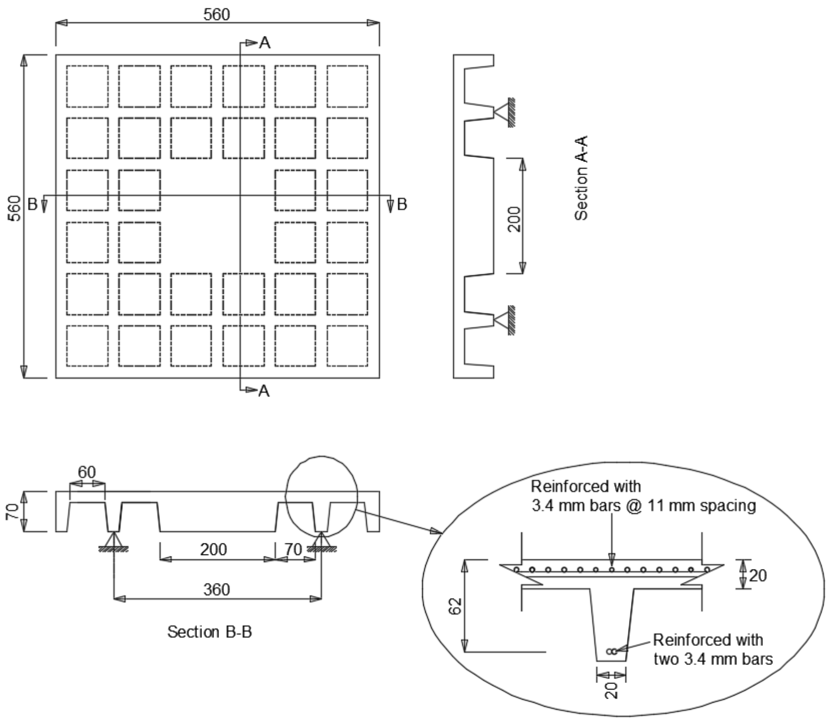

Figure 3.16 Schematic diagram of reinforcement for Internal Column Series

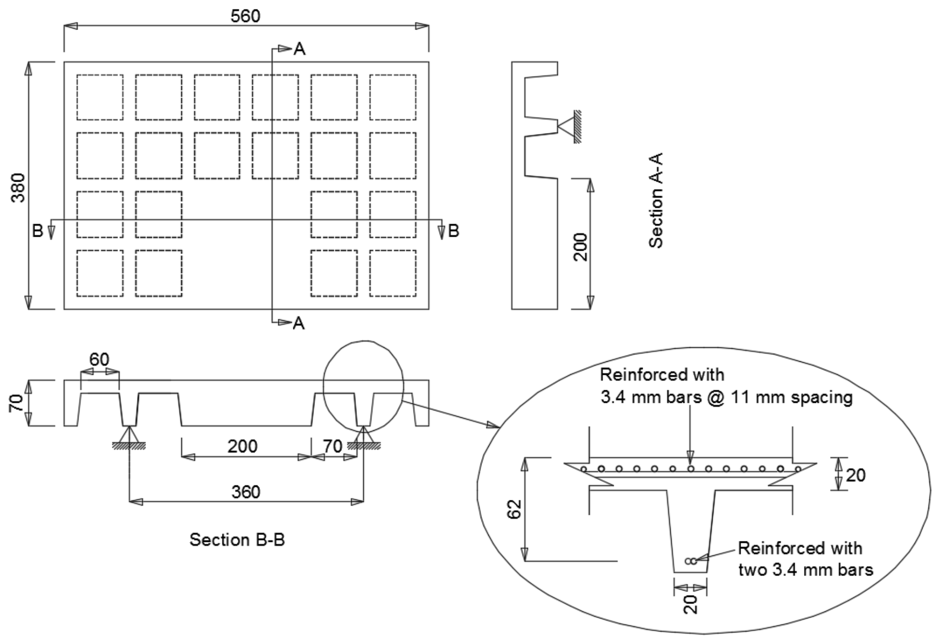

Figure 3.17 Schematic diagram of reinforcement for Edge Column Series

(a) Compression Side

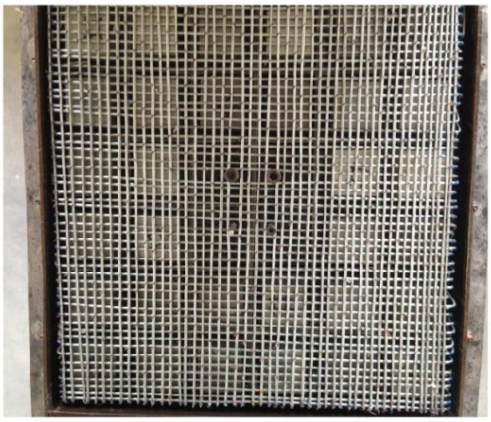

(b) Tension Side

Figure 3.18 Placement of reinforcement cage right before concreting works

Figure 3.19 Test Setup

Figure 3.20 Test Setup for IWSB 9 (Internal Column Series)

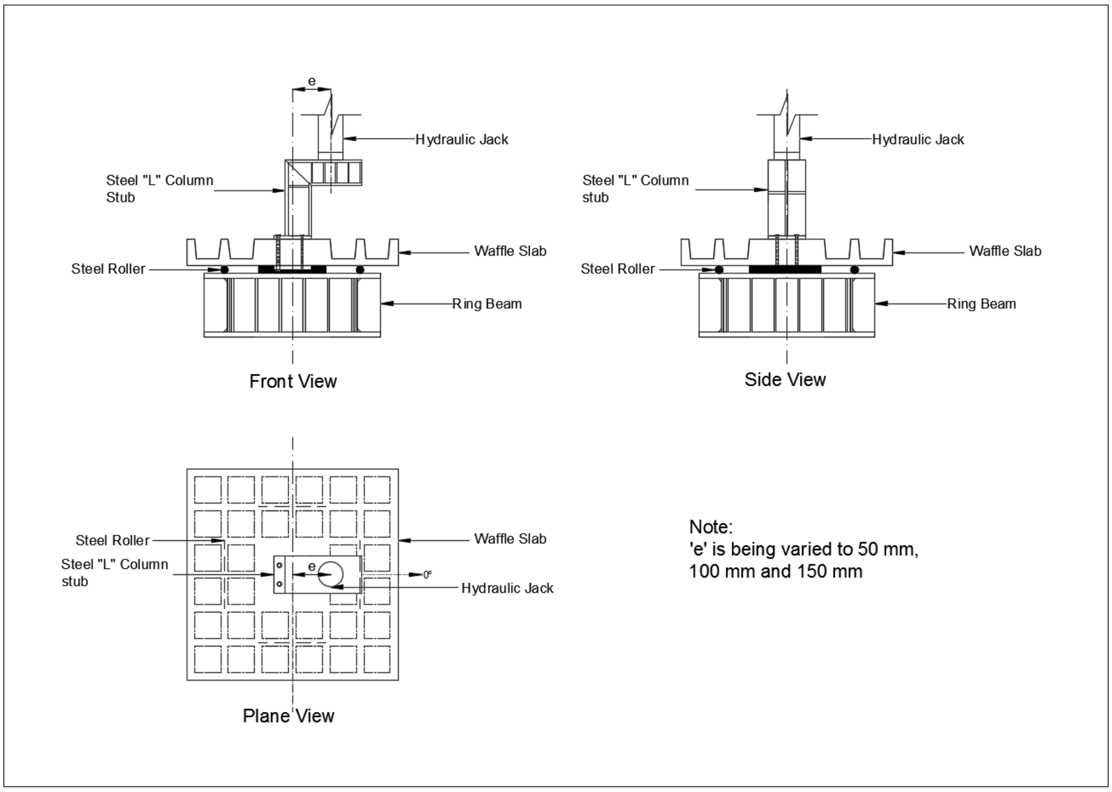

Figure 3.21 Schematic diagram of test setup for IWSB 1, 4 and 7

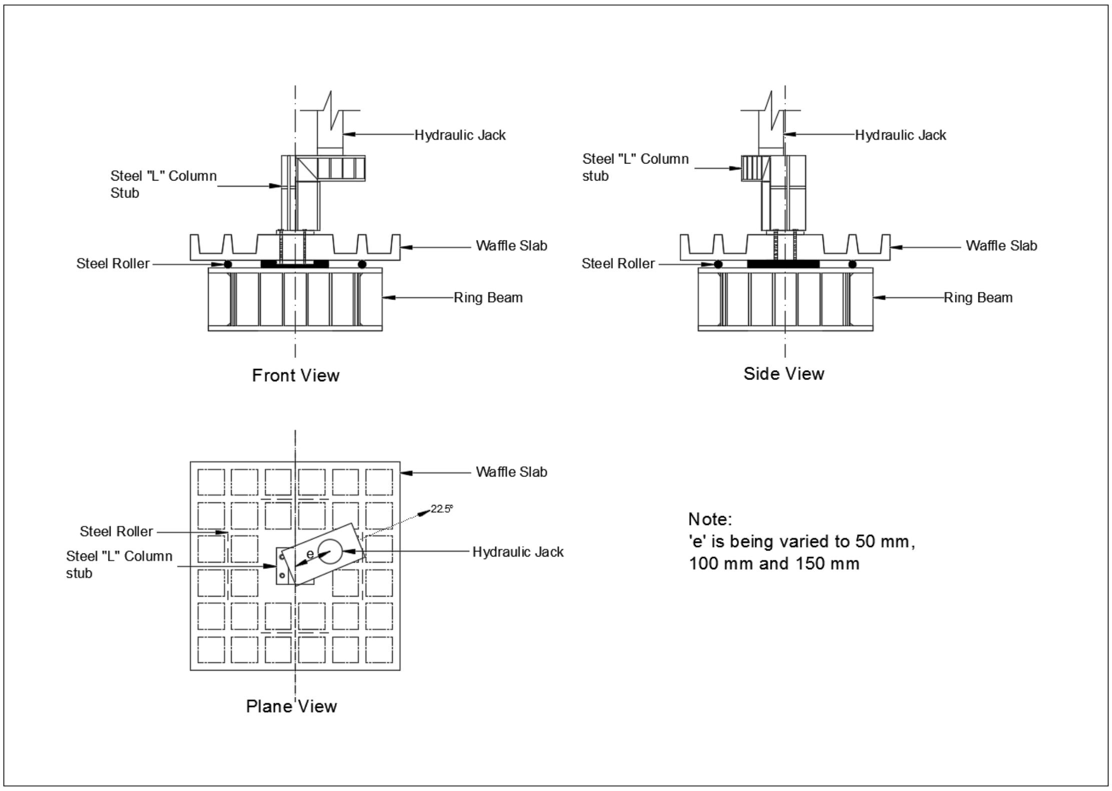

Figure 3.22 Schematic diagram of test setup for IWSB 2, 5 and 8

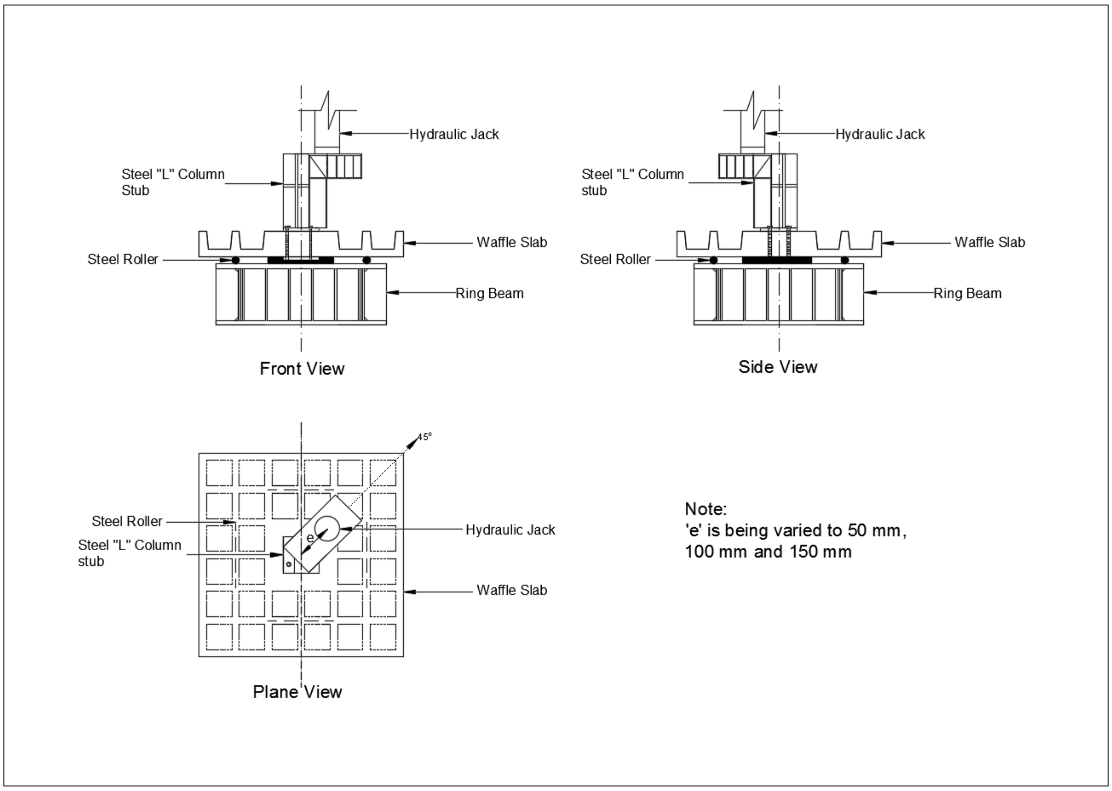

Figure 3.23 Schematic diagram of test setup for IWSB 3, 6 and 9

Figure 3.24 Test Setup for EWSB 3

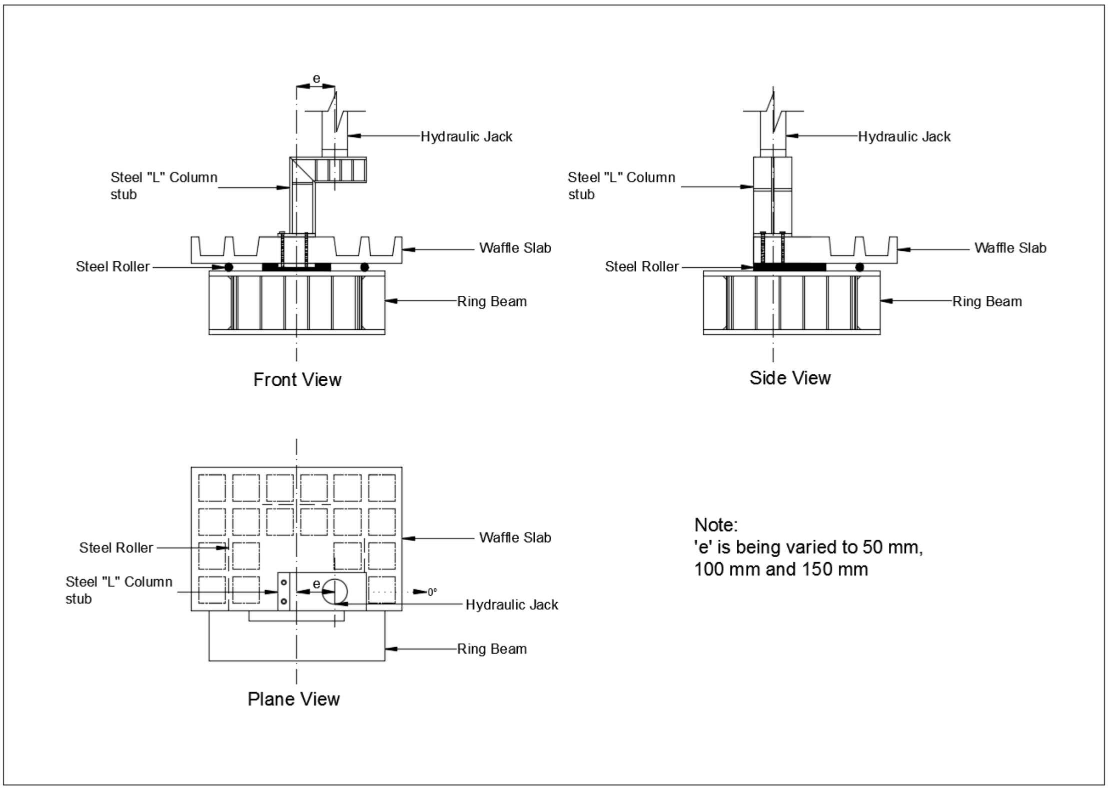

Figure 3.25 Schematic diagram of test setup for EWSB 1, 6 and 11

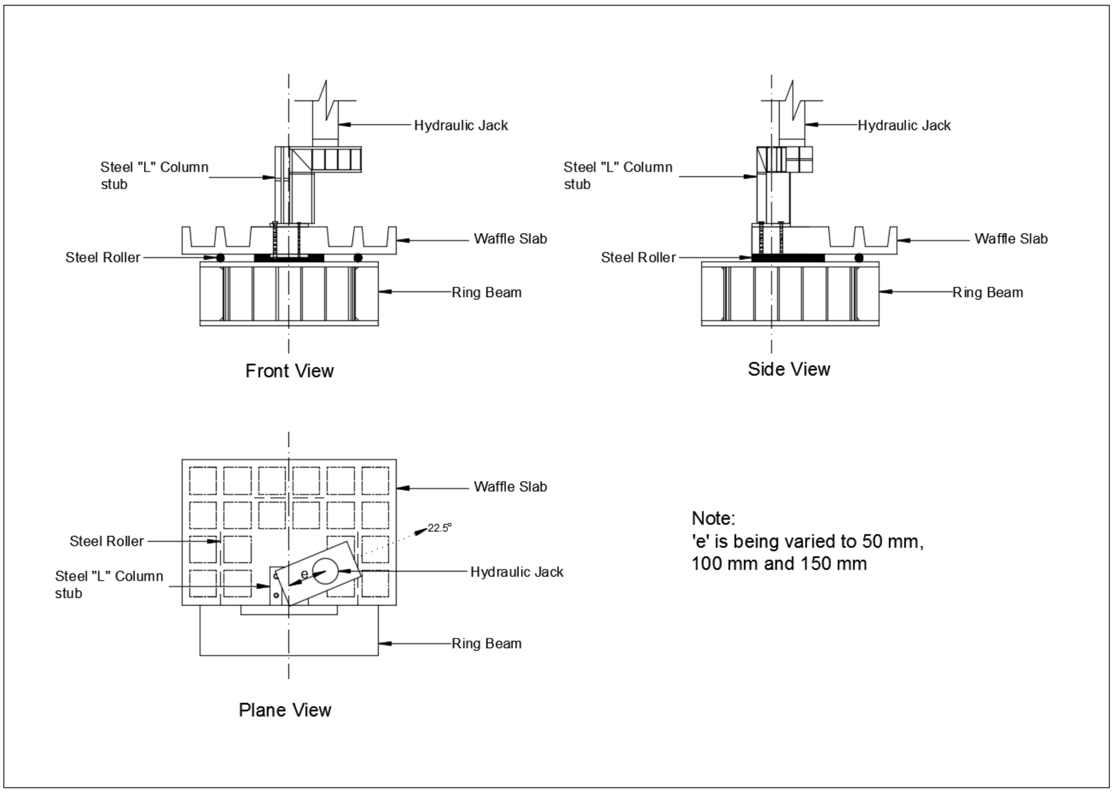

Figure 3.26 Schematic diagram of test setup for EWSB 2, 7 and 12

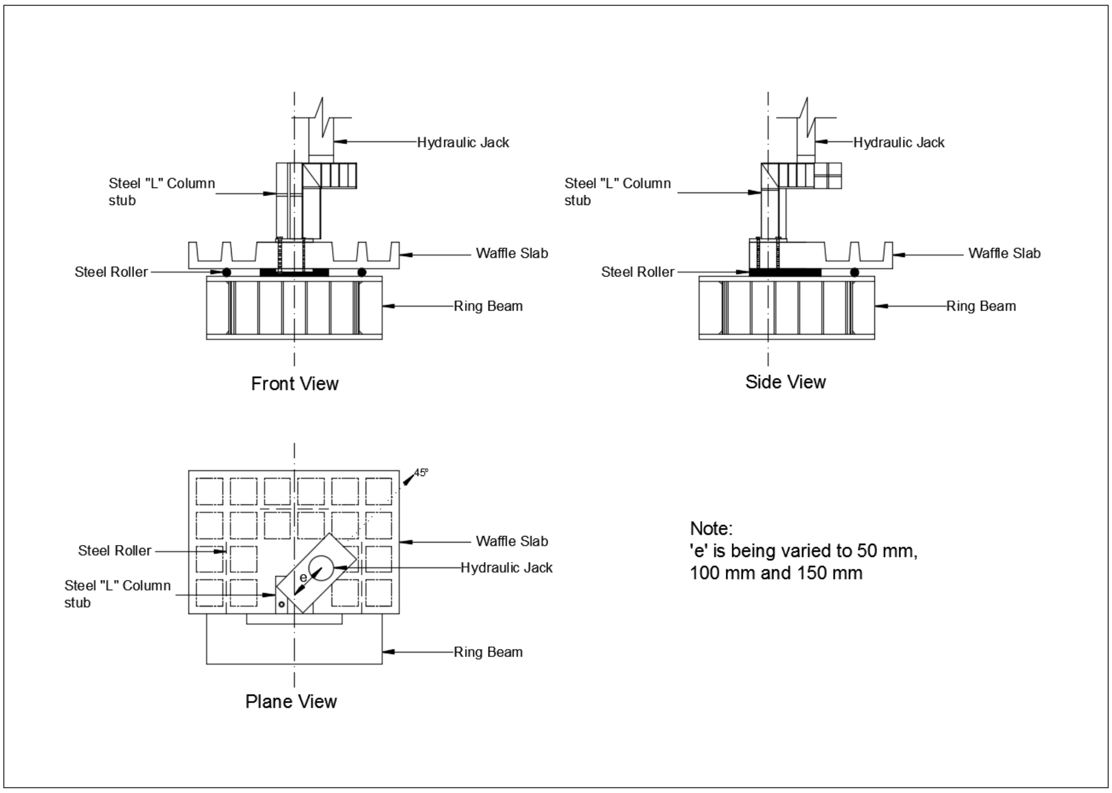

Figure 3.27 Schematic diagram of test setup for EWSB 3, 8 and 12

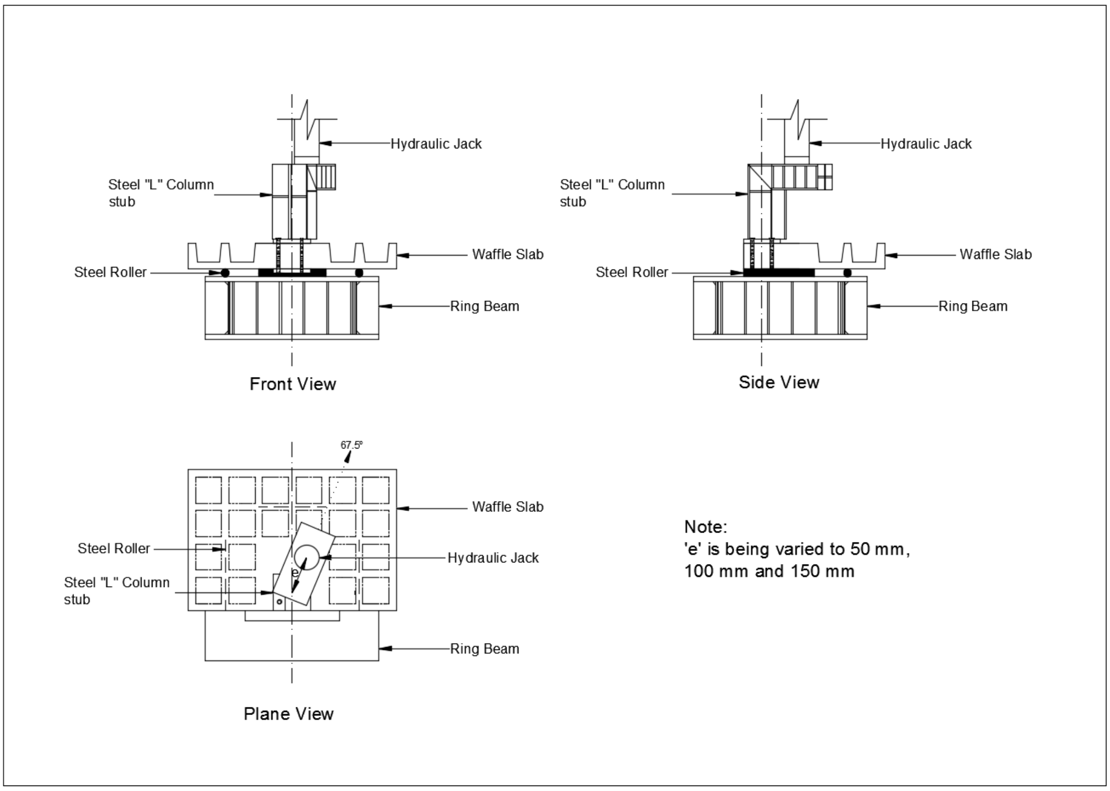

Figure 3.28 Schematic diagram of test setup for EWSB 4, 9 and 13

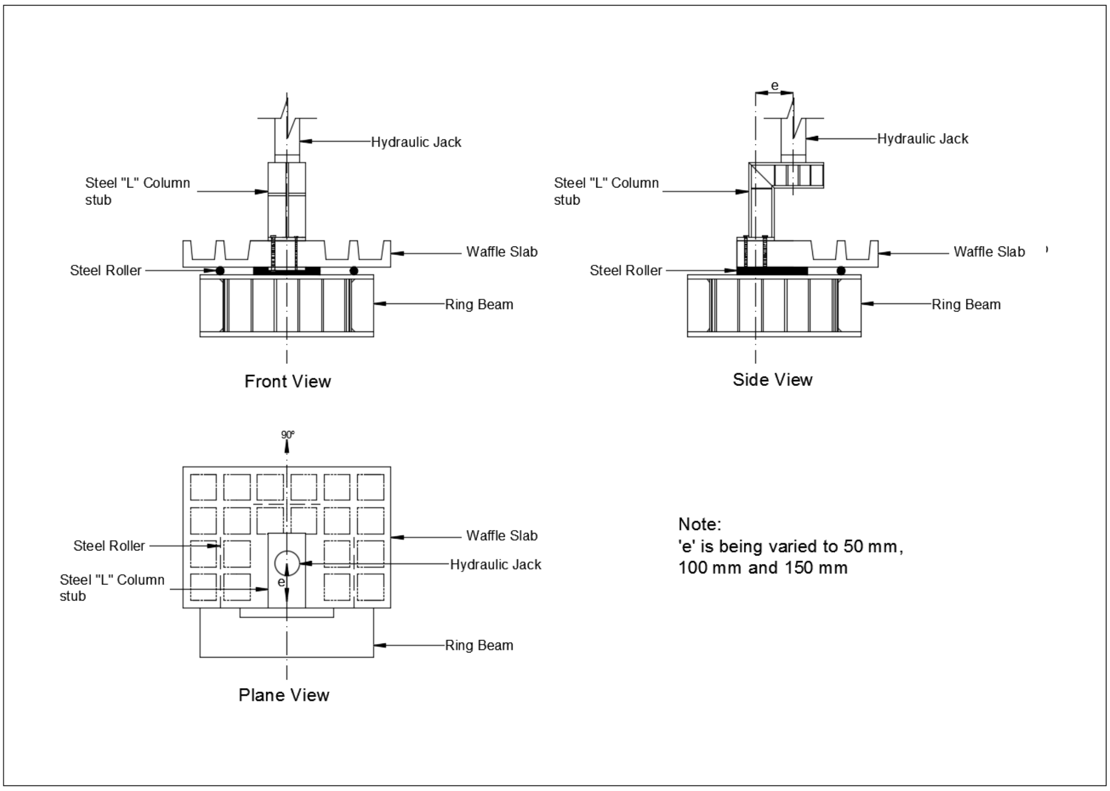

Figure 3.29 Schematic diagram of test setup for EWSB 5, 10 and 15

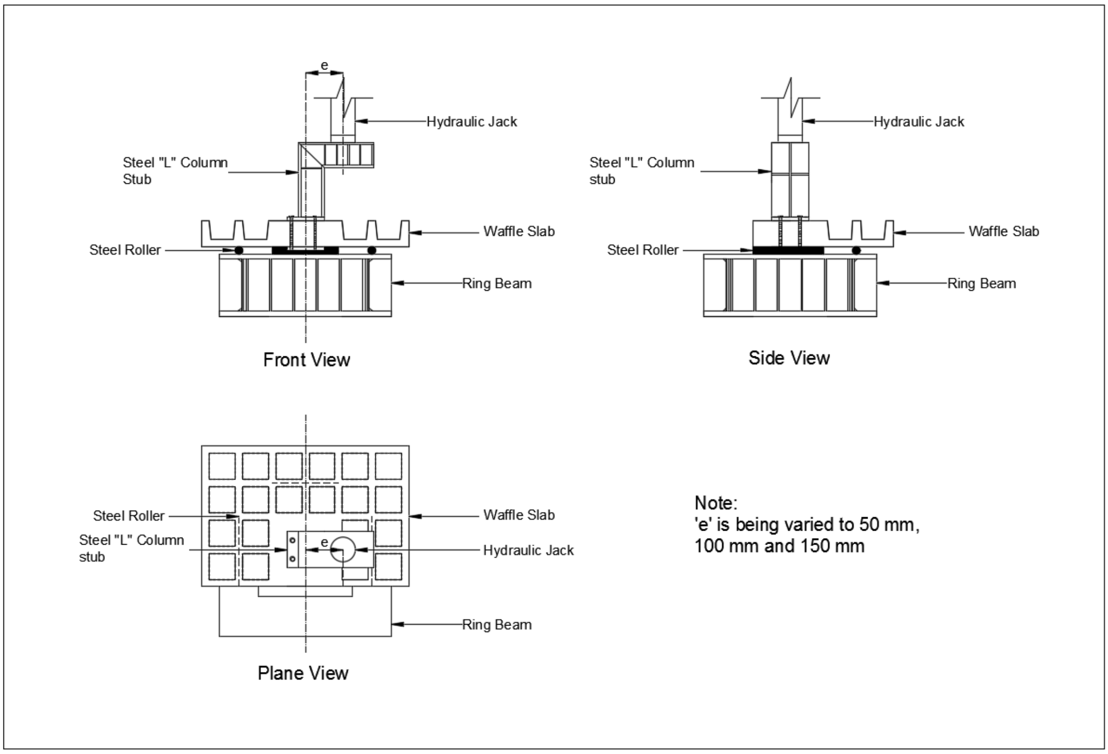

Figure 3.30 Schematic diagram of test setup for EWSCE 1, 2 and 3

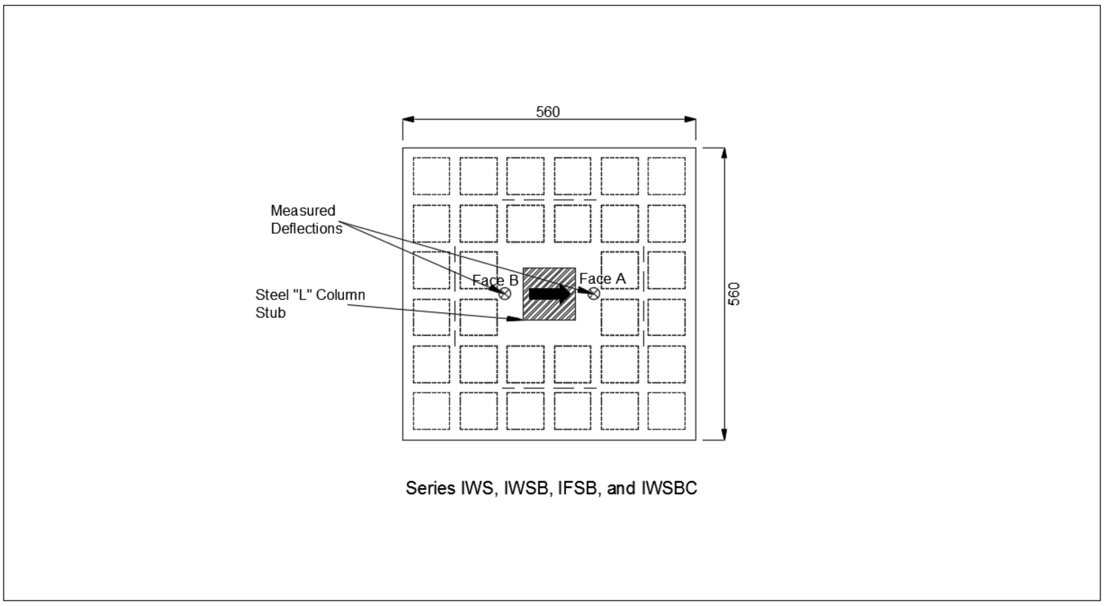

Figure 3.31 Locations of dial gauges in Internal Column Series

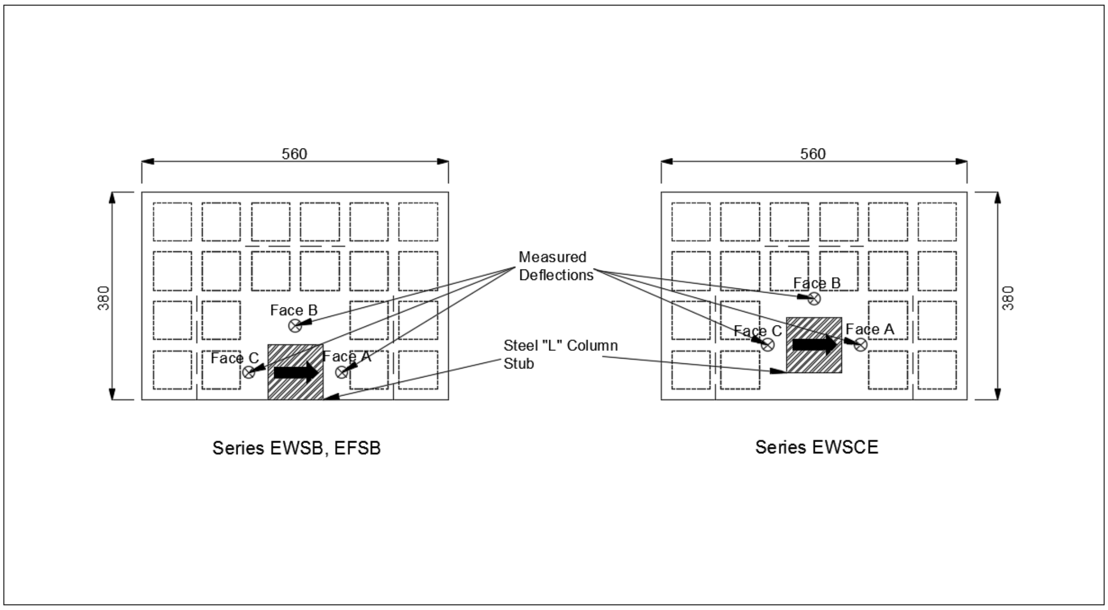

Figure 3.32 Locations of dial gauges in Edge Column Series

Chapter 4 Failure Mechanisms and Test Results

4.1 Introduction

The experimental details for all types of slabs tested in this research are described in Chapter 3. For the internal column series, the variables tested were principle angle of biaxial moment transfer, column's eccentricity, column's orientation, and size of solid section. For the edge column series, the variables tested were principle angle of biaxial moment transfer, column's eccentricity, column's location, and size of solid section.

A total of thirty-eight slab specimens were tested and studied: fifteen slabs in the internal column series; and twenty-three slabs in the edge column series. All slab specimens were observed to fail in a sudden rupture punching failure and with a sudden drop of shear resistance from the peak. The internal shear cracks were found to propagate from the vicinity of the column to the support, otherwise 21 degree inclination (or a distance of 2.6 times the slab depth from the column face) was observed. A solid revolution was formed, which separated from the main slab vertically.

This chapter presents the overall behaviour of the slabs under loading, the failure mechanisms, the punching capacity and the deflections of the slab specimens described in Chapter 3.

4.2 Internal Column Series

4.2.1 Concentric Loading

4.2.1.1 Series IWS

In this series, only one waffle slabs was tested. The internal punching mechanism investigated in this series was waffle slabs with a solid section of 200 mm x 200 mm, loaded to failure, without the presence of moment transfer. (see Table 4.1)

4.2.1.2 Behaviour of Slab during Punching Shear Failure

The internal punching failure mechanism investigated in this series was in the absence of unbalanced moment transfer from the column to the slab. One waffle slab was tested and the result was found to agree with the previous findings[3,4]. However, the result has been used to form the benchmark for further comparison with Internal Column Series loaded with eccentric moments.

The slab specimen was observed to exhibit a punching failure mechanism similar to that at an internal flat slab-column connection[66], where the specimen failed in a sudden rupture punching failure with a sudden drop of shear resistance from its peak. The observed punching failure surface was characterized by internal cracks propagated from the vicinity of column through the slab thickness at about 28 degree inclination and intersecting the top surface of the slab at a distance of about 1.9 times the slab depth from the column face to the root of the supports (see Figure 4.1). In plan, a complete solid revolution of concrete was formed, with the column at its center, which separated from the main slab vertically leaving the rest of the slab remaining rigid.

However, the distinct difference between the punching failure mechanisms observed from in waffle slabs and the flat slabs is the reduced solid section at the column vicinity to form a complete solid of revolution, as such; some of the potential failure surface was lost when it entered the waffle section, as shown in Figure 4.2 and 4.3. The consequence of having less shear failure surface existed within the waffle slab to absorb the applied energy resulted in a lower ultimate punching capacity.

The loss of punching capacity depends on the geometry of the solid section and the column. If the width of the solid section was sufficient such that the complete solid revolution of concrete was formed within the region, there would be no difference between the waffle slabs and the flat slabs. However, if the width of the solid section was smaller than the complete solid revolution of concrete, the punching mechanism differs in having smaller shear failure surface, thus reducing the punching capacities of waffle slabs.

The formation of cracks was first observed on the tension side of the slab, directly above the column stub. The observed cracking load was found to be 52% of the ultimate capacity of the slabs. Upon further loading, more cracks appeared on the tension side of the slabs as well as the waffle sections on the compression side of the slabs. These cracks were induced by the negative moment on the column face. At failure, all specimens were observed to punch in a sudden rupture manner and the width of the shear cracks at the vicinities of the column of the solid section increased.

Figure 4.4 shows the plan views of the punched specimen and its cracks patterns. The cracks were marked with marker pens to highlight the cracks patterns.

4.2.1.3 Punching Capacity of Slab

The applied load was increased and recorded at every 4.21 kN interval for the slab specimen. The punching capacity was taken prior to its punching shear failure. The result of the punched slab specimen is presented in Table 4.1.

4.2.1.4 Deflections

The deflections of the slab specimen were measured using dial gauges at the vicinity of the column stub. The readings were taken and recorded after every increment of the applied load. A curve of load-deflection of the slab specimen is presented in Figure 4.5.

In general, the load-deflection curve was found to agree with the previous researchers' findings[4,47]. The load-deflection curve is initiated with a linear elastic behavior and later, a sudden spike in deflection, followed by a second linear elastic behavior until failure occurred. As reported by Marzouk & Hussein[49], the first slope represents the stiffness of an un-cracked section, while the second slope represents the stiffness of a cracked section.

The comparison between the observed cracking load and the actual cracking load inferred from the load-deflection curve is presented in Table 4.2. The observed cracking load was found to be about 17% of the failure load higher than the actual cracking load obtained from the load-deflection curve. This phenomenon is believed to happen due to the formation of micro-cracks formed within the slab specimen and could not be seen by the naked eye.

4.2.2 Eccentric Loading

4.2.2.1 Components of the Series

4.2.2.1.1 Series IWSB

In this series, a total of nine waffle slabs were tested. The internal punching mechanism investigated in this series was carried out on waffle slabs with a solid section of 200 mm x 200 mm, in the presence of biaxial moment transfer with varying load eccentricities and principle angles. (see Table 4.3 and Section 3.2.2)

4.2.2.1.2 Series IFSB

In this series, a total of three flat slabs were tested. The internal punching mechanism investigated in this series was carried out on solid slabs with a solid section of 360 mm x 360mm, being loaded to failure, in the presence of biaxial moment transfer with uniform eccentricity but varying principle angles. (see Table 4.3 and Section 3.2.3)

4.2.2.1.3 Series IWSBC

In this series, a total of two waffle slabs were tested. The internal punching mechanism investigated in this series was carried out on waffle slabs with a solid section of 200 mm x 200 mm, in the presence of biaxial moment transfer with uniform eccentricity but varying column orientation. (see Table 4.3 and Section 3.2.4)

4.2.2.2 Behaviour of Slabs during Punching Shear Failure

The observed punching shear failure mechanisms were found to be similar amongst the tested series mentioned in Section 4.2.2.1. It is similar to the punching failure mechanism observed from an internal flat slab-column connection that is the specimens failed in an abrupt manner at the last load increment with a sudden drop of shear resistance from its peak. The observed punching failure shear surface was characterized by internal cracks propagated from the vicinity of column through the slab thickness at about 28 degree inclination and intersecting the top surface of the slab at the roots of the supports, which is located at a distance of about 1.9 times the slab depth from the column face, as shown in Figure 4.1.

However, the distinct difference between the punching failure mechanisms observed from waffle slabs and the flat slabs is the reduced solid section at the column vicinity to form a complete solid of revolution, as such; some of the potential failure surface was lost when it entered the waffle section, as shown in Figure 4.6 to Figure 4.8. The consequence of having less shear failure surface existed within the waffle slab to absorb the applied energy resulted in a lower ultimate punching capacity.

In eccentric loading, the shear surface were observed to be dependent on the ratio of the column eccentricity, e, to the column size, C_x. When the ratio, $\frac{e}{C_x}$, was 0.5, the punching failure surface was found to propagate from the corners of the lightly loaded region of the column to the heavily loaded region of the column. When the ratio, $\frac{e}{C_x}$, was ≥ 1, the punching failure surface was found to propagate from the side regions of the column to the heavily loaded region of the column. A schematic diagram summarizing these eccentric effects is shown in Figure 4.9.

In the presence of biaxial moment transfer, the failure shear surface was observed to be different among all three principle angles (0°, 22.5°, and 45° from the orthogonal axis) investigated in this research. A schematic diagram showing the test observations is shown in Figure 4.10.

In general, when the principle angle was set to 0°, the punching failure surface was observed to be the largest (denoted as '1' in Figure 4.10), followed by those having their principle angle set to 45^o (denoted as '3' in Figure 4.10), and those having their principle angle set to 22.5^o were observed to be the least (denoted as '2' in Figure 4.10). In addition, when the principle angle of biaxial moment transfer was set to 22.5^o, it was observed that the punching failure surface was unsymmetrical that is the far side of the failure surface did not propagate to the side regions of the column as observed from those having their principle angles set to 0^o and 45^o. The loss of potential shear area derived from this unsymmetrical failure surface resulted with a lower punching capacity being mobilized.

The formation of cracks was first observed on the tension side of the slab specimens, directly above the column stub. The observed tensile cracking loads, in general, about 52% of the ultimate punching failure capacity of the slabs (see Table 4.4). Upon further loading, more cracks appeared on the tension side of the slabs as well as the shear cracks on the waffle sections in the compression region of the slabs. Torsion cracks[56] were formed at a distance of 0.5d away from the column side faces.

Figure 4.11 to Figure 4.24 show the punched specimens and their cracks patterns. The cracks were marked with marker pens to enhance the cracks patterns.

4.2.2.3 Punching Capacity

The applied load was increased and recorded at every 4.21 kN interval for all slab specimens. The punching capacities were taken prior to punching shear failure. The results of the punched slab specimens are presented in Table 4.3.

In general, the results showed that an increase in the size of solid section, or a reduction in the column's eccentricity, or an increase in the concrete compressive strength increases the load carrying capacity. On the other hand, the effects from principle angles of biaxial moment transfer appear to be inconsistent when the principle angle is increased from 0^o to

22.5^{o} and 45^{o}. Details of these effects on the slab specimens' punching capacity are further explained in Section 4.2.2.5.

4.2.2.4 Deflection

The deflections of the slab specimens were measured using two digital gauges positioned adjacent to the heavily loaded side of the column stub (front face of the column) and the least loaded side of the column stub (back face of the column). The deflections were taken and recorded after every increment of applied load. For every specimen, two curves of load versus deflection are presented; see Figure 4.25 to Figure 4.38.

From all these figures, it can be observed that the deflections at the front face of the column are always higher than that at the back face of the column. This phenomenon can be attributed to the eccentric loading, which transformed into rotation as the loads transferred from the column to the slab.

However, these load-deflection curves are found to be similar in nature to those carrying concentric loading (as compared to Figure 4.5). In general, the load-deflection curves are initiated with a linear elastic behavior, and later, a sudden spike in deflection, followed by a second linear elastic behavior until failure occurred. As reported by Marzouk & Hussein[49], the first slope represents the stiffness of an un-cracked section, while the second slope represents the stiffness of a cracked section.

The observed cracking loads and the actual cracking loads inferred from the load-deflection curves are compared in Table 4.4. In average, the observed cracking loads were found to be about 14% higher than the actual inferred cracking loads obtained from the load-deflection curves. This phenomenon is believed to happen due to the formation of micro-cracks formed within the slab specimen and could not be seen by the naked eye.

4.2.2.5 Effects of test variables

4.2.2.5.1 Principle angle of biaxial moment transfer

The effects of principle angle of biaxial moment transfer on punching resistance observed in this research are summarized and presented in Figure 4.39. The test results exhibit that punching resistance of waffle slabs, in the presence of biaxial moment transfer, is at its peak when the principle angle is zero. Further analysis into these test results reveal that punching resistance of slab specimens loaded with principle angle of 22.5^o exhibited the lowest punching resistance amongst three principle angles investigated. That is, the sequential order of moment principle angles with respect to punching shear capacities were 0^o, followed by 45^o, and lastly, 22.5^o, as demonstrated in Figure 4.39.

Such sequential order was also observed with regards to column eccentricities. That is, at 50 mm column eccentricity, comparisons between IWSB 1, having loaded with a principle angle of biaxial moment transfer of 0^o, with IWSB 2 and IWSB 3, having loaded with a principle angle of biaxial moment transfer of 22.5^o and 45^o, portrayed a reduction in ultimate capacity of 23% and 15%, respectively.

At 100 mm column eccentricity, comparisons between IWSB 4, having loaded with a principle angle of biaxial moment transfer of 0^o, with IWSB 5 and IWSB 6, having loaded with a principle angle of biaxial moment transfer of 22.5^o and 45^o, portrayed a reduction in ultimate capacity of 23% and 18%, respectively.

At 150 mm column eccentricity, comparisons between IWSB 7, having loaded with a principle angle of biaxial moment transfer of 0^o, with IWSB 8 and IWSB 9, having loaded with a principle angle of biaxial moment transfer of 22.5^o and 45^o, portrayed a reduction in ultimate capacity of 22% and 11%, respectively.

By taking an average for all three series, a reduction of 23% is anticipated when the principle angle of biaxial moment transfer is changed from 0^o to 22.5^o and a reduction of 15% is anticipated when the principle angle of biaxial moment transfer is changed from 0^o to 45^o.

In general, it is observed that the reduction of punching capacities from 0^o to 22.5^o and 45^o are due to the decrease in shear surface area that is being mobilized. That is, when the principle angle of biaxial moment transfer was set at 0^o, the associating shear surface area being mobilized was observed to be the greatest, followed by a smaller shear surface area when the principle angle set at 45^o, and lastly, at 22.5^o. Such phenomenon is mainly due to the fact that far side of the failure surface did not propagate to the side regions of the column (see Figure 4.10 and Section 4.2.2.2).

4.2.2.5.2 Column eccentricity

The punching shear capacities were observed to reduce when the column eccentricity increases, as shown in Figure 4.40. These findings were found agreeable in the presence of all three principle angles.

When the principle angle of biaxial moment transfer is set to 0^o, comparisons between IWSB 1, having a column eccentricity of 50 mm, with IWSB 4 and IWSB 7, having column eccentricities of 100 mm and 150 mm, indicated a reduction in punching capacity of 15% and 31%, respectively.

When the principle angle of biaxial moment transfer is set to 22.5^o, comparisons between IWSB 2, having a column eccentricity of 50 mm, with IWSB 5 and IWSB 8, having column eccentricities of 100 mm and 150 mm, indicated a reduction in punching capacity of 15% and 30%, respectively.

When the principle angle of biaxial moment transfer is set to 45^o, comparisons between IWSB 3, having a column eccentricity of 50 mm, with IWSB 6 and IWSB 9, having column eccentricities of 100 mm and 150 mm, indicated a reduction in punching capacity of 18% and 27%, respectively.

It is believed that the reductions in punching capacity as column eccentricity increases are due to the increasing unbalanced moment being transferred from the column to the slab. This unbalanced moment then transformed into non-uniformly distributed shear stresses around the vicinity of the column, and hence, torsion stresses at the sides of the column. As a result, led to non-simultaneous formation of shear cracks hence shear failure surface to be mobilized, thus, leading to a lower punching shear capacity.

4.2.2.5.3 Column Orientation

The punching shear capacities were found to be slightly affected when the column orientation is rotated according to the principle angle of biaxial moment transfer. As mentioned in Section 4.2.2.5.1, the punching shear capacities were found to be the higher when the principle angle of biaxial moment transfer is at 45^{o} than that at 22.5^{o}. However, when the column orientation is rotated in accordance to the principle angle of biaxial moment transfer, the punching capacity of specimens having their principle angle at 22.5^{o} were found to have higher punching resistance than those set at 45^{o}.

In comparison with IWSB 5, with the column not rotated, IWSCC1 exhibited an increase in punching strength of 15% as the column orientation rotated in accordance to the principle angle (22.5^{o}) of biaxial moment transfer. Conversely, in comparison with IWSB6, with the column not rotated, IWSCC2 exhibited no increase in punching strength as the column orientation rotated in accordance to the principle angle (45^{o}) of biaxial moment transfer, as shown in Figure 4.41.

This increment is due to shear surface area being mobilized within the waffle slab. When the principle angle of biaxial moment transfer is set to 22.5^{o}, it was observed that one face of the column is limiting the extension of the shear surface area when the column orientation is not rotated in accordance to the principle angle, but the otherwise, when the column orientation rotated in accordance to the principle angle. On the other hand, when the principle angle of biaxial moment transfer is set to 45^o, it was observed that the shear surface areas, being mobilized by both column orientations, were indifferent.

4.2.2.5.4 Size of Solid Section

The punching capacities were observed to increase with the size of solid section, as shown in Figure 4.42. By comparing IFSB 1, with a solid section of 360 mm, with IWSB4, with a solid section of 200 mm, the shear capacity was observed to increase by 35% when the principle angle of biaxial moment transfer is set to 0^o. The second comparison is done by comparing IFSB2, with a solid section of 360 mm, with IWSB 5, with a solid section of 200 mm, the shear capacity was observed to increase by 47% when the principle angle of biaxial moment transfer is set to 22.5^o. Lastly, by comparing IFSB 3, with a solid section of 360 mm, with IWSB 6, with a solid section of 200 mm, the shear capacity was observed to increase by 40% when the principle angle of biaxial moment transfer is set to 45^o.

By taking an average for all three principle angles of biaxial moment transfer, an increase of 41% can be anticipated when the size of solid section increases from 200 mm to 360 mm.

In addition, it was found that specimens IFSB 1, IFSB 2 and IFSB 3 punched in a steeper angle as compared to specimens IWSB 4, IWSB 5 and IWSB 6, respectively (see Figure 4.43). It was also noticed that specimens with larger solid section does not punch towards the support at 28^o but rather a steeper angle of 35^o.

The increase in punching shear capacities was expected due to the increase in the size of solid section, which in turn, requires more work to be done to separate the solid section from the main slab vertically.

4.3 Edge Column Series

4.3.1 Components of the Series

4.3.1.1 Series EWSB

In this series, a total of fifteen edge waffle slabs were tested. The edge punching mechanism investigated in this series was carried out on waffle slabs with a solid section of 200 mm x 200 mm, in the presence of biaxial moment transfer with varying principle angle and eccentricities (see Table 4.5 and Section 3.3.1)

4.3.1.2 Series EFSB

In this series, a total of five flat slabs were tested. The edge punching mechanism investigated in this series was waffle slabs with a solid section of 360 mm x 280mm, in the presence of biaxial moment transfer with their eccentricity set at 100 mm from the column centroid and varying principle angle (see Table 4.5 and Section 3.3.2)

4.3.1.4 Series EWSCE

In this series, a total of three waffle slabs were tested. The edge punching mechanism investigated in this series was waffle slabs with a solid section of 200 mm x 200 mm, in the presence of moment transfer (parallel to the slab edge) with varying column and column position (see Table 4.5 and Section 3.3.3)

4.3.2 Behaviour of Slabs during Punching Shear Failure

Regardless of the direction of the principle angle of biaxial moment transfer, all specimens were observed to fail in an abrupt manner with a sudden drop of shear resistance from its peak similar to the punching mechanism observed in flat slabs. The observed punching failure shear surface was characterized by internal cracks propagated inner face and the adjacent faces of column through the slab thickness at about 21 degrees (inner face) to 28 degrees (adjacent faces) inclination and intersecting the top surface of the slab at a distance of about 1.9 times to 2.6 times the slab depth from the column face (due to support constraints), as shown in Figure 4.44.

However, unlike flat slabs, the edge punching mechanism in waffle slabs differs in that the reduced solid section at the column vicinity to form a complete half solid of revolution due to some of the potential failure surface was lost when it entered the waffle section, as shown in Figure 4.45 and Figure 4.46. Thus, waffle slabs have lesser shear failure surface to absorb the applied energy, hence would result in a lower ultimate punching capacity.

The shear surface of specimens, loaded with moment parallel to slab edge (EWSCE series), was observed to be dependent on the ratio of the column eccentricity, e, to the column size, C_x. When the ratio, $\frac{e}{C_x}$, was 0.5, the punching failure surface was found to be extended further away from the heaviest loaded face of the column as compared to specimens having ratio, $\frac{e}{C_x}$, ≥ 1. Figure 4.47 illustrates the observed effect of the ratio, $\frac{e}{C_x}$ to the punching mechanism.

With respect to the effects of principle angle of biaxial moment transfer to the punching failure shear surface, five principle angles were tested; it was observed that the area of punching failure surface increased as the punching angles increase (see Figure 4.48). That is, when the principle angle was set to 0^{o}, where the moment transfer was parallel to the slab edge, the punching failure surface was found to be the smallest, followed by the specimens loaded with principle angle of 45^{o}, 67.5^{o}, 22.5^{o} and 90^{o}, respectively.

Similar to those of eccentric punching at internal column, cracks were first observed on the tension surface of the slabs, directly above the column stub. These cracks were first observed at an average 52% (see Table 4.6) of the ultimate failure loads, which are similar to those failed in eccentric punching at internal column mechanism. However, as the load increased, cracks noted on the compression surface (within the waffle sections), while, more cracks also noted on the tension surface.

Figure 4.49 to Figure 4.70 show the punched specimens and their crack patterns. The cracks were marked with marker pens to enhance the readability.

4.3.3 Punching Capacity

The applied load was increased and recorded at every 4.21 kN interval for all slab specimens. The punching capacities were taken prior to punching shear failure. The results of the punched slab specimens are presented in Table 4.5.

In general, the results show that an increase in the size of solid section, or a reduction in the column's eccentricity, an increase in the principle angles of biaxial moment transfer (from loading parallel to the slab edge (0^{o}) to loading perpendicular to the slab edge (90^{o})) or an increase in the concrete compressive strength increases the punching capacity. These effects on the slab specimens' punching capacity are further explained in Section 4.3.5.

4.3.4 Deflection

Three digital gauges were used to measure the deflections of the slab specimens. Unlike the eccentric punching at internal column series, due to space constraints, the arrangement of the digital gauges were different. Instead of placing at the heavily loaded side, the least loaded side and one adjacent side of the column stub, these three digital gauges were placed at fixed positions throughout the edge punching series, as shown in Figure 3.31. The deflections were taken and recorded after every increment of applied load. For every specimen, a curve of load versus deflection is presented, in Figure 4.71 to Figure 4.93.

Throughout the edge loading series, the deflections were observed to be higher at the front region of the column compared to the back region of the column. This is regarded to the eccentric loading, which transform into rotation from the column to the slab.

The load-deflection curves of the slab specimens are again found to be similar to those in the concentric and eccentric loading at internal column series. An initial linear elastic behaviour was first observed, followed by an increase in the rate of deflection until failure. As explained earlier, the first slope represents the stiffness of the un-cracked section, while the second slope represents the stiffness of the cracked section[49].

The observed cracking loads and the actual inferred cracking loads from the load-deflection curves are summarized and compared in Table 4.6. It can be concluded that the observed cracking loads are about 16% higher than the actual inferred cracking loads obtained from the load-deflection curves. This is due to the fact that the formation of micro-cracks within the slab specimen and could not be noticed by the naked eye.

4.3.5 Effects of Test Variables

4.3.5.1 Principle angle of biaxial moment transfer

In the edge punching series, two principle angles (67.5^{o} and 90^{o}) of biaxial moment transfer were added into the existing angles (0^{o}, 22.5^{o}, and 45^{o}) for the internal punching series. The tested principle angles of biaxial moment transfer are therefore: 0^{0}, 22.5^{o}, 45^{o}, 67.5^{o} and lastly, 90^{o}. A consensus was formed that the punching shear capacity of the waffle slab specimens were found to be the highest when the principle angle of biaxial moment transfer is set to 90^o, followed by 22.5^o, 67.5^o, 45^o and lastly 0^o, as shown in Figure 4.94.

At 50 mm column eccentricity, comparisons between EWSB 5, having loaded with a principle angle of biaxial moment transfer of 90^o, with EWSB 1, EWSB 2, EWSB 3 and EWSB 4, having loaded with a principle angle of 0^o, 22.5^o, 45^o and 67.5^o, portrayed a reduction in ultimate capacity of 40%, 16%, 24% and 20%, respectively.

At 100 mm column eccentricity, comparisons between EWSB 10, having loaded with a principle angle of biaxial moment transfer of 90^o, with EWSB 6, EWSB 7, EWSB 8 and EWSB 9, having loaded with a principle angle of 0^o, 22.5^o, 45^o and 67.5^o, portrayed a reduction in ultimate capacity of 33%, 29%, 38% and 33%, respectively.

At 150 mm column eccentricity, comparisons between EWSB 15, having loaded with a principle angle of biaxial moment transfer of 90^o, with EWSB 11, EWSB 12, EWSB 13 and EWSB 14, having loaded with a principle angle of 0^o, 22.5^o, 45^o and 67.5^o, portrayed a reduction in ultimate capacity of 32%, 32%, 37% and 37%, respectively.

Based on the experimental observations, an average reduction of 35% is anticipated when the principle angle of biaxial moment transfer is changed from 90^o to 0^o, an average reduction of 26% is anticipated when the principle angle of biaxial moment transfer is changed from 90^o to 22.5^o, an average reduction of 33% is anticipated when the principle angle of biaxial moment transfer is changed from 90^o to 45^o, and lastly, an average reduction of 30% is anticipated when the principle angle of biaxial moment transfer is changed from 90^o to 67.5^o.

Therefore, by rearranging the principle angles of biaxial moment transfer, the punching capacities were found to be the highest when set to 90^o, followed by 22.5^o, 67.5^o, 45^o and lastly 0^o. These reductions are due to the decrease in shear surface mobilized as observed from the experimental results.

4.3.5.2 Column Eccentricity

Similar to the internal punching series, the punching shear capacities of edge series were observed to reduce when the column eccentricity increases, as shown in Figure 4.95. These findings are consistent throughout the principle angles of biaxial moment transfer studied in this research.

When the principle angle of biaxial moment transfer is set to 0^o, comparisons between EWSB 1, having a column eccentricity of 50 mm, with EWSB 6 and EWSB 11, having column eccentricities of 100 mm and 150 mm, indicated a reduction in punching capacity of 7% and 13%, respectively.

When the principle angle of biaxial moment transfer is set to 22.5^o, comparisons between EWSB 2, having a column eccentricity of 50 mm, with EWSB 7 and EWSB 12, having column eccentricities of 100 mm and 150 mm, indicated a reduction in punching capacity of 29% and 38%, respectively.

When the principle angle of biaxial moment transfer is set to 45^o, comparisons between EWSB 3, having a column eccentricity of 50 mm, with EWSB 8 and EWSB 13, having column eccentricities of 100 mm and 150 mm, indicated a reduction in punching capacity of 32% and 37%, respectively.

When the principle angle of biaxial moment transfer is set to 67.5^o, comparisons between EWSB 4, having a column eccentricity of 50 mm, with EWSB 9 and EWSB 14, having column eccentricities of 100 mm and 150 mm, indicated a reduction in punching capacity of 30% and 40%, respectively.

When the principle angle of biaxial moment transfer is set to 90°, comparisons between EWSB 5, having a column eccentricity of 50 mm, with EWSB 10 and EWSB 15, having column eccentricities of 100 mm and 150 mm, indicated a reduction in punching capacity of 16% and 30%, respectively.

The punching capacities reduce as column eccentricities increased are believed to be due to the amount of unbalanced moment being transferred from the column to the slab. These unbalanced moments were then transformed to non-uniformly distributed shear stresses around the vicinity of the column and torsion stresses at the side of the columns. Thus, leading to a lower punching shear capacity.

4.3.5.3 Column Location

Two column locations (free-edge and center-edge) (see Figure 3.31) were tested to investigate the column location variable. However, the difference from the internal punching series in that the column were not rotated with respect to the principle angle of biaxial moment transfer, but, was repositioned to a new location. Comparisons between edge punching at the free-edge column and edge punching at the center-edge column are illustrated in Figure 4.96.

Experimental results indicate that higher punching capacities are observed when the column location set to center-edge throughout three different column eccentricities.

When the column eccentricity was set to 50 mm, comparison between EWSCE 1, having the column location at center-edge, with EWSB 1, having the column location at free-edge, indicated a reduction in punching capacity of 23%.

When the column eccentricity was set to 100 mm, comparison between EWSCE 2, having the column location at center-edge, with EWSB 2, having the column location at free-edge, indicated a reduction in punching capacity of 20%.

When the column eccentricity was set to 150 mm, comparison between EWSCE 3, having the column location at center-edge, with EWSB 3, having the column location at free-edge, indicated a reduction in punching capacity of 13%.

Based on shear failure surface observations, both column locations portrayed similar failure surface area. The increases in punching capacities noted from specimens having their column positioned at center-edge was mainly due to a steeper angle of inclination of shear surface, which exhibited higher shear resistance. The steeper angle of inclination portrayed when the column positioned at center-edge was mainly due to the support boundary condition being shorter than the other.

4.3.5.4 Size of Solid Section

The effect of size of solid section on the edge punching series was found to be identical to the internal punching series. The punching capacities were observed to increase with the size of solid section, as shown in Figure 4.97.

By comparing EFSB1, with a solid section of 360 mm, with EWSB 6, with a solid section of 200 mm, the punching capacity was found to be 33% higher when the principle angle of biaxial moment transfer is set to 0^0. Furthermore, comparisons between specimens loaded with principle angle of biaxial moment transfer set to 22.5^o, 45^o, 67.5^o and 90^o exhibited similar outcomes, in which, the specimens cast with larger solid section were found to have higher punching capacity than those cast with smaller solid section, by 29%, 41%, 39% and 16%, respectively. In general, an average increase of 32% can be anticipated when the size of solid section increases from 200 mm to 360 mm.

Similar observations were made from the eccentric punching series, where slabs cast with larger solid section were found to punch in a steeper angle as compared to those cast with smaller solid section. The increase in punching shear capacities was expected due to the increase in the size of solid section, in which, more work is required to remove the revolution apart from the slab specimen.

4.4 Summary

All slab specimens were observed to fail in punching mechanism similar to that at an internal flat slab-column connection, where the specimens failed in a sudden rupture failure mechanism with a sudden drop of shear resistance from its peak. In general, the observed punching failure surface was characterised by internal cracks propagated from the vicinity of column through the slab thickness at about 21 degree inclination or steeper (depending on the boundary conditions) and intersecting the top surface of the slab at a distance of about 2.6 times the slab depth or lesser (depending on the boundary conditions) from the column face. In plan, a solid revolution of concrete was formed, with the column at its centre, which separated from the main slab vertically leaving the rest of the slab remaining rigid. The punching capacities of the slab specimens were found to be highly dependent on the size of solid revolution of concrete formed within the slab.

The distinct difference between the punching mechanism in waffle slabs and the flat slab-column connection is the reduced solid section at the column vicinity to form a complete solid of revolution due to some of the potential failure surface was lost when it entered the waffle section, as shown in Figure 4.2 and Figure 4.3. The consequence of having less shear failure surface existed within the waffle slab to absorb the applied energy resulted in a lower ultimate punching capacity.

A general observation among all the series is that the punching shear mechanism can be characterized according to the three-dimensional failure surface, leading to the proposal of three theoretical models; concentric punching at internal column theoretical model, eccentric punching at internal column theoretical model, and edge punching theoretical model; based upon the plastic approach, which have been developed and proposed in Chapter 5.

Table 4.1 Test result of concentric punching at internal column waffle slabs series

Specimen No	Size of Solid Section (mm)	Column Size, C_x (mm)	Column Shape	Height of Slab, h (mm)	Effective Depth of Slab, d (mm)	Concrete Compressive Strength, f_{cu50} (N/mm^2)	Failure Load, P (kN)
IWS 1	200 x 200	100	Square	70	62	41.077	65.26

Table 4.2 Cracking Loads of concentric punching at internal column waffle slabs series

Specimen No	Observed Cracking Load $P_{crack\ (Observed)}$ (kN)	Inferred Cracking Load $P_{crack\ (Inferred)}$ (kN)	Failure Load P (kN)
IWS 1	33.68 (52%)	23.16 (35%)	65.26

Table 4.3 Test results of eccentric punching at internal column waffle slabs series

Specimen No	Size of Solid Section (mm)	Principle Angle of Moment Transfer (°)	Load Eccentricity, e (mm)	Column Orientation (°)	Concrete Compressive Strength, f_{cu50} (N/mm^2)	Failure Moment, M_U (kNm)	Ultimate Failure Load, P_{test} (kN)
IWSB 1	200 x 200	0	50	0	40.244	2.7365	54.73
IWSB 2	200 x 200	22.5	50	0	40.283	2.105	42.10
IWSB 3	200 x 200	45	50	0	39.291	2.3155	46.31
IWSB 4	200 x 200	0	100	0	41.486	4.631	46.31
IWSB 5	200 x 200	22.5	100	0	40.598	3.579	35.79
IWSB 6	200 x 200	45	100	0	39.633	3.789	37.89
IWSB 7	200 x 200	0	150	0	40.3	5.6835	37.89
IWSB 8	200 x 200	22.5	150	0	40.719	4.4205	29.47
IWSB 9	200 x 200	45	150	0	42.532	5.052	33.68
IFSB 1	360 x 360	0	100	0	41.238	7.157	71.57
IFSB 2	360 x 360	22.5	100	0	40.336	6.736	67.36
IFSB 3	360 x 360	45	100	0	40.896	6.315	63.15
IWSBC 1	200 x 200	22.5	100	22.5	42.298	4.21	42.10
IWSBC 2	200 x 200	45	100	45	43.652	3.789	37.89

Note: Column Size, C_x = 100 mm (Square)
Height of Slab, h = 70 mm
Effective Depth of Slab, d = 62 mm

Table 4.4 Cracking loads of eccentric punching at internal column waffle slabs series

Specimen No	Observed Cracking Load, $P_{crack(observed)}$ (kN)	Inferred Cracking Load, $P_{crack(inferred)}$ (kN)	Ultimate Failure Load, P_{test} (kN)
IWSB 1	29.47 (54%)	18.95 (35%)	54.73
IWSB 2	21.05 (50%)	14.74 (35%)	42.10
IWSB 3	25.26 (55%)	18.95 (41%)	46.31
IWSB 4	25.26 (47%)	14.74 (32%)	46.31
IWSB 5	16.84 (56%)	14.74 (41%)	35.79
IWSB 6	21.05 (56%)	14.74 (39%)	37.89
IWSB 7	21.05 (56%)	14.74 (39%)	37.89
IWSB 8	16.84 (57%)	10.53 (35%)	29.47
IWSB 9	16.84 (50%)	14.74 (44%)	33.68
IFSB 1	37.89 (53%)	27.37 (38%)	71.57
IFSB 2	33.68 (50%)	25.26 (38%)	67.36
IFSB 3	29.47 (47%)	23.16 (37%)	63.15
IWSCC 1	21.05 (50%)	14.74 (35%)	42.10
IWSCC 2	16.84 (44%)	14.74 (39%)	37.89

Table 4.5 Test results of edge punching waffle slabs series

Specimen No	Size of Solid Section (mm)	Principle Angle of Moment Transfer (°)	Load Eccentricity, e (mm)	Column Location*	Concrete Compressive Strength, f_{cu50} (N/mm^2)	Failure Moment, M_U (kNm)	Ultimate Failure Load, P_{test} (kN)
EWSB 1	200 x 200	0	50	Free	41.873	1.579	31.58
EWSB 2	200 x 200	22.5	50	Free	45.295	2.211	44.21
EWSB 3	200 x 200	45	50	Free	41.536	2.000	40.00
EWSB 4	200 x 200	67.5	50	Free	40.563	2.105	42.10
EWSB 5	200 x 200	90	50	Free	41.477	2.630	52.60
EWSB 6	200 x 200	0	100	Free	40.831	2.947	29.47
EWSB 7	200 x 200	22.5	100	Free	42.577	3.158	31.58
EWSB 8	200 x 200	45	100	Free	40.307	2.737	27.37
EWSB 9	200 x 200	67.5	100	Free	39.779	2.947	29.47
EWSB 10	200 x 200	90	100	Free	48.037	4.421	44.21
EWSB 11	200 x 200	0	150	Free	36.688	4.106	27.37
EWSB 12	200 x 200	22.5	150	Free	45.107	4.106	27.37
EWSB 13	200 x 200	45	150	Free	40.988	3.789	25.26
EWSB14	200 x 200	67.5	150	Free	40.746	3.789	25.26
EWSB15	200 x 200	90	150	Free	41.032	6.000	40.00
EFSB 1	360 x 280	0	100	Free	52.946	4.421	44.21
EFSB 2	360 x 280	22.5	100	Free	48.190	4.421	44.21
EFSB 3	360 x 280	45	100	Free	46.085	4.631	46.31
EFSB 4	360 x 280	67.5	100	Free	48.533	4.842	48.42
EFSB 5	360 x 280	90	100	Free	36.168	5.263	52.63
EWSCE 1	200 x 200	0	50	Centre	40.593	2.053	41.05
EWSCE 2	200 x 200	0	100	Centre	40.510	3.684	36.84
EWSCE 3	200 x 200	0	150	Centre	42.385	4.737	31.58

Note: Column Size, C_x = 100 mm (Square)
Height of Slab, h = 70 mm
Effective Depth of Slab, d = 62 mm
*see Figure 3.24 and Figure 3.29

Table 4.6 Cracking loads of edge punching waffle slabs series

Specimen No	Observed Cracking Load $P_{crack\ (Observed)}$ (kN)	Inferred Cracking Load $P_{crack\ (Inferred)}$ (kN)	Failure Load P (kN)
EWSB 1	18.95 (60%)	12.63 (40%)	31.58
EWSB 2	23.16 (52%)	14.74 (33%)	44.21
EWSB 3	18.95 (47%)	14.74 (37%)	40.00
EWSB 4	21.05 (50%)	14.74 (35%)	42.10
EWSB 5	27.37 (52%)	18.95 (36%)	52.60
EWSB 6	14.74 (50%)	10.53 (36%)	29.47
EWSB 7	16.84 (53%)	12.63 (40%)	31.58
EWSB 8	14.74 (54%)	10.53 (38%)	27.37
EWSB 9	14.74 (50%)	10.53 (36%)	29.47
EWSB 10	23.16 (52%)	16.84 (38%)	44.21
EWSB 11	14.74 (54%)	10.53 (38%)	27.37
EWSB 12	14.74 (54%)	10.53 (38%)	27.37
EWSB 13	12.63 (50%)	8.42 (33%)	25.26
EWSB14	12.63 (50%)	8.42 (33%)	25.26
EWSB15	18.95 (47%)	14.74 (37%)	40.00
EFSB 1	23.16 (52%)	16.84 (38%)	44.21
EFSB 2	25.26 (57%)	16.84 (38%)	44.21
EFSB 3	25.26 (55%)	16.84 (36%)	46.31
EFSB 4	25.26 (52%)	16.84 (35%)	48.42
EFSB 5	25.26 (48%)	18.95 (36%)	52.63
EWSCE 1	23.16 (56%)	12.63 (31%)	41.05
EWSCE 2	16.84 (46%)	10.53 (29%)	36.84
EWSCE 3	16.84 (53%)	10.53 (33%)	31.58

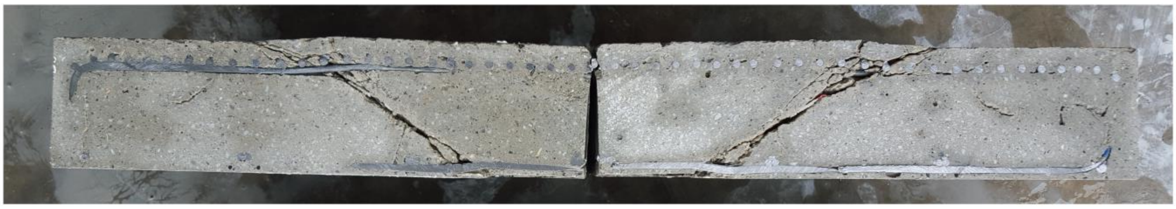

Figure 4.1 Section of internal punching failure surface

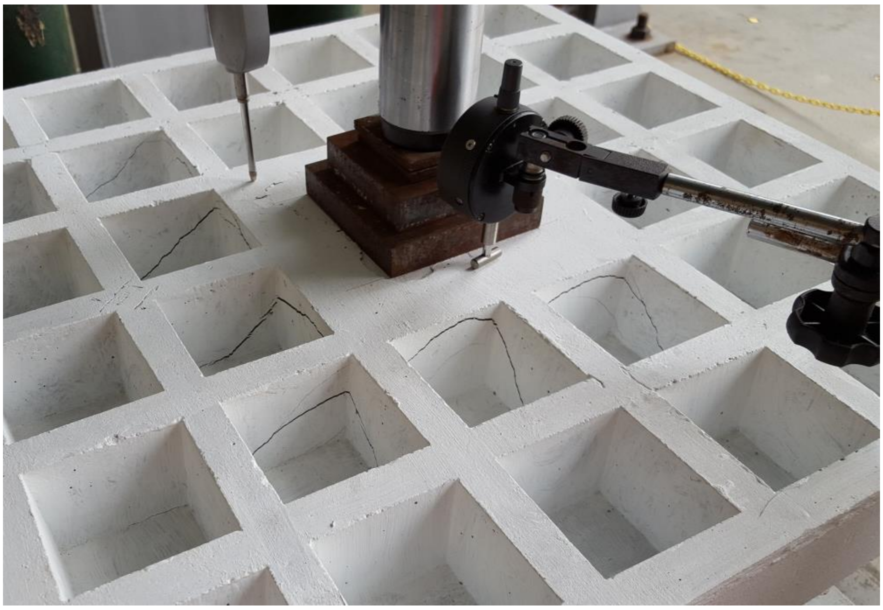

Figure 4.2 Loss of Potential Failure Surface in Waffle Section, IWS1 (during loading)

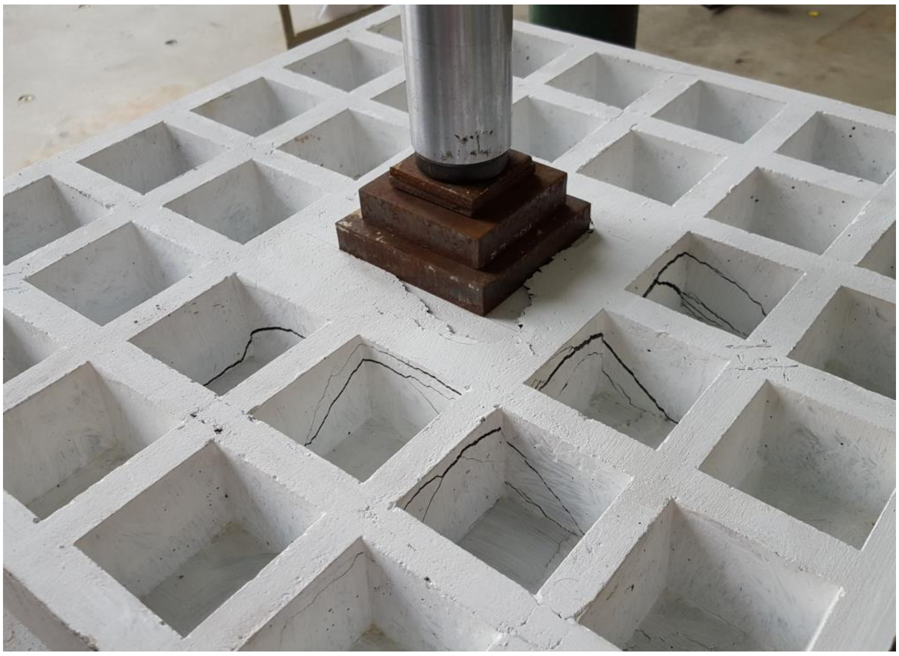

Figure 4.3 Loss of Potential Failure Surface in Waffle Section, IWS 1 (after punching failure)

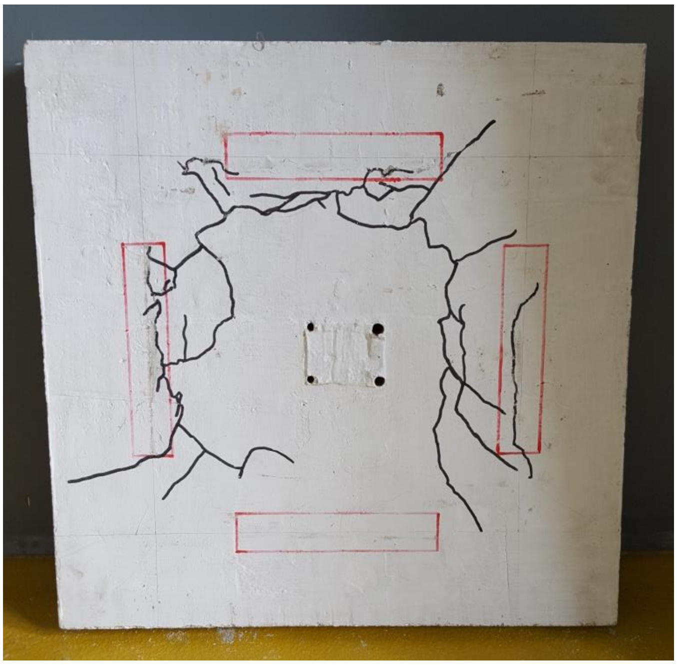

(a) Top View

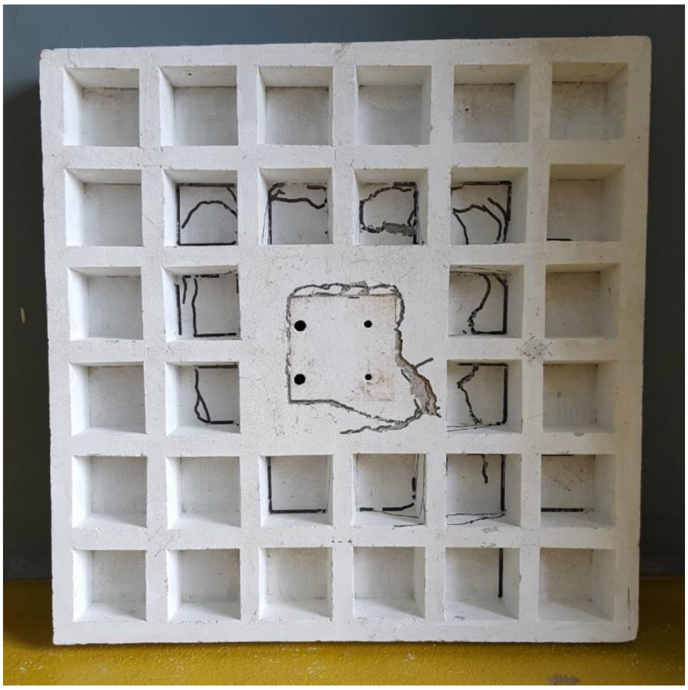

(b) Bottom View

Figure 4.4 Concentric Punching of Waffle Slab, IWS1

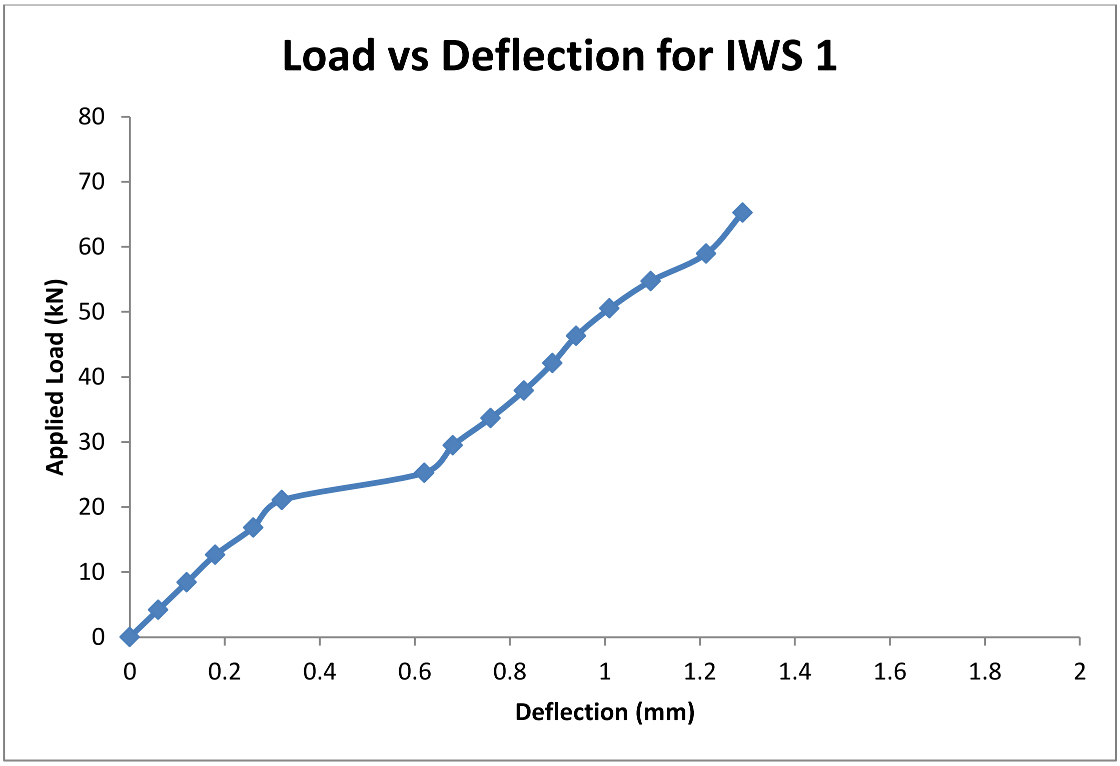

Figure 4.5 Load vs Deflection for IWS 1

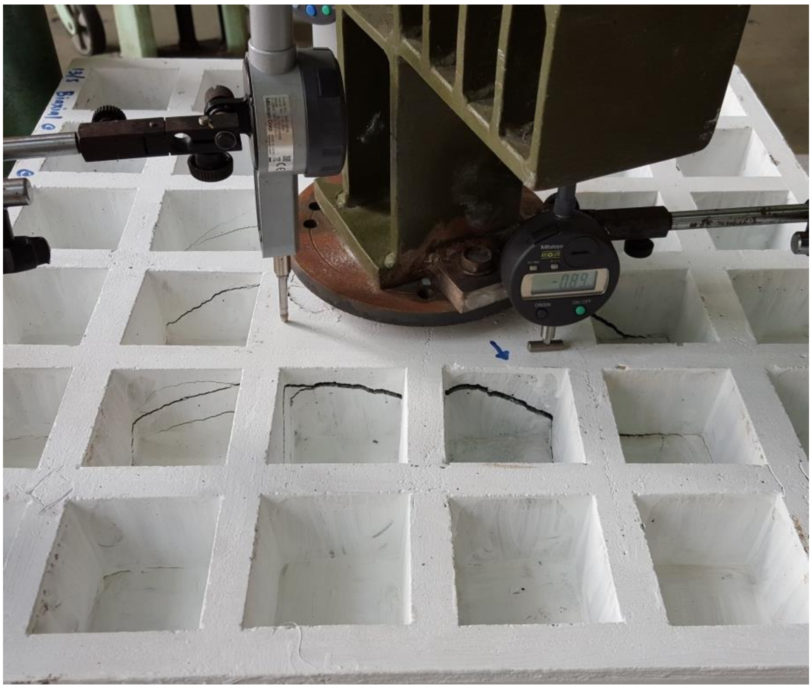

Figure 4.6 Loss of Potential Failure Surface in Waffle Section for IWSB 2 (Front Face – heavily loaded region)

Figure 4.7 Loss of Potential Failure Surface in Waffle Section for IWSB 2 (Side Face)

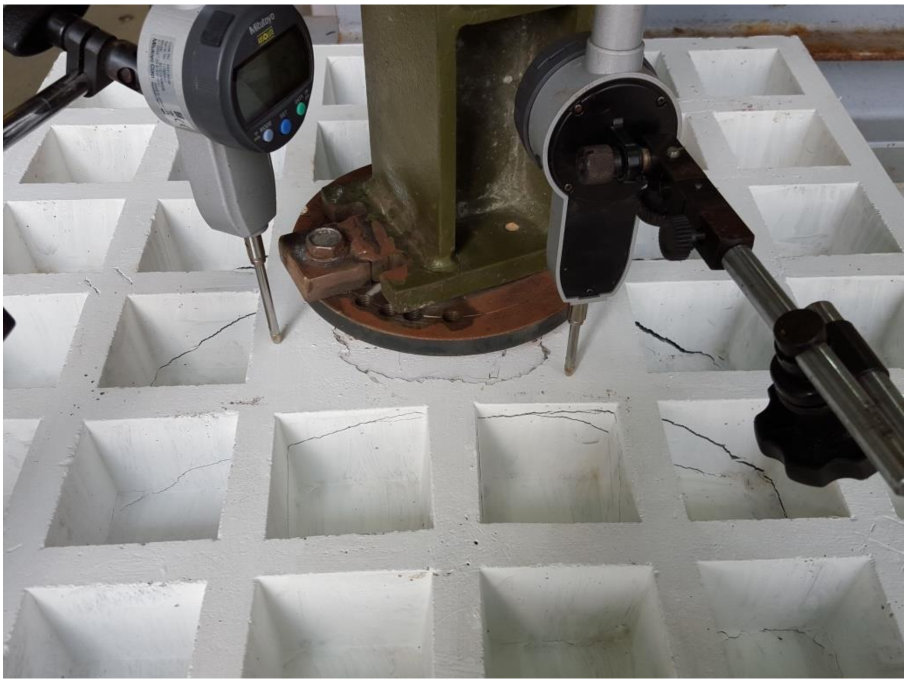

Figure 4.8 Loss of Potential Failure Surface in Waffle Section for IWSB 2 (Back Face - lightly loaded region)

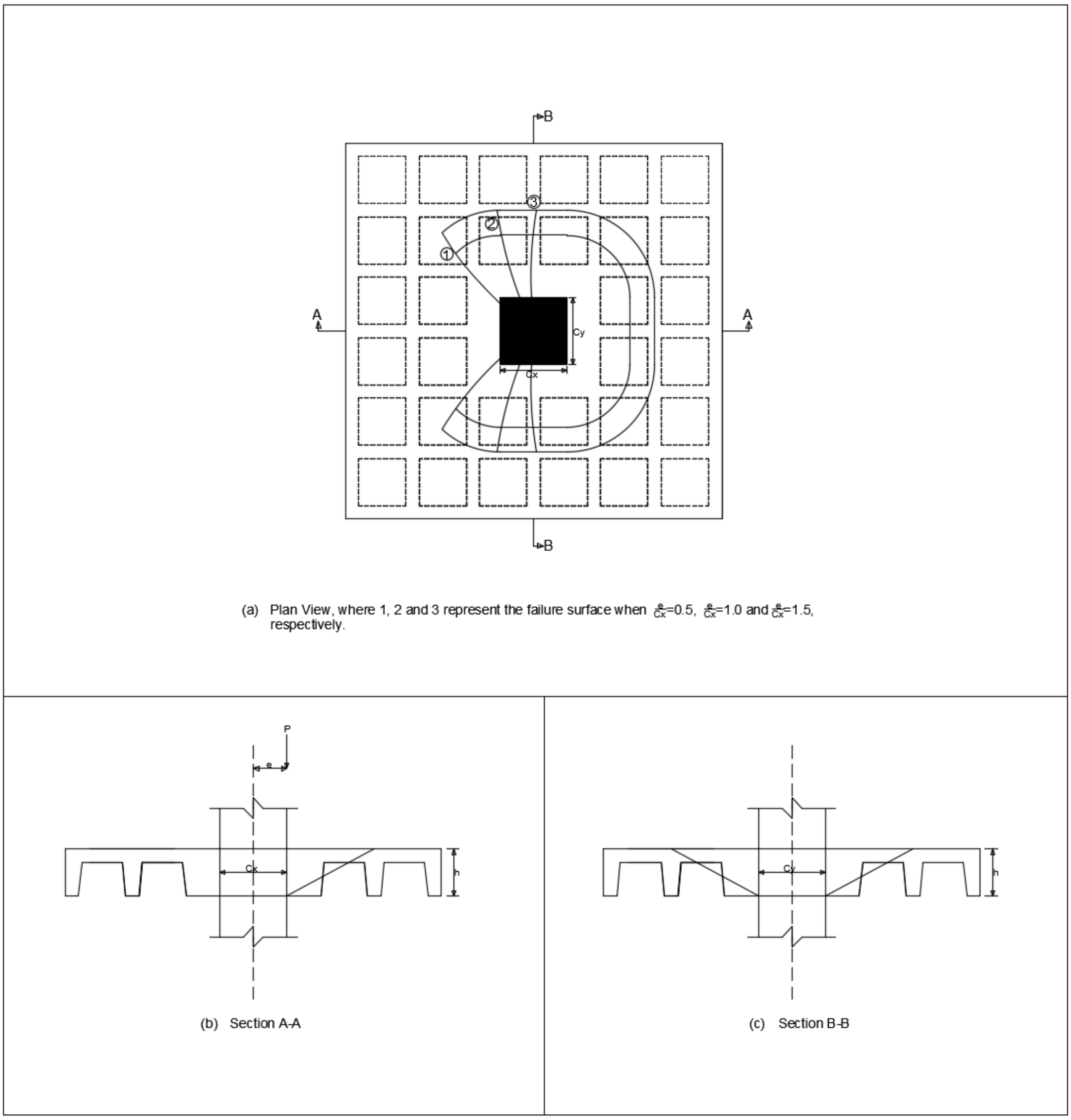

Figure 4.9 Schematic diagram of the observed column eccentricities on internal punching shear mechanism

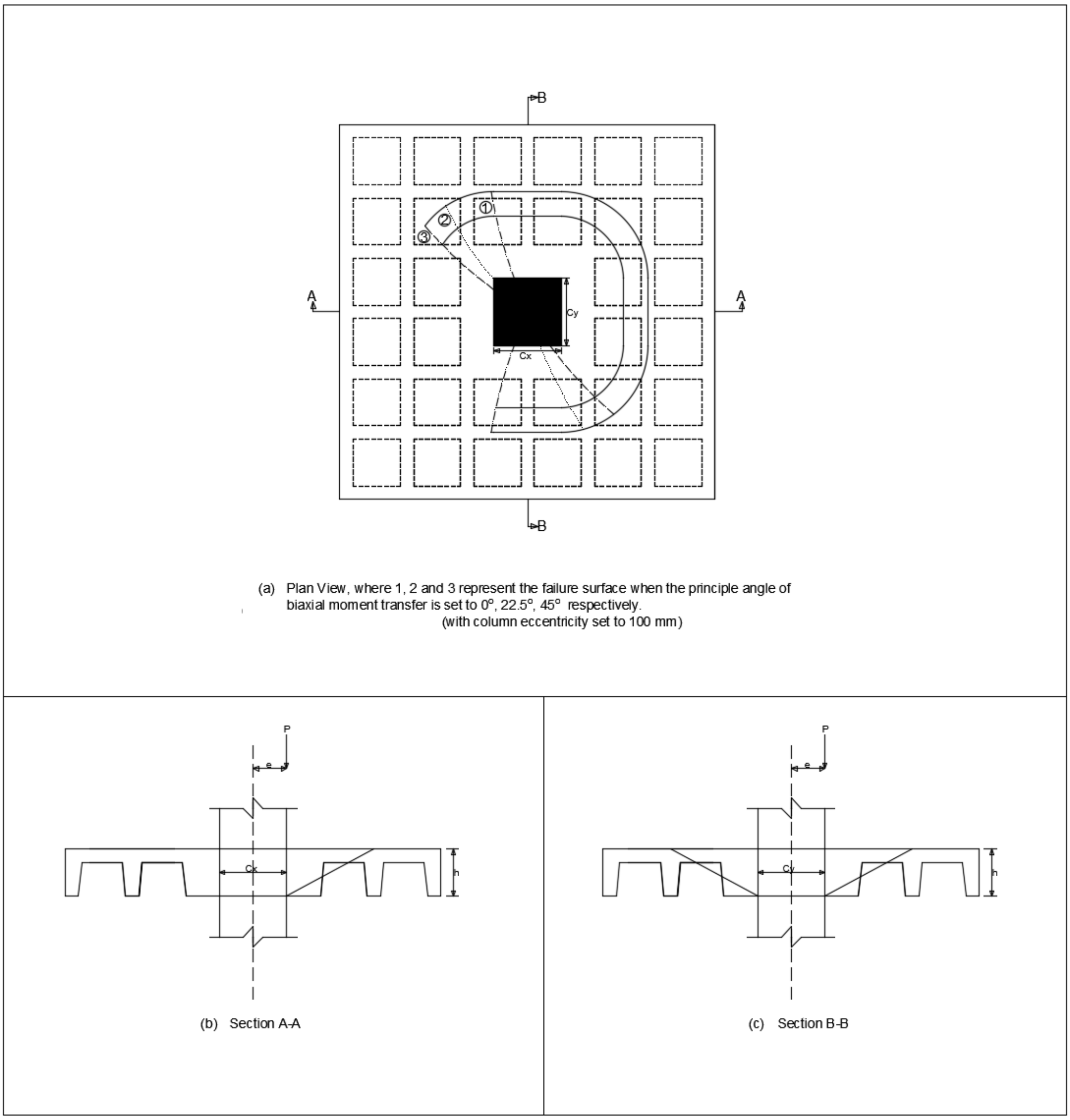

Figure 4.10 Schematic sketch of the observed effect of principle angle of biaxial moment transfer on internal punching shear mechanism

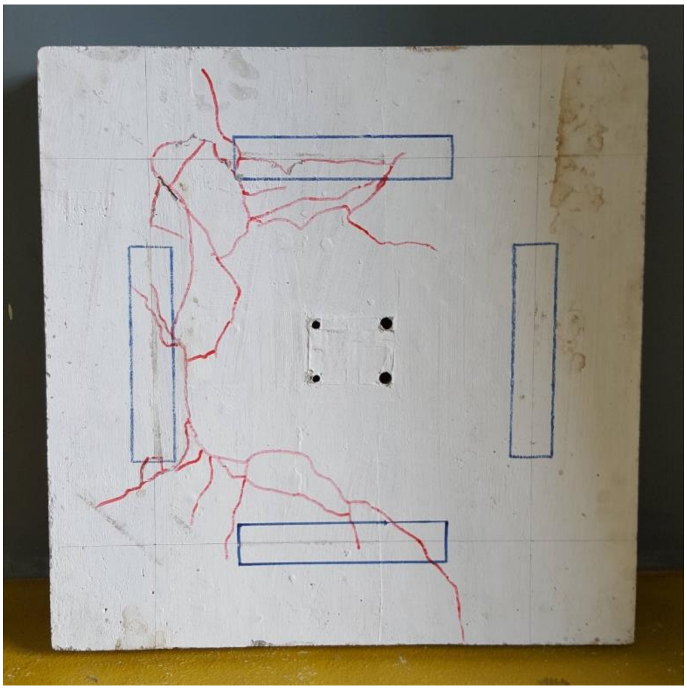

(a) Top View

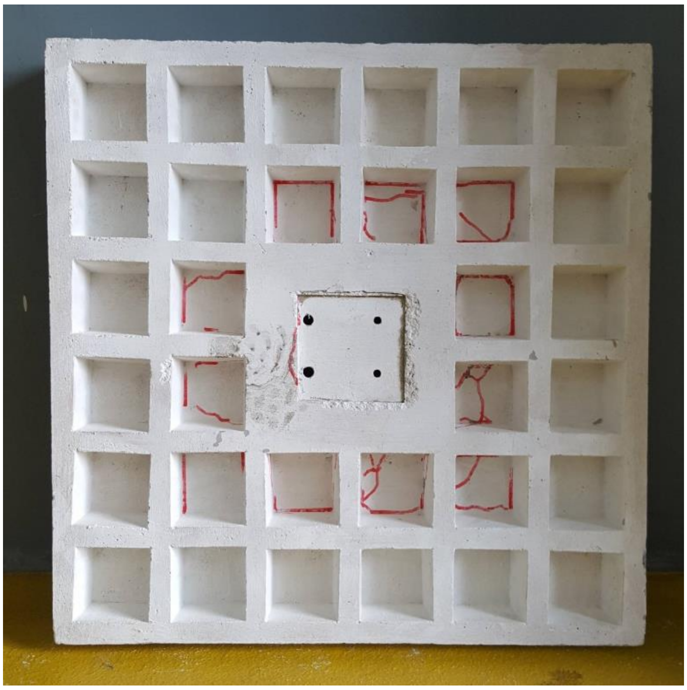

(b) Bottom View

Figure 4.11 Eccentric Punching of Waffle Slab, IWSB1

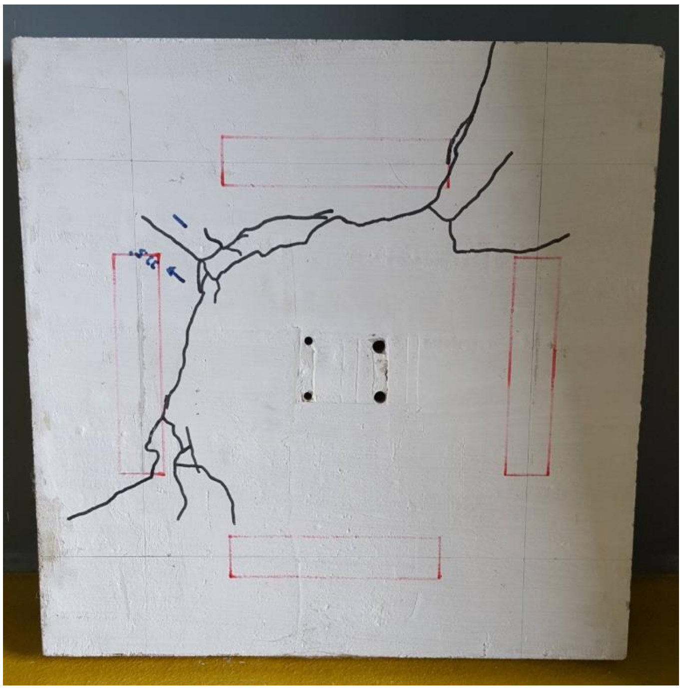

(a) Top View

(b) Bottom View

Figure 4.12 Eccentric Punching of Waffle Slab, IWSB2

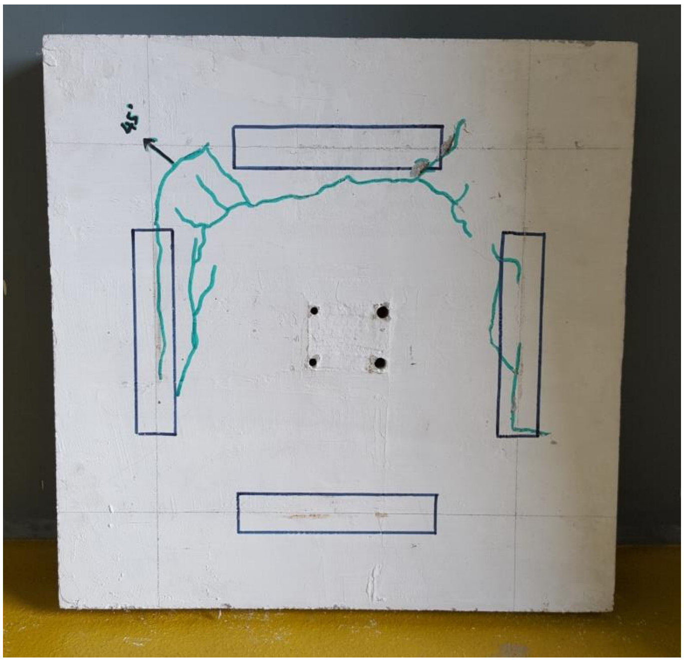

(a) Top View

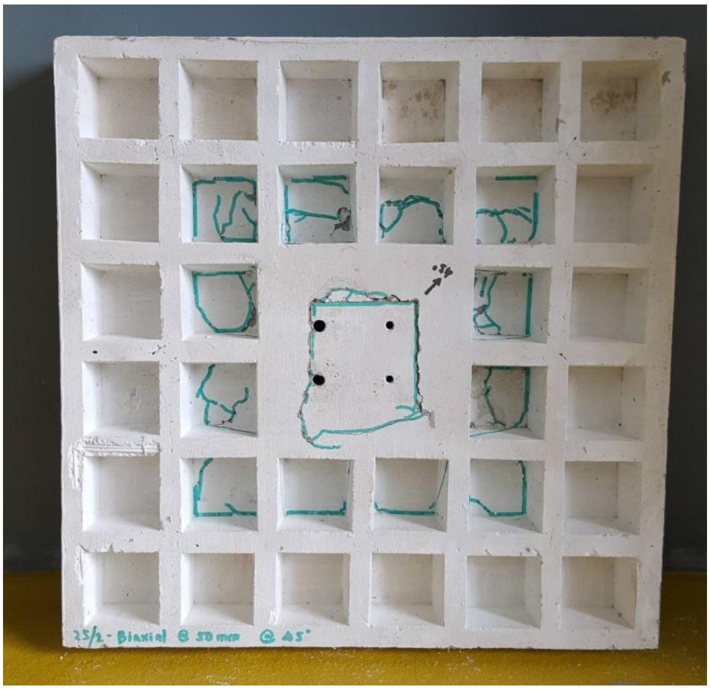

(b) Bottom View

Figure 4.13 Eccentric Punching of Waffle Slab, IWSB3

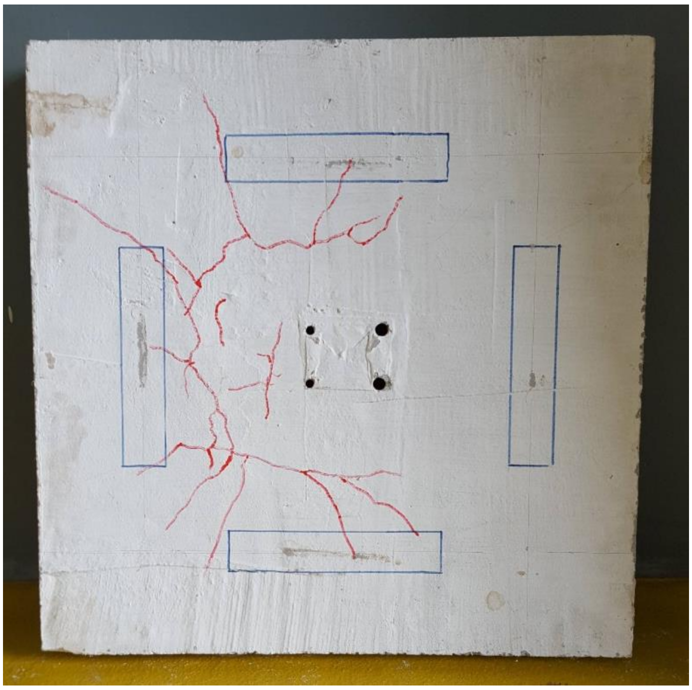

(a) Top View

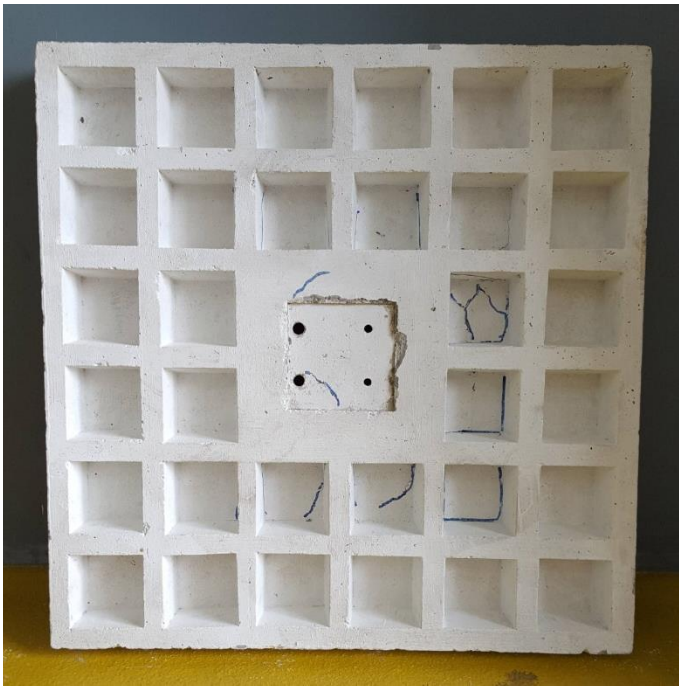

(b) Bottom View

Figure 4.14 Eccentric Punching of Waffle Slab, IWSB4

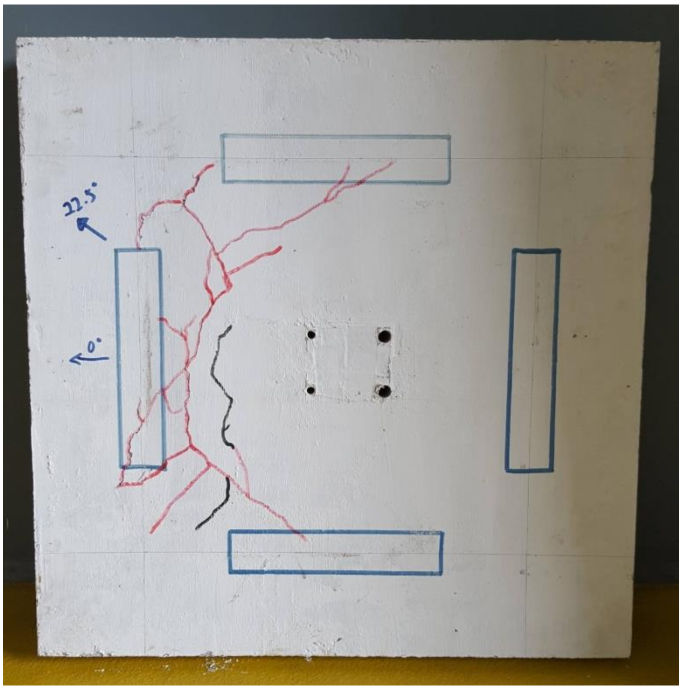

(a) Top View

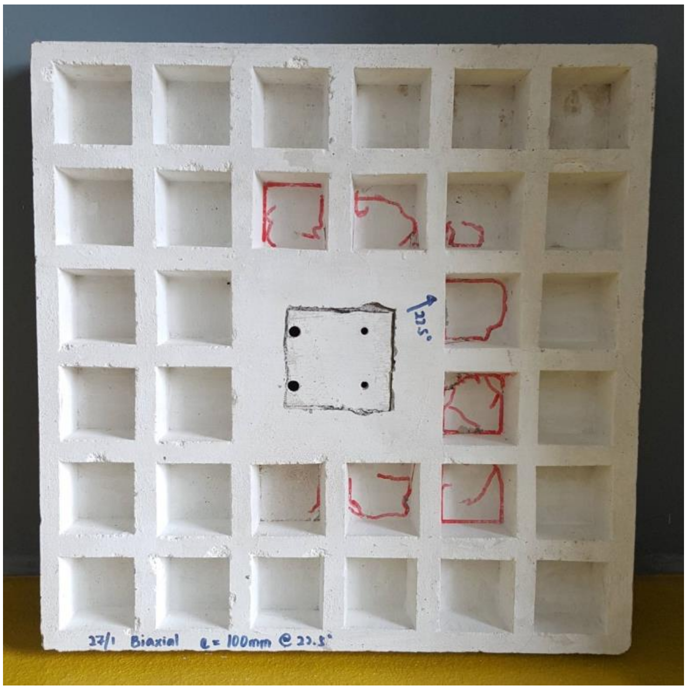

(b) Bottom View

Figure 4.15 Eccentric Punching of Waffle Slab, IWSB5

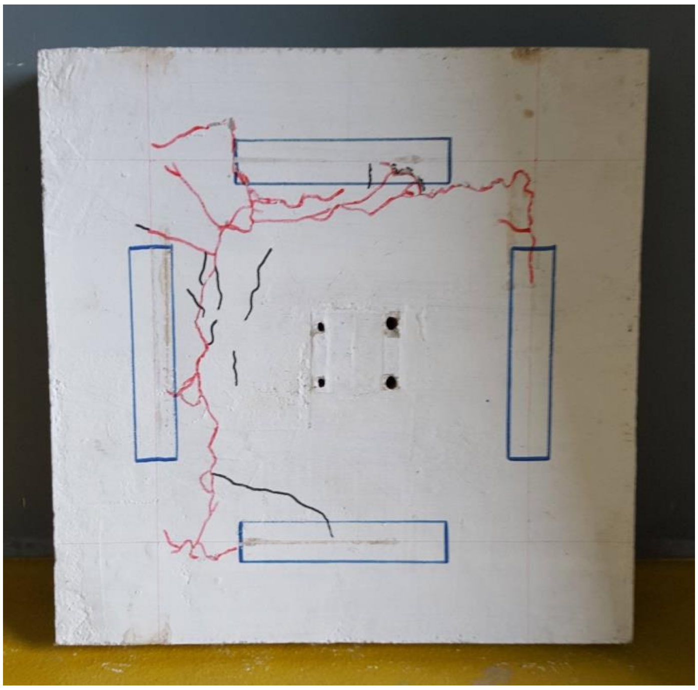

(a) Top View

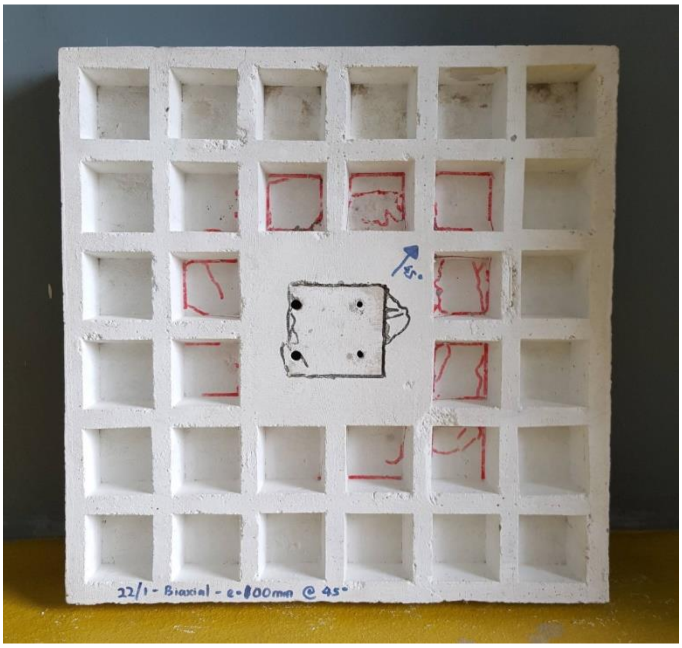

(b) Bottom View

Figure 4.16 Eccentric Punching of Waffle Slab, IWSB6

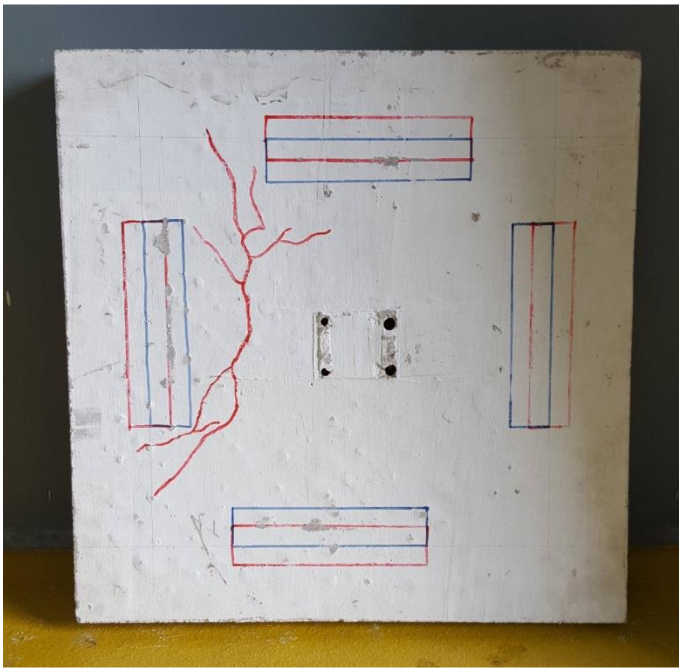

(a) Top View

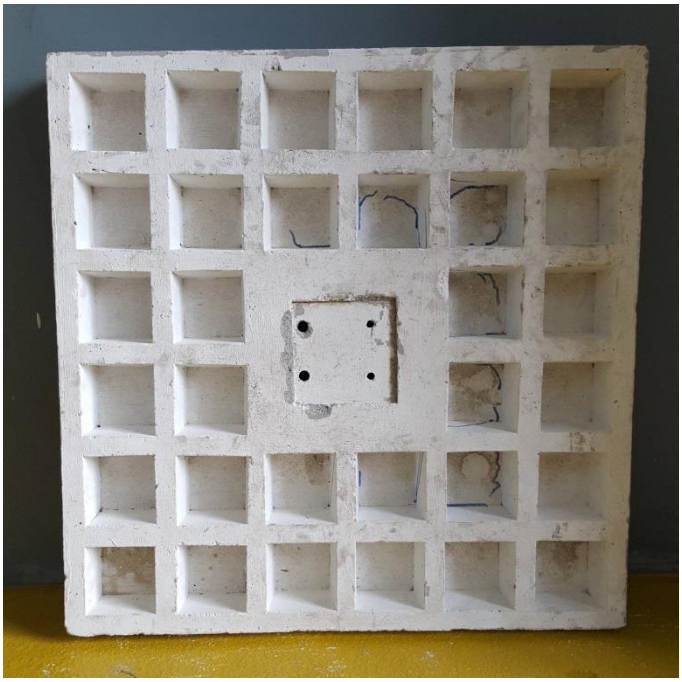

(b) Bottom View

Figure 4.17 Eccentric Punching of Waffle Slab, IWSB7

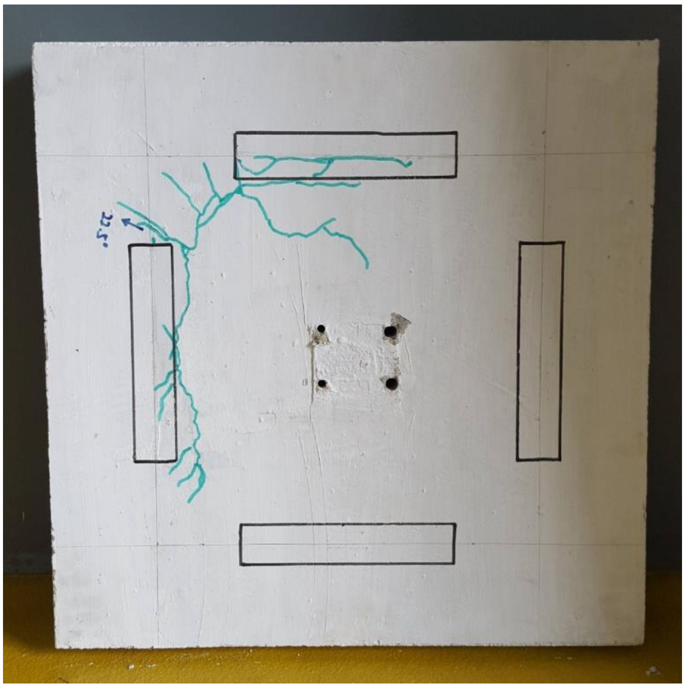

(a) Top View

(b) Bottom View

Figure 4.18 Eccentric Punching of Waffle Slab, IWSB8

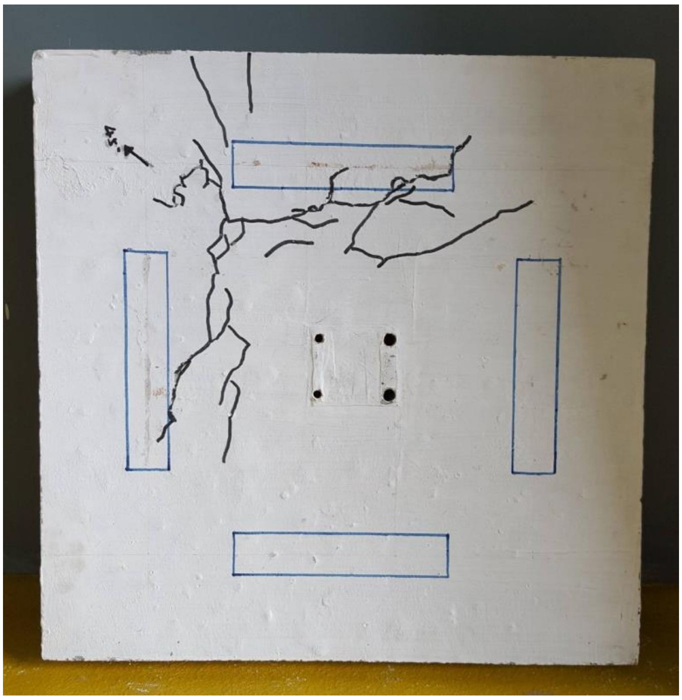

(a) Top View

(b) Bottom View

Figure 4.19 Eccentric Punching of Waffle Slabs, IWSB9

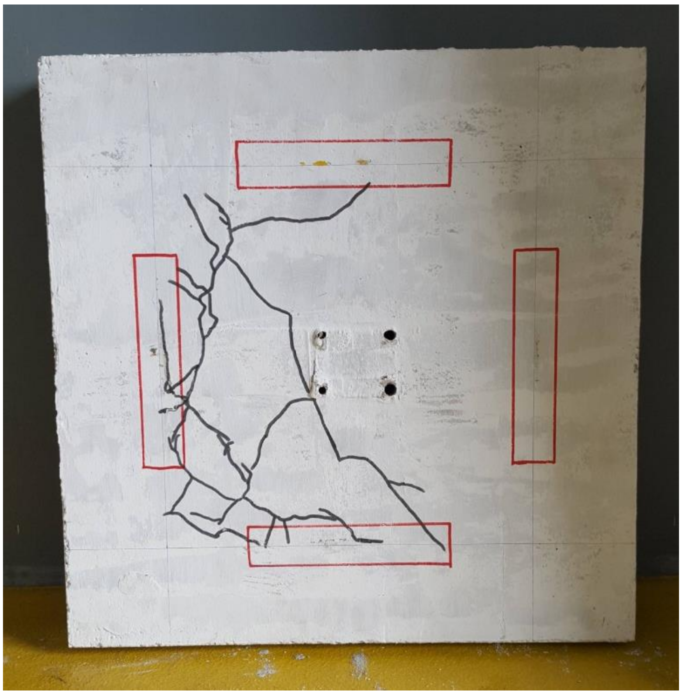

(a) Top View

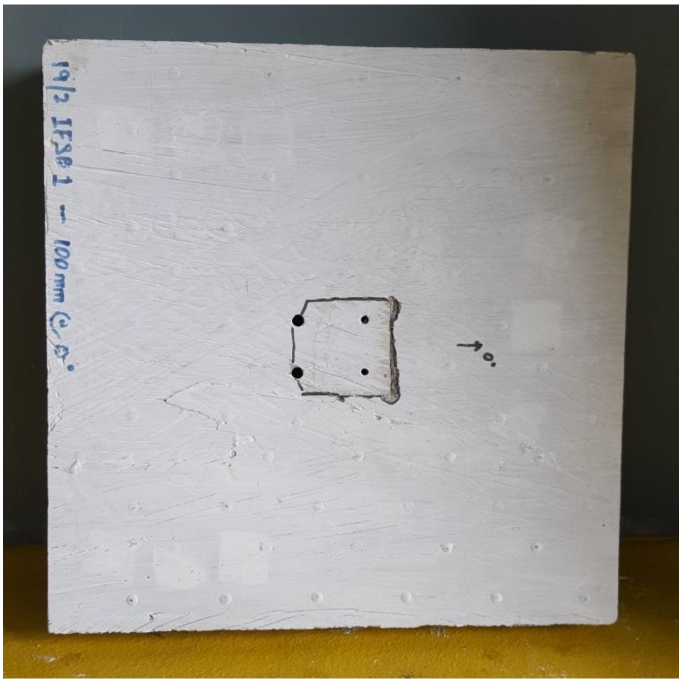

(b) Bottom View

Figure 4.20 Eccentric Punching of Flat Slab, IFSB1

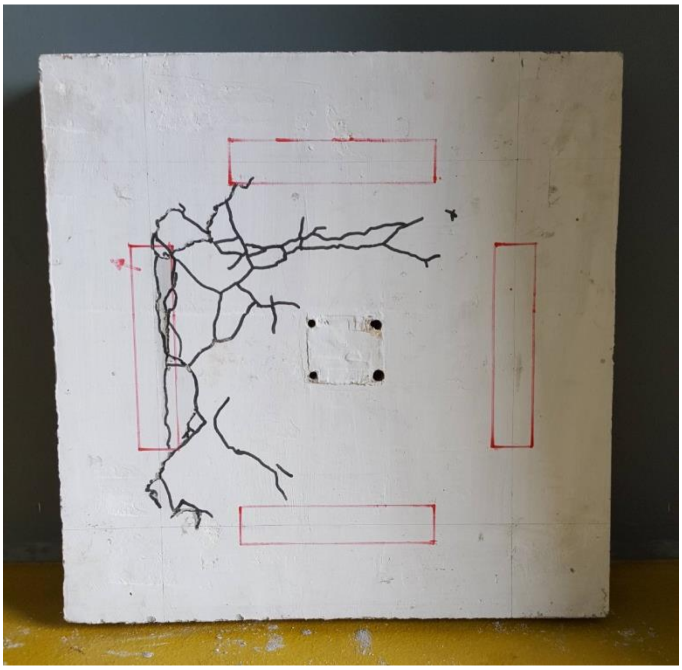

(a) Top View

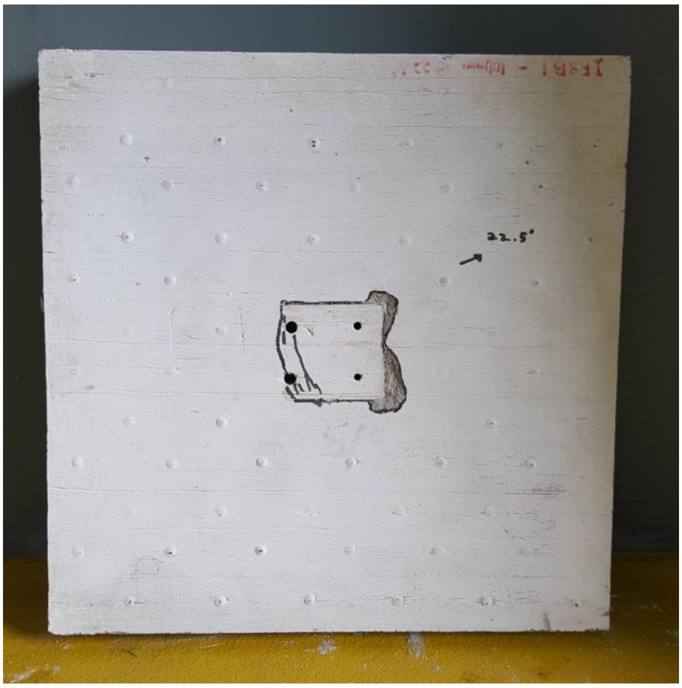

(b) Bottom View

Figure 4.21 Eccentric Punching of Flat Slab, IFSB2

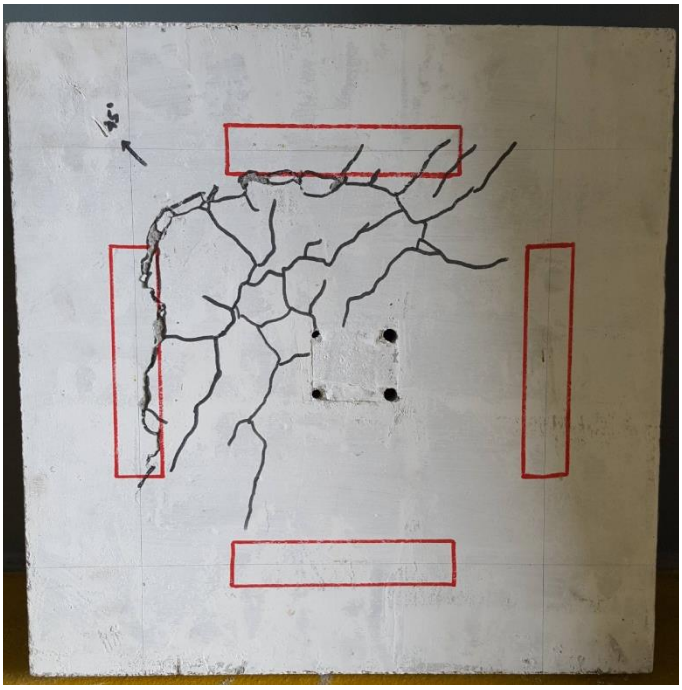

(a) Top View

(b) Bottom View

Figure 4.22 Eccentric Punching of Flat Slab, IFSB3

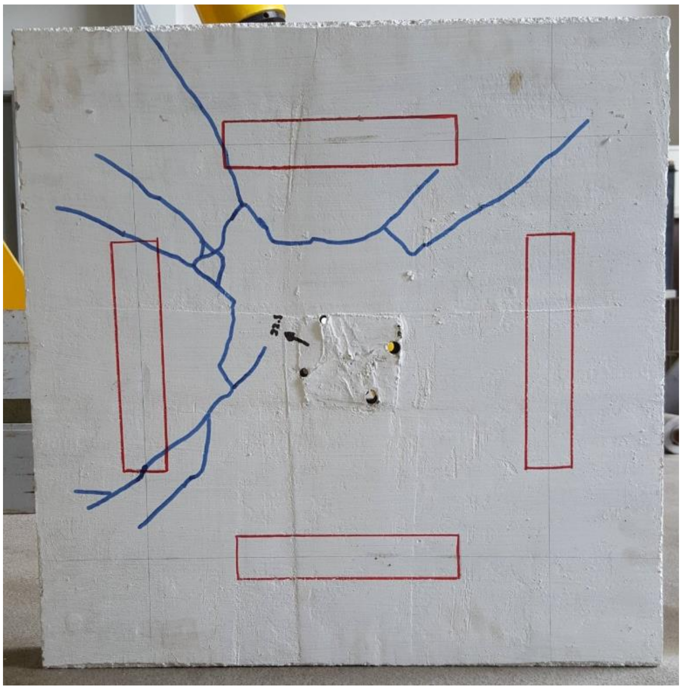

(a) Top View

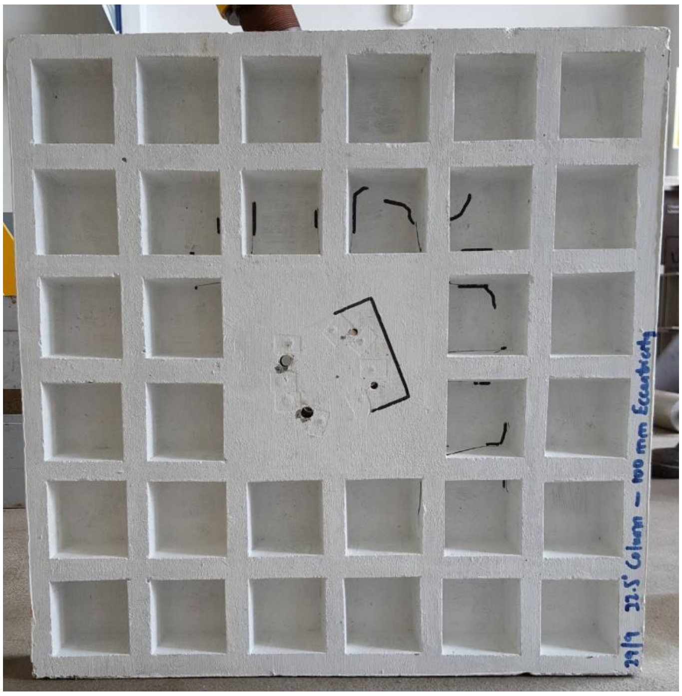

(b) Bottom View

Figure 4.23 Eccentric Punching of Waffle Slab with different column orientation, IWSBC1

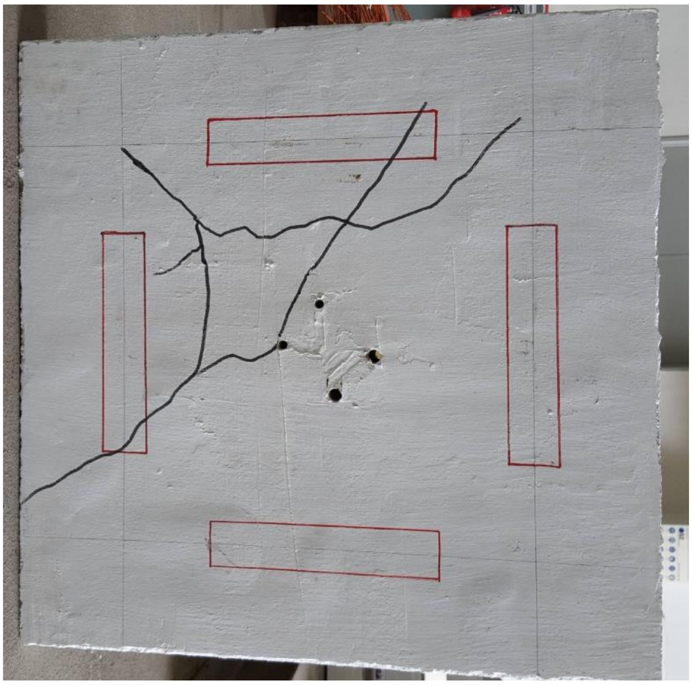

(a) Top View

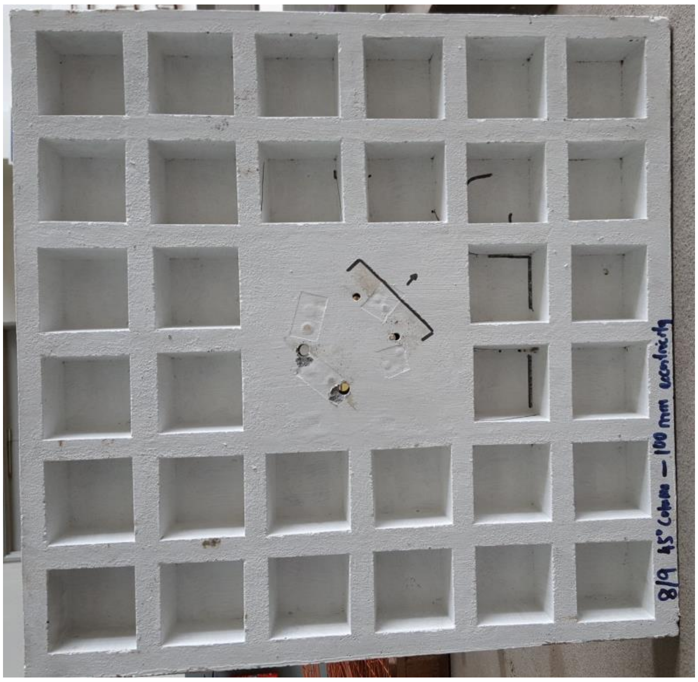

(b) Bottom View

Figure 4.24 Eccentric Punching of Waffle Slab with different column orientation, IWSBC2

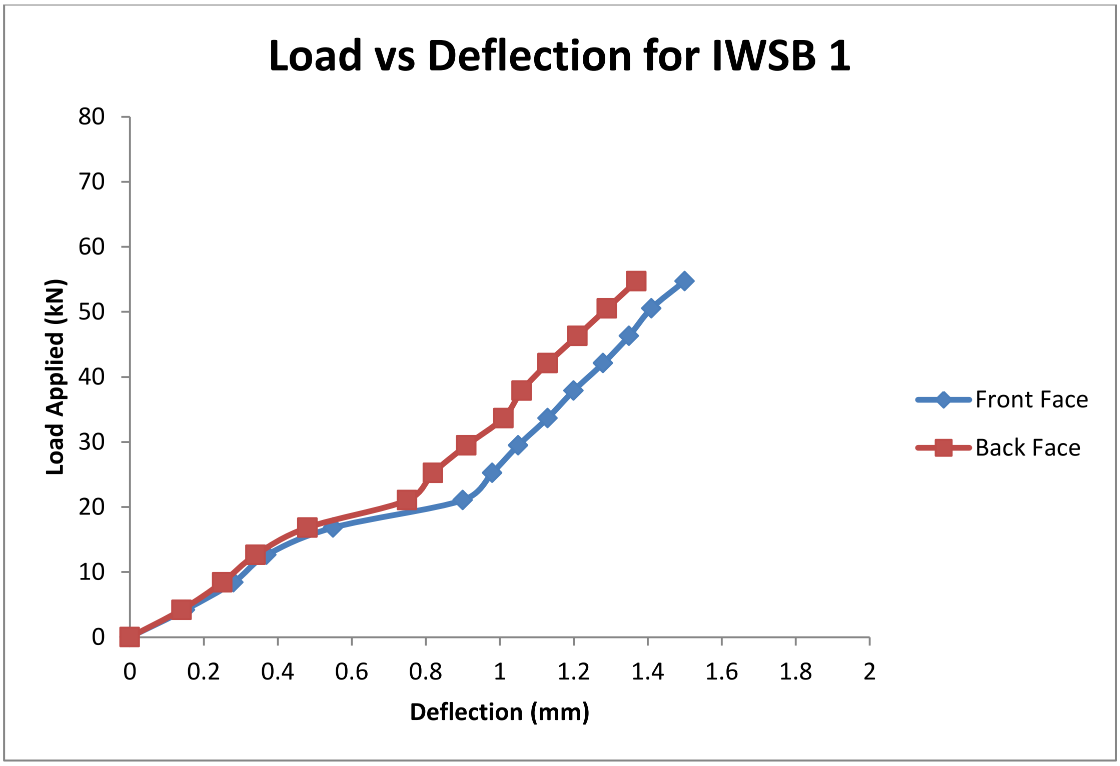

Figure 4.25 Load vs Deflection Curve for IWSB 1

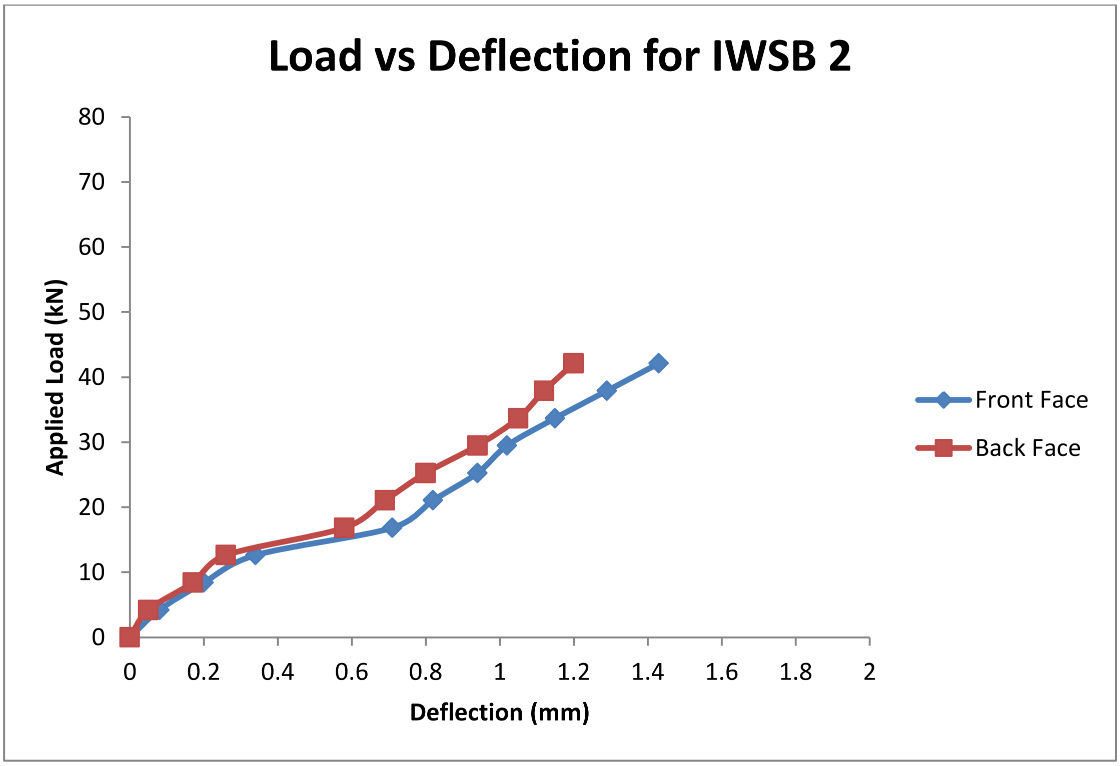

Figure 4.26 Load vs Deflection Curve for IWSB 2

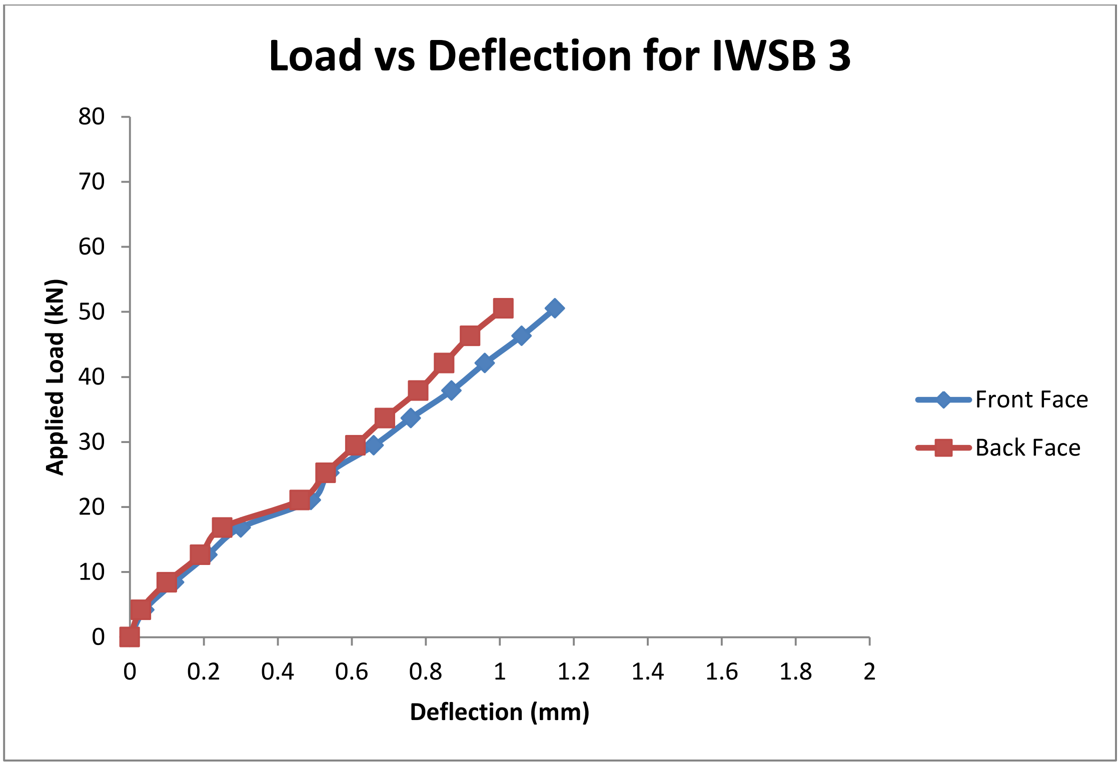

Figure 4.27 Load vs Deflection Curve for IWSB 3

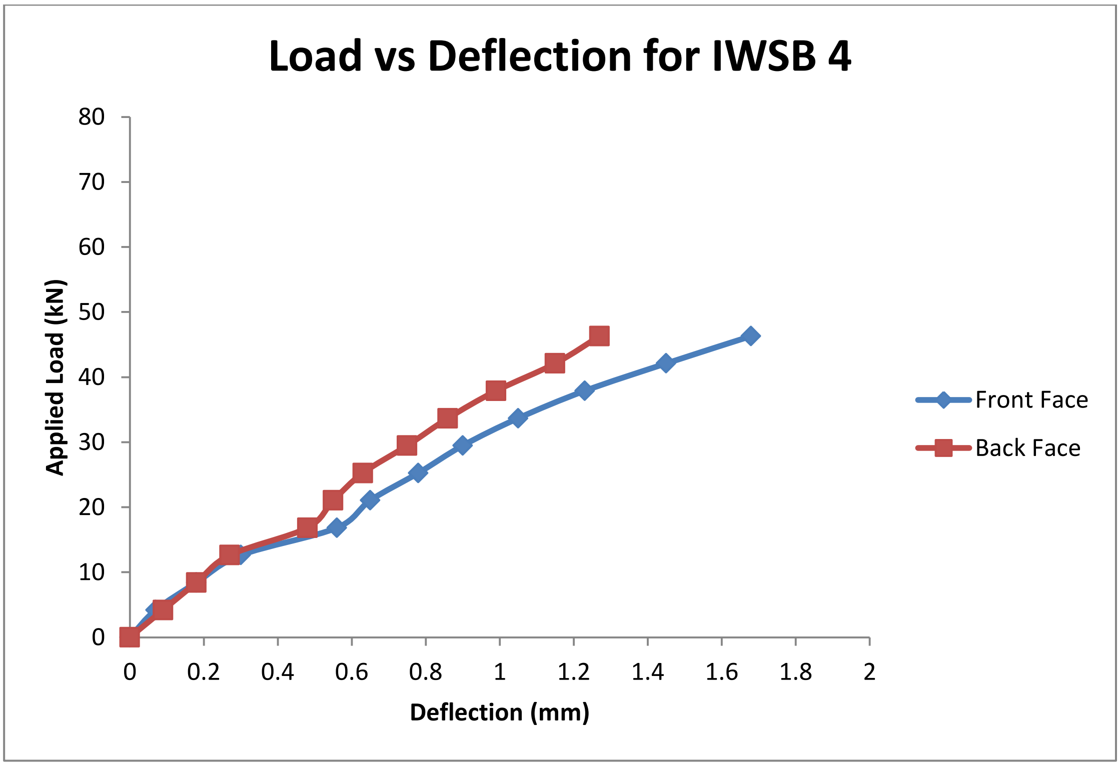

Figure 4.28 Load vs Deflection Curve for IWSB 4

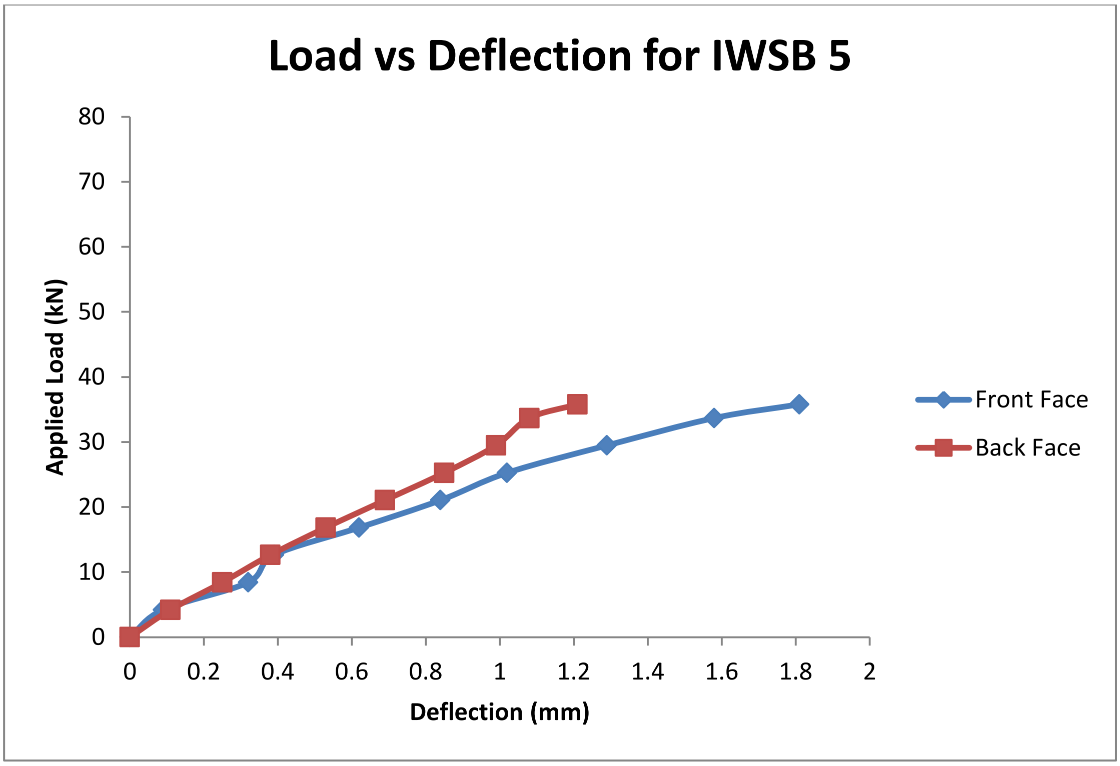

Figure 4.29 Load vs Deflection Curve for IWSB 5

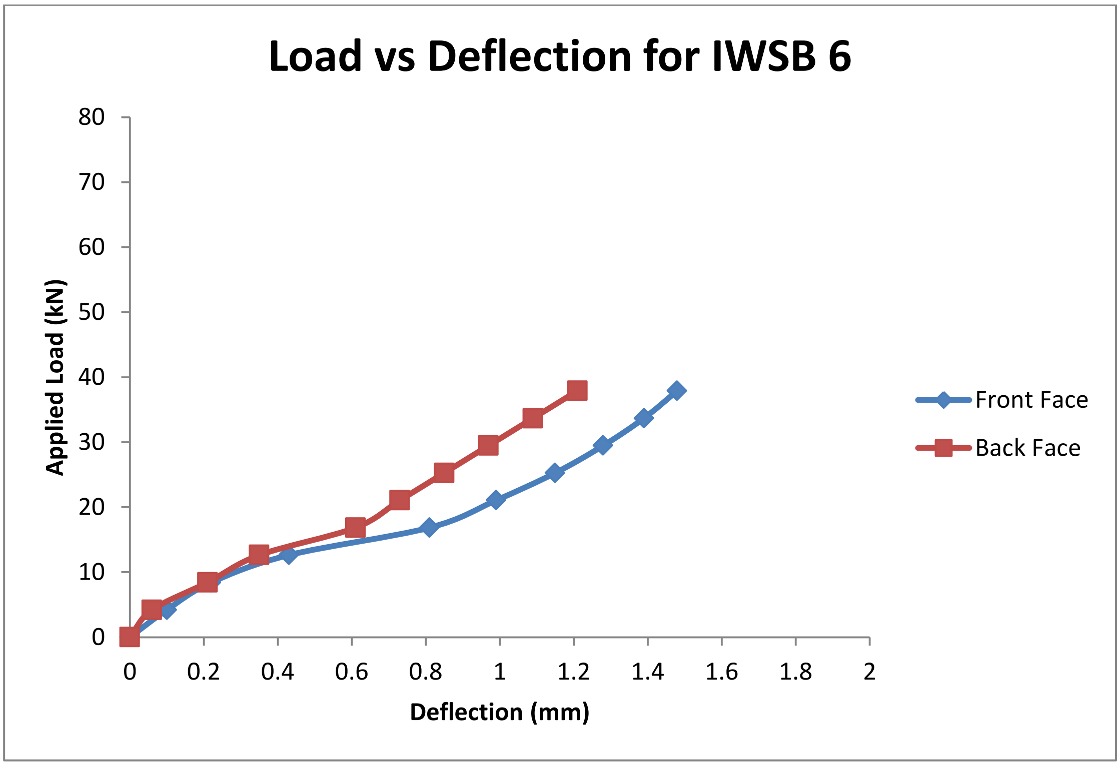

Figure 4.30 Load vs Deflection Curve for IWSB 6

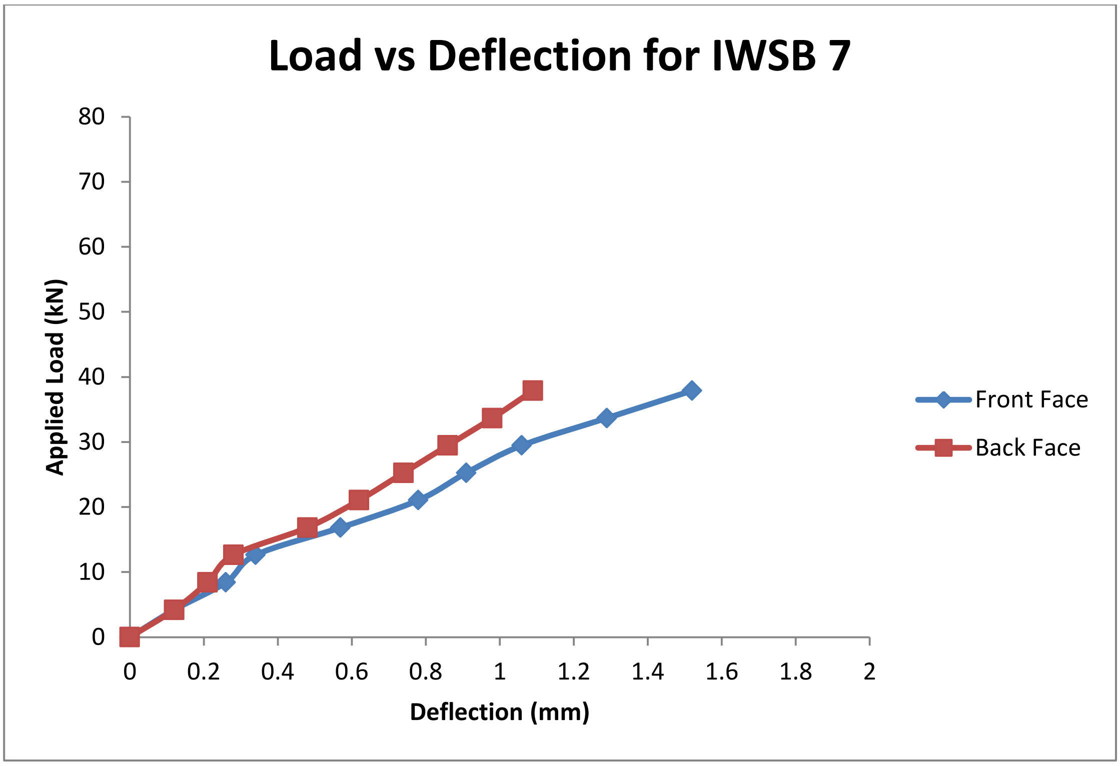

Figure 4.31 Load vs Deflection Curve for IWSB 7

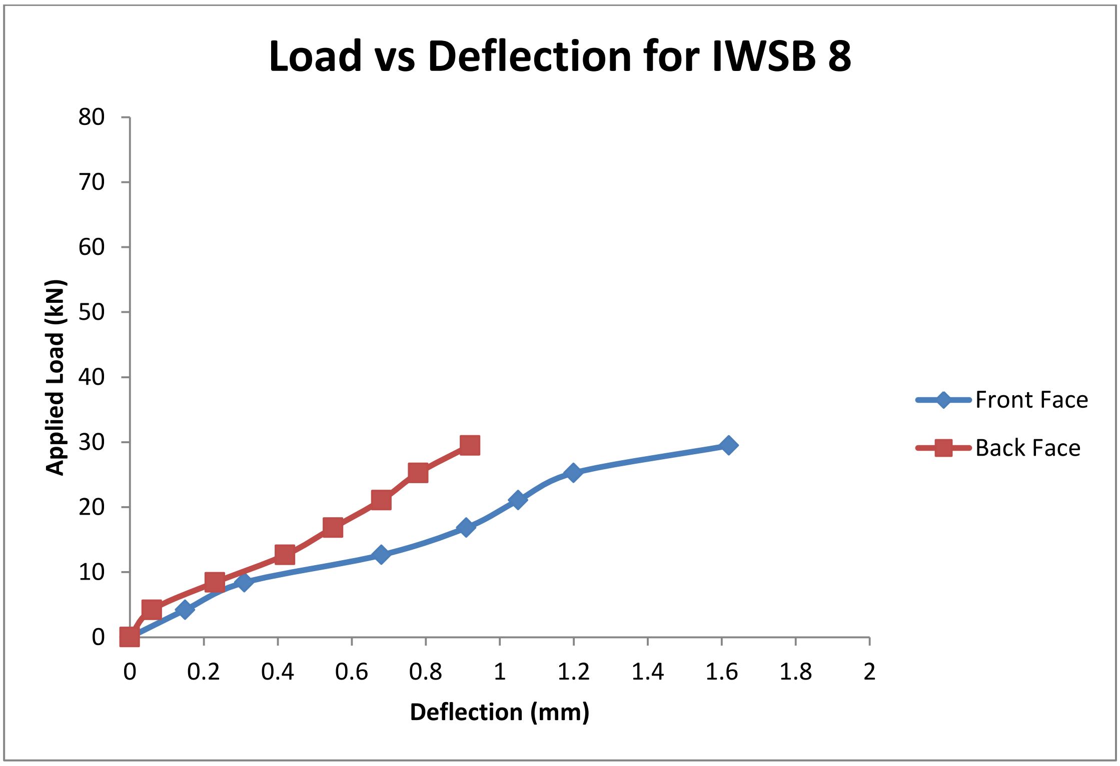

Figure 4.32 Load vs Deflection Curve for IWSB 8

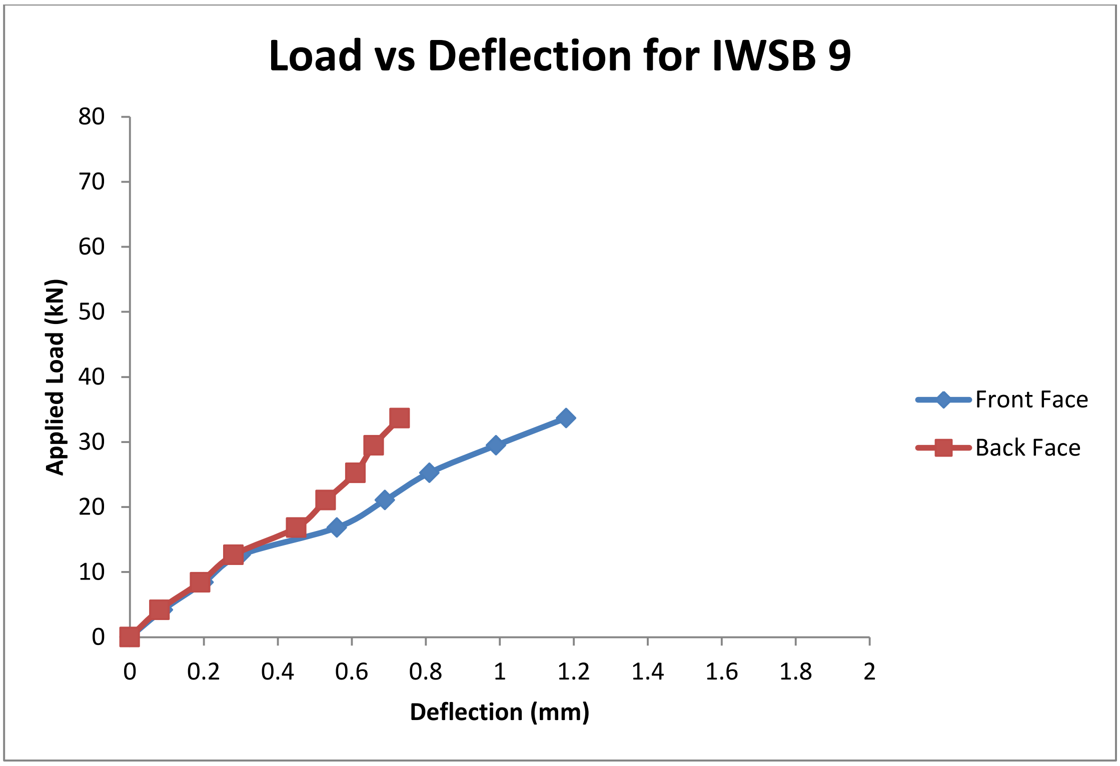

Figure 4.33 Load vs Deflection for IWSB 9

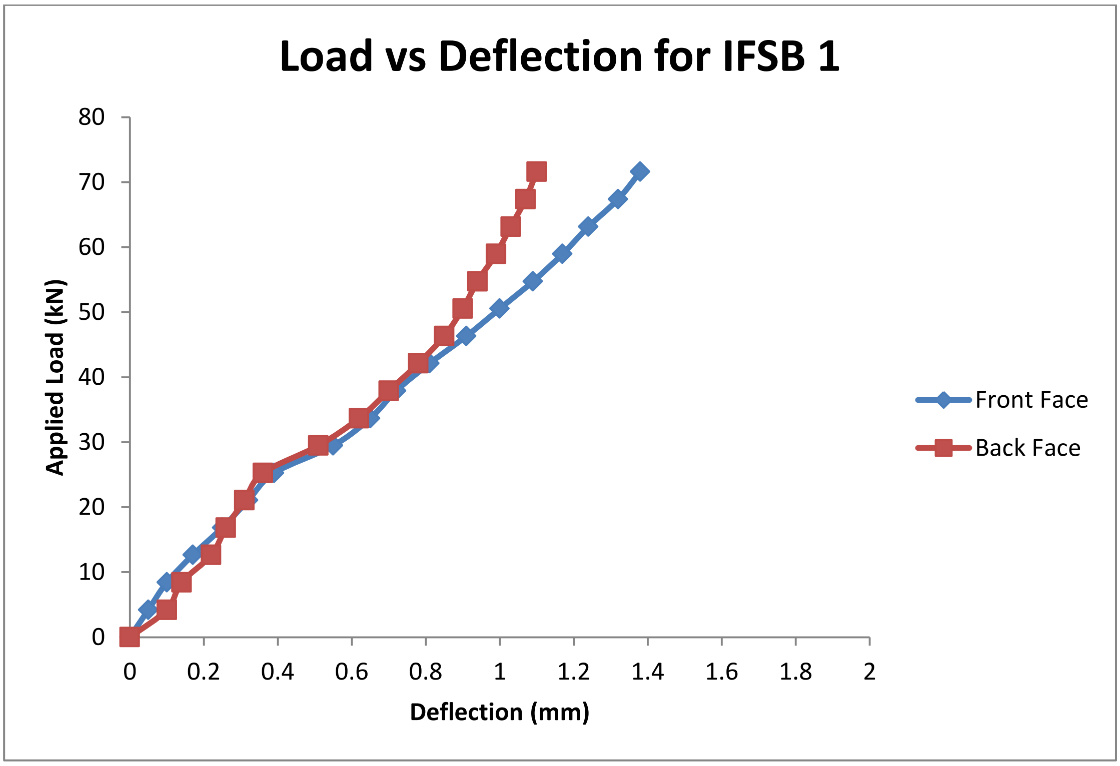

Figure 4.34 Load vs Deflection for IFSB 1

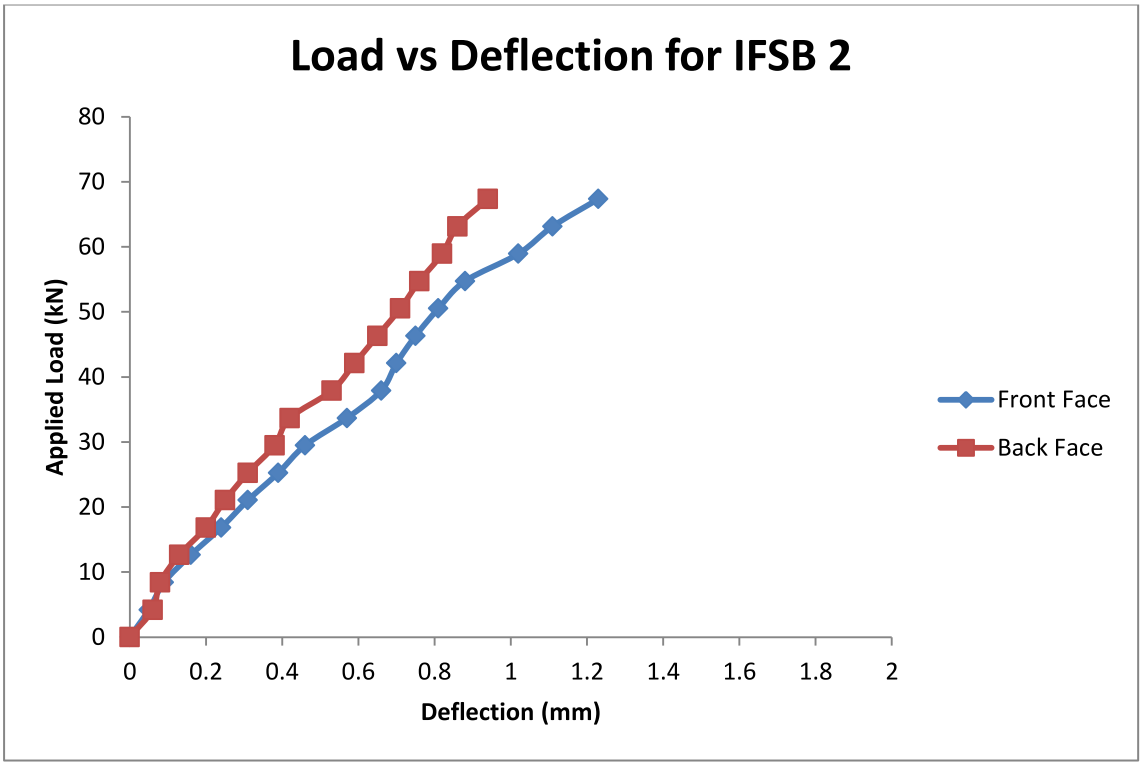

Figure 4.35 Load vs Deflection for IFSB 2

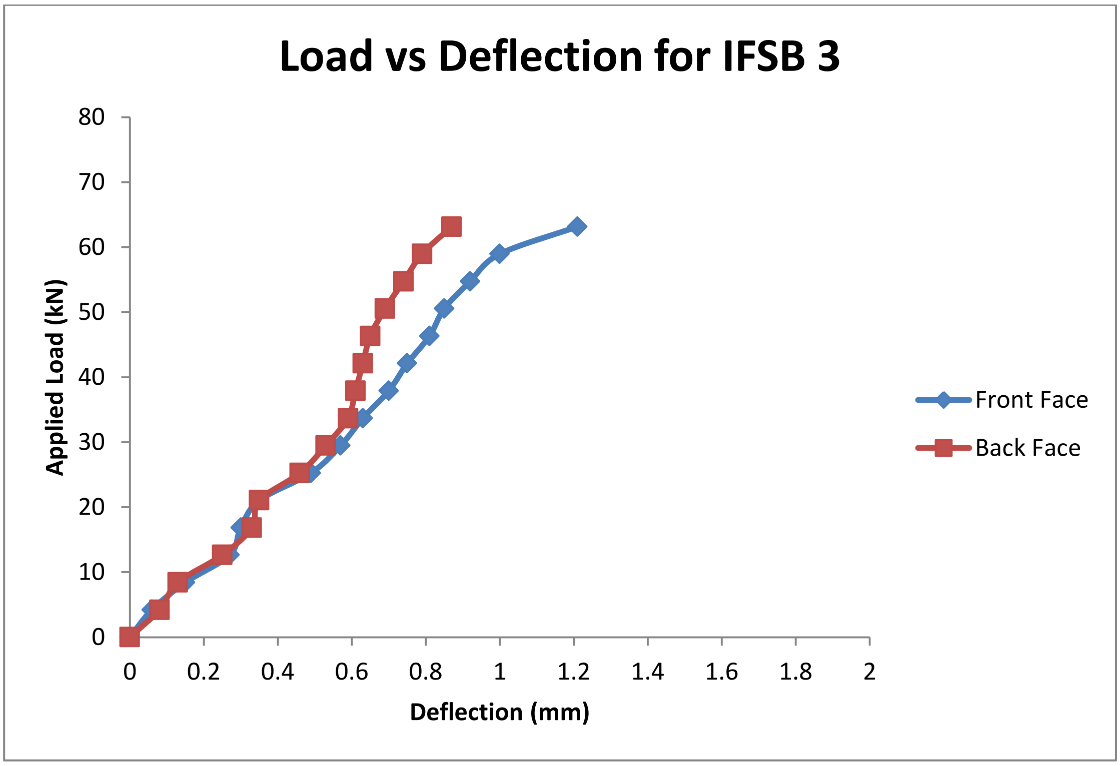

Figure 4.36 Load vs Deflection for IFSB 3

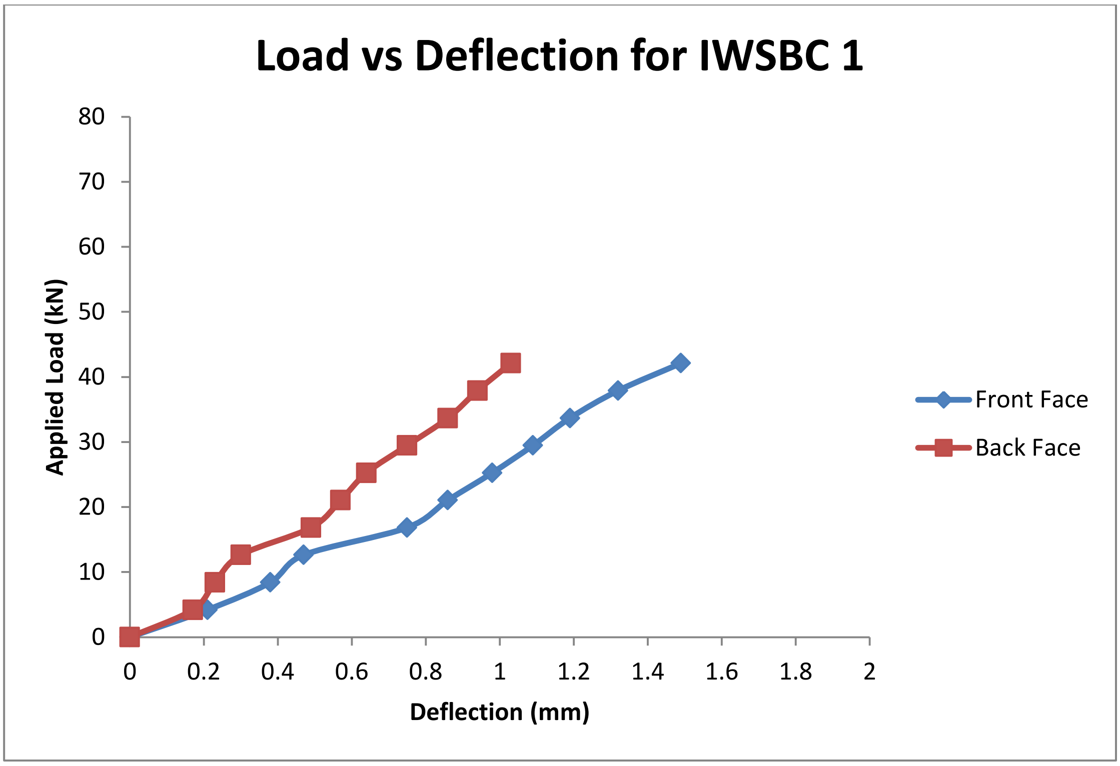

Figure 4.37 Load vs Deflection for IWSBC 1

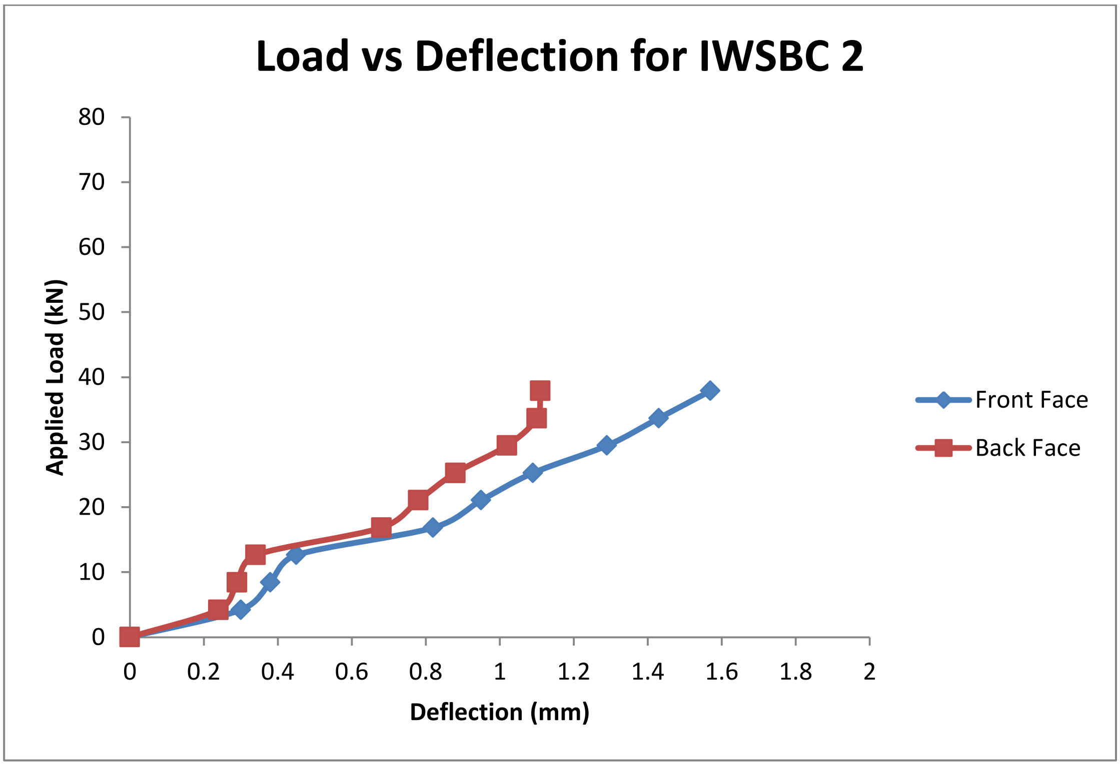

Figure 4.38 Load vs Deflection for IWSBC 2

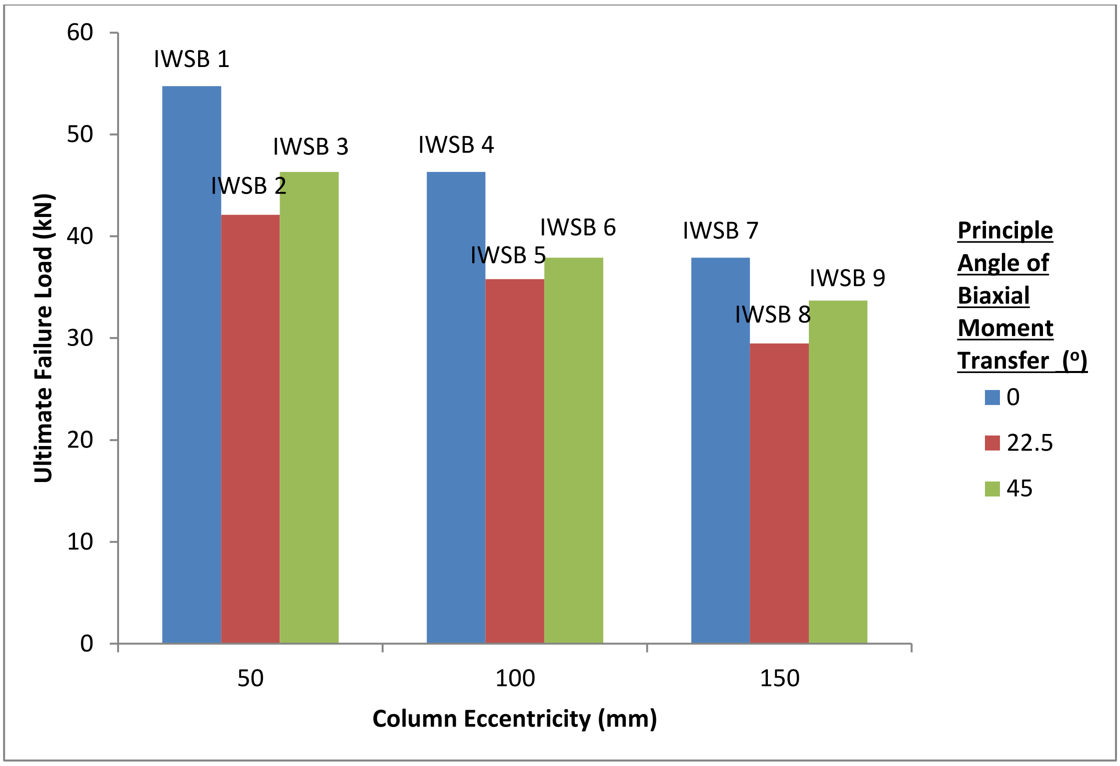

Figure 4.39 Effects of Principle Angle of Biaxial Moment on Punching Capacity

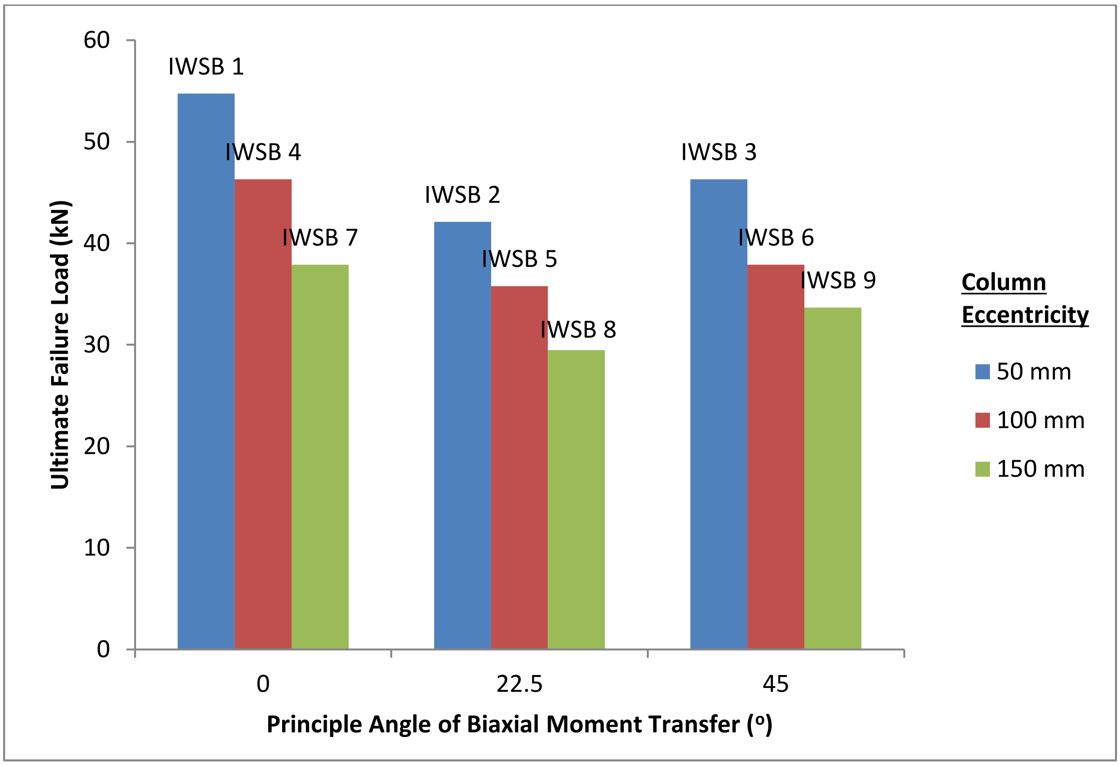

Figure 4.40 Effects of Column Eccentricity on Punching Capacity

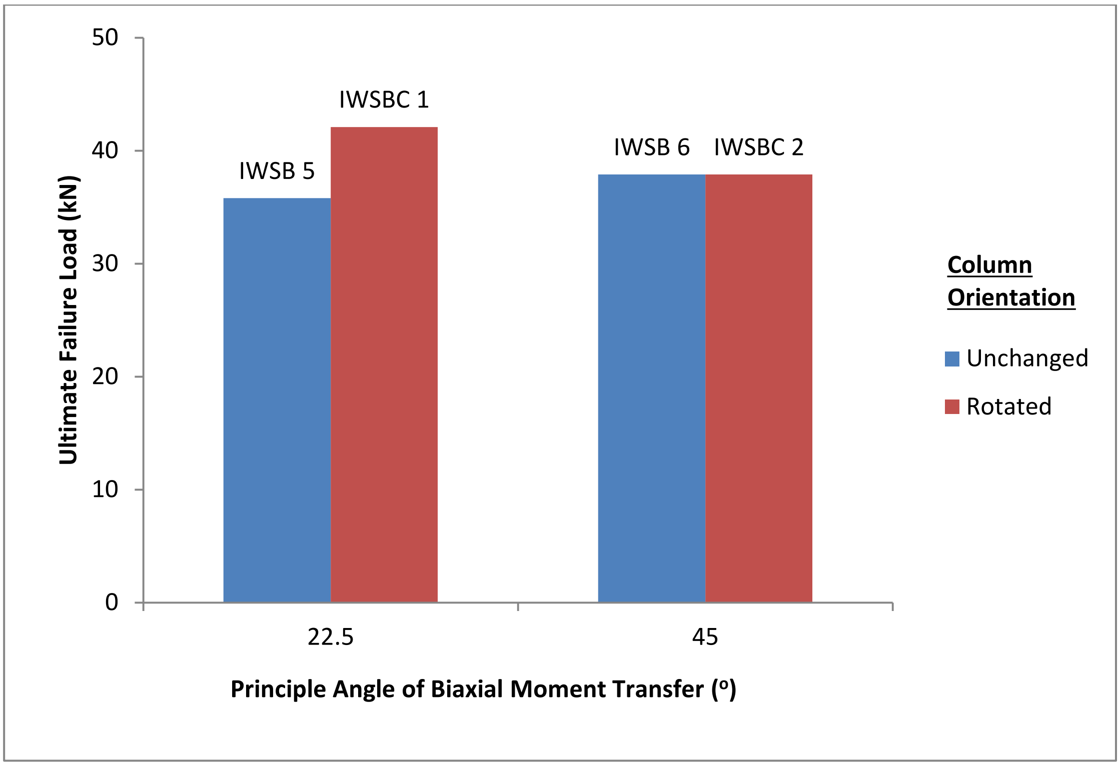

Figure 4.41 Effects of Column Orientation on Punching Capacity

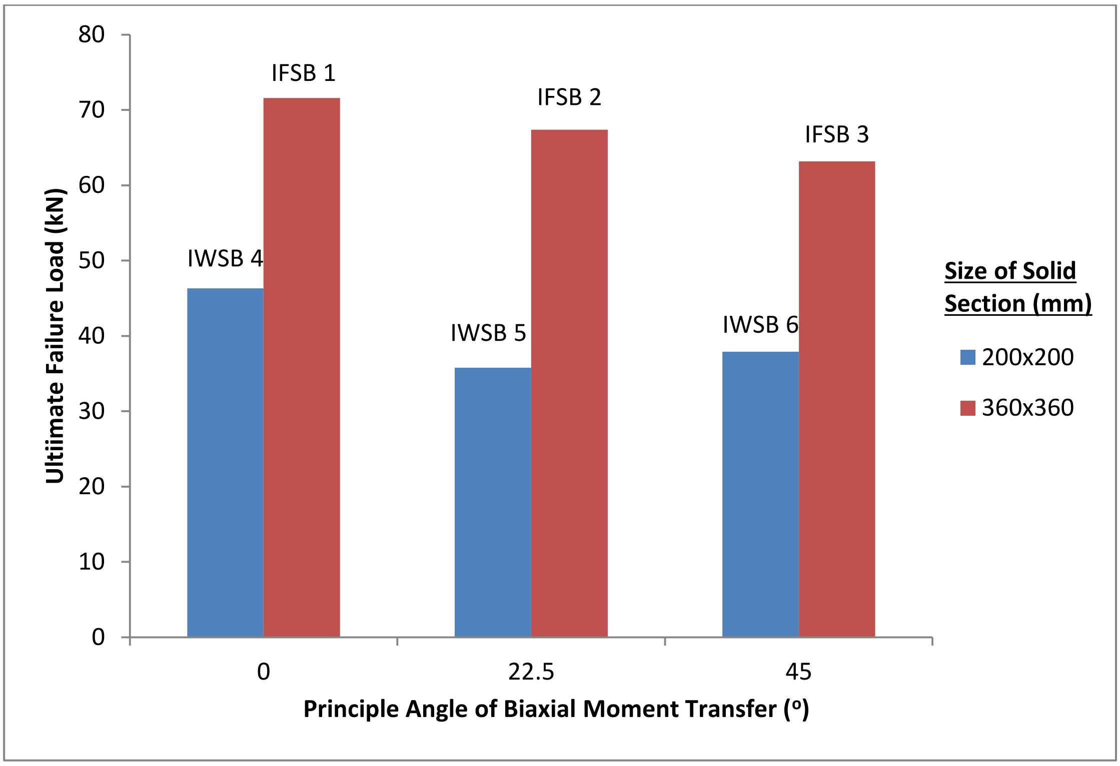

Figure 4.42 Effect of Solid Section on Punching Capacity

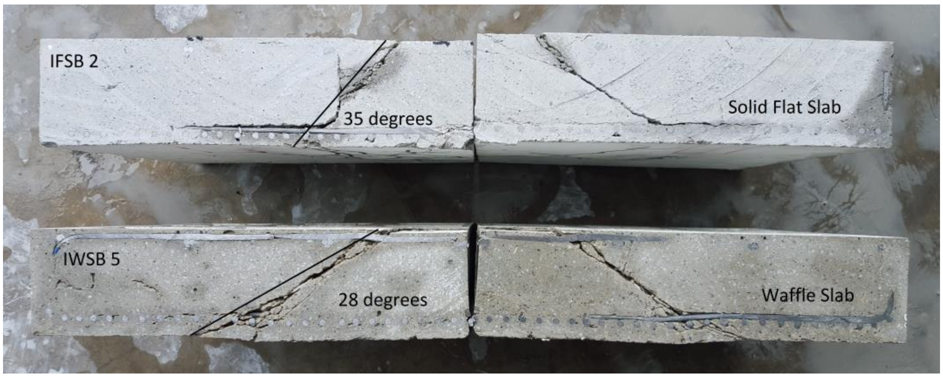

Figure 4.43 Comparisons between IFSB 2 and IWSB 5

Figure 4.44 Edge Punching Mechanism

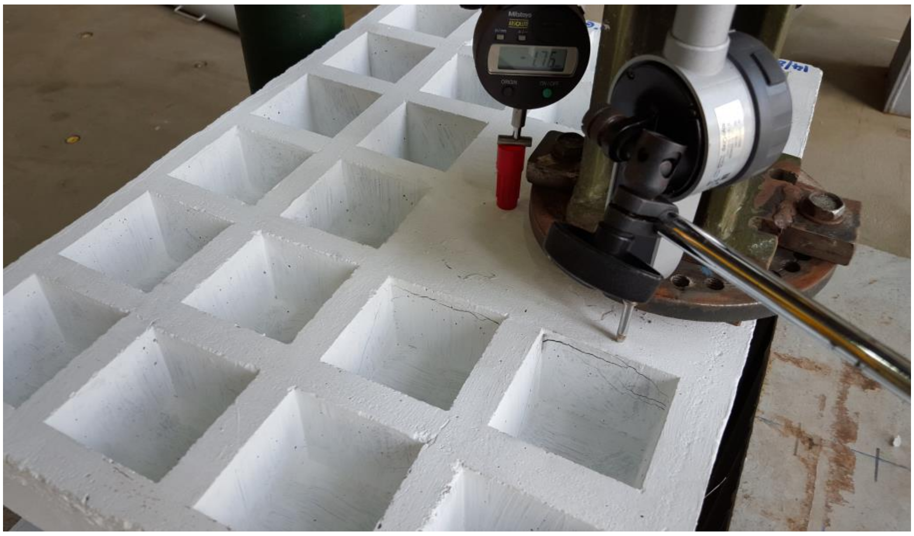

Figure 4.45 Loss of Potential Failure Surface in Waffle Section, EWSB 5 (during loading)

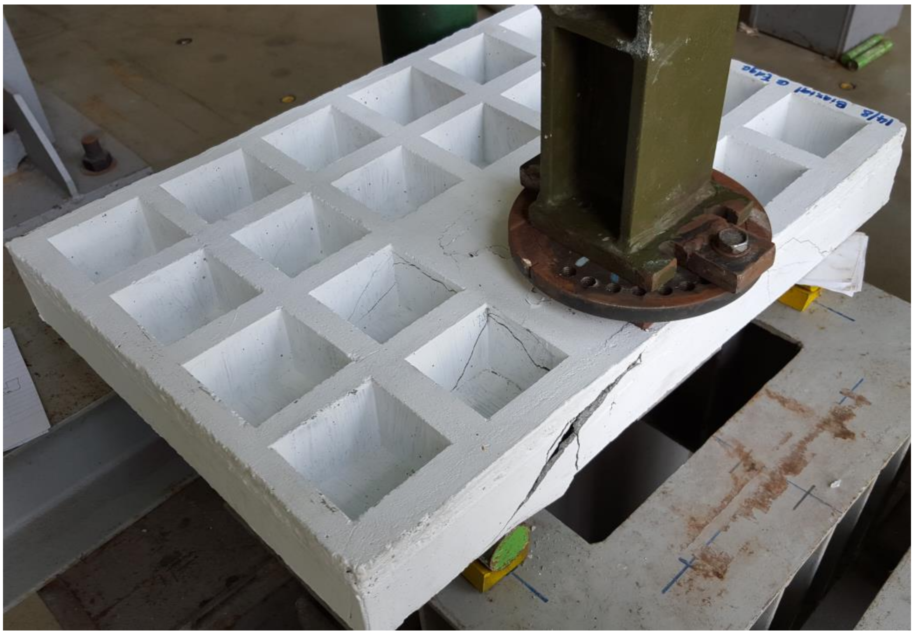

Figure 4.46 Loss of Potential Failure Surface in Waffle Section, EWSB 5 (after punching failure)

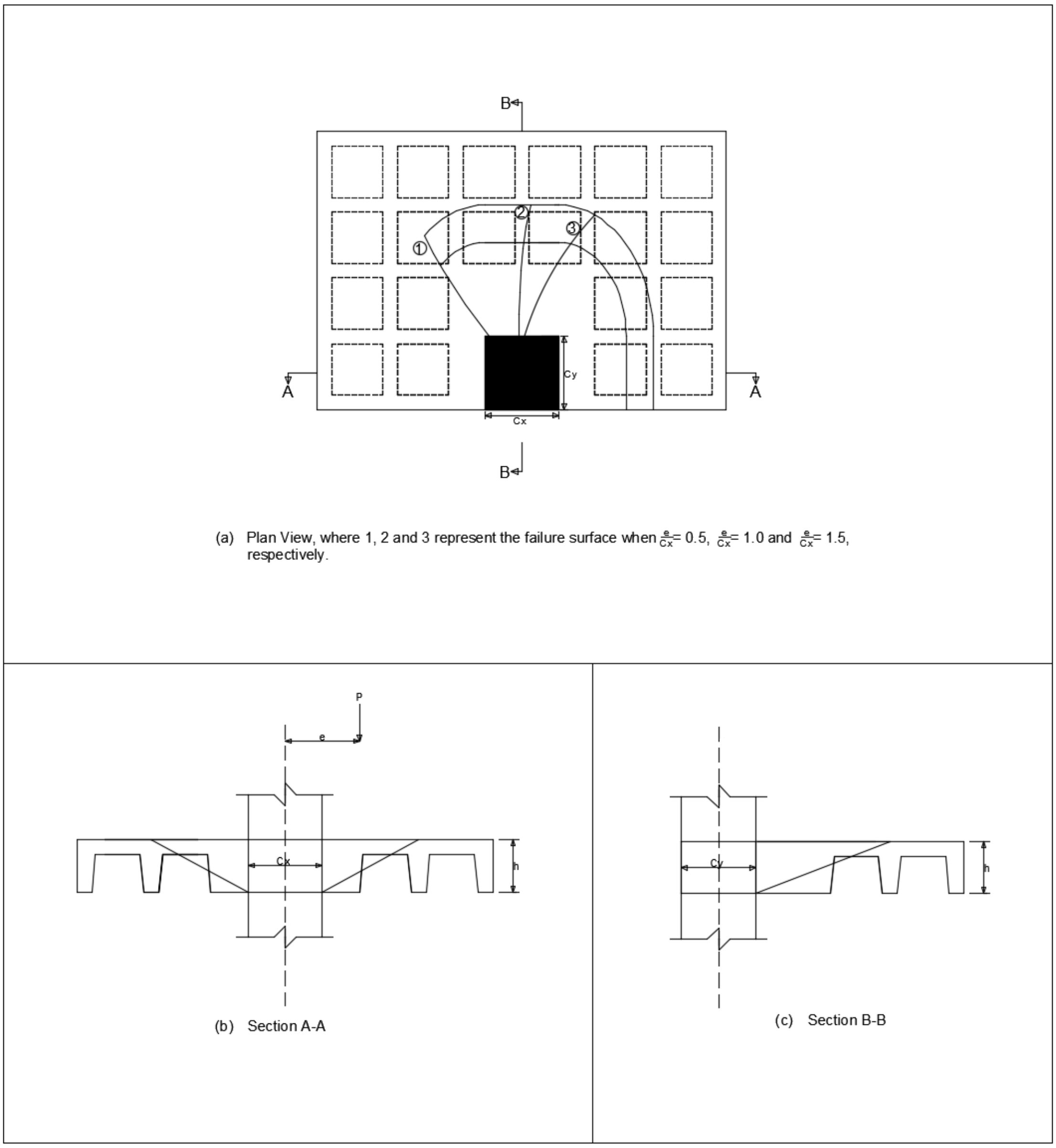

Figure 4.47 Schematic sketches of the observed effects of column eccentricities (parallel to slab edge) on edge punching shear mechanism

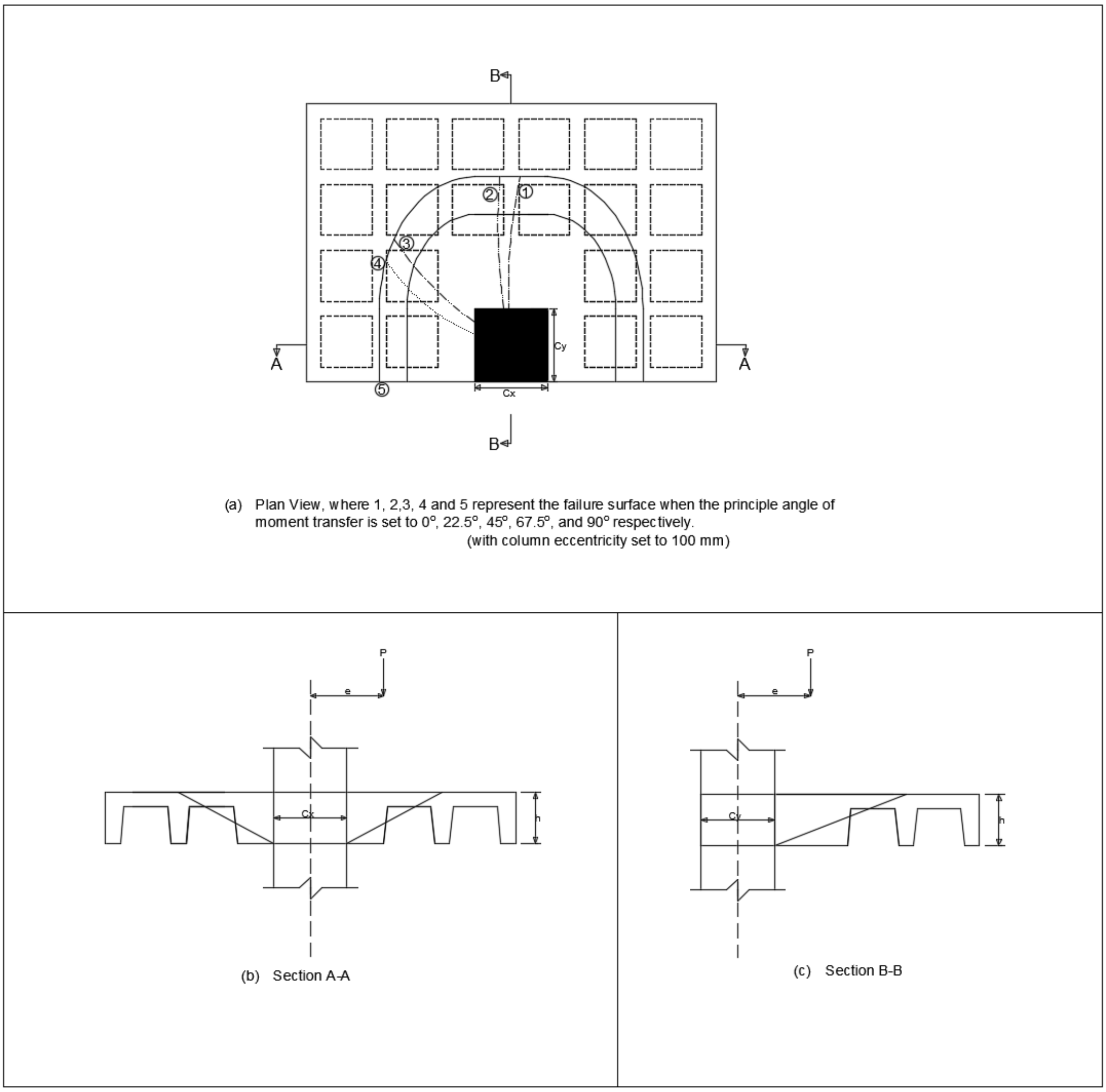

Figure 4.48 Schematic sketches of the observed effects of the principle angles of biaxial moment transfer on edge punching shear mechanism

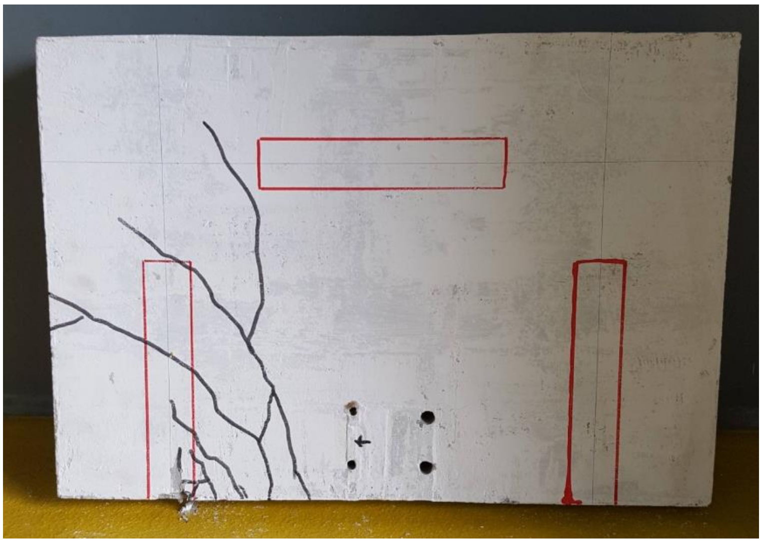

(a) Top View

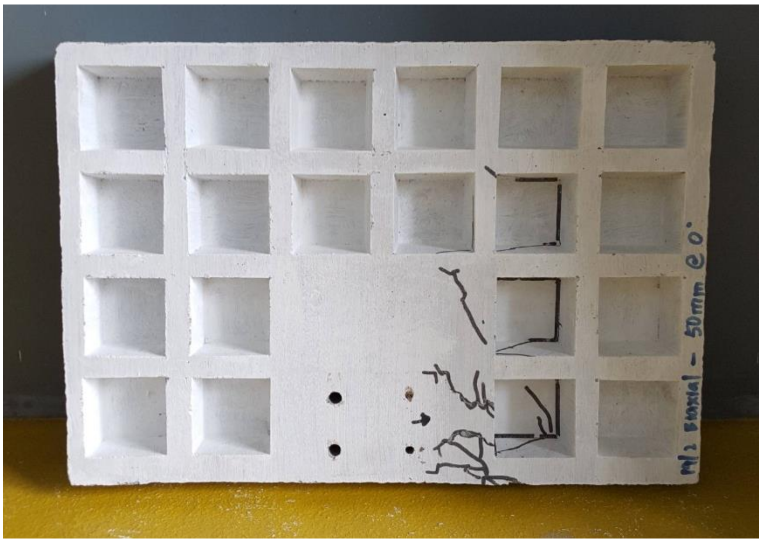

(b) Bottom View

(c) Side View

Figure 4.49 Edge Punching of Waffle Slab, EWSB 1

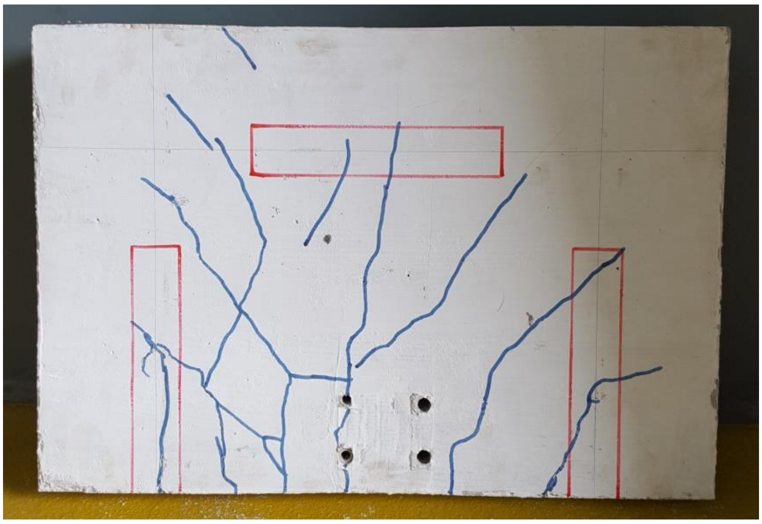

(a) Top View

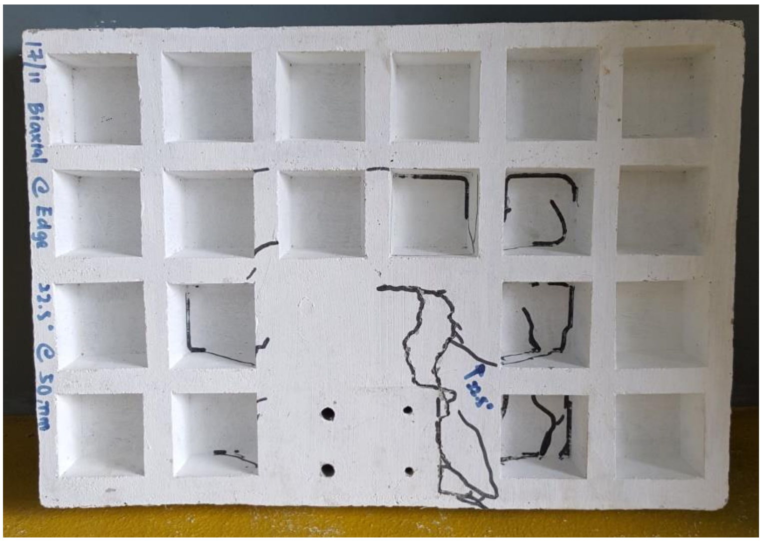

(b) Bottom View

(c) Side View

Figure 4.50 Edge Punching of Waffle Slab, EWSB 2

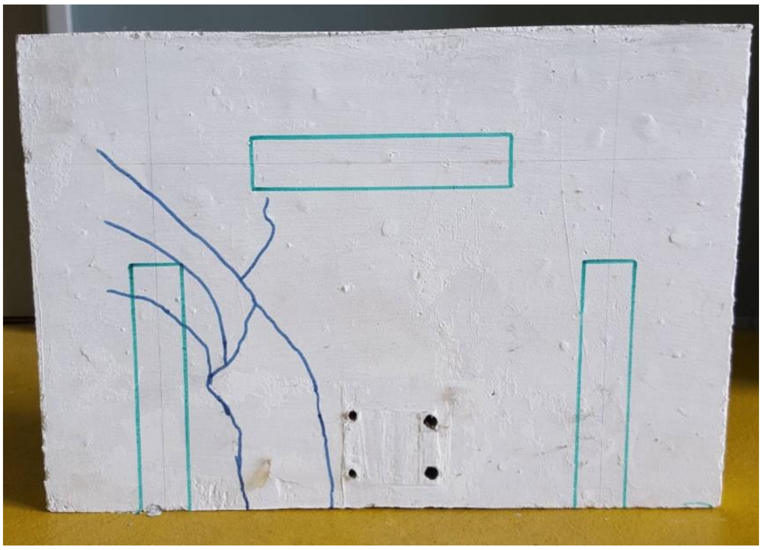

(d) Top View

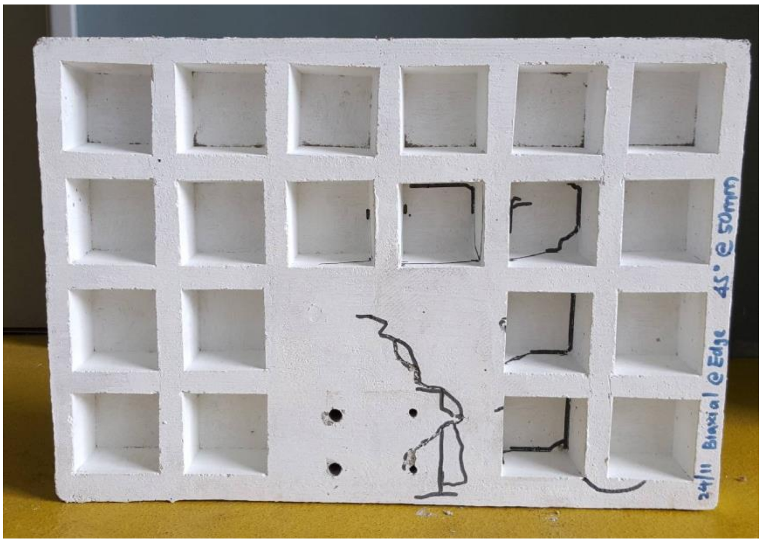

(e) Bottom View

(f) Side View

Figure 4.51 Edge Punching of Waffle Slab, EWSB 3

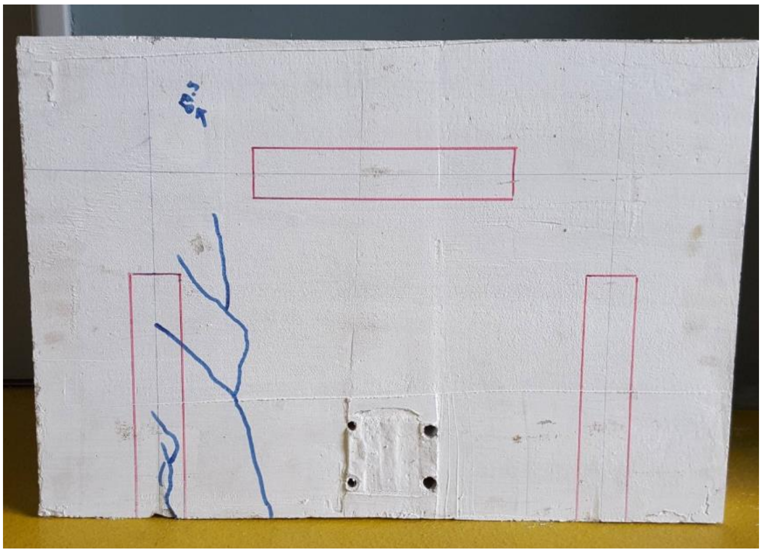

(a) Top View

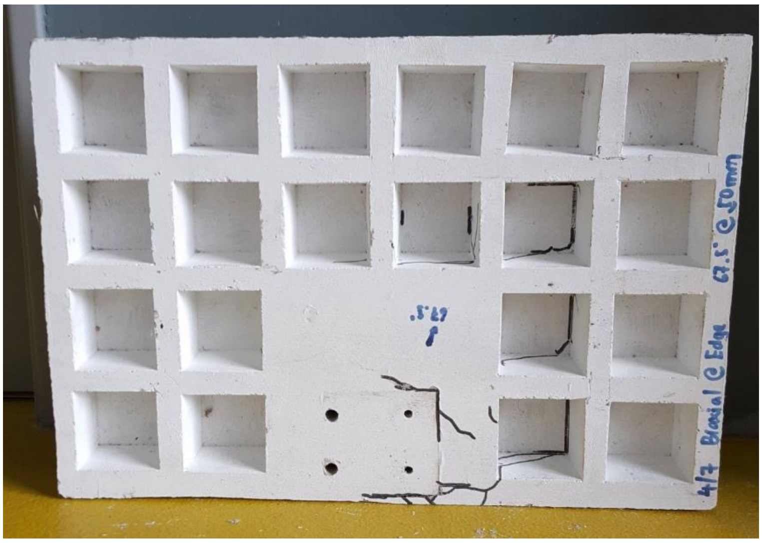

(b) Bottom View

(c) Side View

Figure 4.52 Edge Punching of Waffle Slab, EWSB 4

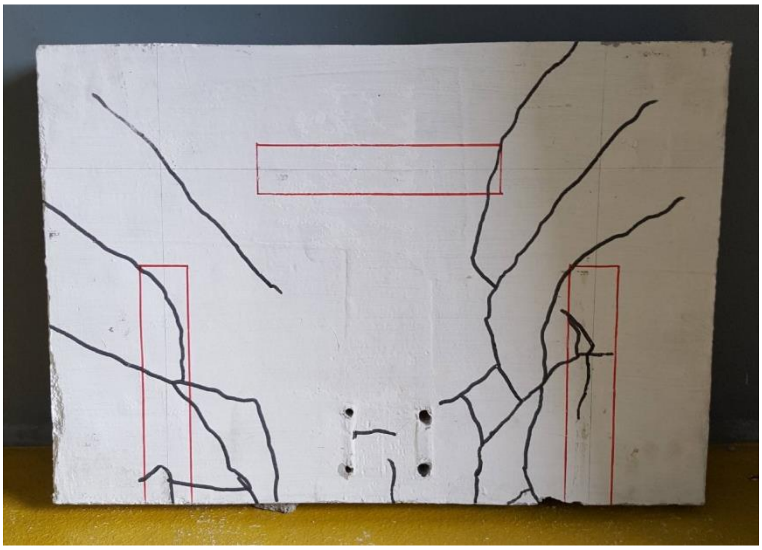

(a) Top View

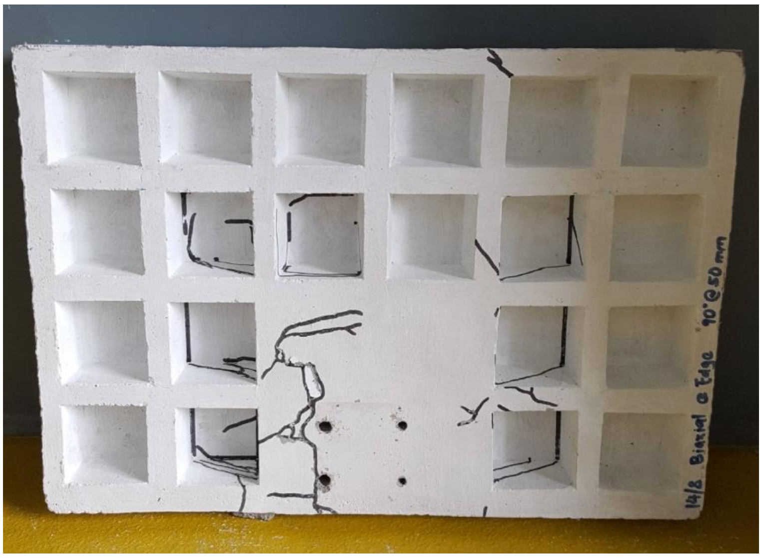

(b) Bottom View

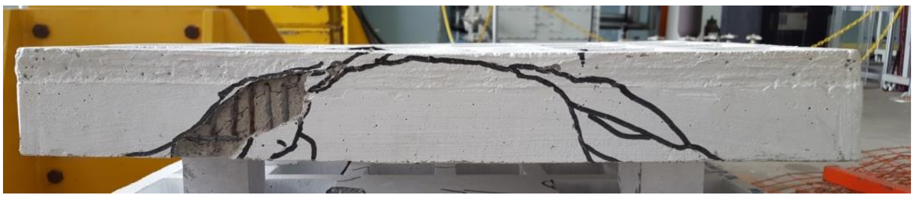

(c) Side View

Figure 4.53 Edge Punching of Waffle Slab, EWSB 5

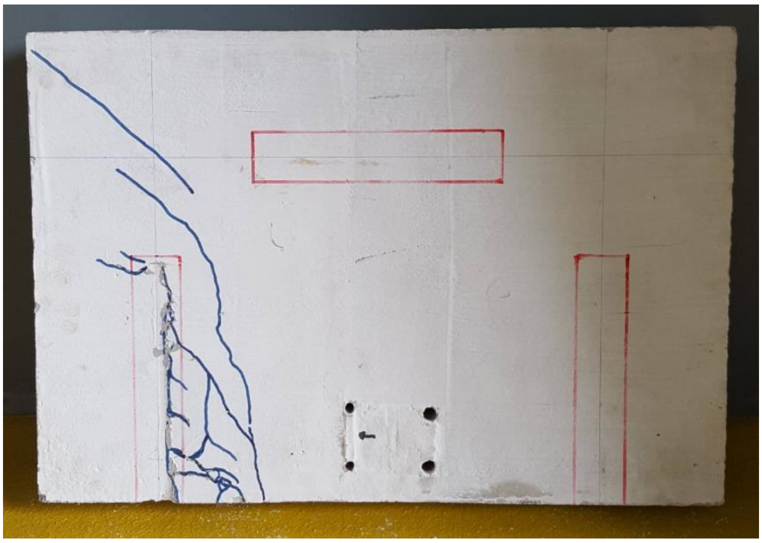

(a) Top View

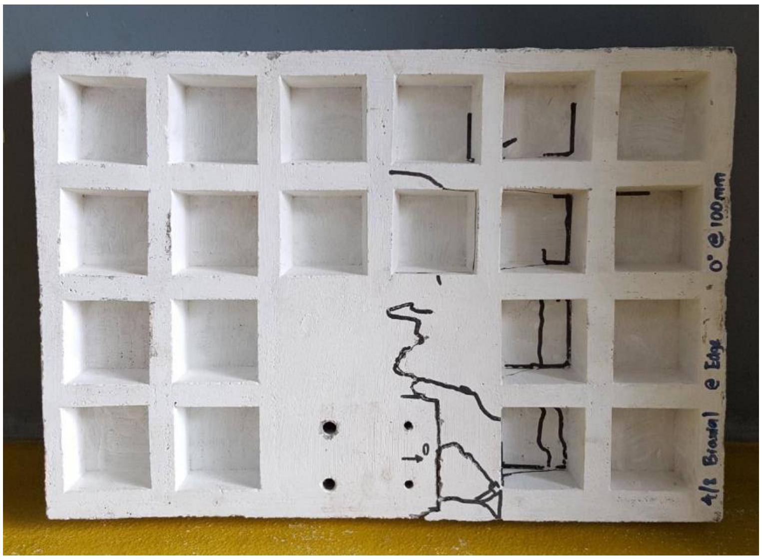

(b) Bottom View

(c) Side View

Figure 4.54 Edge Punching of Waffle Slab, EWSB 6

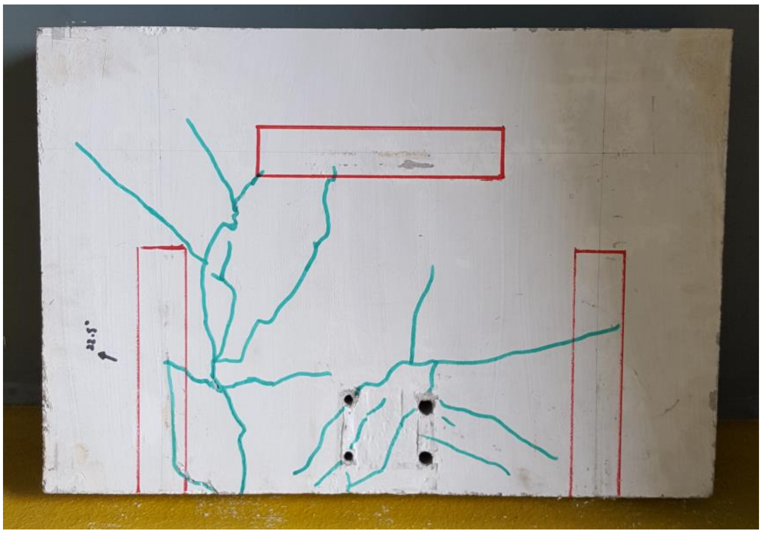

(a) Top View

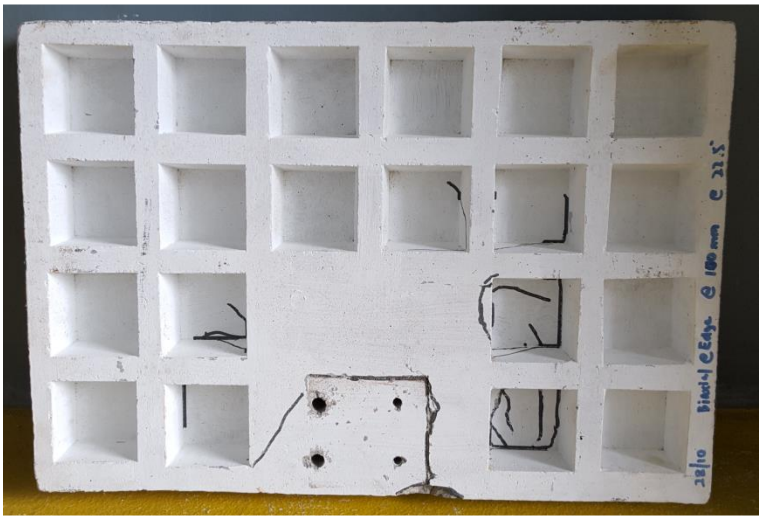

(b) Bottom View

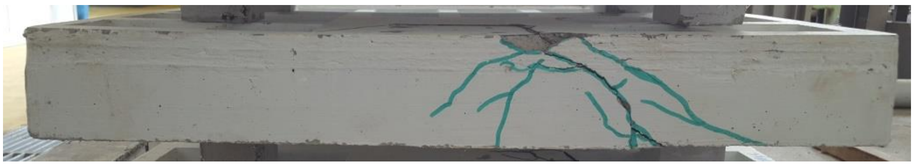

(c) Side View

Figure 4.55 Edge Punching of Waffle Slab, EWSB 7

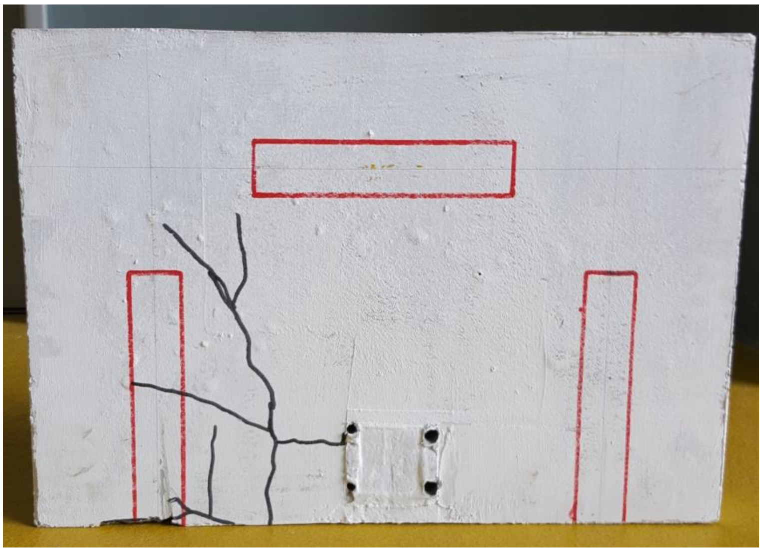

(a) Top View

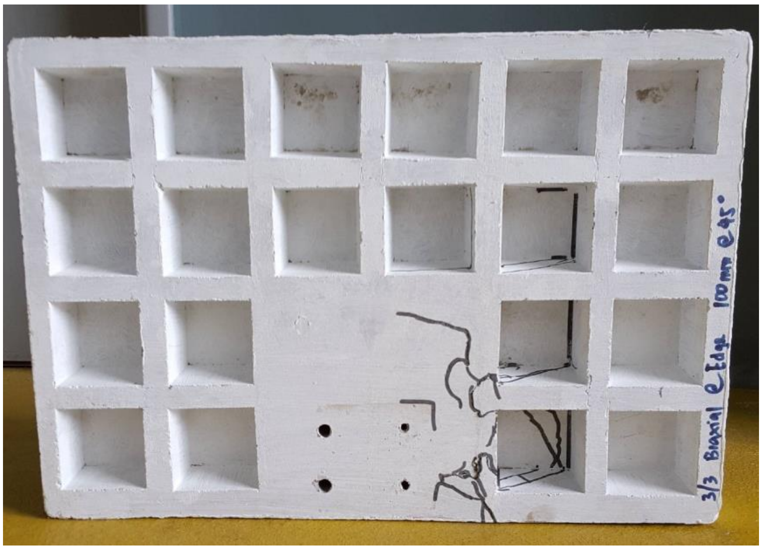

(b) Bottom View

(c) Side View

Figure 4.56 Edge Punching of Waffle Slab, EWSB 8

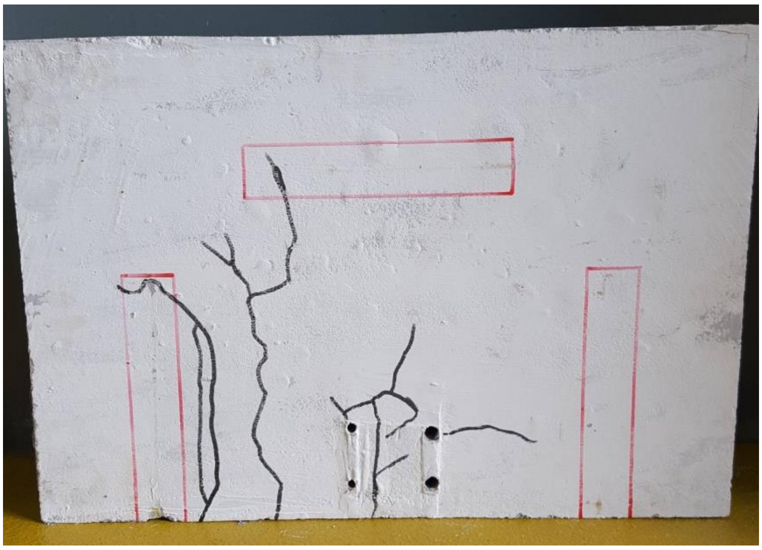

(a) Top View

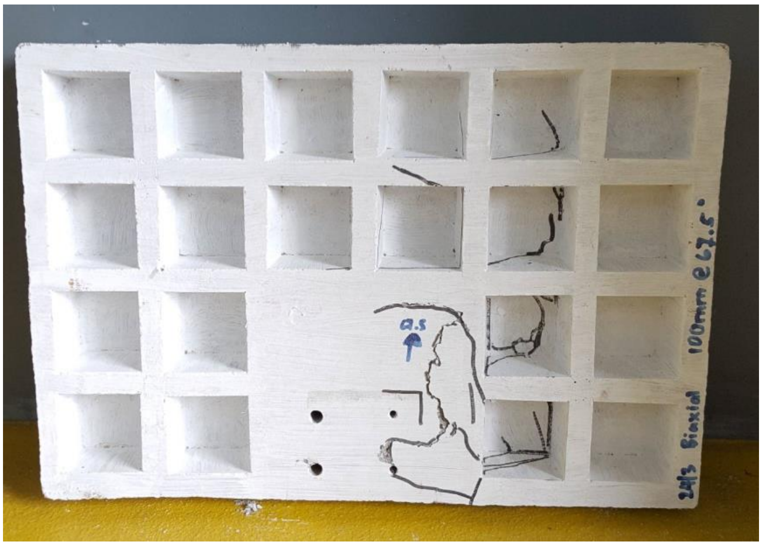

(b) Bottom View

(c) Side View

Figure 4.57 Edge Punching of Waffle Slab, EWSB 9

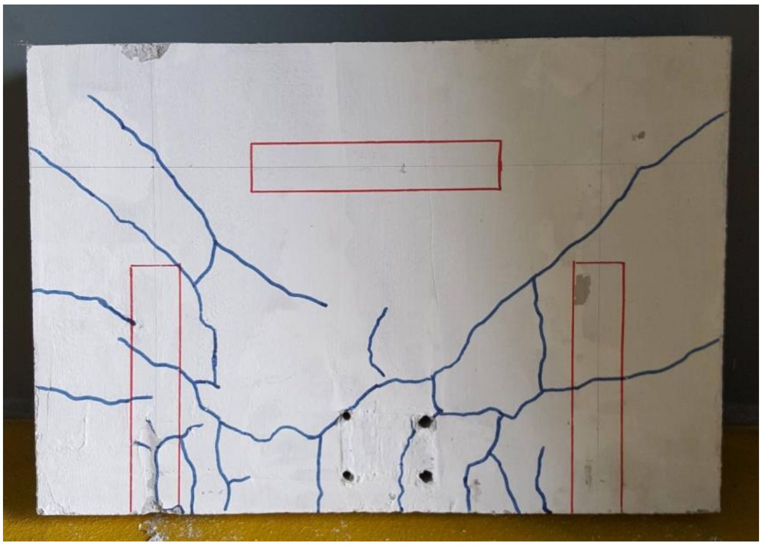

(a) Top View

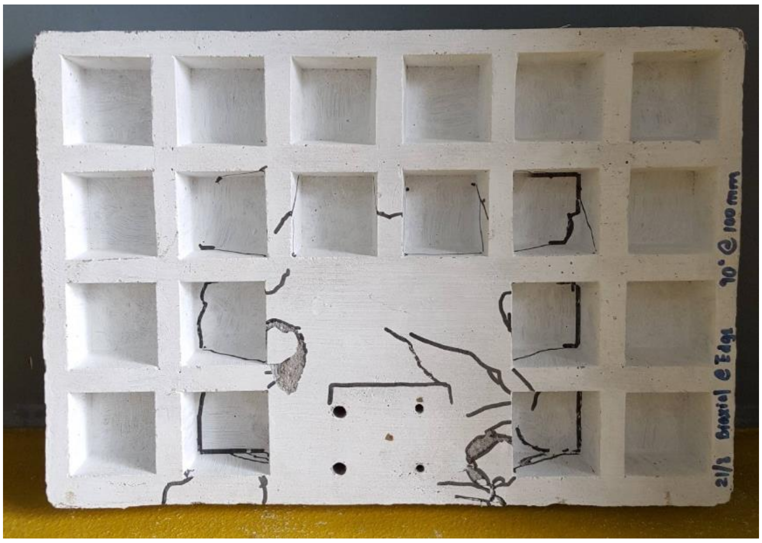

(b) Bottom View

(c) Side View

Figure 4.58 Edge Punching of Waffle Slab, EWSB 10

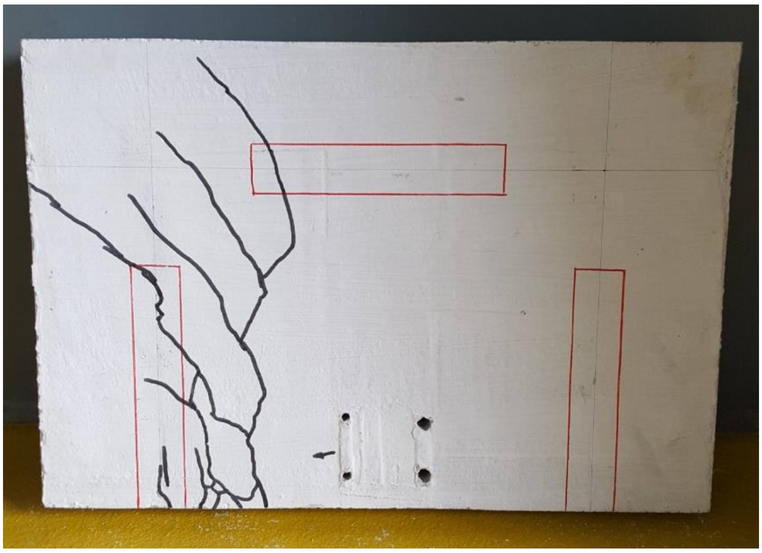

(a) Top View

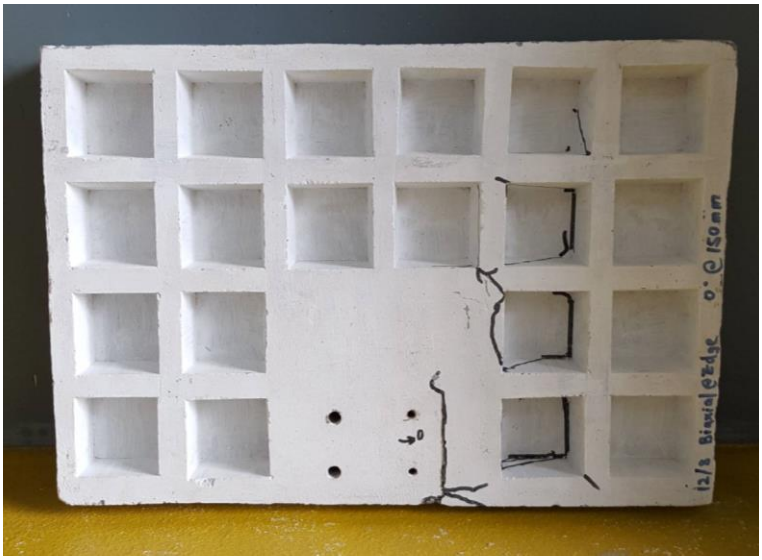

(b) Bottom View

(c) Side View

Figure 4.59 Edge Punching of Waffle Slab, EWSB 11

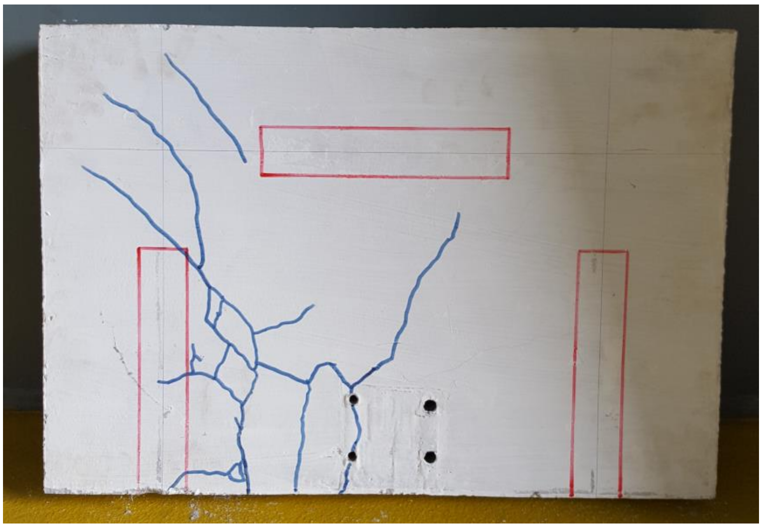

(a) Top View

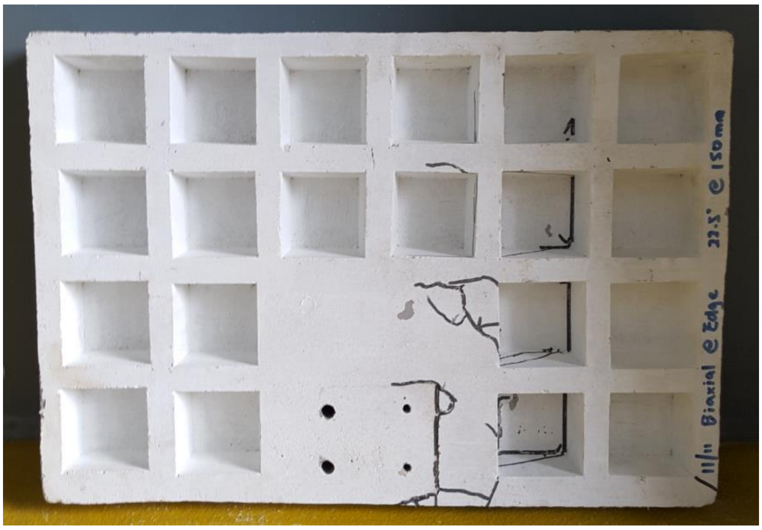

(b) Bottom View

(c) Side View

Figure 4.60 Edge Punching of Waffle Slab, EWSB 12

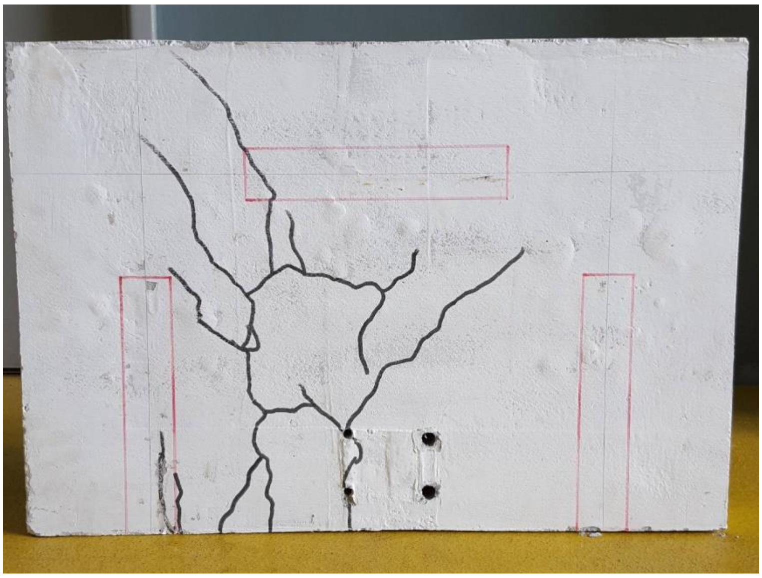

(a) Top View

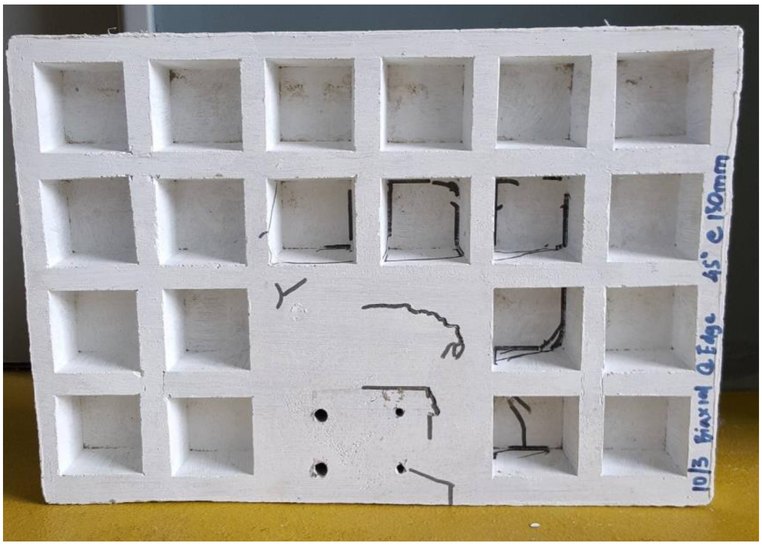

(b) Bottom View

(c) Side View

Figure 4.61 Edge Punching of Waffle Slab, EWSB 13

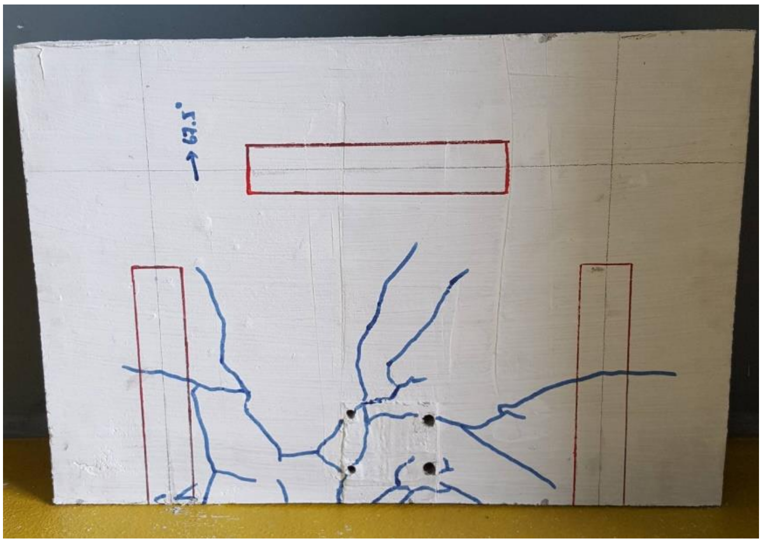

(a) Top View

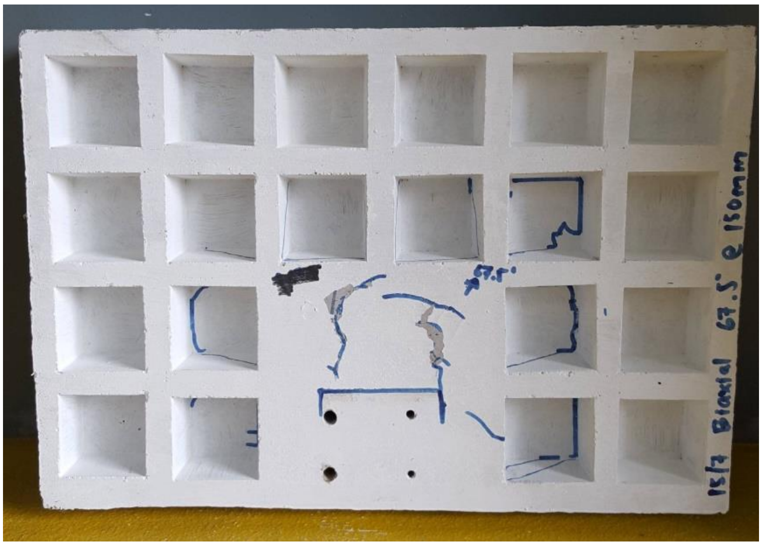

(b) Bottom View

(c) Side View

Figure 4.62 Edge Punching of Waffle Slab, EWSB 14

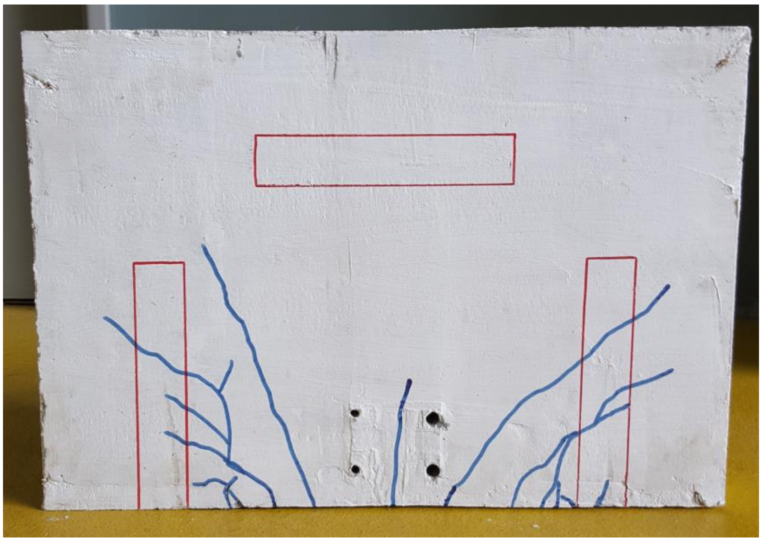

(a) Top View

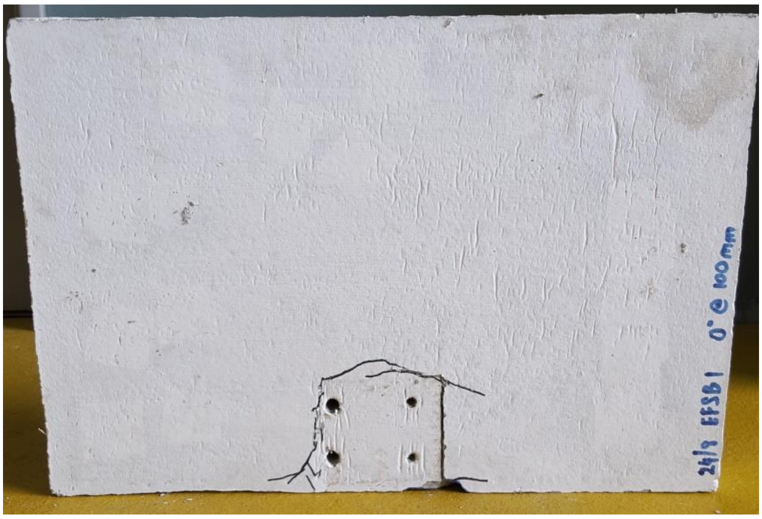

(b) Bottom View

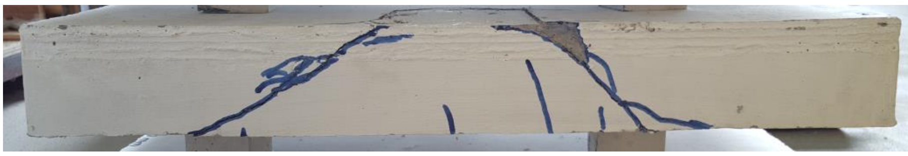

(c) Side View

Figure 4.63 Edge Punching of Flat Slab, EWSB 1

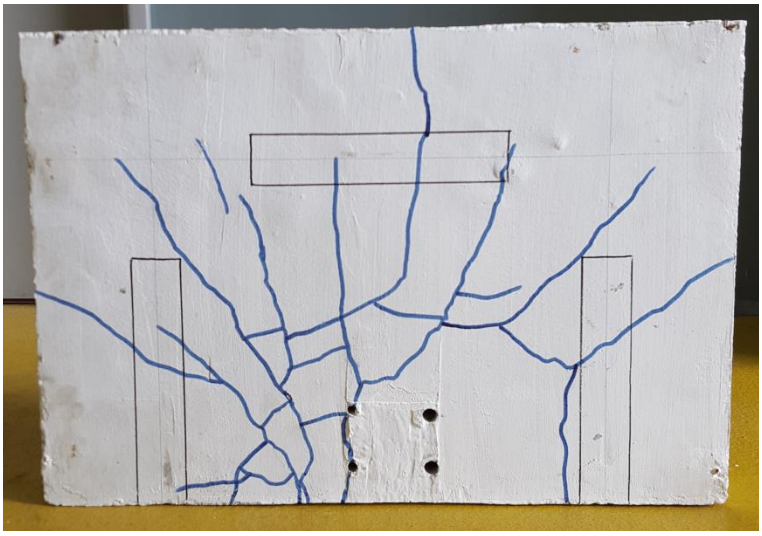

(a) Top View

(b) Bottom View

(c) Side View

Figure 4.64 Edge Punching of Flat Slab, EWSB 2

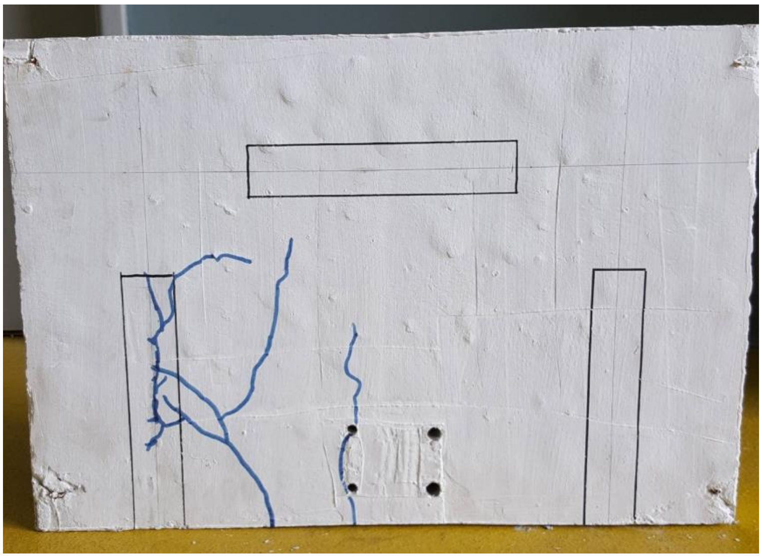

(a) Top View

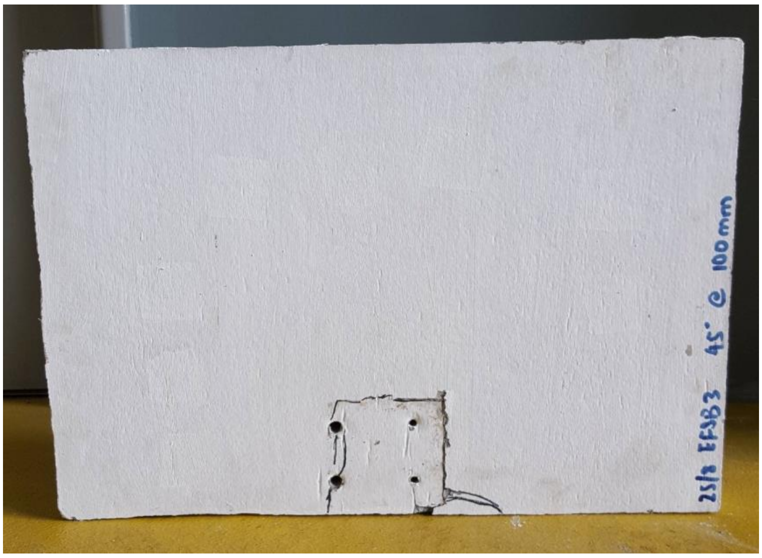

(b) Bottom View

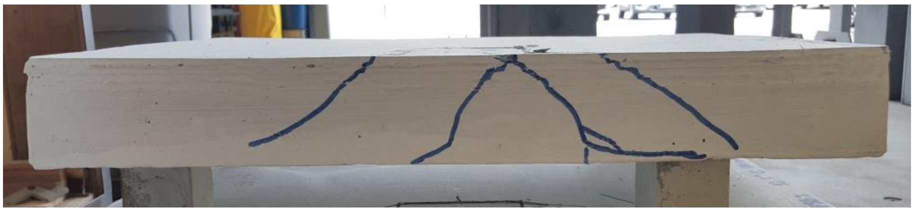

(c) Side View

Figure 4.65 Edge Punching of Flat Slab, EWSB 3

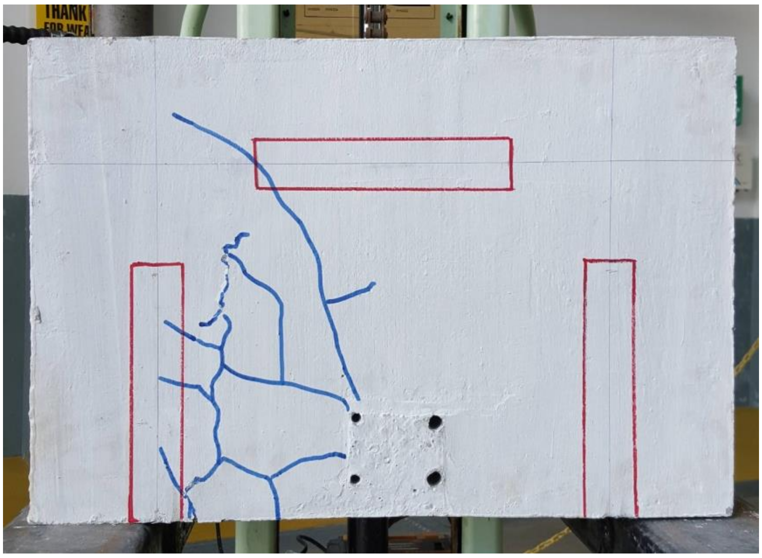

(a) Top View

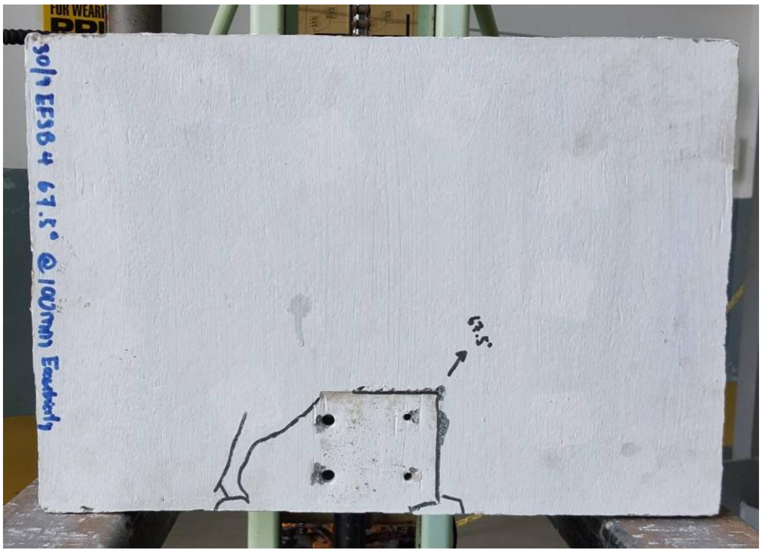

(b) Bottom View

(c) Side View

Figure 4.66 Edge Punching of Flat Slab, EWSB 4

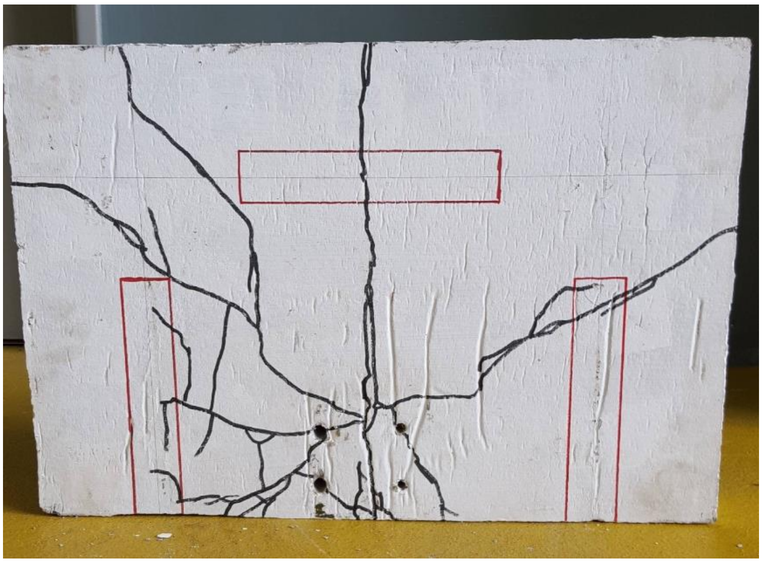

(a) Top View

(b) Bottom View

(c) Side View

Figure 4.67 Edge Punching of Flat Slab, EWSB 5

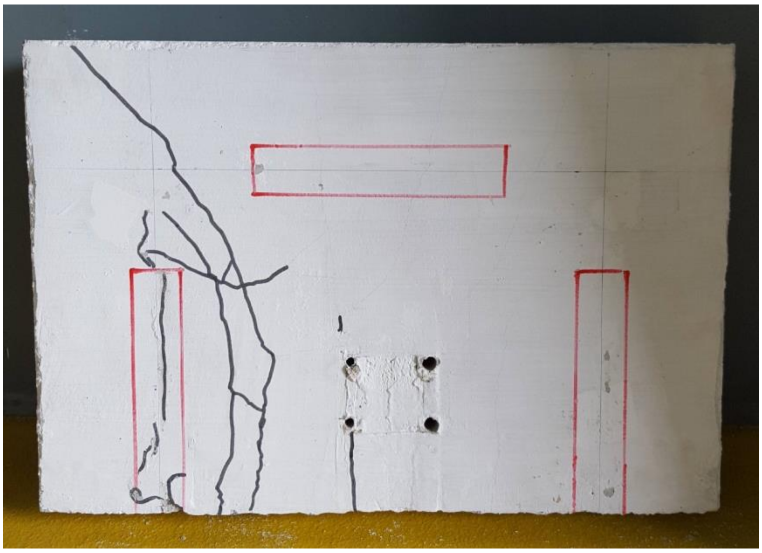

(a) Top View

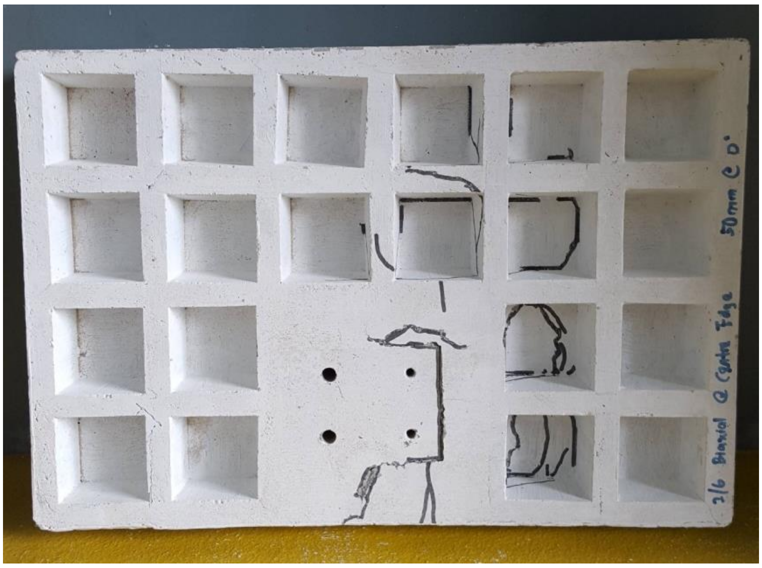

(b) Bottom View

(c) Side View

Figure 4.68 Edge Punching of Waffle Slab with different location, EWSCE 1

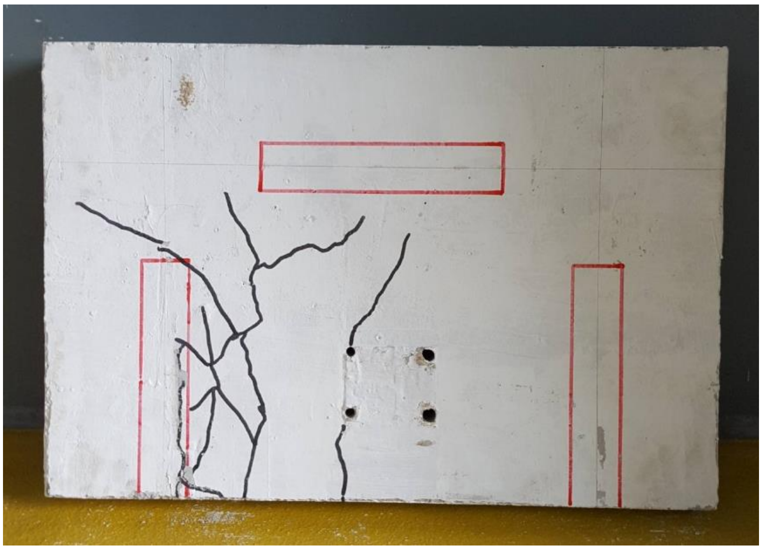

(a) Top View

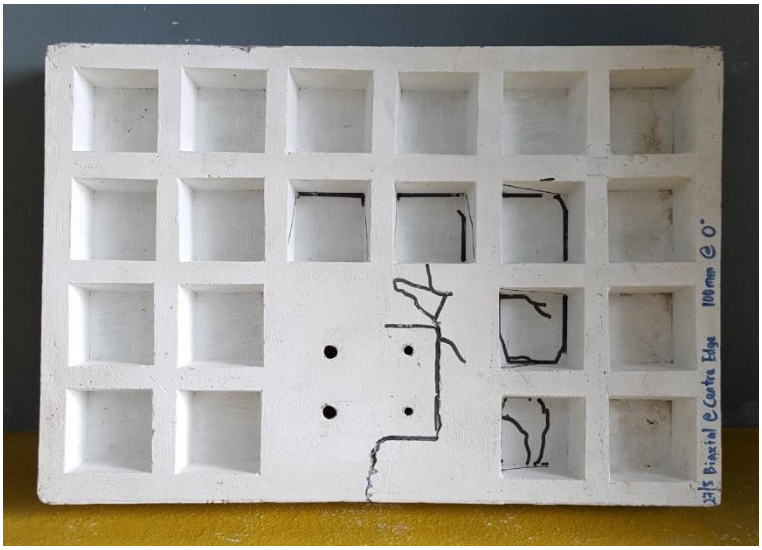

(b) Bottom View

(c) Side View

Figure 4.69 Edge Punching of Waffle Slab with different location, EWSCE 2

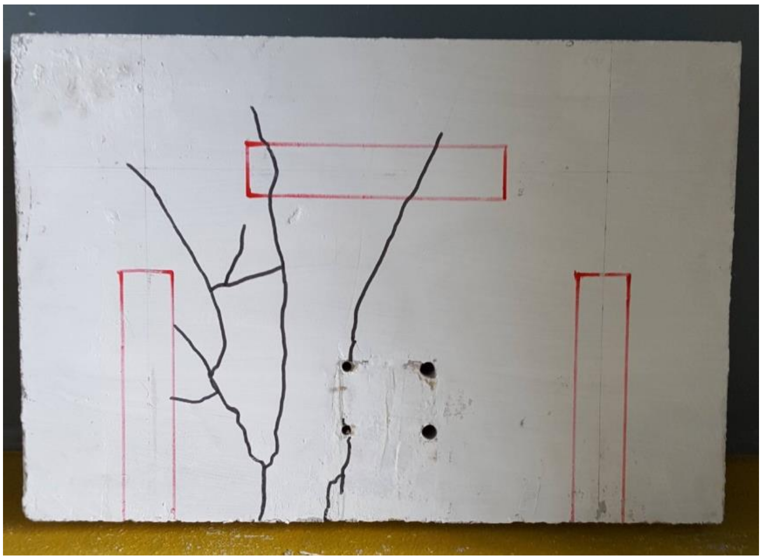

(a) Top View

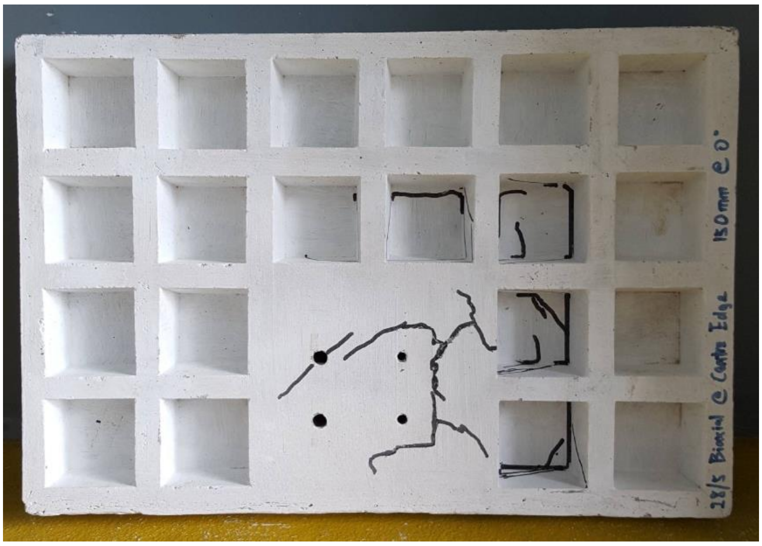

(b) Bottom View

(c) Side View

Figure 4.70 Edge Punching of Waffle Slab with different location, EWSCE 3

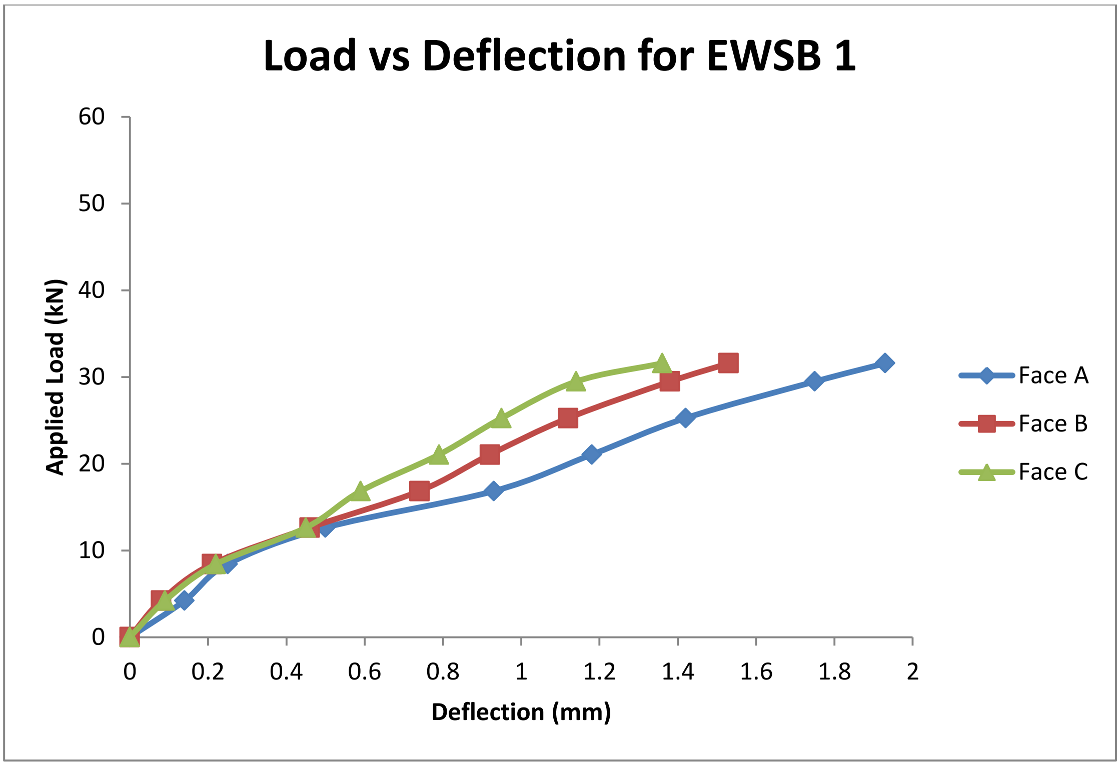

Figure 4.71 Load vs Deflection for EWSB 1

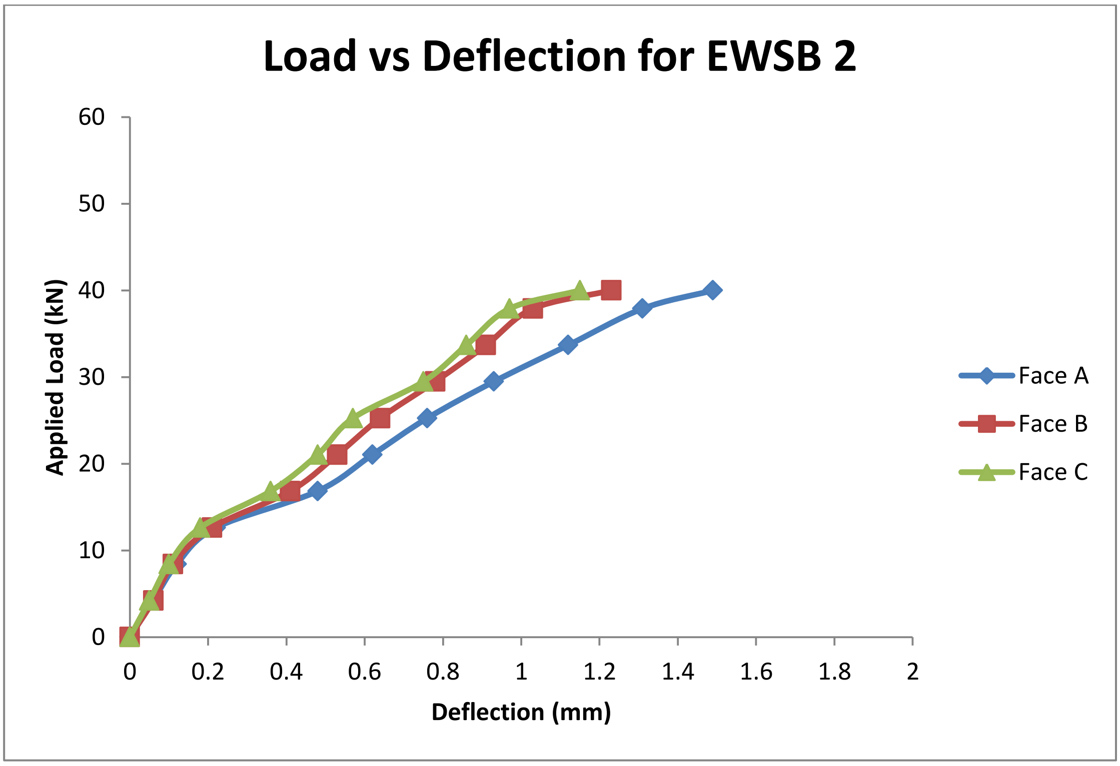

Figure 4.72 Load vs Deflection for EWSB 2

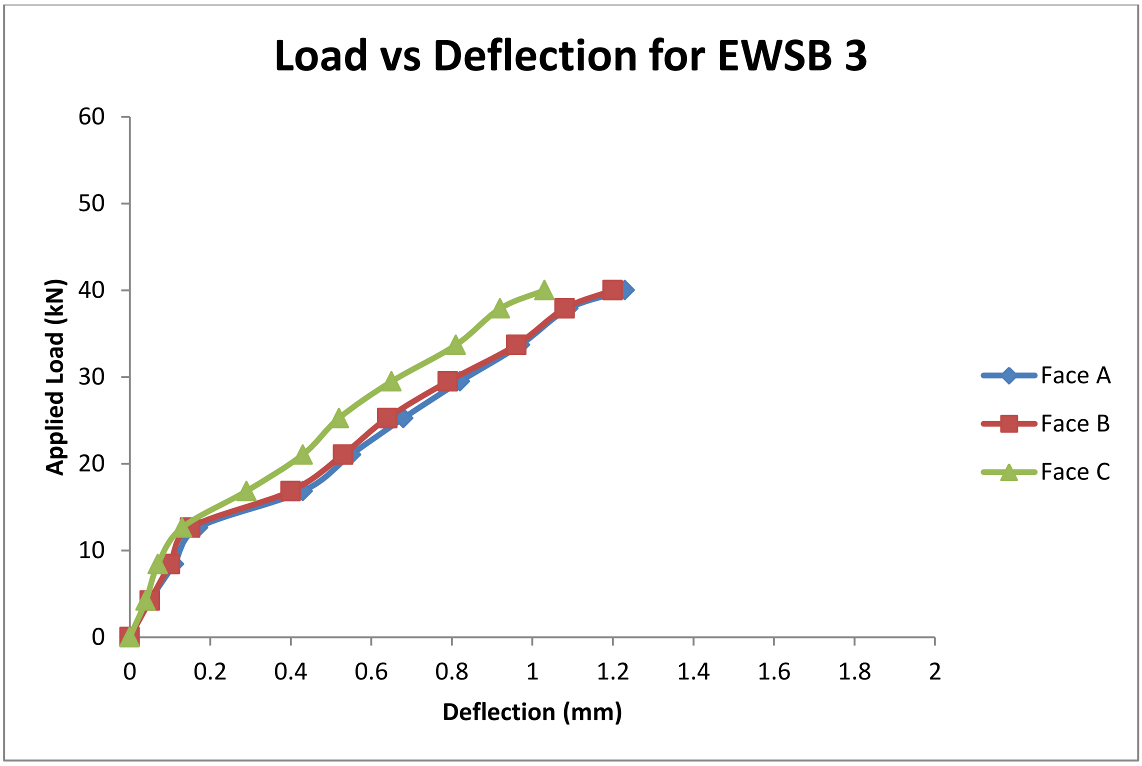

Figure 4.73 Load vs Deflection for EWSB 3

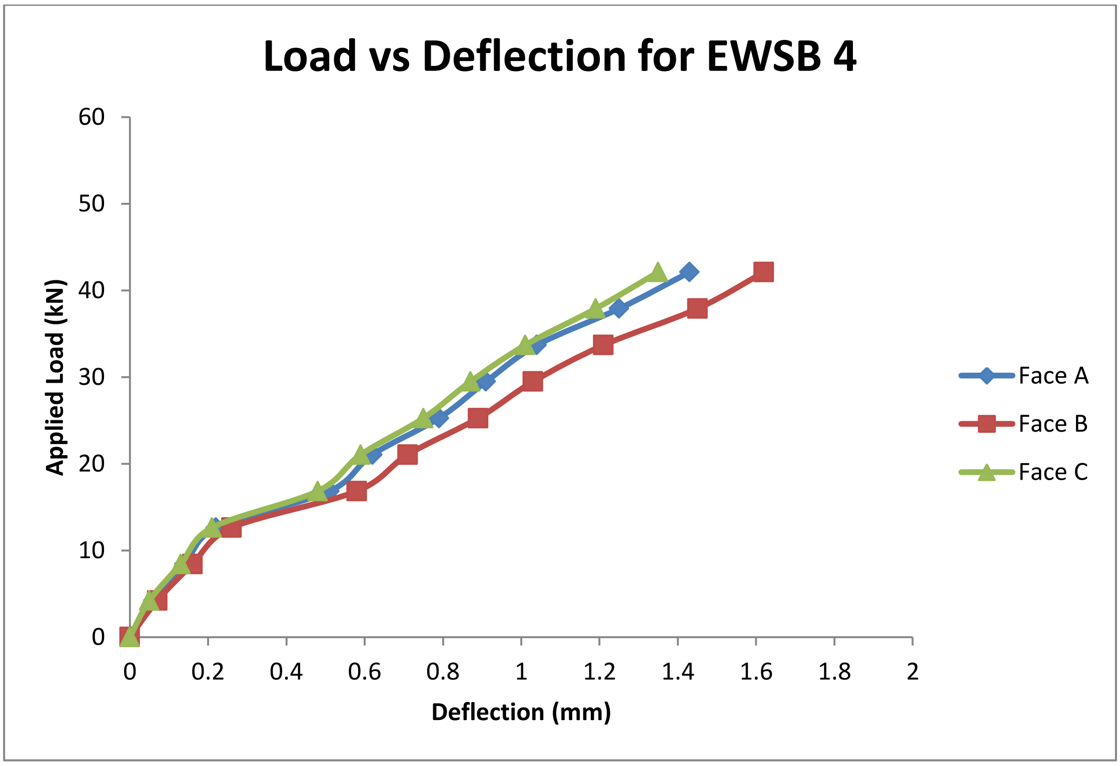

Figure 4.74 Load vs Deflection for EWSB 4

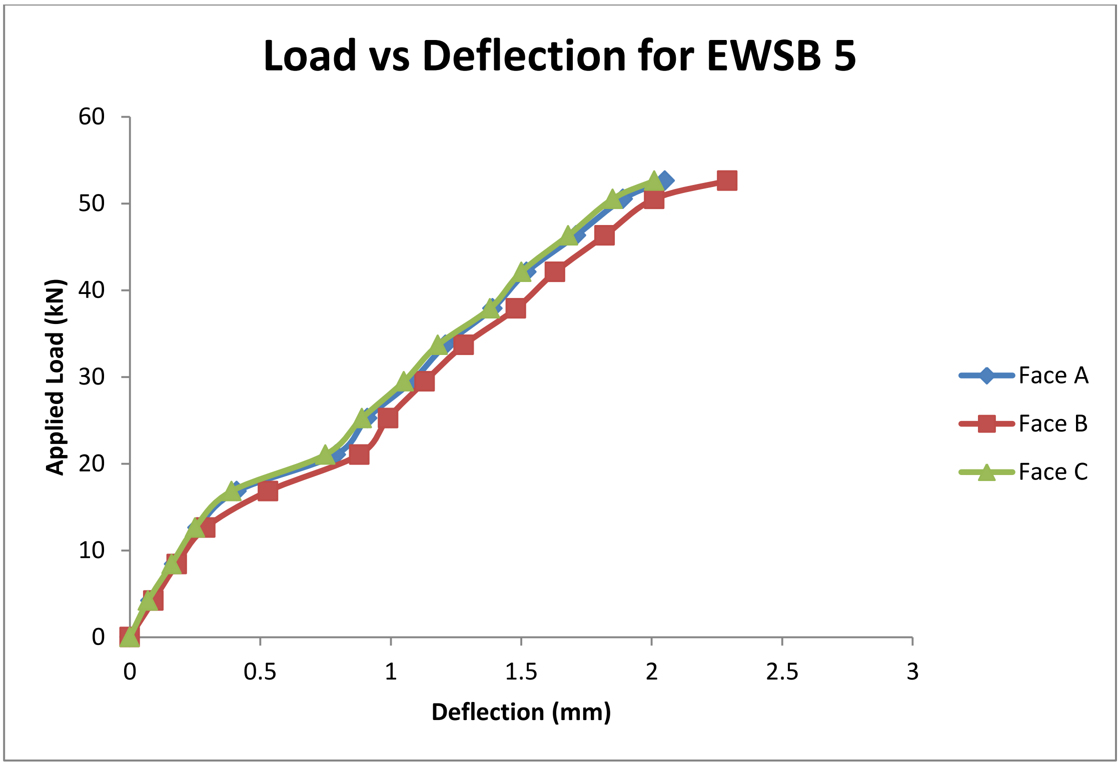

Figure 4.75 Load vs Deflection for EWSB 5

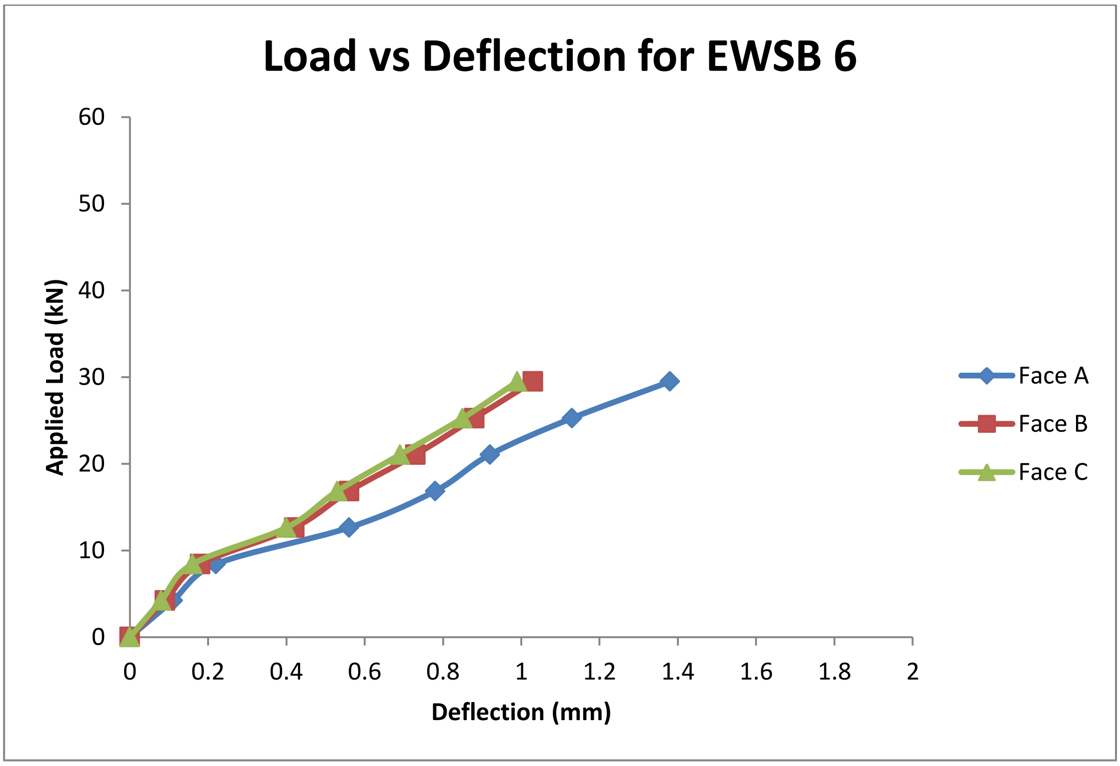

Figure 4.76 Load vs Deflection for EWSB 6

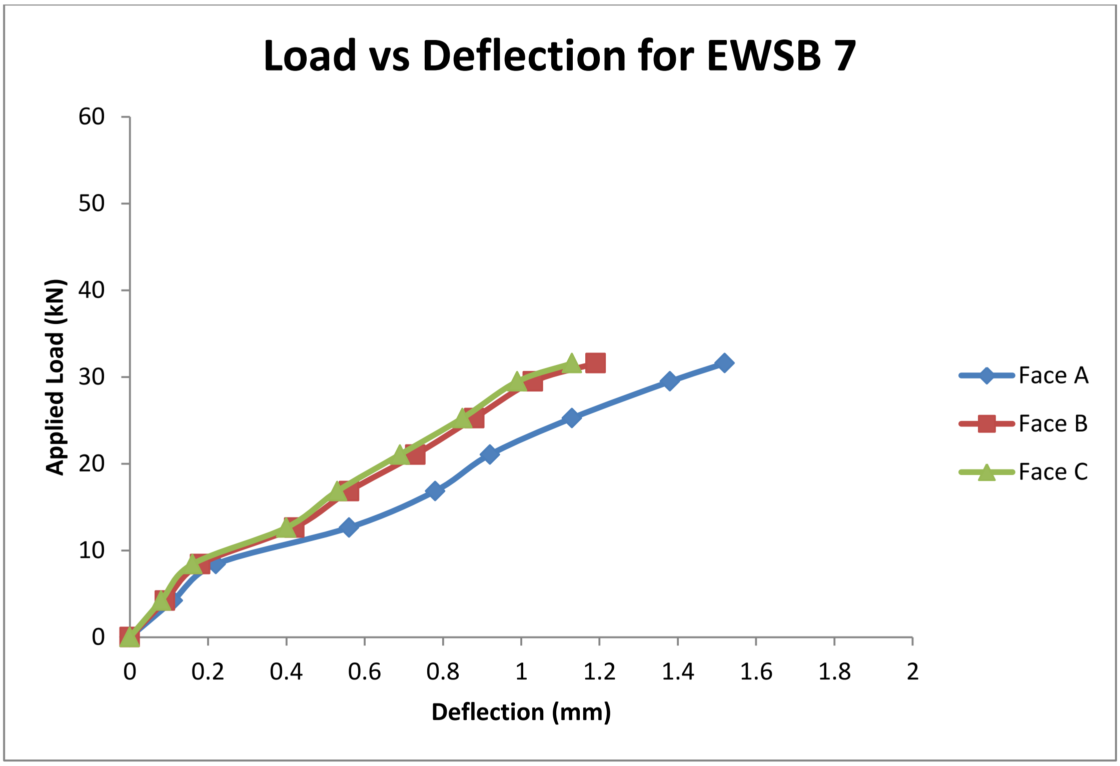

Figure 4.77 Load vs Deflection for EWSB 7

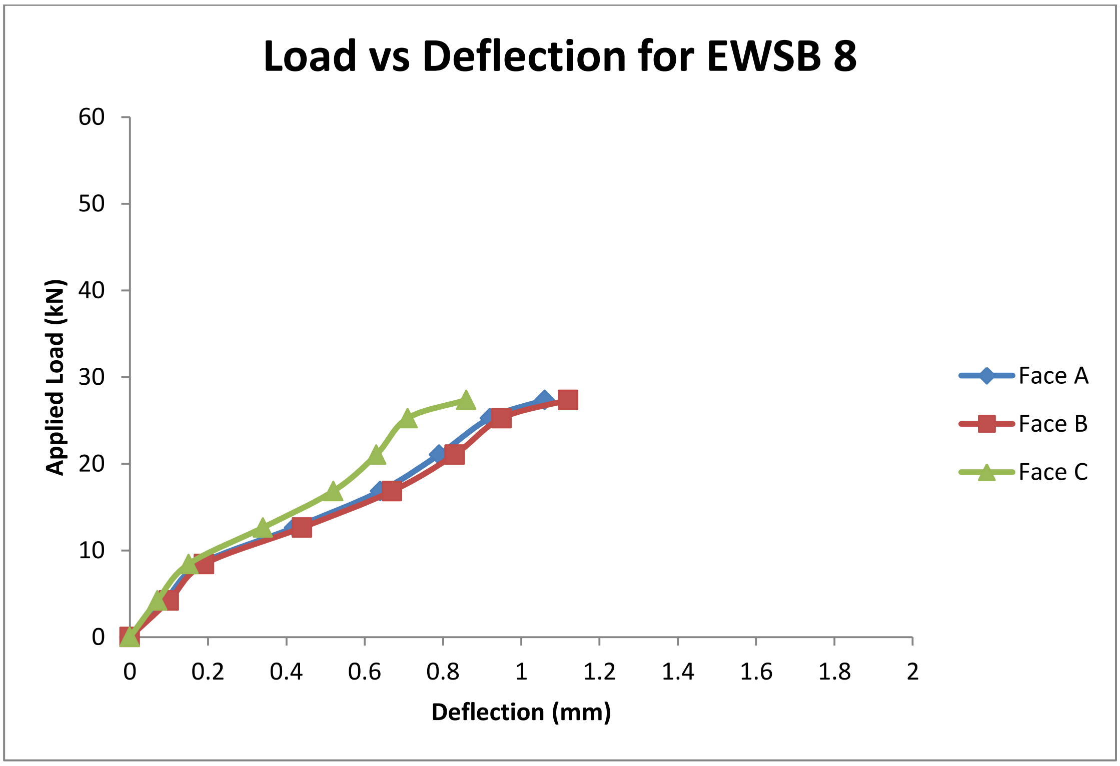

Figure 4.78 Load vs Deflection for EWSB 8

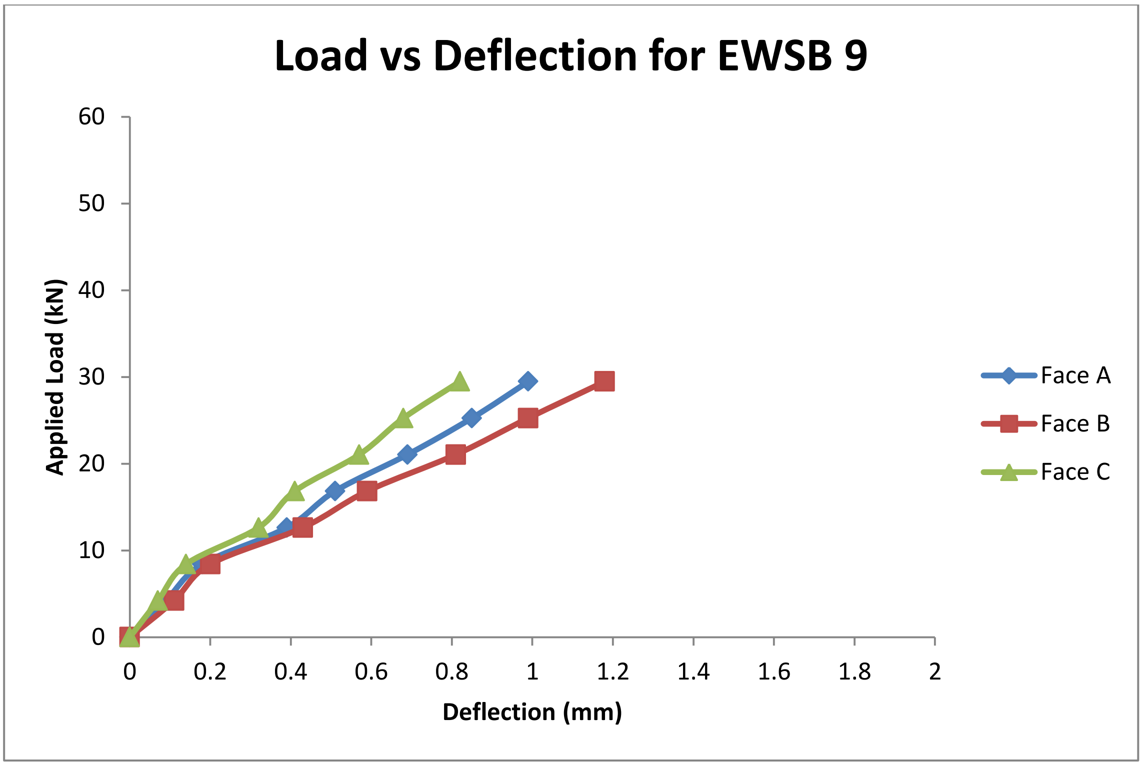

Figure 4.79 Load vs Deflection for EWSB 9

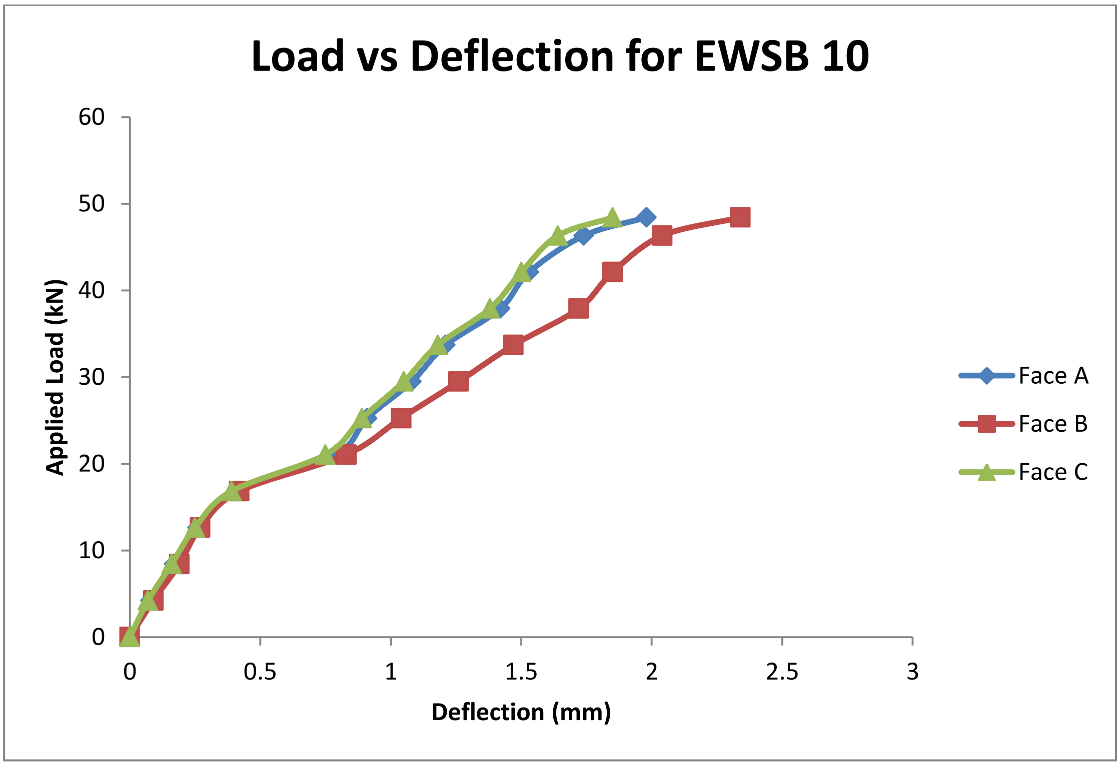

Figure 4.80 Load vs Deflection for EWSB 10

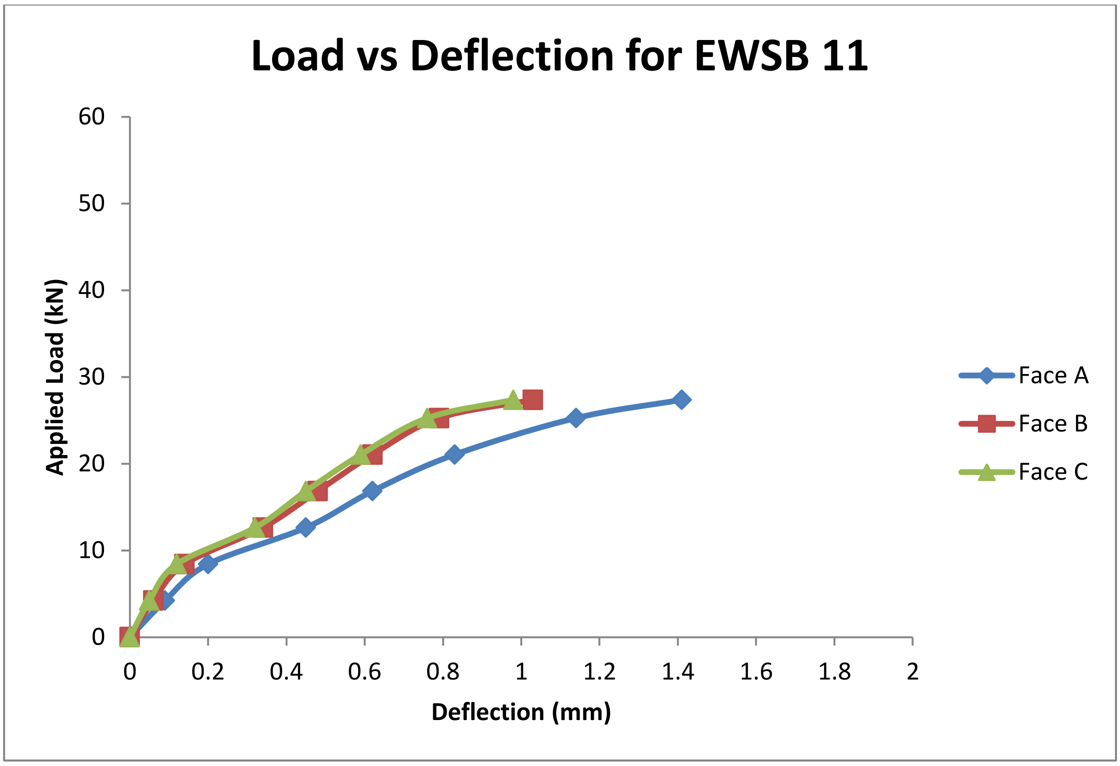

Figure 4.81 Load vs Deflection for EWSB 11

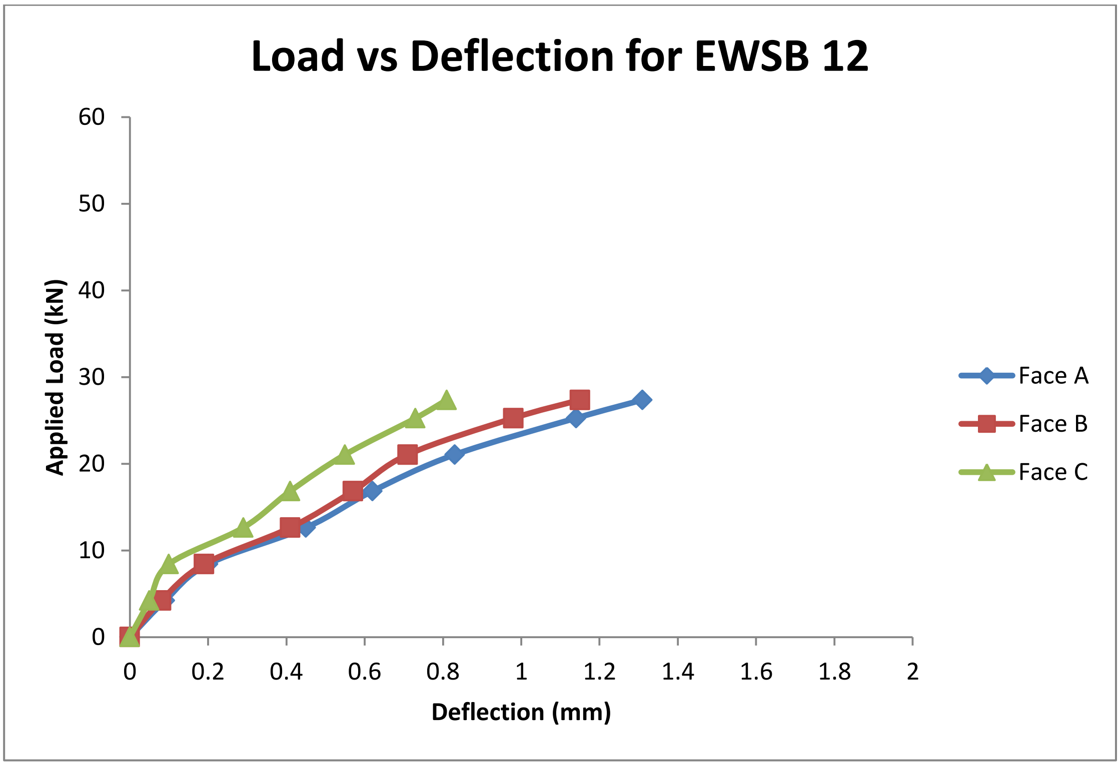

Figure 4.82 Load vs Deflection for EWSB 12

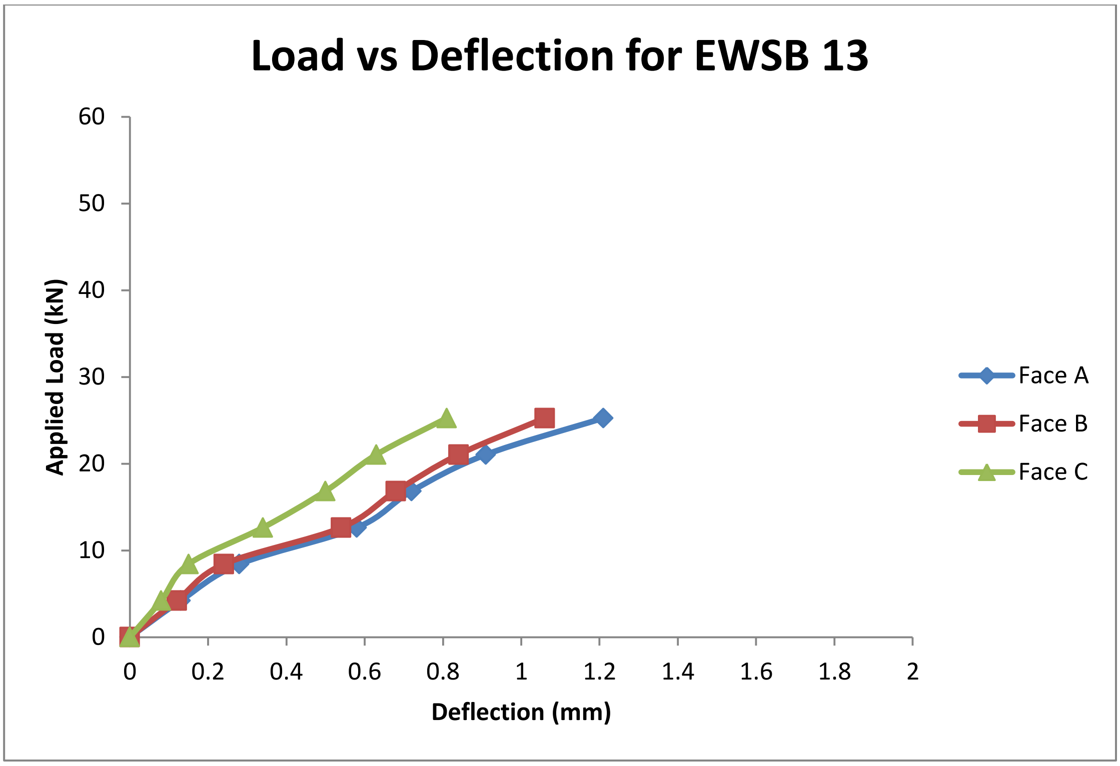

Figure 4.83 Load vs Deflection for EWSB 13

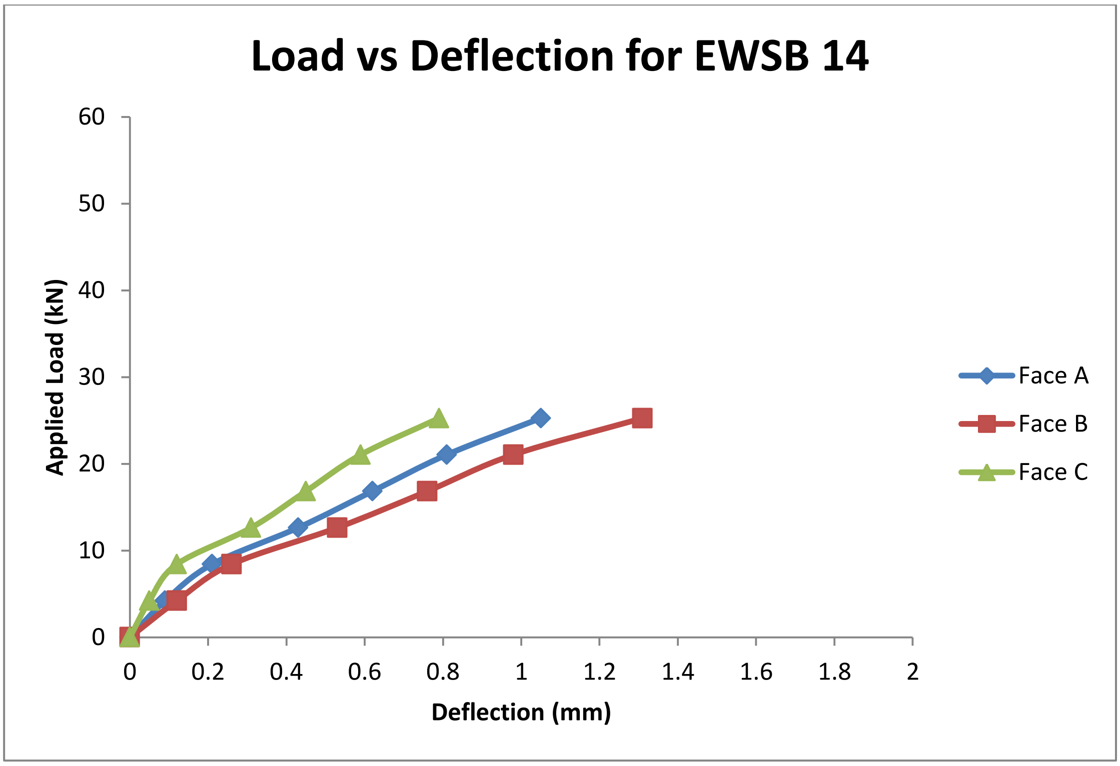

Figure 4.84 Load vs Deflection for EWSB 14

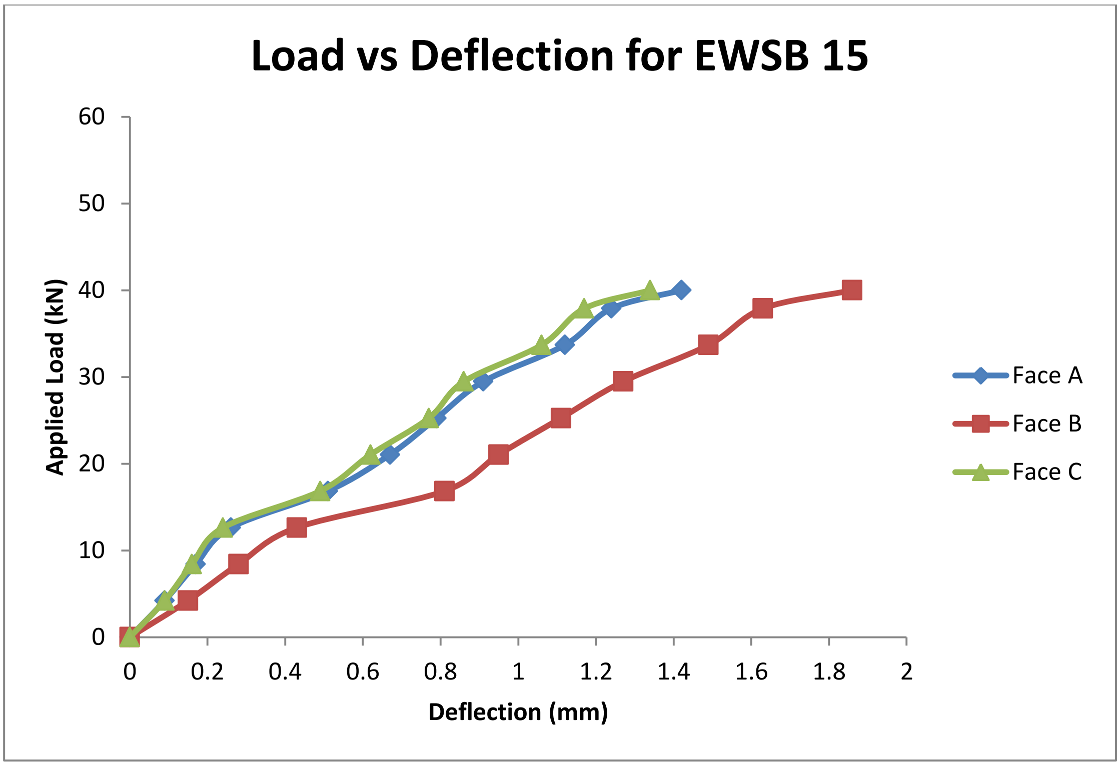

Figure 4.85 Load vs Deflection for EWSB 15

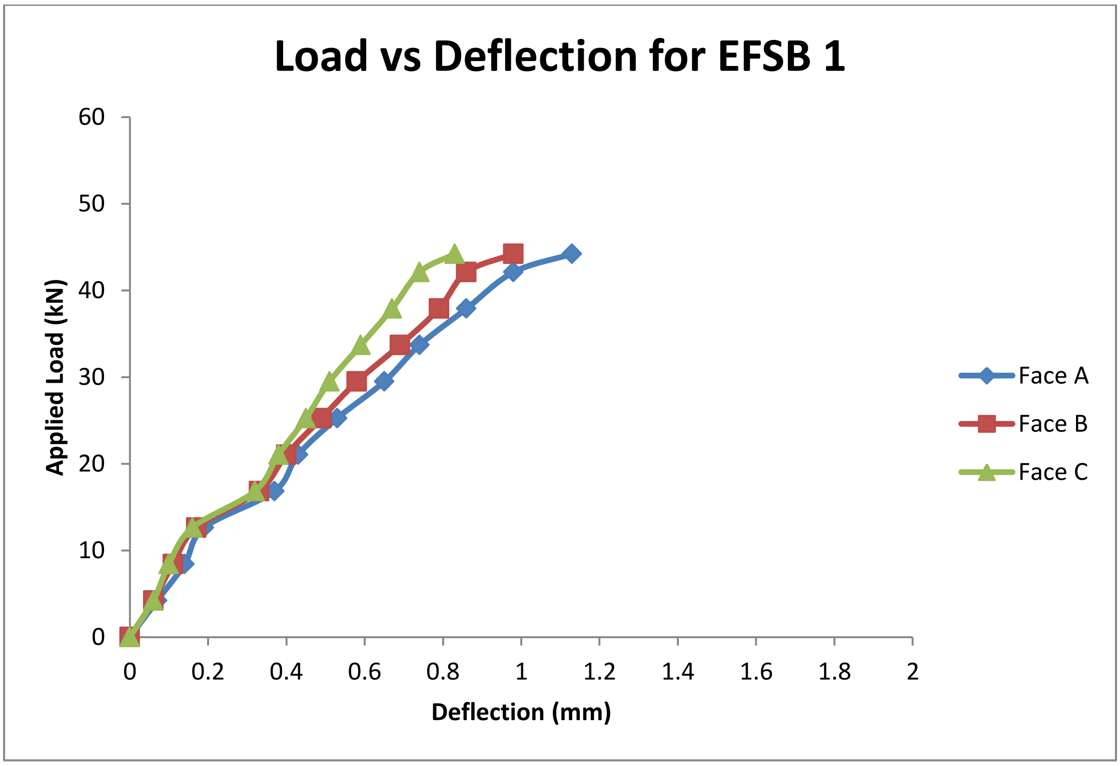

Figure 4.86 Load vs Deflection for EFSB 1

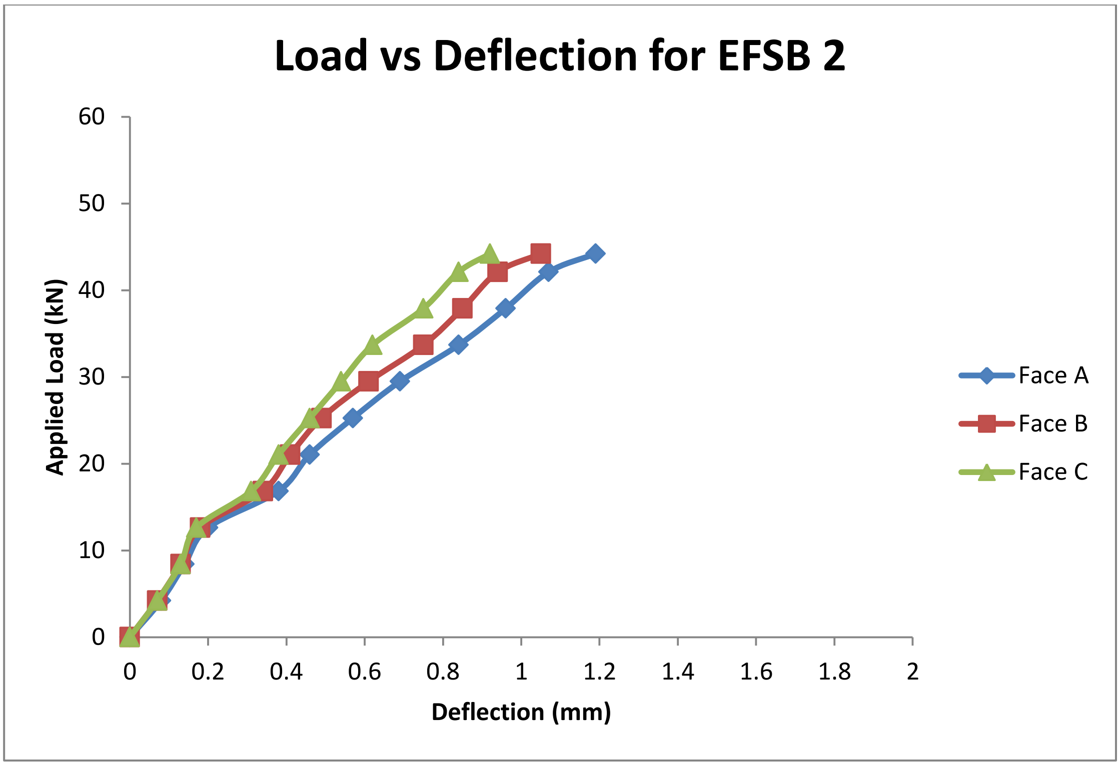

Figure 4.87 Load vs Deflection for EFSB 2

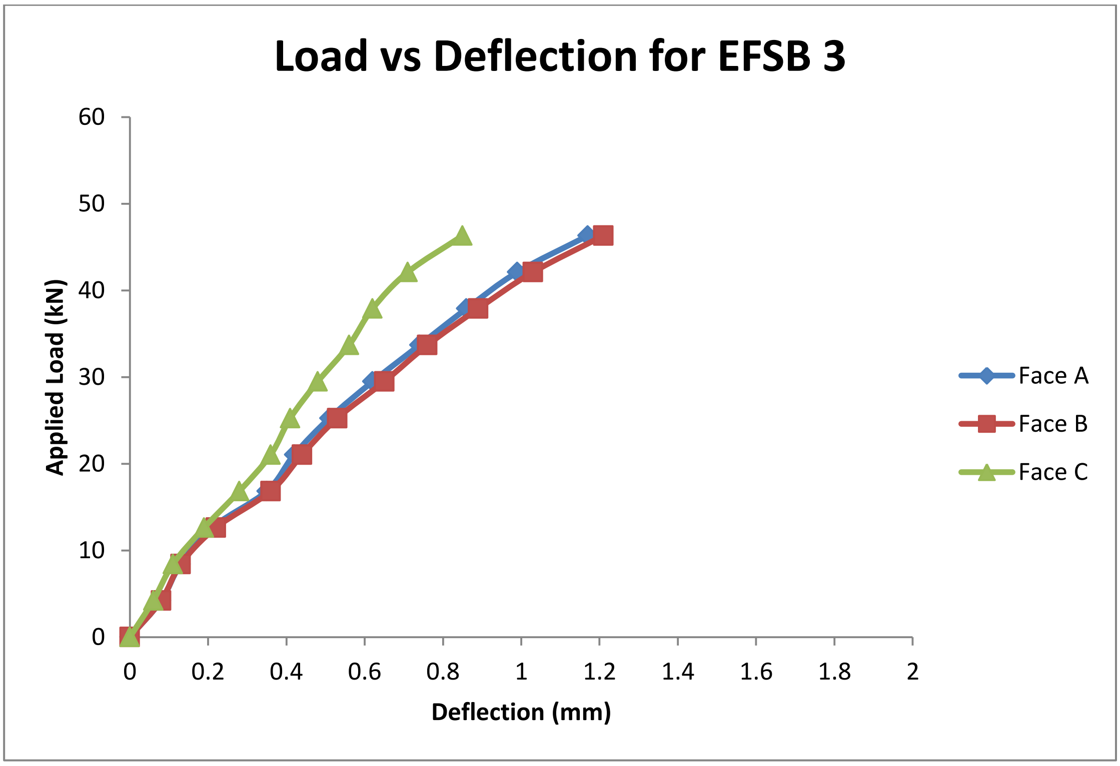

Figure 4.88 Load vs Deflection for EFSB 3

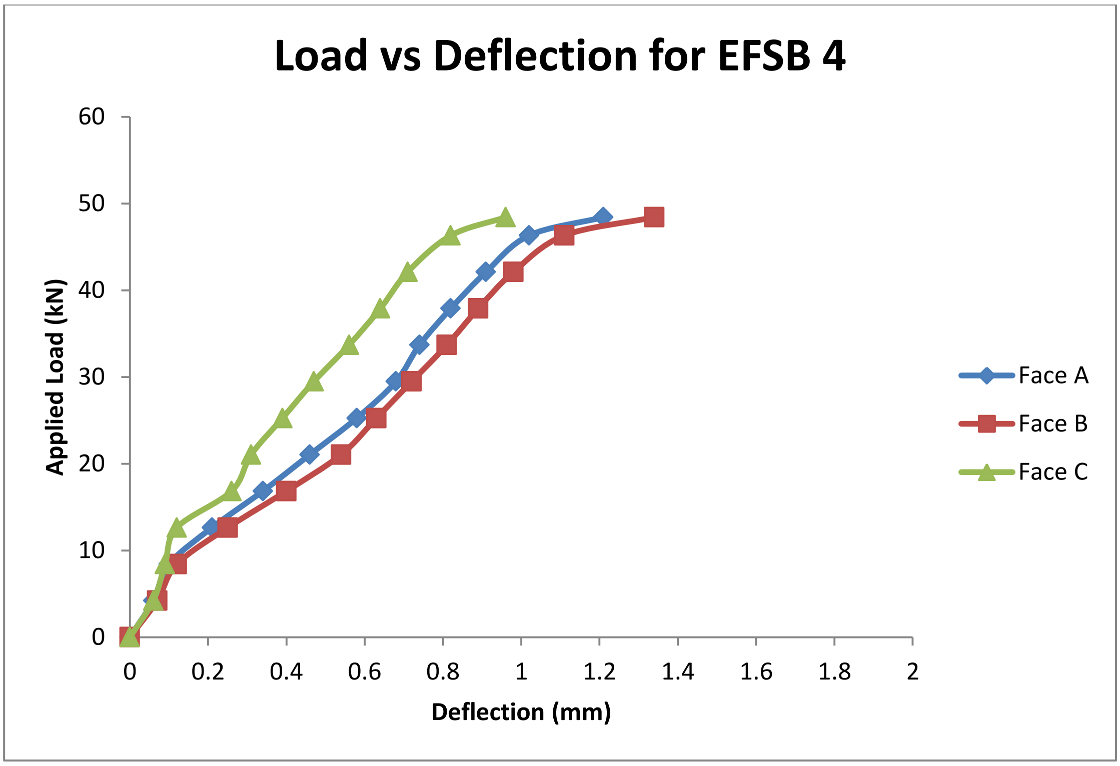

Figure 4.89 Load vs Deflection for EFSB 4

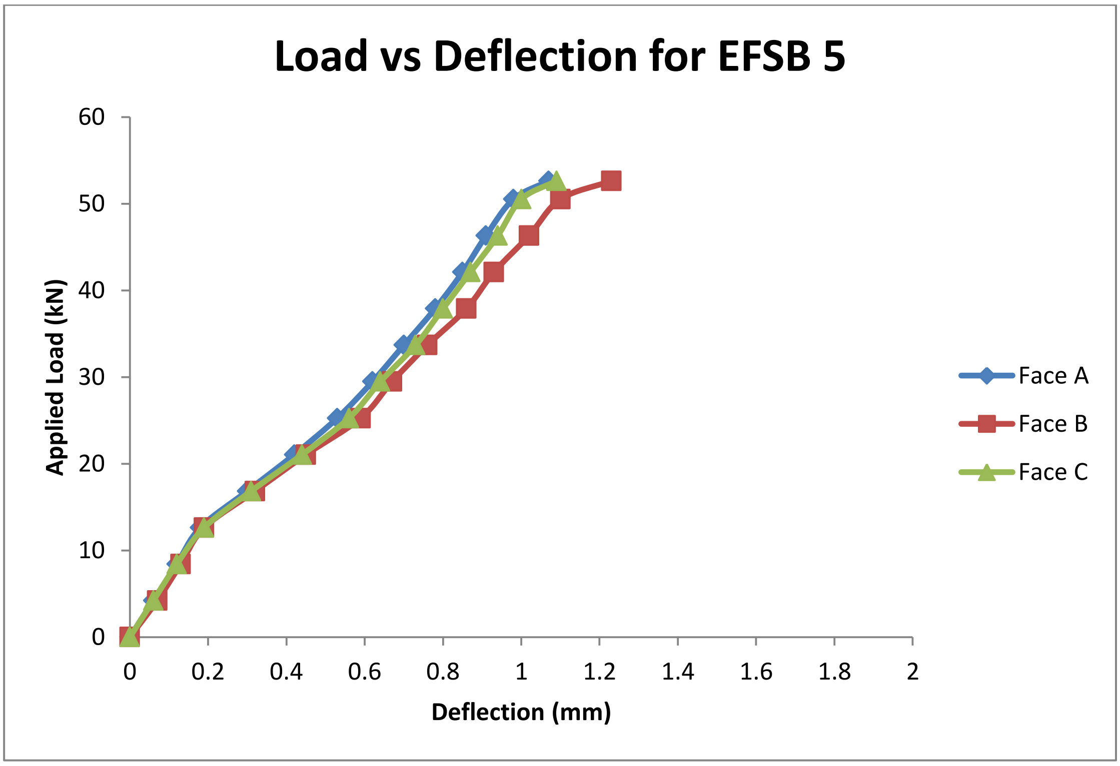

Figure 4.90 Load vs Deflection for EFSB 5

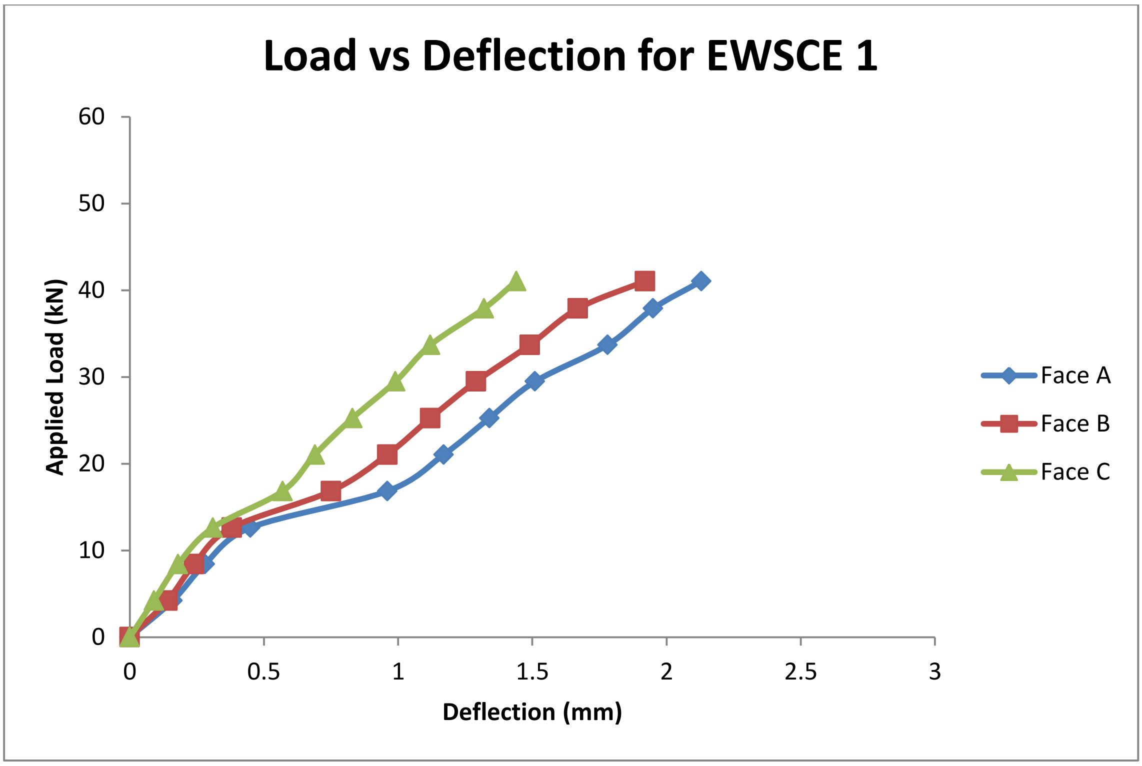

Figure 4.91 Load vs Deflection for EWSCE 1

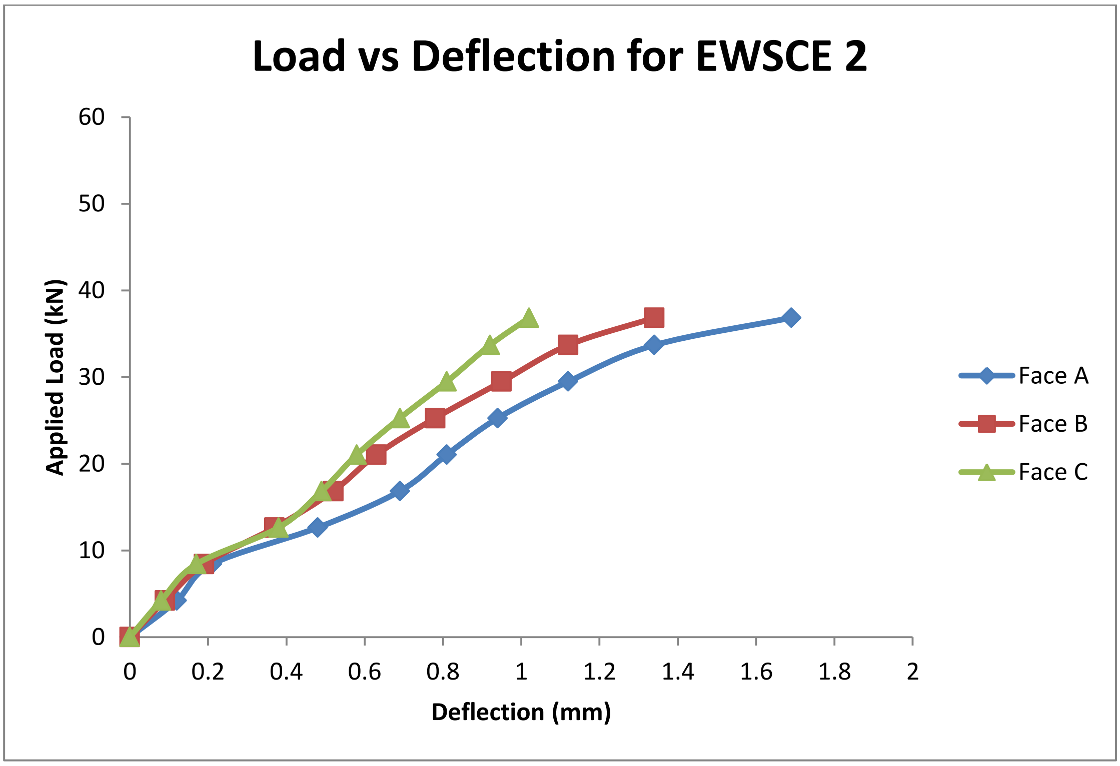

Figure 4.92 Load vs Deflection for EWSCE 2

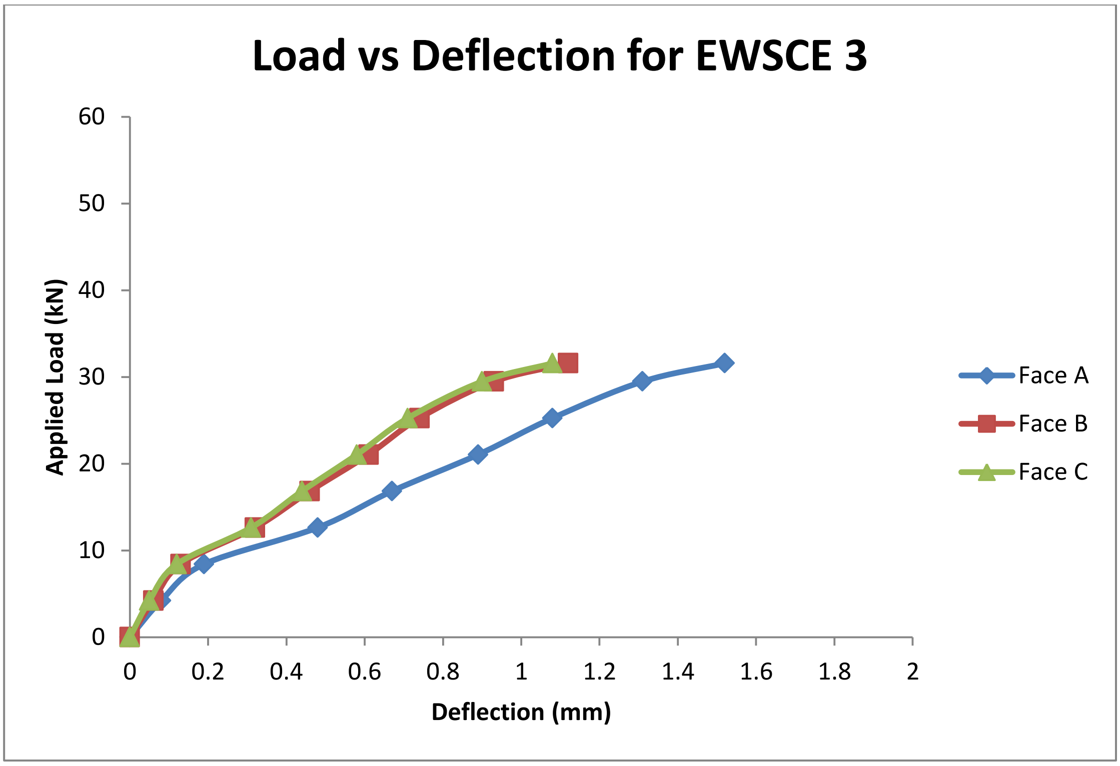

Figure 4.93 Load vs Deflection for EWSCE 3

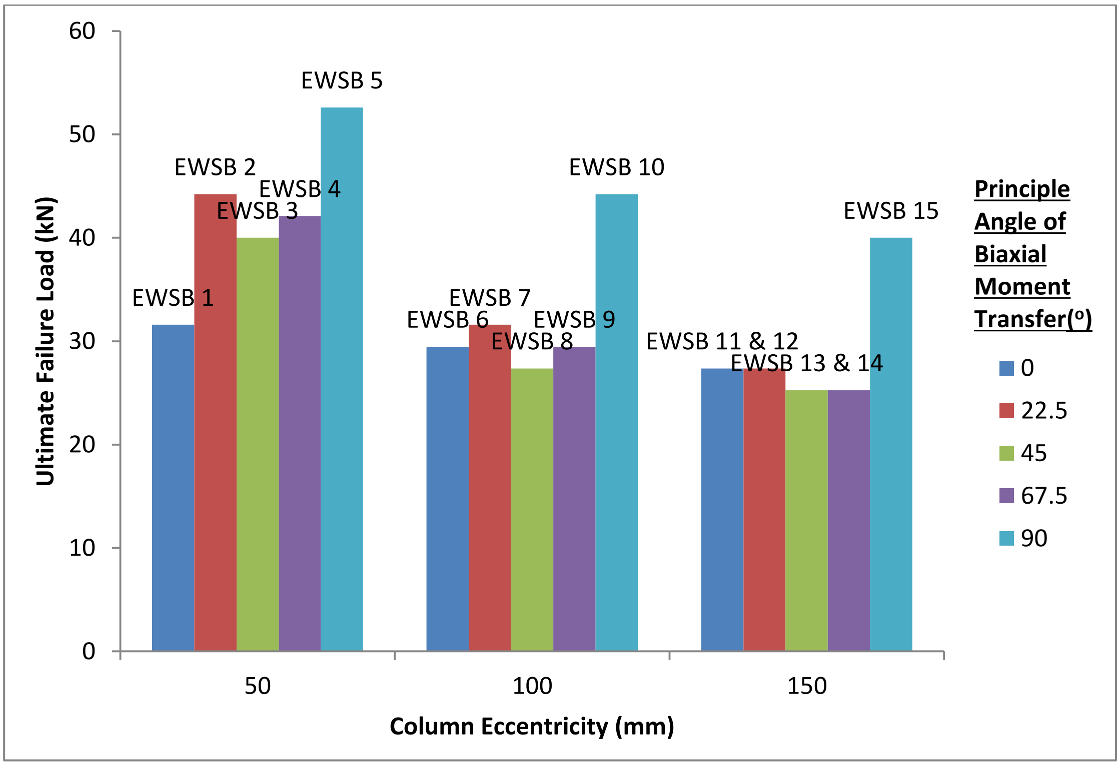

Figure 4.94 Effects of Principle Angle of Biaxial Moment on Punching Capacity

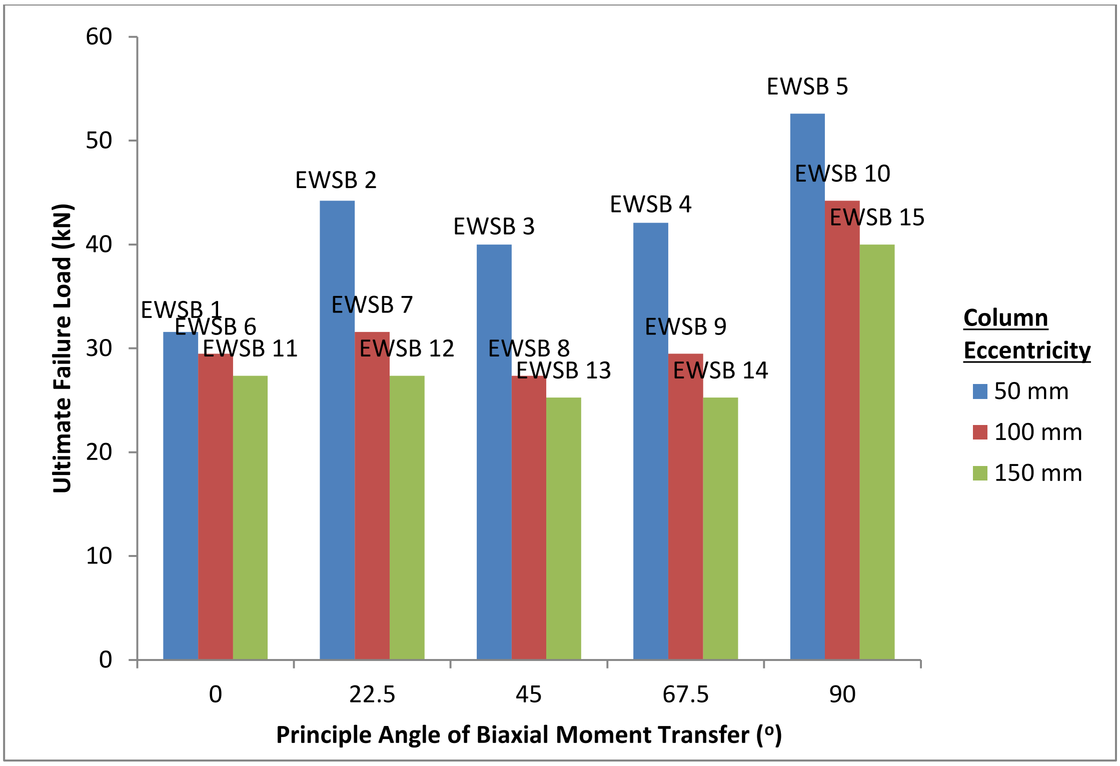

Figure 4.95 Effects of Column Eccentricity on Punching Capacity

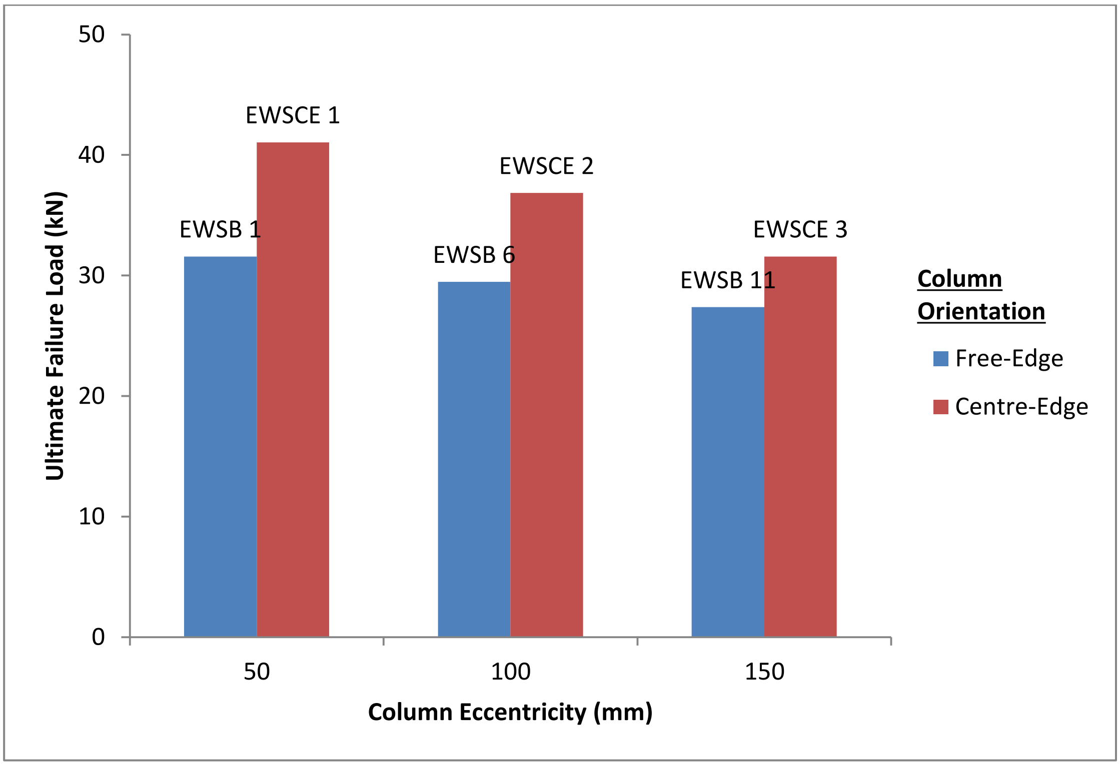

Figure 4.96 Effects of Column Location on Punching Capacity

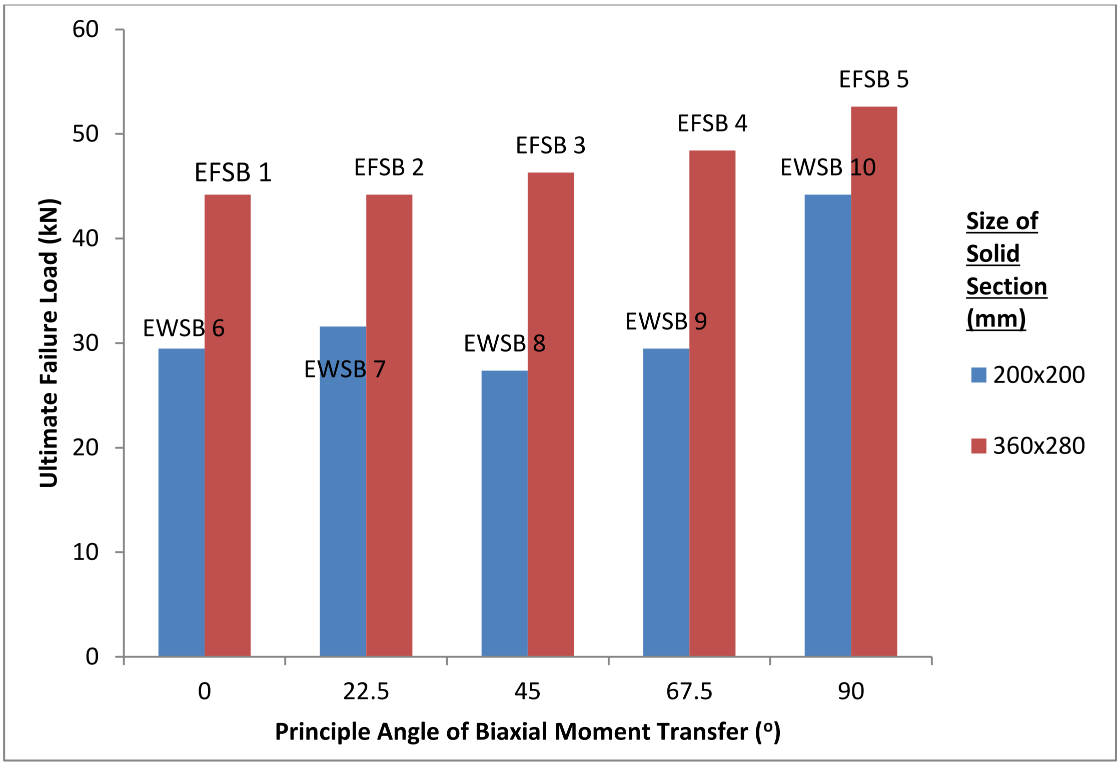

Figure 4.97 Effects of Solid Section on Punching Capacity

Chapter 5 Theoretical Models

5.1 Introduction

In chapter 4, observations made on the tested specimens and failure mechanisms were reported. In this chapter, three theoretical models are proposed to predict the punching capacities of observed; the concentric punching at internal column mechanism; the eccentric punching at internal column mechanism; and the edge punching mechanism.

The main focus in this research is to study the behaviour of waffle slabs in the presence of biaxial moment transfer with the solid of revolution extends into the waffle section causing:

(i) a reduction in the shear failure surface as well as the punching capacity; and

(ii) no reduction in the shear failure surface and the punching capacity.

The proposed theoretical models are extended from the upper bound plasticity approach for internal and edge punching shear mechanisms of flat solid slabs. This derivation is supported by the fact that plastic theory is based on the amount of shear strength per unit area, and hence it is able to take account of any sectional geometry changes, such as waffle sections, on the slab specimens. Therefore, these theoretical models calculate the total plastic work dissipated on the actual shear area of different failure mechanisms before equating to the external work done. The effectiveness factor, proposed by Al-Bayati[3,4], forms the basis of these models.

Both the internal and edge punching theoretical models are developed to account for any changes in the section details of the slabs (the waffle width and the top slab thickness) allowing these theoretical models applicable for both the flat slabs and the waffle slabs.

For the concentric punching at internal column mechanism, it is assumed that a complete solid revolution of concrete is formed within the slab at failure. For the eccentric punching at internal column mechanism, the size of the solid revolution of concrete formed within the slab ranges from a quarter to a complete revolution depending on the principle angle of biaxial moment transfer and the column eccentricity. Lastly, for the edge column punching mechanism, the solid revolution of concrete also varies in size similarly to that in the eccentric punching at internal column mechanism. In general, the shear failure surface is considered to be an inclined surface separating the solid of revolution from the remaining part of the slab.

As introduced by Boswell & Wong[11] in 1981, a shear retention factor '$\propto$', has to be included on specimens cast with micro-aggregate size (2 mm). This is further validated by Fong in 2015 that the shear resistance of micro-concrete specimens reduced from its peak to a residual value of about 70% of the peak value for specimens cast with 2 mm aggregates. Thus, this factor is adopted in these theoretical models as a shear retention factor of 0.70 for concrete specimens cast with 2 mm aggregates and 1.0 for concrete specimens cast with normal size aggregates.

5.2 Theoretical Model for Concentric Punching at Internal Column

5.2.1 Punching Failure Surface

This model is developed to predict the concentric punching capacity of flat slabs and waffle slabs in the absence of moment transfer at internal column. From experimental observation, the model predicts that, upon failure, a complete solid revolution of concrete is formed within the slab surrounding the column. The solid revolution of concrete is separated by inclined shear cracks at 21^{o} from the faces of the column, and intercepting the tension surface of the slab at a distance 2.6 times the height of the slab, as shown in Figure 5.1. By modifying Regan's approach[67] to predict the shear failure surface, the punching shear failure is defined as according to the plasticity approach as:

$$A_{IC} = h\sqrt{1 + (\cot\theta)^2}\left(2C_x + 2C_y + \pi h \cot\theta\right) \qquad \text{(Eq. 5.1)}$$

Where:

h = height of slab

θ = inclination angle of shear cracks

C = column size

In Regan's approach[67], the effective depth was used to calculate the punching shear failure surface whereas Braestrup et al.[12] argued that the height of the slab is a better indication to justify the shear failure surface in plasticity approach. Therefore, such changes were made to the original prediction.

The model allows accurate predictions for waffle slabs as the model considers any changes in the slab thickness that extend into the assumed solid of revolution which cause a reduction in the shear failure surface, and subsequently reduce the punching capacity of the slab. (see Figure 5.2). The reduction in punching capacity of the slab depends on the reduced shear surface area, which, in turn, depends on the size of waffle sections and top slabs' thickness. Therefore, two distinct outcomes were proposed based on the following geometries:

a. Reduction is applied to the shear failure surface when:
   - the solid of revolution extends into the waffle section and resulting losses in the shear failure surface (see Figure 5.2)

b. Reduction is not applied to the shear failure surface when:

- the solid of revolution extends into the waffle section but resulting no losses in the shear failure surface (see Figure 5.3)
- the size of solid section is wider than the solid of revolution (see Figure 5.4)

Having categorised the slab, the shear failure surface of the slab, A_{IC}, can be computed and subsequently the punching capacity can be determined. The predicted punching capacity, V_{IC}, is computed as follows:

$$V_{IC} = \propto w_i A_{IC} \quad \text{(Eq. 5.2)}$$

Where:

$\propto$ = shear retention factor, 0.7 for micro-concrete; and 1.0 for normal-concrete

w_i = sum of internal plastic work dissipated (see Eq. 2.19)

A_{IC} = the shear area, derived from Equation 5.1 or Appendix A.

5.2.2 Effectiveness Factor

The effective compressive strength f_c of concrete, used in the plasticity approach, can be obtained by modifying the cylindrical compressive strength, σ_c, obtained from experimental results, with an effectiveness factor, v, as shown below:

$$f_c = v\sigma_c \quad \text{(Eq. 5.3)}$$

By introducing the effectiveness factor, this allows to account the limited ductility of concrete and to accommodate any shortcomings of applying the plasticity theory to predict the concrete compressive strength. In the early days, Braestrup et al.[12] proposed that the effectiveness factor is a function of only concrete compressive strength, but was further proven by Salim & Sebastian[71] and Sigurdsson[72], to be better when the effectiveness factor is a function of concrete compressive strength, total height and the reinforcement ratio of the slab.

In 2015, Al-Bayati[3,4] then proposed to modify the Sigurdsson's effectiveness factor[70] by comparing with 93 flat slabs from previous researchers[4]. Based on Al-Bayati's findings, Sigurdsson's factors were found to be overestimating the punching strength when using Al-Bayati's proposed models. These discrepancies were believed to occur due to the difference in the inclination angles of the shear cracks used. In Salim & Sebastian's models, an angle ranging from 31 to 38^{o} were used, while in Ahmed's models, an angle of 21^{o} was used. This resulted in that higher shear strength would be required to couple with smaller failure surface in order to achieve good agreement with test results. Furthermore, Al-Bayati's modification on Sigurdsson's effectiveness factor also found to have better agreement (see section 5.2.3) with author's test results. The modified effectiveness factor from Al-Bayati's works is shown as:

$$v = \frac{0.9}{\sqrt{\sigma_c}}\left(0.7 + \frac{0.5}{\sqrt{h}}\right)(1 + 0.14\rho) \qquad \text{(Eq. 5.4)}$$

Where:

σ_c = cylindrical compressive strength

h = height of slab

ρ = reinforcement ratio

5.2.3 Comparisons with Results

The comparisons between the model's predictions and the historical tests results for flat slabs and the author's waffle slab tests are presented in Table 5.1 to Table 5.7. Summarising these comparisons (with 88 tests[7,20,49,53,77,82]) which comprising of solid slabs with normal strength concrete, solid slabs with high strength concrete, and waffle slabs, a mean ratio of test failure loads to predicted failure loads of 1.00, and a standard deviation of 0.15, has been achieved. (see Table 5.8)

In view of the micro-concrete behaviour in shear and in cube compression tests, both the shear retention factor, $\propto$, and the concrete cube size effect have been taken into account when comparing with test results in Table 5.7.

Based on these findings, it can be inferred that the proposed model by Al-Bayati[3,4] provided more realistic punching strength estimations than that of Salim & Sebastian[71]. The modified Sigurdsson's effectiveness factor[72] (see Eq. 5.4) is compatible to the modified Regan's shear surface area, and therefore, will be used as a basis to form the eccentric punching at internal column and edge punching shear theoretical model proposed by author (see Section 5.3 and Section 5.4).

5.3 Theoretical Model for Eccentric Punching at Internal Column

5.3.1 Introduction

This model is developed to predict the eccentric punching capacity of flat slabs and waffle slabs in the presence of moment transfer at internal column. Similar to concentric punching model, eccentric model allows accurate predictions for waffle slabs. The eccentric punching model assumes that any section thickness changes that extend into the solid revolution of concrete incur a reduction on the shear surface area (see Figure 5.2), and subsequently reduce the ultimate punching capacity. Therefore, two distinct outcomes were proposed based on the following geometries:

a. Reduction is applied to the shear failure surface when:
   - the solid of revolution extends into the waffle section and resulting losses in the shear failure surface (see Figure 5.2)

b. Reduction is not applied to the shear failure surface when:

- the solid of revolution extends into the waffle section but resulting no losses in the shear failure surface (see Figure 5.3)
- the size of solid section is wider than the solid of revolution or similarly to solid flat slabs (see Figure 5.4)

However, unlike the concentric punching model, the observed eccentric punching failure surface was found to be dependent on the reductions in shear failure surface deriving from the effects of the principle angle of biaxial moment transfer (see Figure 4.10) and the column eccentricity (see Figure 4.9). As reported in Section 4.2.2.5.2, the observed punching failure surface was found to be dependent on the applied column eccentricity. The observed punching failure surface (at the back face of the column) was observed to decrease as the applied eccentricity increased. This phenomenon was found to be consistent with the increase in the principle angle of biaxial moment transfer (zero at orthogonal of both axis) (see Section 4.2.2.5.1). From the information above, it was evident that there is an opening at the back face of the column prompting the decrease in observed punching failure surface in the presence of column eccentricity and principle angle of biaxial moment transfer.

In order to replicate this mechanism, an angle opening, δ, is introduced to simulate the reduction observed in the effective shear area on the failure surface of revolution at the back face of the column, as shown in Figure 5.7, and explained in Section 5.3.2 and Section 5.3.3.

5.3.2 Moment Transfer Mechanism

From the observed punching shear failure surface, the total moment transfer and torsion are factors to be considered in estimating the eccentric punching capacity. As explained by M.P.

Nielsen[57], when moving the force from a con-centrical position to an eccentrical position, the loaded area is moved and reduced (see Figure 5.6). This reduction is mainly due to shorter control perimeter. The reduction is not significant in cases with small eccentricities but becomes significant as the eccentricities increase. From observations, the failure surface along lightly loaded side of the column, as shown in Figure 5.6, would be rather steep and thus, reducing the punching failure surface.

In order to replicate the observed punching failure surface, this model applies an opening angle in relation to the linear distribution of shear stress introduced by DiStasio & Van Buren's[17] (see Chapter 2). This method is widely appreciated and has been implemented by the ACI codes[1]. DiStasio & Van Buren proposed that the critical section be taken as $h/2$ from the face of the column and that the total height of the slab is used in calculations of A_C and J_C, leading us to the equation:

For front face of the column:

$$v_{AB} = \frac{V_U}{A_C} + \frac{(M_U - M_f)c_{AB}}{J_C} \quad \text{(Eq. 5.5)}$$

For back face of the column:

$$v_{CD} = \frac{V_U}{A_C} + \frac{(M_U - M_f)c_{CD}}{J_C} \quad \text{(Eq. 5.6)}$$

Where:

V_U = the applied load

$A_C = 2(b_x + b_y)h$

M_U = the applied moment

M_f = flexural capacity of front face and back face of column

c_{AB}, c_{CD} = distance from column centroid to the critical perimeter (see Eq. 5.8 – Eq. 5.10)

$$J_C = 2\left(\frac{b_x h^3}{12}\right) + 2\left(\frac{h {b_x}^3}{12}\right) + 2b_x h\left(\frac{b_y}{2}\right)^2$$

5.3.2.1 Flexural Capacities, M_f

The slab flexural capacities are based on the plasticity equation acting on a beam with rectangular cross section stressed to pure bending. The total flexural resistance of the connection, M_f, is the sum of the flexural capacities developed at the front face and back face to the column, M_{ft} and M_{fc}, respectively:

$$M_f = M_{ft} + M_{fc} \qquad \text{(Eq. 5.7)}$$

Where:

$$M_{ft} = \left(1 - \frac{\Phi}{2}\right)\Phi \mathrm{b}_1 {d_1}^2 f_{cb}$$

$$M_{fc} = \left(1 - \frac{\Phi}{2}\right)\Phi \mathrm{b}_2 {d_2}^2 f_{cb}$$

Φ degree of reinforcement, $\Phi = \frac{A_s}{bd} * \frac{f_y}{f_{cb}}$

f_{cb} plastic concrete compressive strength in bending, $f_{cb} = v_b \sigma_c$

v_b effectiveness factor for concrete in bending,

$$v_b = 0.97 - \frac{f_y}{5000} - \frac{f_{cb}}{300} \qquad \text{if } f_y < 900 \text{ MPa}, f_{cb} < 60 \text{ MPa}$$

$\mathrm{b}_1, \mathrm{b}_2$ effective bending width of the connection at front and back faces of the column, respectively, $\mathrm{b} = C_x + d$

d_1, d_2 effective depth of the connection at front and back faces of the column, respectively

As reported by Hawkins et al.[33], in cases when the reinforcement was not concentrated in the column region, tensile strains only extended to a distance of about one slab thickness from the column faces, before these strains become compressive between the location and the slab edge. (see Figure 5.10). By noting the similarities in the arrangement of steel reinforcement and the moment transfer mechanism between the slab specimens tested by the author and those reported in the previous research, the effective bending width, $(\mathrm{C} + d)$, is proposed in this eccentric punching theoretical model.

5.3.2.2 Distance c_{AB}, c_{CD}

For an interior punching shear perimeter, the centroid of shear perimeter is always half the distance of the effective breadth of the critical section perimeter[17]. (see Figure 5.11)

$$c_{AB(0)} = \frac{b_x}{2} \quad \text{(Eq. 5.8a)}$$

$$c_{CD(0)} = \frac{b_x}{2} \quad \text{(Eq. 5.8b)}$$

When the principle angle of biaxial moment transfer is 22.5°, (see Figure 5.13)

$$c_{AB(22.5)}, c_{CD(22.5)} = \frac{c_{AB(0)}}{cos(22.5°)} \quad \text{(Eq. 5.9)}$$

When the principle angle of biaxial moment transfer is 45°, (see Figure 5.15)

$$c_{AB(45)}, c_{CD(45)} = \frac{c_{AB(0)}}{cos(45°)} \quad \text{(Eq. 5.10)}$$

5.3.3 Opening angle, δ

As mentioned above in Section 5.3.1, in the presence of column eccentricity and varying principle angles, an opening on the shear failure surface was observed at the back face of the column (see Figure 5.7, 5.8 and 5.9). As a result, a smaller shear surface was formed thus a lower punching capacity was mobilised. Such mechanism will be modelled in the calculation using the angle opening factor, δ.

The total punching shear strength is the sum of the shear strengths on opposite ends (front and back) of the column that corresponds to the top and bottom reinforcement, respectively. In deriving the opening angle factor, δ, a ratio of the shear strength on the front face with respect to the total shear strength is proposed to simulate the opening angle at the back face of them column.

Ratio to calculate the opening angle:

$$\frac{v_{AB}}{v_{AB}+v_{CD}} = \frac{\frac{V_U}{A_C}+\frac{(M_U-M_f)c_{AB}}{J_C}}{\frac{2V_U}{A_C}+\frac{(M_U-M_f)(c_{AB}-c_{CD})}{J_C}}$$

$$\frac{v_{AB}}{v_{AB}+v_{CD}} = \frac{V_U J_C+(M_U-M_f)c_{AB}A_C}{2V_U J_C+(M_U-M_f)(c_{AB}-c_{CD})} \qquad \text{(Eq. 5.11)}$$

After obtaining the maximum shear stress values at the front face of the column and at the back face of the column, shear stress distribution were sketched based on the findings from the experiment observations along with DiStasio and Buren's theory[17]. The shear stress distribution diagrams were found to vary as the principle angles of biaxial moment transfer differed. (see the effect of the principle angle of biaxial moment transfer when set at 0°, 22.5° and 45°, as shown in Figure 5.12, Figure 5.14 and Figure 5.16, respectively)

A further reduction of 0.5 is applied to this ratio to enable the prediction for concentric punching at internal column mechanism, converting the ratio to the actual opening angle observed in the slabs.

$$Opening\ angle, \delta = 87.682 * \left(\frac{v_{AB}}{v_{AB}+v_{CD}} - 0.5\right)^{0.5056} \qquad \text{(Eq. 5.12)}$$

5.3.4 Punching Failure Surface

As explained in the Section 5.3.2, the model predicts that, upon failure, the size of solid revolution of concrete formed within the slab surrounding the column is dependent on the ratio of concrete shear strength at the front of the column to the sum of concrete shear strength at both the front and the back of the column. The shear cracks at the front face of the column propagates at 21^{o} inclination through slab thickness and intercepting the tension surface of the slab at a distance 2.6 times the height of the slab as shown in Figure 5.1. However, the shear surfaces at the adjacent faces and back face of the column separated by inclined shear cracks inclined at various angles due to the different sizes of solid revolution (see Chapter 4) formed within the slab. Upon computing the opening angle at the back face of the column, the effective punching failure surface of revolution, A_{IE}, can be derived from the following:

(i) When the principle angle of moment transfer is 0^{0}, (see Figure 5.7)

$$A_{IE(0)} = h\sqrt{1 + (\cot\theta)^2}\left[2C_x + C_y + \frac{3\pi h \cot\theta}{4} + \gamma * \left(C_y + \frac{\pi h \cot\theta}{4}\right)\right] \qquad \text{(Eq. 5.13)}$$

Where:

h = height of slab

θ = inclination angle of shear cracks

C_x = column size parallel to the column eccentricity

C_y = column size perpendicular to the column eccentricity

γ = ratio of angle opening = $\frac{45°-\delta}{45°}$, where $0° < \delta \leq 125°$ (anything more than $125°$, use $125°$)

e.g.: if $\delta = 0°$, then $\gamma = 1$

if $\delta = 125°$, then $\gamma = -1.778$

δ = angle opening

(ii) When the principle angle of moment transfer is 22.5°, (see Figure 5.8)

$$A_{IE(22.5)} = h\sqrt{1+(\cot\theta)^2}\left[1.92C_x + 1.08C_y + \frac{3\pi h\cot\theta}{4} + \gamma * \left(0.08C_x + 0.92C_y + \frac{\pi h\cot\theta}{4}\right)\right]$$

(Eq. 5.14)

(iii) When the principle angle of moment transfer is 45°, (see Figure 5.9)

$$A_{IE(45)} = h\sqrt{1+(\cot\theta)^2}\left[\frac{3C_x}{2} + \frac{3C_y}{2} + \frac{3\pi h\cot\theta}{4} + \gamma * \left(\frac{C_x}{2} + \frac{C_y}{2} + \frac{\pi h\cot\theta}{4}\right)\right]$$ (Eq. 5.15)

Having categorised the slab, the shear failure surface of the slab, A_{IE}, can be computed and subsequently the punching capacity can be determined. The predicted punching capacity, V_{IE}, is computed as follows:

$$V_{IE} = \propto w_i A_{IE}$$ (Eq. 5.16)

Where:

$\propto$ = shear retention factor, 0.7 for micro-concrete; and 1.0 for normal-concrete

w_i = sum of internal plastic work dissipated (see Eq. 2.19)

A_{IE} = the shear area, derived from Eq. 5.13 – Eq. 5.15 or Appendix B.

5.3.5 Comparisons with test results

The comparisons between the eccentric punching theoretical model's predictions and the test results of other researchers for solid flat slabs[18,19,26,27,35,44,50,53,59] and of the Author's test results for waffle slabs are presented from Table 5.9 to Table 5.15.

As mentioned earlier, the model predicts the solid flat slabs' punching capacity by assuming there is no losses in punching shear failure surface while the model predicts that the waffle slabs' punching capacities by accommodating the losses in punching shear failure surface when the solid revolution extends into the waffle section, otherwise similar to solid flat slabs.

By applying the theoretical model on the Author's test specimens, opening angles for different waffle slab specimens were sketched and shown in Figure 5.17 to Figure 5.19. These sketches were found to be almost identical to the experimental observations, where, reductions in punching failure surfaces and punching strength were observed when the principle angles of biaxial moment transfer and the column eccentricity increased.

Comparisons with 56 test results comprising of both solid and waffle of slabs (see Table 5.16), with or without moment transfer, the total mean ratio of test failure loads to predicted failure loads was 0.98, with a standard deviation of 0.14. (see Figure 5.20)

5.4 Theoretical Model for Edge Punching

5.4.1 Introduction

This model is developed to predict the edge punching capacity of flat slabs and waffle slabs in the presence of moment transfer. Similar to the previous two models for internal column punching, this edge punching model also allows for accurate predictions for punching on waffle slabs. The edge punching model assumes that any section thickness changes that extend into the solid revolution of concrete incur a reduction on the shear surface area (see Figure 5.21), and subsequently reduce the ultimate punching capacity. Therefore, two distinct outcomes were proposed based on the following geometries:

a. Reduction is applied to the shear failure surface when:
   - the solid of revolution extends into the waffle section and resulting with losses in the shear failure surface (see Figure 5.22)

b. Reduction is not applied to the shear failure surface when:
   - the solid of revolution extends into the waffle section but resulting with no losses in the shear failure surface (see Figure 5.23)
   - the size of solid section is wider than the solid of revolution (see Figure 5.24)

Similar to the eccentric punching at internal column model, the size of the edge punching failure surface was observed to be dependent on the change in the column eccentricity (see Figure 4.47) and the change in the principle angle of moment transfer (see Figure 4.48). The observed punching failure surface (at the back face of the column) was found to decrease as the load eccentricity increased (see Section 4.3.5.1) and as the principle angle of moment transfer reduces (from perpendicular to parallel to the slab edge). Furthermore, the edge punching model predicts that there will be an opening or reduction on the shear failure surface at the back face of the column in the presence of load eccentricity. However, this opening and its associating reduction caused on the shear surface area was observed to reduce as the principle angle increased (see Figure 4.48)

Similar to the eccentric punching at internal column model, an opening angle factor, δ, is introduced to simulate the reduction observed on the failure surface at the back face of the column as shown in Figure 5.25. Basis and derivations of this factor will be explained in detail in Section 5.4.2 and Section 5.4.3.

5.4.2 Moment Transfer Mechanism

Similar to the eccentric punching at internal column model, the edge model derives the opening angle on the basis of DiStasio and Van Buren's works[17] in relation to the linear distribution of shear stress (see Chapter 2). DiStasio and Van Buren assumed that when the unbalanced moment exceeds the flexural capacity of the connection, the unbalanced moment would be transformed into unbalanced shear stresses. These unbalanced shear stresses are then combined with the induced vertical load, and the resultant stresses are distributed linearly with respect to the centroid of the critical section.

5.4.2.1 Flexural Capacities, M_f

The slab flexural capacities are based on the plasticity equation acting on a beam with rectangular cross section stressed to pure bending. The total flexural resistance of the connection, M_f, is the sum of the flexural capacities developed at the front face and back face to the column, M_{ft} and M_{fc}, respectively:

$$M_f = M_{ft} + M_{fc} \qquad \text{(Eq. 5.17)}$$

Where:

$$M_{ft} = \left(1 - \frac{\Phi}{2}\right)\Phi \mathrm{b}_1 {d_1}^2 f_{cb}$$

$$M_{fc} = \left(1 - \frac{\Phi}{2}\right)\Phi \mathrm{b}_2 {d_2}^2 f_{cb}$$

Φ degree of reinforcement, $\Phi = \frac{A_s}{bd} * \frac{f_y}{f_{cb}}$

f_c plastic concrete compressive strength in bending, $f_{cb} = v_b \sigma_c$

v_b effectiveness factor for concrete in bending,

$$v_b = 0.97 - \frac{f_y}{5000} - \frac{f_{cb}}{300} \qquad \text{if } f_y < 900 \text{ MPa}, f_{cb} < 60 \text{ MPa}$$

$\mathrm{b}_1, \mathrm{b}_2$ effective bending width of the connection at front and back faces of the column, respectively;

$\mathrm{b} = C_x + d$ (for perpendicular loading);

$\mathrm{b} = C_x + 0.5d$ (for parallel loading)

d_1, d_2 effective depth of the connection at front and back faces of the column, respectively

When the moment transfer is perpendicular to the slab free edge, the effective width for flexure capacity is considered to be $(\mathrm{C} + d)$. Such effective width derives from the works of Hawkins & Corley[33] and Park & Choi[62], where the strains of the top steel reinforcement were measured to investigate the effective width of the slab that is effective in resisting the applied moment, where, the results indicated that the tensile strains extended to a distance of about one slab thickness from the column faces. However, when the moment transfer is parallel to the slab free edge, the effective bending width was proposed to be reduced to $(\mathrm{C} + 0.5d)$, as one side of the slab becomes non-existent. This assumption is found to be consistent with works of Stamenkovic & Chapman[73], Park & Choi[62] and Ahmed[4].

In the Author's test, where the principle angle of moment transfer was being varied, the Author found that the predicted punching capacity has good agreement with test results, where the principle angles of biaxial moment transfer set as 0°, 22.5° and 45,° when using the same effective bending width similarly to the one used when the moment transfer is parallel to the slab free edge. On the other hand, when the principle angles of biaxial moment transfer is set to 67.5° and 90°, the predicted punching capacity has good agreement with test results when using the same effective bending width similarly to the one used when the moment transfer is perpendicular to the slab free edge.

In cases where the moment transfer is perpendicular to the slab free edge, the total flexural resistance of the connection is the flexural capacities developed at the front face of the column, M_{ft}. This theory applies similarly to the other scenarios when there is a principle angle of biaxial moment transfer, as follows:

$$M_{f(principle\ angle)} = M_{ft} + \left(1 - \frac{principle\ angle\ in\ °}{90°}\right) * M_{fc} \qquad \text{(Eq. 5.18)}$$

5.4.2.2 Distance c_{AB}, c_{CD}

For an edge connection, the centroid location of the shear perimeter differs from that of the interior connection. The centroid of the shear perimeter is calculated as the ratio of moment of shear area on the shear perimeter with respect to the area of the adjacent sides.

When the principle angle of moment transfer is 0^0, (see Figure 5.30)

$$c_{AB(0)} = \frac{moment\ of\ area\ of\ side\ about\ AB}{area\ of\ sides} = \frac{2(b_y h)(\frac{b_y}{2})}{2(b_x h) + b_y h} \qquad \text{(Eq. 5.19a)}$$

$$c_{CD(0)} = b_y - c_{AB(0)} \qquad \text{(Eq. 5.19b)}$$

When the principle angle of moment transfer is 90^0, (see Figure 5.38)

$$c_{AB(90)} = \frac{moment\ of\ area\ of\ side\ about\ AB}{area\ of\ sides} = \frac{2(b_x h)(\frac{b_x}{2})}{2(b_x h)+b_y h} \quad \text{(Eq. 5.20a)}$$

$$c_{CD(90)} = b_x - c_{AB(90)} \quad \text{(Eq. 5.20b)}$$

When the principle angle of moment transfer is 22.5°, (see Figure 5.32)

$$c_{AB(22.5)} = \frac{c_{AB(0)}}{cos(22.5°)} \quad \text{(Eq. 5.21a)}$$

$$c_{CD(22.5)} = \frac{c_{CD(0)}}{cos(22.5°)} \quad \text{(Eq. 5.21b)}$$

When the principle angle of moment transfer is 45°, (see Figure 5.34)

$$c_{AB(45)} = \frac{c_{AB(0)}}{cos(45°)} \quad \text{(Eq. 5.22a)}$$

$$c_{CD(45)} = \frac{c_{CD(0)}}{cos(45°)} \quad \text{(Eq. 5.22b)}$$

When the principle angle of moment transfer is 67.5°, (see Figure 5.36)

$$c_{AB(67.5)} = \frac{c_{AB(0)}}{cos(67.5°)} \quad \text{(Eq. 5.23a)}$$

$$c_{CD(67.5)} = \frac{c_{CD(0)}}{cos(67.5°)} \quad \text{(Eq. 5.23b)}$$

5.4.2.3 Opening angle, δ

After obtaining the shear strength for the front face and the back face of the eccentrically loaded column, according to the theory of elasticity, the shear strength corresponding to punching capacity is the sum of the shear strengths on opposite ends of the column corresponding to the top and bottom reinforcement. From this, a ratio of the shear strength on the front face against the total shear strength corresponding to punching capacity is proposed as the basis for simulating the opening angle at the back face of them column.

Ratio to calculate the opening angle:

$$\frac{v_{AB}}{v_{AB}+v_{CD}} = \frac{\frac{V_U}{A_C}+\frac{(M_U-M_f)c_{AB}}{J_C}}{\frac{2V_U}{A_C}+\frac{(M_U-M_f)(c_{AB}-c_{CD})}{J_C}}$$

$$\frac{v_{AB}}{v_{AB}+v_{CD}} = \frac{V_U J_C+(M_U-M_f)c_{AB}A_C}{2V_U J_C+(M_U-M_f)(c_{AB}-c_{CD})} \qquad \text{(Eq. 5.24)}$$

Where:

V_U = the applied load

$A_C = 2(b_x + b_y)h$

M_U = the applied moment

M_f = flexural capacity of front face and back face of column

c_{AB}, c_{CD} = distance from column centroid to the critical perimeter

(see Eq. 5.19 – Eq. 5.23)

$$J_C = 2\left(\frac{b_x h^3}{12}\right) + 2\left(\frac{h {b_x}^3}{12}\right) + 2b_x h\left(\frac{b_x}{2} - c_{AB}\right)^2 + b_y h {c_{AB}}^2$$

After obtaining the maximum shear stress values at the front face of the column and at the back face of the column, shear stress distribution diagrams were sketched based on the findings from the experiment along with DiStasio & Buren's theory[17]. The shear stress distribution diagrams were found to vary as the principle angles of moment transfer changes. (see the effect of the principle angle of biaxial moment transfer when set at 0°, 22.5°, 45°, 67.5° and 90° as shown in Figure 5.31, Figure 5.33, Figure 5.35, Figure 5.37 and Figure 5.39, respectively)

A further reduction of 0.5 is applied to this ratio in order to enable the prediction for edge punching mechanism, before converting the ratio to the actual opening angle observed in the slabs.

$$Opening\ angle, \delta = 87.682 * \left(\frac{v_{AB}}{v_{AB}+v_{CD}} - 0.5\right)^{0.5056} \quad \text{(Eq. 5.25)}$$

5.4.4 Punching Failure Surface

From experimental observations, the model predicts that, upon failure, where the moment transfer is perpendicular to the slab free edge, the solid revolution of concrete formed within the slab at the front face of the column and its adjacent sides are dependent on the ratio of concrete shear strength at the front of the column to the sum of concrete shear strength at the front and back of the column. A semi-circle solid revolution of concrete is separated by inclined shear cracks at 21° from the sides of the column, and cutting through the tension surface of the slab at a distance 2.6 times the height of the slab as shown in Figure 5.21. Hence, the edge punching failure surface, A_E, can be derived from the followings:

(i) When the principle angle of moment transfer is 0^0, (see Figure 5.25)

If the opening angle was found to be between $0°$ and $45°$, the effective punching failure surface for eccentric punching is defined as according to the plasticity approach as:

$$A_{E(0)} = h\sqrt{1 + (\cot\theta)^2}\left[C_x + C_y + \frac{3\pi \mathrm{h} \cot\theta}{8} + \gamma * \left(C_y + \frac{\pi \mathrm{h} \cot\theta}{8}\right)\right] \quad \text{(Eq. 5.26a)}$$

Where:

h = height of slab

θ = inclination angle of shear cracks

C_x = column size parallel to the column eccentricity

C_y = column size perpendicular to the column eccentricity

γ = ratio of angle opening = $\frac{45°-\delta}{45°}$, where $0° < \delta \leq 45°$

δ = angle opening

If the opening angle was found to be between $45°$ and $90°$, the effective punching failure surface for eccentric punching is defined as according to the plasticity approach as:

$$A_{E(0)} = h\sqrt{1 + (\cot\theta)^2}\left[\frac{C_x}{2} + C_y + \frac{\pi \mathrm{h} \cot\theta}{4} + \gamma * \left(\frac{C_x}{2} + \frac{\pi \mathrm{h} \cot\theta}{8}\right)\right] \quad \text{(Eq. 5.26b)}$$

Where:

γ = ratio of angle opening = $\frac{90°-\delta}{45°}$, where $45° < \delta \leq 90°$

If the opening angle was found to be between $90°$ and $135°$, the effective punching failure surface for eccentric punching is defined as according to the plasticity approach as:

$$A_{E(0)} = h\sqrt{1 + (\cot\theta)^2}\left[C_y + \frac{\pi \mathrm{h} \cot\theta}{8} + \gamma * \left(\frac{C_x}{2} + \frac{\pi \mathrm{h} \cot\theta}{8}\right)\right] \quad \text{(Eq. 5.26c)}$$

Where:

γ = ratio of angle opening = $\frac{135°-\delta}{45°}$, where $90° < \delta \leq 125°$ (anything more than $125°$, use $125°$)

(ii) When the principle angle of moment transfer is 22.5°, (see Figure 5.26)

If the opening angle was found to be between $0°$ and $45°$, the effective punching failure surface for eccentric punching is defined as according to the plasticity approach as:

$$A_{E(22.5)} = h\sqrt{1+(\cot\theta)^2}\left[C_x + 1.08C_y + \frac{1.95\pi h \cot\theta}{4} + \gamma * \left(0.92C_y + \frac{0.05\pi h \cot\theta}{4}\right)\right]$$

(Eq. 5.27a)

Where:

γ = ratio of angle opening = $\frac{45°-\delta}{45°}$, where $0° < \delta \leq 45°$

If the opening angle was found to be between $45°$ and $90°$, the effective punching failure surface for eccentric punching is defined as according to the plasticity approach as:

$$A_{E(22.5)} = h\sqrt{1+(\cot\theta)^2}\left[0.92C_x + C_y + \frac{1.05\pi h \cot\theta}{4} + \gamma * \left(0.08C_x + 0.08C_y + \frac{0.9\pi h \cot\theta}{4}\right)\right]$$

(Eq. 5.27b)

Where:

γ = ratio of angle opening = $\frac{90°-\delta}{45°}$, where $45° < \delta \leq 90°$

If the opening angle was found to be between $90°$ and $135°$, the effective punching failure surface for eccentric punching is defined as according to the plasticity approach as:

$$A_{E(22.5)} = h\sqrt{1+(\cot\theta)^2}\left[0.08C_x + 0.92C_y + \frac{0.95\pi h \cot\theta}{4} + \gamma * \left(0.84C_x + 0.08C_y + \frac{0.1\pi h \cot\theta}{4}\right)\right]$$

(Eq. 5.27c)

Where:

γ = ratio of angle opening = $\frac{135°-\delta}{45°}$, where $90° < \delta \leq 125°$ (anything more than $125°$, use $125°$)

(iii) When the principle angle of moment transfer is 45°, (see Figure 5.27)

If the opening angle was found to be between $0°$ and $45°$, the effective punching failure surface for eccentric punching is defined as according to the plasticity approach as:

$$A_{E(45)} = h\sqrt{1 + (\cot\theta)^2}\left[C_x + \frac{3C_y}{2} + \frac{\pi h \cot\theta}{2} + \gamma * \left(\frac{C_y}{2}\right)\right] \qquad \text{(Eq. 5.28a)}$$

Where:

γ = ratio of angle opening = $\frac{45°-\delta}{45°}$, where $0° < \delta \leq 45°$

If the opening angle was found to be between $45°$ and $90°$, the effective punching failure surface for eccentric punching is defined as according to the plasticity approach as:

$$A_{E(45)} = h\sqrt{1 + (\cot\theta)^2}\left[C_x + C_y + \frac{3\pi h \cot\theta}{8} + \gamma * \left(\frac{C_y}{2} + \frac{\pi h \cot\theta}{8}\right)\right] \qquad \text{(Eq. 5.28b)}$$

Where:

γ = ratio of angle opening = $\frac{90°-\delta}{45°}$, where $45° < \delta \leq 90°$

If the opening angle was found to be between $90°$ and $135°$, the effective punching failure surface for eccentric punching is defined as according to the plasticity approach as:

$$A_{E(45)} = h\sqrt{1 + (\cot\theta)^2}\left[\frac{C_x}{2} + \frac{C_y}{2} + \frac{\pi h \cot\theta}{4} + \gamma * \left(\frac{C_x}{2} + \frac{C_y}{2} + \frac{\pi h \cot\theta}{8}\right)\right] \qquad \text{(Eq. 5.28c)}$$

Where:

γ = ratio of angle opening = $\frac{135°-\delta}{45°}$, where $90° < \delta \leq 125°$ (anything more than $125°$, use $125°$)

(iv) When the principle angle of moment transfer is 67.5°, (see Figure 5.28)

If the opening angle was found to be between $0°$ and $45°$, the effective punching failure surface for eccentric punching is defined as according to the plasticity approach as:

$$A_{E(67.5)} = h\sqrt{1+(\cot\theta)^2}\left[C_x + 1.92C_y + \frac{\pi h \cot\theta}{2} + \gamma * \left(0.08C_y\right)\right] \quad \text{(Eq. 5.29a)}$$

Where:

γ = ratio of angle opening = $\frac{45°-\delta}{45°}$, where $0° < \delta \leq 45°$

If the opening angle was found to be between $45°$ and $90°$, the effective punching failure surface for eccentric punching is defined as according to the plasticity approach as:

$$A_{E(67.5)} = h\sqrt{1+(\cot\theta)^2}\left[C_x + C_y + \frac{1.95\pi h \cot\theta}{4} + \gamma * \left(0.92C_y + \frac{0.05\pi h \cot\theta}{4}\right)\right] \quad \text{(Eq. 5.29b)}$$

Where:

γ = ratio of angle opening = $\frac{90°-\delta}{45°}$, where $45° < \delta \leq 90°$

If the opening angle was found to be between $90°$ and $135°$, the effective punching failure surface for eccentric punching is defined as according to the plasticity approach as:

$$A_{E(67.5)} = h\sqrt{1+(\cot\theta)^2}\left[0.92C_x + 0.08C_y + \frac{\pi h \cot\theta}{4} + \gamma * \left(0.08C_x + 0.92C_y + \frac{0.95\pi h \cot\theta}{4}\right)\right] \quad \text{(Eq. 5.29c)}$$

Where:

γ = ratio of angle opening = $\frac{135°-\delta}{45°}$, where $90° < \delta \leq 125°$ (anything more than $125°$, use $125°$)

(v) When the principle angle of moment transfer is 90^0, (see Figure 5.29)

If the opening angle was found to be between $0°$ and $45°$, the effective punching failure surface for eccentric punching is defined as according to the plasticity approach as:

$$A_{E(90)} = h\sqrt{1 + (\cot\theta)^2}\left[C_x + 2C_y + \frac{\pi h \cot\theta}{2} + \gamma * (0)\right] \quad \text{(Eq. 5.30a)}$$

Where:

γ = ratio of angle opening = $\frac{45°-\delta}{45°}$, where $0° < \delta \leq 45°$

If the opening angle was found to be between $45°$ and $90°$, the effective punching failure surface for eccentric punching is defined as according to the plasticity approach as:

$$A_{E(90)} = h\sqrt{1 + (\cot\theta)^2}\left[C_x + C_y + \frac{\pi h \cot\theta}{2} + \gamma * \left(C_y\right)\right] \quad \text{(Eq. 5.30b)}$$

Where:

γ = ratio of angle opening = $\frac{90°-\delta}{45°}$, where $45° < \delta \leq 90°$

If the opening angle was found to be between $90°$ and $135°$, the effective punching failure surface for eccentric punching is defined as according to the plasticity approach as:

$$A_{E(90)} = h\sqrt{1 + (\cot\theta)^2}\left[C_x + \frac{\pi h \cot\theta}{4} + \gamma * \left(C_y + \frac{\pi h \cot\theta}{4}\right)\right] \quad \text{(Eq. 5.30c)}$$

Where:

γ = ratio of angle opening = $\frac{135°-\delta}{45°}$, where $90° < \delta \leq 125°$ (anything more than $125°$, use $125°$)

Having categorised the slab, the shear failure surface of the slab, A_E, can be computed and subsequently the punching capacity can be determined. The punching capacity, V_E, to be computed as follows:

$$V_E = \propto w_i A_E \quad \text{(Eq. 5.31)}$$

Where:

$\propto$ = shear retention factor, 0.7 for micro-concrete; and 1.0 for normal-concrete

w_i = sum of internal plastic work dissipated (see Eq. 2.19)

A_E = the shear area, derived from Eq. 5.26 – Eq. 5.30 or Appendix C.

5.4.5 Comparisons with test results

The comparisons between the edge theoretical model's predictions and the test results of other researchers for solid flat slabs[24,73,74,83] and the Author's tests for waffle slabs are presented from Table 5.17 to Table 5.21.

As mentioned earlier, the model predicts the solid flat slabs' punching capacity by assuming there is no losses in punching shear failure surface while the model predicts that the waffle slabs' punching capacities by accommodating the losses in punching shear failure surface when the solid revolution extends into the waffle section.

By applying the theoretical model on the Author's tests, an opening angle(s) was predicted for individual waffle slab specimen, which were sketched and shown in Figure 5.40 to Figure 5.44. These sketches were found to be almost identical to that observed from the tests as reductions in punching failure surfaces and punching strength were noticed when the principle angles of moment transfer is reduced and the column eccentricity are increased.

Based on the comparison with 45 test results comprising of different of slabs (see Table 5.22), e.g, edge solid slabs and edge waffle slabs in the presence of moment transfer, the total mean ratio of test failure loads to predicted failure loads was 0.90, with a standard deviation of 0.19. (see Figure 5.45)

5.5 Summary

Three theoretical models based on the upper bound plastic approach have been developed and proposed in this chapter: the concentric punching at internal column mechanism; the eccentric punching at internal column mechanism; and lastly, the edge punching mechanism.

All three models simulate the observed failure mechanisms of waffle slabs with an opening angle at the back face of the column and able to take into account the reduction in punching strength of the waffle slabs when there are losses in the punching failure surface.

In general, all theoretical models have achieved good agreement for both the test results of other researchers' for solid flat slabs and for the test results of the Author's for waffle slabs. However, the application of these theoretical models would be too sophisticated for a day-to-day design purposes. Therefore, empirical design models have been developed and proposed in Chapter 6.

Table 5.1 Test and predicted failure loads of slab specimens reported by Moe[53] using proposed model

Specimen No	Column Size, C_x (mm)	Height of Slab, h (mm)	Cylindrical Compressive Strength, σ_c (N/mm^2)	Reinforcement Ratio, ρ (%)	Failure Load, P_{test} (kN)	Predicted Load, V_{IC} (kN)	$\frac{P_{test}}{V_{IC}}$
S1-60	254	152	23.3	1.1	389.0	402.9	0.97
S5-60	203	152	22.2	1.1	343.0	357.8	0.96
S1-70	254	152	24.5	1.1	393.0	413.1	0.95
S5-70	203	152	23.0	1.1	378.0	364.2	1.04
H1	254	152	26.1	1.1	372.0	426.4	0.87
R2	152	152	27.6	1.4	394.0	366.5	1.08
M1A	305	152	20.8	1.5	433.0	425.8	1.02
						Mean	0.98
						Standard Deviation	0.07

Table 5.2 Test and predicted failure loads of slab specimens reported by Eltsner & Hognestad[20] using proposed model

Specimen No	Column Size, C_x (mm)	Height of Slab, h (mm)	Cylindrical Compressive Strength, σ_c (N/mm^2)	Reinforcement Ratio, ρ (%)	Failure Load, P_{test} (kN)	Predicted Load, V_{IC} (kN)	$\frac{P_{test}}{V_{IC}}$
A1a	254	152	11.3	1.2	303.0	280.3	1.08
A1b	254	152	20.2	1.2	365.0	374.7	0.97
A1c	254	152	23.2	1.2	356.0	402.0	0.89
A1d	254	152	29.4	1.2	351.0	452.8	0.78
A1e	254	152	16.2	1.2	356.0	336.3	1.06
A2a	254	152	10.9	2.5	334.0	298.9	1.12
A2b	254	152	15.6	2.5	400.0	357.9	1.12
A2c	254	152	29.9	2.5	467.0	495.7	0.94
A7b	254	152	22.3	2.5	512.0	428.1	1.20
A3a	254	152	10.2	3.7	356.0	311.3	1.14
A3b	254	152	18.1	3.7	445.0	413.7	1.08
A3c	254	152	21.2	3.7	534.0	447.9	1.19
A3d	254	152	27.6	3.7	547.0	511.1	1.07
A4	356	152	20.9	1.2	400.0	450.2	0.89
A5	356	152	22.2	2.5	534.0	504.5	1.06
A6	356	152	20.0	3.7	498.0	513.6	0.97
B4	254	152	38.2	1.0	334.0	510.2	0.65
B9	254	152	35.1	2.0	505.0	521.9	0.97
B11	254	152	10.8	3.0	329.0	307.2	1.07
B14	254	152	40.4	3.0	578.0	594.2	0.97
						Mean	1.01
						Standard Deviation	0.14

Table 5.3 Test and predicted failure loads of slab specimens reported by Base[7] using proposed model

Specimen No	Column Size, C_x (mm)	Height of Slab, h (mm)	Cylindrical Compressive Strength, σ_c (N/mm^2)	Reinforcement Ratio, ρ (%)	Failure Load, P_{test} (kN)	Predicted Load, V_{IC} (kN)	$\frac{P_{test}}{V_{IC}}$
A1/M2	203	140	15.5	1.5	346.0	274.9	1.26
A1/M3	203	140	14.2	1.9	307.0	269.9	1.14
A1/M4	203	140	14.0	1.0	259.0	252.8	1.02
A1/M5	203	140	21.0	1.2	346.0	313.8	1.10
A2/M2	203	140	32.8	1.5	419.0	399.9	1.05
A2/M3	203	140	32.5	1.9	430.0	408.4	1.05
A2/T1	203	140	39.3	1.0	419.0	423.6	0.99
A2/T2	203	140	41.4	1.7	439.0	455.1	0.96
A3/M1	203	140	18.8	1.0	247.0	293.0	0.84
A3/M2	203	140	19.3	1.7	336.0	310.7	1.08
A3/M3	203	140	27.3	1.9	298.0	374.3	0.80
A3/T1	203	140	20.6	1.0	328.0	306.7	1.07
A3/T2	203	140	16.0	1.2	298.0	273.9	1.09
A4/M1	203	140	38.3	1.1	259.0	421.0	0.62
A4/M2	203	140	29.2	1.5	341.0	377.3	0.90
A4/M3	203	140	32.2	1.9	541.0	406.5	1.33
A4/T1	203	140	32.8	1.1	384.0	389.6	0.99
A4/T2	203	140	29.3	1.2	402.0	370.7	1.08
						Mean	1.02
						Standard Deviation	0.16

Table 5.4 Test and predicted failure loads of slab specimens reported by Yitzhaki[82] using proposed model

Specimen No	Column Size, C_x (mm)	Height of Slab, h (mm)	Cylindrical Compressive Strength, σ_c (N/mm^2)	Reinforcement Ratio, ρ (%)	Failure Load, P_{test} (kN)	Predicted Load, V_{IC} (kN)	$\frac{P_{test}}{V_{IC}}$
II-1	221	102	10.5	1.2	181.0	156.5	1.16
II-4a	221	102	17.9	0.9	245.0	200.4	1.22
II-4b	201	102	9.8	0.9	162.0	141.6	1.14
II-4c	201	102	13.9	0.9	215.0	168.4	1.28
IIB20-2	201	102	15.0	0.9	307.0	174.6	1.76
IIB30-1	300	102	17.6	2.0	239.0	253.6	0.94
II-2	221	102	9.8	1.3	152.0	152.1	1.00
II-6	221	102	21.6	1.3	240.0	226.3	1.06
II-9	201	102	9.3	8.5	157.0	212.1	0.74
III-3	221	102	18.1	1.2	201.0	205.6	0.98
7	119	102	10.0	0.7	117.0	112.5	1.04
II-10	119	102	11.7	1.0	98.0	124.3	0.79
						Mean	1.09
						Standard Deviation	0.26

Table 5.5 Test and predicted failure loads of slab specimens reported by Tomaszewicz[77] using proposed model

Specimen No	Column Size, C_x (mm)	Height of Slab, h (mm)	Cylindrical Compressive Strength, σ_c (N/mm^2)	Reinforcement Ratio, ρ (%)	Failure Load, P_{test} (kN)	Predicted Load, V_{IC} (kN)	$\frac{P_{test}}{V_{IC}}$
ND65-1-1	200	320	64.3	1.4	2050.0	1763.3	1.16
ND65-2-1	150	240	70.2	1.7	1200.0	1133.7	1.06
ND95-1-1	200	320	83.7	1.4	2250.0	2011.8	1.12
ND95-1-3	200	320	89.9	2.5	2400.0	2205.7	1.09
ND95-2-1	150	240	88.2	1.7	1100.0	1270.7	0.87
ND95-2-1D	150	240	86.7	1.7	1300.0	1259.9	1.03
ND95-2-3	150	240	89.5	2.5	1450.0	1340.8	1.08
ND95-2-3D	150	240	80.3	2.5	1250.0	1270.0	0.98
ND95-2-3D+	150	240	98.0	2.5	1450.0	1403.0	1.03
ND95-3-1	100	120	85.1	1.7	330.0	414.9	0.80
ND115-1-1	200	320	112.0	1.4	2450.0	2327.1	1.05
ND115-2-1	150	240	119.0	1.7	1400.0	1476.0	0.95
ND115-2-3	150	240	108.1	2.5	1550.0	1473.5	1.05
						Mean	1.02
						Standard Deviation	0.10

Table 5.6 Test and predicted failure loads of slab specimens reported by Marzouk & Hussein[49] using proposed model

Specimen No	Column Size, C_x (mm)	Height of Slab, h (mm)	Cylindrical Compressive Strength, σ_c (N/mm^2)	Reinforcement Ratio, ρ (%)	Failure Load, P_{test} (kN)	Predicted Load, V_{IC} (kN)	$\frac{P_{test}}{V_{IC}}$
HS1	150	120	67.0	0.4	178.0	385.0	0.46
HS2	150	120	70.0	0.7	249.0	402.0	0.62
HS3	150	120	69.0	1.2	356.0	413.1	0.86
HS4	150	120	66.0	2.1	418.0	428.7	0.98
HS7	150	120	74.0	0.9	356.0	419.1	0.85
HS5	150	150	68.0	0.5	365.0	528.0	0.69
HS6	150	150	70.0	0.5	489.0	535.8	0.91
HS8	150	150	69.0	1.0	436.0	550.0	0.79
HS9	150	150	74.0	1.5	543.0	588.3	0.92
HS10	150	150	80.0	2.1	645.0	635.1	1.02
HS11	150	90	70.0	0.7	196.0	278.8	0.70
HS12	150	90	75.0	1.2	258.0	299.2	0.86
HS13	150	90	68.0	1.6	267.0	293.1	0.91
HS14	220	120	72.0	1.2	498.0	496.7	1.00
HS15	300	120	71.0	1.2	560.0	578.0	0.97
NS1	150	120	42.0	1.2	320.0	322.3	0.99
NS2	150	150	30.0	0.5	396.0	350.7	1.13
						Mean	0.86
						Standard Deviation	0.17

Table 5.7 Test and predicted failure loads of slab specimens reported by Author using proposed model

Specimen No	Column Size, C_x (mm)	Height of Slab, h (mm)	Concrete Compressive Strength, f_{cu50} (N/mm^2)	Reinforcement Ratio, ρ (%)	Failure Load, P_{test} (kN)	Predicted Load, V_{IC} (kN)	$\frac{P_{test}}{V_{IC}}$
IWS 1	100	70	41.1	1.3	65.3	65.6	0.99

Table 5.8 Comparison between test failure loads and predicted failure loads for concentric punching at internal column series

Researcher	Number of Slab	Mean	Standard Deviation
Moe[53]	7	0.98	0.07
Elstner & Hognestad[20]	20	1.01	0.14
Base[7]	18	1.02	0.16
Yitzhaki[82]	12	1.09	0.26
Tomaszewicz[77]	13	1.02	0.1
Marzouk & Hussein[49]	17	0.86	0.17
Author's	1	0.99	-
Total	88	1.00	0.15

Table 5.9 Test and predicted failure loads of slab specimens reported by Moe[53] using proposed model

Specimen No	Column Size, C_x (mm)	Height of Slab, h (mm)	Cylindrical Compressive Strength, σ_c (N/mm^2)	Reinforcement Ratio (Tension), ρ (%) with steel yield strength, f_{yt} (N/mm^2)	Reinforcement Ratio (Compression), ρ (%) with steel yield strength, f_{yc} (N/mm^2)	Moment Transferred, M_u (kNm)	Failure Load, P_{test} (kN)	Predicted Load, V_{IE} (kN)	$\frac{P_{test}}{V_{IE}}$
M1A	305	152.4	20.82	1.50 (481)	0.00	0.00	432.8	364.5	1.19
M2A	305	152.4	15.51	1.50 (481)	0.00	39.42	212.6	252.3	0.84
M4A	305	152.4	17.65	1.50 (481)	0.00	62.45	143.7	195.9	0.73
M2	305	152.4	25.75	1.50 (481)	0.00	57.21	292.2	302.9	0.96
M3	305	152.4	22.72	1.50 (481)	0.00	70.05	207.3	238.3	0.87
M6	254	152.4	26.48	1.34 (327)	0.00	40.23	239.3	269.0	0.89
M7	254	152.4	24.96	1.34 (327)	0.00	19.00	311.4	350.0	0.89
M8	254	152.4	24.61	1.34 (327)	0.57 (327)	65.32	149.5	191.1	0.78
M9	254	152.4	23.24	1.34 (327)	0.00	33.90	266.9	271.0	0.99
M10	254	152.4	21.10	1.34 (327)	0.57 (327)	54.76	177.9	210.3	0.85
								Mean	0.90
								Standard Deviation	0.13

Table 5.10 Test and predicted failure loads of slab specimens reported by Ghali et al.[26,27] using proposed model

Specimen No	Column Size, C_x (mm)	Height of Slab, h (mm)	Cylindrical Compressive Strength, σ_c (N/mm^2)	Reinforcement Ratio (Tension), ρ (%) with steel yield strength, f_{yt} (N/mm^2)	Reinforcement Ratio (Compression), ρ (%) with steel yield strength, f_{yc} (N/mm^2)	Moment Transferred, M_u (kNm)	Failure Load, P_{test} (kN)	Predicted Load, V_{IE} (kN)	$\frac{P_{test}}{V_{IE}}$
SM0.5	305	152	36.8	0.50 (476)	0.17 (476)	99.98	129.0	142.8	0.90
SM1.0	305	152	33.4	1.00 (476)	0.33 (476)	126.94	129.0	124.2	1.04
SM1.5	305	152	39.9	1.50 (476)	0.50 (476)	133.00	129.0	172.4	0.75
								Mean	0.90
								Standard Deviation	0.15

Table 5.11 Test and predicted failure loads of slab specimens reported by Elgabry & Ghali[18,19] using proposed model

Specimen No	Column Size, C_x (mm)	Height of Slab, h (mm)	Cylindrical Compressive Strength, σ_c (N/mm^2)	Reinforcement Ratio (Tension), ρ (%) with steel yield strength, f_{yt} (N/mm^2)	Reinforcement Ratio (Compression), ρ (%) with steel yield strength, f_{yc} (N/mm^2)	Moment Transferred, M_u (kNm)	Failure Load, P_{test} (kN)	Predicted Load, V_{IE} (kN)	$\frac{P_{test}}{V_{IE}}$
1	250	150	35.0	1.07 (452)	0.46 (452)	130.05	150.0	133.7	1.12
								Mean	1.12
								Standard Deviation	-

Table 5.12 Test and predicted failure loads of slab specimens reported by Kruger[44] using proposed model

Specimen No	Column Size, C_x (mm)	Height of Slab, h (mm)	Cylindrical Compressive Strength, σ_c (N/mm^2)	Reinforcement Ratio (Tension), ρ (%) with steel yield strength, f_{yt} (N/mm^2)	Reinforcement Ratio (Compression), ρ (%) with steel yield strength, f_{yc} (N/mm^2)	Moment Transferred, M_u (kNm)	Failure Load, P_{test} (kN)	Predicted Load, V_{IE} (kN)	$\frac{P_{test}}{V_{IE}}$
P0A	300	150	34.6	1.00 (460)	0.00	0.00	423.0	430.9	0.98
P16A	300	150	38.6	1.00 (460)	0.00	53.12	332.0	339.1	0.98
P30A	300	150	30.4	1.00 (460)	0.00	86.40	270.0	234.1	1.15
							Mean		1.04
							Standard Deviation		0.10

Table 5.13 Test and predicted failure loads of slab specimens reported by Marzouk et al.[50,59] using proposed model

Specimen No	Column Size, C_x (mm)	Height of Slab, h (mm)	Cylindrical Compressive Strength, σ_c (N/mm^2)	Reinforcement Ratio (Tension), ρ (%) with steel yield strength, f_{yt} (N/mm^2)	Reinforcement Ratio (Compression), ρ (%) with steel yield strength, f_{yc} (N/mm^2)	Moment Transferred, M_u (kNm)	Failure Load, P_{test} (kN)	Predicted Load, V_{IE} (kN)	$\frac{P_{test}}{V_{IE}}$
HSLW0.5L	250	150	72	0.50 (400)	0.00	40.50	257.1	356.5	0.72
HSLW1.0L	250	150	72	1.00 (400)	0.00	64.39	342.8	367.0	0.93
HSLW0.5M	250	150	72	0.50 (400)	0.00	76.70	216.2	252.9	0.85
HSLW1.0M	250	150	72	1.00 (400)	0.00	98.65	287.0	281.9	1.02
HSLW0.5H	250	150	72	0.50 (400)	0.00	102.75	184.2	175.8	1.05
HSLW1.0H	250	150	72	1.00 (400)	0.00	133.60	223.3	180.8	1.23
HSLW1.5H	250	150	72	1.50 (400)	0.00	132.00	265.1	239.0	1.11
NSNW1.0L	250	150	35	1.00 (400)	0.00	62.00	360.8	262.2	1.38
								Mean	1.04
								Standard Deviation	0.21

Table 5.14 Test and predicted failure loads of slab specimens reported by Hawkins et al.[35] using proposed model

Specimen No	Column Size, C_x (mm)	Height of Slab, h (mm)	Cylindrical Compressive Strength, σ_c (N/mm^2)	Reinforcement Ratio (Tension), ρ (%) with steel yield strength, f_{yt} (N/mm^2)	Reinforcement Ratio (Compression), ρ (%) with steel yield strength, f_{yc} (N/mm^2)	Moment Transferred, M_u (kNm)	Failure Load, P_{test} (kN)	Predicted Load, V_{IE} (kN)	$\frac{P_{test}}{V_{IE}}$
6AH	305	153	31.3	0.52 (472)	0.25 (462)	90.40	169.0	173.2	0.98
9.6AH	305	153	30.7	0.83 (415)	0.44 (472)	97.70	187.0	193.2	0.97
14AH	305	153	30.3	1.21 (420)	0.54 (472)	100.20	205.0	221.1	0.93
6AL	305	153	22.7	0.52 (472)	0.25 (462)	32.70	244.0	270.0	0.90
9.6AL	305	153	28.9	0.83 (415)	0.44 (472)	34.60	257.0	345.4	0.74
14AL	305	153	27.0	1.21 (420)	0.54 (472)	43.40	319.0	353.4	0.90
7.3BH	305	114	22.2	0.62 (472)	0.35 (462)	39.00	80.0	112.3	0.71
9.5BH	305	114	19.8	0.86 (472)	0.42 (462)	45.40	94.0	112.1	0.84
14.2BH	305	114	29.5	1.19 (415)	0.64 (472)	51.00	102.0	145.7	0.70
7.3BL	305	114	18.1	0.52 (472)	0.35 (462)	12.80	130.0	189.0	0.69
9.5BL	305	114	20.0	0.83 (472)	0.42 (462)	16.60	142.0	208.1	0.68
14.2BL	305	114	20.5	1.21 (415)	0.64 (472)	20.90	162.0	221.0	0.73
6CH	305	153	52.4	0.52 (472)	0.25 (462)	95.10	186.0	229.3	0.81
9.6CH	305	153	57.2	0.83 (415)	0.44 (472)	113.10	218.0	257.7	0.85
14CH	305	153	54.7	1.21 (420)	0.54 (472)	133.30	252.0	267.4	0.94
6CL	305	153	49.5	0.52 (472)	0.25 (462)	36.80	273.0	392.2	0.70
14CL	305	153	47.7	1.21 (420)	0.54 (472)	49.40	362.0	455.1	0.80
							Mean		0.82
							Standard Deviation		0.11

Table 5.15 Test and predicted failure loads of slab specimens reported by Author using proposed model

Specimen No	Column Size, C_x (mm)	Height of Slab, h (mm)	Cylindrical Compressive Strength, σ_c (N/mm^2)	Reinforcement Ratio (Tension), ρ (%) with steel yield strength, f_{yt} (N/mm^2)	Reinforcement Ratio (Compression), ρ (%) with steel yield strength, f_{yc} (N/mm^2)	Moment Transferred, M_u (kNm)	Failure Load, P_{test} (kN)	Predicted Load, V_{IE} (kN)	$\frac{P_{test}}{V_{IE}}$
IWSB1	100	70	36.6	1.31 (460)	0.6 (460)	2.74	54.73	46.56	1.18
IWSB2	100	70	36.6	1.31 (460)	0.6 (460)	2.11	42.10	46.51	0.91
IWSB3	100	70	35.7	1.31 (460)	0.6 (460)	2.32	46.31	42.81	1.08
IWSB4	100	70	37.7	1.31 (460)	0.6 (460)	4.63	46.31	38.07	1.22
IWSB5	100	70	36.9	1.31 (460)	0.6 (460)	3.58	35.79	37.25	0.96
IWSB6	100	70	36.0	1.31 (460)	0.6 (460)	3.79	37.89	33.5	1.13
IWSB7	100	70	36.6	1.31 (460)	0.6 (460)	5.68	37.89	31.13	1.22
IWSB8	100	70	37.0	1.31 (460)	0.6 (460)	4.42	29.47	30.76	0.96
IWSB9	100	70	38.7	1.31 (460)	0.6 (460)	5.052	33.68	28.35	1.19
IFSB1	100	70	37.5	1.31 (460)	0.6 (460)	7.16	71.57	65.24	1.10
IFSB2	100	70	36.7	1.31 (460)	0.6 (460)	6.74	67.36	65.25	1.03
IFSB3	100	70	37.2	1.31 (460)	0.6 (460)	6.32	63.15	65.13	0.97
IWSBC1	100	70	38.5	1.31 (460)	0.6 (460)	4.21	42.10	39.91	1.05
IWSBC2	100	70	39.7	1.31 (460)	0.6 (460)	3.79	37.89	41.84	0.91
								Mean	1.06
								Standard Deviation	0.11

Table 5.16 Comparison between test failure loads and predicted failure loads for eccentric punching at internal column series

Researcher	Number of Slab	Mean	Standard Deviation
Moe[53]	10	0.90	0.13
Ghali et al.[26,27]	3	0.90	0.15
Elgabry and Ghali[18,19]	1	1.12	-
Kruger[44]	3	1.04	0.10
Marzouk, Osman and Helmy[50,59]	8	1.04	0.21
Hawkins et. al.[35]	17	0.82	0.11
Author's	14	1.06	0.11
Total	56	0.98	0.14

Table 5.17 Test and predicted failure loads of slab specimens reported by Stamenkovic & Chapman[73] using proposed model

Specimen No	Column Size, C_x (mm)	Column Size, C_y (mm)	Height of Slab, h (mm)	Cylindrical Compressive Strength, σ_c (N/mm^2)	Reinforcement Ratio (Tension), ρ (%) with steel yield strength, f_{yt} (N/mm^2)	Reinforcement Ratio (Compression), ρ (%) with steel yield strength, f_{yc} (N/mm^2)	Moment Transferred, M_u (kNm)	Failure Load, P_{test} (kN)	Predicted Load, V_{IE} (kN)	$\frac{P_{test}}{V_{IE}}$
V/E/1	127	127	76	29.2	1.09 (496)	1.09 (496)	0.00	74.73	73.15	1.02
C/E/1	127	127	76	31.5	1.39 (448)	1.09 (448)	5.59	73.39	78.80	0.93
C/E/2	127	127	76	33.0	1.39 (496)	1.09 (496)	9.18	54.71	71.18	0.77
C/E/3	127	127	76	34.0	1.39 (496)	1.09 (496)	10.06	24.91	46.77	0.53
C/E/4	127	127	76	27.8	1.39 (496)	1.09 (496)	8.84	10.94	11.51	0.95
									Mean	0.84
									Standard Deviation	0.20

Table 5.18 Test and predicted failure loads of slab specimens reported by Zaghlool[83] using proposed model

Specimen No	Column Size, C_x (mm)	Column Size, C_y (mm)	Height of Slab, h (mm)	Cylindrical Compressive Strength, σ_c (N/mm^2)	Reinforcement Ratio (Tension), ρ (%) with steel yield strength, f_{yt} (N/mm^2)	Reinforcement Ratio (Compression), ρ (%) with steel yield strength, f_{yc} (N/mm^2)	Moment Transferred, M_u (kNm)	Failure Load, P_{test} (kN)	Predicted Load, V_{IE} (kN)	$\frac{P_{test}}{V_{IE}}$
Z-IV(1)	178	178	152	27.4	2.41 (476)	2.29 (476)	44.97	122.32	199.90	0.62
Z-V(1)	267	267	152	34.3	1.60 (474)	1.52 (474)	84.64	215.28	234.99	0.92
Z-V(2)	267	267	152	40.5	2.00 (474)	1.72 (474)	93.56	246.86	270.20	0.91
Z-V(3)	267	267	152	38.8	1.65 (475)	1.75 (475)	103.62	268.21	247.58	1.08
Z-V(5)	267	267	152	35.2	1.60 (476)	1.52 (476)	0.00	279.33	276.51	1.01
Z-V(6)	267	267	152	31.3	1.60 (476)	1.52 (476)	88.14	116.98	162.84	0.72
Z-VI(1)	356	356	152	26.0	2.41 (476)	1.14 (476)	106.90	265.10	263.36	1.00
								Mean		0.89
								Standard Deviation		0.17

Table 5.19 Test and predicted failure loads of slab specimens reported by Gardner & Shao[24] using proposed model

Specimen No	Column Size, C_x (mm)	Column Size, C_y (mm)	Height of Slab, h (mm)	Cylindrical Compressive Strength, σ_c (N/mm^2)	Reinforcement Ratio (Tension), ρ (%) with steel yield strength, f_{yt} (N/mm^2)	Reinforcement Ratio (Compression), ρ (%) with steel yield strength, f_{yc} (N/mm^2)	Moment Transferred, M_u (kNm)	Failure Load, P_{test} (kN)	Predicted Load, V_{IE} (kN)	$\frac{P_{test}}{V_{IE}}$
2	199	199	140	21.5	0.92 (460)	0.82 (460)	14.60	159.00	154.73	1.03
3	254	254	140	21.5	0.92 (460)	0.82 (460)	14.60	144.00	176.55	0.82
4	254	254	140	21.5	0.92 (460)	0.82 (460)	19.00	207.00	176.55	1.17
5	254	254	140	21.5	0.92 (460)	0.82 (460)	14.60	144.00	176.55	0.82
									Mean	0.96
									Standard Deviation	0.17

Table 5.20 Test and predicted failure loads of slab specimens reported by Surdasana[74] using proposed model

Specimen No	Column Size, C_x (mm)	Column Size, C_y (mm)	Height of Slab, h (mm)	Cylindrical Compressive Strength, σ_c (N/mm^2)	Reinforcement Ratio (Tension), ρ (%) with steel yield strength, f_{yt} (N/mm^2)	Reinforcement Ratio (Compression), ρ (%) with steel yield strength, f_{yc} (N/mm^2)	Moment Transferred, M_u (kNm)	Failure Load, P_{test} (kN)	Predicted Load, V_{IE} (kN)	$\frac{P_{test}}{V_{IE}}$
E1	203	203	140	43.6	0.90 (480)	0.70 (480)	34.40	127.00	204.14	0.62
E2	203	203	140	42.4	0.90 (480)	0.70 (480)	0.00	220.00	218.97	1.00
E2-1	203	203	140	52.8	1.20 (480)	0.90 (480)	34.70	130.50	239.20	0.55
E2-2	203	203	140	52.8	1.20 (480)	0.90 (480)	25.30	178.90	253.47	0.71
E2-3	203	203	140	55.0	1.20 (480)	0.90 (480)	9.60	328.00	258.70	1.27
E2-4	203	203	140	55.0	1.20 (480)	0.90 (480)	16.40	199.00	258.70	0.77
								Mean		0.82
								Standard Deviation		0.27

Table 5.21 Test and predicted failure loads of slab specimens reported by Author using proposed model

Specimen No	Column Size, C_x (mm)	Column Size, C_y (mm)	Height of Slab, h (mm)	Cylindrical Compressive Strength, σ_c (N/mm^2)	Reinforcement Ratio (Tension), ρ (%) with steel yield strength, f_{yt} (N/mm^2)	Reinforcement Ratio (Compression), ρ (%) with steel yield strength, f_{yc} (N/mm^2)	Moment Transferred, M_u (kNm)	Failure Load, P_{test} (kN)	Predicted Load, V_{IE} (kN)	$\frac{P_{test}}{V_{IE}}$
EWSB1	100	100	70	38.1	1.31 (460)	0.6 (460)	1.58	31.58	39.30	0.80
EWSB2	100	100	70	41.2	1.31 (460)	0.6 (460)	2.21	44.21	38.00	1.16
EWSB3	100	100	70	37.8	1.31 (460)	0.6 (460)	2.00	40.00	44.85	0.89
EWSB4	100	100	70	36.9	1.31 (460)	0.6 (460)	2.11	42.10	49.41	0.86
EWSB5	100	100	70	37.7	1.31 (460)	0.6 (460)	2.63	52.60	49.74	1.06
EWSB6	100	100	70	37.1	1.31 (460)	0.6 (460)	2.95	29.47	29.14	1.01
EWSB7	100	100	70	38.7	1.31 (460)	0.6 (460)	3.16	31.58	30.03	1.05
EWSB8	100	100	70	36.7	1.31 (460)	0.6 (460)	2.74	27.37	36.58	0.75
EWSB9	100	100	70	36.2	1.31 (460)	0.6 (460)	2.95	29.47	36.03	0.82
EWSB10	100	100	70	43.7	1.31 (460)	0.6 (460)	4.84	48.42	43.77	1.11
EWSB11	100	100	70	33.3	1.31 (460)	0.6 (460)	4.11	27.37	20.92	1.31
EWSB12	100	100	70	41.0	1.31 (460)	0.6 (460)	4.11	27.37	24.30	1.13
EWSB13	100	100	70	37.3	1.31 (460)	0.6 (460)	3.79	25.26	22.20	1.14
EWSB14	100	100	70	37.0	1.31 (460)	0.6 (460)	3.79	25.26	28.43	0.89
EWSB15	100	100	70	37.3	1.31 (460)	0.6 (460)	6.00	40.00	34.94	1.15
EFSB1	100	100	70	48.1	1.31 (460)	0.6 (460)	4.42	44.21	47.03	0.94
EFSB2	100	100	70	43.8	1.31 (460)	0.6 (460)	4.42	44.21	50.09	0.88
EFSB3	100	100	70	41.9	1.31 (460)	0.6 (460)	4.63	46.31	55.34	0.84
EFSB4	100	100	70	44.1	1.31 (460)	0.6 (460)	4.84	48.42	65.14	0.74
EFSB5	100	100	70	32.9	1.31 (460)	0.6 (460)	5.26	52.63	59.50	0.88
EWSCE1	100	100	70	36.9	1.31 (460)	0.6 (460)	2.05	41.05	44.50	0.92
EWSCE2	100	100	70	36.8	1.31 (460)	0.6 (460)	3.68	36.84	31.12	1.18

EWSCE3	100	100	70	38.5	1.31 (460)	0.6 (460)	4.74	31.58	25.92	1.22
									Mean	0.99
									Standard Deviation	0.16

Table 5.22 Comparison between test failure loads and predicted failure loads for edge punching series

Researcher	Number of Slab	Mean	Standard Deviation
Stamenkovic and Chapman[73]	5	0.84	0.20
Zaghlool[83]	7	0.89	0.17
Gardner and Shao[24]	4	0.96	0.17
Surdasana[74]	6	0.82	0.27
Author's	23	0.99	0.16
Total	45	0.90	0.19

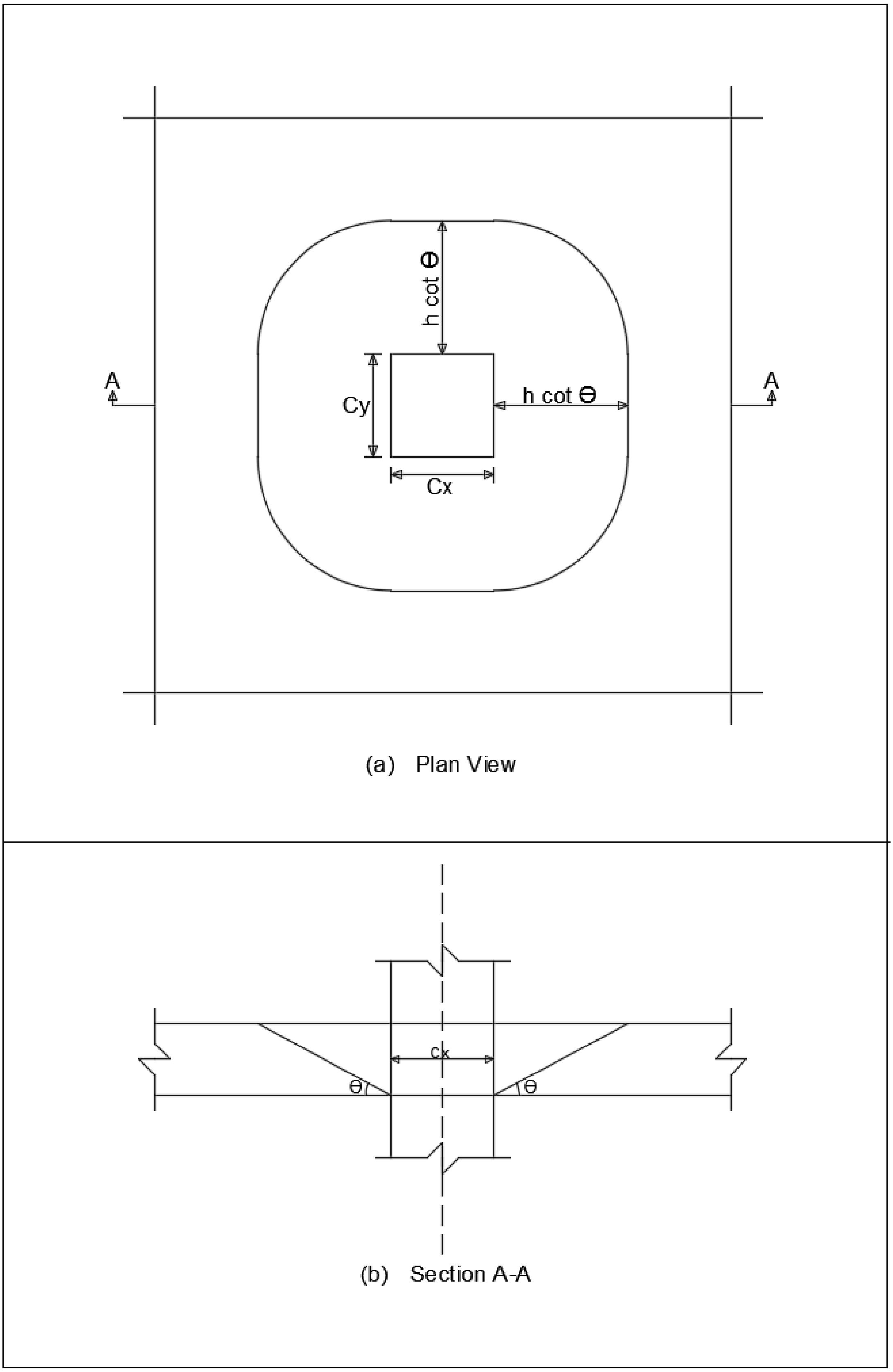

Figure 5.1 Proposed concentric punching at internal column shear failure surface

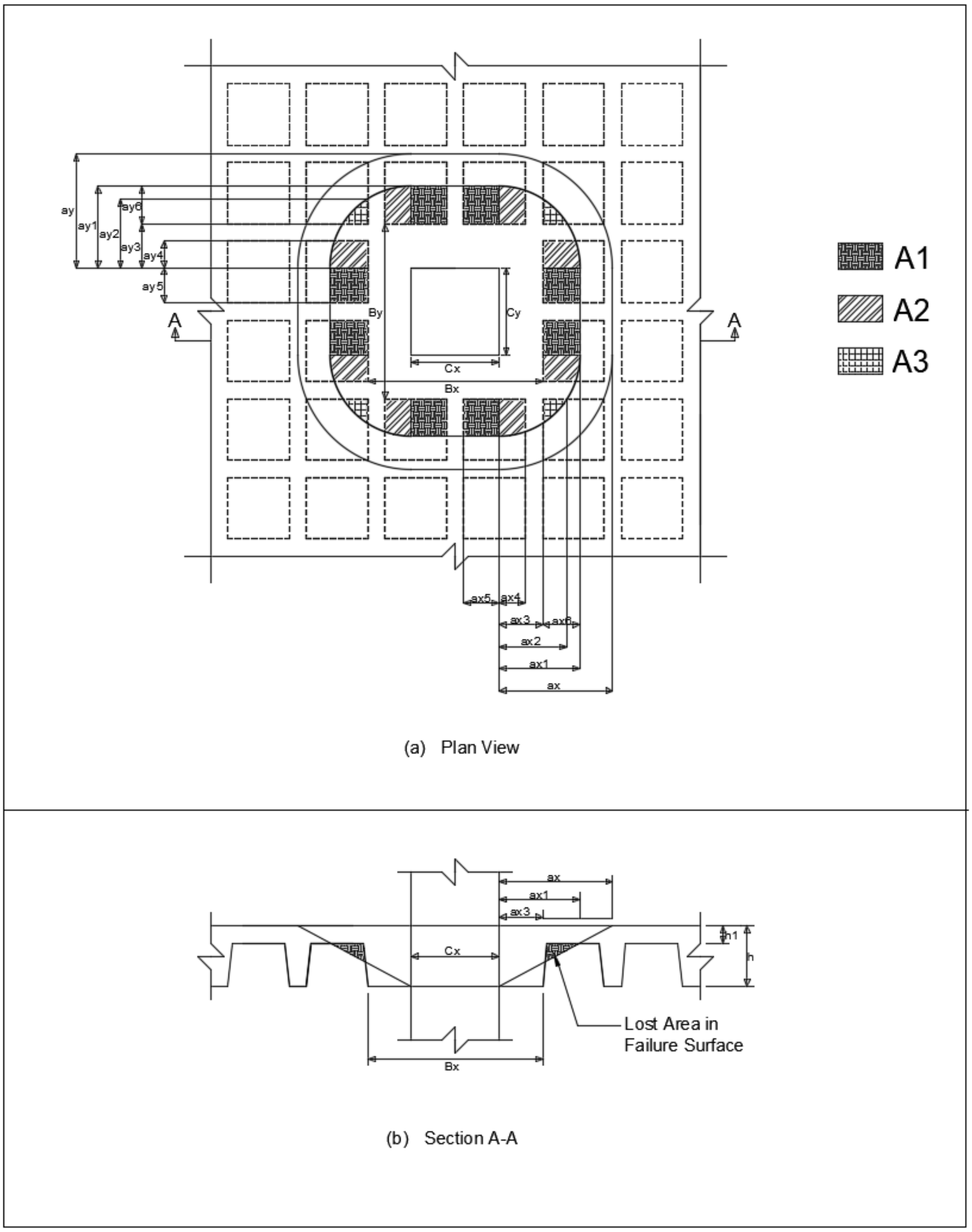

Figure 5.2 Proposed concentric punching at internal column shear failure surface for waffle slabs with losses

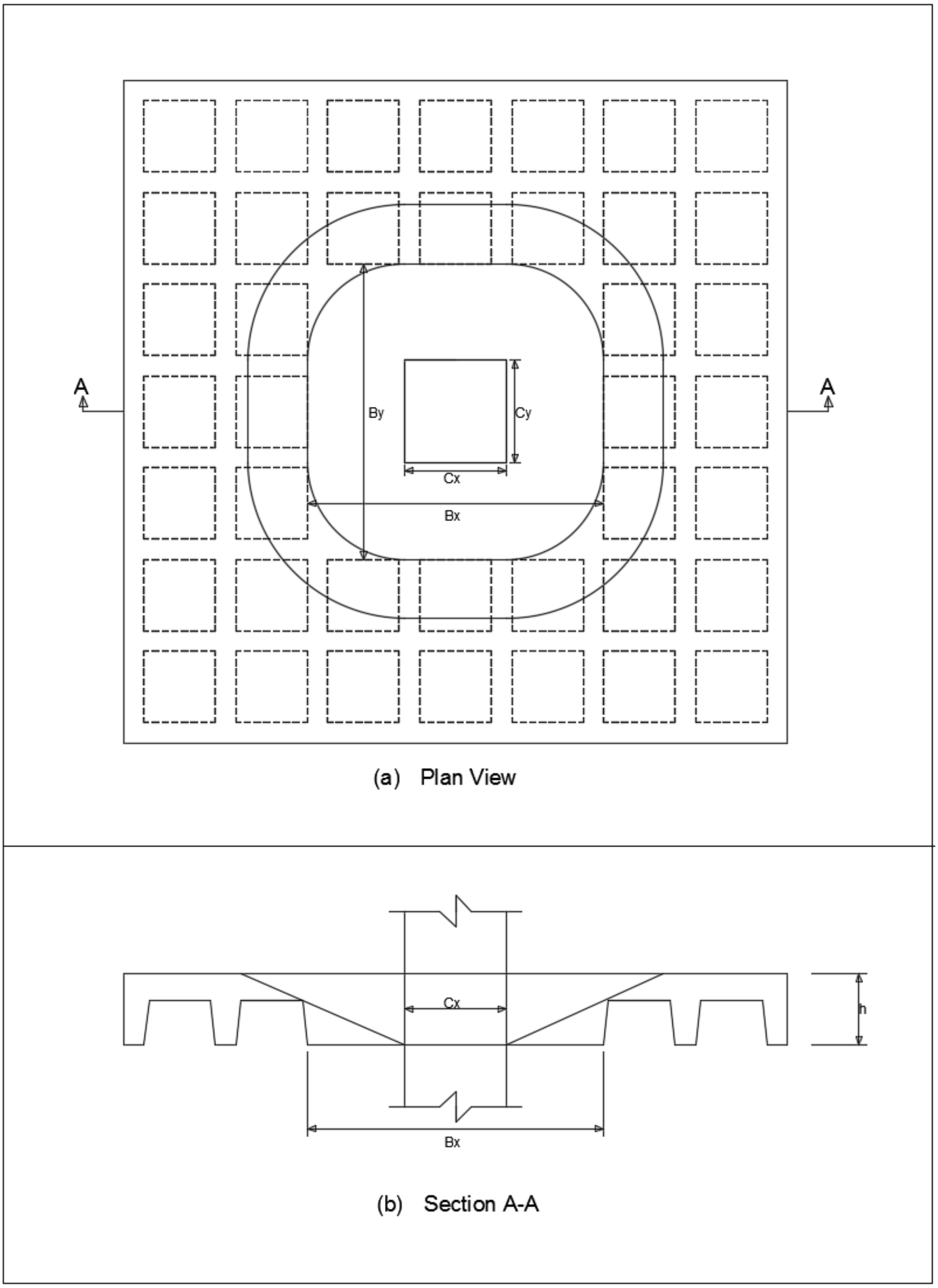

Figure 5.3 Proposed concentric punching at internal column shear failure surface for waffle slabs with no losses

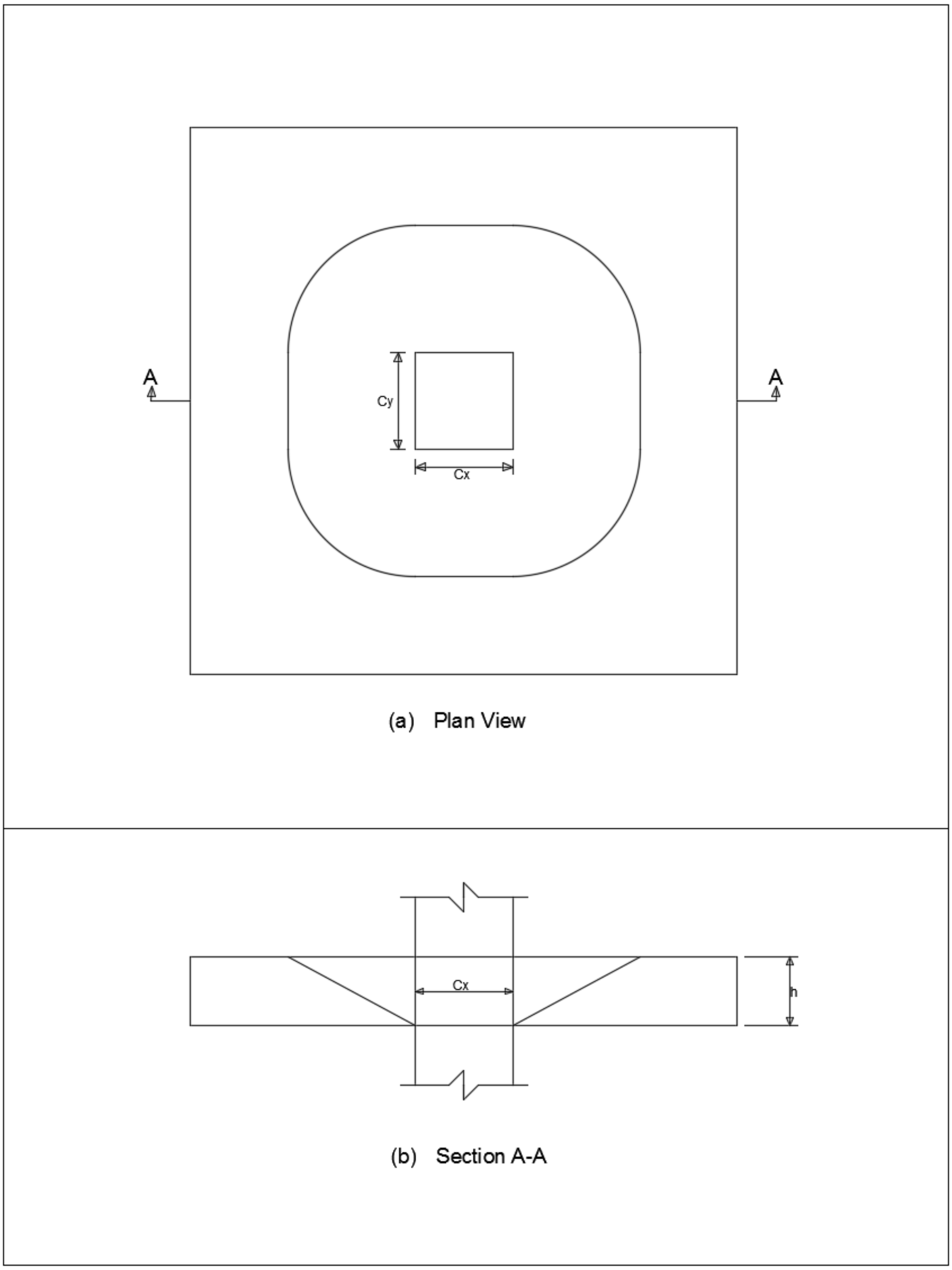

Figure 5.4 Proposed concentric punching at internal column shear failure surface for solid flat slabs with no losses

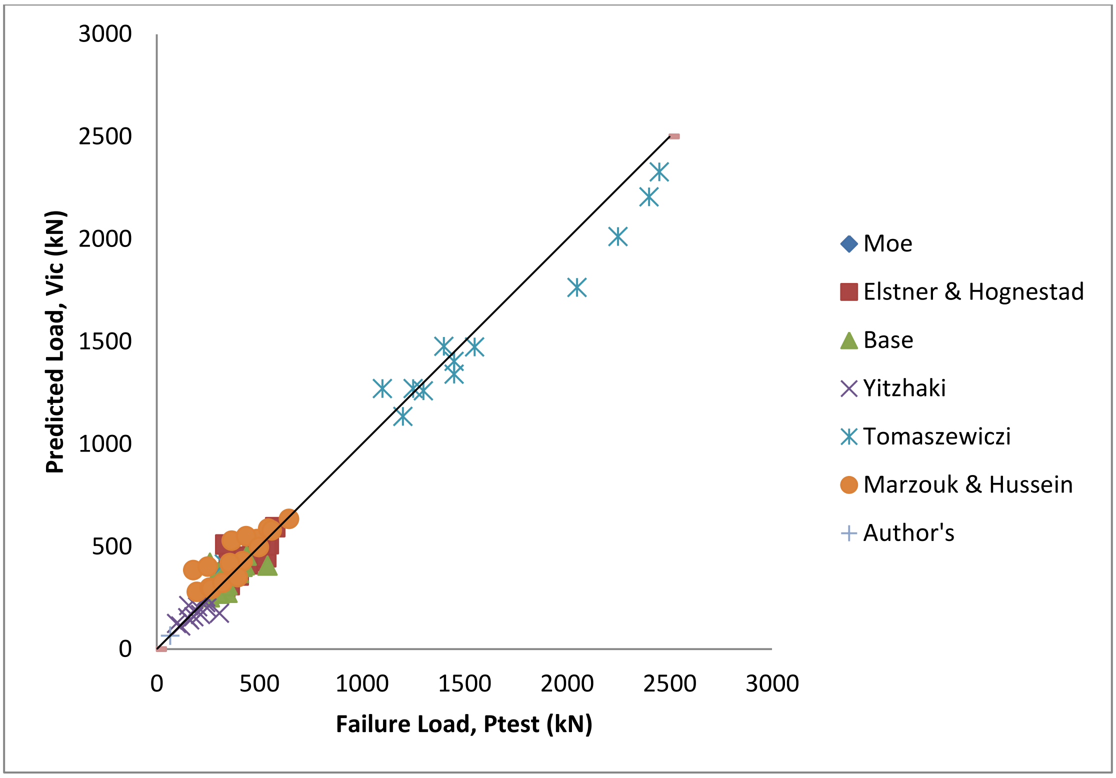

Figure 5.5 Comparison between predicted loads and test failure loads for waffle slabs and solid flat slabs using proposed concentric punching at internal column

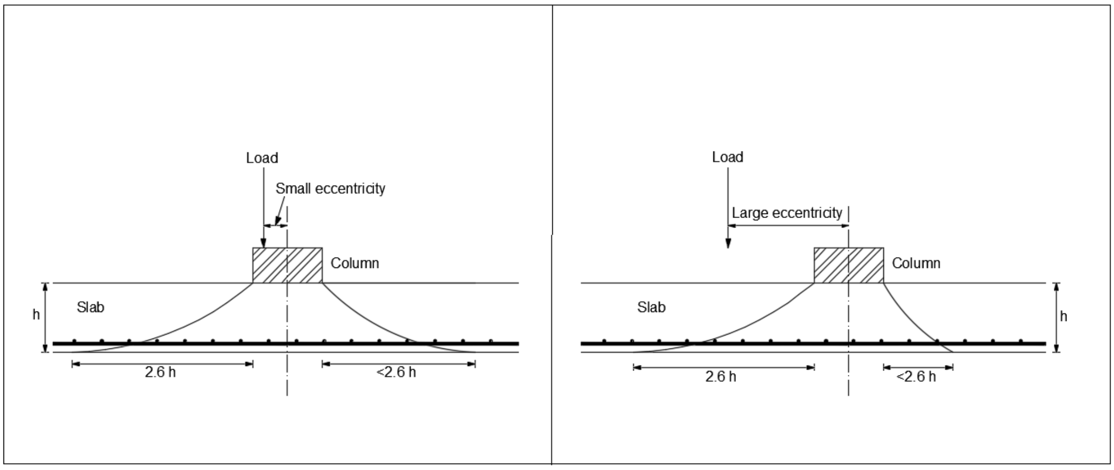

Figure 5.6 Effect of eccentricity on punching shear failure surface

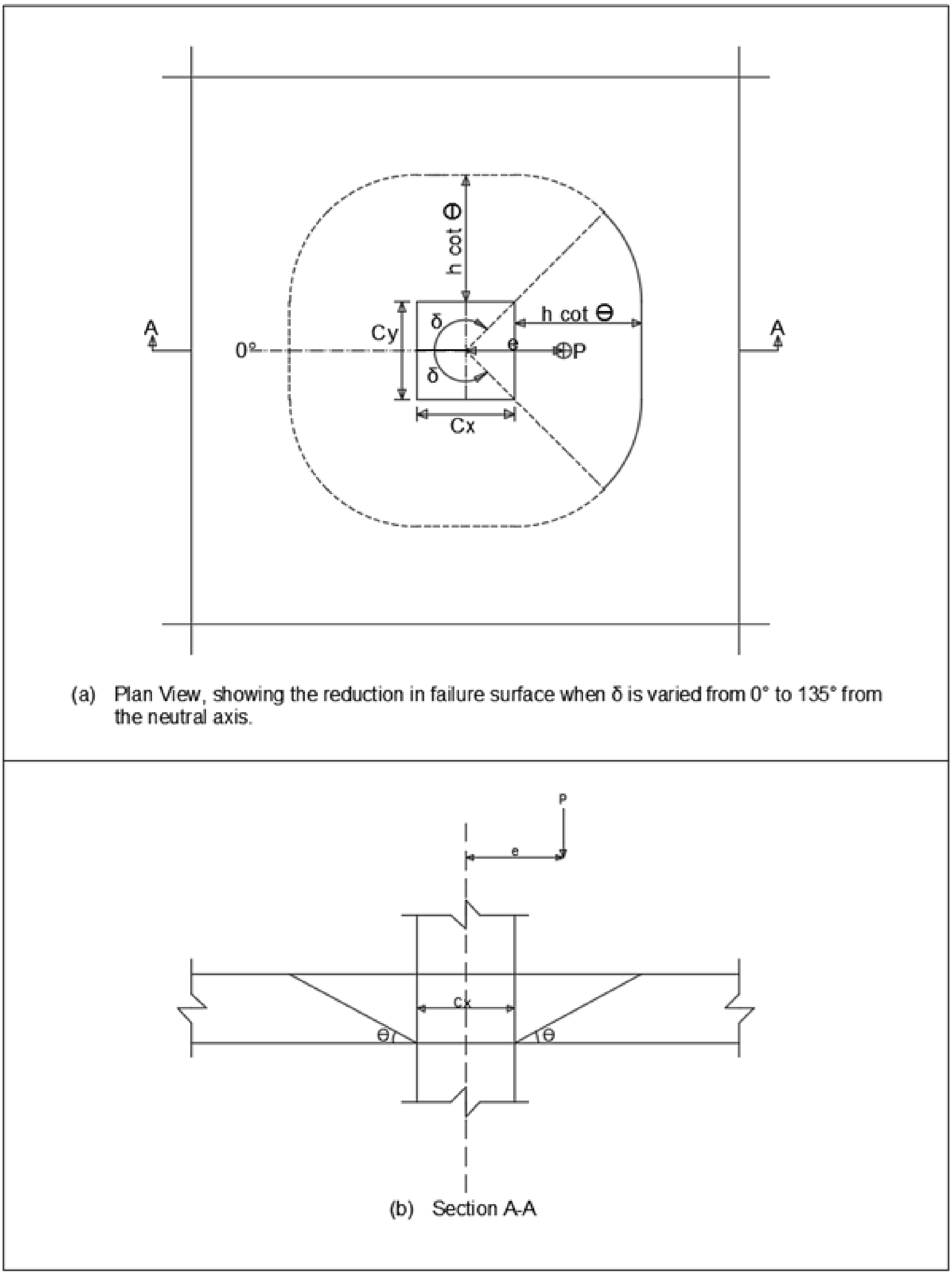

(a) Plan View, showing the reduction in failure surface when δ is varied from 0° to 135° from the neutral axis.

(b) Section A-A

Figure 5.7 Proposed eccentric punching at internal column shear failure surface when the principle angle of moment transfer is 0^{o}

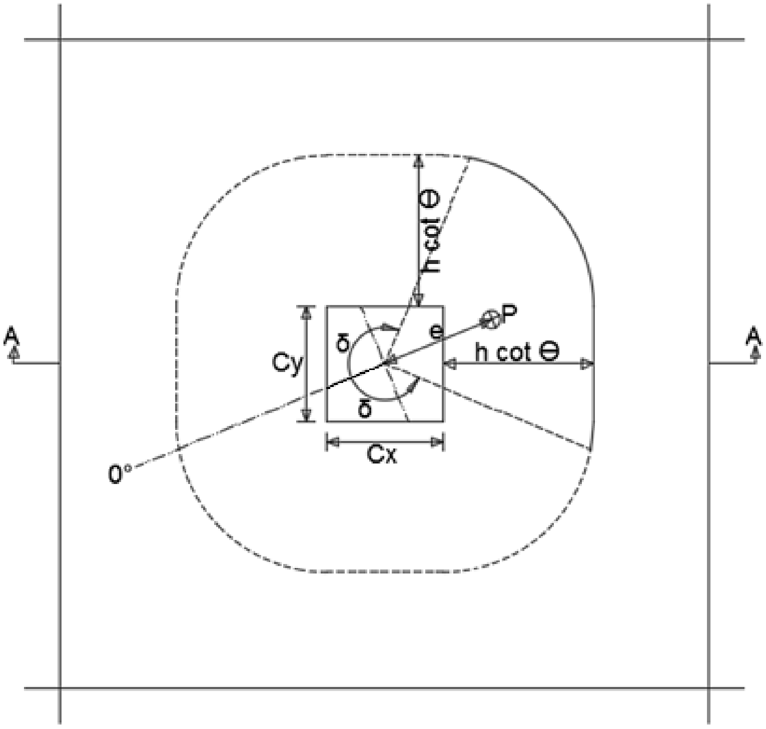

(a) Plan View, showing the reduction in failure surface when δ is varied from 0° to 135° from the neutral axis.

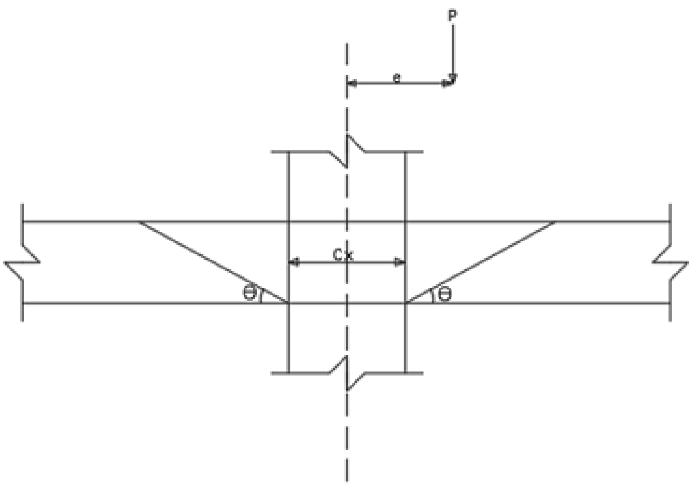

(b) Section A-A

Figure 5.8 Proposed eccentric punching at internal column shear failure surface when the principle angle of moment transfer is 22.5°

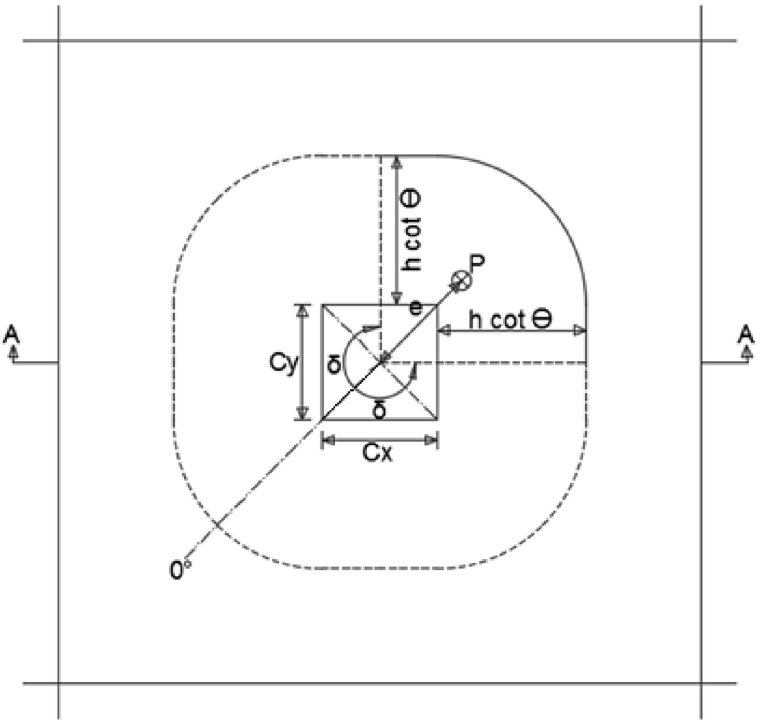

(a) Plan View, showing the reduction in failure surface when δ is varied from 0° to 135° from the neutral axis.

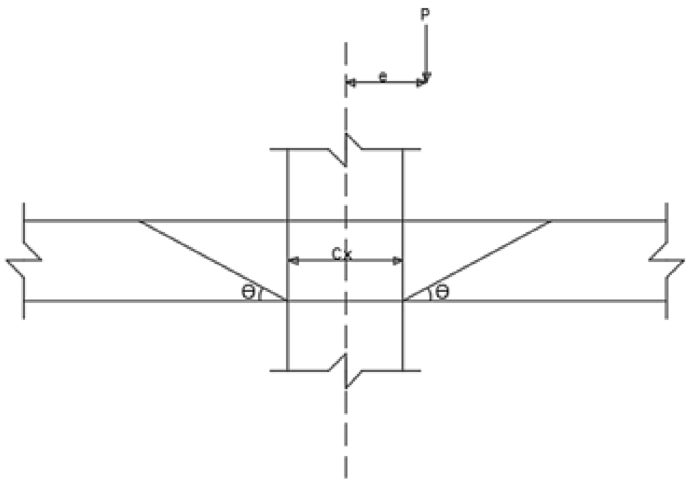

(b) Section A-A

Figure 5.9 Proposed eccentric punching at internal column shear failure surface when the principle angle of moment transfer is 45°

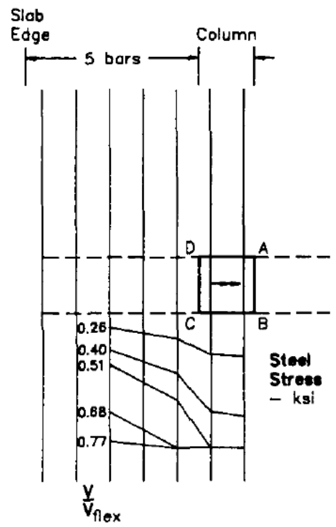

(a) Low moment transfer

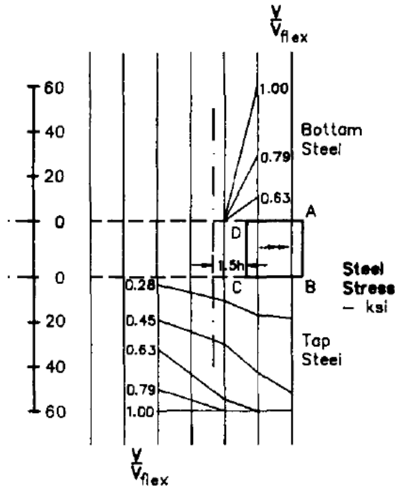

(b) High moment transfer

Figure 5.10 Distribution of steel strain at solid flat slab connections

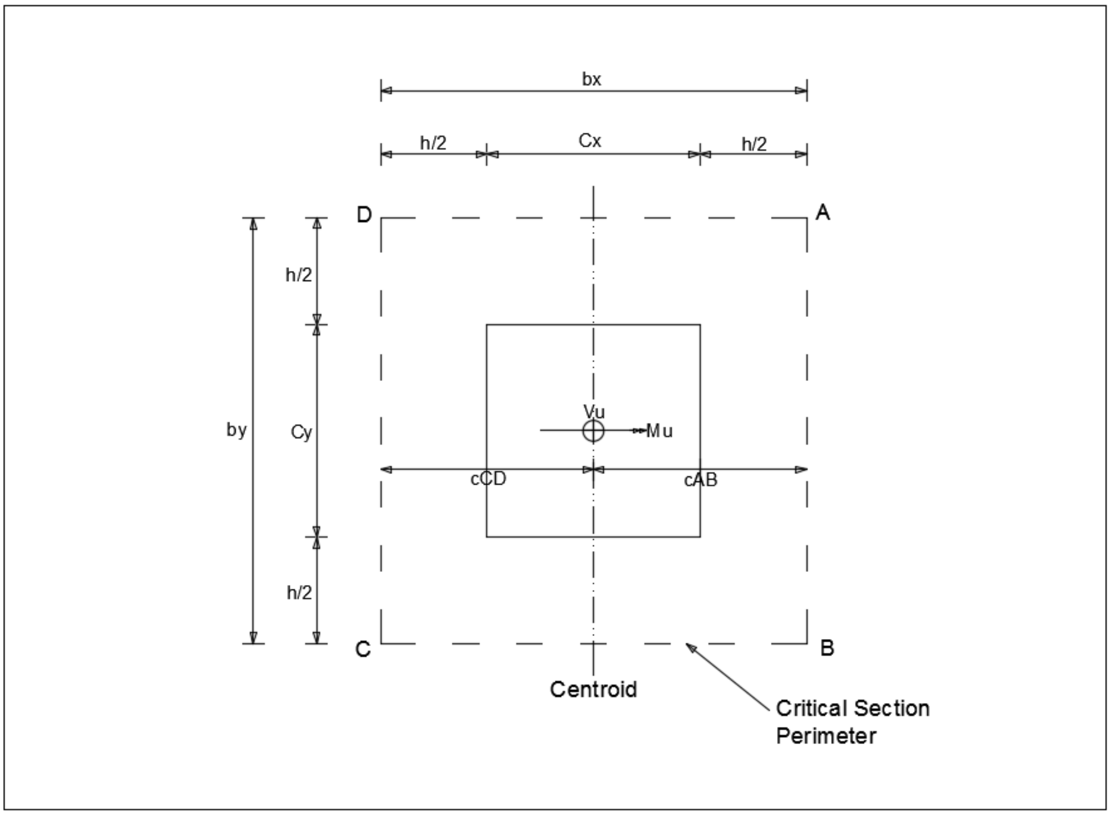

Figure 5.11 Critical section perimeter when the principle angle of moment transfer is 0°

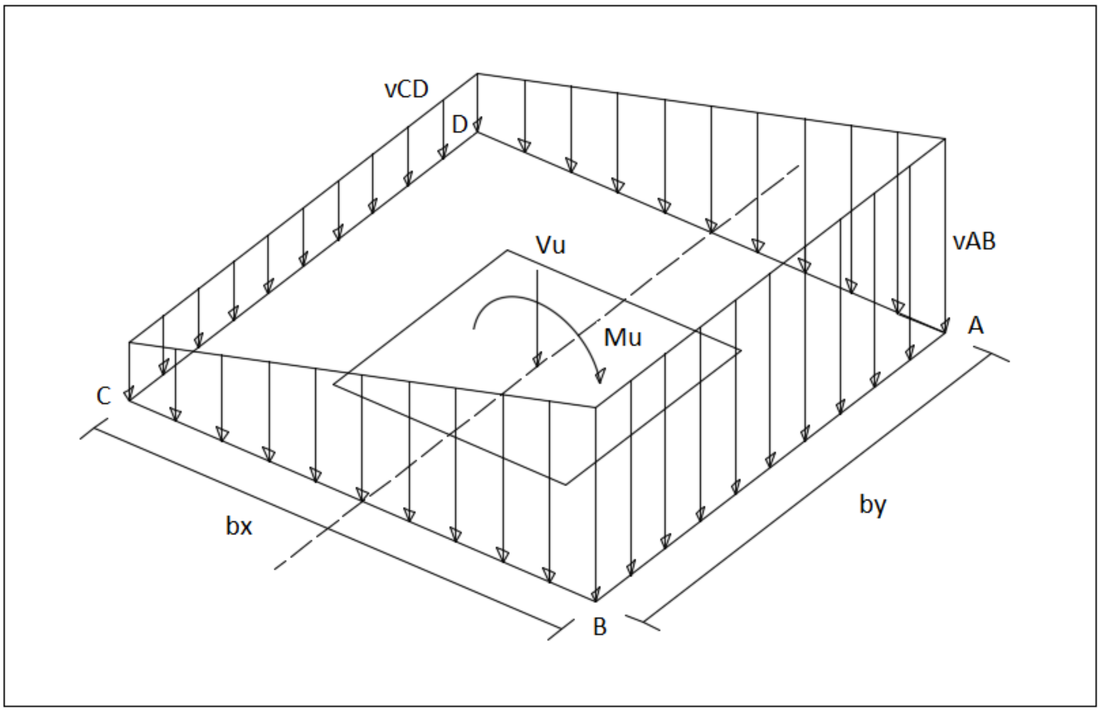

Figure 5.12 Shear stress distribution when the principle angle of moment transfer is 0°

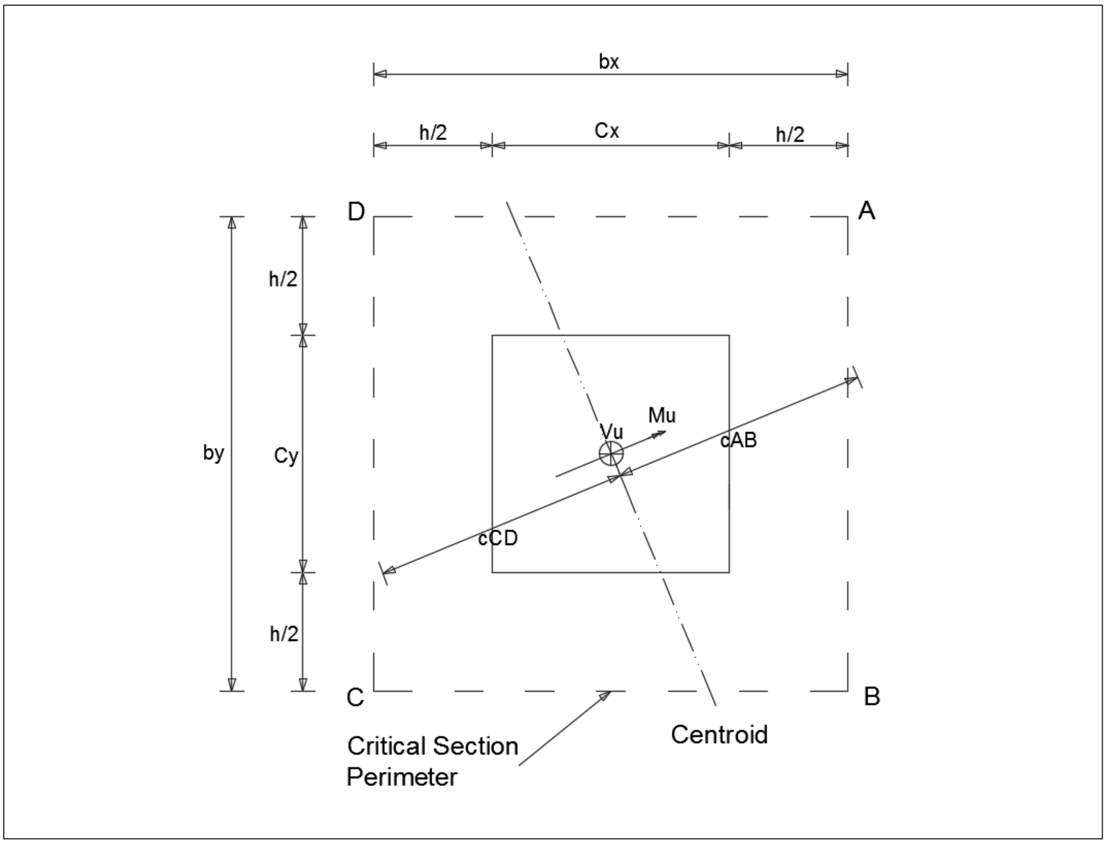

Figure 5.13 Critical section perimeter when the principle angle of moment transfer is 22.5°

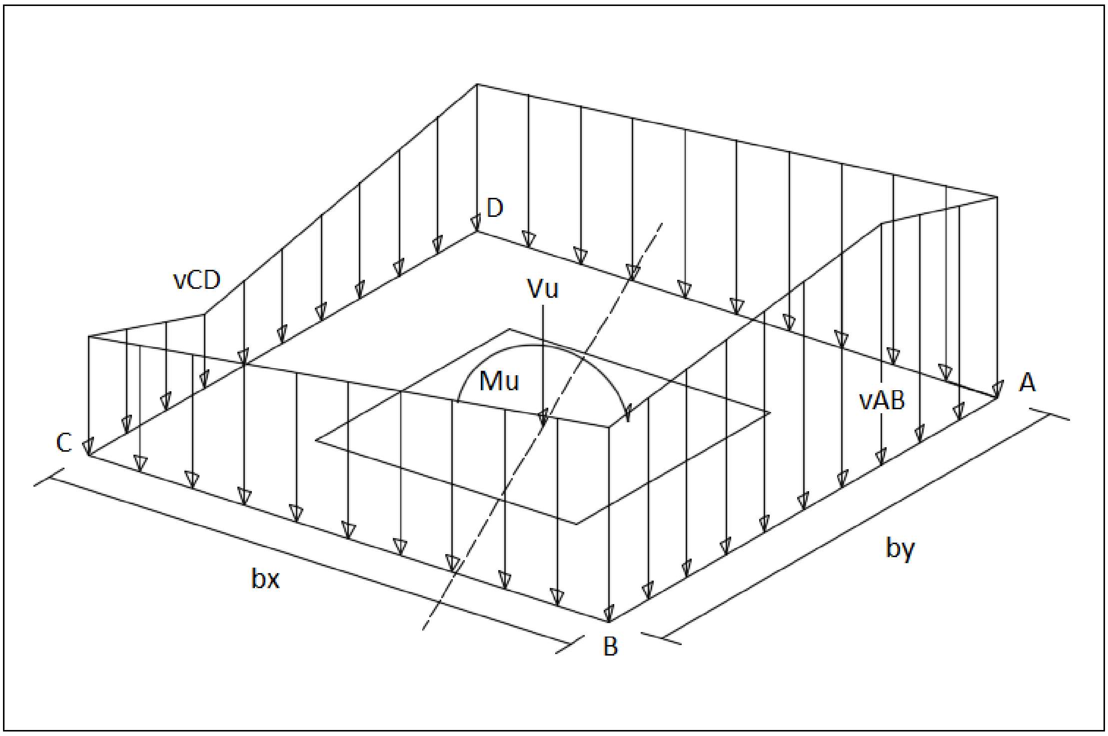

Figure 5.14 Shear stress distribution when the principle angle of moment transfer is 22.5°

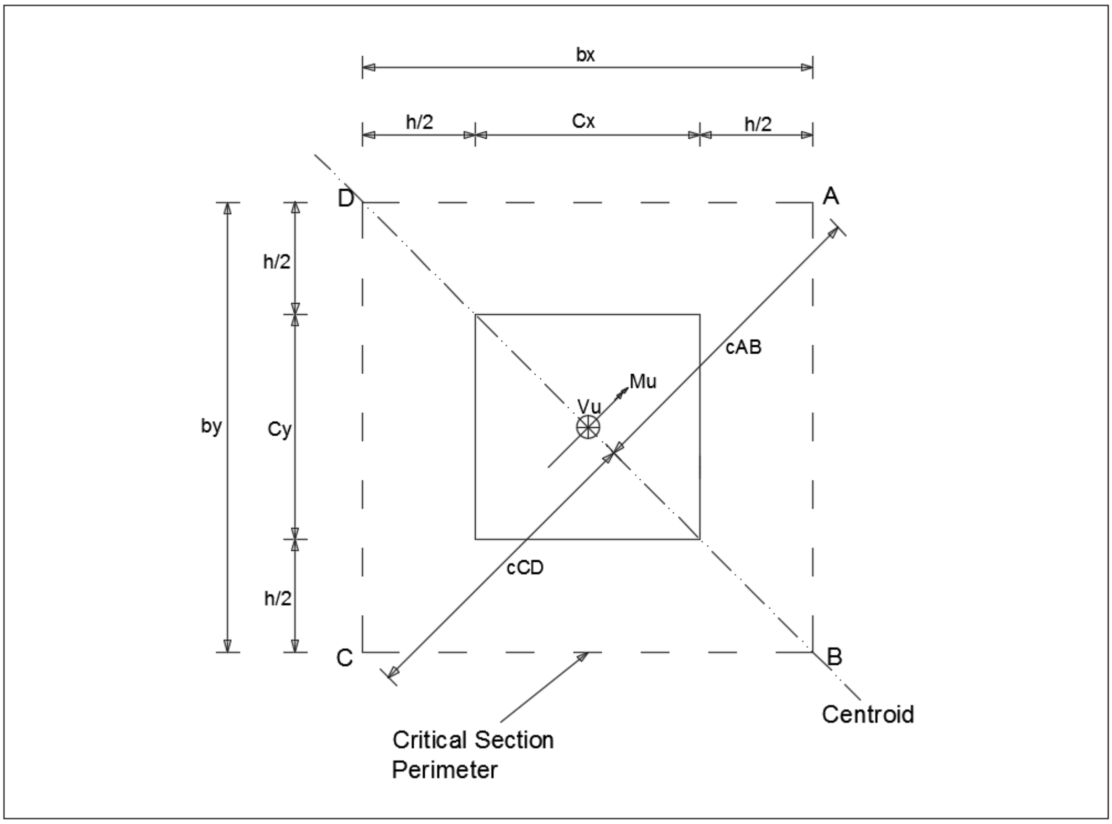

Figure 5.15 Critical section perimeter when the principle angle of moment transfer is 45°

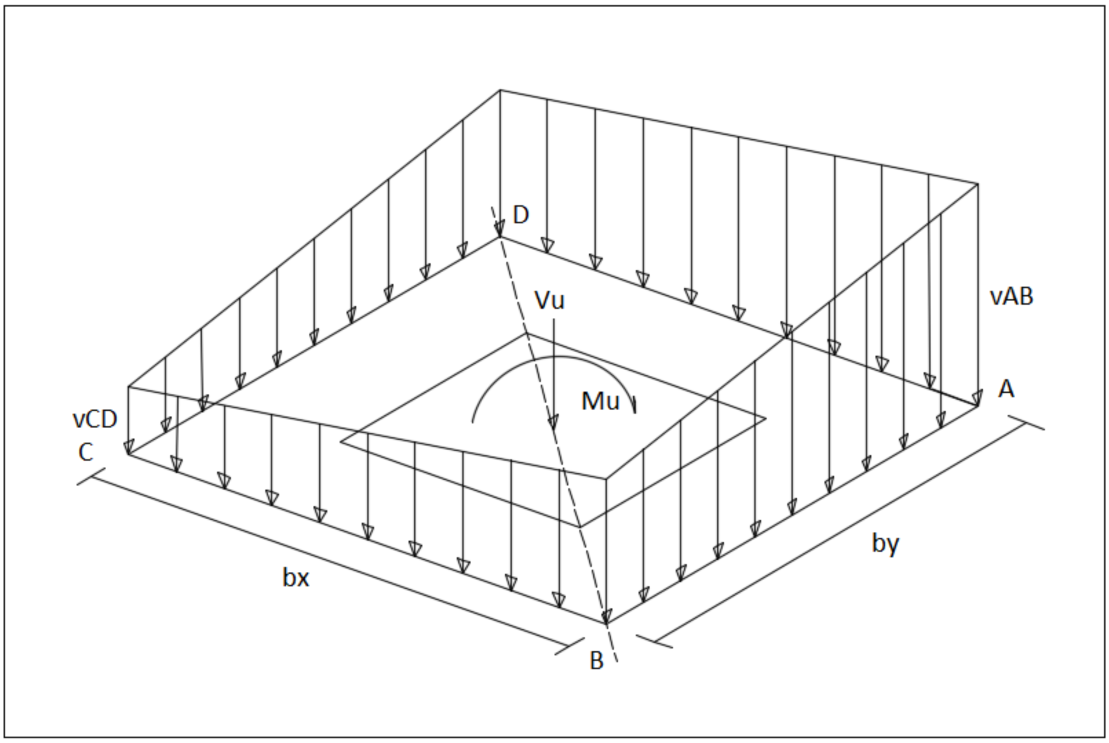

Figure 5.16 Shear stress distribution when the principle angle of moment transfer is 45°

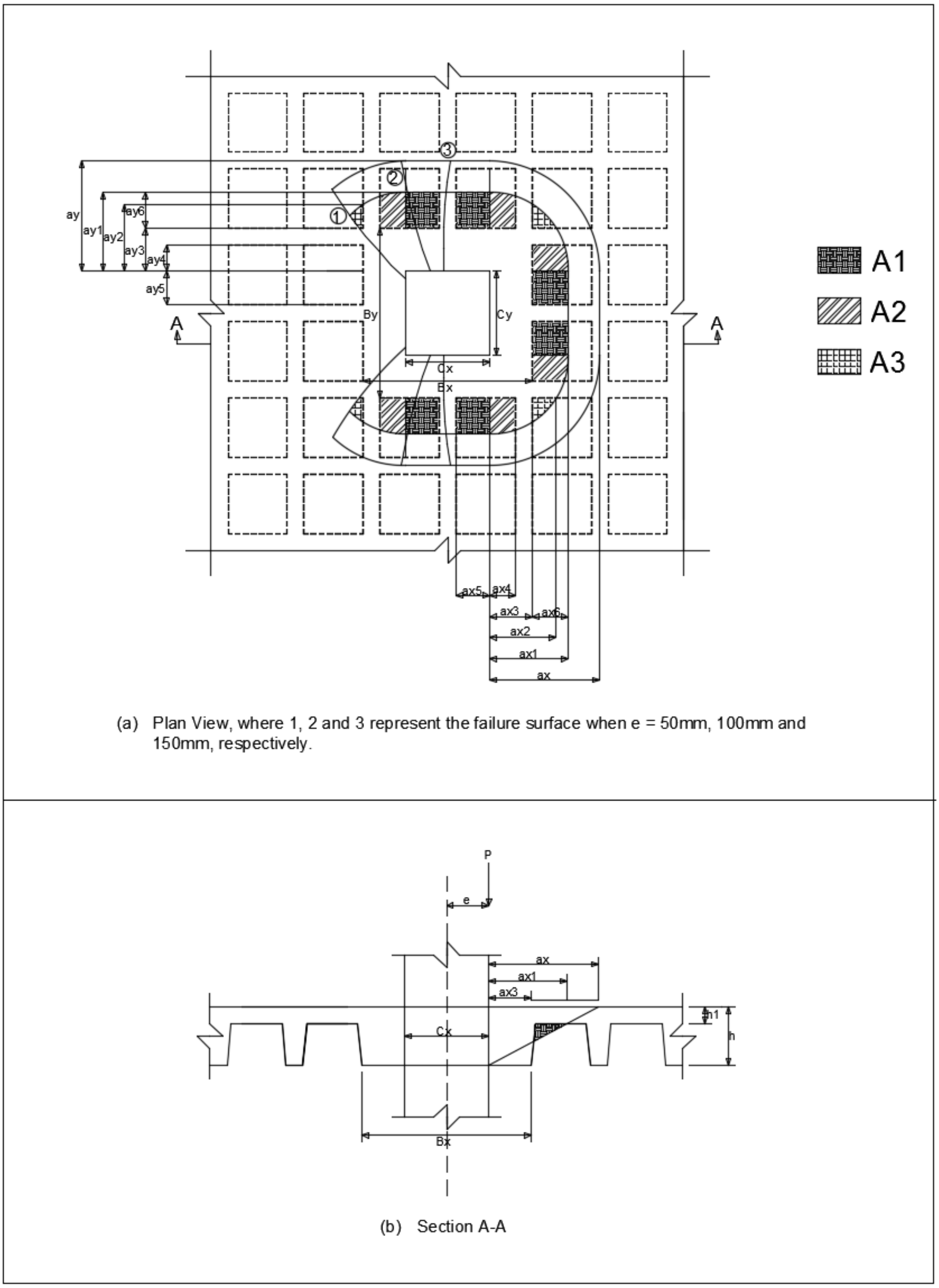

(a) Plan View, where 1, 2 and 3 represent the failure surface when e = 50mm, 100mm and 150mm, respectively.

(b) Section A-A

Figure 5.17 Schematic diagram of eccentric punching at internal column shear failure surface when the principle angle of moment transfer is 0^{o}

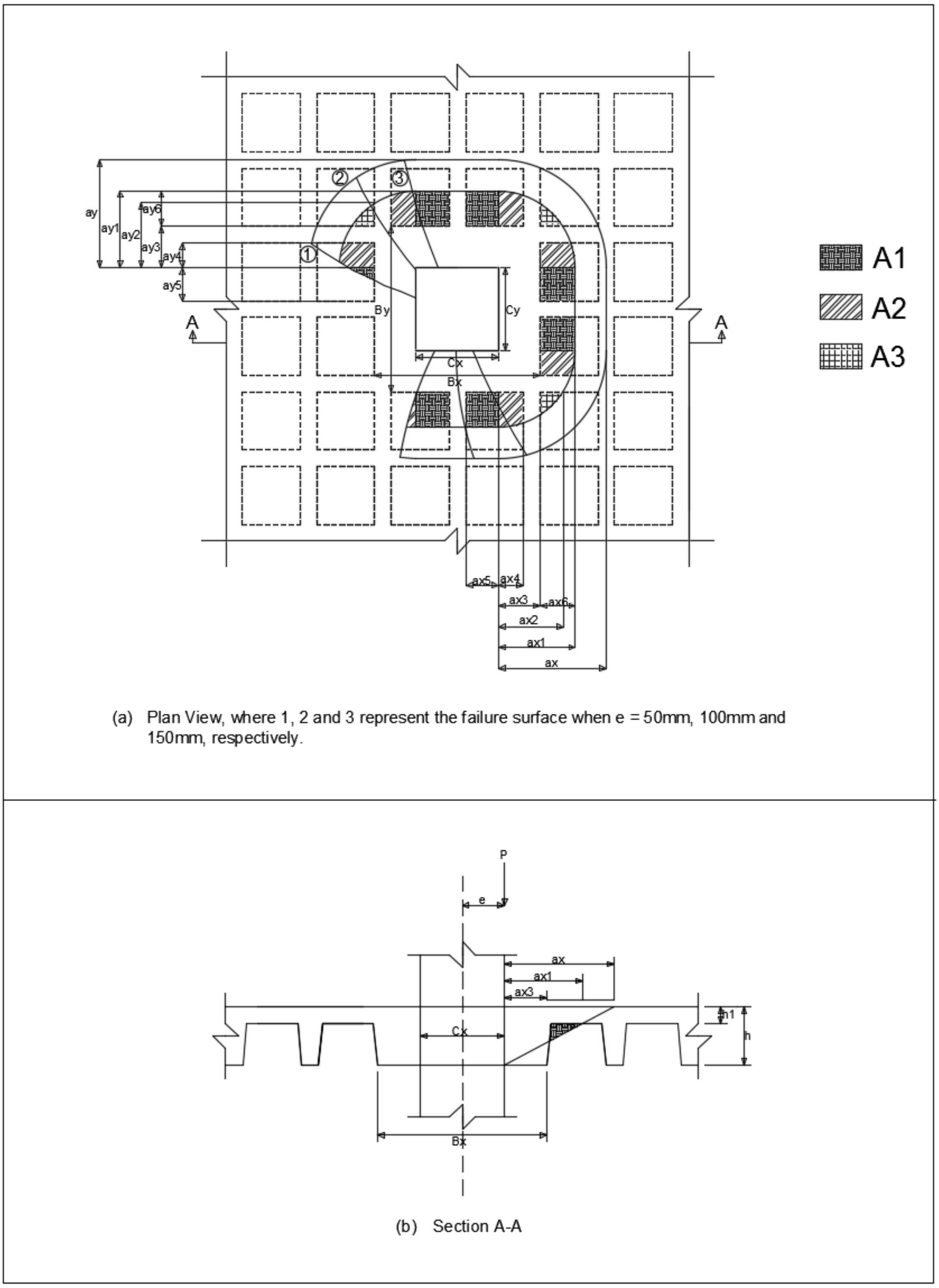

(a) Plan View, where 1, 2 and 3 represent the failure surface when e = 50mm, 100mm and 150mm, respectively.

(b) Section A-A

Figure 5.18 Schematic diagram of eccentric punching at internal column shear failure surface when the principle angle of moment transfer is 22.5^{o}

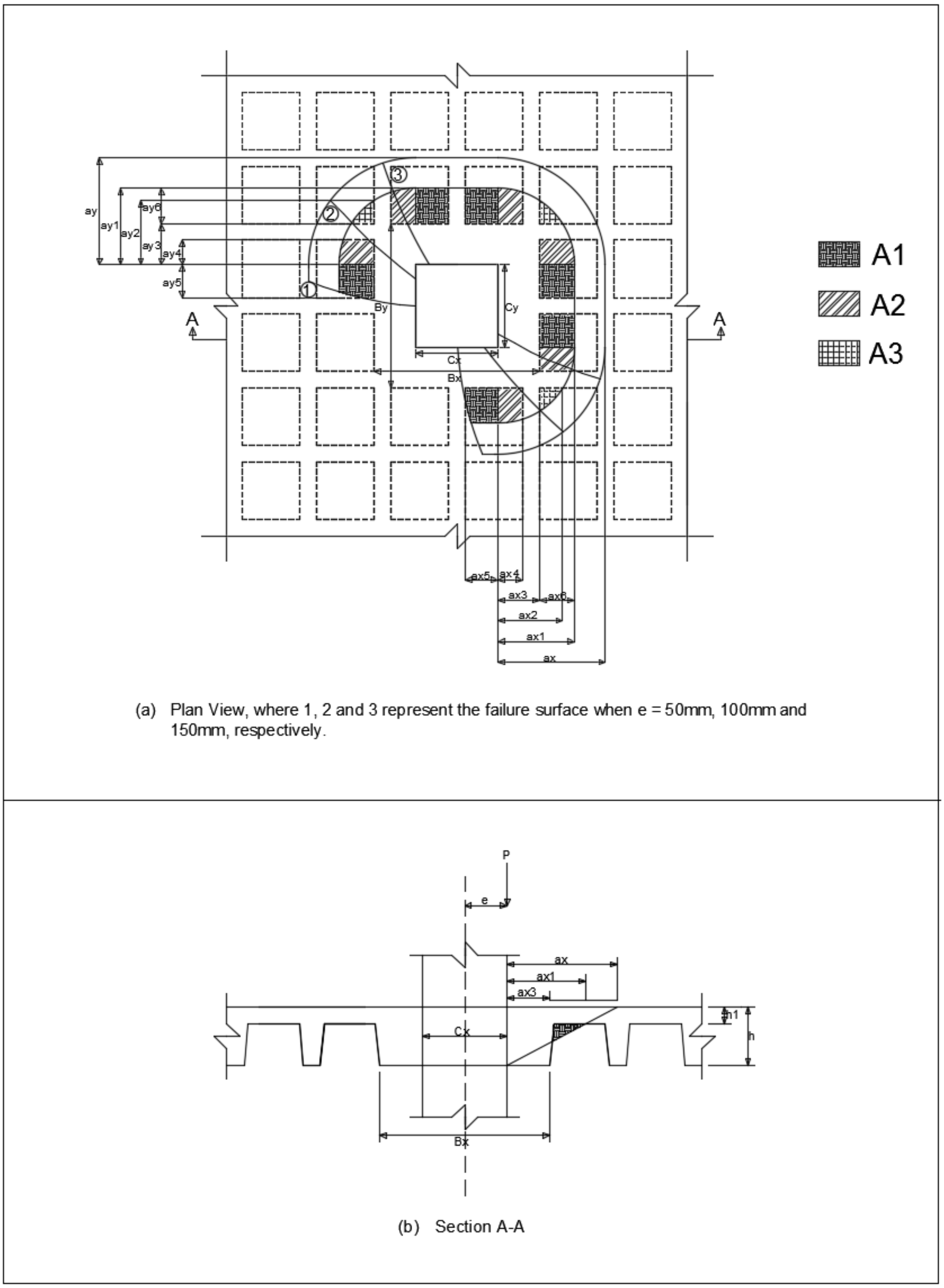

Figure 5.19 Schematic diagram of eccentric punching at internal column shear failure surface when the principle angle of moment transfer is 45°

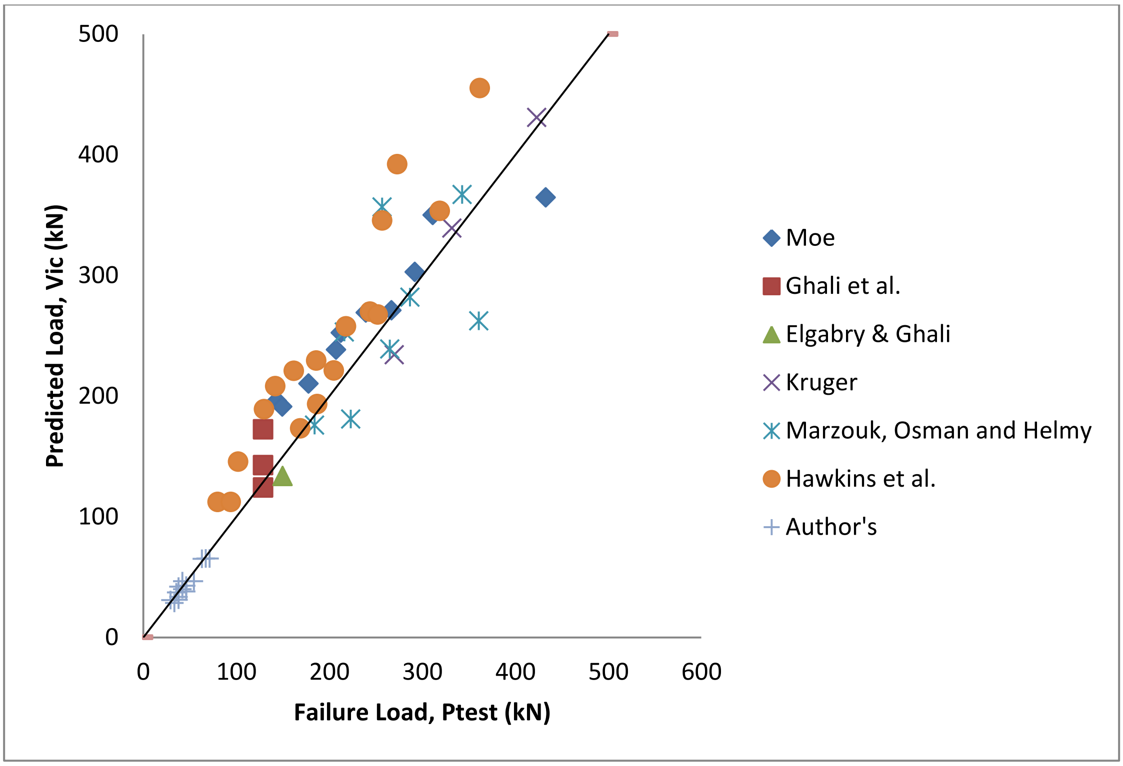

Figure 5.20 Comparison between predicted loads and test failure loads for waffle slabs and solid flat slabs using proposed eccentric punching at internal column model

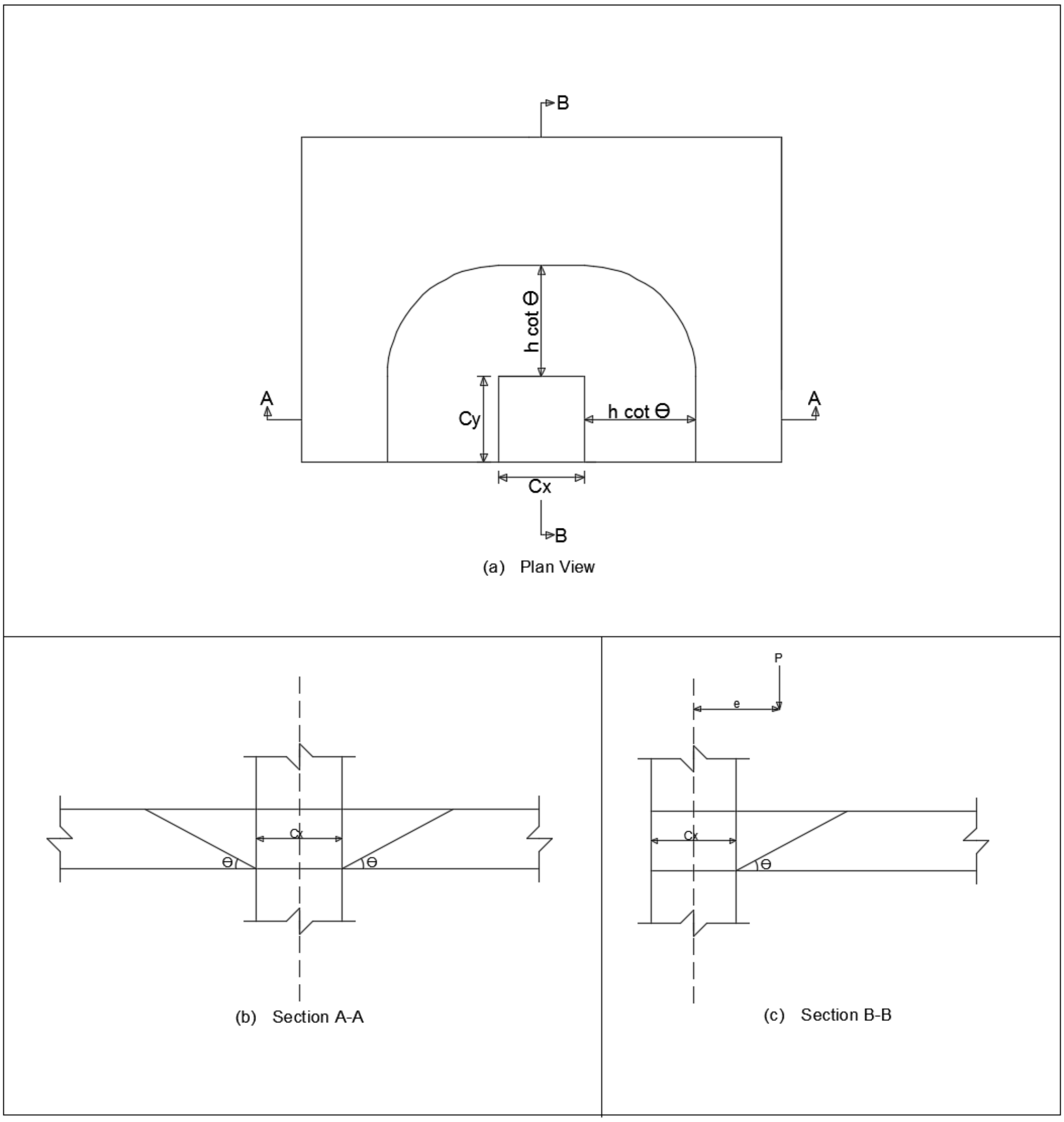

Figure 5.21 Proposed edge punching shear failure surface

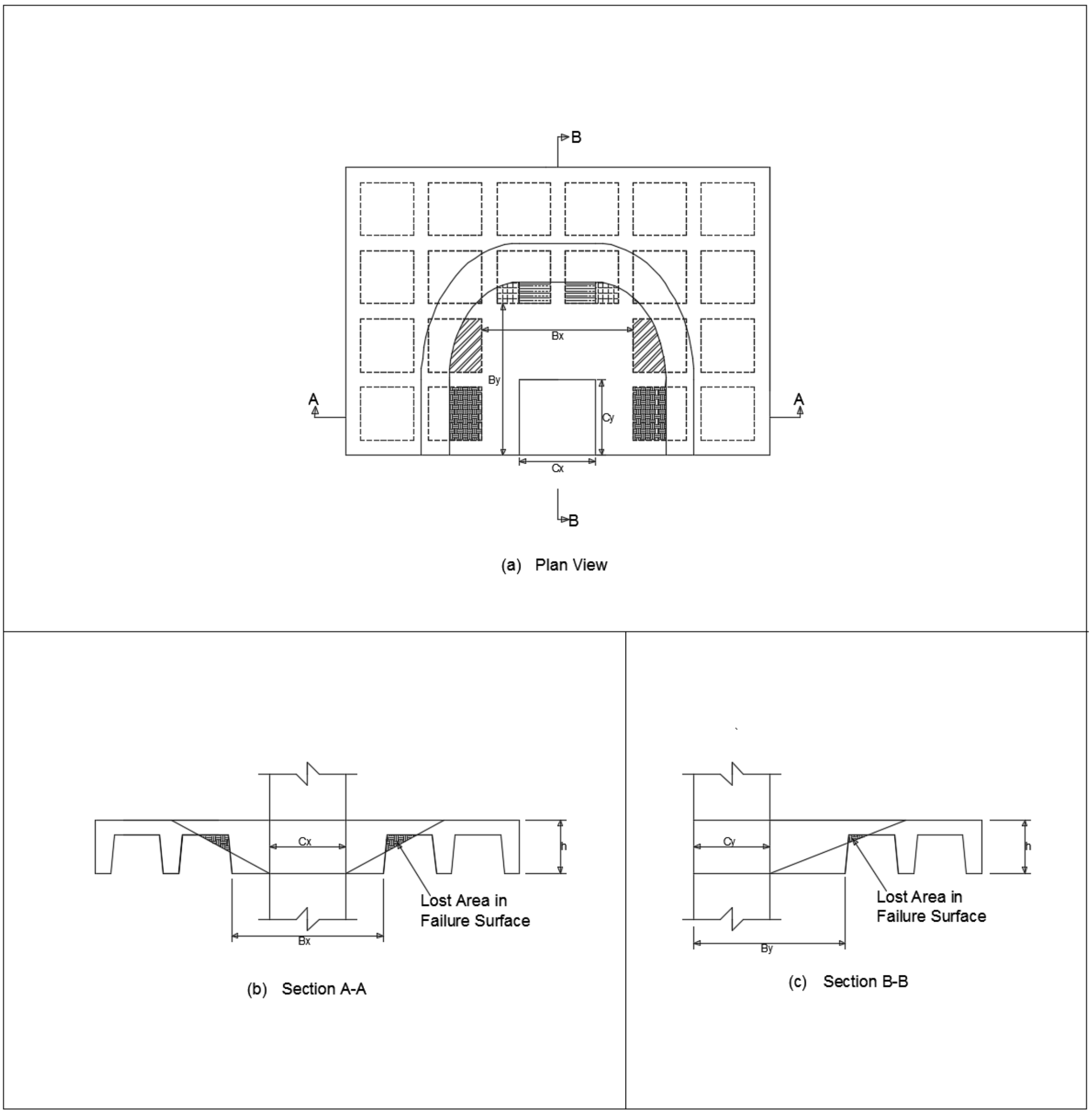

Figure 5.22 Proposed edge punching shear failure surface for waffle slabs with losses

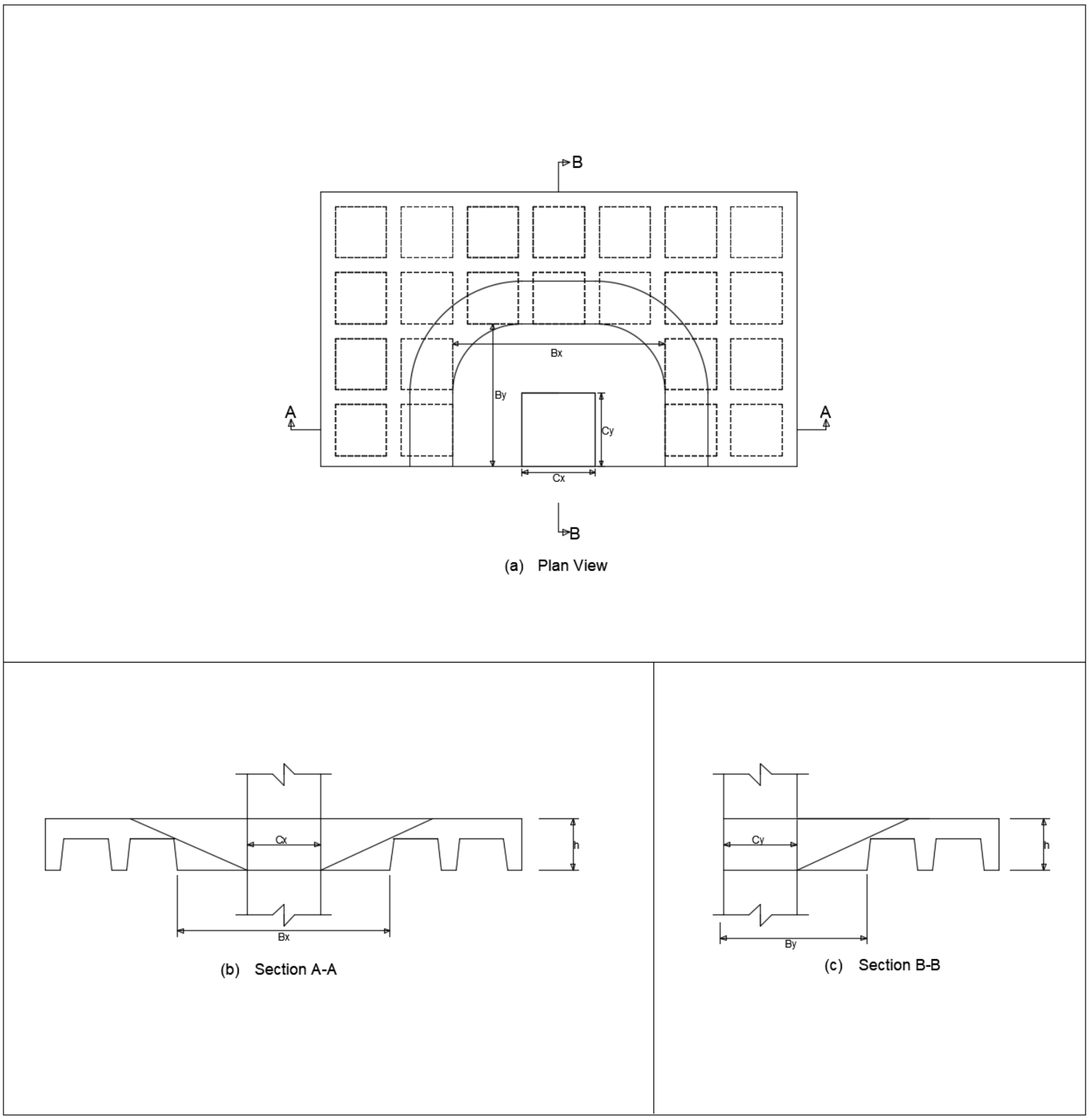

Figure 5.23 Proposed edge punching shear failure surface for waffle slabs with no losses

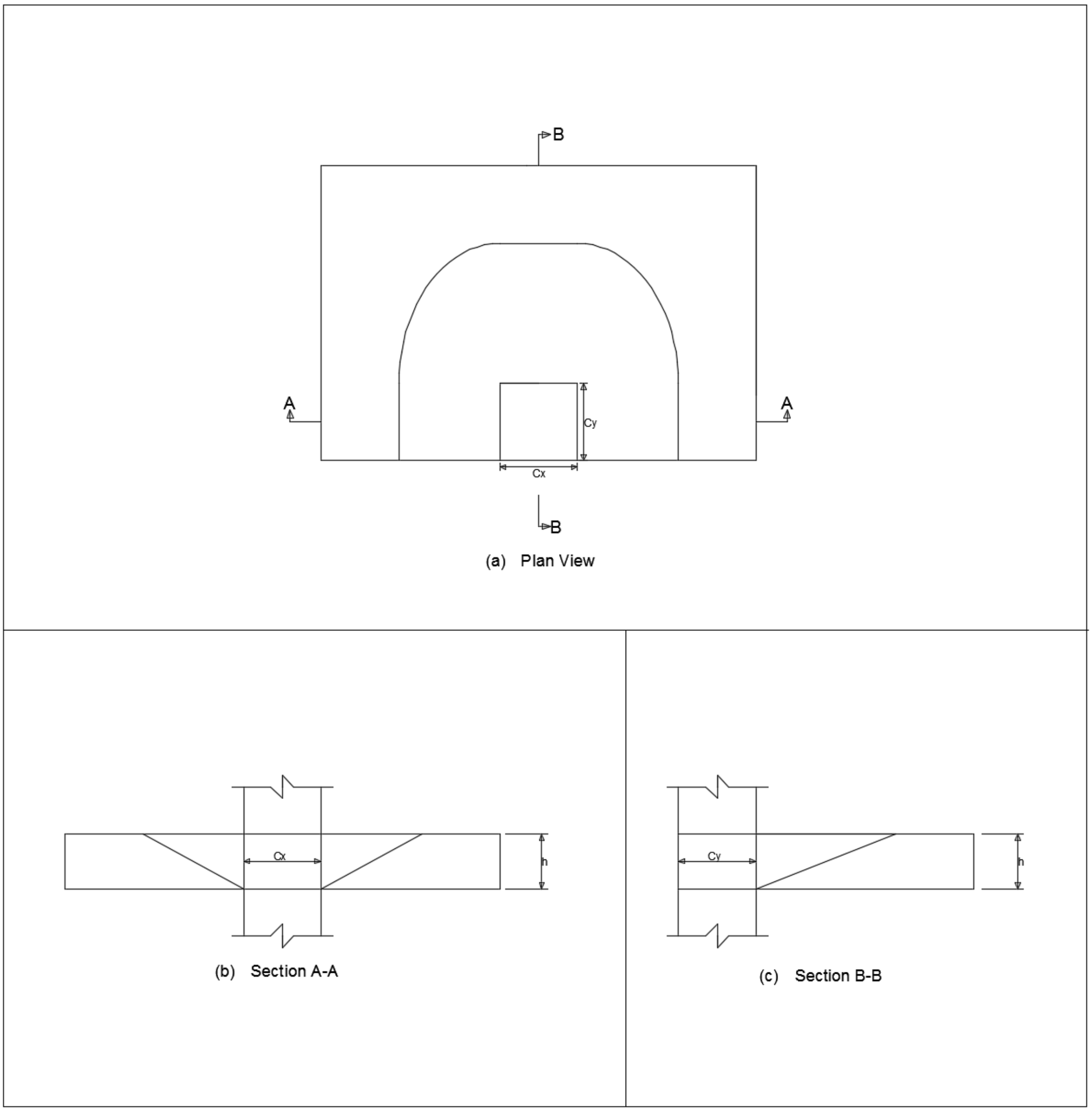

Figure 5.24 Proposed edge punching shear failure surface for solid flat slabs with no losses

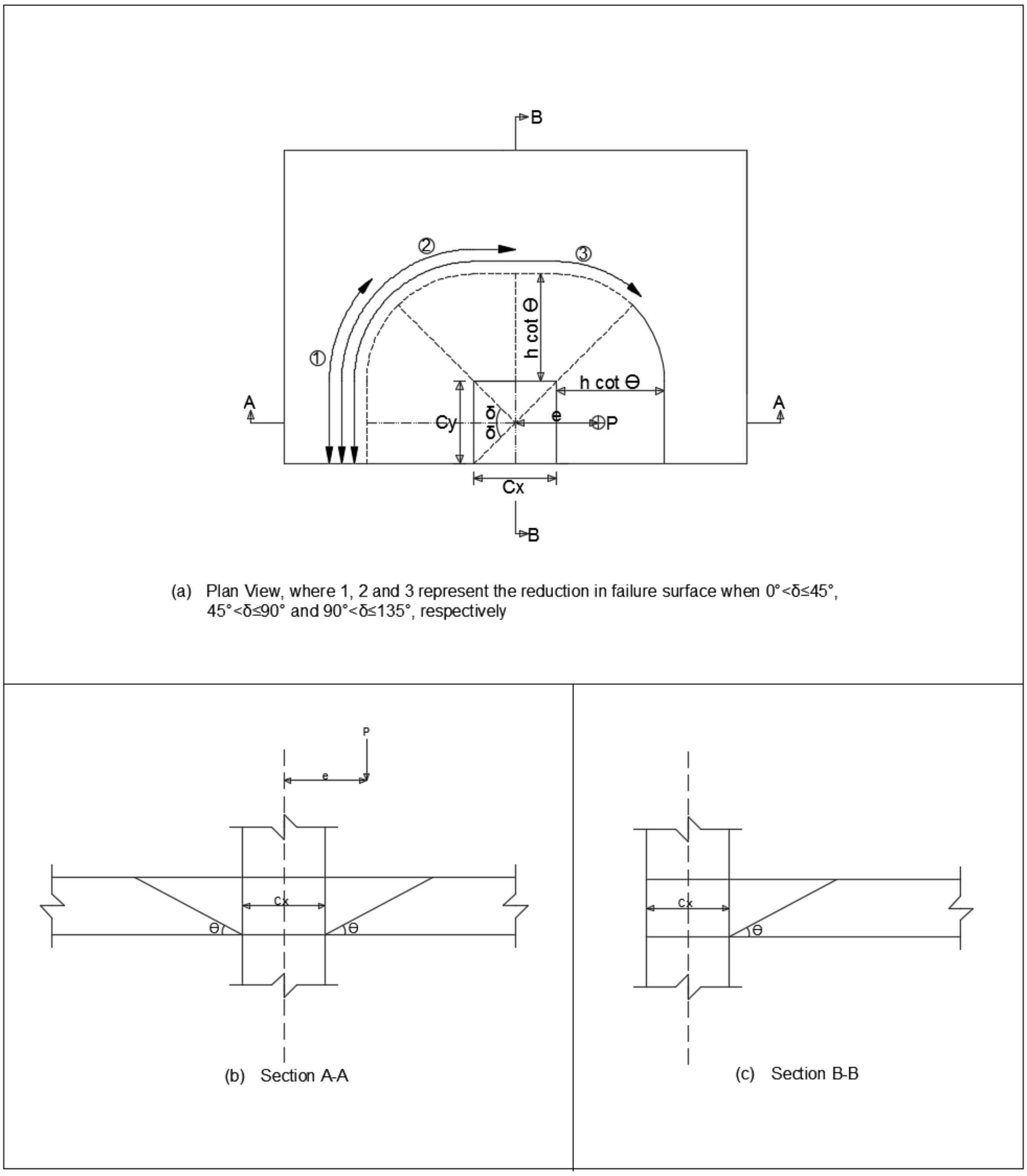

Figure 5.25 Proposed edge punching shear failure surface when the principle angle of moment transfer is 0° from column axis (parallel to the slab edge)

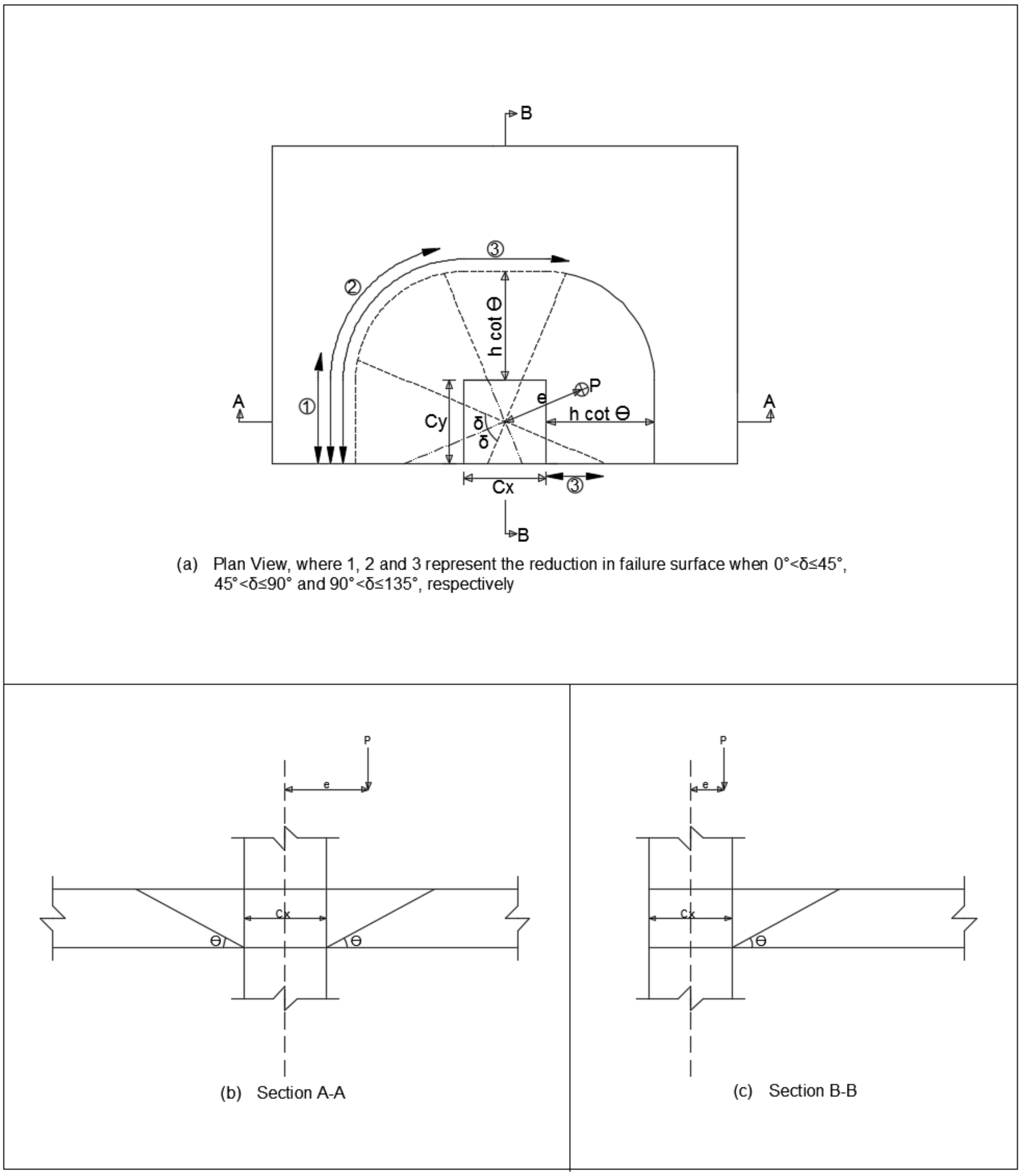

Figure 5.26 Proposed edge punching shear failure surface when the principle angle of moment transfer is 22.5^{o} from column axis

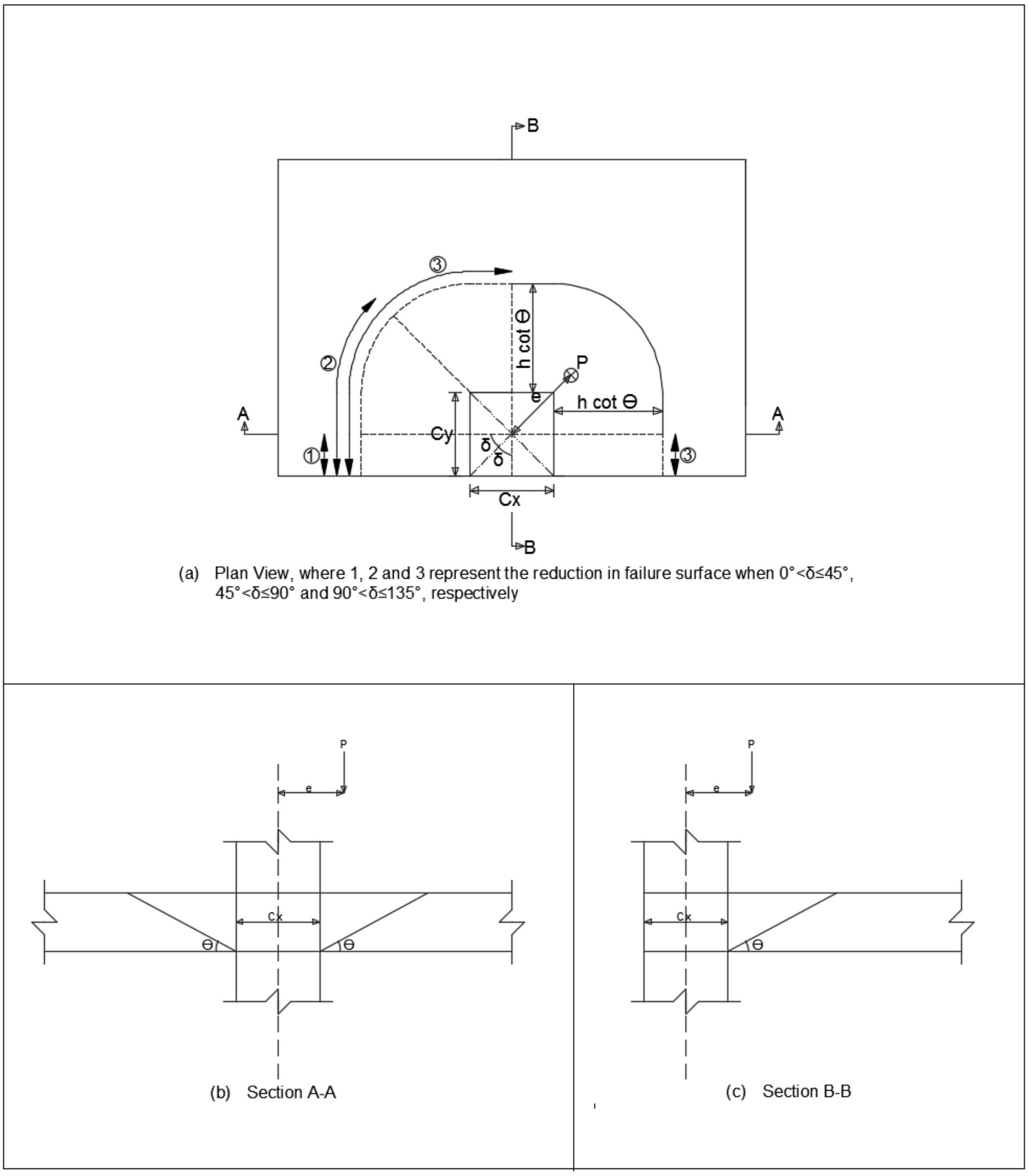

Figure 5.27 Proposed edge punching shear failure surface when the principle angle of moment transfer is 45° from column axis

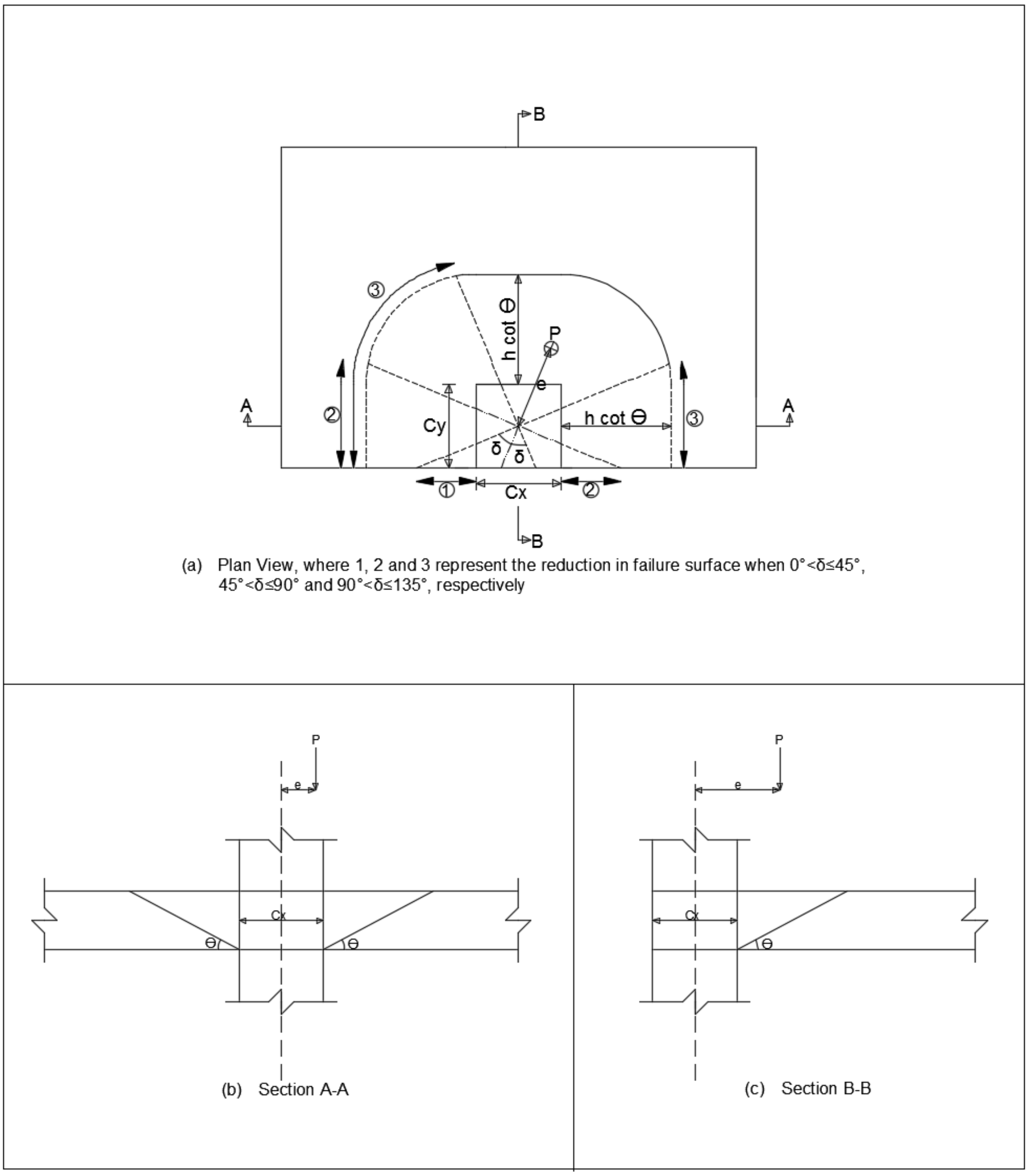

Figure 5.28 Proposed edge punching shear failure surface when the principle angle of moment transfer is 67.5° from column axis

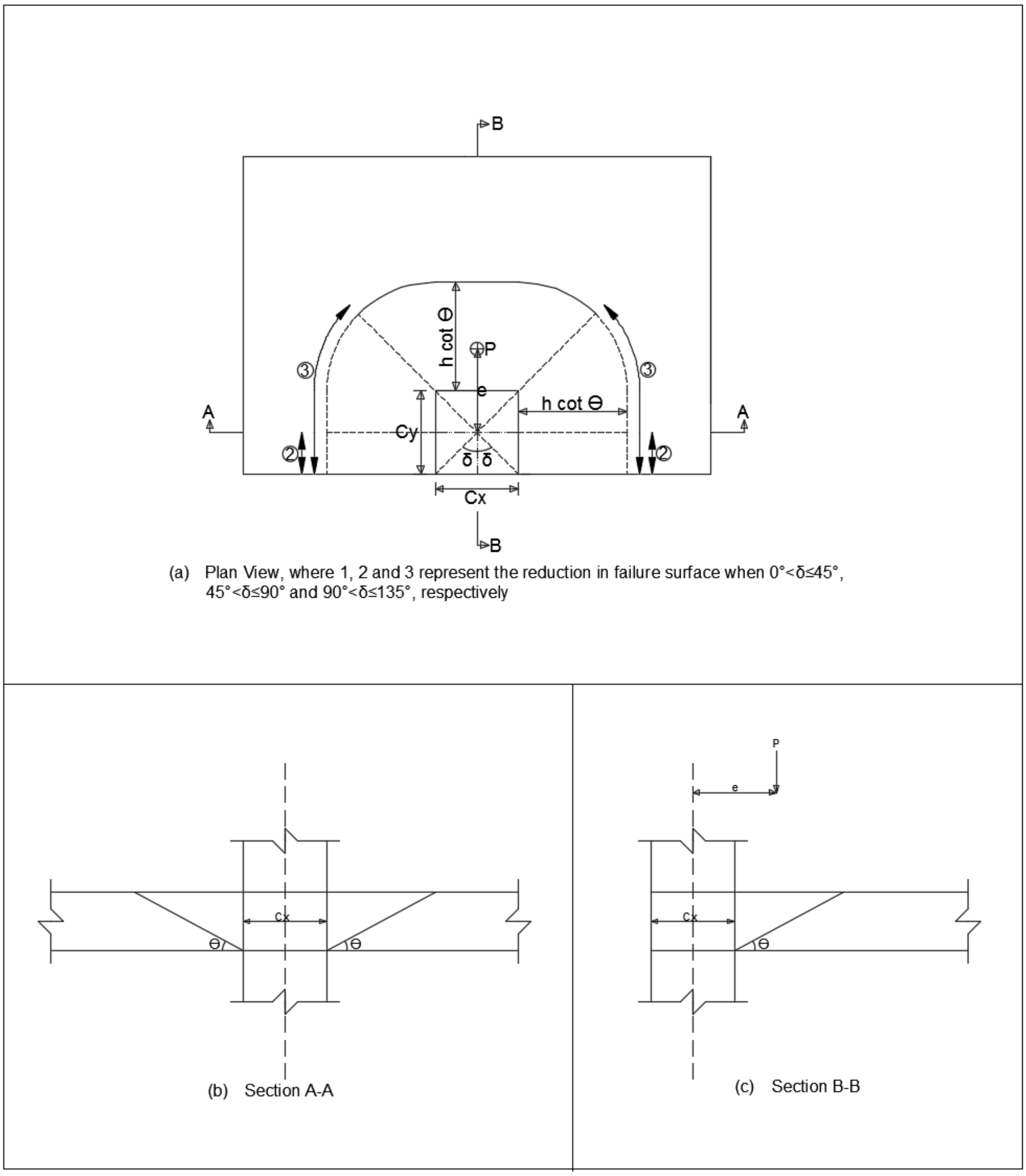

Figure 5.29 Proposed edge punching shear failure surface when the principle angle of moment transfer is 90° from column axis (perpendicular to the slab edge)

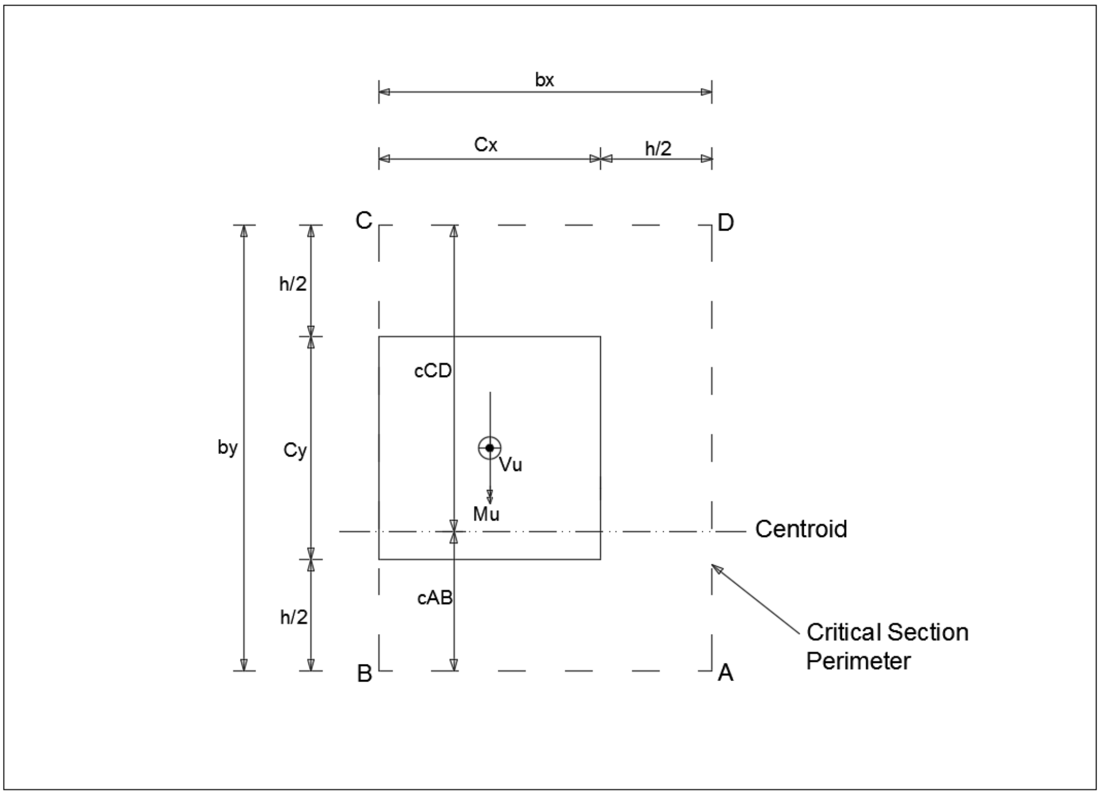

Figure 5.30 Critical section perimeter when the principle angle of moment transfer is 0°
(parallel to the slab edge)

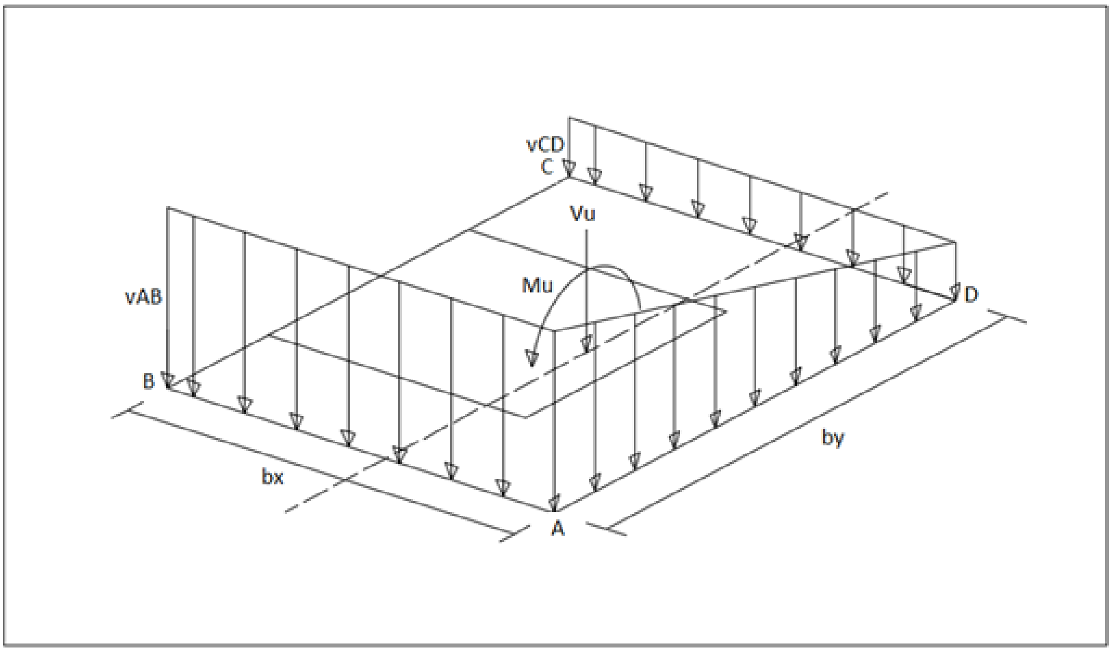

Figure 5.31 Shear stress distribution when the principle angle of moment transfer is 0°
(parallel to the slab edge)

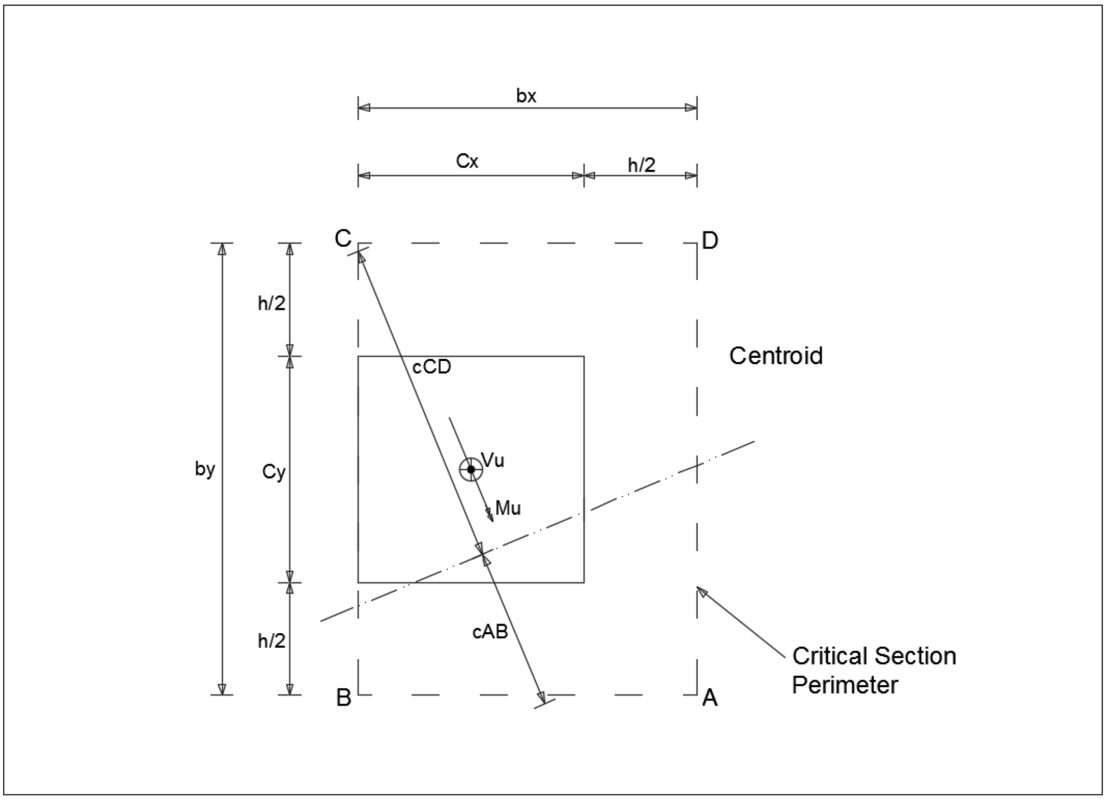

Figure 5.32 Critical section perimeter when the principle angle of moment transfer is 22.5°

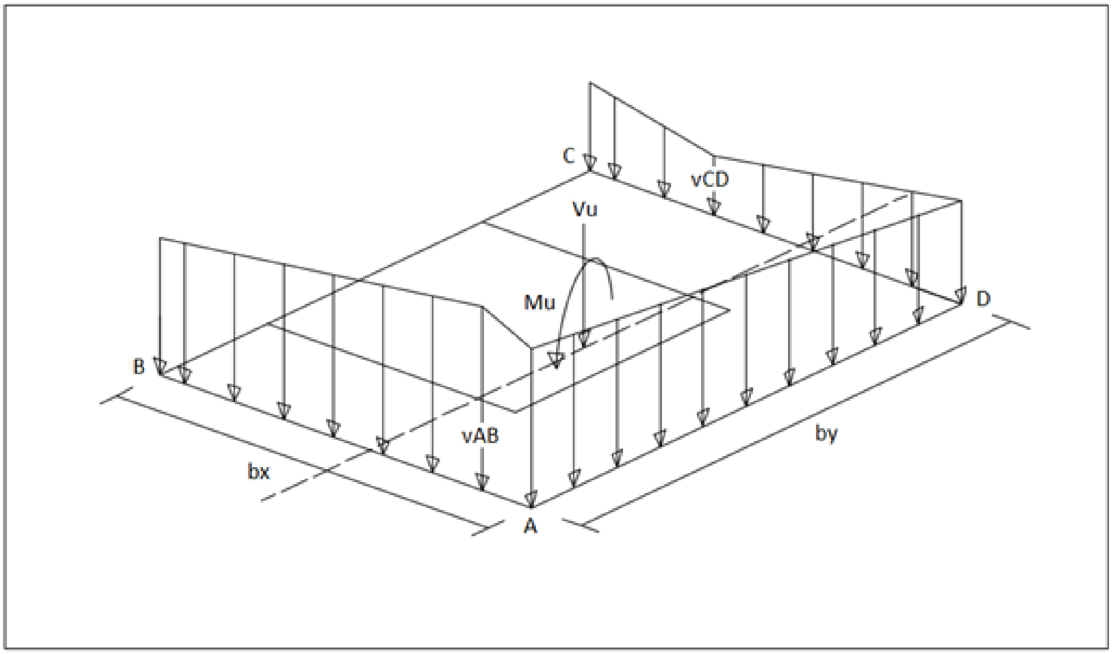

Figure 5.33 Shear stress distribution when the principle angle of moment transfer is 22.5°

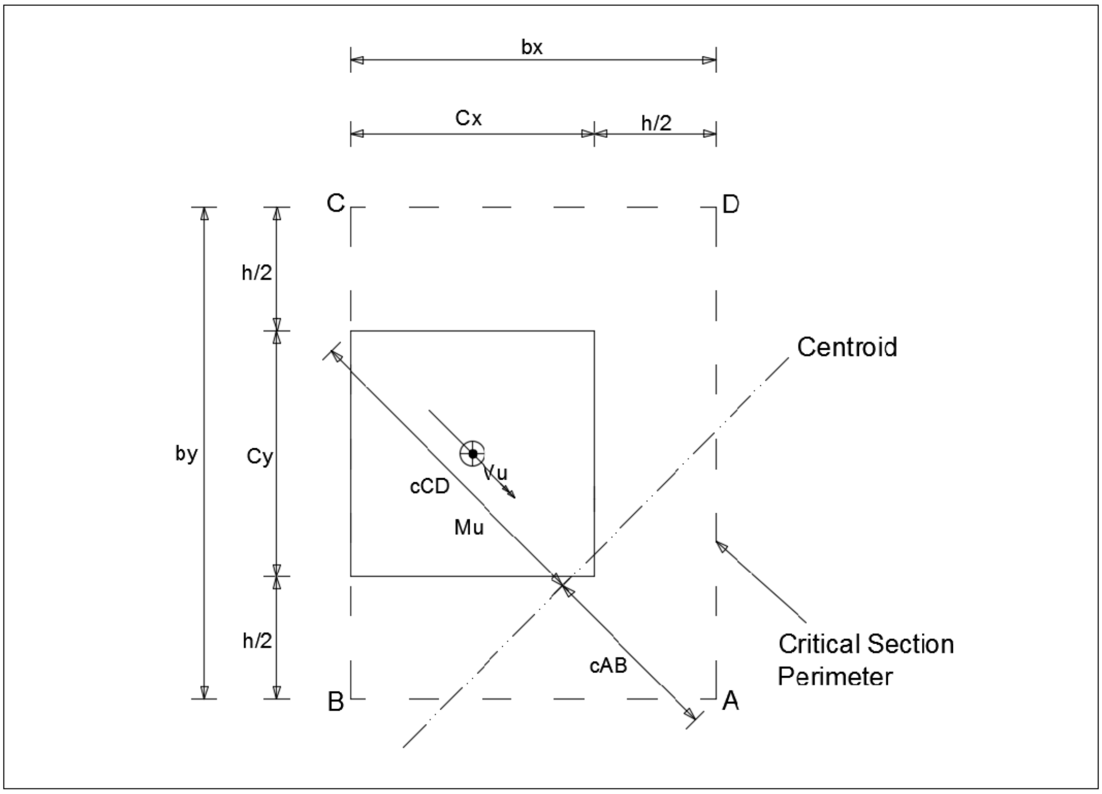

Figure 5.34 Critical section perimeter when the principle angle of moment transfer is 45°

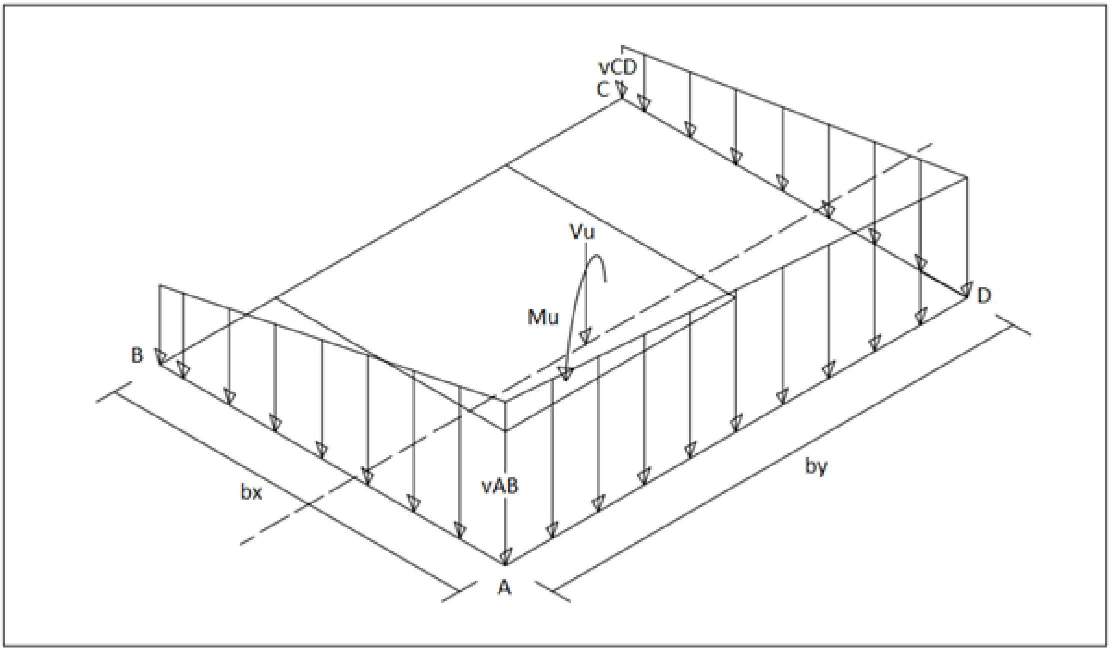

Figure 5.35 Shear stress distribution when the principle angle of moment transfer is 45°

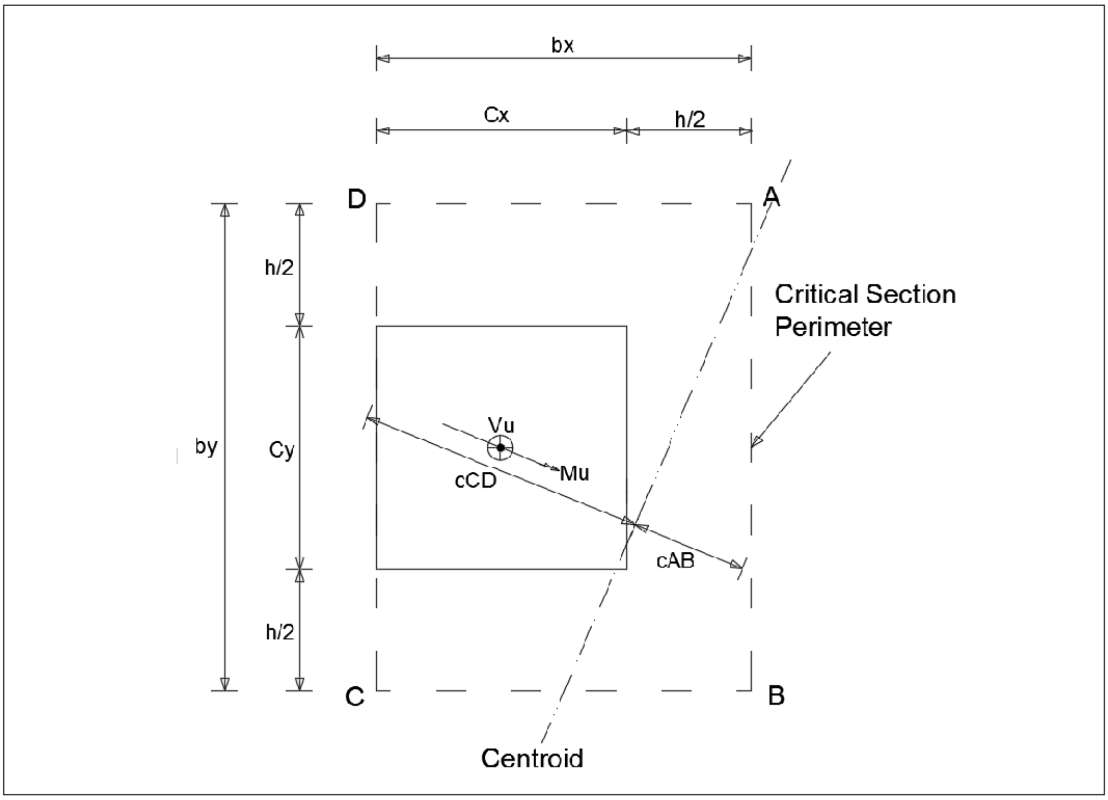

Figure 5.36 Critical section perimeter when the principle angle of moment transfer is 67.5°

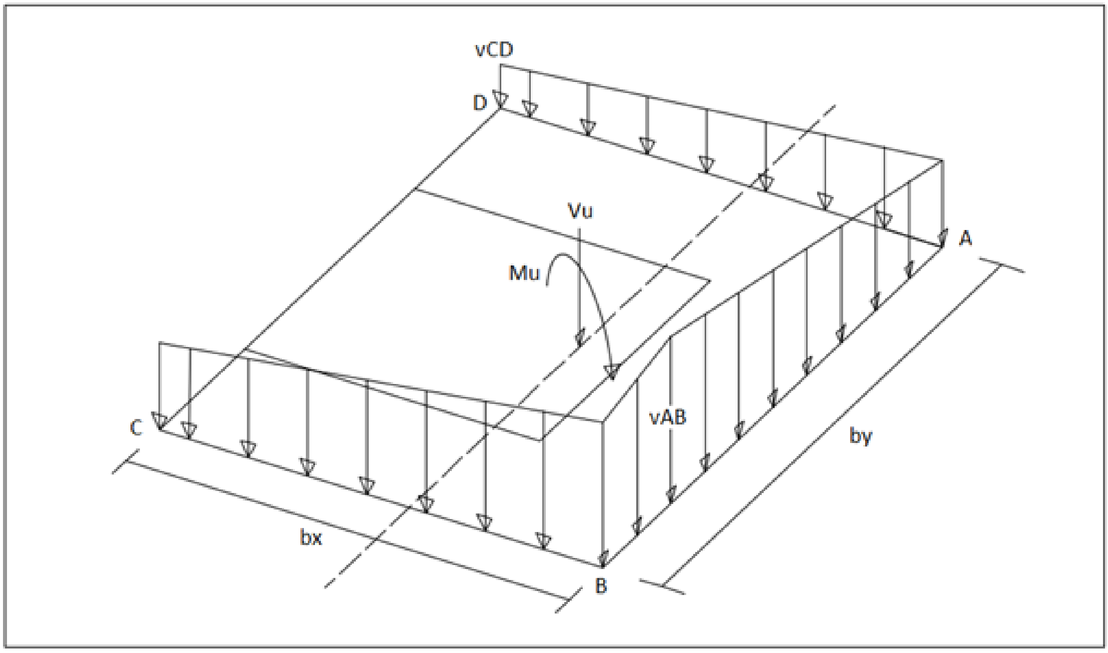

Figure 5.37 Shear stress distribution when the principle angle of moment transfer is 67.5°

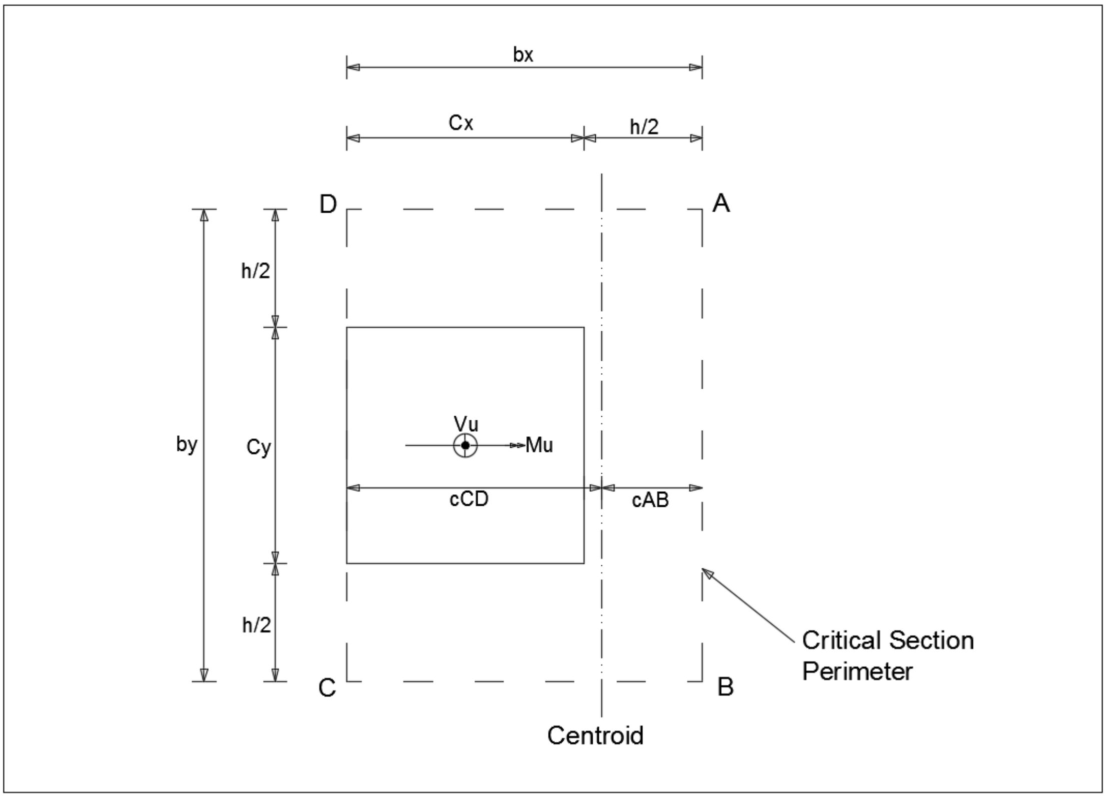

Figure 5.38 Critical section perimeter when the principle angle of moment transfer is 90°
(perpendicular to the slab edge)

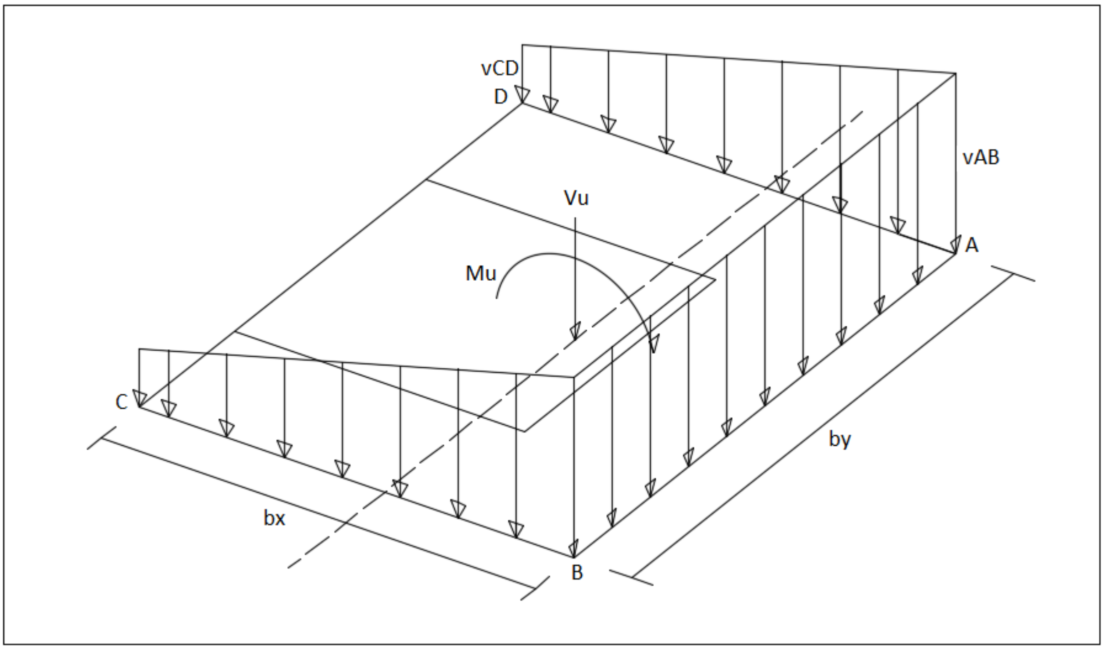

Figure 5.39 Shear stress distribution when the principle angle of moment transfer is 90°
(perpendicular to the slab edge)

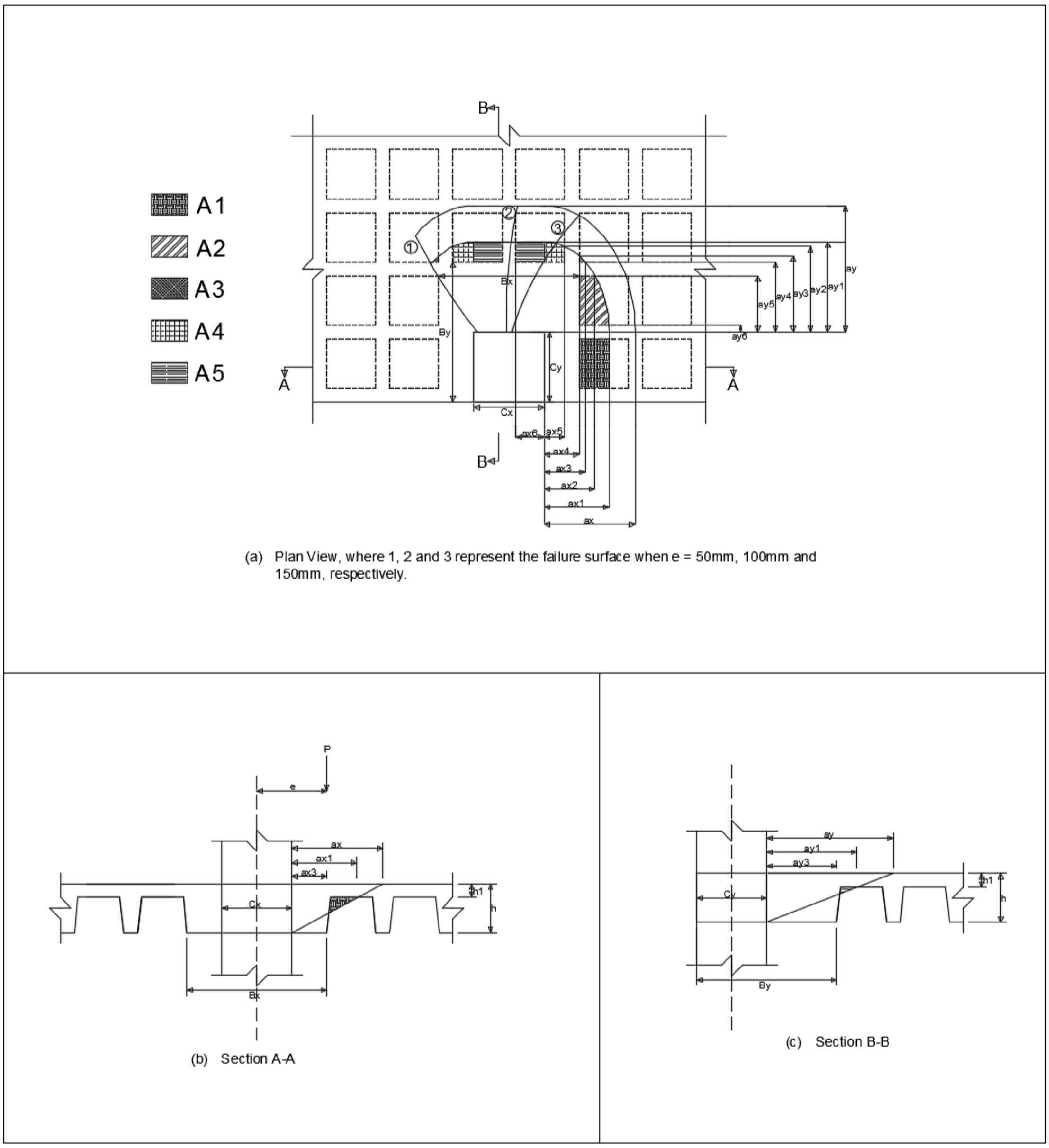

Figure 5.40 Schematic diagram of edge punching shear failure surface when the principle angle of moment transfer is 0^{o} (parallel to the slab edge)

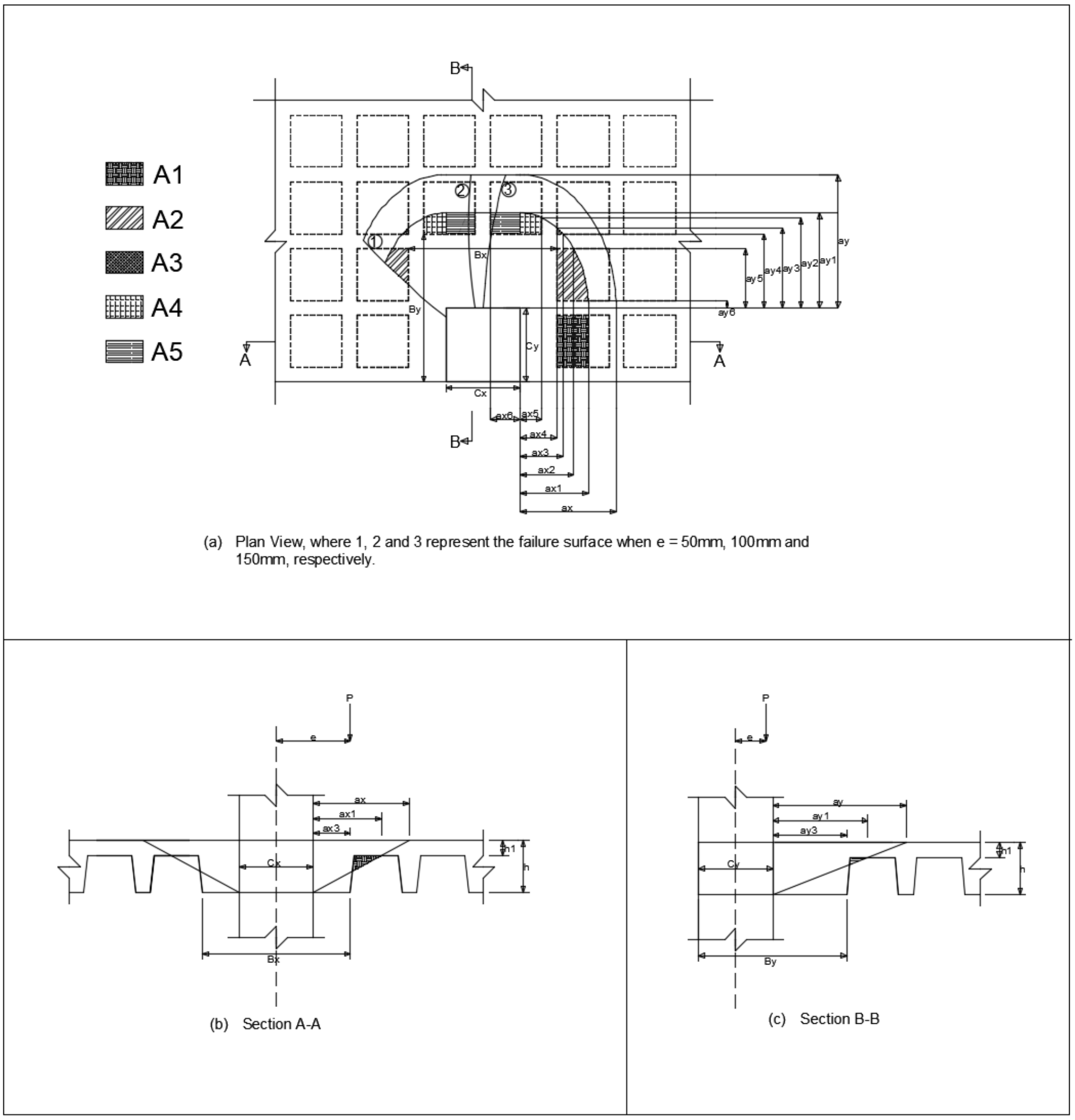

Figure 5.41 Schematic diagram of edge punching shear failure surface when the principle angle of moment transfer is 22.5°

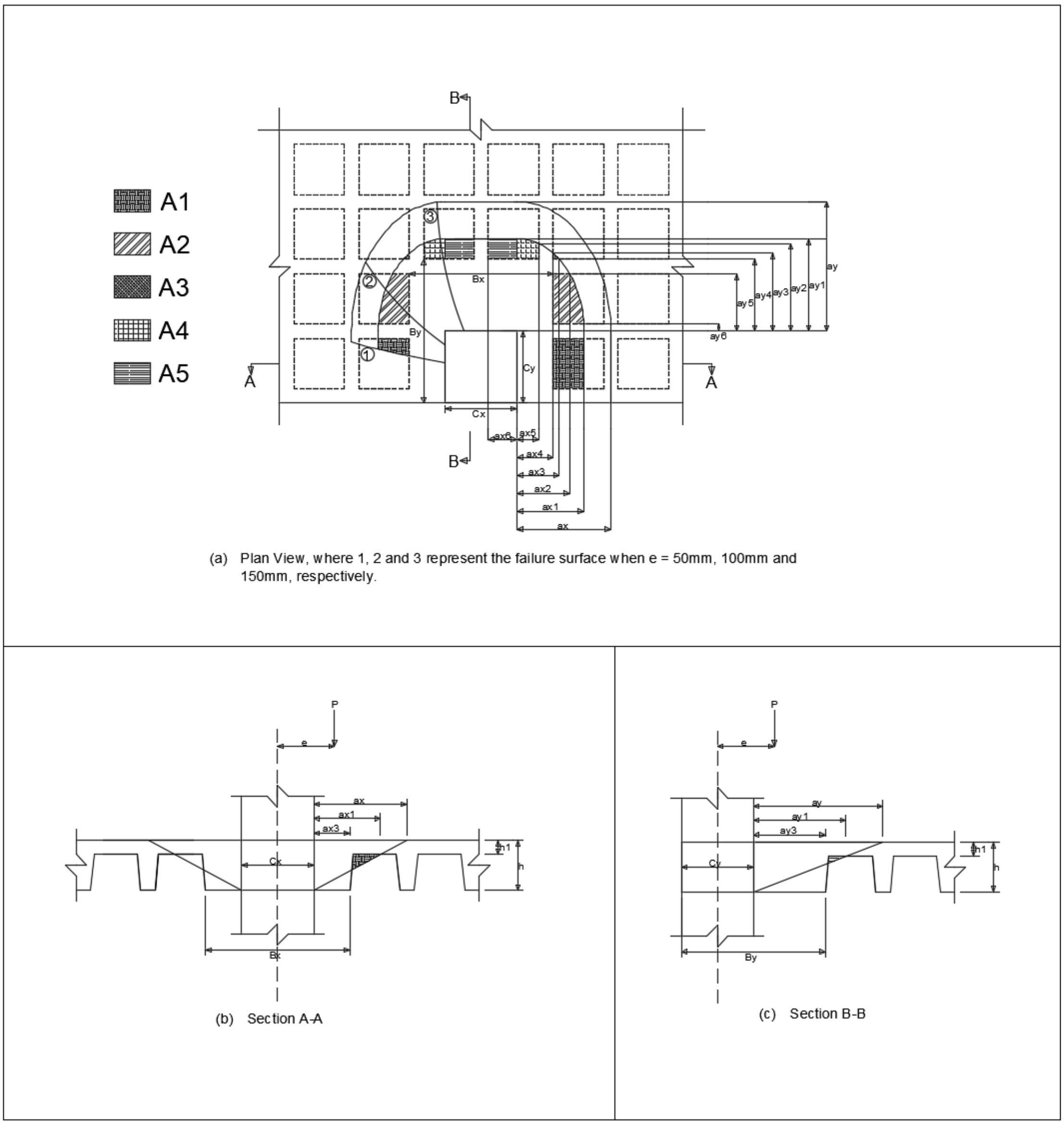

Figure 5.42 Schematic diagram of edge punching shear failure surface when the principle angle of moment transfer is 45^{o}

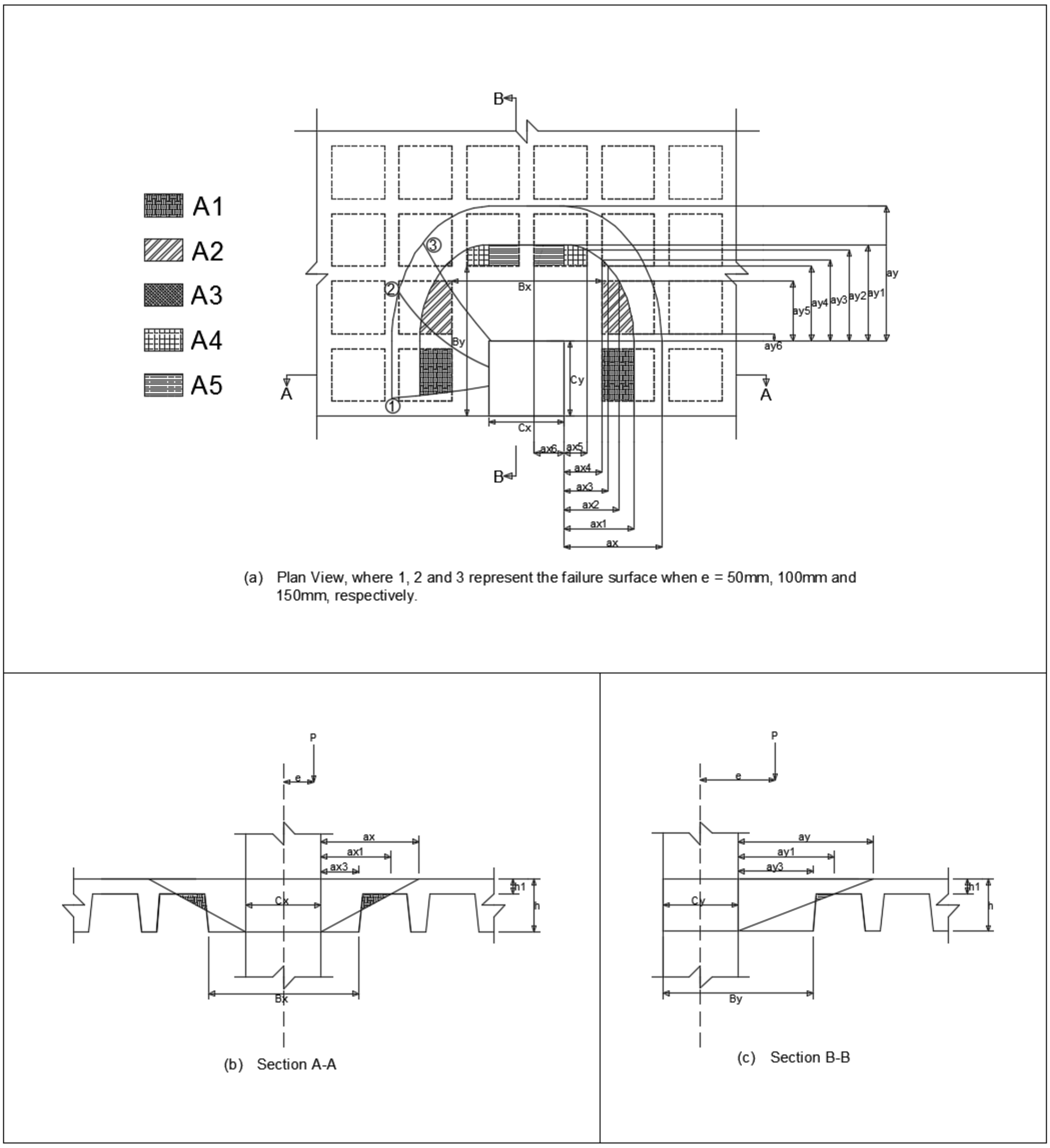

Figure 5.43 Schematic diagram of edge punching shear failure surface when the principle angle of moment transfer is 67.5°

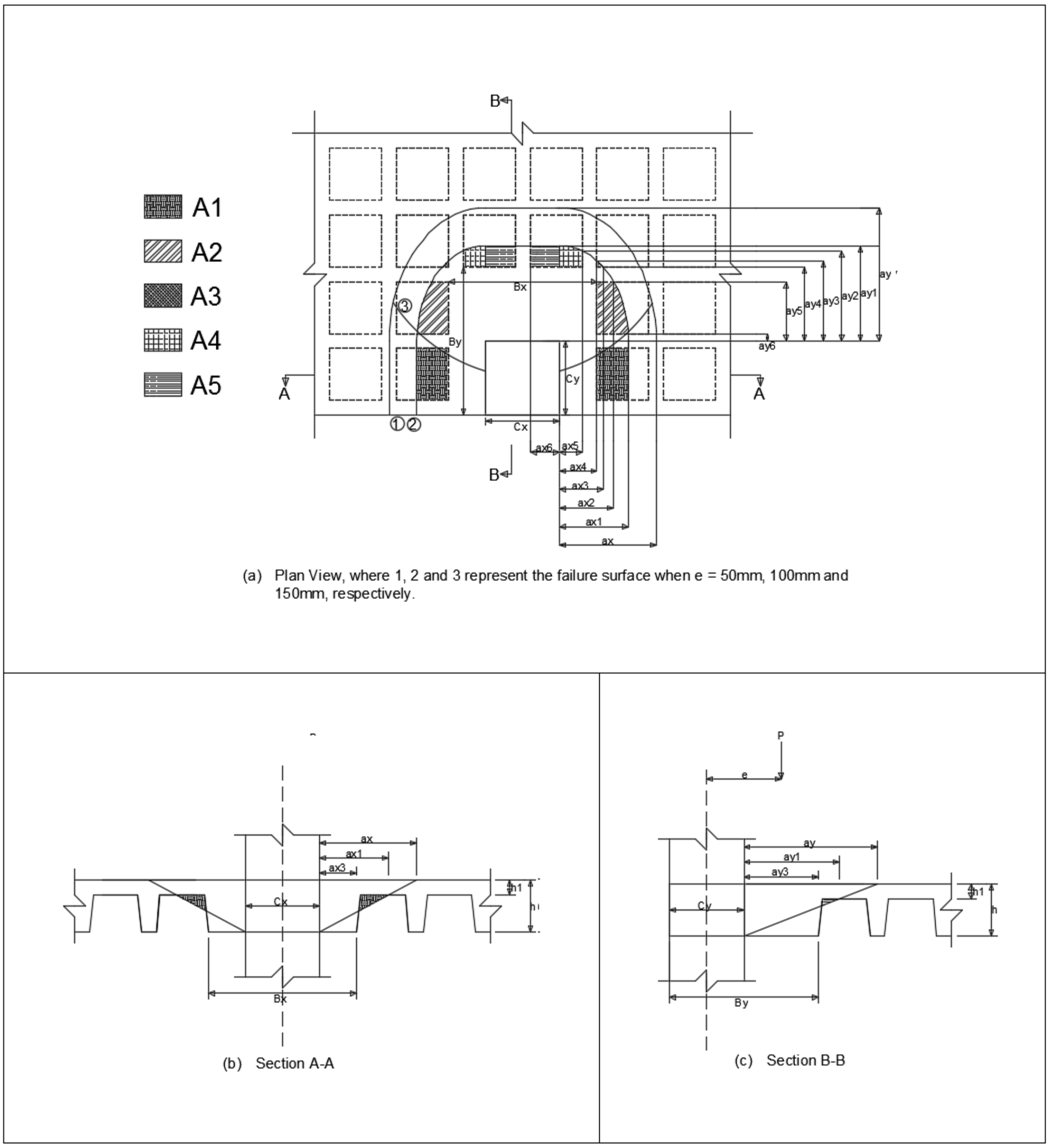

Figure 5.44 Schematic diagram of edge punching shear failure surface when the principle angle of moment transfer is 90^{o} (perpendicular to the slab edge)

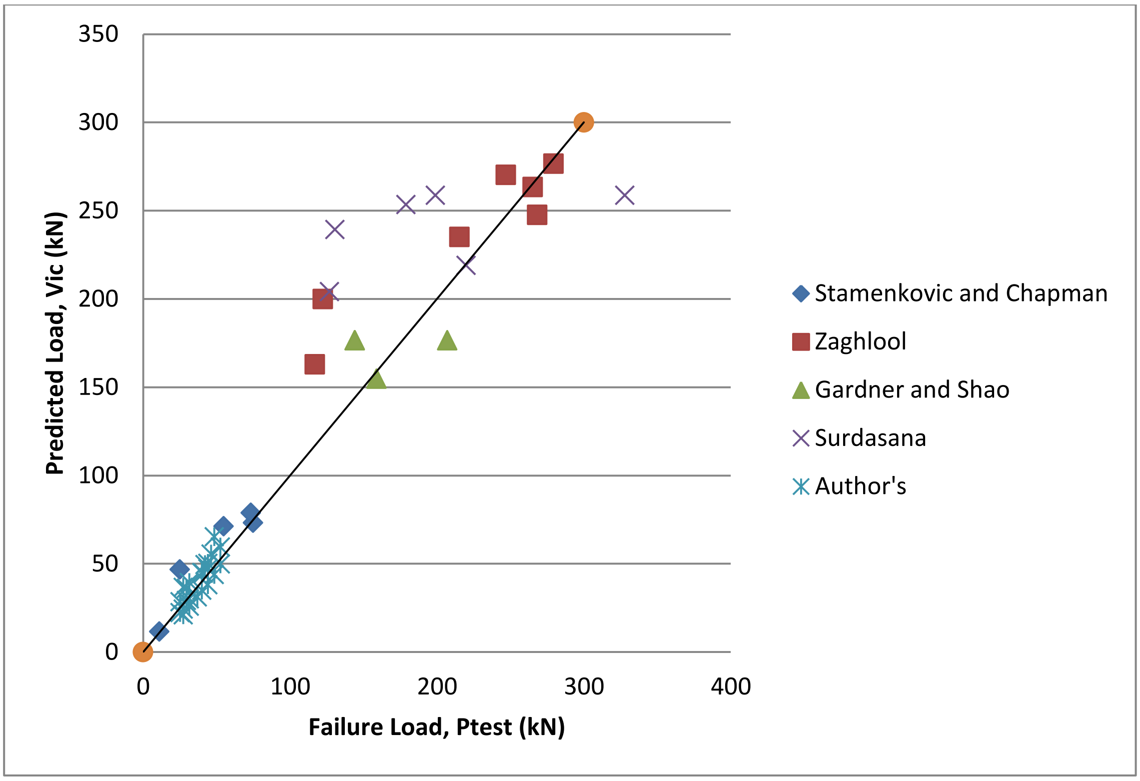

Figure 5.45 Comparison between predicted loads and test failure loads for waffle slabs and solid flat slabs using proposed edge punching model

Chapter 6 Design Models

6.1 Introduction

As reported in Chapter 4, there were two main series investigated in this research: the internal column and edge column series. The internal column series was further split to the concentric punching series and the eccentric punching series. Thus, in Chapter 5, three theoretical models for predicting the observed failure mechanism were proposed which gave good agreements with both the historical and the author's test results.

The current codes of practice (ACI-318[1], BS8110[14] and Eurocode 2[22]) have adopted the control surface approach for the design of punching shear mechanism, as explained in Chapter 2. The similarities among these three codes are that the control failure surface is a virtual vertical shear surface at an assumed distance from the column faces. The differences between these codes are the variation in the assumed distance. However, these codes do not cover the design of waffle slabs.

In this chapter, three empirical design models are proposed to predict the failure load of the waffle slabs. For the concentric series at internal column, the proposed design model is basically a modified version of that in the current Eurocode 2 model for solid flat slabs in accommodating the section losses observed in the waffle slabs. For the eccentric series at internal column, the proposed design model is also a modified version of that in the current Eurocode 2 for solid flat slabs in accommodating the section losses observed in the waffle slabs with the introduction of a new variable in the moment transfer factor, β, to account for the effect of the principle angle of biaxial moment transfer. Lastly, for the edge column series, the proposed design model replicates the same basis as the eccentric punching at internal column series.

The shear strength equation used in the proposed empirical design models is maintained as reported by the Eurocode 2, without any modifications required. However, when comparing with test results, the partial safety factor, γ_m, is set to 1 in the shear strength equation and the shear retention factor, α, is also introduced into the proposed design models when comparing micro-concrete waffle slab specimens cast with maximum aggregate size of 2 mm.

6.2 Design model for internal column series

6.2.1 Introduction

The design models proposed for the internal column series are divided into 2 categories: EC2-IC and EC2-IE; where the former allows the prediction of concentric punching capacities and the latter allows the prediction of eccentric punching capacities.

The concrete shear strength of the models adopted that of the current EC2, as shown below:

$$v_c = \frac{0.18}{\gamma_m} k(100\rho\sigma_c)^{1/3} \qquad \text{(Eq. 6.1)}$$

Where:

k = the size effect factor, where $k = 1 + \sqrt{\frac{200}{d}}$

ρ = the steel reinforcement ratio

σ_c= the concrete cylindrical compressive strength.

The location of the critical perimeter also remains unchanged at a distance, 2d, away from the column faces, (see Figure 6.1), but the critical shear perimeter will be reduced depending on the geometry of the waffle slab (see Sections 6.2.2. and 6.2.3)

$$u = 2C_x + 2C_y + 4\pi d \qquad \text{(Eq. 6.2)}$$

Where:

C_x= the column size at x-axis

C_y= the column size at y-axis

d = the effective depth

6.2.2 Model EC2-IC

Similar to the geometrical categories in Chapter 5, the proposed design model calculates the reduction on the critical shear perimeter when the width of the solid section is narrower than $(C + 5.2d)$, but otherwise, the critical shear perimeter will be identical to that of EC2 for a solid flat slab. Depending on the width of the waffles and the top slab's thickness, the effective shear surface of the punching revolution for a waffle slab could be less than that for a solid flat slab. Therefore, an effective shear factor, φ, has been introduced to determine the degree of the reductions incurred.

The effective shear factor calculates the ratio of the loss in the projected area in the presence of waffles to the total projected area in the absence of waffles, as shown in Figure 6.2.

$$\varphi_x = 1 - \frac{a_{x1}d_2}{a_x d} \qquad \text{(Eq. 6.3)}$$

$$\varphi_y = 1 - \frac{a_{y1} d_2}{a_y d} \tag{Eq. 6.4}$$

Where:

a_{x1}, a_{y1}, d_2 = as defined in Figure 6.2

a_x, a_y = shear span which is $\leq 2.6d$, in x-direction and y-direction, respectively

d = the effective depth

The effective critical shear perimeter for punching mechanism on a waffle slab is therefore defined as the following equation:

$$u = 2(\varphi_x)^3 C_x + 2(\varphi_y)^3 C_y + 4\pi \left(\frac{\varphi_x + \varphi_y}{2}\right)^3 d \tag{Eq. 6.5}$$

Where:

φ_x, φ_y = effective shear factor, in x-direction and y-direction, respectively

C_x, C_y = column size, in x-direction and y-direction, respectively

d = the effective depth

Therefore, the concentric punching capacity of a waffle slab can be computed from the following equation:

$$V_{IC} = \alpha\ v_c\ u\ d \tag{Eq. 6.6}$$

Where:

α = shear retention factor, 0.7 for micro-concrete and 1.0 for normal-concrete.

v_c = concrete shear strength, as defined in Eq. 6.1

u = effective critical shear perimeter, as defined in Eq. 6.5

d = the effective depth

From Eq. 6.6, the punching capacity of a waffle slab can be predicted using the existing design equations with the introduction of an effective shear perimeter factor, u. That is, if the width of the solid section is wider than $2.6d$ (at one side of the column), the effective shear factor will resolve to unity making the Model EC2-IC identical to the code's model, and hence, predicts the punching capacities for solid flat slabs.

6.2.2.1 Comparison with test results

The comparisons between the Eurocode 2's model, the proposing Model EC2-IC, and the historical test results for solid flat slabs are presented from Table 6.1 to Table 6.6 and summarized in Table 6.7. While comparisons with waffle slab are presented in Table 6.8.

In these comparisons, the partial safety factor in these design codes has been set to 1. An important factor adopted in the proposed design model is the micro-concrete shear retention factor, α, which was identified by Boswell & Wong[11] and later, verified by Fong[23]. They revealed that the shear resistance of micro-concrete specimens (cast with maximum aggregate size of 2mm) reduced from its peak to a residual value (about 70% of the peak) as compared to normal-concrete specimen (maximum aggregate size of 20 mm). Therefore, the shear retention factor of 0.7 is applied for micro-concrete specimens.

Table 6.7 summarises the comparisons with 87 historical test results[7,20,49,53,77,82] and it can be inferred that the Eurocode 2's model underestimates the concentric punching capacity by 10%, which is still deemed within the acceptable range when the material partial safety factor is taken into account. However, in Table 6.8, Eurocode 2's model exhibits an overestimation of about 31% on the author's waffle slab test results, while, Model EC2-IC (which carries the critical shear area factor, u) exhibits good agreement with mean ratio of 1.00 with the test results. Such agreement inferred that the effective shear area factor, u, has been able to account for the observed loss of punching capacity on the waffle slab specimens.

6.2.3 Model EC2-IE

This model allows the prediction of punching shear capacity of waffle slabs at the internal column in the presence of biaxial moment transfer. As reported in Chapter 5, the proposed design model will account for the reduction on the critical shear perimeter when the width of the solid section is narrower than $(C + 5.2d)$, but otherwise, the critical shear perimeter will be identical to that of EC2 for a solid flat slab. Depending on the width of the waffles and the top slab's thickness, the effective shear surface of the punching revolution for a waffle slab could be less than that for a solid flat slab. Therefore, the effective shear factor, φ, as indicated in Eq. 6.3 and Eq. 6.4, is applied.

Similar to Model EC2-IC, the perimeter of the critical section is assumed to be a function of the sectional geometrical properties of the waffle slabs and the effective shear perimeter is calculated as according to Eq. 6.5.

6.2.3.1 Moment transfer factor, β

In the presence of moment transfer, EC2 introduces a moment transfer factor, β in the equation to predict the punching capacity of the slab specimens. EC2 assumes that the unbalanced moment at a slab-internal column connection is redistributed into unbalanced shear stresses as shown in Figure 6.3. These unbalanced shear stresses are assumed to be added to the shear stresses contributed from the vertical load.

The moment transfer factor, β is therefore defined as follows:

$$\beta_{internal} = 1 + k \frac{M_{test}}{P_{test}} \frac{u}{w_1} \qquad \text{(Eq. 6.7)}$$

Where:

k = coefficient dependent on ratio between column dimensions (can be obtained from EC2 Table 6.1)

M_{test} = total unbalanced moment transferred

P_{test} = applied vertical load

u = perimeter of critical section (for internal column)

w_1 = corresponds to distribution of shear stress, where for rectangular column,

$$w_1 = \frac{{C_x}^2}{2} + C_x C_y + 4C_y d + 16d^2 + 2\pi d C_x$$

C_x, C_y = column size, in x-direction and y-direction, respectively

d = the effective depth

In the calculation of moment transfer factor, EC2 does not take account of the effect of the principle angle of biaxial moment transfer. In this research, the principle angle of biaxial moment transfer portrayed a reduction in punching capacity when the principle angle was rotated away from orthogonal axis, 0°. The author therefore proposed a new moment transfer factor to account for the effect of the principle angle of biaxial moment transfer, which is:

$$\beta_{EC2-IE} = 1 + k\frac{M_{test}}{P_{test}}\frac{u}{w_1}\frac{1}{(\cos\forall)^2} \qquad \text{(Eq. 6.8)}$$

Where:

$\forall$ = the principle angle of biaxial moment transfer

Therefore, the eccentric punching capacity of a waffle slab can be computed from the following equation:

$$V_{IE} = \frac{1}{\beta_{EC2-IE}} \alpha \, v_c \, u \, d \qquad \text{(Eq. 6.9)}$$

6.2.3.2 Comparison with test results

The comparisons between the previous researchers' test failure loads and the calculated punching capacity as according to EC2 was carried out to evaluate the accuracy of Eurocode 2 with regards to the eccentric punching shear mechanism on solid flat slabs are presented from Table 6.10 to Table 6.15. In this calculation, the material partial safety factor in this design equation is set to 1.

Another important factor adopted in the current codes approach is the micro-concrete shear retention factor, a, which was introduced by Wong and later, verified by Fong. They revealed that the shear resistance of micro-concrete specimens reduced from its peak to a residual value (about 70% of the peak) as compared to normal-concrete specimen. Therefore, the shear retention factor of 0.70 is applied for micro-concrete specimens.

Table 6.16 shows the summary of comparisons of the previous researcher's test results[18,19,26,27,35,44,50,53,59] against the EC2 predicted punching capacities. From the 42 slab specimens, the mean ratio of test results to predicted strength was 0.98 with a standard deviation of 0.09. This again proves that no modification to the existing EC2 is required.

However, based on Table 6.17, EC2 overestimates the author's waffle slab specimens by 27%. The overestimation was found to be mainly due to the fact that EC2 does not acknowledge the loss of shear surface within the critical shear perimeter and the reduction of punching capacity due to the effect of increasing the principle angle of biaxial moment transfer. By applying the modified critical shear perimeter and the modified moment transfer factor as proposed by Model EC2-IE, the mean ratio of test results to predicted strength was increased to 0.98 with a standard deviation of 0.16, as shown in Table 6.18. This finding verifies that Model EC2-IE allows a good estimation on the punching capacity of waffle slab specimens by maintaining the same control surface approach in EC2.

6.3 Design model for edge column series

6.3.1 Introduction

In EC2, two instances of edge punching are introduced in the prediction of edge punching failure loads of slab specimens, which are: in the presence of moment transfer parallel to the slab edge and in the presence of moment transfer perpendicular to the slab edge.

A design model is proposed in this section to predict the edge punching capacities of solid flat slabs and waffle slabs in the presence of moment transfer parallel and perpendicular to the slab edge. The design model will be compared with previous researchers' test results and author's test results to gain confidence on the proposed model.

The concrete shear strength of this design model remains the same as that of the current EC2 (see Eq 6.1). In the calculation to predict the punching shear capacity at the edge column, EC2 proposed a reduced critical shear perimeter within the column's dimensions but the location of the critical perimeter remains unchanged at a distance, 2d, away from the column faces (see Figure 6.4).

$$u_* = C_x + C_y + 2\pi d \quad \text{(Eq. 6.10)}$$

Where:

C_x= the column size at x-axis

C_y= the column size at y-axis

d = the effective depth

This proposed design model allows a reduction in the critical shear perimeter depending on the geometry of the waffle slabs.

6.3.2 Model EC2-E

Similar to the geometrical categories in Chapter 5, the proposed design model calculates the reduction on the critical shear perimeter when the width of the solid section is narrower than $(C + 5.2d)$, but otherwise, the critical shear perimeter will be identical to that of EC2 for a solid flat slab. Depending on the width of the waffles and the top slab's thickness, the effective shear surface of the punching revolution for an edge waffle slab could be less than that for a solid flat slab. Therefore, the similar effective shear factor, φ, has been determined from Eq. 6.3 and Eq. 6.4, but with different dimensions to accommodate for the edge boundary conditions as shown in Figure 6.5.

The effective shear perimeter of the critical section for edge punching mechanism in the presence of waffles in the slab specimen is defined as the following equation:

$$u_* = (\varphi_x)^3 C_x + \left(\varphi_y\right)^3 C_y + 2\pi \left(\frac{\varphi_x+\varphi_y}{2}\right)^3 d \qquad \text{(Eq. 6.11)}$$

6.3.2.1 Moment transfer factor, β

In the presence of moment transfer, EC2 introduces a moment transfer factor, β into the equation to predict the punching capacity of the slab specimens. EC2 assumes that the unbalanced moment at a slab-edge column connection is distributed into unbalanced shear stresses as shown in Figure 6.6. These unbalanced shear stresses are assumed to be added to the shear stresses contributed from the vertical load.

However, the moment transfer factor differs for two types of loading in the edge column. When the eccentricity of the loading is towards the interior of the slab, EC2 proposed that

β is set to unity, where the assumption of no moment is being transferred with the reduced critical shear perimeter. However, when the moment transfer is parallel to the slab edge, EC2 proposed that β is calculated using the following equation:

$$\beta_{edge} = 1 + k\frac{M_{test}}{P_{test}}\frac{u_*}{w_1} \quad \text{(Eq. 6.12)}$$

Where:

k = coefficient dependent on ratio between column dimensions (can be obtained from EC2 Table 6.1)

M_{test} = total unbalanced moment transferred

P_{test} = applied vertical load

u_* = reduced perimeter of critical section (edge)

w_1 = corresponds to distribution of shear stress, where for rectangular column,

$$w_1 = \frac{{C_x}^2}{2} + C_xC_y + 4C_yd + 16d^2 + 2\pi dC_x$$

C_x, C_y = column size, in x-direction and y-direction, respectively

d = the effective depth

As mentioned in Model EC2-IE, the moment transfer factor does not allow the effect of the principle angle of biaxial moment transfer to take place in the prediction of the punching capacity of edge slab specimens. In Chapter 4, the principle angle of biaxial moment transfer displayed an increase in the punching capacity when the column with parallel loading is being rotated away and towards the column with perpendicular loading. Therefore, an attempt was made to account this effect. The author therefore proposed a new moment transfer factor for the edge column series, in order to account the effect of the principle angle of biaxial moment transfer, which is:

$$\beta_{EC2-E} = 1 + k\frac{M_{test}}{P_{test}}\frac{u_*}{w_1}(\cos\forall)^2 \qquad \text{(Eq. 6.13)}$$

Where:

$\forall$ = the principle angle of biaxial moment transfer,

0^0 when the moment transfer is parallel to the slab edge,

90^0 when the moment transfer is perpendicular to the slab edge,

Therefore, the edge punching capacity of a waffle slab can be computed from the following equation:

$$V_E = \frac{1}{\beta_{EC2-E}}\,\alpha\, v_c\, u_*\, d \qquad \text{(Eq. 6.14)}$$

6.3.2.2 Comparison with test results

The comparisons between the previous researchers' test failure loads and the calculated punching capacity as according to EC2 was carried out to evaluate the accuracy of Eurocode 2 with regards to the edge punching shear mechanism on solid flat slabs are presented from Table 6.19 to Table 6.22. In this calculation, the material partial safety factor in these design codes has been set to 1.

An important factor adopted in the proposing design model is the micro-concrete shear retention factor, a, which was introduced by Boswell & Wong[11] and later, verified by Fong[23]. They revealed that the shear resistance of micro-concrete specimens reduced from its peak to a residual value (about 70% of the peak) as compared to normal-concrete specimen. Therefore, the shear retention factor of 0.70 is applied for micro-concrete specimens.

Table 6.23 shows the summary of comparisons of the previous researcher's test results[24,73,74,83] against the EC2 predicted punching capacities. From the 22 slab specimens, the mean ratio of test results to predicted strength was 0.91 with a standard deviation of 0.32. By accounting the use of material partial safety factor in the actual real world's design, the mean ratio of 0.91 becomes acceptable and therefore, no modification is proposed to the current EC2 edge punching mechanism.

In the EC2 edge punching mechanism, the design code introduced two different moment transfer factor, one in which the moment transfer is parallel to the slab edge and the other in which the moment transfer is perpendicular to the slab edge. There is no explanation in EC2 on the punching capacity of slab specimens if the moment transfer lies between the two axes. Therefore, comparisons between both moment transfer factors and test results with different principle angles of biaxial moment transfer are tabulated in Table 6.24. It is evident that the moment transfer factors for perpendicular loading to be more conservative by 10% as compared to for parallel loading but both do still overestimate the actual punching capacity of edge slab specimens. This overestimation was mainly due to not accounting the critical surface losses in the waffle sections of the waffle slabs and the reducing effect of the principle angle of biaxial moment transfer. Thus, after applying the modified critical shear perimeter and the modified moment transfer factor as proposed by Model EC2-E, the mean ratio of test results to predicted strength was increased to 1.05 with a standard deviation of 0.16, as shown in Table. This finding verifies that Model EC2-E allows a good estimation on the punching capacity of edge waffle slab specimens by maintaining the same control surface approach in EC2.

6.4 Summary

Three empirical design models based on the current Eurocode 2 have been proposed for the use of design; Model EC2-IC for concentric punching at internal column mechanism, Model EC2-IE for eccentric punching at internal column mechanism and Model EC2-E for edge punching mechanism.

By comparing previous researchers' test results with the EC2 predicted loads, the mean ratio between test and prediction was found to be very good and no modification is required to enhance the accuracy of EC2. However, for all three series, EC2 overestimates the punching capacities of all waffle slab specimens mainly due to not accounting the critical shear losses and the effect of the principle angle of biaxial moment transfer. Therefore, an effective shear factor was introduced to the perimeter of the critical section so as to simulate the actual loss of shear area within the waffle sections and a modified moment transfer factor was recommended to simulate the effect of the principle angle of biaxial moment transfer.

In general, when the perimeter of the critical shear area reduces and the moment transfer factor increases, the punching capacity reduces due to less effective shear area available and more moment being transferred, respectively. All the proposed design models achieved very good agreement with the author's test result.

Table 6.1 Test and predicted failure loads of slab specimens reported by Moe[53] as according to EC2[22] and using Model EC2-IC

Specimen No	Column Size, C_x (mm)	Effective depth, d (mm)	Cylindrical Compressive Strength, σ_c (N/mm^2)	Reinforcement Ratio, ρ (%)	Test Failure Load, P_{test} (kN)	EC2 Predicted Load, V_{IC} (kN)	Model EC2-IC Predicted Load, V_{EC2-IC} (kN)	$\frac{P_{test}}{V_{IC}}$	$\frac{P_{test}}{V_{EC2-IC}}$
S1-60	254	114	23.3	1.1	389.0	345.5	345.5	1.42	1.42
S5-60	203	114	22.2	1.1	343.0	311.7	311.7	1.46	1.46
S1-70	254	114	24.5	1.1	393.0	351.4	351.4	1.36	1.36
S5-70	203	114	23.0	1.1	378.0	315.4	315.4	1.42	1.42
H1	254	114	26.1	1.1	372.0	358.9	358.9	1.29	1.29
R2	152	114	27.6	1.4	394.0	330.3	330.3	1.14	1.14
M1A	305	114	20.8	1.5	433.0	399.6	399.6	1.45	1.45
						Mean		1.36	1.36
						Standard Deviation		0.12	0.12

Table 6.2 Test and predicted failure loads of slab specimens reported by Eltsner & Hognestad[20] as according to EC2[22] and using Model EC2-IC

Specimen No	Column Size, C_x (mm)	Effective depth, d (mm)	Cylindrical Compressive Strength, σ_c (N/mm^2)	Reinforcement Ratio, ρ (%)	Test Failure Load, P_{test} (kN)	EC2 Predicted Load, V_{IC} (kN)	Model EC2-IC Predicted Load, V_{EC2-IC} (kN)	$\frac{P_{test}}{V_{IC}}$	$\frac{P_{test}}{V_{EC2-IC}}$
A1a	254	118	11.3	1.2	303.0	287.1	287.1	1.06	1.06
A1b	254	118	20.2	1.2	365.0	348.4	348.4	1.05	1.05
A1c	254	118	23.2	1.2	356.0	365.1	365.1	0.98	0.98
A1d	254	118	29.4	1.2	351.0	395.2	395.2	0.89	0.89
A1e	254	118	16.2	1.2	356.0	324.1	324.1	1.10	1.10
A2a	254	114	10.9	2.5	334.0	349.8	349.8	0.95	0.95
A2b	254	114	15.6	2.5	400.0	394.5	394.5	1.01	1.01
A2c	254	114	29.9	2.5	467.0	490.1	490.1	0.95	0.95
A7b	254	114	22.3	2.5	512.0	444.5	444.5	1.15	1.15
A3a	254	114	10.2	3.7	356.0	392.3	392.3	0.91	0.91
A3b	254	114	18.1	3.7	445.0	474.1	474.1	0.94	0.94
A3c	254	114	21.2	3.7	534.0	500.0	500.0	1.07	1.07
A3d	254	114	27.6	3.7	547.0	545.9	545.9	1.00	1.00
A4	356	114	20.9	1.2	400.0	393.1	393.1	1.02	1.02
A5	356	114	22.2	2.5	534.0	518.0	518.0	1.03	1.03
A6	356	114	20.0	3.7	498.0	572.1	572.1	0.87	0.87
B4	254	114	38.2	1.0	334.0	391.9	391.9	0.85	0.85
B9	254	114	35.1	2.0	505.0	481.9	481.9	1.05	1.05
B11	254	114	10.8	3.0	329.0	372.3	372.3	0.88	0.88
B14	254	114	40.4	3.0	578.0	578.0	578.0	1.00	1.00
						Mean		0.99	0.99
						Standard Deviation		0.08	0.08

Table 6.3 Test and predicted failure loads of slab specimens reported by Base[7] as according to EC2[22] and using Model EC2-IC

Specimen No	Column Size, C_x (mm)	Effective depth, d (mm)	Cylindrical Compressive Strength, σ_c (N/mm^2)	Reinforcement Ratio, ρ (%)	Test Failure Load, P_{test} (kN)	EC2 Predicted Load, V_{IC} (kN)	Model EC2-IC Predicted Load, V_{EC2-IC} (kN)	$\frac{P_{test}}{V_{IC}}$	$\frac{P_{test}}{V_{EC2-IC}}$
A1/M2	203	117	15.5	1.5	346.0	316.5	316.5	1.09	1.09
A1/M3	203	121	14.2	1.9	307.0	348.3	348.3	0.88	0.88
A1/M4	203	124	14.0	1.0	259.0	289.4	289.4	0.89	0.89
A1/M5	203	117	21.0	1.2	346.0	325.2	325.2	1.06	1.06
A2/M2	203	117	32.8	1.5	419.0	406.4	406.4	1.03	1.03
A2/M3	203	121	32.5	1.9	430.0	459.0	459.0	0.94	0.94
A2/T1	203	124	39.3	1.0	419.0	408.3	408.3	1.03	1.03
A2/T2	203	124	41.4	1.7	439.0	495.8	495.8	0.89	0.89
A3/M1	203	124	18.8	1.0	247.0	319.3	319.3	0.77	0.77
A3/M2	203	102	19.3	1.7	336.0	295.4	295.4	1.14	1.14
A3/M3	203	117	27.3	1.9	298.0	413.6	413.6	0.72	0.72
A3/T1	203	121	20.6	1.0	328.0	318.3	318.3	1.03	1.03
A3/T2	203	119	16.0	1.2	298.0	303.9	303.9	0.98	0.98
A4/M1	203	114	38.3	1.1	259.0	372.5	372.5	0.70	0.70
A4/M2	203	119	29.2	1.5	341.0	400.1	400.1	0.85	0.85
A4/M3	203	117	32.2	1.9	541.0	437.0	437.0	1.24	1.24
A4/T1	203	114	32.8	1.1	384.0	353.8	353.8	1.09	1.09
A4/T2	203	117	29.3	1.2	402.0	363.3	363.3	1.11	1.11
							Mean	0.97	0.97
							Standard Deviation	0.15	0.15

Table 6.4 Test and predicted failure loads of slab specimens reported by Yitzhaki[82] as according to EC2[22] and using Model EC2-IC

Specimen No	Column Size, C_x (mm)	Effective depth, d (mm)	Cylindrical Compressive Strength, σ_c (N/mm^2)	Reinforcement Ratio, ρ (%)	Test Failure Load, P_{test} (kN)	EC2 Predicted Load, V_{IC} (kN)	Model EC2-IC Predicted Load, V_{EC2-IC} (kN)	$\frac{P_{test}}{V_{IC}}$	$\frac{P_{test}}{V_{EC2-IC}}$
II-1	221	82	10.5	1.2	181.0	168.3	168.3	1.08	1.08
II-4a	221	82	17.9	0.9	245.0	182.9	182.9	1.34	1.34
II-4b	201	82	9.8	0.9	162.0	143.5	143.5	1.13	1.13
II-4c	201	82	13.9	0.9	215.0	161.1	161.1	1.33	1.33
IIB20-2	201	83	15.0	0.9	307.0	167.5	167.5	1.83	1.83
IIB30-1	300	80	17.6	2.0	239.0	268.6	268.6	0.89	0.89
II-2	221	82	9.8	1.3	152.0	168.8	168.8	0.90	0.90
II-6	221	82	21.6	1.3	240.0	220.0	220.0	1.09	1.09
II-9	201	79	9.3	8.5	157.0	283.9	283.9	0.55	0.55
III-3	221	82	18.1	1.2	201.0	201.9	201.9	1.00	1.00
7	119	82	10.0	0.7	117.0	109.0	109.0	1.07	1.07
II-10	119	82	11.7	1.0	98.0	129.2	129.2	0.76	0.76
							Mean	1.08	1.08
							Standard Deviation	0.32	0.32

Table 6.5 Test and predicted failure loads of slab specimens reported by Tomaszewicz[77] as according to EC2[22] and using Model EC2-IC

Specimen No	Column Size, C_x (mm)	Effective depth, d (mm)	Cylindrical Compressive Strength, σ_c (N/mm^2)	Reinforcement Ratio, ρ (%)	Test Failure Load, P_{test} (kN)	EC2 Predicted Load, V_{IC} (kN)	Model EC2-IC Predicted Load, V_{EC2-IC} (kN)	$\frac{P_{test}}{V_{IC}}$	$\frac{P_{test}}{V_{EC2-IC}}$
ND65-1-1	200	275	64.3	1.4	2050.0	1757.6	1757.6	1.17	1.17
ND65-2-1	150	200	70.2	1.7	1200.0	1094.9	1094.9	1.10	1.10
ND95-1-1	200	275	83.7	1.4	2250.0	1919.0	1919.0	1.17	1.17
ND95-1-3	200	275	89.9	2.5	2400.0	2369.9	2369.9	1.01	1.01
ND95-2-1	150	200	88.2	1.7	1100.0	1181.4	1181.4	0.93	0.93
ND95-2-1D	150	200	86.7	1.7	1300.0	1174.7	1174.7	1.11	1.11
ND95-2-3	150	200	89.5	2.5	1450.0	1359.0	1359.0	1.07	1.07
ND95-2-3D	150	200	80.3	2.5	1250.0	1310.8	1310.8	0.95	0.95
ND95-2-3D+	150	200	98.0	2.5	1450.0	1400.7	1400.7	1.04	1.04
ND95-3-1	100	88	85.1	1.7	330.0	315.2	315.2	1.05	1.05
ND115-1-1	200	275	112.0	1.4	2450.0	2114.7	2114.7	1.16	1.16
ND115-2-1	150	200	119.0	1.7	1400.0	1305.5	1305.5	1.07	1.07
ND115-2-3	150	200	108.1	2.5	1550.0	1447.3	1447.3	1.07	1.07
							Mean	1.07	1.07
							Standard Deviation	0.08	0.08

Table 6.6 Test and predicted failure loads of slab specimens reported by Marzouk & Hussein[49] as according to EC2[22] and using Model EC2-IC

Specimen No	Column Size, C_x (mm)	Effective depth, d (mm)	Cylindrical Compressive Strength, σ_c (N/mm^2)	Reinforcement Ratio, ρ (%)	Test Failure Load, P_{test} (kN)	EC2 Predicted Load, V_{IC} (kN)	Model EC2-IC Predicted Load, V_{EC2-IC} (kN)	$\frac{P_{test}}{V_{IC}}$	$\frac{P_{test}}{V_{EC2-IC}}$
HS1	150	95	67.0	0.4	178.0	225.0	225.0	0.79	0.79
HS2	150	95	70.0	0.7	249.0	275.1	275.1	0.91	0.91
HS3	150	95	69.0	1.2	356.0	327.7	327.7	1.09	1.09
HS4	150	90	66.0	2.1	418.0	361.5	361.5	1.16	1.16
HS7	150	95	74.0	0.9	356.0	304.7	304.7	1.17	1.17
HS5	150	125	68.0	0.5	365.0	358.4	358.4	1.02	1.02
HS6	150	120	70.0	0.5	489.0	341.2	341.2	1.43	1.43
HS8	150	120	69.0	1.0	436.0	427.8	427.8	1.02	1.02
HS9	150	120	74.0	1.5	543.0	501.3	501.3	1.08	1.08
HS10	150	120	80.0	2.1	645.0	575.6	575.6	1.12	1.12
HS11	150	70	70.0	0.7	196.0	183.5	183.5	1.07	1.07
HS12	150	70	75.0	1.2	258.0	224.8	224.8	1.15	1.15
HS13	150	70	68.0	1.6	267.0	239.4	239.4	1.12	1.12
HS14	220	95	72.0	1.2	498.0	384.2	384.2	1.30	1.30
HS15	300	95	71.0	1.2	560.0	441.5	441.5	1.27	1.27
NS1	150	95	42.0	1.2	320.0	277.7	277.7	1.15	1.15
NS2	150	120	30.0	0.5	396.0	257.3	257.3	1.54	1.54
							Mean	1.14	1.14
							Standard Deviation	0.18	0.18

Table 6.7 Comparison between test failure loads and predicted failure loads for concentric punching at internal column series as according EC2[22] and using Model EC2-IC

Researcher	Number of Slab	Mean	Standard Deviation
Moe[53]	7	1.36	0.12
Elstner & Hognestad[20]	20	0.99	0.08
Base[7]	18	0.97	0.15
Yitzhaki[82]	12	1.08	0.32
Tomaszewicz[77]	13	1.07	0.08
Marzouk & Hussein[49]	17	1.14	0.18
Total	87	1.10	0.15

Table 6.8 Test and predicted failure loads of slab specimens reported by Author as according to EC2[22] and using Model EC2-IC

Specimen No	Column Size, C_x (mm)	Effective depth, d (mm)	Cylindrical Compressive Strength, σ_c (N/mm^2)	Reinforcement Ratio, ρ (%)	Test Failure Load, P_{test} (kN)	EC2 Predicted Load, V_{IC} (kN)	Model EC2-IC Predicted Load, V_{EC2-IC} (kN)	$\frac{P_{test}}{V_{IC}}$	$\frac{P_{test}}{V_{IC}}$
IWS 1	100	62	41.1	1.3	65.2	94.1	65.2	0.69	1.00

Table 6.9 Test and predicted failure loads of slab specimens reported by Moe[53] as according to EC2[22] and using Model EC2-IE

Specimen No	Column Size, C_x, C_y (mm)	Effective depth, d (mm)	Cylindrical Compressive Strength, σ_c (N/mm^2)	Reinforcement Ratio, ρ (%)	Moment Transferred, M_{test} (kNm)	Test Failure Load, P_{test} (kN)	EC2 Predicted Load, V_{IE} (kN)	Model EC2-IE Predicted Load, V_{EC2-IE} (kN)	$\frac{P_{test}}{V_{IE}}$ & $\frac{P_{test}}{V_{EC2-IE}}$
M1A	305	114	20.82	1.50	0.00	432.8	398.4	398.4	1.09
M2A	305	114	15.51	1.50	39.42	212.6	254.6	254.6	0.83
M4A	305	114	17.65	1.50	62.45	143.7	190.4	190.4	0.75
M2	305	114	25.75	1.50	57.21	292.2	296.6	296.6	0.99
M3	305	114	22.72	1.50	70.05	207.3	232.7	232.7	0.89
M6	254	114	26.48	1.34	40.23	239.3	272.2	272.2	0.88
M7	254	114	24.96	1.34	19.00	311.4	327.6	327.6	0.95
M8	254	114	24.61	1.34	65.32	149.5	181.3	181.3	0.82
M9	254	114	23.24	1.34	33.90	266.9	280.6	280.6	0.95
M10	254	114	21.10	1.34	54.76	177.9	203.3	203.3	0.88
								Mean	0.90
								Standard Deviation	0.09

Table 6.10 Test and predicted failure loads of slab specimens reported by Ghali et al.[26,27] as according to EC2[22] and using Model EC2-IE

Specimen No	Column Size, C_x, C_y (mm)	Effective depth, d (mm)	Cylindrical Compressive Strength, σ_c (N/mm^2)	Reinforcement Ratio, ρ (%)	Moment Transferred, M_{test} (kNm)	Test Failure Load, P_{test} (kN)	EC2 Predicted Load, V_{IE} (kN)	Model EC2-IE Predicted Load, V_{EC2-IE} (kN)	$\frac{P_{test}}{V_{IE}}$ & $\frac{P_{test}}{V_{EC2-IE}}$
SM0.5	305	127	36.8	0.50	99.98	129.0	144.9	144.9	0.89
SM1.0	305	127	33.4	1.00	126.94	129.0	151.3	151.3	0.85
SM1.5	305	127	39.9	1.50	133.00	129.0	178.1	178.1	0.72
								Mean	0.82
								Standard Deviation	0.09

Table 6.11 Test and predicted failure loads of slab specimens reported by Elgabry & Ghali[18,19] as according to EC2[22] and using Model EC2-IE

Specimen No	Column Size, C_x, C_y (mm)	Effective depth, d (mm)	Cylindrical Compressive Strength, σ_c (N/mm^2)	Reinforcement Ratio, ρ (%)	Moment Transferred, M_{test} (kNm)	Test Failure Load, P_{test} (kN)	EC2 Predicted Load, V_{IE} (kN)	Model EC2-IE Predicted Load, V_{EC2-IE} (kN)	$\frac{P_{test}}{V_{IE}}$ & $\frac{P_{test}}{V_{EC2-IE}}$
1	250	116	35.0	1.07	130.05	150.0	127.9	127.9	1.17
								Mean	1.17
								Standard Deviation	-

Table 6.12 Test and predicted failure loads of slab specimens reported by Kruger[44] as according to EC2[22] and using Model EC2-IE

Specimen No	Column Size, C_x, C_y (mm)	Effective depth, d (mm)	Cylindrical Compressive Strength, σ_c (N/mm^2)	Reinforcement Ratio, ρ (%)	Moment Transferred, M_{test} (kNm)	Test Failure Load, P_{test} (kN)	EC2 Predicted Load, V_{IE} (kN)	Model EC2-IE Predicted Load, V_{EC2-IE} (kN)	$\frac{P_{test}}{V_{IE}}$ & $\frac{P_{test}}{V_{EC2-IE}}$
P0A	300	150	34.6	1.00	0.00	423.0	427.4	427.4	0.99
P16A	300	150	38.6	1.00	53.12	332.0	326.7	326.7	1.02
P30A	300	150	30.4	1.00	86.40	270.0	238.9	238.9	1.13
							Mean		1.05
							Standard Deviation		0.08

Table 6.13 Test and predicted failure loads of slab specimens reported by Marzouk et al.[50,59] as according to EC2[22] and using Model EC2-IE

Specimen No	Column Size, C_x, C_y (mm)	Effective depth, d (mm)	Cylindrical Compressive Strength, σ_c (N/mm^2)	Reinforcement Ratio, ρ (%)	Moment Transferred, M_{test} (kNm)	Test Failure Load, P_{test} (kN)	EC2 Predicted Load, V_{IE} (kN)	Model EC2-IE Predicted Load, V_{EC2-IE} (kN)	$\frac{P_{test}}{V_{IE}}$ & $\frac{P_{test}}{V_{EC2-IE}}$
HSLW0.5L	250	118	72.0	0.50	40.50	257.1	294.6	294.6	0.87
HSLW1.0L	250	118	72.0	1.00	64.39	342.8	371.2	371.2	0.92
HSLW0.5M	250	118	72.0	0.50	76.70	216.2	214.9	214.9	1.01
HSLW1.0M	250	118	72.0	1.00	98.65	287.0	270.8	270.8	1.06
HSLW0.5H	250	118	72.0	0.50	102.75	184.2	172.6	172.6	1.07
HSLW1.0H	250	118	72.0	1.00	133.60	223.3	217.5	217.5	1.03
HSLW1.5H	250	118	72.0	1.50	132.00	265.1	249.0	249.0	1.06
NSNW1.0L	250	118	35.0	1.00	62.00	360.8	291.9	291.9	1.24
							Mean		1.03
							Standard Deviation		0.11

Table 6.14 Test and predicted failure loads of slab specimens reported by Hawkins et al.[35] as according to EC2[22] and using Model EC2-IE

Specimen No	Column Size, C_x, C_y (mm)	Effective depth, d (mm)	Cylindrical Compressive Strength, σ_c (N/mm^2)	Reinforcement Ratio, ρ (%)	Moment Transferred, M_{test} (kNm)	Test Failure Load, P_{test} (kN)	EC2 Predicted Load, V_{IE} (kN)	Model EC2-IE Predicted Load, V_{EC2-IE} (kN)	$\frac{P_{test}}{V_{IE}}$ & $\frac{P_{test}}{V_{EC2-IE}}$
6AH	305	127	31.3	0.52	90.40	169.0	165.4	165.4	1.02
9.6AH	305	125	30.7	0.83	97.70	187.0	187.2	187.2	1.00
14AH	305	124	30.3	1.21	100.20	205.0	208.7	208.7	0.98
6AL	305	127	22.7	0.52	32.70	244.0	259.2	259.2	0.94
9.6AL	305	125	28.9	0.83	34.60	257.0	321.1	321.1	0.80
14AL	305	124	27.0	1.21	43.40	319.0	351.9	351.9	0.91
7.3BH	305	89	22.2	0.62	39.00	80.0	90.3	90.3	0.89
9.5BH	305	89	19.8	0.86	45.40	94.0	97.0	97.0	0.97
14.2BH	305	87	29.5	1.19	51.00	102.0	119.4	119.4	0.85
7.3BL	305	89	18.1	0.52	12.80	130.0	148.3	148.3	0.88
9.5BL	305	89	20.0	0.83	16.60	142.0	179.1	179.1	0.79
14.2BL	305	87	20.5	1.21	20.90	162.0	198.8	198.8	0.81
6CH	305	127	52.4	0.52	95.10	186.0	196.4	196.4	0.95
9.6CH	305	125	57.2	0.83	113.10	218.0	230.4	230.4	0.95
14CH	305	124	54.7	1.21	133.30	252.0	254.1	254.1	0.99
6CL	305	127	49.5	0.52	36.80	273.0	336.1	336.1	0.81
14CL	305	124	47.7	1.21	49.40	362.0	425.4	425.4	0.85
								Mean	0.91
								Standard Deviation	0.08

Table 6.15 Comparison between test failure loads and predicted failure loads for eccentric punching at internal column series as according EC2 and using Model EC2-IE

Researcher	Number of Slab	M6ean	Standard Deviation
Moe[53]	10	0.90	0.09
Ghali et al.[26,27]	3	0.82	0.09
Elgabry & Ghali[18,19]	1	1.17	-
Kruger[44]	3	1.05	0.07
Marzouk, Osman and Helmy[50,59]	8	1.03	0.11
Hawkins et. al.[35]	17	0.91	0.08
Total	42	0.98	0.09

Table 6.16 Test and predicted failure loads of slab specimens reported by Author as according to EC2[22] and using Model EC2-IE

Specimen No	Column Size, C_x, C_y (mm)	Effective depth, d (mm)	Cylindrical Compressive Strength, σ_c (N/mm^2)	Reinforcement Ratio, ρ (%)	Principle Angle of Biaxial Moment Transfer, ∀ (°)	Moment Transferred, M_{test} (kNm)	Test Failure Load, P_{test} (kN)	EC2 Predicted Load, V_{IE} (kN)	Model EC2-IE Predicted Load, V_{EC2-IE} (kN)	$\frac{P_{test}}{V_{IE}}$	$\frac{P_{test}}{V_{EC2-IE}}$
IWSB1	100	62	36.6	1.31	0	2.74	54.73	74.6	0.73	0.73	0.99
IWSB2	100	62	36.6	1.31	22.5	2.11	42.10	74.6	0.56	0.56	0.78
IWSB3	100	62	35.7	1.31	45	2.32	46.31	74.0	0.63	0.63	0.97
IWSB4	100	62	37.7	1.31	0	4.63	46.31	62.7	0.74	0.74	0.96
IWSB5	100	62	36.9	1.31	22.5	3.58	35.79	62.3	0.57	0.57	0.78
IWSB6	100	62	36.0	1.31	45	3.79	37.89	61.8	0.61	0.61	1.00
IWSB7	100	62	36.6	1.31	0	5.68	37.89	53.2	0.71	0.71	0.89
IWSB8	100	62	37.0	1.31	22.5	4.42	29.47	53.4	0.55	0.55	0.73
IWSB9	100	62	38.7	1.31	45	5.052	33.68	54.2	0.62	0.62	1.05
IFSB1	100	62	37.5	1.31	0	7.16	71.57	62.6	1.14	1.14	1.14
IFSB2	100	62	36.7	1.31	22.5	6.74	67.36	62.2	1.08	1.08	1.15
IFSB3	100	62	37.2	1.31	45	6.32	63.15	62.5	1.01	1.01	1.35
IWSBC1	100	62	38.5	1.31	22.5	4.21	42.10	63.2	0.67	0.67	0.90
IWSBC2	100	62	39.7	1.31	45	3.79	37.89	63.8	0.59	0.59	0.97
								Mean		0.73	0.98
								Standard Deviation		0.20	0.16

Table 6.17 Test and predicted failure loads of slab specimens reported by Stamenkovic & Chapman[73] as according to EC2[22] and using Model EC2-E

Specimen No	Column Size, C_x, C_y (mm)	Effective depth, d (mm)	Cylindrical Compressive Strength, σ_c (N/mm^2)	Reinforcement Ratio, ρ (%)	Moment Transferred, M_{test} (kNm)	Test Failure Load, P_{test} (kN)	EC2 Predicted Load, V_E (kN)	Model EC2-E Predicted Load, V_{EC2-E} (kN)	$\frac{P_{test}}{V_E}$ & $\frac{P_{test}}{V_{EC2-E}}$
V/E/1	127	56	29.2	1.09	0.00	74.73	55.93	55.93	1.34
C/E/1	127	56	31.5	1.39	5.59	73.39	62.20	62.20	1.18
C/E/2	127	56	33.0	1.39	9.18	54.71	63.18	63.18	0.87
C/E/3	127	56	34.0	1.39	10.06	24.91	63.81	63.81	0.39
C/E/4	127	56	27.8	1.39	8.84	10.94	59.67	59.67	0.18
								Mean	0.79
								Standard Deviation	0.50

Table 6.18 Test and predicted failure loads of slab specimens reported by Zaghlool[83] as according to EC2[22] and using Model EC2-E

Specimen No	Column Size, C_x, C_y (mm)	Effective depth, d (mm)	Cylindrical Compressive Strength, σ_c (N/mm^2)	Reinforcement Ratio, ρ (%)	Moment Transferred, M_{test} (kNm)	Test Failure Load, P_{test} (kN)	EC2 Predicted Load, V_E (kN)	Model EC2-E Predicted Load, V_{EC2-E} (kN)	$\frac{P_{test}}{V_E}$ & $\frac{P_{test}}{V_{EC2-E}}$
Z-IV(1)	178	121	27.4	2.41	44.97	122.32	224.61	224.61	0.54
Z-V(1)	267	121	34.3	1.60	84.64	215.28	244.85	244.85	0.88
Z-V(2)	267	121	40.5	2.00	93.56	246.86	278.77	278.77	0.89
Z-V(3)	267	121	38.8	1.65	103.62	268.21	257.75	257.75	1.04
Z-V(5)	267	121	35.2	1.60	0.00	279.33	246.97	246.97	1.13
Z-V(6)	267	121	31.3	1.60	88.14	116.98	237.49	237.49	0.49
Z-VI(1)	356	121	26.0	2.41	106.90	265.10	291.11	291.11	0.91
								Mean	0.84
								Standard Deviation	0.24

Table 6.19 Test and predicted failure loads of slab specimens reported by Gardner & Shoa[24] as according to EC2[22] and using Model EC2-E

Specimen No	Column Size, C_x, C_y (mm)	Effective depth, d (mm)	Cylindrical Compressive Strength, σ_c (N/mm^2)	Reinforcement Ratio, ρ (%)	Moment Transferred, M_{test} (kNm)	Test Failure Load, P_{test} (kN)	EC2 Predicted Load, V_E (kN)	Model EC2-E Predicted Load, V_{EC2-E} (kN)	$\frac{P_{test}}{V_E}$ & $\frac{P_{test}}{V_{EC2-E}}$
2	199	120	21.5	0.92 (460)	14.60	159.00	154.17	154.17	1.03
3	254	120	21.5	0.92 (460)	14.60	144.00	168.89	168.89	0.85
4	254	120	21.5	0.92 (460)	19.00	207.00	168.89	168.89	1.23
5	254	120	21.5	0.92 (460)	14.60	144.00	168.89	168.89	0.85
								Mean	0.99
								Standard Deviation	0.18

Table 6.20 Test and predicted failure loads of slab specimens reported by Surdasana[74] as according to EC2[22] and using Model EC2-E

Specimen No	Column Size, C_x, C_y (mm)	Effective depth, d (mm)	Cylindrical Compressive Strength, σ_c (N/mm²)	Reinforcement Ratio, ρ (%)	Moment Transferred, M_{test} (kNm)	Test Failure Load, P_{test} (kN)	EC2 Predicted Load, V_E (kN)	Model EC2-E Predicted Load, V_{EC2-E} (kN)	$\frac{P_{test}}{V_E}$
E1	203	110	43.6	0.90 (480)	34.40	127.00	173.36	173.36	0.73
E2	203	110	42.4	0.90 (480)	0.00	220.00	171.75	171.75	1.28
E2-1	203	110	52.8	1.20 (480)	34.70	130.50	203.38	203.38	0.64
E2-2	203	110	52.8	1.20 (480)	25.30	178.90	203.38	203.38	0.88
E2-3	203	110	55.0	1.20 (480)	9.60	328.00	206.17	206.17	1.59
E2-4	203	110	55.0	1.20 (480)	16.40	199.00	206.17	206.17	0.97
							Mean		1.02
							Standard Deviation		0.36

Table 6.21 Comparison between test failure loads and predicted failure loads for edge punching series as according EC2 and using Model EC2-E

Researcher	Number of Slab	Mean	Standard Deviation
Stamenkovic and Chapman[73]	5	0.79	0.50
Zaghlool[83]	7	0.84	0.24
Gardner and Shao[24]	4	0.99	0.18
Surdasana[74]	6	1.02	0.36
Total	22	0.91	0.32

Table 6.22 Test and predicted failure loads of slab specimens by Author as according to EC2[22]

Specimen No	Column Size, C_x, C_y (mm)	Effective depth, d (mm)	Cylindrical Compressive Strength, σ_c (N/mm^2)	Reinforcement Ratio, ρ (%)	Principle Angle of Biaxial Moment Transfer, $\forall$ (°)	Test Failure Load, P_{test} (kN)	EC2 Predicted Load (Parallel Loading), $V_{E(par)}$ (kN)	EC2 Predicted Load (Perpendicular Loading), $V_{E(per)}$ (kN)	$\frac{P_{test}}{V_{E(par)}}$	$\frac{P_{test}}{V_{E(per)}}$
EWSB1	100	62	38.1	1.31	0	31.58	42.48	-	0.74	-
EWSB2	100	62	41.2	1.31	22.5	44.21	43.61	49.10	1.01	0.90
EWSB3	100	62	37.8	1.31	45	40.00	42.38	47.71	0.94	0.84
EWSB4	100	62	36.9	1.31	67.5	42.10	42.03	47.33	1.00	0.89
EWSB5	100	62	37.7	1.31	90	52.60	-	47.68	-	1.10
EWSB6	100	62	37.1	1.31	0	29.47	37.88	-	0.78	-
EWSB7	100	62	38.7	1.31	22.5	31.58	38.41	48.10	0.82	0.66
EWSB8	100	62	36.7	1.31	45	27.37	37.73	47.21	0.73	0.58
EWSB9	100	62	36.2	1.31	67.5	29.47	37.55	47.02	0.78	0.63
EWSB10	100	62	43.7	1.31	90	48.42	-	50.08	-	0.88
EWSB11	100	62	33.3	1.31	0	27.37	33.21	-	0.82	-
EWSB12	100	62	41.0	1.31	22.5	27.37	35.58	49.04	0.77	0.56
EWSB13	100	62	37.3	1.31	45	25.26	34.46	47.50	0.73	0.53
EWSB14	100	62	37.0	1.31	67.5	25.26	34.39	47.40	0.73	0.53
EWSB15	100	62	37.3	1.31	90	40.00	-	47.51	-	0.84
EFSB1	100	62	48.1	1.31	0	44.21	41.31	-	1.07	-
EFSB2	100	62	43.8	1.31	22.5	44.21	40.03	50.13	1.10	0.88
EFSB3	100	62	41.9	1.31	45	46.31	39.44	49.39	1.17	0.94
EFSB4	100	62	44.1	1.31	67.5	48.42	40.13	50.25	1.21	0.96
EFSB5	100	62	32.9	1.31	90	52.63	-	45.56	-	1.16
EWSCE1	100	62	36.9	1.31	0	41.05	37.81	-	1.09	-
EWSCE2	100	62	36.8	1.31	0	36.84	37.78	-	0.98	-
EWSCE3	100	62	38.5	1.31	0	31.58	38.36	-	0.82	-

Mean	0.91	0.81
Standard Deviation	0.16	0.20

Table 6.23 Test and predicted failure loads of slab specimens reported by Author using Model EC2-E

Specimen No	Column Size, C_x (mm)	Column Size, C_y (mm)	Effective depth, d (mm)	Cylindrical Compressive Strength, σ_c (N/mm^2)	Reinforcement Ratio, ρ (%)	Principle Angle of Biaxial Moment Transfer, ∀ (°)	Moment Transferred, M_{test} (kNm)	Test Failure Load, P_{test} (kN)	Model EC2-E Predicted Load, V_E (kN)	$\frac{P_{test}}{V_E}$
EWSB1	100	100	62	38.1	1.31	0	1.58	31.58	34.72	0.91
EWSB2	100	100	62	41.2	1.31	22.5	2.21	44.21	35.89	1.23
EWSB3	100	100	62	37.8	1.31	45	2.00	40.00	35.59	1.12
EWSB4	100	100	62	36.9	1.31	67.5	2.11	42.10	36.43	1.16
EWSB5	100	100	62	37.7	1.31	90	2.63	52.60	38.12	1.38
EWSB6	100	100	62	37.1	1.31	0	2.95	29.47	31.50	0.94
EWSB7	100	100	62	38.7	1.31	22.5	3.16	31.58	32.36	0.98
EWSB8	100	100	62	36.7	1.31	45	2.74	27.37	33.02	0.83
EWSB9	100	100	62	36.2	1.31	67.5	2.95	29.47	34.89	0.84
EWSB10	100	100	62	43.7	1.31	90	4.84	48.42	40.04	1.21
EWSB11	100	100	62	33.3	1.31	0	4.11	27.37	28.01	0.98
EWSB12	100	100	62	41.0	1.31	22.5	4.11	27.37	30.57	0.90
EWSB13	100	100	62	37.3	1.31	45	3.79	25.26	31.24	0.81
EWSB14	100	100	62	37.0	1.31	67.5	3.79	25.26	33.92	0.74
EWSB15	100	100	62	37.3	1.31	90	6.00	40.00	37.98	1.05
EFSB1	100	100	62	48.1	1.31	0	4.42	44.21	40.88	1.08
EFSB2	100	100	62	43.8	1.31	22.5	4.42	44.21	40.24	1.10
EFSB3	100	100	62	41.9	1.31	45	4.63	46.31	41.49	1.12
EFSB4	100	100	62	44.1	1.31	67.5	4.84	48.42	45.35	1.07
EFSB5	100	100	62	32.9	1.31	90	5.26	52.63	45.10	1.17

EWSCE1	100	100	62	36.9	1.31	0	2.05	41.05	34.35	1.20
EWSCE2	100	100	62	36.8	1.31	0	3.68	36.84	31.41	1.17
EWSCE3	100	100	62	38.5	1.31	0	4.74	31.58	29.40	1.07
									Mean	1.05
									Standard Deviation	0.16

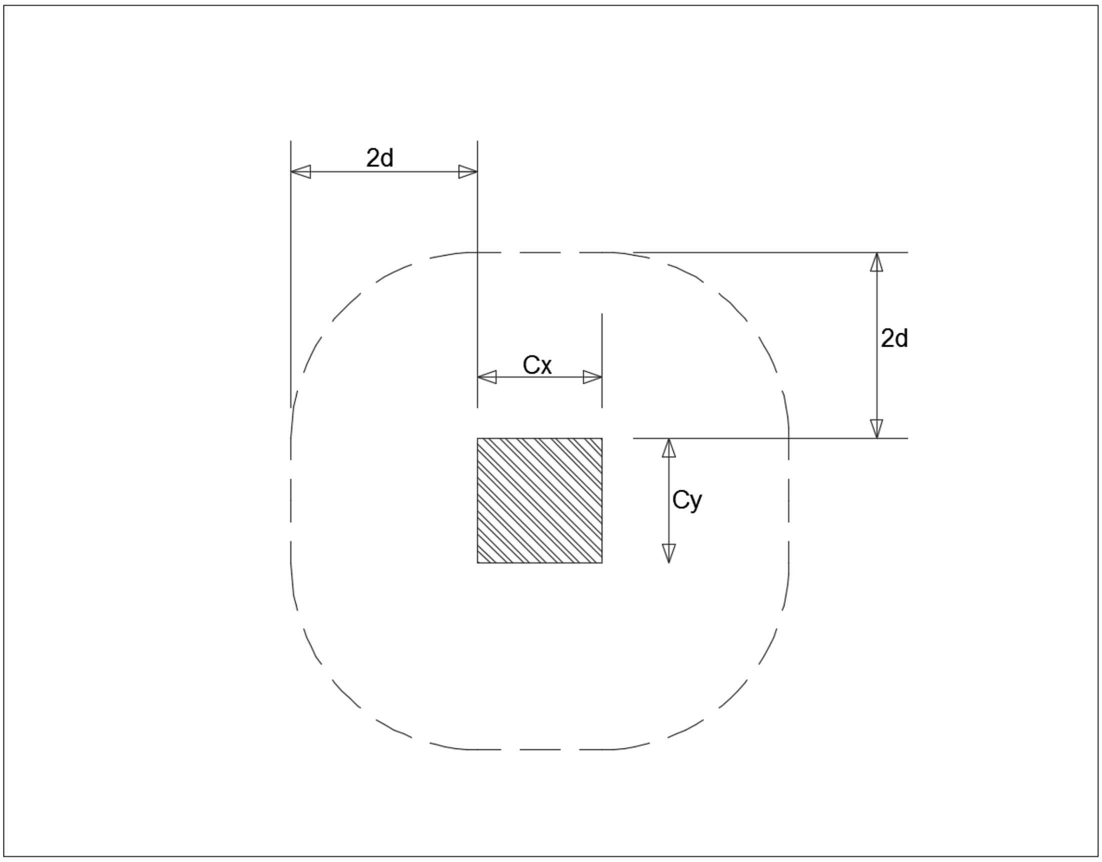

Figure 6.1 Critical shear perimeter for internal column by EC2[22]

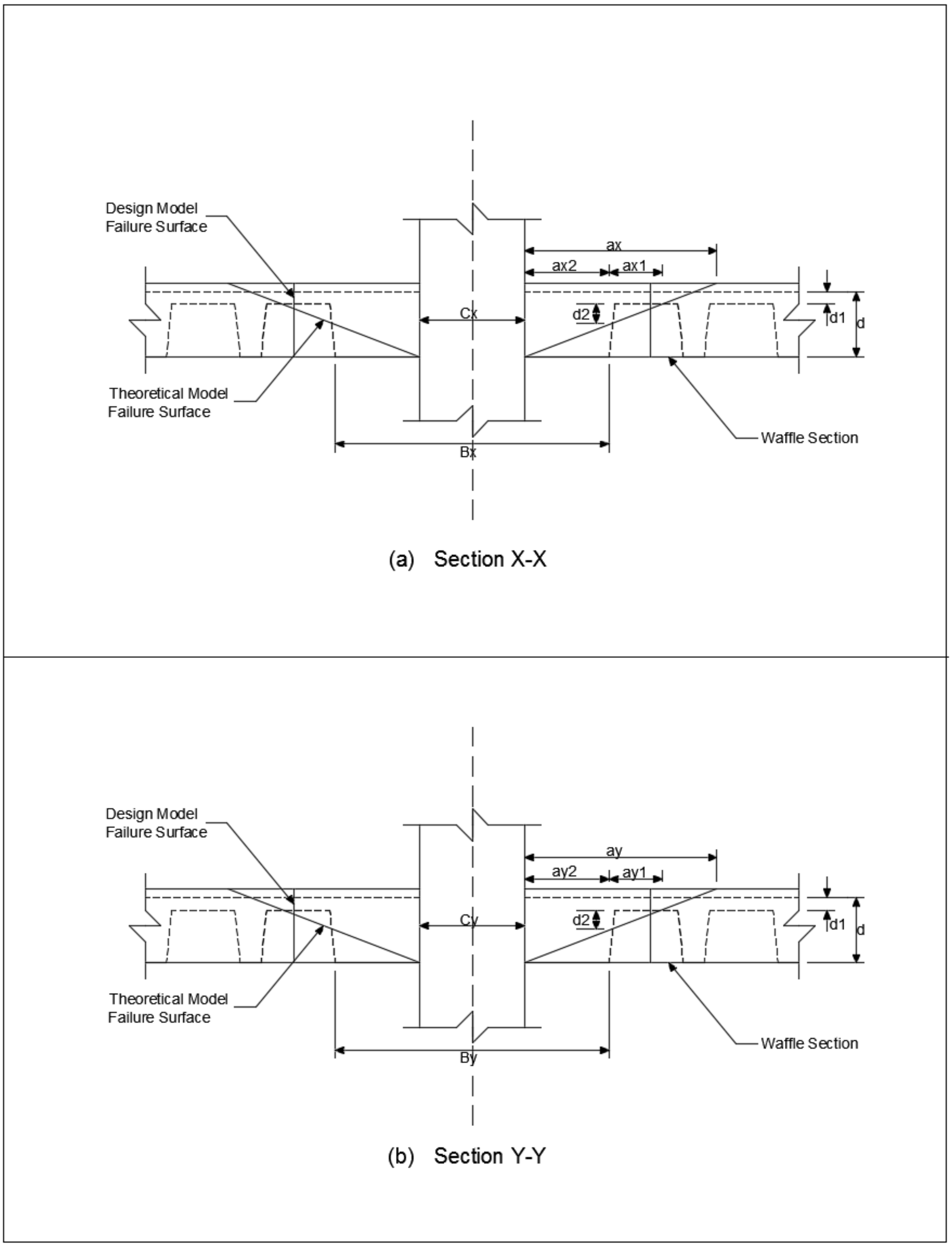

Figure 6.2 Design model EC2-IC and EC2-IE – critical shear area

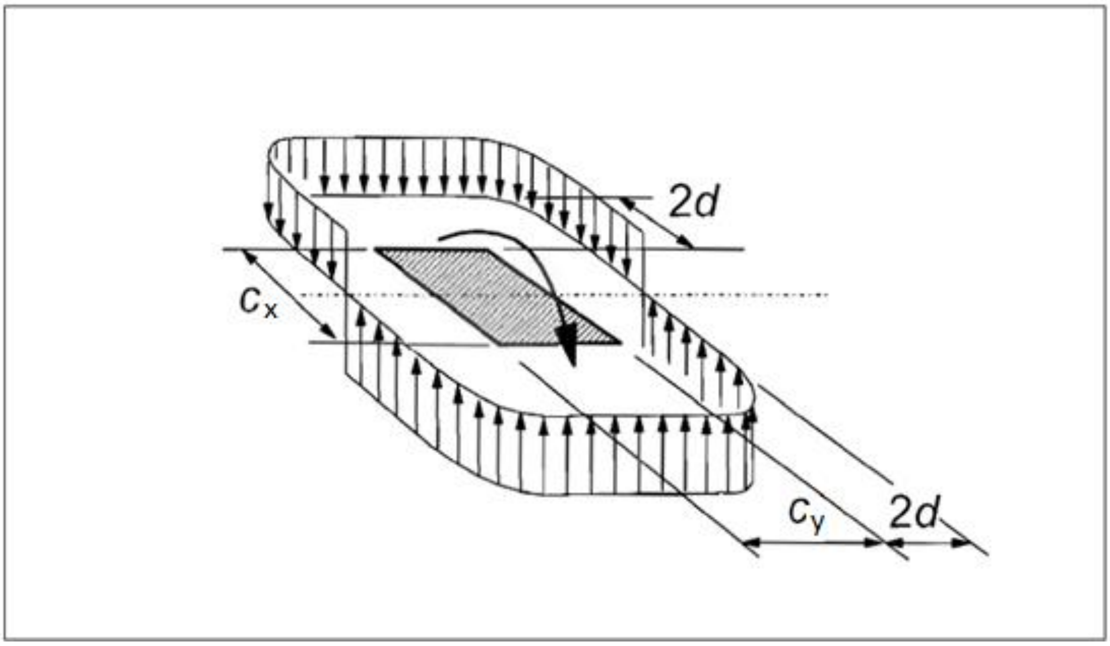

Figure 6.3 Moment transfer mechanism for internal column by EC2[22]

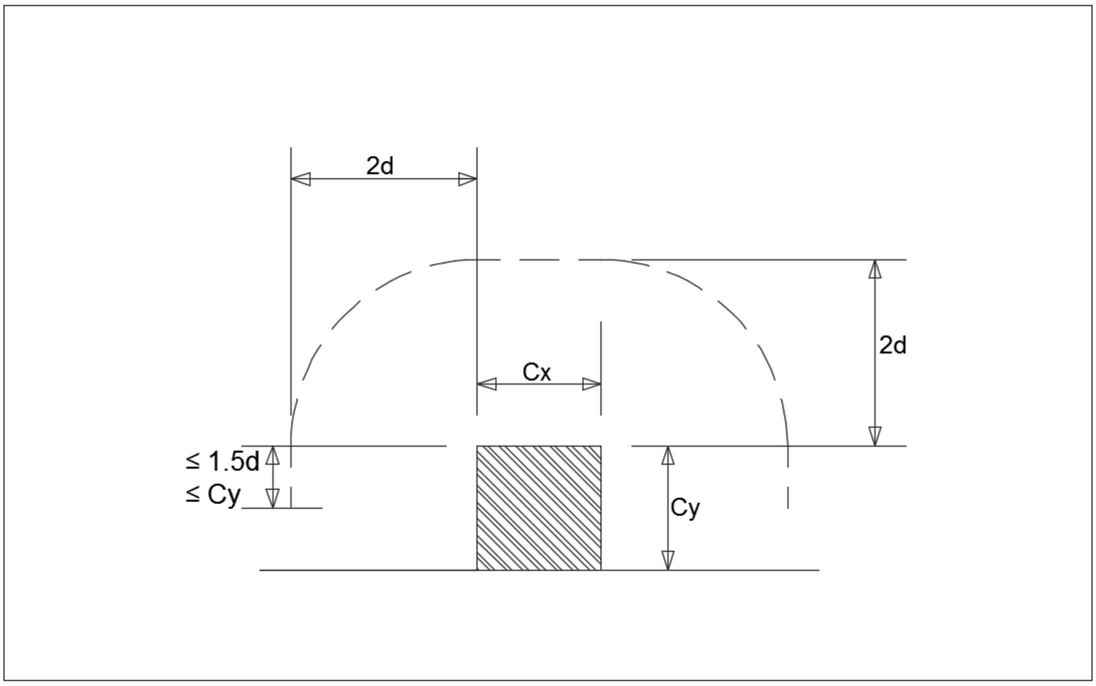

Figure 6.4 Critical shear perimeter for edge column by EC2[22]

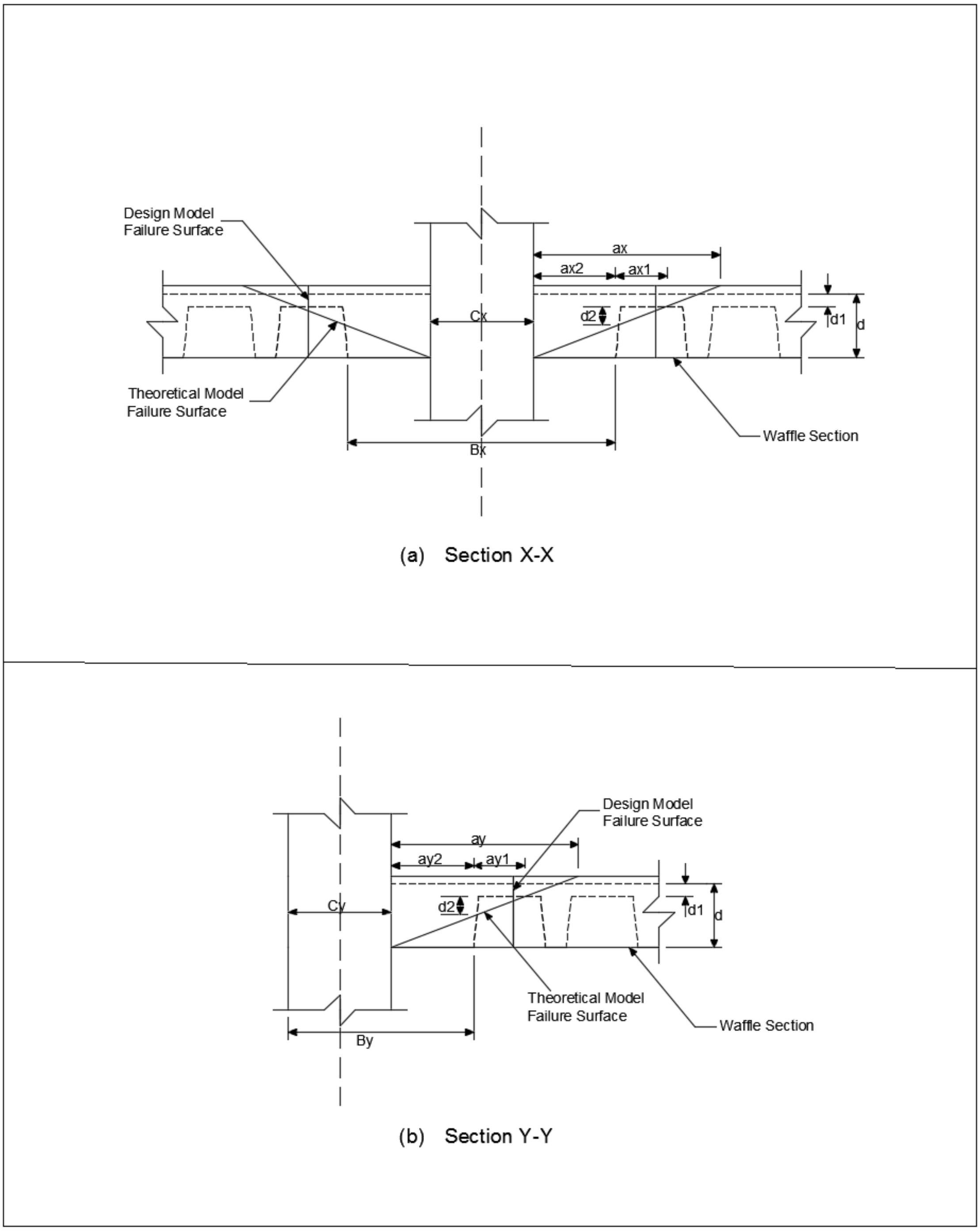

Figure 6.5 Design model EC2-E – critical shear area

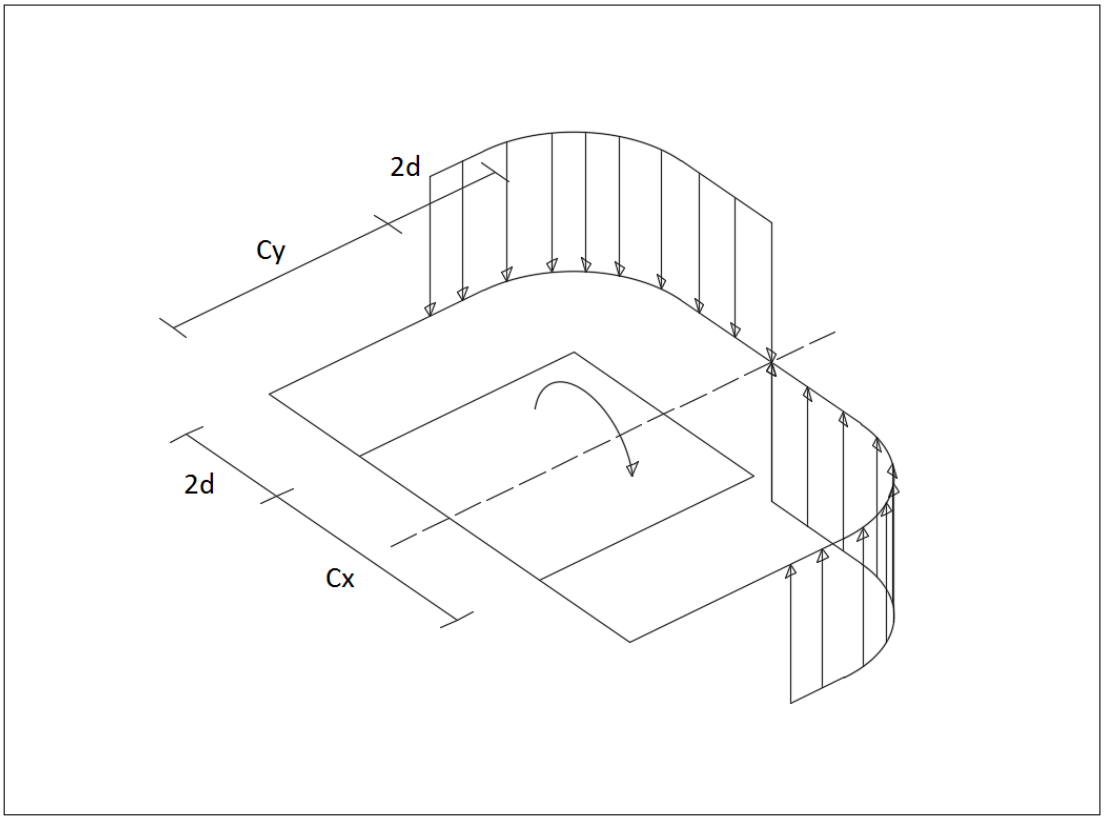

Figure 6.6 Moment transfer mechanism for edge column by EC2[22]

Chapter 7 Conclusions and Suggestions to Future Works

7.1 Introduction

The main objective of this research was to investigate, through experimental and analytical studies, the punching shear mechanism in waffle slabs in the presence of biaxial moment transfer at the internal and edge column connections. The experimental works involved destructive testing of slab specimens, which consisted of internal and edge column slabs. Three distinct punching shear failures were observed, which were: the concentric punching at internal column mechanism, the eccentric punching at internal column mechanism and the edge punching mechanism.

Based on the experimental findings, an analytical study, based on the plasticity approach, was carried out on all slab specimens; and three theoretical models were developed for the observed punching shear failure mechanisms. Furthermore, three design models extended from that of the EC2[22] have also been proposed.

7.2 Experimental Programme

A total of thirty-eight 1/10th scale slab specimens, of which fifteen were internal column specimens and twenty-three were edge column specimens, were tested and all specimens failed in punching shear failure.

The experimental programme observed three distinct punching shear failures, which were: the concentric punching at internal column mechanism, the eccentric punching at internal column mechanism and the edge punching mechanism.

7.2.1 Internal Column Series

7.2.1.1 Concentric Punching at Internal Column Series

In this series, the slab specimen was tested in the absence of moment transfer from the column to the slab at internal column connection.

The concentric punching mechanism of waffle slab at internal column was observed to be similar to that of a solid flat slab. The specimen failed in a sudden rupture failure and in a sudden drop of shear resistance from its peak. At failure, the failure surface was characterized by internal cracks propagated from the vicinity of column, through the slab thickness, to the support at about 28 degrees inclination. In cases where the supports were further away, 22 degrees inclination was observed. In plan, a complete solid revolution of concrete was formed at the centre of the slab specimen, which was separated from the main slab vertically leaving the rest of the slab remaining rigid. However, the distinct difference between a waffle slab specimen and a solid flat slab is the reduced solid section at the column vicinity to form a complete solid of revolution due to some of the potential failure surface was lost when it entered the waffle section.

Cracks were first observed on the tension side of the slab, directly above the column stub. The observed cracking load was found to be 52% of ultimate capacity of the slab. The observed cracking load was found to be 17% higher than the actual cracking load mainly due to the formation of micro-cracks formed within the slab specimen and could not be identified by the naked eye.

Prior to punching shear failure, the width of the cracks at the vicinities of the column widened and more cracks were observed on the tension side of the slab as well as within the waffle sections on the compression side of the slabs.

7.2.1.2 Eccentric Punching at Internal Column Series

In this series, the punching mechanism was tested in the presence of biaxial moment transfer from the column to the slab at internal column connection.

The eccentric punching mechanism of waffle slab was found to be similar to that of the concentric punching mechanism at internal column. However, due to the presence of eccentric loading, an incomplete solid revolution was formed upon failure and the size of the solid revolution was dependent on the ratio of load eccentricity to column size. The principle angle of moment transfer was also observed to influence the orientation and size of the solid of revolution within the slab specimens.

Cracks were first observed on the tension side of the slab, directly above the column stub. The observed cracking loads were found to be 52% of ultimate capacity of the slabs. The observed cracking loads were found to be 14% higher than the actual cracking loads mainly due to the formation of micro-cracks formed within the slab specimen and could not be identified by the naked eye.

The punching shear capacity among the waffle slab specimens were observed to be the highest when the principle angle of moment transfer was orthogonal to the column axis (0^o), followed by 45^o and lastly, 22.5^o. These were due to the decrease in shear surface being mobilized as the principle angle rotated.

An increase in the load eccentricity increased the moment transferred on the slab, thus reducing the punching capacity of the slab specimens.

Limited differential findings were found when the column orientation is rotated according to the principle angle of moment transfer. The punching capacity of the waffle slab specimens was indifferent in regard to the change of column location.

An increase in the size of solid section of waffle slab specimens increased the punching capacity, mainly due to the increase in the shear failure surface formed within the solid region.

7.2.2 Edge Column Series

In this series, the edge slab specimens were tested in the presence of biaxial moment transfer from the column to the slab.

The edge punching mechanism of waffle slab was observed to fail similarly to that of a solid flat slab. All specimens were found to fail in a very abrupt manner at the last load increment with a sudden drop of shear resistance from its peak. The observed failure surface was characterised by internal cracks propagated from the heavily loaded side and the adjacent side of the column through the slab thickness at about 21 degrees to 28 degrees inclination. In plan, a complete quarter to half solid of revolution was formed, which was separated from the main slab vertically. The distinct difference between a waffle slab specimen and a solid flat slab specimen is the reduced shear failure surface to absorb the applied energy, thus reducing the ultimate punching capacity of the waffle slab specimen.

The size of the solid revolution of concrete formed upon failure was found to be highly dependent on the ratio of the column eccentricity to the column size. The principle angle of biaxial moment transfer was also observed to influence the size of the failure surface within the slab specimens

Cracks were first observed on the tension side of the slab, directly above the column stub. The observed cracking loads were found to be 52% of ultimate capacity of the slabs on average. The observed cracking loads were found to be 16% higher than the actual cracking loads mainly due to the formation of micro-cracks formed within the slab specimen and could not be identified by the naked eye.

The punching shear capacity of the waffle slab specimens were observed to be the highest when the principle angle of moment transfer was set to 90^{o} (perpendicular to slab free edge), followed by 22.5^{o}, 67.5^{o}, 45^{o} and lastly 0^{o} (parallel to slab free edge). The decrease in punching shear capacity was due to the decrease in shear surface being mobilized as the principle angle rotated.

An increase in the load eccentricity increased the moment transferred on the slab specimens, thus reducing the punching capacity of the slab specimens

The punching shear capacity of the waffle slab specimens were found to be higher when the column was placed at the free-edge of the slab and at the centre-edge of the slab. The increase in punching shear capacity was mainly due to a steeper angle of inclination separating the solid revolution of concrete from the remaining part of the slab when the column was loaded at the centre-edge, therefore more work required to mobilize the solid revolution of concrete.

An increase in the size of solid section of waffle slab specimens increased the punching capacity, mainly due to the increase portions of the potential failure surface formed within the solid section.

7.3 Theoretical Model

Three theoretical models were proposed to predict the ultimate punching capacity of the slab specimens: concentric punching at internal column; eccentric punching at internal column and edge punching. The theoretical models were derived based on the observation of punching failure mechanism as reported in the experimental programme.

All theoretical models were derived from the upper bound approach using the theory of plasticity for internal and edge punching shear of flat solid slabs. These theoretical models calculate the total plastic work dissipated on the loss of shear area for different failure mechanism before equating to the predicted failure loads.

The punching strength of a waffle slab was differentiated into two main geometrical categories:

a. Causing a reduction in shear failure surface:
    i) Solid of revolution extends into the waffle section with losses in the shear failure surface
b. Causing no reduction in shear failure surface:
    i) Solid of revolution extends into the waffle section with no losses in the shear failure surface
    ii) Size of solid section wider than solid of revolution

A shear retention factor was also applied to the theoretical models in the prediction of the ultimate punching capacity of slab specimens cast from micro-concrete having maximum aggregates size of 2.36 mm.

7.3.1 Internal Column Series

7.3.1.1 Concentric Punching at Internal Column Series

The concentric punching at internal column theoretical model predicts the punching capacity of both waffle and solid slab specimens in the absence of moment transfer at internal column.

This model is able to predict for punching capacities of waffle slabs as the model considers changes in the slab thickness that extend into the assumed solid of revolution which cause a reduction in the shear failure surface, thus reduce the punching capacity of the slab.

In predicting the shear failure surface, the model adopted Regan's approach[67] but modified the effective depth to the height of the slab. This is mainly due to Braestrup et al.'s argument[12] that the height of the slab specimen is a better justification of shear failure surface as according to the plasticity approach.

The effectiveness factor, v, of concrete was used to account the limited ductility of concrete and to accommodate any shortcomings of applying the plasticity theory to predict the plastic concrete compressive strength.

The proposed model achieved good agreements when compared with test results reported in the literatures for solid flat slabs (mean of 1.00 and standard deviation of 0.15); and also achieved good agreement with the Author's test results on waffle slab (mean of 1.00).

7.3.1.2 Eccentric Punching at Internal Column Series

The eccentric punching at internal column theoretical model predicts the punching capacity of both waffle and solid slab specimens in the presence of biaxial moment transfer at internal column.

Similarly to the concentric punching theoretical model, this model is able to predict accurately for waffle slabs by accommodating any changes in the slab thickness and applies the same modification to the Regan's approach[67] to predict the shear failure surface. Besides that, the same effectiveness factor is maintained in this model to predict the plastic concrete compressive strength.

In order to simulate the reduced shear failure surface as pointed out by Braestrup et al[12], an opening angle at the back of the column face was introduced, which was derived from the linear shear stress distribution method by DiStasio & Van Buren[17]. After obtaining the opening angle, the effective punching failure surface of revolution can be calculated and thus, the punching capacity can be determined by finding the product of the sum of internal plastic work dissipated and the total shear area.

The proposed model achieved good agreements when compared with test results reported in the literatures for solid flat slabs (mean of 0.97 and standard deviation of 0.14); and also achieved good agreements when compared with the Author's test results for waffle slabs (mean of 1.06 and standard deviation of 0.11).

7.3.2 Edge Column Series

The edge punching theoretical model predicts the edge punching capacity of both waffle and solid slab specimens in the presence of biaxial moment transfer.

Similarly to the two earlier models, this model is able to predict accurately for waffle slabs by accommodating any changes in the slab thickness and applies the same modification to the Regan's approach to predict the shear failure surface. Besides that, the same effectiveness factor is maintained in this model to predict the plastic concrete compressive strength.

As explained in the eccentric punching at internal column theoretical model, this model also calculates an opening angle, derived from the shear stress distribution within the column vicinity. After obtaining the opening angle, the effective punching failure surface of revolution can be calculated and thus, the punching capacity can be determined by finding the product of the sum of internal plastic work dissipated and the total shear area.

The proposed model achieved good agreements when compared with test results reported in the literatures for solid flat slabs (mean of 0.88 and standard deviation of 0.20); and also achieved good agreements with the Author's test results on edge waffle slabs (mean of 0.99 and standard deviation of 0.19).

7.4 Design Model

Three empirical design models based on the current code of practice, Eurocode 2[22], were proposed to predict the ultimate punching capacity of the waffle slab specimens: concentric punching; eccentric punching and edge punching. These design models were based on the observations made on the ultimate punching capacity of the slab specimens as reported in Chapter 4.

In general, it adopted the current Eurocode 2 control surface approach, but reduces the control surface by projecting the loss of shear surface with respect to the total potential shear surface. The concrete shear strength remains as that reported in the Eurocode 2.

A shear retention factor was introduced to the design models in the prediction of the ultimate punching capacity of slab specimens cast from micro-concrete with a maximum aggregate size of 2.36 mm.

7.4.1 Internal Column Series

7.4.1.1 Concentric Punching Series

EC2 adopts the control surface approach and calculates the punching shear capacities from the sum of the shear stresses on an imaginary critical shear area positioned at a distance “2d” from the column faces. However, EC2 does not cover the prediction of punching capacity of a waffle slab as it does not account for the loss of shear surface area in the waffle sections. Therefore, an effective shear factor is introduced to simulate the loss of shear area when computing for the critical shear area.

The current design code EC2 achieved good agreements with the test results reported in the literatures (mean of 1.10 and standard deviation of 0.15), but overestimated the Author’s test result (mean of 0.69) due to the presence of waffles. However, with the proposing effective shear factor, the proposed design model achieved good agreement with the Author’s test result (mean of 1.00).

7.4.1.2 Eccentric Punching Series

EC2 introduces a moment transfer factor, β to reduce the punching capacity when the slab specimens are loaded at the column in the presence of moment transfer. In this proposed design model, the effect of the biaxial moment transfer is taken into account by accommodating the principle angle of biaxial moment transfer within the modified moment transfer factor, β_{EC2-IE}.

Similarly to the concentric proposed design model, an effective shear factor is introduced to simulate the shear area losses within the waffle sections when computing the imaginary critical shear area.

The current design code EC2 achieved good agreement with the test results reported in the literatures (mean of 0.98 and standard deviation of 0.09), but overestimated the Author's test results (mean of 0.73 and standard deviation of 0.20). However, with the proposing effective shear factor, the proposed design model achieved good agreements with the Author's test results (mean of 0.98 and standard deviation of 0.16).

7.4.2 Edge Column Series

EC2 states that when the moment transfer is perpendicular to the slab free edge, the moment transfer factor, β is set to unity, whereas, when the moment transfer is parallel to the slab free edge, the moment transfer factor, β is calculated similarly to the eccentric punching model's moment transfer factor. However, no explanation was provided by the EC2 regarding the presence of moment transfer between a parallel loading and a perpendicular loading. Therefore, this model introduces a modified moment transfer factor, β_{EC2-E} which accounts the principle angle of biaxial moment transfer.

Similarly to the earlier two design models, an effective shear factor is introduced to simulate the shear area losses within the waffle sections when computing the imaginary critical shear area.

The current design code EC2 achieved good agreement with the test results reported in the literatures (mean of 0.91 and standard deviation of 0.32), but overestimated the Author's test results (for parallel loading, mean of 0.91 and standard deviation of 0.16; for perpendicular loading, mean of 0.81 and standard deviation of 0.20) like the internal column series. However, by including the proposing effective shear factor, the proposed design model achieved good agreements with the Author's test results (mean of 1.05 and standard deviation of 0.16).

7.5 Future Work

Based on the literature review, no study had previously been carried out to investigate the effect of punching shear in biaxial moment transfer, and that the investigation undertaken here is only a preliminary exploration in this area, future research is required.

The followings are therefore suggested for future research:

1. Since the study has not covered the corner column slab connection, destructive testing are required to investigate the effect of punching shear mechanism in the presence of biaxial moment transfer for waffle slabs in the corner column connection.
2. Since the study only covered slab specimens cast from micro-concrete, destructive testing to verify the behaviour of full scale slab specimens are favourable as the size effect on concrete shear strength is significant.
3. Since the study only covered two different sizes of solid section, destructive testing on various sizes of solid section in waffle slab specimens are required to establish the similar effect of punching shear mechanism in the presence of biaxial moment transfer.
4. Since the study has not covered the punching shear mechanism with the presence of shear reinforcement, destructive testing are required to investigate the effect of shear reinforcement in the punching capacity of waffle slabs in the presence of biaxial moment transfer.

References

1. ACI Committee 318. Building Code Requirements for Structural Concrete (ACI 318-11) and Commentary Farmington Hills, Michigan: American Concrete Institute; 2011.

2. ACI-ASCE Committee 326. Shear and Diagonal Tension. ACI Journal Proceedings. 1962 March; 59(3): p. 277-330; and 353-395.

3. Al-Bayati AF, Lau TL, Clark LA. Concentric Punching Shear of Waffle Slab. ACI Structural Journal. 2015 Sep-Oct; 112(5): p. 533-542.

4. Al-Bayati AF. Punching Shear Mechanisms of Waffle Slabs. 2013. Ph.D. Thesis. Department of Civil Engineering, The University of Nottingham, Malaysia Campus. 311 p.

5. Alexander SDB, Simmonds SH. Moment Transfer at Interior Slab-Column Connections. ACI Structural Journal. 2003 Mar-Apr; 100(2): p. 197-202.

6. Andersson JL. Punching of Concrete Slabs with Shear Reinforcement. Meddelande Nr 47, Institutionen for Byggnadsstatik, Kungliga Tekniska Hogskolan, Stockholm. 1963.

7. Base GD. Some Tests on the Punching Shear Strength of Reinforced Concrete Slabs. Technical Report TRA/321. London: Cement and Association; 1959.

8. Bazant ZP, Cao ZP. Size Effect in Punching Shear Failure of Slabs. ACI Journal Proceedings. 1987 Jan-Feb; 84(1): p. 44-53.

9. Bazant ZP, Kim JK. Size Effect in Shear Failure of Longitudinally Reinforced Beams. ACI Journal Proceedings. 1984 Sep-Oct; 81(5): p. 456-468.

10. Bazant ZP, Sun HH. Size Effect in Diagonal Shear Failure: Influence of Aggregate Size and Stirrups. ACI Journal Proceedings. 1987 Jul-Aug; 84: p. 259-272.

11. Boswell LF, Wong SS. The Shear Behavior of Micro-Concrete and its Inclusion in a Proposed Yield Criterion. Proceedings of Cement and Concrete Association Research Seminar. 1981;: p. 217-227.

12. Braestrup MW, Nielsen MP, Jensen BC, Bach F. Axissymmetric Punching of Plain and Reinforced Concrete. Report R75. Copenhagen: Technical University of Denmark, Structural Research Laboratory; 1976.

13. British Standard Instituition, CP110. The Structural Use of Concrete: Part I - Design, Materials and Workmanship; 1972.

14. British Standards Instituition. BS 8110 Structural Use of Concrete - Part I: Code of

Practice for Design and Construction London; 1997.

15. Broms CE. Design Method for Imposed Rotations of Interior Slab-Column Connections. ACI Structural Journal. 2009 Sep-Oct; 106(5): p. 636-645.

16. CEB-FIB. Punching of Structural Concrete Slabs: Bulletin 12 Lausanne: International Federation for Structural Concrete; 2001.

17. Di Stasio J, Van Buren MP. Transfer of Bending Moment between Flat Plate Floor and Column. Journal of American Concrete Institute. 1960 Sep; 57(14): p. 299-314.

18. Elgabry AA, Ghali A. Moment Transfer by Shear in Slab-Column Connections. ACI Structural Journal. 1996 Mar-Apr; 93(2): p. 187-196.

19. Elgabry AA, Ghali A. Tests on Concrete Slab-Column Connections with Stud Shear Reinforcement Subjected to Shear-Moment Transfer. ACI Structural Journal. 1987 Sep-Oct; 84(5): p. 433-442.

20. Elstner RC, Hognestad E. Shearing Strength of Reinforced Concrete Slab. ACI Journal Proceedings. 1956 July; 28(1): p. 29-58.

21. Endersbee LA. Discussion of Reference 49. ACI Journal Proceedings. 1966 Nov; 63(11): p. 1572-1573.

22. Eurocode 2. Design of Concrete Structurees - Part I: General Rules for Building: European Prestandard ENV 1992-1-1; 1991.

23. Fong WJ, Lau TL. Effect of Aggregate Size on Punching Strength of Reinforced Concrete Slabs. Applied Mechanics and Materials. 2016 May; 835: p. 450-454.

24. Gardner NJ, Shao XY. Punchiing Shear of Continuous Flat Reinforced Concrete Slabs. ACI Structural Journal. 1996 Mar-Apr; 93(2): p. 218-228.

25. Gardner NJ. Relationship of the Punching Shear Capacity of Reinforced Concrete Slabs with Shear Strength. ACI Structural Journal. 1990 Jan-Feb; 87(1): p. 66-71.

26. Ghali A, Elmasri MZ, Dilger W. Punching of Flat Plates Under Static and Dynamic Horizontal Forces. ACI Journal Proceedings. 1976 Oct; 73(10): p. 566-572.

27. Ghali A, Megally S. Design for Punching Shear Strength with ACI 318-95. ACI Structural Journal. 1999 Jul-Aug; 96(4): p. 539-548.

28. Ghannoum WM. Size Effect on Shear Strength of Reinforced Concrete Beams. 1998. MSc Thesis. Department of Civil Engineering and Applied Mechanics, McGill University, Canada. 115p.

29. Gonnerman HF. Effect of Size and Shape of Test Specimen on Compressive Strength

of Concrete. Proceedings ASTM. 1925; 25(II): p. 237-250.

30. Hanson NW, Hanson JM. Shear and Moment Transfer between Concrete Slabs and Columns. Journal of the Research and Development Laboratories, Portland Cement Association. 1968 Jan; 10(1): p. 2-16.

31. Harris HG, Sabnis GM,WRN. Small Scale Direct Model of Reinforced and Prestressed Concrete Structures. Report No. 326. Ithaca, N.Y.: Cornell University, Department of Civil Engineering; 1966.

32. Harris HG, Schwindt R, Taaher I, Werner S. Techniques and Materials in the Modelling of Reinforced Concrete Structures under Dynamic Loads. Report 63-54. Port Hueneme, C.A. : Massachusetts Institute of Engineering Laboratory, Department of Civil Engineering; 1963.

33. Hawkins NM, Bao A, Yamazaki J. Moment Transfer from Concrete Slabs to Columns. ACI Structural Journal. 1989 Nov-Dec; 86(6): p. 705-716.

34. Hawkins NM, Corley WG. Transfer of Unbalanced Moment and Shear from Flat Plates to Columns. Publication SP-42, ACI Detroit. 1971; 2: p. 147-176.

35. Hawkins NM, Wong CF, Yang CH. Slab Edge Column Connections Transferring High Intensity Reversing Moments Normal to the Edge of the slab. Structures and Mechanics Report No: SM78-1. Seattle: University of Washington, Department of Civil Engineering; May 1978.

36. Hognested E. Shearing Strength of Reinforced Concrete Column Footings. ACI Journal Proceedings. 1953 Nov; 50: p. 189-208.

37. Hussein AF. Punching Shear Strength at Edge Columns in Ribbed Flat Slabs. 1994. Ph.D. Thesis. Department of Civil Engineering, University of Leeds.

38. Islam S, Park R. Test on Slab-Column Connections with Shear and Unbalanced Flexure. Journal of the Structural Division, ASCE. 1976 Mar; 102(3): p. 549-568.

39. Jiang D, Shen J. Strength of Concrete Slabs in Punching Shear. Journal of Structural Engineering, ASCE. 1986 Dec; 112(12): p. 2578-2591.

40. Johnson RP. Strength Tests on Scaled-down Concrete Suitable for Models, with a Note on Mix Design. Magazine of Concrete Research. 1962 Mar; 14(40).

41. Kadlecek VS, Modry S, Kadlecek VJ. Size Effect of Test Specimens on Tensile Splitting Strength of Concrete: General Relation. Materials and Structures. 2002 Jan-Feb; 35: p. 28-34.

42. Kani GNJ. How Safe are Our Large Concrete Beams? ACI Journal Proceedings. 1967

Mar;: p. 128-141.

43. Kinnunen S, Nylander H. Punching of Concrete Slabs without Shear Reinforcement. Meddelande Nr 38, Institutionen for Byggnadsstatik, Kungliga Tekniska Hogskolan, Stockholm. 1960.

44. Kruger G, Burdet O, Favre R. Punching Strength of R.C. Flat Slabs with Moment Trasnfer. Swiss Federal Institute of Technology, Civil Engineering Department. 2000.

45. Lau TL, Clark LA. Shear Transfer between Ribbed Slab and Edge Column. Magazine of Concrete Research. 2008 Aug; 60(6): p. 411-419.

46. Lau TL, Clark LA. Shear Transfer between Ribbed Slab and Internal Column. Magazine of Concrete Research. 2007 Sep; 59(7): p. 507-516.

47. Lau TL. Shear Transfer Mechanism between Reinforced Concrete Ribbed Slabs and Columns. 2004. Ph.D. Thesis. Department of Civil Engineering, University of Birmingham. 314 p.

48. Long AE. A Two Phase Approach to the Prediction of the Punching Strength of Slabs. Journal of American Concrete Institution. 1975 Feb; 72(2): p. 37-47.

49. Marzouk H, Hussein A. Experimental Investigation on the Behavior of High-Strength Concrete Slabs. ACI Structural Journal. 1991; 88(6): p. 701-713.

50. Marzouk H, Osman M, Helmy S. Behavior of High-Strength Lightweight Aggregatee Concrete Slabs under Column Load and Unbalanced Moment. ACI Structural Journal. 2000 Nov-Dec; 97(6): p. 860-866.

51. Mattock AH, Ibrahim IO, Hofbeck JA. Shear Transfer in Reinforced Concrete. ACI Journal Proceedings. 1969; 66(2): p. 119-128.

52. Megally S, Ghali A. Punching of Concrete Slabs due to Column Moment Transfer. Journal of Structural Engineering. 2000 Feb; 126(2): p. 180-189.

53. Moe J. Shearing Stregnth of Reinforced Concretre Slabs and Footings under Concentrated Loads. Development Department Bulletin D47, Portland Cement Association, Research and Development Laboratories, Skokie, Illinois. 1961.

54. Moehle JP. Strength of Slab-Column Edge Connections. ACI Structural Journal. 1988 Jan-Feb; 85(1): p. 89-98.

55. Neville AM. A General Relation for Strengths of Concrete Specimens of Different Shapes and Sizes. ACI Journal Proceedings. 1966; 63(3): p. 1095-1110.

56. Newmark NM. Torsion in Reinforced Concrete. Structural Research Series No. 226.

Urbana, Illinois: University of Illinois, The University Research Board; 1961.

57. Nielsen MP, Hoang LC. Limit Analysis and Concrete Plasticity Florida, United States: CRC Press, Taylor & Francis Group; 2011.

58. O'Clearly DP, Byrne JG. Testing of Concrete and Mortar in Tension. Engineering, London. 1960 Mar;: p. 384-5.

59. Osman M, Marzouk H, Helmy S. Behavior of High-Strenght Lightweight Concrete Slabs under Punching Loads. ACI Structural Journal. 2000 May-Jun; 97(3): p. 492-498.

60. Pahl PJ, Soosaar K. Structual Models for Architectural and Engineering Education. Report No: R64-3. Cambridge, M.A.: Massachusetts Institute of Technology, Department of Civil Engineering; 1964.

61. Pan AD, Moehle JP. An Experimental Study of Slab-Column Connections. ACI Structural Journal. 1992 Nov-Dec; 89(6): p. 626-638.

62. Park H, Choi K. Improved Strength Model for Interior Flat Plate-Column Connections Subjected to Unbalanced Moment. Journal of Structural Engineering ASCE. 2006 May; 132(5): p. 694-704.

63. Park R, Gamble WL. Reinforced Concrete Slabs. 2nd ed. Danvers, M.A.: John Wiley & Sons, Inc; 2000.

64. Popovics S. Effect of Curing Method and Final Moisture Condition on Compressive Strength of Concrete. ACI Journal Proceedings. 1986; 83(4): p. 650-657.

65. Rankin GIB, Long AE. Predicting the Punching Strength of Conventional Slab-Column Specimens. Proceedings Instituition of Civil Engineers. 1987 Apr; 82(1): p. 327-346.

66. Regan PE, Braestrup MW. Punching Shear in Reinforced Concrete: A State of Art Report. CEB-Bulletin No. 168. Lausanne:, Comite Euro-Intenrational; 1985.

67. Regan PE. Behavior of Reinforced Concrete Flat Slabs. CIRIA Report 89. London:, Construction Industry Research and Information Association; 1981.

68. Richart FE. Reinforced Concrete Wall and Column Footings. ACI Journal Proceedings. 1948 Oct-Nov; 45: p. 237-260.

69. Rossi P. Effect d'echelle sur le comportement du beton en traction. Bulletin Liaison Laboratorires des Ponts et Chaussees. 1992 Nov-Dec; 182: p. 11-20.

70. Sabnis GM. Size Effects in Material Systems and their Impact on Model Studies: A Theoretical Approach. In Proceeding of SECT AM X Conference; 1980; Knoxville. p. 649-668.

71. Salim W, Sebastiam WM. Plasticity Model for Predicting Punching Shear Strenghts of Reinforced Concrete Slabs. ACI Structural Journal. 2002 Nov-Dec; 99(6): p. 827-835.

72. Sigurdsson TG. Punching Shear by Eccentric Loading. 1991. MSc Thesis. Department of Structural Engineering, Technical University of Denmark.

73. Stamenkovic A, Chapman JC. Local Strength at Column Heads in Flat Slabs subjected to a Combined Vertical and Horizontal Loading. Proceedings Instituition of Civil Engineers (London). 1974 Jun; 57(II): p. 205-232.

74. Surdasana KI. Punching Shear in Edge and Corner Column Slab Connections of Flat Plate Structures. 2001 Dec. Ph.D. Thesis. Department of Engineering, The University of Ottawa, Ottawa. 225 p.

75. Swamy RN, Falih FM. Development of a Small Aggregate Concrete for Structural Similitude of Slab-Column Connections. Design of Concrete Structures, The Use of Model Analysis, Elzevier Applied Science Publishers, Barking U.K. 1985;: p. 25-37.

76. Talbot AN. Reinforced Concrete Wall Footings and Column Footings. Bulletin No. 67. Urbana: University of Illinois , Engineering Experiment Station; 1913.

77. Tomaszewics A. High-Strength Concrete: SP2-Plates and Shells - Report 2.3, Punching Shear of Capacity of Reinforced Concrete Slabs. Report No. STE70 A93082. Norway: Trondheim, SINTEF Structures and Concrete; 1993.

78. Whitney C.S.. Ultimate Shear Strength of Reinforced Concrete Flat Slabs, Footings, Beams and Frames Members without Shear Reinforcement. ACI Journal Proceedings. 1957 Oct;: p. 265-298.

79. William AL, Mario P. Size Effects in Small-Scale Models. ACI Journal Proceedings. 1966 Nov; 63(11): p. 1191-1204.

80. Wright PJF. The Effect of the Method of Test on the Flexural Strength of Concrete. Magazine of Concrete Research. 1952; 4(11): p. 67-76.

81. Xiang XZ. Punching Shear Strength of Waffle Slabs at Internal Column. 1993. Ph.D. Thesis. Department of Civil Engineering, University of Leeds.

82. Yitzhaki R. Punching Shear of Reinforced Concrete Slabs. ACI Journal Proceedings. 1966 May; 63(5): p. 527-542.

83. Zaghlool ERF. Strength and Behavior of Corner and Edge Column-Slab Connections in Reinforced Concrete Flat Plates. 1977. Ph.D. Thesis, Department of Civil Engineering, The University of Calgary, Calgary. 366p.

Appendix A

Theoretical Model for Concentric Punching at Internal Column

A.1 Flow Chart of Concentric Punching at Internal Column Theoretical Model

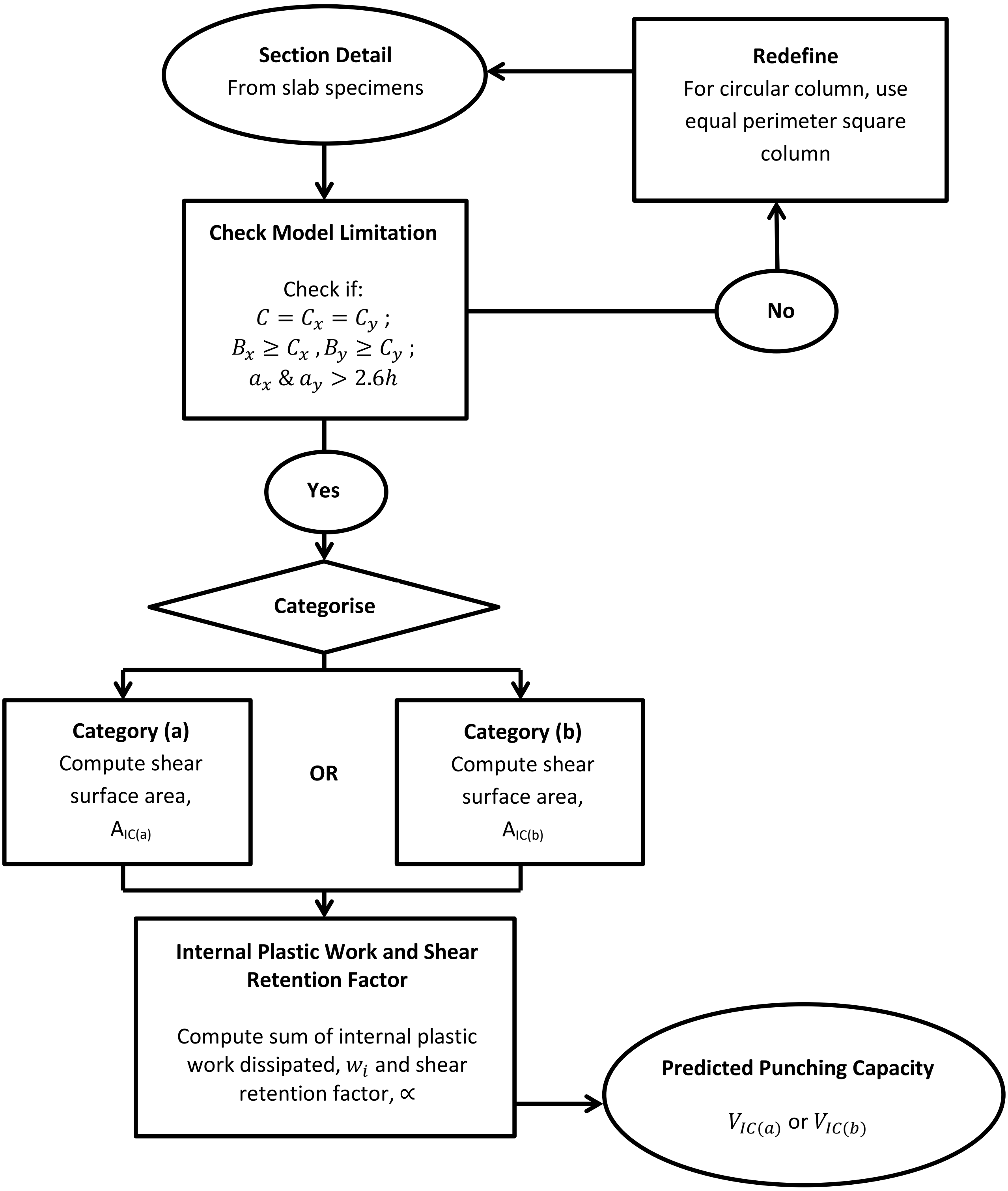

A.2 Section Details

For any given slab, the following information are required to predict the punching capacity:

Column Size: C_x, C_y

(for circular column, use square column with equivalent perimeter)

Size of Solid Section: B_x, B_y

Top Slab Thickness and Overall Height of Slab: h_1, h

Waffle Width: w

Waffle Rib Width: b_{rib}

Shear Spans: a_x, a_y

Cylindrical Concrete Compressive Strength: σ_c

Reinforcement Ratios: ρ_x, ρ_y

A.3 Limits and Assumption

If the actual a_x; or a_y is less than $2.6h$, use $2.6h$.

A.4 Categories

If $a_{x4} < a_{x1}\ or\ a_x$; and $a_{y4} < a_{y1}\ or\ a_y$, then Category (a)

If $a_{x4} \geq a_{x1}\ or\ a_x$; and $a_{y4} \geq a_{y1}\ or\ a_y$, then Category (b)

A.5 Category (a)

A.5.1 General Equations (see Figure 5.2)

$$a_{x1} = a_x\left(1 - \frac{h_1}{h}\right) \qquad a_{y1} = a_y\left(1 - \frac{h_1}{h}\right)$$

$$a_{x2} = \sqrt{{a_{x1}}^2\left(1 - \frac{{a_{y3}}^2}{{a_{y1}}^2}\right)} \qquad a_{y2} = \sqrt{{a_{y1}}^2\left(1 - \frac{{a_{x3}}^2}{{a_{x1}}^2}\right)}$$

$$a_{x3} = \frac{B_x - C_x}{2} \qquad a_{y3} = \frac{B_y - C_y}{2}$$

$$a_{x4} = a_{x3} - b_{rib} \qquad a_{y4} = a_{y3} - b_{rib}$$

$$a_{x5} = w - a_{x4} \qquad a_{y5} = w - a_{y4}$$

$a_{x6} = a_{x1} - a_{x3}$ $\quad$ $a_{y6} = a_{y1} - a_{y3}$

$\theta_{zx} = \tan^{-1}\left(\frac{h}{a_x}\right)$ $\quad$ $\theta_{zy} = \tan^{-1}\left(\frac{h}{a_y}\right)$

$\theta_{avg} = \tan^{-1}\left(\frac{2h}{a_x+a_y}\right)$

$$A_1 = a_{x5}a_{y6}$$

$$A_2 = \int_0^{a_{x4}} \sqrt{{a_{x1}}^2 - x^2}\,dx - \int_0^{a_{x4}} a_{y3}\,dx$$

$$A_2 = \left[\frac{a_{x4}\sqrt{{a_{x1}}^2 - {a_{x4}}^2} + {a_{x1}}^2 \sin^{-1}\left(\frac{a_{x4}}{a_{x1}}\right)}{2}\right] - \left[a_{x4}a_{y3}\right]$$

$$A_3 = \int_{a_{x3}}^{a_{x2}} \sqrt{{a_{x1}}^2 - x^2}\,dx - \int_{a_{x3}0}^{a_{x2}} a_{y3}\,dx$$

$$A_3 = \left\{\left[\frac{a_{x2}\sqrt{{a_{x1}}^2 - {a_{x2}}^2} + {a_{x1}}^2 \sin^{-1}\left(\frac{a_{x2}}{a_{x1}}\right)}{2}\right] - \left[\frac{a_{x3}\sqrt{{a_{x1}}^2 - {a_{x3}}^2} + {a_{x1}}^2 \sin^{-1}\left(\frac{a_{x3}}{a_{x1}}\right)}{2}\right]\right\} - \left\{\left[a_{x2}a_{y3}\right] - \left[a_{x3}a_{y3}\right]\right\}$$

A.5.2 Total Shear Area in Plan

$$A_{total} = \pi {a_x}^2 + 2a_xC_x + 2a_yC_y$$

A.5.3 Total Shear Area Loss in Plan

$$A_{loss} = 8A_1 + 8A_2 + 4A_3$$

A.5.4 Shear Surface Area, $A_{IC(a)}$

$$A_{IC(a)} = \frac{\left[\pi {a_x}^2 - (8A_2 + 4A_3)\right]}{\cos\theta_{avg}} + \frac{\left[2a_xC_x - 4A_1\right]}{\cos\theta_{zx}} + \frac{\left[2a_yC_y - 4A_1\right]}{\cos\theta_{zy}}$$

A.6 Category (b)

A.6.1 Shear surface area, $A_{IC(b)}$

$$A_{IC(b)} = h\sqrt{1 + \left(\cot\theta_{avg}\right)^2}\left(2C_x + 2C_y + \pi h \cot\theta_{avg}\right)$$

A.7 Punching Capacity

$$V_{IC} = \propto w_i A_{IC}$$

Where:

$\propto$ = shear retention factor, 0.7 for micro-concrete; and 1.0 for normal-concrete

w_i = sum of internal plastic work dissipated (see Eq. 2.19)

Appendix B

Theoretical Model for Eccentric Punching at Internal Column

B.1 Flow Chart of Eccentric Punching at Internal Column Theoretical Model

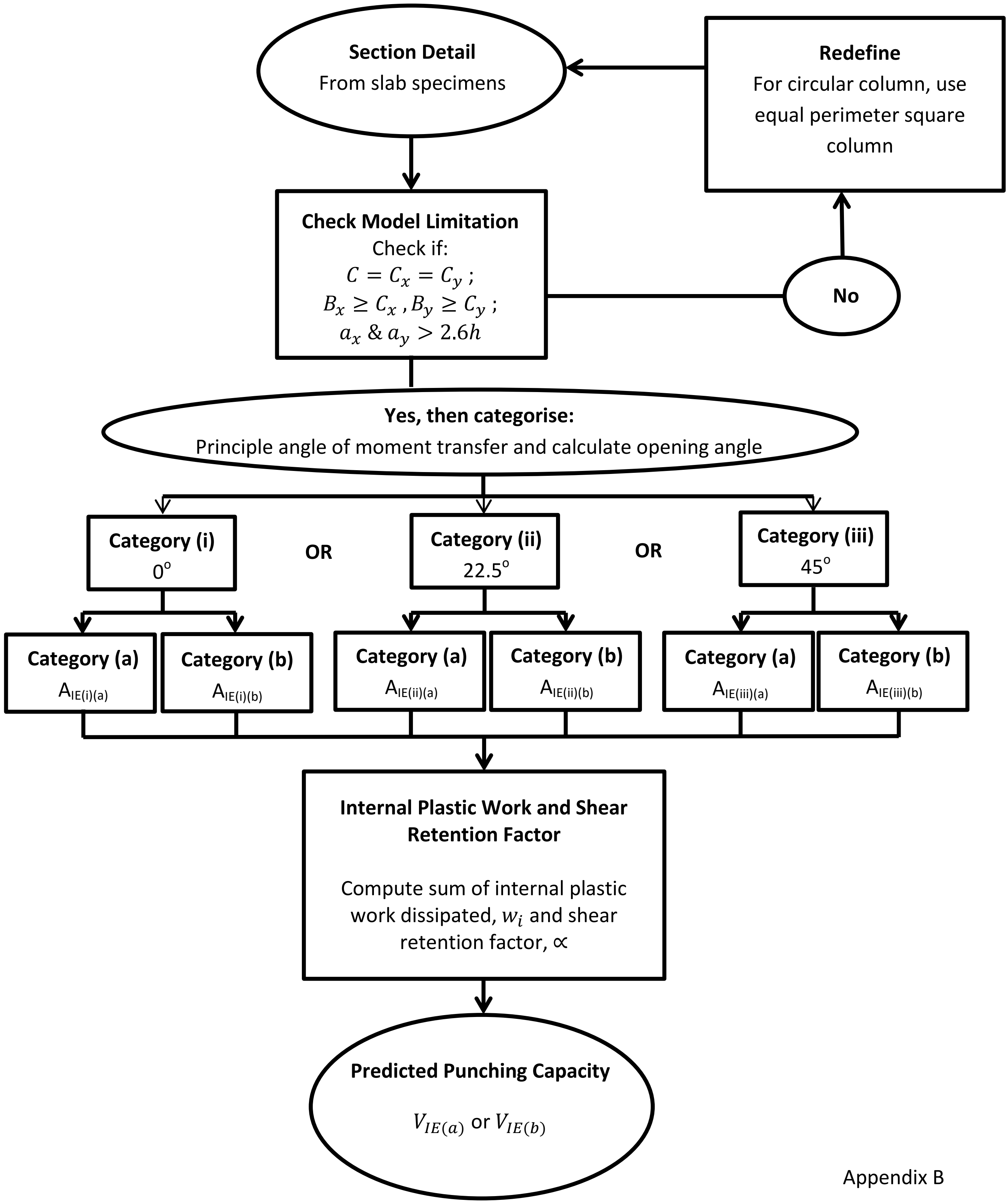

B.2 Section Details

For any given slab, the following information are required to predict the punching capacity:

Column Size: C_x, C_y

(for circular column, use square column with equivalent perimeter)

Size of Solid Section: B_x, B_y

Top Slab Thickness and Overall Height of Slab: h_1, h

Waffle Width: w

Waffle Rib Width: b_{rib}

Shear Spans: a_x, a_y

Cylindrical Concrete Compressive Strength: σ_c

Reinforcement Ratios: ρ_x, ρ_y

B.3 Limits and Assumption

If the actual a_x or a_y is less than $2.6h$, use $2.6h$.

B.4 Categories

B.4.1 Principle Angles of Biaxial Moment Transfer

If principle angle of biaxial moment transfer is set to 0^{o}, then category (i)

If principle angle of biaxial moment transfer is set to 22.5^{o}, then category (ii)

If principle angle of biaxial moment transfer is set to 45^{0}, then category (iii)

B.4.2 Size Reduction

If $a_{x4} < a_{x1}\ or\ a_x$; and $a_{y4} < a_{y1}\ or\ a_y$, then Category (a)

If $a_{x4} \geq a_{x1}\ or\ a_x$; and $a_{y4} \geq a_{y1}\ or\ a_y$, then Category (b)

B.5 Opening Angle, δ

$$Opening\ angle, \delta = 87.682 * \left(\frac{v_{AB}}{v_{AB} + v_{CD}} - 0.5\right)^{0.5056}$$

Where, $$\frac{v_{AB}}{v_{AB}+v_{CD}} = \frac{V_U J_C + (M_U - M_f) c_{AB} A_C}{2V_U J_C + (M_U - M_f)(c_{AB} - c_{CD})}$$

B.6

B.6.1 General Equations (see Figure 5.17, 5.18 or 5.19)

$$a_{x1} = a_x\left(1 - \frac{h_1}{h}\right) \qquad a_{y1} = a_y\left(1 - \frac{h_1}{h}\right)$$

$$a_{x2} = \sqrt{{a_{x1}}^2\left(1 - \frac{{a_{y3}}^2}{{a_{y1}}^2}\right)} \qquad a_{y2} = \sqrt{{a_{y1}}^2\left(1 - \frac{{a_{x3}}^2}{{a_{x1}}^2}\right)}$$

$$a_{x3} = \frac{B_x - C_x}{2} \qquad a_{y3} = \frac{B_y - C_y}{2}$$

$$a_{x4} = a_{x3} - b_{rib} \qquad a_{y4} = a_{y3} - b_{rib}$$

$$a_{x5} = w - a_{x4} \qquad a_{y5} = w - a_{y4}$$

$$a_{x6} = a_{x1} - a_{x3} \qquad a_{y6} = a_{y1} - a_{y3}$$

$$\theta_{zx} = \tan^{-1}\left(\frac{h}{a_x}\right) \qquad \theta_{zy} = \tan^{-1}\left(\frac{h}{a_y}\right)$$

$$\theta_{avg} = \tan^{-1}\left(\frac{2h}{a_x + a_y}\right)$$

$$A_1 = a_{x5} a_{y6}$$

$$A_2 = \int_0^{a_{x4}} \sqrt{{a_{x1}}^2 - x^2}\,dx - \int_0^{a_{x4}} a_{y3}\,dx$$

$$A_2 = \left[\frac{a_{x4}\sqrt{{a_{x1}}^2 - {a_{x4}}^2} + {a_{x1}}^2 \sin^{-1}\left(\frac{a_{x4}}{a_{x1}}\right)}{2}\right] - \left[a_{x4} a_{y3}\right]$$

$$A_3 = \int_{a_{x3}}^{a_{x2}} \sqrt{{a_{x1}}^2 - x^2}\,dx - \int_{a_{x3}0}^{a_{x2}} a_{y3}\,dx$$

$$A_3 = \left\{\left[\frac{a_{x2}\sqrt{{a_{x1}}^2 - {a_{x2}}^2} + {a_{x1}}^2 \sin^{-1}\left(\frac{a_{x2}}{a_{x1}}\right)}{2}\right] - \left[\frac{a_{x3}\sqrt{{a_{x1}}^2 - {a_{x3}}^2} + {a_{x1}}^2 \sin^{-1}\left(\frac{a_{x3}}{a_{x1}}\right)}{2}\right]\right\} - \left\{\left[a_{x2} a_{y3}\right] - \left[a_{x3} a_{y3}\right]\right\}$$

B.6.2.1 For category (i)

B.6.2.1.1 For category (a)

B.6.2.1.1.1 Total Shear Area in Plan

$$A_{total} = \frac{3\pi a_x a_y}{4} + a_x C_y + 2a_y C_x + \gamma * \left(a_x C_y + \frac{\pi a_x a_y}{4}\right)$$

Where: γ = ratio of angle opening = $\frac{45°-\delta}{45°}$, where $0° < \delta \leq 125°$

B.6.2.1.1.2 Total Shear Area Loss in Plan

When $e = 50mm$,

$$A_{loss} = 6A_1 + 6A_2 + 3A_3$$

When $e = 100mm$,

$$A_{loss} = 5.62A_1 + 4A_2 + 2A_3$$

When $e = 150mm$,

$$A_{loss} = 4A_1 + 4A_2 + 2A_3$$

B.6.2.1.1.3 Shear Surface Area, $A_{IE(i)(a)}$

When $e = 50mm$,

$$A_{IE(i)(a)} = \frac{\left[\left(\frac{3\pi a_x a_y}{4} + \gamma * \left(\frac{\pi a_x a_y}{4}\right)\right) - (6A_2 + 3A_3)\right]}{\cos\theta_{avg}} + \frac{\left[\left(a_x C_y + \gamma * \left(a_x C_y\right)\right) - (2A_1)\right]}{\cos\theta_{zx}} + \frac{\left[\left(2a_y C_x\right) - (4A_1)\right]}{\cos\theta_{zy}}$$

When $e = 100mm$,

$$A_{IE(i)(a)} = \frac{\left[\left(\frac{3\pi a_x a_y}{4} + \gamma * \left(\frac{\pi a_x a_y}{4}\right)\right) - (4A_2 + 2A_3)\right]}{\cos\theta_{avg}} + \frac{\left[\left(a_x C_y + \gamma * \left(a_x C_y\right)\right) - (2A_1)\right]}{\cos\theta_{zx}} + \frac{\left[\left(2a_y C_x\right) - (3.62A_1)\right]}{\cos\theta_{zy}}$$

When $e = 150mm$,

$$A_{IE(i)(a)} = \frac{\left[\left(\frac{3\pi a_x a_y}{4} + \gamma * \left(\frac{\pi a_x a_y}{4}\right)\right) - (4A_2 + 2A_3)\right]}{\cos\theta_{avg}} + \frac{\left[\left(a_x C_y + \gamma * \left(a_x C_y\right)\right) - (2A_1)\right]}{\cos\theta_{zx}} + \frac{\left[\left(2a_y C_x\right) - (2A_1)\right]}{\cos\theta_{zy}}$$

B.6.2.1.2 For category (b)

B.5.2.1.2.1 Shear Surface Area, $A_{IE(i)(b)}$

$$A_{IE(i)(b)} = h\sqrt{1 + (\cot\theta)^2}\left[2C_x + C_y + \frac{3\pi h \cot\theta}{4} + \gamma * \left(C_y + \frac{\pi h \cot\theta}{4}\right)\right]$$

Where: γ = ratio of angle opening = $\frac{45° - \delta}{45°}$, where $0° < \delta \leq 125°$

B.6.2.2 For category (ii)

B.6.2.2.1 For category (a)

B.6.2.2.1.1 Total Shear Area in Plan

$$A_{total} = \frac{3\pi a_x a_y}{4} + 1.08a_x C_y + 1.92a_y C_x + \gamma * \left(0.92a_x C_y + 0.08a_y C_x + \frac{\pi a_x a_y}{4}\right)$$

Where: γ = ratio of angle opening = $\frac{45° - \delta}{45°}$, where $0° < \delta \leq 125°$

B.6.2.2.1.2 Total Shear Area Loss in Plan

When $e = 50mm$,

$A_{loss} = 6.15A_1 + 6.18A_2 + 3A_3$

When $e = 100mm$,

$A_{loss} = 5A_1 + 5A_2 + 2A_3$

When $e = 150mm$,

$A_{loss} = 4A_1 + 3.87A_2 + 2A_3$

B.6.2.2.1.3 Shear Surface Area, $A_{IE(ii)(a)}$

When $e = 50mm$,

$$A_{IE(ii)(a)} = \frac{\left[\left(\frac{3\pi a_x a_y}{4} + \gamma * \left(\frac{\pi a_x a_y}{4}\right)\right) - (6.18A_2 + 3A_3)\right]}{\cos\theta_{avg}} + \frac{\left[\left(1.08a_x C_y + \gamma * \left(0.92a_x C_y\right)\right) - (2.15A_1)\right]}{\cos\theta_{zx}} + \frac{\left[\left(1.92a_y C_x + \gamma * \left(0.08a_y C_x\right)\right) - (4A_1)\right]}{\cos\theta_{zy}}$$

When $e = 100mm$,

$$A_{IE(ii)(a)} = \frac{\left[\left(\frac{3\pi a_x a_y}{4} + \gamma * \left(\frac{\pi a_x a_y}{4}\right)\right) - (5A_2 + 2A_3)\right]}{\cos\theta_{avg}} + \frac{\left[\left(1.08a_x C_y + \gamma * \left(0.92a_x C_y\right)\right) - (2A_1)\right]}{\cos\theta_{zx}} + \frac{\left[\left(1.92a_y C_x + \gamma * \left(0.08a_y C_x\right)\right) - (3A_1)\right]}{\cos\theta_{zy}}$$

When $e = 150mm$,

$$A_{IE(ii)(a)} = \frac{\left[\left(\frac{3\pi a_x a_y}{4} + \gamma * \left(\frac{\pi a_x a_y}{4}\right)\right) - (3.87A_2 + 2A_3)\right]}{\cos\theta_{avg}} + \frac{\left[\left(1.08a_x C_y + \gamma * \left(0.92a_x C_y\right)\right) - (2A_1)\right]}{\cos\theta_{zx}} + \frac{\left[\left(1.92a_y C_x + \gamma * \left(0.08a_y C_x\right)\right) - (2A_1)\right]}{\cos\theta_{zy}}$$

B.6.2.2.2 For category (b)

B.6.2.2.2.1 Shear Surface Area, $A_{IE(ii)(b)}$

$$A_{IE(ii)(b)} = h\sqrt{1 + (\cot\theta)^2}\left[1.92C_x + 1.08C_y + \frac{3\pi h \cot\theta}{4} + \gamma * \left(0.08C_x + 0.92C_y + \frac{\pi h \cot\theta}{4}\right)\right]$$

Where: γ = ratio of angle opening = $\frac{45° - \delta}{45°}$, where $0° < \delta \leq 125°$

B.6.2.3 For category (iii)

B.6.2.3.1 For category (a)

B.6.2.3.1.1 Total Shear Area in Plan

$$A_{total} = \frac{3\pi a_x a_y}{4} + 1.5a_x C_y + 1.5a_y C_x + \ \gamma * \left(0.5a_x C_y + 0.5a_y C_x + \frac{\pi a_x a_y}{4}\right)$$

Where: γ = ratio of angle opening = $\frac{45°-\delta}{45°}$, where $0° < \delta \leq 125°$

B.6.2.3.1.2 Total Shear Area Loss in Plan

When $e = 50mm$,

$$A_{loss} = 6A_1 + 6A_2 + 3A_3$$

When $e = 100mm$,

$$A_{loss} = 4A_1 + 4A_2 + 3A_3$$

When $e = 150mm$,

$$A_{loss} = 4A_1 + 3.32A_2 + A_3$$

B.6.2.3.1.3 Shear Surface Area, $A_{IE(iii)(a)}$

When $e = 50mm$,

$$A_{IE(iii)(a)} = \frac{\left[\left(\frac{3\pi a_x a_y}{4} + \gamma * \left(\frac{\pi a_x a_y}{4}\right)\right) - (6A_2 + 3A_3)\right]}{\cos\theta_{avg}} + \frac{\left[\left(1.5a_x C_y + \gamma * \left(0.5a_x C_y\right)\right) - (3A_1)\right]}{\cos\theta_{zx}} + \frac{\left[\left(1.5a_y C_x + \gamma * \left(0.5a_y C_x\right)\right) - (3A_1)\right]}{\cos\theta_{zy}}$$

When $e = 100mm$,

$$A_{IE(iii)(a)} = \frac{\left[\left(\frac{3\pi a_x a_y}{4} + \gamma * \left(\frac{\pi a_x a_y}{4}\right)\right) - (4A_2 + 3A_3)\right]}{\cos\theta_{avg}} + \frac{\left[\left(1.5a_x C_y + \gamma * \left(0.5a_x C_y\right)\right) - (2A_1)\right]}{\cos\theta_{zx}} + \frac{\left[\left(1.5a_y C_x + \gamma * \left(0.5a_y C_x\right)\right) - (2A_1)\right]}{\cos\theta_{zy}}$$

When $e = 150mm$,

$$A_{IE(iii)(a)} = \frac{\left[\left(\frac{3\pi a_x a_y}{4} + \gamma * \left(\frac{\pi a_x a_y}{4}\right)\right) - (3.32A_2 + A_3)\right]}{\cos\theta_{avg}} + \frac{\left[\left(1.5a_x C_y + \gamma * \left(0.5a_x C_y\right)\right) - (2A_1)\right]}{\cos\theta_{zx}} + \frac{\left[\left(1.5a_y C_x + \gamma * \left(0.5a_y C_x\right)\right) - (2A_1)\right]}{\cos\theta_{zy}}$$

B.6.2.3.2 For category (b)

B.6.2.3.2.1 Shear Surface Area, $\boldsymbol{A_{IE(iii)(b)}}$

$$A_{IE(iii)(b)} = h\sqrt{1 + (\cot\theta)^2}\left[\frac{3C_x}{2} + \frac{3C_y}{2} + \frac{3\pi h\cot\theta}{4} + \gamma * \left(\frac{C_x}{2} + \frac{C_y}{2} + \frac{\pi h\cot\theta}{4}\right)\right]$$

Where: γ = ratio of angle opening = $\frac{45° - \delta}{45°}$, where $0° < \delta \leq 125°$

B.7.1 Punching Capacity

$V_{IE} = \propto w_i A_{IE}$

Where:

$\propto$ = shear retention factor, 0.7 for micro-concrete; and 1.0 for normal-concrete

w_i = sum of internal plastic work dissipated (see Eq. 2.19)

Appendix C

Theoretical Model for Punching at Edge Column

C.1 Flow Chart of Edge Punching Theoretical Model

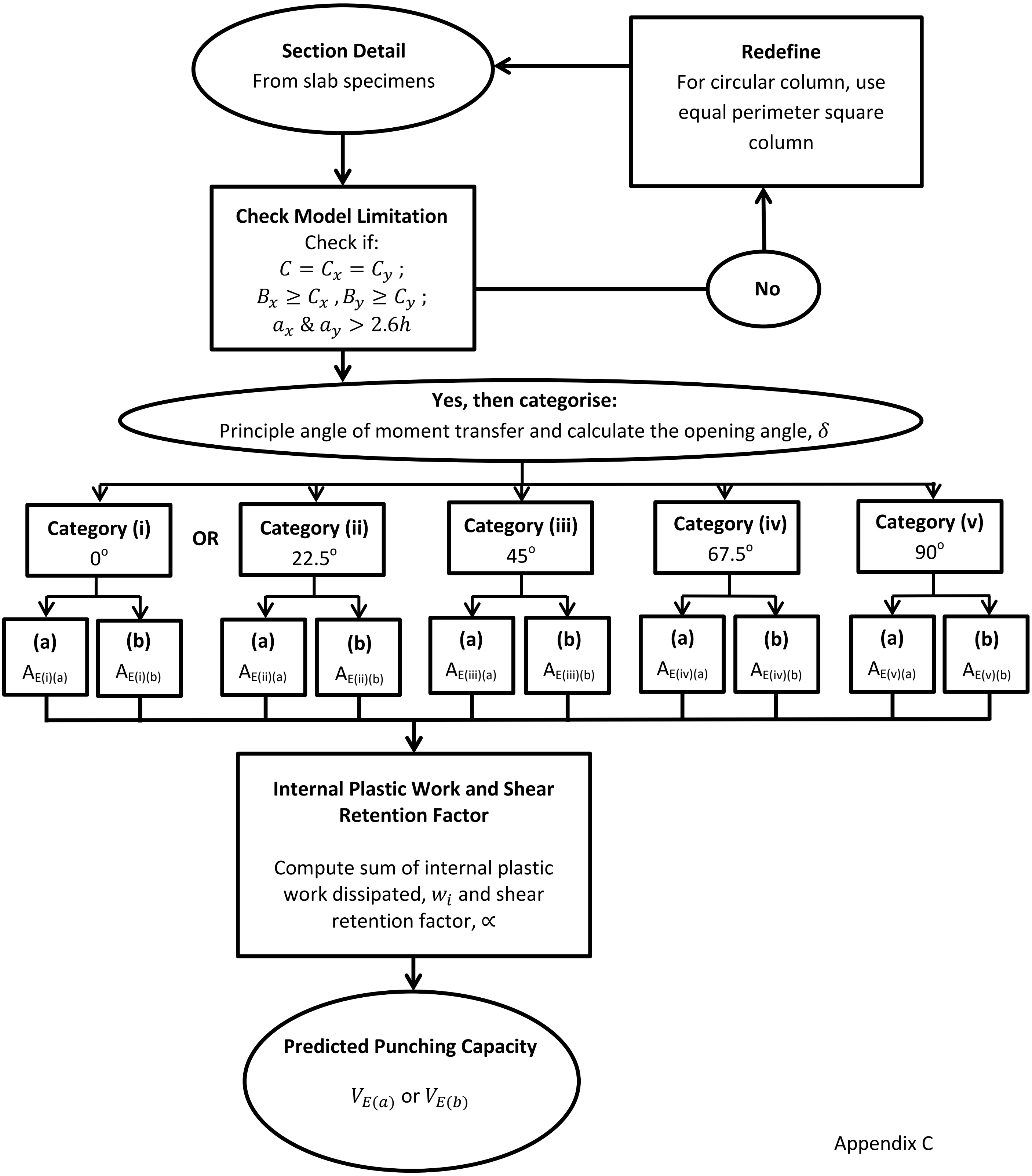

C.2 Section Details

For any given slab, the following information are required to predict the punching capacity:

Column Size: C_x, C_y

(for circular column, use square column with equivalent perimeter)

Size of Solid Section: B_x, B_y

Top Slab Thickness and Overall Height of Slab: h_1, h

Waffle Width: w

Waffle Rib Width: b_{rib}

Shear Spans: a_x, a_y

Cylindrical Concrete Compressive Strength: σ_c

Reinforcement Ratios: ρ_x, ρ_y

C.3 Limits and Assumption

If the actual a_x or a_y is less than $2.6h$, use $2.6h$.

C.4 Categories

C.4.1 Principle Angles of Biaxial Moment Transfer

If principle angle of biaxial moment transfer is set to 0^o, then category (i)

If principle angle of biaxial moment transfer is set to 22.5^o, then category (ii)

If principle angle of biaxial moment transfer is set to 45^0, then category (iii)

If principle angle of biaxial moment transfer is set to 67.5^o, then category (iv)

If principle angle of biaxial moment transfer is set to 90^0, then category (v)

C.4.2 Size Reduction

If $a_{x4} < a_{x1}\ or\ a_x$; and $a_{y4} < a_{y1}\ or\ a_y$, then Category (a)

If $a_{x4} \geq a_{x1}\ or\ a_x$; and $a_{y4} \geq a_{y1}\ or\ a_y$, then Category (b)

C.5 Opening Angle, δ

$$Opening\ angle, \delta = 87.682 * \left(\frac{v_{AB}}{v_{AB} + v_{CD}} - 0.5\right)^{0.5056}$$

Where, $\frac{v_{AB}}{v_{AB}+v_{CD}} = \frac{V_U J_C + (M_U - M_f) c_{AB} A_C}{2V_U J_C + (M_U - M_f)(c_{AB} - c_{CD})}$

C.6

C.6.1 General Equations (see Figure 5.40, 5.41, 5.42, 5.43 or 5.44)

$$a_{x1} = a_x \left(1 - \frac{h_1}{h}\right) \qquad a_{y1} = a_y \left(1 - \frac{h_1}{h}\right)$$

$$a_{x2} = \sqrt{{a_{x1}}^2 \left(1 - \frac{{a_{y5}}^2}{{a_{y1}}^2}\right)} \qquad a_{y2} = \sqrt{{a_{y1}}^2 \left(1 - \frac{{a_{x5}}^2}{{a_{x1}}^2}\right)}$$

$$a_{x3} = \sqrt{{a_{x1}}^2 \left(1 - \frac{{a_{y4}}^2}{{a_{y1}}^2}\right)} \qquad a_{y3} = \sqrt{{a_{y1}}^2 \left(1 - \frac{{a_{x4}}^2}{{a_{x1}}^2}\right)}$$

$$a_{x4} = B_x - C_x \qquad a_{y4} = B_x - C_x$$

$$a_{x5} = a_{x4} - b_{rib} \qquad a_{y5} = a_{y4} - b_{rib}$$

$$a_{x6} = w - a_{x5} \qquad a_{y6} = a_{y5} - w$$

$$\theta_{zx} = \tan^{-1}\left(\frac{h}{a_x}\right) \qquad \theta_{zy} = \tan^{-1}\left(\frac{h}{a_y}\right)$$

$$\theta_{avg} = \tan^{-1}\left(\frac{2h}{a_x + a_y}\right)$$

$$A_1 = w * (a_{x1} - a_{x4})$$

$$A_2 = \int_{a_{y6}}^{a_{y5}} \sqrt{{a_{x1}}^2 - \frac{{a_{x1}}^2 y^2}{{a_{y1}}^2}}\, dy - \int_{a_{y6}}^{a_{y5}} a_{x4}\, dy$$

$$A_2 = \left\{\left[\frac{a_{x1} a_{y5} \sqrt{{a_{y1}}^2 - {a_{y5}}^2} + a_{x1} {a_{y1}}^2 \sin^{-1}\left(\frac{a_{y5}}{a_{y1}}\right)}{2a_{y1}}\right] - \left[\frac{a_{x1} a_{y6} \sqrt{{a_{y1}}^2 - {a_{y6}}^2} + a_{x1} {a_{y1}}^2 \sin^{-1}\left(\frac{a_{y6}}{a_{y1}}\right)}{2a_{y1}}\right]\right\} - \{[a_{x4} a_{y5}] - [a_{x4} a_{y6}]\}$$

$$A_3 = \int_{a_{y4}}^{a_{y3}} \sqrt{{a_{x1}}^2 - \frac{{a_{x1}}^2 y^2}{{a_{y1}}^2}}\, dy - \int_{a_{y4}}^{a_{y3}} a_{x4}\, dy$$

$$A_3 = \left\{\left[\frac{a_{x1}a_{y3}\sqrt{{a_{y1}}^2 - {a_{y3}}^2} + a_{x1}{a_{y1}}^2 \sin^{-1}\left(\frac{a_{y3}}{a_{y1}}\right)}{2a_{y1}}\right] - \left[\frac{a_{x1}a_{y4}\sqrt{{a_{y1}}^2 - {a_{y4}}^2} + a_{x1}{a_{y1}}^2 \sin^{-1}\left(\frac{a_{y4}}{a_{y1}}\right)}{2a_{y1}}\right]\right\} - \{[a_{x4}a_{y3}] - [a_{x4}a_{y4}]\}$$

$$A_4 = \int_{0}^{a_{x5}} \sqrt{{a_{y1}}^2 - \frac{{a_{y1}}^2 x^2}{{a_{x1}}^2}}\, dx - \int_{0}^{a_{x5}} a_{y4}\, dx$$

$$A_4 = \left[\frac{a_{x5}a_{y1}\sqrt{{a_{x1}}^2 - {a_{x5}}^2} + {a_{x1}}^2 a_{y1} \sin^{-1}\left(\frac{a_{x5}}{a_{x1}}\right)}{2a_{x1}}\right] - [a_{x5}a_{y4}]$$

$$A_5 = a_{x6} * (a_{y1} - a_{y4})$$

C.6.2.1 For category (i)

C.6.2.1.1 For category (a)

C.6.2.1.1.1 Total Shear Area in Plan

$$A_{total} = \frac{3\pi a_x a_y}{8} + a_x C_y + a_y C_x + \gamma * \left(a_x C_y + \frac{\pi a_x a_y}{8}\right)$$

Where: γ = ratio of angle opening = $\frac{45°-\delta}{45°}$, where $0° < \delta \leq 45°$

$$A_{total} = \frac{\pi a_x a_y}{4} + a_x C_y + \frac{a_y C_x}{2} + \gamma * \left(\frac{a_y C_x}{2} + \frac{\pi a_x a_y}{8}\right)$$

Where: γ = ratio of angle opening = $\frac{90°-\delta}{45°}$, where $45° < \delta \leq 90°$

$$A_{total} = \frac{\pi a_x a_y}{8} + a_x C_y + \gamma * \left(\frac{a_y C_x}{2} + \frac{\pi a_x a_y}{8}\right)$$

Where: γ = ratio of angle opening = $\frac{135°-\delta}{45°}$, where $90° < \delta \leq 125°$ (anything more than 125°, use 125°)

C.6.2.1.1.2 Total Shear Area Loss in Plan

For 50 mm,

$$A_{loss} = A_1 + A_2 + 2A_3 + 2A_4 + 2A_5$$

For 100 mm,

$$A_{loss} = A_1 + A_2 + A_3 + A_4 + A_5$$

For 150 mm,

$$A_{loss} = A_1 + A_2 + A_3 + 0.71A_4$$

C.6.2.1.1.3 Shear Surface Area, $A_{E(i)(a)}$

For 50 mm,

$$A_{E(i)(a)} = \frac{\left[\left(\frac{3\pi a_x a_y}{8} + \gamma * \left(\frac{\pi a_x a_y}{8}\right)\right) - (A_2 + 2A_3 + 2A_4)\right]}{\cos\theta_{avg}} + \frac{\left[(a_x C_y) - A_1\right]}{\cos\theta_{zx}} + \frac{\left[\left(a_y C_x + \gamma * (a_y C_x)\right) - (2A_5)\right]}{\cos\theta_{zy}}$$

For 100 mm,

$$A_{E(i)(a)} = \frac{\left[\left(\frac{\pi a_x a_y}{8} + \gamma * \left(\frac{\pi a_x a_y}{8}\right)\right) - (A_2 + A_3 + A_4)\right]}{\cos\theta_{avg}} + \frac{\left[a_x C_y - A_1\right]}{\cos\theta_{zx}} + \frac{\left[\gamma * \left(a_y C_x\right) - A_5\right]}{\cos\theta_{zy}}$$

For 150 mm,

$$A_{E(i)(a)} = \frac{\left[\left(\frac{\pi a_x a_y}{8} + \gamma * \left(\frac{\pi a_x a_y}{8}\right)\right) - (A_2 + A_3 + 0.71A_4)\right]}{\cos\theta_{avg}} + \frac{\left[a_x C_y - A_1\right]}{\cos\theta_{zx}} + \frac{\left[\gamma * \left(a_y C_x\right)\right]}{\cos\theta_{zy}}$$

C.6.2.1.2 For category (b)

C.6.2.1.2.1 Shear Surface Area, $A_{E(i)(b)}$

$$A_{E(i)(b)} = h\sqrt{1 + (\cot\theta)^2}\left[C_x + C_y + \frac{3\pi\mathrm{h}\cot\theta}{8} + \gamma * \left(C_y + \frac{\pi\mathrm{h}\cot\theta}{8}\right)\right]$$

Where: γ = ratio of angle opening = $\frac{45° - \delta}{45°}$, where $0° < \delta \leq 45°$

$$A_{E(i)(b)} = h\sqrt{1 + (\cot\theta)^2}\left[\frac{C_x}{2} + C_y + \frac{\pi\mathrm{h}\cot\theta}{4} + \gamma * \left(\frac{C_x}{2} + \frac{\pi\mathrm{h}\cot\theta}{8}\right)\right]$$

Where: γ = ratio of angle opening = $\frac{90° - \delta}{45°}$, where $45° < \delta \leq 90°$

$$A_{E(i)(b)} = h\sqrt{1 + (\cot\theta)^2}\left[C_y + \frac{\pi\mathrm{h}\cot\theta}{8} + \gamma * \left(\frac{C_x}{2} + \frac{\pi\mathrm{h}\cot\theta}{8}\right)\right]$$

Where: γ = ratio of angle opening = $\frac{135° - \delta}{45°}$, where $90° < \delta \leq 125°$ (anything more than 125°, use 125°)

C.6.2.2 For category (ii)

C.6.2.2.1 For category (a)

C.6.2.2.1.1 Total Shear Area in Plan

$$A_{total} = \frac{1.95\pi a_x a_y}{4} + 1.08a_x C_y + a_y C_x + \gamma * \left(0.92a_x C_y + \frac{0.05\pi a_x a_y}{4}\right)$$

Where: γ = ratio of angle opening = $\frac{45° - \delta}{45°}$, where $0° < \delta \leq 45°$

$$A_{total} = \frac{1.05\pi a_x a_y}{4} + a_x C_y + 0.92a_y C_x + \gamma * \left(0.08a_x C_y + 0.08a_y C_x + \frac{0.9\pi a_x a_y}{4}\right)$$

Where: γ = ratio of angle opening = $\frac{90° - \delta}{45°}$, where $45° < \delta \leq 90°$

$$A_{total} = \frac{0.95\pi a_x a_y}{4} + 0.92a_x C_y + 0.08a_y C_x + \gamma * \left(0.08a_x C_y + 0.84a_y C_x + \frac{0.1\pi a_x a_y}{4}\right)$$

Where: γ = ratio of angle opening = $\frac{135° - \delta}{45°}$, where $90° < \delta \leq 125°$ (anything more than 125°, use 125°)

C.6.2.2.1.2 Total Shear Area Loss in Plan

For 50 mm,

$$A_{loss} = A_1 + 1.41A_2 + 2A_3 + 2A_4 + 2A_5$$

For 100 mm,

$$A_{loss} = A_1 + A_2 + A_3 + A_4 + 1.21A_5$$

For 150 mm,

$$A_{loss} = A_1 + A_2 + A_3 + A_4 + 0.9A_5$$

C.6.2.2.1.3 Shear Surface Area, $A_{E(ii)(a)}$

For 50 mm,

$$A_{E(ii)(a)} = \frac{\left[\left(\frac{1.05\pi a_x a_y}{4} + \gamma * \left(\frac{0.9\pi a_x a_y}{8}\right)\right) - (1.41A_2 + 2A_3 + 2A_4)\right]}{\cos\theta_{avg}} + \frac{\left[\left(a_x C_y + \gamma * \left(0.08 a_x C_y\right)\right) - (A_1)\right]}{\cos\theta_{zx}} + \frac{\left[\left(0.92 a_y C_x + \gamma * \left(0.08 a_y C_x\right)\right) - (2A_5)\right]}{\cos\theta_{zy}}$$

For 100 mm,

$$A_{E(ii)(a)} = \frac{\left[\left(\frac{0.95\pi a_x a_y}{4} + \gamma * \left(\frac{0.1\pi a_x a_y}{4}\right)\right) - (A_2 + A_3 + A_4)\right]}{\cos\theta_{avg}} + \frac{\left[\left(0.92 a_x C_y + \gamma * \left(0.08 a_x C_y\right)\right) - (A_1)\right]}{\cos\theta_{zx}} + \frac{\left[\left(0.08 a_y C_x + \gamma * \left(0.84 a_y C_x\right)\right) - (1.21A_5)\right]}{\cos\theta_{zy}}$$

For 150 mm,

$$A_{E(ii)(a)} = \frac{\left[\left(\frac{0.95\pi a_x a_y}{4} + \gamma * \left(\frac{0.1\pi a_x a_y}{4}\right)\right) - (A_2 + A_3 + A_4)\right]}{\cos\theta_{avg}} + \frac{\left[\left(0.92 a_x C_y + \gamma * \left(0.08 a_x C_y\right)\right) - (A_1)\right]}{\cos\theta_{zx}} + \frac{\left[\left(0.08 a_y C_x + \gamma * \left(0.84 a_y C_x\right)\right) - (0.9A_5)\right]}{\cos\theta_{zy}}$$

C.6.2.2.2 For category (b)

C.6.2.2.2.1 Shear Surface Area, $A_{E(ii)(b)}$

$$A_{E(ii)(b)} = h\sqrt{1 + (\cot\theta)^2}\left[C_x + 1.08C_y + \frac{1.95\pi h \cot\theta}{4} + \gamma * \left(0.92C_y + \frac{0.05\pi h \cot\theta}{4}\right)\right]$$

Where: γ = ratio of angle opening = $\frac{45° - \delta}{45°}$, where $0° < \delta \leq 45°$

$$A_{E(ii)(b)} = h\sqrt{1 + (\cot\theta)^2}\left[0.92C_x + C_y + \frac{1.05\pi\mathrm{h}\cot\theta}{4} + \gamma * \left(0.08C_x + 0.08C_y + \frac{0.9\pi\mathrm{h}\cot\theta}{4}\right)\right]$$

Where: γ = ratio of angle opening = $\frac{90°-\delta}{45°}$, where $45° < \delta \leq 90°$

$$A_{E(ii)(b)} = h\sqrt{1 + (\cot\theta)^2}\left[0.08C_x + 0.92C_y + \frac{0.95\pi\mathrm{h}\cot\theta}{4} + \gamma * \left(0.84C_x + 0.08C_y + \frac{0.1\pi\mathrm{h}\cot\theta}{4}\right)\right]$$

Where: γ = ratio of angle opening = $\frac{135°-\delta}{45°}$, where $90° < \delta \leq 125°$ (anything more than $125°$, use $125°$)

C.6.2.3 For category (iii)

C.6.2.3.1 For category (a)

C.6.2.3.1.1 Total Shear Area in Plan

$$A_{total} = \frac{\pi a_x a_y}{2} + \frac{3a_x C_y}{2} + a_y C_x + \gamma * \left(\frac{a_x C_y}{2}\right)$$

Where: γ = ratio of angle opening = $\frac{45°-\delta}{45°}$, where $0° < \delta \leq 45°$

$$A_{total} = \frac{3\pi a_x a_y}{8} + a_x C_y + a_y C_x + \gamma * \left(\frac{a_x C_y}{2} + \frac{\pi a_x a_y}{8}\right)$$

Where: γ = ratio of angle opening = $\frac{90°-\delta}{45°}$, where $45° < \delta \leq 90°$

$$A_{total} = \frac{\pi a_x a_y}{4} + \frac{a_x C_y}{2} + \frac{a_y C_x}{2} + \gamma * \left(\frac{a_x C_y}{2} + \frac{a_y C_x}{2} + \frac{\pi a_x a_y}{8}\right)$$

Where: γ = ratio of angle opening = $\frac{135°-\delta}{45°}$, where $90° < \delta \leq 125°$ (anything more than 125°, use 125°)

C.6.2.3.1.2 Total Shear Area Loss in Plan

For 50 mm,

$$A_{loss} = 1.28A_1 + 2A_2 + 2A_3 + 2A_4 + 2A_5$$

For 100 mm,

$$A_{loss} = A_1 + 1.49A_2 + 2A_3 + 2A_4 + 2A_5$$

For 150 mm,

$$A_{loss} = A_1 + A_2 + A_3 + A_4 + 2A_5$$

C.6.2.3.1.3 Shear Surface Area, $A_{E(iii)(a)}$

For 50 mm,

$$A_{E(iii)(a)} = \frac{\left[\left(\frac{3\pi a_x a_y}{8} + \gamma * \left(\frac{\pi a_x a_y}{8}\right)\right) - (2A_2 + 2A_3 + 2A_4)\right]}{\cos\theta_{avg}} + \frac{\left[\left(a_x C_y + \gamma * (0.5a_x C_y)\right) - (1.28A_1)\right]}{\cos\theta_{zx}} + \frac{\left[(a_y C_x) - (2A_5)\right]}{\cos\theta_{zy}}$$

For 100 mm,

$$A_{E(iii)(a)} = \frac{\left[\left(\frac{3\pi a_x a_y}{8} + \gamma * \left(\frac{\pi a_x a_y}{8}\right)\right) - (1.49A_2 + 2A_3 + 2A_4)\right]}{\cos\theta_{avg}} + \frac{\left[\left(a_x C_y + \gamma * (0.5a_x C_y)\right) - (A_1)\right]}{\cos\theta_{zx}} + \frac{\left[(a_y C_x) - (2A_5)\right]}{\cos\theta_{zy}}$$

For 150 mm,

$$A_{E(iii)(a)} = \frac{\left[\left(\frac{\pi a_x a_y}{4} + \gamma * \left(\frac{\pi a_x a_y}{8}\right)\right) - (A_2 + A_3 + A_4)\right]}{\cos\theta_{avg}} + \frac{\left[\left(0.5a_x C_y + \gamma * (0.5a_x C_y)\right) - (A_1)\right]}{\cos\theta_{zx}} + \frac{\left[\left(0.5a_y C_x + \gamma * (0.5a_y C_x)\right) - (2A_5)\right]}{\cos\theta_{zy}}$$

C.6.2.3.2 For category (b)

C.6.2.3.2.1 Shear Surface Area, $A_{E(iii)(b)}$

$$A_{E(iii)(b)} = h\sqrt{1 + (\cot\theta)^2}\left[C_x + \frac{3C_y}{2} + \frac{\pi h \cot\theta}{2} + \gamma * \left(\frac{C_y}{2}\right)\right]$$

Where: γ = ratio of angle opening = $\frac{45° - \delta}{45°}$, where $0° < \delta \leq 45°$

$$A_{E(iii)(b)} = h\sqrt{1 + (\cot\theta)^2}\left[C_x + C_y + \frac{3\pi h \cot\theta}{8} + \gamma * \left(\frac{C_y}{2} + \frac{\pi h \cot\theta}{8}\right)\right]$$

Where: γ = ratio of angle opening = $\frac{90° - \delta}{45°}$, where $45° < \delta \leq 90°$

$$A_{E(iii)(b)} = h\sqrt{1 + (\cot\theta)^2}\left[\frac{C_x}{2} + \frac{C_y}{2} + \frac{\pi h \cot\theta}{4} + \gamma * \left(\frac{C_x}{2} + \frac{C_y}{2} + \frac{\pi h \cot\theta}{8}\right)\right]$$

Where: γ = ratio of angle opening = $\frac{135° - \delta}{45°}$, where $90° < \delta \leq 125°$ (anything more than 125°, use 125°)

C.6.2.4 For category (iv)

C.6.2.4.1 For category (a)

C.6.2.4.1.1 Total Shear Area in Plan

$$A_{total} = \frac{\pi a_x a_y}{2} + 1.92 a_x C_y + a_y C_x + \gamma * (0.08 a_x C_y)$$

Where: γ = ratio of angle opening = $\frac{45°-\delta}{45°}$, where $0° < \delta \leq 45°$

$$A_{total} = \frac{1.95\pi a_x a_y}{4} + a_x C_y + a_y C_x + \gamma * \left(0.92 a_x C_y + \frac{0.05\pi a_x a_y}{4}\right)$$

Where: γ = ratio of angle opening = $\frac{90°-\delta}{45°}$, where $45° < \delta \leq 90°$

$$A_{total} = \frac{\pi a_x a_y}{4} + 0.08 a_x C_y + 0.92 a_y C_x + \gamma * \left(0.92 a_x C_y + 0.08 a_y C_x + \frac{0.95\pi a_x a_y}{4}\right)$$

Where: γ = ratio of angle opening = $\frac{135°-\delta}{45°}$, where $90° < \delta \leq 125°$ (anything more than 125°, use 125°)

C.6.2.4.1.2 Total Shear Area Loss in Plan

For 50 mm,

$$A_{loss} = 1.86A_1 + 2A_2 + 2A_3 + 2A_4 + 2A_5$$

For 100 mm,

$$A_{loss} = A_1 + 2A_2 + 2A_3 + 2A_4 + 2A_5$$

For 150 mm,

$$A_{loss} = A_1 + A_2 + 2A_3 + 2A_4 + 2A_5$$

C.6.2.4.1.3 Shear Surface Area, $A_{E(iv)(a)}$

For 50 mm,

$$A_{E(iv)(a)} = \frac{\left[\left(\frac{1.95\pi a_x a_y}{4} + \gamma * \left(\frac{0.05\pi a_x a_y}{4}\right)\right) - (2A_2 + 2A_3 + 2A_4)\right]}{\cos\theta_{avg}} + \frac{\left[\left(a_x C_y + \gamma * (0.92 a_x C_y)\right) - (1.86A_1)\right]}{\cos\theta_{zx}} + \frac{\left[(a_y C_x) - (2A_5)\right]}{\cos\theta_{zy}}$$

For 100 mm,

$$A_{E(iv)(a)} = \frac{\left[\left(\frac{\pi a_x a_y}{4} + \gamma * \left(\frac{0.95\pi a_x a_y}{4}\right)\right) - (2A_2 + 2A_3 + 2A_4)\right]}{\cos\theta_{avg}} + \frac{\left[\left(0.08a_x C_y + \gamma * \left(0.92a_x C_y\right)\right) - (A_1)\right]}{\cos\theta_{zx}} + \frac{\left[\left(0.92a_y C_x + \gamma * \left(0.08a_y C_x\right)\right) - (2A_5)\right]}{\cos\theta_{zy}}$$

For 150 mm,

$$A_{E(iv)(a)} = \frac{\left[\left(\frac{\pi a_x a_y}{4} + \gamma * \left(\frac{0.95\pi a_x a_y}{4}\right)\right) - (A_2 + 2A_3 + 2A_4)\right]}{\cos\theta_{avg}} + \frac{\left[\left(0.08a_x C_y + \gamma * \left(0.92a_x C_y\right)\right) - (A_1)\right]}{\cos\theta_{zx}} + \frac{\left[\left(0.92a_y C_x + \gamma * \left(0.08a_y C_x\right)\right) - (2A_5)\right]}{\cos\theta_{zy}}$$

C.6.2.4.2 For category (b)

C.6.2.4.2.1 Shear Surface Area, $A_{E(iv)(b)}$

$$A_{E(iv)(b)} = h\sqrt{1 + (\cot\theta)^2}\left[C_x + 1.92C_y + \frac{\pi h \cot\theta}{2} + \gamma * \left(0.08C_y\right)\right]$$

Where: γ = ratio of angle opening = $\frac{45° - \delta}{45°}$, where $0° < \delta \leq 45°$

$$A_{E(iv)(b)} = h\sqrt{1 + (\cot\theta)^2}\left[C_x + C_y + \frac{1.95\pi h \cot\theta}{4} + \gamma * \left(0.92C_y + \frac{0.05\pi h \cot\theta}{4}\right)\right]$$

Where: γ = ratio of angle opening = $\frac{90° - \delta}{45°}$, where $45° < \delta \leq 90°$

$$A_{E(iv)(b)} = h\sqrt{1 + (\cot\theta)^2}\left[0.92C_x + 0.08C_y + \frac{\pi h \cot\theta}{4} + \gamma * \left(0.08C_x + 0.92C_y + \frac{0.95\pi h \cot\theta}{4}\right)\right]$$

Where: γ = ratio of angle opening = $\frac{135° - \delta}{45°}$, where $90° < \delta \leq 125°$ (anything more than 125°, use 125°)

C.6.2.5 For category (v)

C.6.2.5.1 For category (a)

C.6.2.5.1.1 Total Shear Area in Plan

$$A_{total} = \frac{\pi a_x a_y}{2} + 2a_x C_y + a_y C_x + \gamma * (0)$$

Where: γ = ratio of angle opening = $\frac{45° - \delta}{45°}$, where $0° < \delta \leq 45°$

$$A_{total} = \frac{\pi a_x a_y}{2} + a_x C_y + a_y C_x + \gamma * \left(a_x C_y\right)$$

Where: γ = ratio of angle opening = $\frac{90° - \delta}{45°}$, where $45° < \delta \leq 90°$

$$A_{total} = \frac{\pi a_x a_y}{4} + a_y C_x + \gamma * \left(a_x C_y + \frac{\pi a_x a_y}{4}\right)$$

Where: γ = ratio of angle opening = $\frac{135° - \delta}{45°}$, where $90° < \delta \leq 125°$ (anything more than 125°, use 125°)

C.6.2.5.1.2 Total Shear Area Loss in Plan

For 50 mm and 100 mm,

$$A_{loss} = 2A_1 + 2A_2 + 2A_3 + 2A_4 + 2A_5$$

For 150 mm,

$$A_{loss} = 2A_2 + 2A_3 + 2A_4 + 2A_5$$

C.6.2.5.1.3 Shear Surface Area, $A_{E(v)(a)}$

For 50 mm,

$$A_{E(v)(a)} = \frac{\left[\left(\frac{\pi a_x a_y}{2}\right) - (2A_2 + 2A_3 + 2A_4)\right]}{\cos\theta_{avg}} + \frac{\left[\left(a_x C_y + \gamma * \left(a_x C_y\right)\right) - (2A_1)\right]}{\cos\theta_{zx}} + \frac{\left[\left(a_y C_x\right) - (2A_5)\right]}{\cos\theta_{zy}}$$

For 100 mm,

$$A_{E(v)(a)} = \frac{\left[\left(\frac{\pi a_x a_y}{4} + \gamma * \left(\frac{\pi a_x a_y}{4}\right)\right) - (2A_2 + 2A_3 + 2A_4)\right]}{\cos\theta_{avg}} + \frac{\left[\left(\gamma * \left(a_x C_y\right)\right) - (2A_1)\right]}{\cos\theta_{zx}} + \frac{\left[\left(a_y C_x\right) - (2A_5)\right]}{\cos\theta_{zy}}$$

For 150 mm,

$$A_{E(v)(a)} = \frac{\left[\left(\frac{\pi a_x a_y}{4} + \gamma * \left(\frac{\pi a_x a_y}{4}\right)\right) - (2A_2 + 2A_3 + 2A_4)\right]}{\cos\theta_{avg}} + \frac{\left[\left(\gamma * \left(a_x C_y\right)\right)\right]}{\cos\theta_{zx}} + \frac{\left[\left(a_y C_x\right) - (2A_5)\right]}{\cos\theta_{zy}}$$

C.6.2.5.2 For category (b)

C.6.2.5.2.1 Shear Surface Area, $A_{E(v)(b)}$

$$A_{E(v)(b)} = h\sqrt{1 + (\cot\theta)^2}\left[C_x + 2C_y + \frac{\pi \mathrm{h} \cot\theta}{2} + \gamma * (0)\right]$$

Where: γ = ratio of angle opening = $\frac{45° - \delta}{45°}$, where $0° < \delta \leq 45°$

$$A_{E(v)(b)} = h\sqrt{1 + (\cot\theta)^2}\left[C_x + C_y + \frac{\pi \mathrm{h} \cot\theta}{2} + \gamma * \left(C_y\right)\right]$$

Where: γ = ratio of angle opening = $\frac{90° - \delta}{45°}$, where $45° < \delta \leq 90°$

$$A_{E(v)(b)} = h\sqrt{1 + (\cot\theta)^2}\left[C_x + \frac{\pi \mathrm{h} \cot\theta}{4} + \gamma * \left(C_y + \frac{\pi \mathrm{h} \cot\theta}{4}\right)\right]$$

Where: γ = ratio of angle opening = $\frac{135° - \delta}{45°}$, where $90° < \delta \leq 125°$ (anything more than 125°, use 125°)

C.7.1 Punching Capacity

$V_E = \propto w_i A_E$

Where:

$\propto$ = shear retention factor, 0.7 for micro-concrete; and 1.0 for normal-concrete

w_i = sum of internal plastic work dissipated (see Eq. 2.19)